

# Atmospheric pressure plasmas for polymer surface modification: Alternating current gliding arcs and ultrasound enhanced plasmas

**Kusano, Yukihiro**

*Publication date:*
2019

*Document Version*
Publisher's PDF, also known as Version of record

# Atmospheric Pressure Plasmas for Polymer Surface Modification - Alternating Current Gliding Arcs and Ultrasound Enhanced Plasmas

Yukihiro Kusano

Department of Wind Energy
Technical University of Denmark

Doctor of Technices thesis

2019

Title: Atmospheric Pressure Plasmas for Polymer Surface Modification - Alternating Current Gliding Arcs and Ultrasound Enhanced Plasmas

Author: Yukihiro KUSANO

Year: 2019

Published by: Department of Wind Energy
Technical University of Denmark
P.O. Box 49, DK-4000 Roskilde, Denmark
www.vindenergi.dtu.dk

ISBN: 978-87-93549-49-4

DTU Wind Energy E-0181

Denne afhandling er af Danmarks Tekniske Universitet antaget til forsvar for den tekniske doktorgrad. Antagelsen er sket efter bedømmelse af den foreliggende afhandling.

Kgs. Lyngby, den 4. februar 2019

Anders O. Bjarklev
Rektor

/Rasmus Larsen
Prorektor

This thesis has been accepted by the Technical University of Denmark for public defence in fulfilment of the requirements for the degree of Doctor Technices. The acceptance is based on an evaluation of the present dissertation.

Kgs. Lyngby, 4 February 2019

Anders O. Bjarklev
President

/Rasmus Larsen
Provost

## Preface

A plasma is an ionized gas. Ions, electrons, radicals and ultra violet photons are generated in a plasma and can be used for a variety of material- and surface-processing. It has been industrially applied in areas including semiconductors, automobiles, aerospace, buildings, glasses, polymers, and textiles. In wind energy industry, there are a plenty of potentials for applying plasmas in manufacture and maintenance of wind turbines, particularly in adhesion improvement.
Among applications of plasmas, modification of material surfaces is promising because of environmental friendliness and high treatment efficiency. They are often employed at low gas pressures, but also possible at atmospheric pressure. One of the challenges for atmospheric pressure plasmas is to achieve high chemical selectivity and efficient productivity simultaneously. High chemical selectivity can be expected with a non-equilibrium state in a plasma so as to influence chemical bonding of the molecules in the plasma and/or at the material surfaces to be treated, since energy of electrons is comparable to that of chemical bonding while gas molecules can retain their chemical properties in a non-equilibrium plasma. Efficient productivity of plasma reactors can be demonstrated with high energy densities. However, plasmas generally cannot provide non-equilibrium states and high energy densities simultaneously.
In the present thesis, after reviewing atmospheric pressure plasmas and polymer adhesion, two approaches to overcome this issue are studied: development of a hybrid plasma at a non-equilibrium state with a high energy density, and plasma processing assisted by external energy input. More specifically, two plasma techniques presented are; a gliding arc as a hybrid plasma and ultrasound enhanced plasma processing as a plasma assisted by external energy input.
The thesis comprises a 9-chapter overview and appendices of two patents and sixteen journal papers, including one Editorial. The overview is intended to provide a description of the work with the focus on the plasma techniques and present their usefulness in solving engineering problems. Details concerning the methods, their limitations, the results obtained and comprehensive references are given in the individual papers and patents.
Chapter 1 introduces adhesion and atmospheric pressure plasmas, and formulates the objectives of the thesis. Chapter 2 presents gliding arcs, demonstrating adhesion improvement. Chapter 3 presents characterization of the gliding arc. Chapter 4 studies the stability of the gliding arc. Chapter 5 presents ultrasound enhanced plasmas. Chapter 6 studies combination of the gliding arc and the ultrasound process. Chapter 7 suggests future developments of the works. Chapter 8 summarizes the major results. Chapter 9 concludes this thesis. Appendices contain eighteen publications that form the basis of this thesis. These publications are (in the order of appearance in the thesis):

[A1] **Y. Kusano** "Atmospheric pressure plasma processing for polymer adhesion – a review" *J. Adhesion* 90(9) (2014) 755-777.
[A2] **Y. Kusano** "Plasma surface modification at atmospheric pressure" *Surf. Eng.* 25(6) (2009) 415-416 (Editorial).
[A3] **Y. Kusano** "An apparatus for treating a surface with at least one gliding arc source" European patent No. 2,514,280 B1 (2014). There is a variation that has been granted in the US (U.S. patent No. 9,420,680 B2 (2016)).

[A4] **Y. Kusano**, B.F. Sørensen, T.L. Andersen, F. Leipold "Adhesion improvement of glass-fibre-reinforced polyester composites by gliding arc discharge treatment" *J. Adhesion* 89(6) (2013) 433-459.

[A5] **Y. Kusano**, B.F. Sørensen, T.L. Andersen, H.L. Toftegaard, F. Leipold, M. Salewski, Z.W. Sun, J.J. Zhu, Z.S. Li, M. Aldén "Water-cooled non-thermal gliding arc for adhesion improvement of glass-fibre-reinforced polyester" *J. Phys. D: Appl. Phys*. 46(13) (2013) 135203.

[A6] **Y. Kusano**, L. Berglund, Y. Aitomäki, K. Oksman, B. Madsen "Gliding arc surface modification of carrot nanofibre coating – perspective for composite processing" *Mater. Sci. Eng.* 139(1) (2016) 012027.

[A7] **Y. Kusano**, A. Bardenshtein, P. Morgen "Fluoropolymer coated alanine films treated by atmospheric pressure plasmas – in comparison with gamma irradiation" *Plasma Proc. Polym*. 15(3) (2018) 1700131.

[A8] Z.W. Sun, J.J. Zhu, Z.S. Li, M. Aldén, F. Leipold, M. Salewski, **Y. Kusano** "Optical diagnostics of a gliding arc" *Optics Express* 21(5) (2013) 6028-6044.

[A9] J.J. Zhu, Z.W. Sun, Z.S. Li, A. Ehn, M, Aldén, M. Salewski, F. Leipold, **Y. Kusano** "Dynamics, OH distributions and UV emission of a gliding arc at various flow-rates investigated by optical measurements" *J. Phys. D: Appl. Phys*. 47 (2014) 295203.

[A10] **Y. Kusano**, M. Salewski, F. Leipold, J.J. Zhu, A. Ehn, Z.S. Li, M. Aldén "Stability of alternating current gliding arcs" *Eur. Phys. J. D* 68 (2014) 319.

[A11] N. Krebs, A. Bardenshtein, **Y. Kusano**, H. Bindslev, H.J. Mortensen "Enhancing plasma surface modification using high intensity and high power ultrasonic acoustic wave" US patent No. 8,399,795 B2 (2013). There is a variation that has been granted in China (Chinese patent No. 101,743,785 B (2012)).

[A12] **Y. Kusano**, S.V. Singh, A. Bardenshtein, N. Krebs, N. Rozlosnik "Plasma surface modification of glass fibre reinforced polyester enhanced by ultrasonic irradiation" *J. Adhesion Sci. Technol*. 24 (2010) 1831-1839.

[A13] **Y. Kusano**, K. Norrman, S.V. Singh, F. Leipold, P. Morgen, A. Bardenshtein, N. Krebs "Ultrasound enhanced 50 Hz plasma treatment of glass-fiber-reinforced polyester at atmospheric pressure" *J. Adhesion Sci. Technol.* 27(7) (2013) 825-833.

[A14] **Y. Kusano**, T.L. Andersen, H.L. Toftegaard, F. Leipold, A. Bardenshtein, N. Krebs "Plasma treatment of carbon fibres and glass-fibre-reinforced polyesters at atmospheric pressure for adhesion improvement" *Int. J. Mater. Eng. Innovation* 5(2) (2014) 122-137.

[A15] **Y. Kusano**, S.V. Singh, K. Norrman, F. Leipold, J. Drews, P. Morgen, A. Bardenshtein, N. Krebs "Ultrasound enhanced plasma treatment of glass-fibre-reinforced polyester in atmospheric pressure air for adhesion improvement" *J. Adhesion* 87 (2011) 720-731.

[A16] **Y. Kusano**, B. Madsen, L. Berglund, Y. Aitomäki, K. Oksman "Dielectric barrier discharge plasma treatment of cellulose nanofibre surfaces" *Surf. Eng.* 34(11) (2018) 825-831.

[A17] **Y. Kusano**, K. Norrman, J. Drews, F. Leipold, S.V. Singh, P. Morgen, A. Bardenshtein, N. Krebs "Gliding arc surface treatment of glass fiber reinforced polyester enhanced by ultrasonic irradiation" *Surf. Coat. Technol*. 205 (2011) S490-S494.

[A18] **Y. Kusano**, J.J. Zhu, A. Ehn, Z.S. Li, M. Aldén, M. Salewski, F. Leipold, A. Bardenshtein, N. Krebs "Observation of gliding arc surface treatment" *Surf. Eng*. 31(4) (2015) 282-288.

**Acknowledgements**

First of all I would like to thank sincerely Bent F. Sørensen for his support, guidance, proofreading, valuable discussion and suggestions.

I would like to thank Hans Lilholt for his proofreading and valuable discussion and advices.

I would like to thank Peter Hauge Madsen and Bo Madsen for their supports to complete the thesis.

I would like to thank Stergios Goutianos for advices on fracture and mechanics of materials. I would like to thank Helga Nørgaard Petersen for the preparation of the Danish abstract. I would like to thank Jens Nørkær Sørensen and Mathias Stolpe for practical advices and encouragement to complete the thesis.

I would like to thank Anna-Maria Lund and Trine Danhøj for various practical advices, supports and encouragement to complete the thesis.

I would like to thank all the co-authors, Frank Leipold, Mirko Salewski, Bent F. Sørensen, Bo Madsen, Helmuth L. Toftegaard, Tom L. Andersen, Joanna Drews, Kion Norrman, Shailendra V. Singh, Alexander Bardenshtein, Niels Krebs, Noemi Rozlosnik, Per Morgen, Zhongshan Li, Jiajian Zhu, Zhiwei Sun, Andreas Ehn, Makus Aldén, Kristiina Oksman, Linn Berglund, and Yvonne Aitomäki
and all the co-inventors, Alexander Bardenshtein, Niels Krebs, Henrik Bindslev and Henrik J. Mortensen for scientific and technical supports and fruitful discussion.

In particular, I would like to thank Alexander Bardenshtein Danish Technological Institute and Niels Krebs FORCE Technology for development of the ultrasound enhanced plasma processing, and Zhongshan Li, Jiajian Zhu, Andreas Ehn, Zhiwei Sun, and Marcus Aldén in Lund University for advanced plasma diagnostics.

I would like to thank Jonas Kreutzfeldt Heininge and Vagn Jensen for design and construction of the plasma devices, and Christian H. Madsen, Jacob Christensen, and Anette Pedersen for specimen preparations.

Financial supports were provided by Danish Research Council (Statens Teknisk-Videnskabelige Forskningsråd (STVF), Forskningsrådet for Teknologi og Produktion (FTP)), the Ministry of Science, Technology and Innovation through the National Danish Proof of Concept (PoC) funding Scheme, the Swedish Energy Agency, Center for Combustion Science and Technology (CECOST), and the European Commission through the Framework VII programme.

I would like to thank DTU for provision of research facilities at Risø and Lyngby.

Finally, I would like to thank my wife, Masako Kusano and our son, Reinosuke Kusano for always encouraging me to complete the thesis.

**Abstract**

A plasma is one of the four states of matter. It is useful for industrial and material processing due to high treatment effects and environmental compatibility. Surface modification for adhesion improvement is among the most promising applications for plasmas. Practically it is realized by introducing electrical energy to a gas to generate a plasma as a reactive gas, in which a material surface is exposed. During plasma surface treatment, addition of polar functional groups, roughening, and removal of weak domains can take place simultaneously. All of them are important to improve adhesion by better interaction with adhesives or uncured polymers in composite manufacturing. For many practical applications, atmospheric pressure plasma processing is much preferable, as it can avoid to use expensive vacuum systems.
In the present thesis, newly developed atmospheric pressure plasmas for surface-processing are summarized. Specifically, a gliding arc and ultrasound enhanced plasma processing were developed. The gliding arc presented is characterized by stable extension of the discharge into air up to several centimetres operated by a high frequency alternating current (AC). In the optimized conditions, highly oxidative radicals are efficiently produced and used for surface processing. In addition, the discharge may not necessarily extinguish at every half period, but can survive over a plurality of AC periods, suppressing unwanted energy consumption for arc ignition. Ultrasound enhanced plasma processing demonstrated enhanced treatment effects, arc suppression, and improved treatment-uniformity, compared to plasma processing without ultrasonic irradiation.

**Dansk Resumé**

Plasma er en af de fire tilstande et stof kan befinde sig i. Det kan være nyttigt indenfor både industrien og indenfor materialeforarbejdning, da effekten af overfladebehandlingen er stor og metoden er miljøvenlig. Overflademodifikation for at øge vedhæftning er en af de mest lovende anvendelser af plasma. Rent praktisk gennemføres plasma behandlingen ved at introducere elektrisk energi til en gas for at skabe plasma i form af en reaktiv gas, som materiale overflade så kan udsættes for. Overfladebehandling med plasma kan bl.a. forårsage: tilføjelsen af polære funktionelle grupper, øgning af ruhed, og fjernelse af svage områder. Alle disse virkninger er vigtige for at kunne forbedre vedhæftningen i kompositmaterialer, da de giver anledning til en bedre interaktion med klæbemidler og uhærdet polymere under fremstillingen. For mange anvendelser vil plasma ved atmosfærisk tryk være at foretrække, da man så kan undgå de meget dyre vakuum systemer. I denne afhandling vil den nyligt udviklede metode for netop plasma behandling af overflader ved atmosfærisk tryk blive sammenfattet. Helt specifikt er det en glidende bue og ultralyds forstærket plasma behandling som er blevet udviklet. Den omtalte glidende bue er karakteriseret ved en stabil forlængelse af afladningen til luften på op til flere centimeter styret af højfrekvent vekselstrøm (AC). Under optimerede forhold bliver stærkt oxiderende radikaler produceret med stor effektivitet og kan derfor anvendes til overfladebehandling. Derudover standser afladningen ikke nødvendigvis ved hver halv-periode, men kan derimod overleve adskillige AC-perioder. Herved minimeres det unødige energiforbrug ved gentagende antændinger af plasma. Sammenlignet med plasmabehandling uden ultralydsbestråling udviser den nye ultralydsforstærkede plasmabehandling øget effekt af behandlingen, undertrykkelse af høj temperaturs plasma og forbedret homogenitet af behandlingen.

**Terminology, abbreviations and symbols**

***Definitions of key concepts***

**Cohesive law**: A traction-separation relationship that describes the tractions transferred across crack faces of the fracture process zone.

**Ablation**: Loss of a part of a material by melting or evaporation.

**Ambient air**: Atmospheric air in its natural state.

**Alanine/electron-paramagnetic resonance (EPR) dosimetry**: A standard method or process for measuring dosages of ionizing radiation.

**Arc**: An arc discharge is a thermal plasma of an electrical discharge at an equilibrium state.

**Bond cleavage**: Cutting of an atomic bond.

**Chemical etching**: Materials removal by means of chemical reactions.

**Cold plasma**: See "Non-equilibrium plasma/non-thermal plasma".

**Contaminant**: A substance that makes a material less pure.

**Corona discharge**: A gas discharge generated when the electric field is significantly non-uniform for example due to asymmetrical geometry of electrodes.

**Deconvolution**: A process of resolving a recorded data into its constituent elements.

**Dielectric barrier discharge (DBD)**: An electrical discharge between electrodes separated by an insulator. It is also called a silent discharge.

**Discharge**: A discharge in this thesis is an electrical gas discharge generated by electrical gas breakdown.

**Electrode fall voltage**: A voltage drop near an electrode.

**Electron avalanche**: A process in which free electrons in a gas are accelerated by an electric field and collide with an atom or a molecule in the gas to ionize them, releasing additional electrons to cause chain reactions. This regime is called a Townsend regime.

**Electron temperature**: Electron temperature $T_e$ is defined by an average kinetic energy of electrons. In an equilibrium state, electron temperature is almost equal to other temperatures. In the non-equilibrium state, it is much higher than a gas temperature, and reaching 1 eV or higher. Also see "Temperature".

**Etching**: See "chemical etching" and "physical etching".

**Equilibrium**: A state of balance among different aspects such as reactions or temperatures.

**Filamentary discharge**: A filament-like micro-discharge with a diameter smaller than a few millimetres, as an opposing concept of a homogeneous glow discharge.

**Gliding arc**: A plasma generated between diverging electrodes and extended and quenched by a gas flow.

**Hybrid plasma**: A plasma in a hybrid condition with high chemical selectivity and efficient productivity simultaneously.

**Impedance matching**: Adjusting an output impedance of a signal source (power supply) to maximize the power transfer or minimize signal reflection from a load (plasma).

**Inelastic collision**: A collision after which a part of kinetic energy is changed to other form of energy.

**Micro-discharge**: See “Filamentary discharge”.

**Mode mixity**: Proportions of the mode I (opening mode) load to the mode II (sliding mode) load. Here, the loads can be stresses, openings or work of tractions.

**Non-equilibrium plasma/non-thermal plasma**: A plasma not in an thermodynamic equilibrium, in which the electron temperature is much higher than the temperatures of heavy species such as ions and neutrals.

**O/C ratio**: Atomic ratio of oxygen to carbon, used for indicating an oxidation level on a polymer surface.

**Physical etching**: Materials removal induced by physical stimulations.

**Plasma column**: A plasma of a columnar shape.

**Rotational temperature**: See “Temperature”.

**Temperature**: A parameter describing energy levels. In a molecular system, it can be separated into translational, rotational, vibrational and electronic. Since translations and rotations of molecules are readily coupled, translational temperature and rotational temperature are often relatively close. Vibrational temperature describes the excitation level of molecular vibrations, while electron temperature refers to a kinetic energy of free electrons.

**Townsend discharge**: See “Electron avalanche”.

**Thermal plasma**: A plasma in an thermodynamic equilibrium such as an arc discharge.

**Vibrational temperature**: See “Temperature”.

**Weak boundary layer**: At an interface/interphase where interactions between materials are insufficient due to various reasons to cause a fracture. In the present thesis, it is also referred to as a weak domain, since it does not necessarily form a layer.

***Abbreviations***

**AC**: Alternating current

**AFM**: Atomic force microscopy

**ATR-FTIR**: Attenuated total reflection-Fourier transform infrared spectroscopy

**CNF**: Cellulose nanofibre

**DBD**: Dielectric barrier discharge

**DC**: Direct current

**DCB**: Double cantilever beam

**FE-SEM**: Field emission type scanning electron microscopy

**EPR**: Electron-paramagnetic resonance

**FCA**: Fluoropolymer coated alanine

**FTIR**: Fourier transform infrared spectroscopy

**GA**: Gliding arc

**GFRP**: Glass fibre reinforced polyester

**HSP**: Hansen solubility parameters

**MW**: Microwave

**OES**: Optical emission spectroscopy

**PLIF**: Planar laser-induced fluorescence

**RF**: Radio frequency

**SLM**: Standard litre per minute

**SPL**: Sound pressure level

**TOF-SIMS**: Time-of-flight secondary ion mass spectrometry

**XPS**: X-ray photoelectron spectroscopy

**Table of contents**

## 1. Adhesion and atmospheric pressure plasmas [A1,A2]

### 1.1. Adhesion of materials

Adhesion can be defined as process of attachment of a substance to the surface of another substance [1]. The force that causes adhesion can be divided into several relevant mechanisms, including mechanical, chemical, dispersive, diffusion, and electrostatic effects.
The mechanical effect can be caused by interlocking of uneven dissimilar surfaces, when they contact with each other. Specifically, increasing surface roughness can increase mechanical interlocking thereby improving adhesion. The interlocking phenomena can be observed on different length scales, from nanometres to centimetres.
The chemical effect is an atomic scale interaction further divided to covalent bonding, ionic bonding and hydrogen bonding. Chemical reactions of contacting surfaces form the strongest joints by a covalent or ionic bond. Difference of the covalent bond and the ionic bond is based on the way of sharing electrons between atoms of the two jointed materials.
If the electrons are significantly attracted by one of the atoms, the bond formed is called ionic. Ionic bonds require both electropositive and electronegative atoms, corresponding to electron-losing and electron-gaining atoms, respectively. In general, metals are electropositive and non-metals are electronegative. Examples of ionic bonds in polymers include crosslinks of polymer chains by metallic ions.
On the other hand, if electrons are shared between atoms, it is the covalent bond. For example, when a polymer surface with hydroxyl (-OH), carboxyl (-COOH) or amino ($-NH_2$) group contacts with an uncured epoxy resin, there is an opportunity for reactions to form covalent bonds as shown in Figure 1.1.

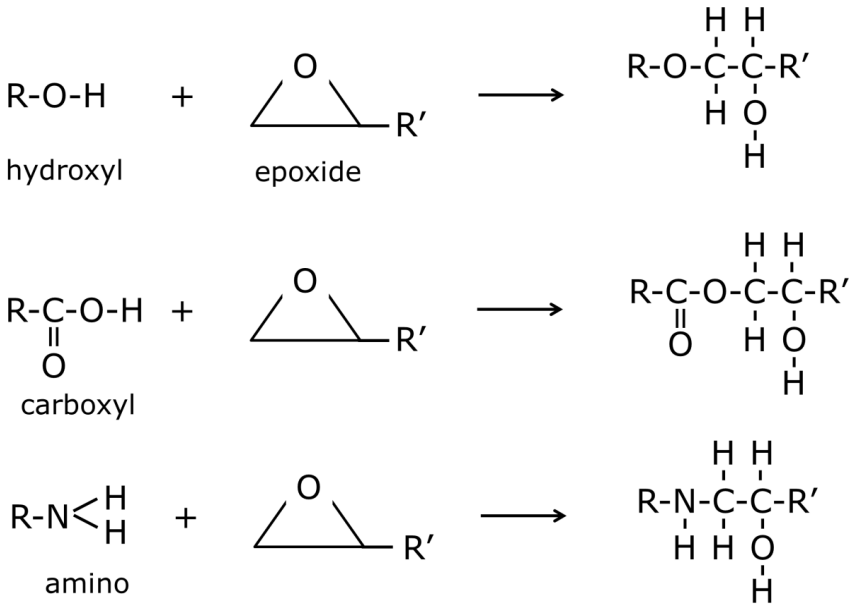


Figure 1.1. Reactions of epoxy group (epoxide) to form covalent bonds. R and R' represent hydrocarbons.

A hydrogen bond is formed when a hydrogen atom in a molecule is attracted by an electronegative atom such as oxygen, nitrogen, or fluorine in another molecule [2]. Examples of the hydrogen bond are illustrated in Figure 1.2. Addition of the electronegative atoms on a surface can be useful to form hydrogen bond.

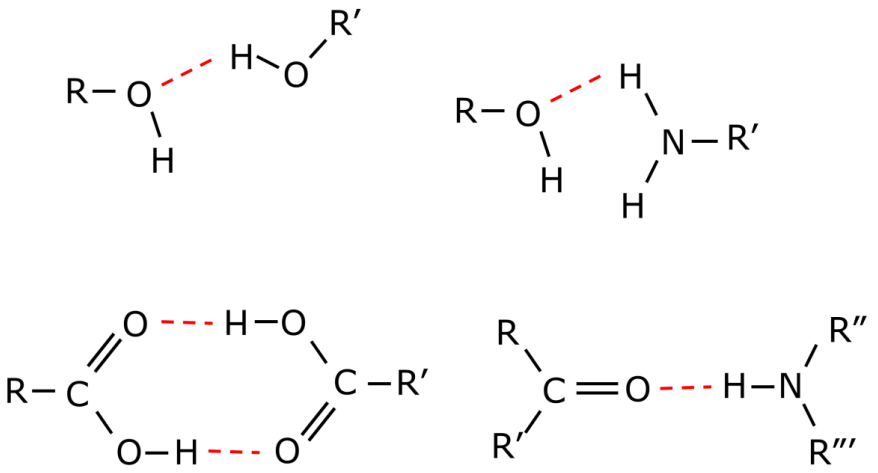

Figure 1.2. Examples of hydrogen bonds, indicated by red broken lines.

The energy of hydrogen bond depends on atoms that constitute the hydrogen bond, geometry of the bond, and environment. It varies between approximately $4 \times 10^3$ and $2 \times 10^5$ J mol$^{-1}$, corresponding to between $4 \times 10^{-2}$ and $2 \times 10^0$ eV per bond [2]. Although it is lower than the typical energy of covalent bonds at several eV, hydrogen bond can play an important role in adhesion. In particular when an adhesive does not contain a significant number of reactive sites that can react with material surfaces, the hydrogen bond can be a primary mechanism for adhesion.

The dispersive effect is based on van der Waals forces. It varies between approximately $4 \times 10^2$ and $4 \times 10^3$ J mol$^{-1}$, corresponding to $4 \times 10^{-3}$ and $2 \times 10^{-2}$ eV per bond. Molecules are polar, and electron density has an uneven distribution permanently or temporarily. This polarity induces a weak attractive force to another polar molecule. Wetting performance of a liquid is related to the dispersive effect. A liquid adhesive applied should wet the surface. If a contact angle of liquid adhesive is lower, adhesion can be improved. Since general liquid adhesives contain substantial electronegative atoms, they have some similarities to water, and thus water is often used as a test liquid for a contact angle measurement.

The diffusive effect is expected when molecules of both materials contacted are mobile and soluble with each other. The electrostatic effect is caused by a charge transfer between dissimilar surfaces in contact [B1]. These two are not considered to be primary effective, while mechanical, chemical and dispersive effects are important for tight adhesion.

It is noted that even though the mechanical, chemical and dispersive effects are fulfilled, adhesion improvement may not be always observed. In such a case, existence of weak domains or weak boundary layers would induce interfacial failure. It is important to remove them for tight adhesion [1].

## 1.2. Plasma and surface modification effects

A plasma is a fully or partially ionized gas, containing electrons, ions, and radicals [3]. It usually accompanies ultraviolet (UV) photoemission. At low gas pressures, non-thermal plasmas can be easily generated, where the electron temperature is approximately 1 eV (ca. 10,000 K) or higher, which is comparable to binding energy of molecules. On the other hand, gas temperatures can be as low as a room temperature. Since it is in a non-equilibrium state, it is reasonable to call it a non-equilibrium plasma, but it is often conventionally called a non-thermal plasma, a low temperature plasma or a cold plasma. Such kinds of non-thermal plasmas are useful especially for polymer surface processing, since high electron temperature ensures production of highly reactive species such as electrons, ions, and radicals which support the main function of the plasma for its use in chemical processing, while avoiding damage of bulk properties due to a low gas temperature. Such highly reactive species can hardly be generated by conventional chemical processing at a moderate temperature without using a plasma. At low gas pressures, free electrons in a plasma can be efficiently accelerated and heated in an electric field without frequent collisions. If the gas pressure increases, however, the inelastic collision frequency of gas molecules with electrons increases, and gas temperature subsequently increases. As collision ionization by electron avalanche sustains the plasma, the input energy must be increased at a higher pressure. Consequently, the discharge is easily evolved to be a thermal plasma, or an arc, at an equilibrium state. Figure 1.3 gives an idea of the evolution of a gas discharge plasma.

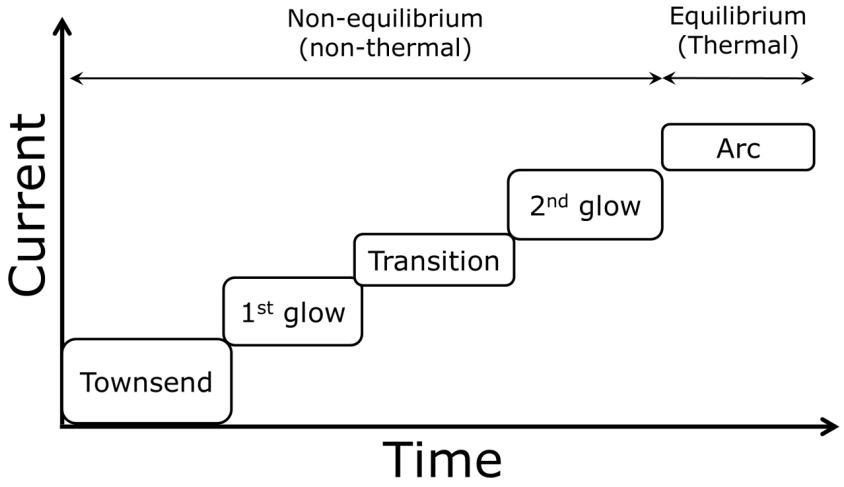


Figure 1.3. Evolution of a plasma (based on [4]).

Even when a voltage applied to a gas is lower than gas breakdown voltage, a current is detected due to a charge generation by cosmic rays or the like. Since it is partially ionized, it is also a plasma. As the applied voltage increases, accelerated free electrons in the gas cause further ionization, and subsequent electron avalanche. This regime is called a Townsend regime with a typical current ranging from femto-amperes to

micro-amperes. When the voltage further increases, in some cases the glow becomes visible as a 1st glow regime. Then, there is an unstable transition phase with a typical current in the order of microampere towards a 2nd glow within a typical current up to 1 ampere. A corona discharge corresponds to the transition regime. The 2nd glow shows strong photoemission. If the plasma is kept on, it will via an abnormal glow evolve to an arc discharge which can be used only for a thermal processing at an equilibrium state. A timescale of each step highly depends on a plasma condition such as gas species and gas pressure [4]. It is indicated in Figure 1.3 that in order to avoid generation of a thermal plasma, the current should be blocked before the discharge becomes an arc. Alternatively, if an arc is generated, it should be forcefully quenched, which will be further described in *Section 1.3.4*.

A plasma can be generated by introducing an electrical energy to a gas. Figure 1.4 illustrates a schematic diagram of an example of a plasma setup, essentially comprising an electrical power supply, also called plasma generator, and a gas handling system. The power supply delivers an electrical power to a gas by direct current (DC) and/or alternating current (AC) with a variety of waveforms including sinusoidal, square, and triangle. When the driving frequency is lower than a radio frequency (RF) (in the range of MHz), electrodes are used. When it is RF, either electrodes or an inductive coupling can be used. On the other hand, if it is in the range of microwave (MW) (in the range of GHz), no electrodes are needed, but a special care for impedance-matching is necessary for example using a waveguide. Another way of power delivery to generate a plasma is pulsed excitation which can be considered as DC biased AC, and is often used for avoiding excess heating of a plasma. A plasma is often surrounded by a chamber so as to separate it from the ambient air. However, a specimen can be exposed to an open space if a plasma can be extended in the ambient air. A plasma gas can be appropriately chosen and fed to the plasma. As chemical properties of gas species are sustained in a non-thermal plasma, choice of a gas is important for optimizing plasma conditions. In addition, electrical power, a way of excitation, frequency, voltage, voltage waveform, a gas flowrate, exposure time, and a specimen can affect treatment effects.

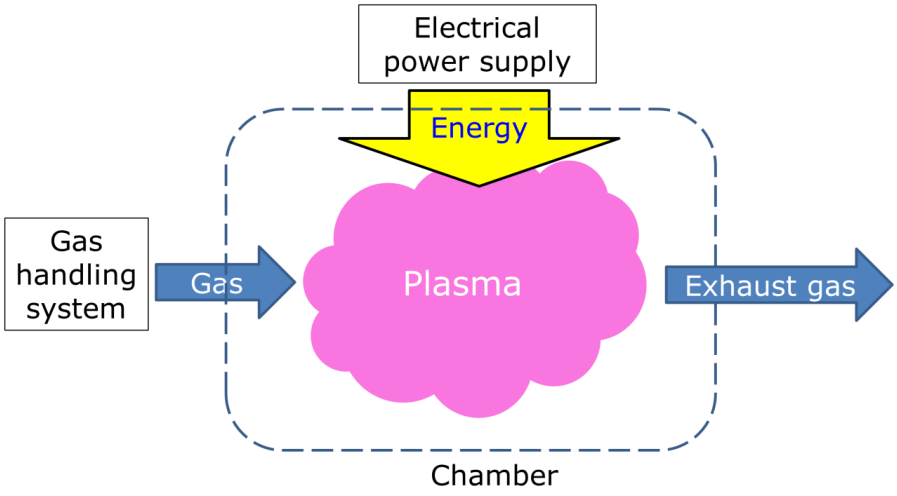


Figure 1.4. A conceptual illustration of a plasma device comprising an electrical power supply, a gas handling system, and a chamber.

During plasma treatment of polymer surfaces, etching and surface-chemistry modification are observed. Depending on the materials and conditions, one of them may be dominated, but in principle both processes occur simultaneously.

- Etching

  Atmospheric pressure non-thermal plasmas are only weakly ionized [3], and chemical etching by neutral species is usually pronounced compared with physical etching. In other words, if effects of ions are desired in a process, atmospheric pressure non-thermal plasma may not be a good choice. Etching includes removal of organic contaminants called "plasma cleaning" and ablation. They are both governed by chemically preferential etching and subsequent gasification of contaminants and weak domains. Here, the weak domains include amorphous and low-molecular-weight domains as well as organic domains compared with inorganic ones. Cleaning is primarily important for adhesion improvement, and often considered to be one of the major reasons of improved bonding after plasma treatment [5]. Ablation, however, is also important in eliminating weak domains and increasing surface roughness for improved mechanical interlocking.

- Surface-chemistry modification

  There are two major effects observed. One is to cut C-C and C-H bonds of polymer surfaces by attachment of electrically excited atoms and molecules, UV emission [5], and creation of free radicals at the surfaces. If there is flexibility in movements of the polymer chains, or if the created radicals would migrate on the polymer chains by thermal fluctuation, there can be recombination, unsaturation, branching or crosslinking. The crosslinking may improve the mechanical properties of the surfaces so that resulting fracture energy can be increased. A helium or argon plasma can enhance this effect if the plasma gas does not contain certain contaminations, since the activated polymer surface does not react with species in the plasma but reacts with molecules in the polymer. If a concentration of the contaminations is high, other effects may dominate due to surface reactions of species derived from the contaminations. However, care should be taken for the effect of bond cleavage, since breaking such bonds in a polymer main chain may result in creation of lower weight molecules (oligomers) so that weak domains may be created instead.

  Another more important chemical effect is functionalization. It can be categorized according to the functions (e.g. hydrophilization, hydrophobization, adhesability, printability and paintability), and the chemistry of the process (e.g. oxidation, nitration and fluorination). They are realized by feeding a specific gas into the plasma volume.

  If a film-forming gas (precursor) is introduced into a plasma volume, a coating can be synthesized on a polymer surface. This process is called plasma polymerization [6]. A plasma-polymerized coating adheres to polymer surfaces tightly [6] since the above mentioned effects of the etching and the functionalization are expected at the beginning of the plasma process.

In summary, plasma treatment can first remove contaminants and/or weak domains to roughen a polymer surface, increasing mechanical interlocking when another material such as an adhesive contacts the plasma treated surface. A plasma at the same time can add polar components at the surface, improving interaction with the adhesive typically by a hydrogen bond. In some specific cases, direct covalent bonds can also be expected. Since the range of the bond strengths is broad, it is difficult to predict

improvement effect quantitatively. However, a rough estimation of the improvement effect is possible, and is attempted in Chapter 2.
Figure 1.5 shows a schematic normal traction-separation relationship describing the fracture process zone in a material when it is fractured [7]. Here, $\sigma_n$ and $\delta_n$ are traction and separation of the fracture, respectively. $\sigma_n^o$ and $\delta_n^o$ are peak traction and critical separation at complete failure, respectively. It is expected that introduction of polar functional groups, surface roughening, and surface hardening can primarily increase a peak traction $\sigma_n^o$, since they are nano-scale interaction.

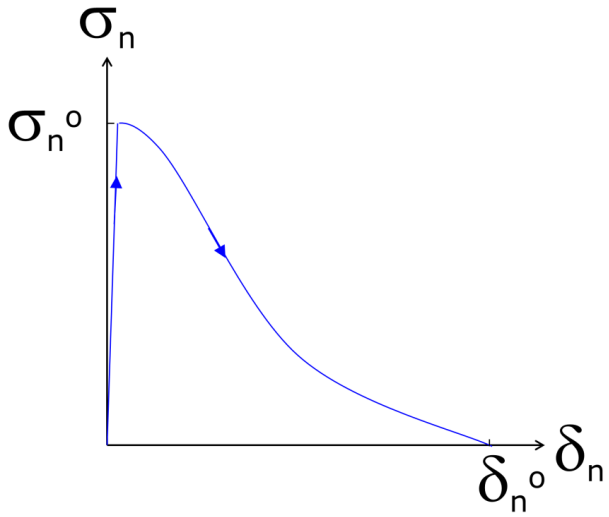


Figure 1.5. Traction separation relation of the cohesive law, representing fracture mechanics of a material.

## 1.3. Atmospheric pressure plasma sources

A variety of atmospheric pressure plasma sources are developed for surface processing, including a corona discharge (*Section 1.3.1*), a dielectric barrier discharge (DBD) (*Section 1.3.2*), and a gliding arc (*Section 1.3.4*). In addition, a DBD and other plasmas can be extended into an ambient air by a gas flow to realize cold plasma torches (*Section 1.3.3*). These plasmas are typically weakly ionized [3].

### *1.3.1. Corona discharge*

Corona discharges can be generated when the electric field is significantly non-uniform [8]. They usually appear in a vicinity of sharp edges and thin wires of an anode or cathode. When it is an anode (cathode), the plasma is called a positive (negative) corona. They are weakly luminous, filamentary, and unstable at the transition regime before 2$^{nd}$ glow in Figure 1.3. General configuration of the corona discharge is schematically illustrated in Figure 1.6. After ignition near a sharp or thin electrode, if the electrical power is kept introduced to the plasma without a special care, a corona discharge extends to the remaining gap of the electrodes between which high voltage is applied, and then in the end transfers to an arc discharge as shown in Figure 1.3. In order to achieve continual operation of a corona discharge, the discharge current must be somehow limited, resulting in low speed of the processing.

It is overcome by applying pulsed high voltages so that the discharge is ignited at the onset of the high voltage pulse and extinguished before arcing. The corona discharge is widely used for polymer surface treatment.

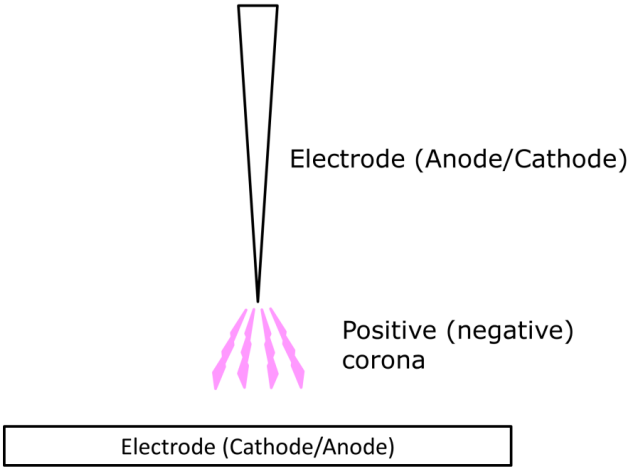


Figure 1.6. Typical configuration of a corona discharge.

*1.3.2. Dielectric barrier discharge (DBD)*

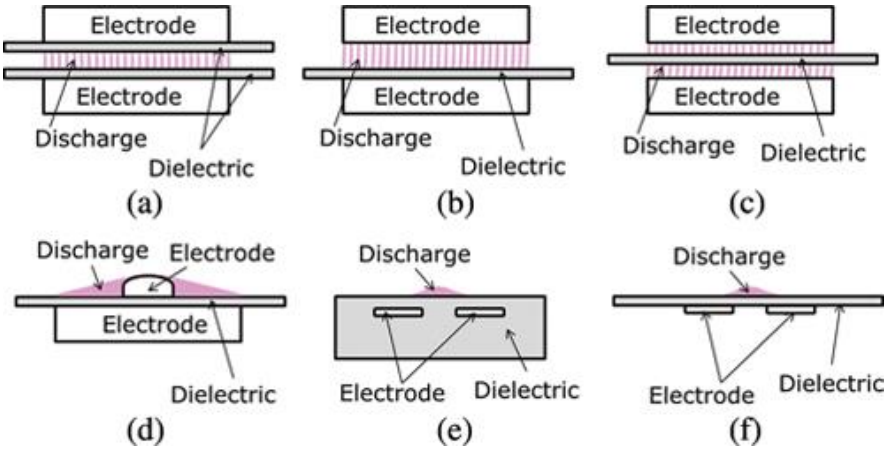


Figure 1.7. Various types of DBDs: volume discharges (a)-(c) and surface discharges (d)-(f).

Another solution for avoiding arcing is to insert at least one insulator (dielectric) between the electrodes, and block DC. It is called a dielectric barrier discharge (DBD), often operated at atmospheric pressure. The DBD is generated between electrodes by applying an AC high voltage [9, B2-B16]. DBDs have been widely used for adhesion improvement of materials [9, B2-B9].

There are two types of basic configuration of DBDs, as shown in Figure 1.7; the first is a volume discharge where the plasma is generated at the gap between the electrodes (Figure 1.7 (a)-(c)). For the plasma surface modification, a specimen is usually placed in the gap and the surface is directly exposed to the DBD. In order to ensure stable DBD operation of the volume discharge scheme, however, the gap between the electrodes is typically limited to several millimetres, which restricts the size and shape of the specimens to be treated. The second is a surface discharge [10]. A typical configuration of the surface discharge is a dielectric with an electrode on one side of the dielectric surface and another electrode on its reverse side [B17] (Figure 1.7 (d)) or all electrodes embedded in the dielectric [11] (Figure 1.7 (e)). Another case is that both electrodes are attached on one side of the dielectric material and the surface discharge is preferably generated on its reverse side [12, B17] (Figure 1.7 (f)). It is achieved by feeding specific gas such as helium or argon near the reverse side.
Frequency for operating a DBD is typically chosen between 500 Hz and 500 kHz, but DBDs driven at 50 Hz or 60 Hz are also reported [13]. As the frequency is lowered, capacitive impedance increases at a fixed gap, and at a fixed applied voltage the power is lowered. Therefore, in general, a higher frequency is preferred for high speed processing. However, as the investment cost for the power supply often dominates the total cost of atmospheric pressure plasma processing, it is attractive to try the low frequency regime at 50 or 60 Hz by using grid-connected power [A1].
In most cases, DBDs are non-uniform and consist of numerous filamentary micro-discharges distributed in the discharge gap. It is called a filamentary mode in the 2$^{nd}$ glow regime. Subsequently the plasma surface treatment is not uniform due to heavily treated regions by the individual filamentary discharge [9]. However, uniform DBDs can also be generated stably. It is called a homogeneous or glow mode, and such a discharge is often called atmospheric pressure glow discharge [B18]. In order to generate a glow discharge at atmospheric pressure the plasma gas should be diluted with helium [14]. One explanation of the effect of helium gas is that helium has the metastable state with a long lifetime in the 1$^{st}$ glow regime [14] in Figure 1.3.
It is reported that a filamentary discharge can be avoided even without using noble gas if a plasma is operated at a high frequency (typically higher than 500 Hz and up to RF (in the range of MHz)), or short pulses [15]. If the frequency is as high as RF or higher, or if the pulse width is short enough, in fact, dielectric may be unnecessary [16]. However, RF operation requires an impedance-matching network in order to deliver RF energy to the plasma efficiently, usually limiting high voltage outputs. Here, the impedance-matching network consists of variable or fixed capacitances and inductances that are tuned to match the impedances of the plasma to the impedance-matching network so as to deliver maximum power to be applied to the plasma. Due to the limitation for the high voltage application, the gap of the electrodes should be significantly close enough for stable ignition of the discharge. Consequently introduction of a specimen between the gap significantly affects the impedance between the gap, and the discharge can be unstable. In this respect, atmospheric pressure RF plasma is rather preferably developed for cold plasma torches (*Section 1.3.3*) which do not require insert of a specimen between the electrodes [16].

### *1.3.3. Cold plasma torches*

Plasma torches that can be extended in the ambient air have been developed for thermal processing, and the plasma in such a case is usually a thermal plasma in an equilibrium state. A plasma spray is a good example. It is widely used for materials synthesis by heating with a high current, and thermally melting and spraying materials

for deposition. However, followed by the recent developments of atmospheric pressure plasmas, non-thermal atmospheric pressure plasma jets (cold plasma torches) have also been developed. It is reported that a cold plasma torch can be operated at a high frequency (in the range of kHz) or RF (in the range of MHz) based on the DBD configuration [B19, B20]. With a high speed flow of argon gas, the plasma is extended to the ambient air. It is also demonstrated that a cold plasma torch can be generated without covering electrodes with the dielectrics [16]. Many different types of atmospheric pressure cold plasma torches have been developed [A1]. Figure 1.8 illustrates an example of a cold plasma torch. A plasma is generated between powered and ground electrodes by introducing electric energy, and a gas flow extends the plasma outside where a specimen to be treated is placed. Cold plasma torches typically use a noble gas such as helium and argon due to easy ignition and operation. Inductively coupled RF plasma torch has been used as a thermal plasma for material synthesis [17], but is not intensively applied for non-thermal processing such as adhesion improvement.

Atmospheric pressure plasmas can also be generated at microwave (in the order of GHz) and extended as a plasma jet by a gas flow [18]. The plasma properties of the atmospheric pressure microwave plasma jet is similar to those of the atmospheric pressure gliding arcs (see Section *1.3.4*); namely the plasma is first significantly heated to be an arc discharge, and subsequently cooled down by the gas flow to be a non-thermal plasma in the 2$^{nd}$ glow regime in Figure 1.3.

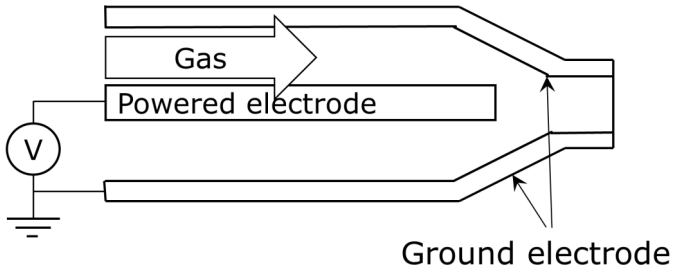


Figure 1.8. A cold plasma torch.

*1.3.4. Gliding arcs*

One of the challenges for atmospheric pressure plasma processing is to achieve a hybrid condition with high chemical selectivity and efficient productivity [19]. Here, the high chemical selectivity of a plasma is supported by high electron temperature (> 1 eV) at a non-equilibrium state, while the efficient productivity relates to high input power to ensure high speed processing. It is noted that general non-thermal (non-equilibrium) plasmas as well as thermal (equilibrium) plasmas cannot provide them simultaneously. Thermal plasmas are at the equilibrium state at high temperature and cannot demonstrate high selectivity. Thermal plasmas can even affect bulk properties of materials severely due to high temperature of gases and molecules. On the other hand, if the input power to a non-thermal plasma is increased, the plasma tends to evolve to an arc regime. However, a gliding arc can potentially achieve a hybrid condition [19], and can be regarded as a hybrid plasma. Here, a gliding arc is a plasma generated between diverging electrodes and extended and quenched by a gas flow [19,20] as shown in Figure 1.9.

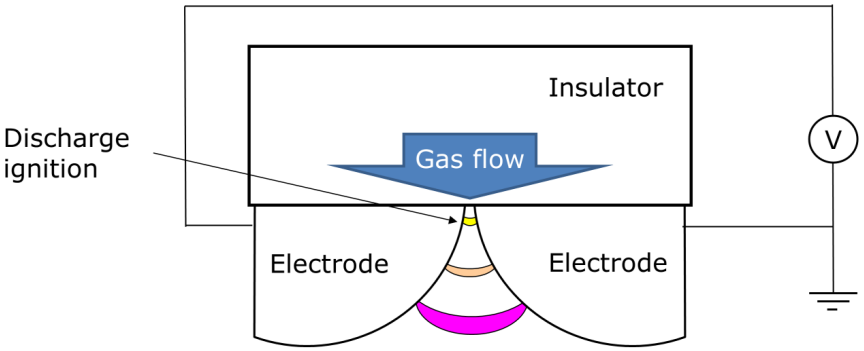


Figure 1.9. A schematic diagram of a gliding arc (based on [19,20]).

A fast transition into a non-equilibrium state occurs once heat losses from the discharge column exceed the supplied energy. The gliding arc combines a number of industrially attractive features of plasma surface treatment: it is an environmentally clean process; it operates well in air at atmospheric pressure with low costs; and it can treat surfaces of bulky objects since it allows open air treatment. It is potentially useful for adhesion improvement of materials [21]. However, the treatment effects of general gliding arcs are often inefficient. It is reported that gliding arcs are generally extinguished almost immediately after transition to the non-equilibrium state [19], suggesting that achieving the hybrid condition may be practically difficult. Typically the discharge can be extended from the edges of the electrodes up to only 2 centimetres in the ambient air [22]. However, it is due to the fact that the conditions of the non-equilibrium state and high energy density are not taken into account properly. More specifically, general gliding arcs typically employ low powers and high gas flowrates so as to prevent thermal damage of electrodes, resulting in low energy density and short lifetime of the discharge.

Plasma processing called open air technology “Plasmatreat®” is also a plasma generated as an arc and extended and quenched by a gas flow, and can also be regarded as a hybrid plasma. Since high voltage electrode is surrounded and shielded by a cylindrical ground electrode, both conductive and insulating materials can be treated [23]. The discharge can be extended up to 1-2 centimetres in the ambient air, and its performance is similar to general gliding arcs.

A preliminary study of gliding arcs was carried out to clarify issues so as to achieve hybrid conditions [B21]. Figure 1.10 shows two gliding arc sources used. The first gliding arc (GA-I) in Figure 1.10 (a) was generated between two 2-mm diameter stainless steel wire electrodes with a diverging configuration, based on a design presented in ref. [24]. The second one (GA-II) is a modification of GA-I and was built with two 1-mm thick stainless steel blade-electrodes with a similar diverging configuration based on ref. [20] (Figure 1.10 (b)). In both cases the high speed air flow was fed between the electrodes to extend and quench the discharges. They were driven by an AC power supply at a frequency of approximately 40 kHz.

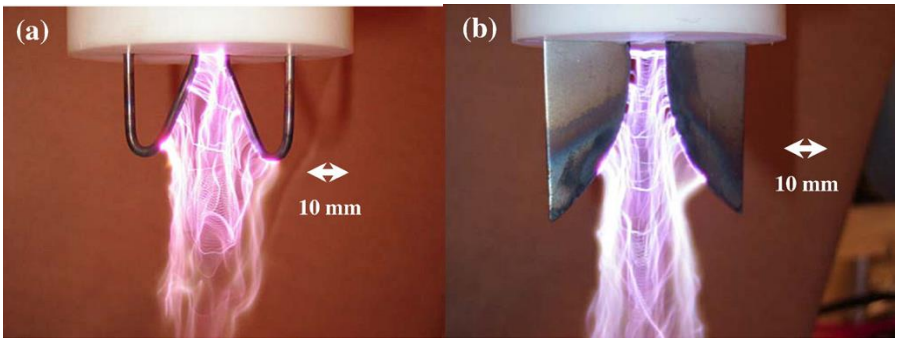


Figure 1.10. Gliding arc sources used for the treatment of polymer plates; GA-I operated at a flowrate of 25 SLM with 250 W (a) and GA-II operated at a flowrate of 30 SLM with 550 W (b) [B21].

The input power and the flowrate are important system parameters to determine the properties of the discharges. Generally, when the flowrate is 30 standard litre per minute (SLM) or lower and at the plasma power of a few hundred W, the gliding arc discharge can be extended toward the air significantly as shown in Figure 1.10. However, with the input power of more than 300 W, the temperature of the wire electrodes of the GA-I increased within 10 s at the flowrate of 25 SLM, recognized by incandescence of the electrodes. Subsequently the plasma became highly fluctuated with the occasional generation of unwanted discharges between the powered electrode and the grounded workbench due to the increase in the electrical resistance of the electrodes. In order to stabilize a discharge using the GA-I, the input power has to be less than 300 W. On the other hand, GA-II can be operated at higher input powers than GA-I possibly due to larger surface areas of the electrodes and easier heat release. However, even with GA-II, when it was continuously operated for more than several minutes at 500 W, the plasma became unstable and the electrodes were excessively heated. Therefore neither of them are practically applicable for high power continuous operation. The design of the gliding arc should be further considered so as to avoid excess heating and operate it stably while applying high power to the discharge, which will be presented in Chapter 2.

## 1.4. Surface characterization techniques [A1]

Surface characterization is vitally important to understand the surface modification effects and to optimize them. Surface characterization is also performed for fractured parts of materials in order to investigate the interfaces and failure mechanisms. Commonly used techniques include contact angle measurement, Fourier transform infrared (FTIR) spectroscopy, X-ray photoelectron spectroscopy (XPS), energy dispersive X-ray spectrometry (EDS), and time-of-flight secondary ion mass spectrometry (TOF-SIMS) for surface chemistry analyses, and atomic force microscopy (AFM), optical microscopy, and scanning electron microscopy (SEM) for morphological analyses.
The contact angle measurement appears to be the simplest method to characterize the surfaces [for example 25]. The measurement relies on the observation of the angle formed by a liquid at the three-phase boundary where the liquid, gas (usually air), and

solid intersect. It can be advantageously performed immediately after the treatment. It is noted that the technique detects the topmost surface property with the analysis depth of approximately 1 nm or less and is extremely sensitive against its changes. One drawback of the contact angle measurement method is that if highly wetting weak domains exist at the material surface, high wettability may not necessarily result in strong adhesion since the weak domains might be easily separated from the material. Aging of plasma-treated surfaces is often monitored by the contact angle measurement. Here, the aging mechanisms include migration of polar functional groups into the material due to rotation of polymer main chains, removal of the polar functional groups, and deposition of contaminations. These changes are detectable by the contact angle measurement, but not necessarily by many other much more sophisticated and expensive methods. However, it is recommended that an adhesion test is performed for the confirmation after aging of plasma-treated surfaces. It is because even if the surface wettability is reduced by the migration or the deposition, applying an uncured adhesive might induce the recovery of the polar functional groups that were migrated beneath the material surfaces or the removal of the contamination by its diffusion into the adhesive, and thus wetting may not directly indicate adhesion properties. There are two types of contact angles reported in the literature. The static contact angle is measured by the sessile drop technique while the dynamic contact angle involves both advancing and receding contact angles. The advancing angle is measured when the liquid is advanced to an unwetted solid surface while the receding angle is measured when the liquid is retracted from a previously wetted surface [26]. The problems of the static contact angle are discussed [26], but the sessile drop technique is widely used in research works and process monitoring in the industry due to the simplicity and flexibility of the measurement.

FTIR spectroscopy is also a relatively simple technique, usually operated in atmospheric pressure air. Photo-absorption in the infrared range is used to identify chemical functional groups. Many important functional groups created by plasma treatment are infrared-active. Attenuated total reflection FTIR (ATR-FTIR) is often used especially when a material to be analyzed itself has strong infrared absorption that disturbs reliable surface analysis. However, even ATR-FTIR detects the bulk information of some micrometres from the surface. Plasma surface treatment generally changes the top layer up to 10 nm or less, and so plasma-treated surfaces are usually insensitive against the FTIR measurement [B8]. On the other hand, if the surface is heavily modified or if the surface volume ratio is significantly high (such as thin fibres or fine powders), the plasma modification effect can be clearly detected [B6].

XPS, or electron spectroscopy for chemical analysis (ESCA), is a powerful tool for characterization of polymer material surfaces after plasma treatment. XPS uses a soft X-ray source for electron emission from the surface at low-gas pressure. The energies of the emitted electrons are measured, and the binding energies of these electrons are obtained. The surface sensitivity of XPS is governed by the attenuation length of the emitted electrons, and XPS typically measures the average surface chemistry up to a depth of approximately 5 nm. Therefore, XPS is less surface sensitive than the contact angle measurement. It can quantitatively measure the elemental composition, and chemical states of elements at a surface. It can also give localized information, depending on instrumentation and spatial resolutions, and maps by multiple measurements.

EDS also provides information of elemental composition at the surface. A focused electron beam bombards a specimen surface to emit an X-ray that can be used for the

analysis. Since EDS is often attached in SEM, they are often performed at the same locations of the specimen. In many cases, however, EDS is not equipped for light elements that are important for polymer surface analysis.
TOF-SIMS uses a short-pulsed ion beam directing the specimen surface causing secondary ions emission. As all the secondary ions are accelerated to the same kinetic energy, their time-of-flight for the determined path provides their masses. TOF-SIMS is destructive but demonstrates high sensitivity (detection limit ppm–ppb, detection depth < 1 nm). For example, uniform distribution of nitrogen-containing functional groups after plasma treatment is detected by TOF-SIMS (Chapters 5 and 6). Since TOF-SIMS measures masses only, a good understanding of the surface chemistry is necessary for the reasonable characterization.
A morphological property of the surface also significantly affects the adhesion property. AFM, SEM, and optical microscopy are commonly used for the observation of the surface morphology. Since plasma treatment usually induces morphological changes in the range of sub-micrometres, high resolution microscopies such as AFM and field emission type SEM (FE-SEM) are preferably used.
In addition to the above-mentioned surface characterization techniques, it is reported that Hansen solubility (cohesive energy) parameter (HSP) can be used for characterizing the thermodynamic properties of plasma-treated surfaces [27, B5]. It is particularly useful for characterizing specimens with high surface volume ratios such as thin fibres and fine particles. The HSP quantitatively describes the physical interactions among molecules. Similar HSP means solubility, permeation, chemical attack, adsorption leading to suspension or slow sedimentation of particulates, or other forms of what might be called positive affinity. Lack of similarity means perhaps only swelling or no physical effect at all, chemical resistance, high barrier properties, and rejection from surfaces such as dewetting, high contact angles, and rapid sedimentation of particulates. The noticeable disadvantage of the XPS is that it is a localized analysis and does not give information on the uniformity and the overall character of the surfaces by a single measurement. XPS cannot tell exactly where the analysis took place, and in order to obtain full understanding, one has to repeat the expensive and time-consuming analyses and then rely on statistical methods. The advantage of the HSP method is that it can characterize the surface and give the macroscopic information. The HSP measurement was tested for characterizing ultra high molecular weight polyethylene (UHMWPE) fibres before and after atmospheric pressure DBD treatment [B5]. Since matching the HSP of fibres and a polymer matrix optimizes physical adhesion, it is important to know the HSP of the oxygenated surfaces of the UHMWPE fibres. HSP correlations of the interaction of solvents with untreated and plasma-treated UHMWPE fibres have shown that there are two types of surfaces. The first is found in both untreated and treated samples and is typical of polyethylene (PE) and is characteristic of aromatic solvents. The second type of surface is the result of oxygenated species. Matching these HSP with the HSP of a polymer matrix, or some entity connected with the polymer matrix will optimize physical adhesion.

## 1.5. Aims of the thesis

Realizing atmospheric pressure plasma processing stably with high selectivity and efficient productivity is a scientific challenge, since it has rarely been achieved. In the present thesis, two possible approaches to overcome this issue are presented: development of a hybrid plasma with a high energy density at a highly non-

equilibrium state, and plasma processing assisted by external energy input, that is, ultrasonic irradiation.
The overview of the thesis is illustrated in Figure 1.11. The objectives are to
(I). Develop gliding arcs that satisfy a hybrid condition stably,
(II). Develop atmospheric pressure plasma processing with ultrasonic irradiation, and
(III). Combine the gliding arcs with the ultrasonic irradiation.

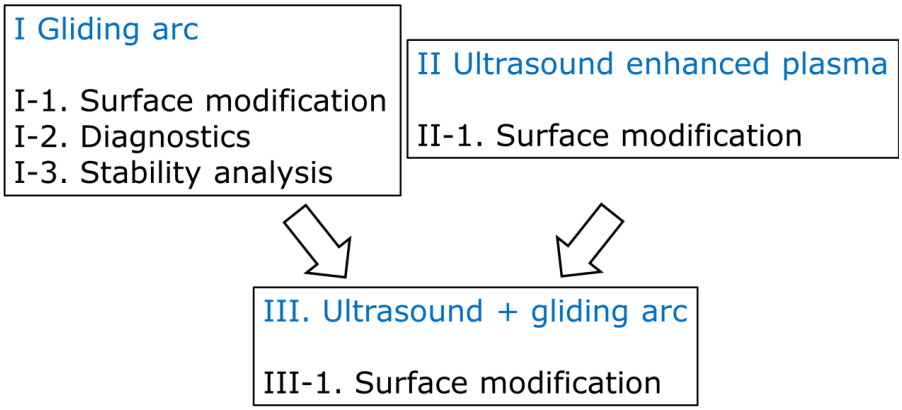


Figure 1.11. Overview of the topics of the thesis.

Under the objective (I), the sub-objectives are to
(I-1). Design, construct and operate gliding arcs to demonstrate polymer surface modification and adhesion improvement (Chapter 2),
(I-2). Diagnose the developed gliding arc to understand its properties (Chapter 3), and
(I-3). Investigate stability of the developed gliding arc using an analytical model (Chapter 4).

Under the objective (II), the sub-objectives are to:
(II-1). Design, construct and operate ultrasound enhanced plasma processing using a DBD to demonstrate polymer surface modification (Chapter 5), and

Under the objective (III), the sub-objectives are to:
(III-1). Demonstrate the processing by combining gliding arcs and the ultrasonic irradiation (Chapter 6).

## 2. Alternating current (AC) gliding arcs for materials processing [A3-A7]

### 2.1. Introduction

In order to achieve the condition of the high energy density, high power must be introduced to the discharge, which inevitably leads to heating of the electrodes. Subsequently, the resistance of the electrodes increases and joule heating of the electrodes is enhanced. This is energy-inefficient, and induces unstable operation of the gliding arc due to the changing electrical impedance of the electrodes. Furthermore, excess heat irradiation may damage the setup and the materials to be treated. Therefore, it is desirable to cool the electrodes efficiently. A common and efficient way of cooling electrodes is internal cooling by flowing coolants, usually water, through hollow electrodes. Electrodes of gliding arcs are rarely water-cooled, probably because surface erosion of the water-cooled tubular electrodes has been observed [28]. However, in the same work it is reported that the lifetime of the electrodes is not affected by the water-cooling. Therefore, the negative aspect of the water cooling has to be sincerely reconsidered.

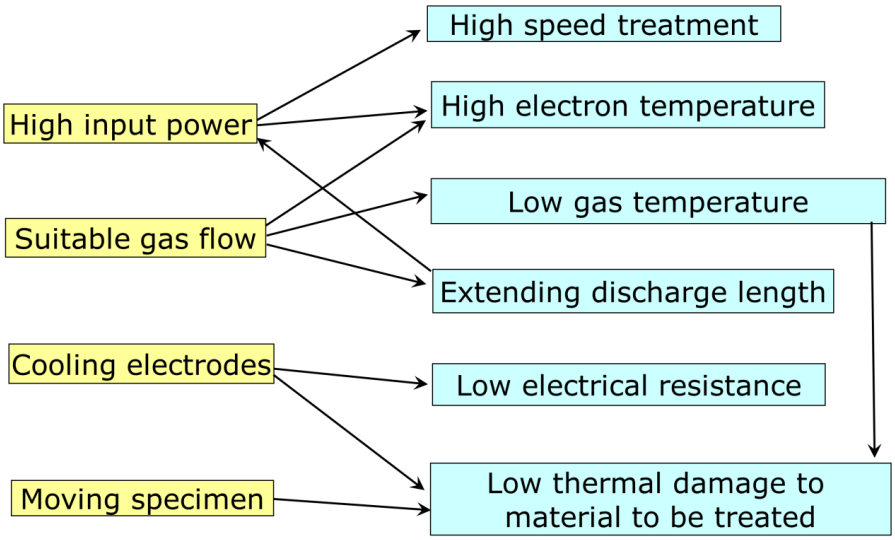


Figure 2.1. Concept of gliding arc sources studied in this chapter.

Based on the results in *Section 1.3.4*, new gliding arc sources are developed in this chapter. Figure 2.1 shows a concept of gliding arc sources to be studied in Chapters 2 to 4. In order to achieve high speed treatment, the input power should be high. On the other hand, the gas flowrate should be not too high in order to avoid lowering the electron temperature, while not too low so that the plasma can be quenched (low gas temperature) and that the length of the discharge can be extended. In addition, it is desirable to efficiently cool the electrodes, and reduce thermal damage and electrical resistance of the electrodes, as well as thermal irradiation to treating specimens. Moving specimens during treatment also avoids thermal damage of the specimens. Furthermore, ignition voltage is desirably low enough so that a power supply can have

sufficient margin to increase the power. The patent [A3] discloses specific ideas of the design, in particular, a curvature of the electrodes facing each other. Among them, a blade welded type (GA-III) and a thin tube type (GA-IV) are presented below.
In this chapter, three different materials, glass fibre reinforced polyester (GFRP) plates, cellulose nanofibre (CNF) coating on a glass plate, and fluoropolymer coated alanine (FCA) films are surface-treated with the gliding arcs (GA-III and GA-IV). Due to their high strength-to-weight ratios and corrosion resistance, GFRP are used for a variety of applications in civil engineering, wind energy, aerospace and automobile industry. Adhesives are often required for joining these materials to components fabricated from similar GFRPs or other types of materials. GFRPs usually have smooth surfaces composed mainly of the polymer matrix with low surface energies. Therefore, an adhesive joint usually requires careful surface preparation. In the case of thermosetting composites such as unsaturated polyester, vinylester and epoxy resins, mechanical roughening has been applied for the surface preparation [29]. However, it needs laborious abrasion followed by solvent cleaning prior to adhesive bonding for achieving high joint strength.
Cellulose, the most abundant biopolymer on earth, is characterized by its renewability, nontoxicity, and biodegradability. Intensive studies on CNFs have been stimulated by their high strength, high modulus, high surface area and unique optical properties [30]. Typical lateral dimensions of the CNFs are approximately 5 – 20 nm, while the longitudinal dimensions are up to several μm [31]. The mechanical properties of CNFs can be effectively availed when the CNFs are impregnated with a polymer to create strong, light-weight composite materials [32]. CNF composites can exhibit optimum mechanical performance when the CNFs are substantially dispersed and when strong interfacial interactions exist between the CNFs and the polymer matrix. If these criteria are not met, interfacial defects are created which may result in non-uniform material properties. In this respect, enhancing the interfacial interaction by surface modification of CNFs is of great importance [B9].
It is generally believed without careful investigation that plasma treatment can modify material surfaces while retaining bulk properties (Chapter 1). In this chapter, a bulk modification effect by GA-IV is measured and compared with a helium DBD. Calibrated gamma-cells with an established traceability to the international radiation dose standard are used for calibrating the alanine dosimeters. The main advantage of the gamma-calibrated alanine-electron paramagnetic resonance (EPR) dosimetry is that it enables a straightforward link between concentration of radiation damages seen as polar defects, radicals, and the like, and the amount of absorbed energy or a dose of radiation. EPR has been used for characterization of polymers after plasma processing [33]. Here, plasma modification effects are considered to happen at material surfaces [33] or within less than 1-μm thin surface layer [34]. However, in this chapter, plasma treatment of the FCA films indicated that both fluoropolymer surfaces and the bulk alanine were modified after the treatment. When plasma processing is used for surface treatment, changes of bulk properties should be avoided. On the other hand, in some medical applications such as plasma medicine [35], it is desirable that the bulk properties can also be affected by plasmas.
First, GFRP plates, also referred to as laminates, are treated with GA-III and GA-IV for adhesion improvement for adhesive bonding by a vinylester adhesive. Optical emission spectroscopy (OES) was used to estimate the rotational temperature in the discharge. The treated surfaces were characterized using contact angle measurement and XPS. The properties of the interface between the GFRP laminate and an adhesive layer are characterized in terms of the fracture energy as a function of mode mixity.

Here, the adhesive layer deforms in peel (Mode I), in shear (Mode II) or in a combination of peel and shear (mixed mode). The mode-mixity is defined by the shear portion of the total energy release rate. The interfacial fracture energy of the plasma treated interface is compared with two other relevant fracture energies: That of adhesive joints made by the use of a standard peel ply and that of the GFRP laminate itself undergo delamination. These comparisons are relevant since adhesive bonds created by applying the adhesive directly to freshly created peel-ply surfaces are considered to give sufficiently strong adhesive joints [36]. Thus, the fracture energy of an adhesive joint made from a peel ply represents an acceptable minimum value for the interfacial fracture energy. Furthermore, the GFRP laminate itself is expected to have a higher fracture energy. It is because if the adhesive and the adhesive/laminate interface possess a fracture energy or a peak traction (Figure 1.5) higher than that of the GFRP laminate, fracture is likely to occur within the GFRP laminate. Thus, the fracture energy or a peak traction of the adhesive joint made from plasma treated surfaces should surpass that of the peel ply interface but not necessarily that of the GFRP laminate. The fracture energy or a peak traction of the GFRP laminate thus usually represents an upper limit for fracture energy of the adhesive joint.
Second, CNF coatings are treated with GA-IV. The treated surfaces were characterized by means of contact angle measurements, XPS, and FE-SEM in order to investigate the treatment effect.
Third, FCA films were treated by a DBD and GA-IV at atmospheric pressure, as well as gamma irradiation to study surface modification effects, thermal effects and influence on the bulk properties by the treatments. The treated specimens were characterized by surface analysis using XPS, and by the values of the absorbed doses for the bulk alanine.

## 2.2. Experimental methods

### *2.2.1. Manufacturing of GFRP, test specimens, GA treatments and characterizations*

Four different types of double cantilever beam (DCB) specimens were used as listed in Table 2.1. Typically “peel ply”, “gliding arc” plasma treated and “crack in glue” test specimens were all based on 8-mm thick GFRP (it is referred to as GFRP-I) plates (290 mm × 30 mm × 8 mm). For testing of the GFRP laminate fracture energy, “crack in laminate”, a 16-mm thick GFRP laminate with crack initiation in the middle was manufactured. They were manufactured with symmetric and almost unidirectional fibre lay-up by resin infusion of orthophthalic polyester. Specimens for surface characterization were further cut into smaller pieces before plasma treatment for easier handling.

Table 2.1. Specimens and types of the adhesion test.

| Type of test specimen | Adhesive | Type of test |
|---|---|---|
| Peel ply | Vinylester | Mode I and mixed mode |
| Gliding arc (GA-III) | Vinylester | Mode I and mixed mode |
| Crack in glue | Vinylester | Mode I |
| Crack in laminate | None | Mode I and mixed mode |

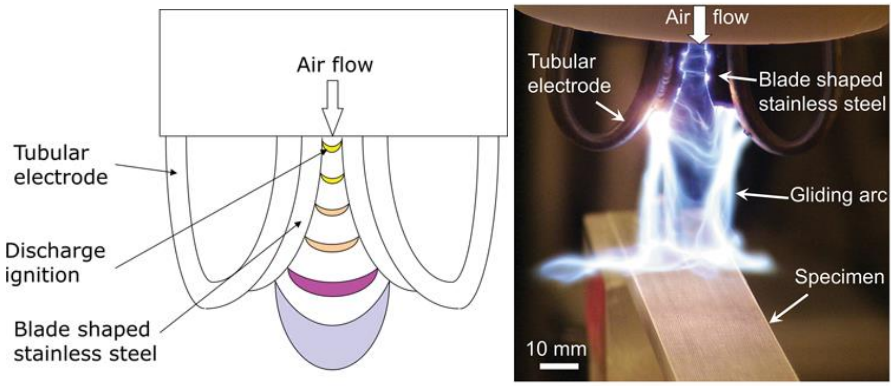


Figure 2.2. Setup of the GA-III. (a) Schematic diagram, and (b) a photo image showing the GA-III treatment of GFRP-I.

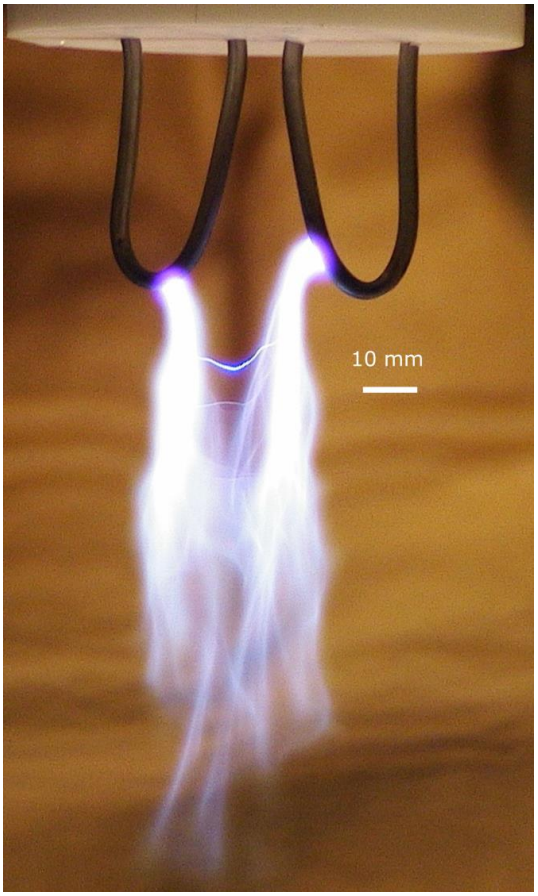


Figure 2.3. A photo of the GA-IV with water-cooled electrodes.

The gliding arcs were generated between two diverging stainless steel tubular electrodes, based on two different designs. In the case of GA-III, cooling water was fed through the 6-mm diameter tubular electrodes during operation as shown in Figure 2.2. It is noted that without water cooling, the electrodes were heated up and subsequently the discharge became unstable in a few minutes. Blade-shaped stainless steel pieces were welded on the tubular electrodes, facing each other. The arc discharge was ignited between these blade-shaped pieces so that ignition voltage can be lowered and that a margin for applying high power can be ensured at a moderate voltage. Here, a power supply usually has a maximum applicable voltage that limits an eventual maximum applicable power which can be lower than the maximum applicable power in a specification. Air flow was fed between the electrodes to extend and quench the discharge.

A potential problem in GA-III is that the blade-shaped stainless steel pieces are not directly water-cooled and can be heated and damaged during operation. GA-IV was generated between two diverging 3-mm outer diameter stainless steel tubular electrodes as shown in Figure 2.3. Cooling water was fed through the electrodes during operation. Smaller diameter decreases cooling efficiency due to an increase in flow resistance, but the electrodes are directly cooled, and the ignition voltage can be lowered compared to larger diameter electrodes without the blades due to the curvature of the small diameter electrodes. Air flow was fed between the electrodes. In Chapter 4, optimal design of the electrodes will be further discussed.

In both cases, the gliding arc was driven by an AC power supply at a frequency of approximately 30-40 kHz. The average power to the gliding arc was obtained by measuring voltage and current with a high-voltage probe and resistors, respectively. In order to treat a GFRP-I plate surface, the plate was fixed on a holder which moved forward and back at a speed of 180 mm $s^{-1}$.

OES measurements of GA-III and GA-IV were performed without the GFRP-I plate using an optical fibre and a spectrometer. The rotational temperature, $T_{rot}$, which is assumed to be close to the gas temperature, was evaluated by the relative intensity of two groups of rotational OES lines corresponding to the R and P branches of the OH A-X (0,0) vibrational band [37]. The OH molecules come from ambient air humidity. The relation between the rotational temperature, $T_{rot}$, and the relative intensity of the R and P branches is given in [37].

The contact angles for deionized water on the GFRP-I surfaces were measured in air at room temperature using a contact angle measurement system.

XPS was employed to study the changes of the elemental composition at the GFRP-I surfaces before and after the GA-III treatment.

For crack initiation in the interface between a vinylester adhesive (glue) and GFRP laminate, a 51-µm thin polytetrafluoroethylene (PTFE) release tape was mounted on the GFRP laminate surface in a position of 70 mm from the tab-end of the beam. On top of the release tape a 2-mm thick PTFE chamfered spacer was placed close to the tip of the crack initiation.

DCB specimens for “crack in laminate” measurements were cut directly from the cured GFRP laminate manufactured from 20 layers of fabric. The crack initiation was established using a 12.7-µm thin ethylene chloro-trifluoroethylene (E-CTFE) film between the middle two fabric layers. Overall geometry of the DCB test specimens used and a close up of the three different crack initiations used are shown in Figure 2.4. Pins were placed 70 mm from the specimen end for mounting extensometers to measure end opening of a crack. The mechanical test was performed by applying even or uneven pure bending moments to the DCB-specimens. The DCB-loaded-by-

uneven-bending-moments test configuration provides stable crack growth for materials having a constant or rising fracture resistance and enables the testing of the whole mode mixity range from Mode I ($\psi = 0°$) to Mode II ($\psi = 90°$) ($\psi$ being the mode mixity, defined as the phase angle of the complex stress intensity factor, see [38]). Here, the fracture resistance and mode mixity were calculated without accounting for the stiffness and thickness of the adhesive layer, i.e., analyzing the specimens as being a homogeneous GFRP laminate. The mode mixity, $\psi$, calculated in this manner is therefore a nominal mode mixity, $\psi_{nom}$.

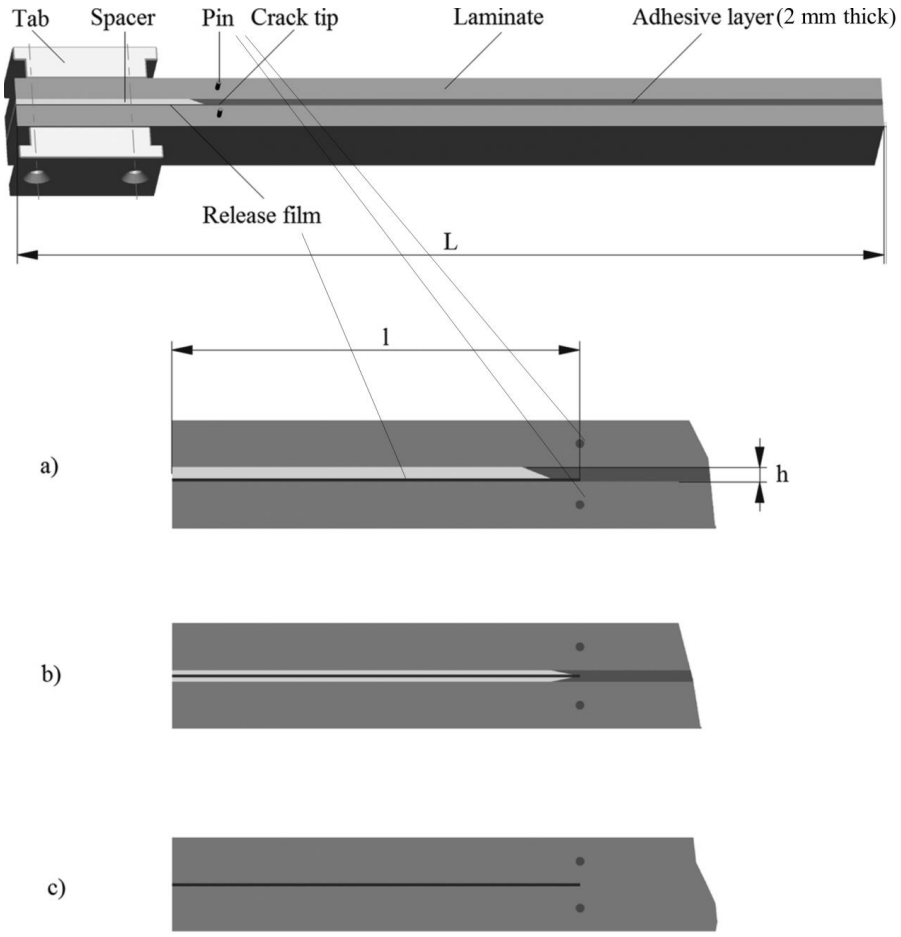


Figure 2.4. Overall geometry of the 290-mm long (L) DCB test specimens illustrated with mounted tabs and 2-mm thick (h) glue. Crack initiation (l) starts 70mm from the specimen end where also the pins for mounting of extensometers (not shown) are positioned. A close-up of the three different crack initiation types: a) interface between glue and GFRP laminate (corresponding to “Peel ply” and “Gliding arc” specimens in Table 2.1), b) center of glue (corresponding to “Crack in glue” specimen in Table 2.1), and c) in the middle of the GFRP laminate (corresponding to “Crack in laminate” specimen in Table 2.1).

*2.2.2. Manufacturing of CNF coatings, GA treatment and characterizations*

CNFs were isolated from carrot residue, bleached and fibrillated by ultrafine grinding to obtained aqueous CNF suspension (2wt% concentration). It was used to prepare coatings on glass plates and dried. The coating thickness was estimated to be approximately 6 μm.

GA-IV was used for surface treatment of CNF coatings.

Contact angles and XPS data were measured similarly to *Section 2.2.1*. The surface morphology of the CNF coating was observed using FE-SEM. The CNF surfaces were sputter-coated with approximately 15-nm thick Au before the observation.

*2.2.3. FCA films, GA treatment, DBD treatment and characterizations*

The fluoropolymer coating of the FCA film is approximately 20μm thick and has a porous structure. FCA films were treated with a DBD and GA-IV.

The DBD was generated between two parallel plane water-cooled electrodes (50 mm × 50 mm) and driven at a frequency of 40 kHz. The water-cooled bottom electrode is grounded and covered with an alumina plate as a dielectric barrier. The distance between the upper powered electrode and the alumina plate was fixed at 5 mm. A similar setup will be presented in Chapters 5 and 6. Helium was fed into the DBD at a flowrate of 3 SLM. The FCA film was placed on the alumina plate and exposed to the DBD at the power of 120 W.

The treatment condition using GA-IV is similar to *Sections 2.2.1 and 2.2.2*.

The treated surfaces were studied by XPS.

The temperature of the specimen surface was measured immediately after plasma treatments by using a thermocouple.

FCA films were irradiated with gamma rays, which delivered the absorbed dose rate of approximately 79 Gy $min^{-1}$.

The application of the EPR for the plasma treated films is considered as follows;

1. Irradiation of a set of virgin FCA films in a calibrated gamma-cell up to predetermined doses to prepare calibration films.
2. Measuring EPR spectra of the gamma-irradiated calibration films.
3. Plotting EPR alanine signal amplitudes vs. absorbed doses and fitting them with a calibration function.
4. Plasma treating another set of virgin FCA films as witnesses of dosages during plasma processing.
5. Measuring EPR spectra of the plasma treated FCA films.
6. Deriving ”absorbed dose” in the bulk alanine using the calibration function obtained from step 3, subtracting that of the virgin FCA film as a background.

## 2.3. Results and discussion

*2.3.1. Treatment of GFRP-I using GA-III*

Figure 2.5 shows the rotational temperature $T_{rot}$ and water contact angles after GA-III treatment at different flowrates. $T_{rot}$ was estimated to be 3800 K at a flowrate of 20 SLM and decreased as the flowrate increased. The contact angle markedly increased at the flowrate of 30 SLM. At this flowrate, the excess cooling reduced the rotational temperature as low as approximately 2000 K (see Figure 2.5), resulting in insufficient treatment effect. In the following experiment in *Section 2.3.1* the air flowrate was fixed at 20 SLM in order to demonstrate efficient adhesion improvement.

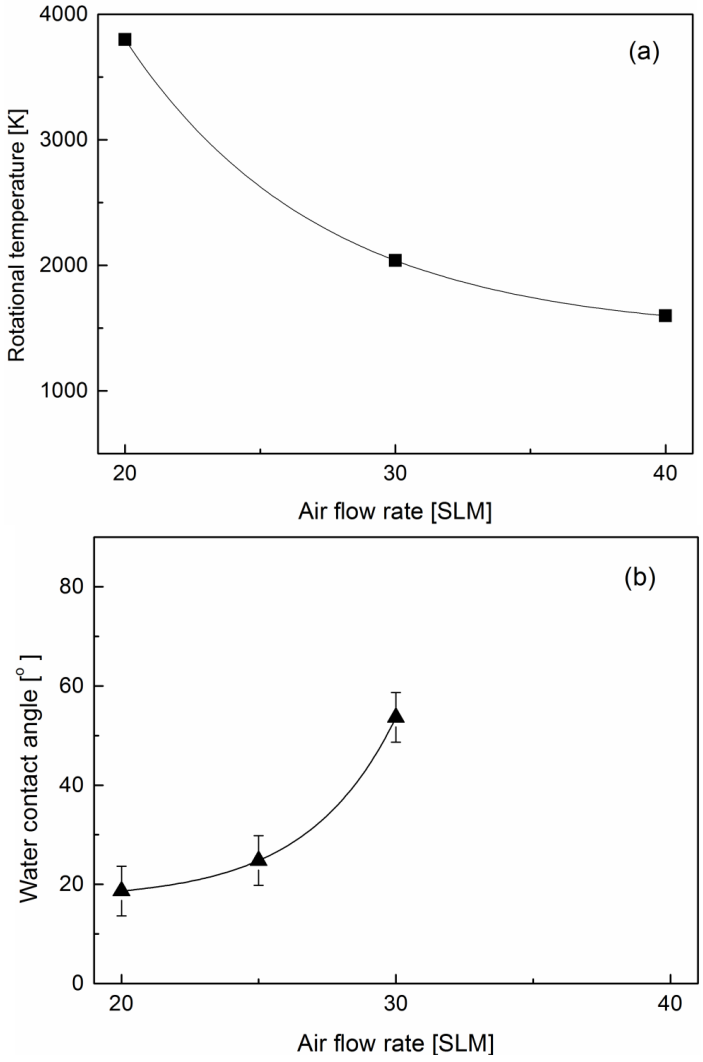


Figure 2.5. Measured rotational temperature (a) and water contact angle of GA-III (b) at different air flowrates and fixed power (720 W), fixed distance to the electrodes (15 mm) and fixed number of exposure (four times).

The contact angles of the GFRP-I plate surfaces, measured before and after GA-III treatment at different number of the exposure, are shown in Figure 2.6. The water contact angles dropped to approximately 20$^{o}$ or lower when the specimen surface was exposed 4 times or more. The XPS analysis indicated that the GFRP-I surfaces were mostly dominated by oxygen (O) and carbon (C) atoms. The O/C ratio of the GFRP-I surfaces before and after the treatment was compared as shown in Figure 2.6. The oxygen content increased more after the longer treatment, approaching to approximately 0.45.

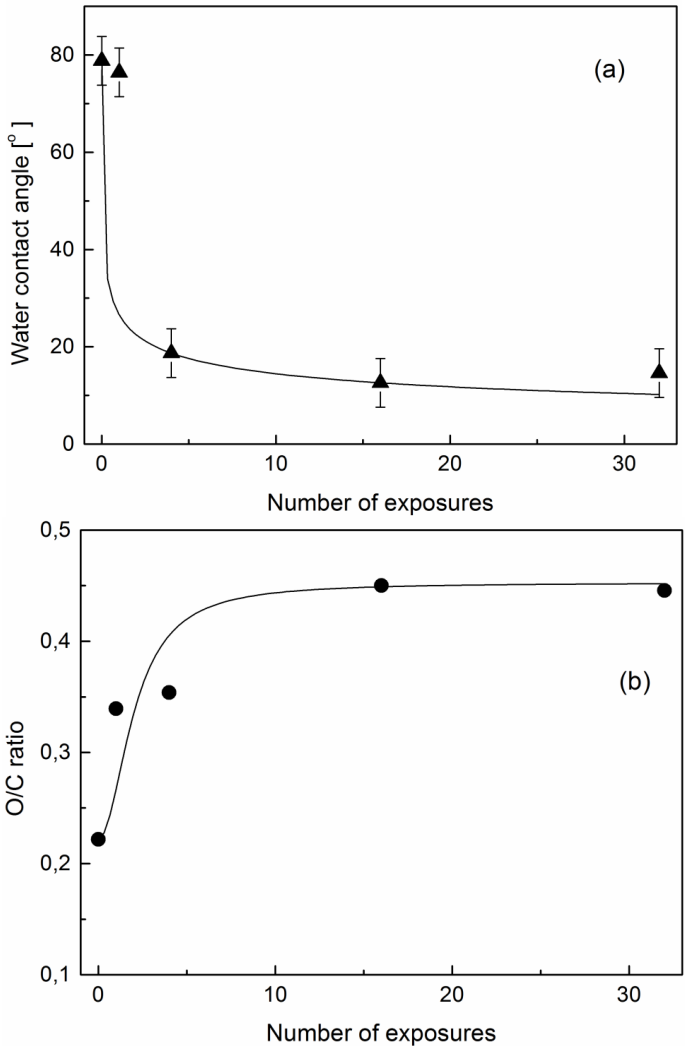


Figure 2.6. Water contact angle (a) and O/C ratio (b) of the GFRP-I plates after GA-III treatment at different number of exposure at fixed air flowrate (20 SLM), fixed power (720 W), and fixed distance to the electrodes (15 mm).

Since the gliding arc discharge can be extended into air up to several centimetres, it is interesting to investigate an effective distance of the treatment. Contact angles were measured after GA-III treatment at different distances from the edges of the electrodes to the GFRP-I plate surface. The water contact angle and O/C ratio at the GFRP-I plate surface after GA-III treatment are shown in Figure 2.7. The results indicate that the GFRP-I plate surface can be substantially oxidized when the distance between the edges of the electrodes and the GFRP-I surface was up to approximately 6 cm.

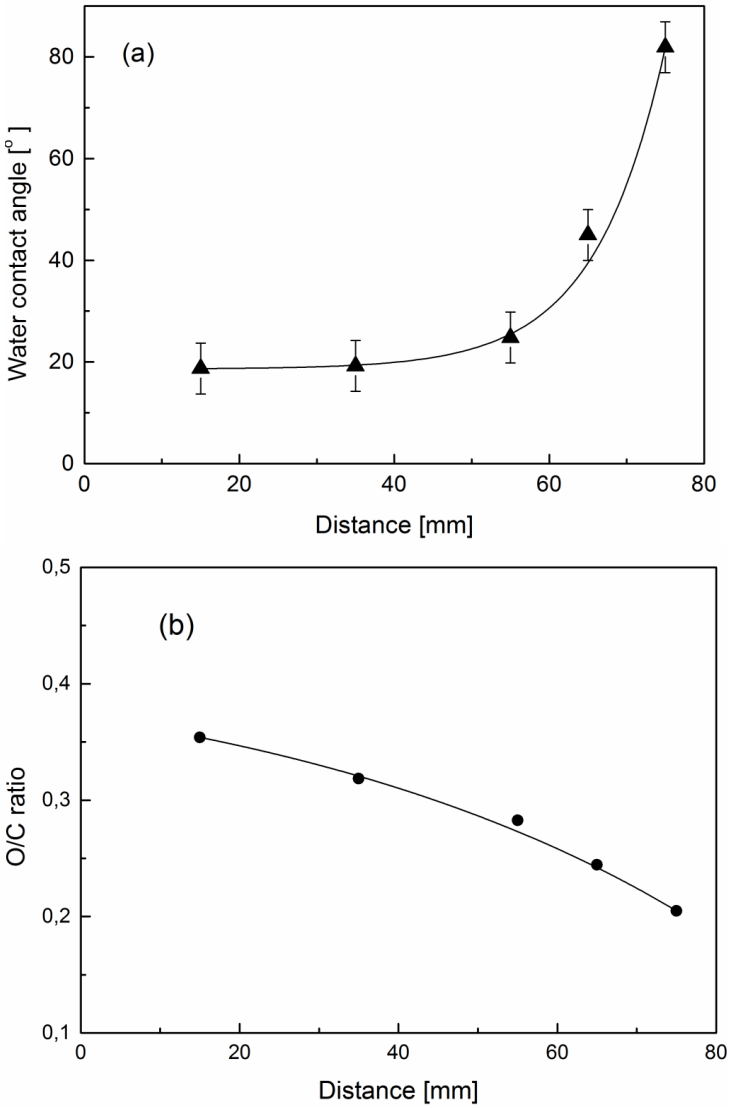


Figure 2.7. Water contact angle (a) and O/C ratio (b) of the GFRP-I plates after GA-III treatment at different distances from the edges of the electrodes to the GFRP-I plate surface at fixed air flowrate (20 SLM), fixed power (720 W), and fixed number of exposure to GA-III (four times).

Figure 2.8 shows the initiation fracture energy as a function of mode mixity for crack growth of the peel ply specimens, GA-III treated specimens and the GFRP laminate. The value of Mode I cracking growth initiation within the adhesive is also included. First, the general trend observed in Figure 2.8 is that the fracture energy increases with increasing mode mixity for configurations (cracking in laminate, adhesive joints made from peel ply, adhesive joints made from plasma treated surfaces). Such trends are in good agreement with results of mixed mode interface fracture [39].

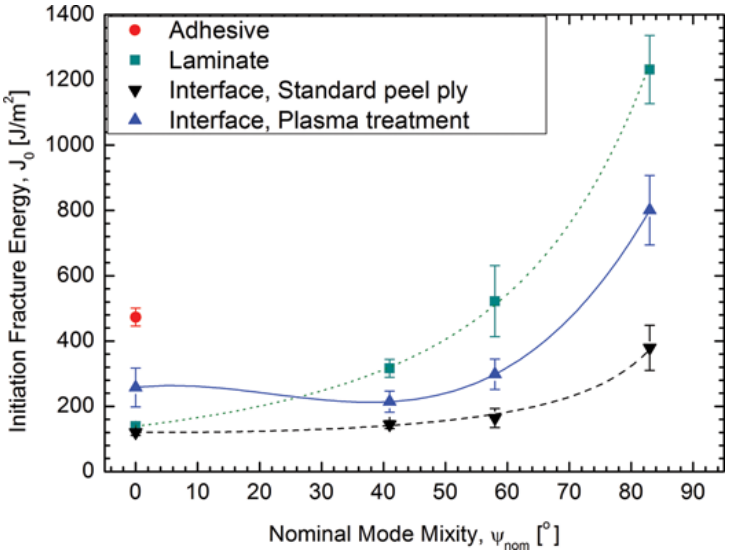


Figure 2.8. Mixed mode initiation fracture energy shown as a function of the mode mixity.

Next, for nominal Mode I ($\psi_{nom}$ = 0.3°), the fracture initiation values of the GFRP laminate and the peel play specimens are comparable, while the fracture initiation values of GA-III treated specimens are higher than those of the GFRP laminates and the peel ply specimens but lower than those within the adhesive layer. For higher values of $\psi_{nom}$, the results associated with the peel ply specimen, GA-III treated specimens and the GFRP laminates are clearly different. This suggests that Mode I testing only may be insufficient for screening and selecting interface treatments.
The most important result from Figure 2.8 is that the fracture energy of GA-III treated specimens is approximately twice as high as that of the peel ply specimens. Thus, the plasma treatment results in a significant increase in the fracture energy of the adhesive joint. The mixed mode fracture energy is, however, not as high as the mixed mode fracture energy of the pure GFRP laminate, i.e., specimens having no adhesive layer. If it is assumed that each carbon atom could bond at most one oxygen atom, the O/C ratio can represent a ratio of carbon atoms which directly bond oxygen atoms. They can induce hydrogen-bond interactions with the adhesive. The O/C ratio of the untreated specimen is approximately 0.23, while it increased 1.6 – 2 times after GA-

III treatment as shown in Figure 2.6. It is therefore roughly estimated that GA-III treatment may increase the fracture energy at the interface by a factor of two. Although this estimation is based on the simplified assumption, it shows good agreement with the initiation fracture energy at the mixed modes in Figure 2.8.

*2.3.2. Treatment of GFRP-I using GA-IV*

Similar experiments were carried out for GA-IV for contact angle measurements, XPS analysis in terms of input power, gas flowrate, the number of exposure, and mechanical properties of DCB specimens. The results are similar to those in *Section 2.3.1.* and thus detailed presentations are omitted in this chapter. In brief, the optimum treatment was demonstrated at the plasma power of 800 W and gas flowrate of 17.5 SLM. In this condition, the GA-IV treated GFRP-I plates was efficiently oxidized and showed improved fracture resistance even when the distance between the edge of the electrodes and the GRFP plate surface is 55 mm.

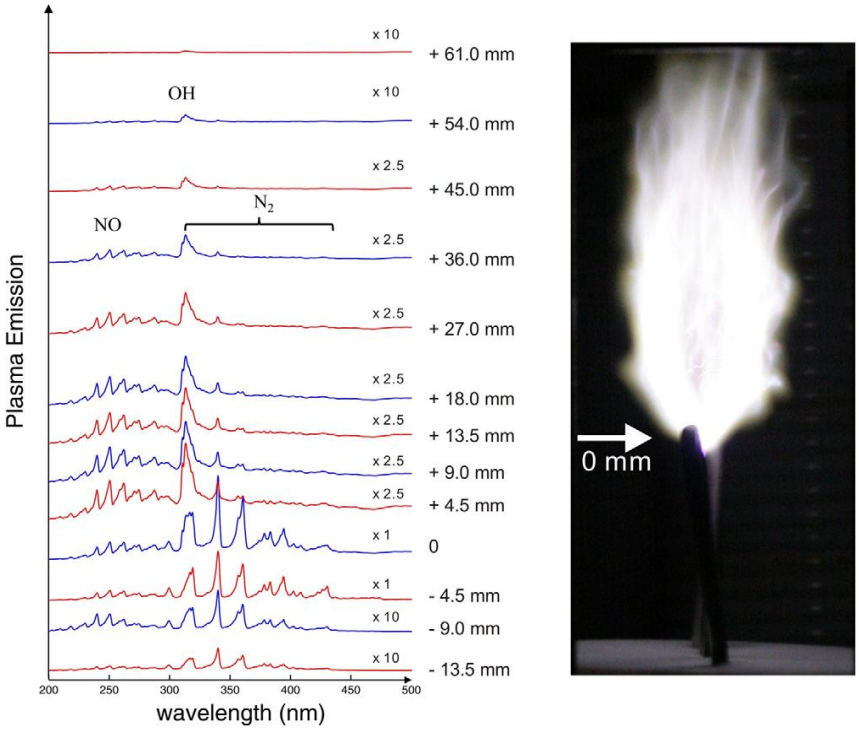


Figure 2.9. OES at different heights and a side-view of the gliding-arc discharge operated at an air flowrate of 17.5 SLM and a power of 800W. The height of the image is approximately 12 cm.

Figure 2.9 shows OES of the GA-IV operated at the air flowrate of 17.5 SLM and the power of 800 W, including NO, $N_2$ and OH bands. In particular the emission from OH(A-X) was detected up to a distance of 60 mm from the edges of the electrodes. Hence increase in the fracture energy of GA-IV treated specimens at distances of 55 mm or shorter is understandable.

*2.3.3. Treatment of CNF coating using GA-IV*

In this section, contact angles of deionized water and glycerol were measured. Figure 2.10 shows measured contact angles at different numbers of exposure. Typically 10 measurements were made for each specimen, and their arithmetic mean was calculated. The contact angles of deionized water and glycerol before GA-IV treatment, corresponding to 0-time exposure, were typically between 20º - 35º and 70º - 80º, respectively. The deionized water contact angles tend to decrease as the number of exposure increases, approaching 0º. The glycerol contact angles also tend to decrease as the number of exposure increases, approaching approximately 30º. Enhancement of glycerol wetting is preferable when CNFs are mixed in a composite, since CNFs are usually dispersed in an organic solvent for mixing it into a polymer matrix. However, it is noted that after 16-time exposure, contact angles of deionized water and glycerol is slightly increased.

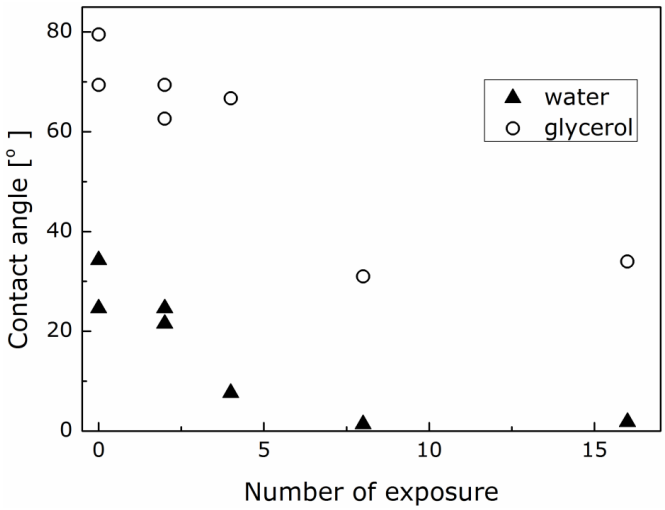


Figure 2.10. Contact angles of deionized water and glycerol on the CNF coatings at different times of exposure to GA-IV. The numbers of exposure are 0 (corresponding to an untreated surface), 2, 4, 8 and 16. Solid triangle: deionized water. Open circle: glycerol.

XPS measurement was carried out to analyze the elemental composition of the CNF coatings before and after the GA-IV treatment. The CNF surfaces typically contain C, O, Ca, and low concentration impurities. The atomic ratios of O/C and Ca/C calculated using the XPS survey spectra are shown in Figure 2.11 (a). After 2-time exposure, the O/C ratio significantly increased from 0.59 to approximately 0.72. The O/C ratio did not significantly increase by further exposure, and eventually decreased to approximately 0.64 after 16-time exposure. The Ca/C ratio also increased, after the GA-IV treatment, from 0.02 to 0.03-0.04. The increase in the Ca/C ratio can be interpreted as preferential etching of organic components in the coatings (see *Section 1.2*). It is indicated that the Ca/C ratio does not monotonically increase as the increase in the exposure to the GA-IV, and that the preferential etching of organic component is not a leading effect of GA-IV treatment.

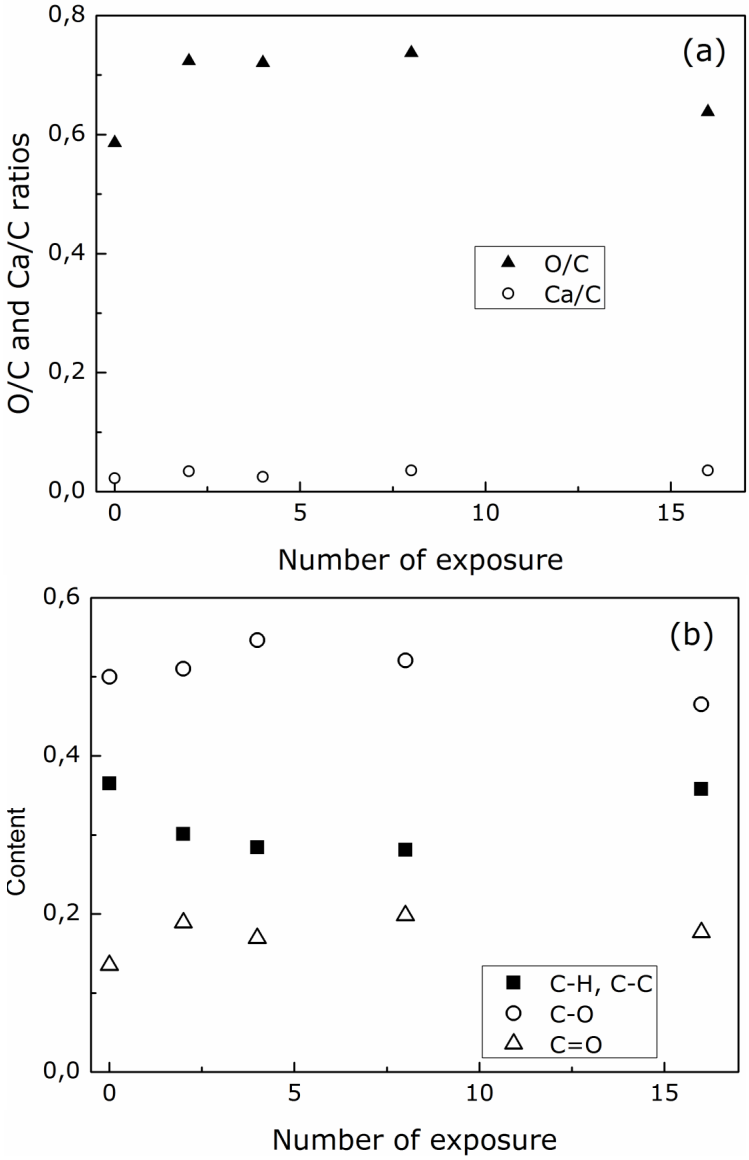


Figure 2.11. (a) O/C and Ca/C ratios of the CNF coating surfaces at different times of exposure to the GA-IV. (b) Contents of peaks obtained by curve-fitting of C1s spectra of the CNF coating surfaces at different times of exposure to the GA-IV.

Deconvolution of the C1s spectra of CNF coatings before and after GA-IV treatment was carried out to study functional groups at the CNF coating surface. The result is shown in Figure 2.11 (b). Peaks at approximately 285 eV, 286.8 eV, and 288.4 eV can be assigned to C-H/C-C, C-O, and C=O (carbonyl), respectively. Here, a content of each peak in Figure 2.11 (b) is a ratio of a peak area to a total area of a C1s spectrum.

A peak corresponding to carboxyl group at approximately 289.5 eV was not detected. Since general plasma treatment can readily create carboxyl group on polymer surfaces by oxidation, it is suggested that GA-IV may result in moderate oxidation on CNF surfaces. After 2-time exposure, the peak corresponding to C-H/C-C decreased, while the peaks corresponding to C-O and C=O increased. Similar to the O/C ratio, they may not significantly change by further exposure, and after 16-time exposure, the peak of C-H/C-C increased and the peaks of C-O and C=O decreased. Therefore, GA-IV treatment can oxidize the CNF coating, but further treatment may rather deoxidize it. It may be the reason why after 16-time exposure, the contact angles slightly increased in Figure 2.10.

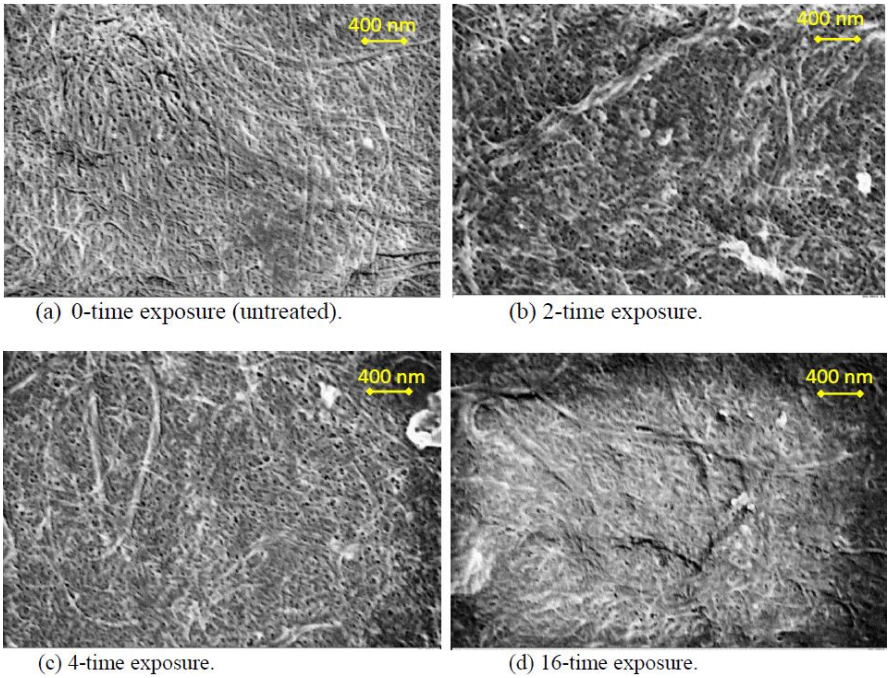

(a) 0-time exposure (untreated). (b) 2-time exposure.

(c) 4-time exposure. (d) 16-time exposure.

Figure 2.12. FE-SEM images of the CNF coating surfaces.

Discussion of the morphological changes after the gliding arc treatment is possible only when nano-scale observation is performed, since plasma surface treatment generally changes the top layer up to 10 nm or less. Figure 2.12 shows FE-SEM images before and after the GA-IV treatment. Figure 2.12 (a) indicates that the untreated CNF coating shows assemblies of nano-cellulose fibrils surrounded by an unstructured phase. 2-time exposure in Figure 2.12 (b) seems to roughen the surface, most likely due to the preferential etching of the surrounding phase, supported by the XPS result of the increase in the Ca/C ratio. However, further exposure may not significantly roughen the CNF coating surfaces in a nano-scale as shown in Figures 2.12 (c) and (d). Instead, these images indicate that the surface becomes smoother in nanoscale, while a larger scale deformation might occur (Figure 2.12 (d)). A possible

explanation of this morphological change by the GA-IV treatment is that the CNF coating surface could be etched and roughened moderately, and that longer exposure could result in microscale melting at the surface.
In summary, after 2- and 4-time exposures of GA-IV treatment to CNF coating surfaces, the contact angles were decreased, the O/C content were increased and the surfaces were roughened. These changes are useful for improving adhesion of the CNF coatings. However, after 16-time exposure, the contact angles were slightly increased, the O/C ratio was slightly decreased and the surfaces were melted. Therefore, there can be an optimal treatment condition for adhesion improvement.

*2.3.4. Thermal effect and influence on bulk materials*

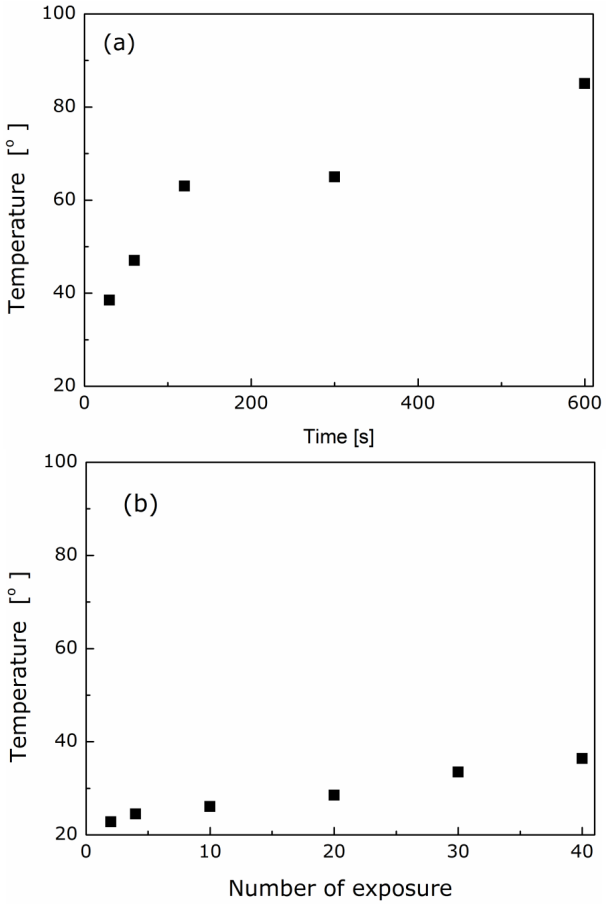


Figure 2.13. Temperature of the FCA surface after DBD treatment (a) and GA-IV treatment (b).

FCA films were treated with the DBD and GA-IV. The results of temperature measurements at the FCA film surfaces are shown in Figure 2.13. As the exposure time or treatment time increases, heat was accumulated and the temperature was increased. After 600 s treatment with the DBD, the temperature exceeded 80 °C. On

the other hand, even after 40 times of exposure by GA-IV, the temperature remained below 40 °C, indicating that GA-IV treatment can prevent the treated films from excess thermal damage. Generation of free radicals in alanine is temperature dependent [40]. Results of alanine/EPR dosimetry therefore depend on the temperature and thus a correction of the alanine dosimeter response was performed when the irradiation temperature was different from the calibration temperature. Elemental compositions of FCA films deduced from the XPS results before and after each treatment are summarized in Table 2.2. Plasma treatment decreases the fluorine content and increases the oxygen content. For the present conditions, GA-IV treatment shows a higher effect in decrease of fluorine and increase of oxygen than the DBD treatment. Gamma radiation also decreases the fluorine content and increases the oxygen content, comparable to the GA-IV treatment.

Table 2.2. Elemental composition of FCA surfaces by XPS [%].

| Treatment | | Untreated | DBD, 15 s | GA-IV, 2 exposures | Gamma irradiated |
|---|---|---|---|---|---|
| Elemental composition [at.%] | C | 48 | 51 | 54 | 56 |
| | F | 48 | 42 | 33 | 32 |
| | O | 4 | 5 | 10 | 9 |
| | N | 0 | 1 | 2 | 2 |

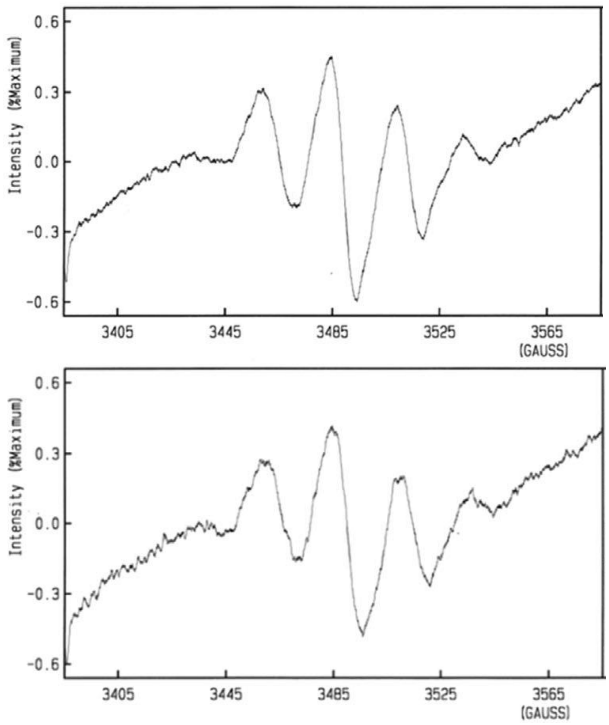


Figure 2.14. EPR spectra of identical FCA films subjected to 80-Gy dose of gamma-radiation (upper image) and DBD treatment for 600 s (lower image). The background subtraction was not performed.

The EPR spectra obtained from gamma irradiated and plasma treated FCA films with the use of an EPR spectrum analyser are shown in Figure 2.14. Both waveforms in Figure 2.14 present typical EPR spectra of alanine radicals [41].

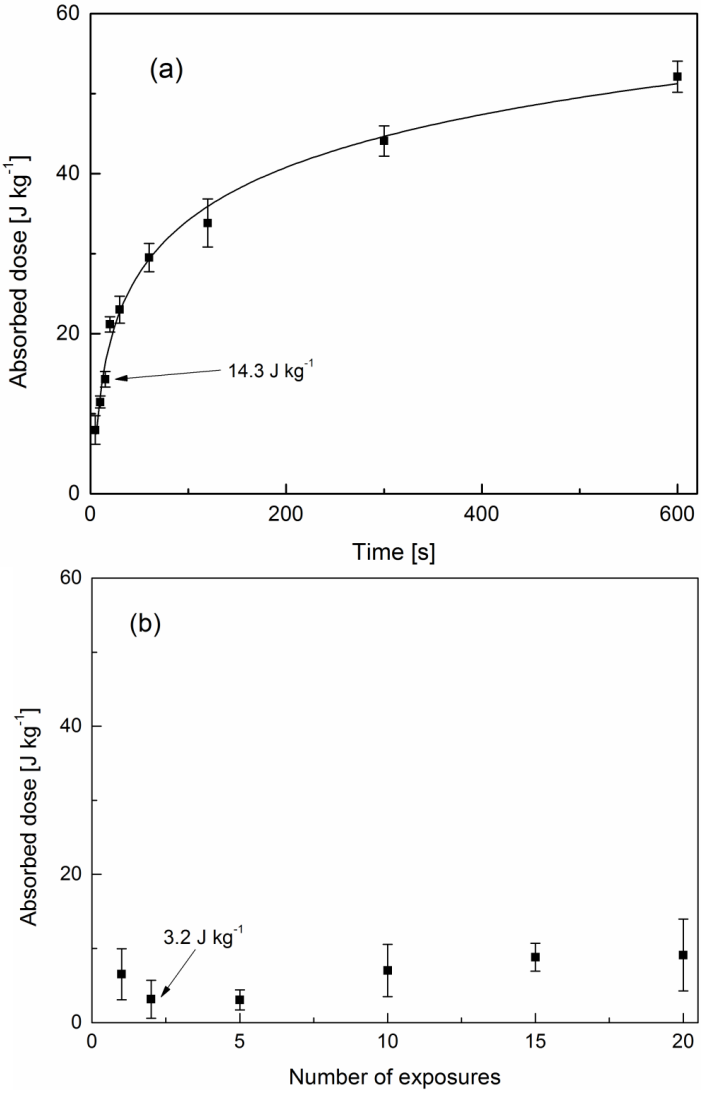


Figure 2.15. Absorbed dose deposited in FCA films treated by the DBD (a) and GA-IV (b).

The results of absorbed dose measurements for DBD and GA-IV treatments of FCA films using EPR spectra with temperature corrections are shown in Figure 2.15. Gamma rays are known to be the most penetrating of the radiations and can pass through the FCA film. If plasma treatment modifies only the surface layer of the

materials up to approximately 1 μm, the bulk material properties of alanine would be retained due to the 20-μm thick fluoropolymer covering alanine. However, Figures 2.14 and 2.15 indicate that plasma treatments eventually modified the bulk alanine, and thus the plasma treatments affected not only surfaces but also bulk materials. Since increase in temperature by the treatment was moderate as shown in Figure 2.13, the bulk modification in the present study is probably caused by high energy photo-emission of the plasmas such as ultraviolet (UV) rays. Penetration depth of UV rays into polymer materials depends on the materials themselves and the wavelength of UV [42]. Fluoropolymers are known to be substantially UV transparent even at short wavelengths [43], while alanine absorbs a broad range of UV [44]. It is therefore likely that UV rays emitted from the plasma can pass through the fluoropolymer layer and easily be absorbed by alanine. This indicates that the alanine/EPR dosimetry can be potentially used as a measure of bulk modification caused by the plasma treatment. Here, modification effects of the surfaces and the bulk for the two different plasma treatments are compared. GA-IV treatment decreased the fluorine content and increased the oxygen content much more than the DBD treatment. On the other hand, the specific deposited energies of the films after GA-IV and the DBD treatments are approximately 3 and 14 J $kg^{-1}$, respectively, as shown in Figure 2.15. These results indicate that in the specific conditions, GA-IV treatment can modify the material surface and retain the bulk properties more efficiently than the DBD treatment. In other words, the gliding arc treatment may be more appropriate for surface modification while the DBD treatment may be the choice for bulk modification. UV emission of the gliding arc includes emissions from NO, OH and $N_2$, and its intensity is lowered in the condition in this section (see Figure 2.9). In addition, the intensity of the UV emission a few centimeters away from the electrodes, where the specimen can be exposed, is substantially lower than that in the vicinity of the electrodes in Figure 2.9. On the other hand, the helium DBD typically has strong UV emissions consisting of $N_2$, $N_2^+$ and NO [45]. The difference of the UV emission between the GA-IV and the helium DBD can be one of the reasons of the higher bulk modification effect of the DBD.

## 2.4. Summary

Gliding arc sources were developed based on a new concept of the design. They demonstrated stable operation with high efficiency in treatment. Surface modification effects were examined for GFRP-I plates and CNF coatings. In each case, the surface was oxidized significantly and roughened. These changes are useful for improving adhesion with adhesives which have polar functional groups. Significant improvement of adhesion with vinylester was demonstrated for GFRP-I plates. Since the gliding arcs developed here can efficiently oxidize the material surfaces when the distance from the edge of the electrodes is up to approximately 6 cm in open air, it can be advantageously applied to plasma surface modification of bulky objects for adhesion improvement of materials.

FCA films were treated by the DBD and the gliding arc at atmospheric pressure as well as gamma irradiation. Each treatment decreased fluorine contents and increased oxygen contents at the surfaces of the fluoropolymer coatings on the alanine films. On the other hand, each treatment also modified the bulk alanine films. It is indicated that the plasma treatments can affect bulk properties, and the changes can be detected by the EPR technique. In the selected conditions, the gliding arc treatment modified the surface more and the bulk less than the DBD treatment.

## 3. Diagnostics of AC gliding arc [A8-A9]

### 3.1. Introduction

In this chapter, properties of the gliding arc (GA-IV) are investigated using optical diagnostics and electric measurements. A typical gliding arc is a plasma column that extends between two diverging electrodes in a turbulent gas flow. When applying high electric power in a gas flow, the generated gliding arc is visualized as a blurred glowing region. The gliding arc of the present thesis reveals its true instantaneous structure in photographs with short exposure time as the ones shown in Figure 3.1. The gliding arc is a thin, string-like plasma column that repeatedly ignites in the closest gap between the diverging electrodes, glides up along the electrodes, and extinguishes. The large-scale motion of the gliding arc is caused by convection in a turbulent free jet that stretches an arc into the quenched plasma column connecting the anchor points on the electrodes. The length of the plasma column increases until its extinction unless the plasma column short-cuts a long current path with a shorter one. After the ignition of a new plasma column at the closest gap of the electrodes at 100 μs (third image from the left in Figure 3.1), the previous plasma column decays, indicated by the lower photoemission intensities. At the ignition stage the plasma is hot but the molecules and ions are quickly cooled, creating non-equilibrium conditions.
Knowledge of the freely developing gliding arc discharge is useful to understand more complicated practical situations, such as surface treatment where the gliding arc interacts with a surface. Free-developing gliding arcs, therefore, have been investigated in modelling [19, 46] and in experiments [3, 46, 47]. Measurements of gliding arcs reported were usually done at temporal resolution that did not allow dynamic processes, such as ignition and small-scale movement, to be tracked.

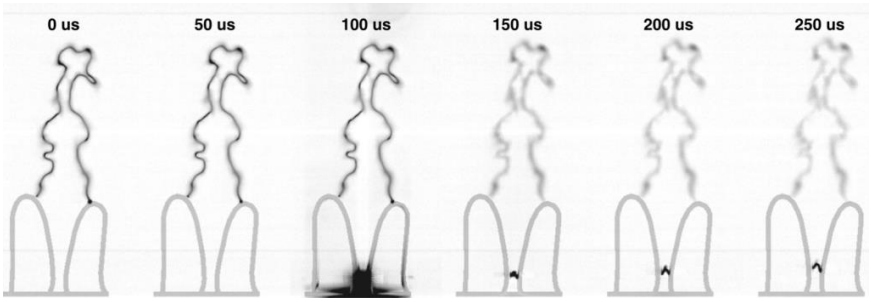


Figure 3.1. Photographs of GA-IV taken every 50 μs. The exposure time of the camera was 13.9 μs. A new arc ignites in the third frame (100 μs) after which the previous discharge above the electrodes extinguishes and the optical emissions decay.

High speed photography reveals the dynamic processes and tracks GA-IV in time including ignition, short-cutting events triggered by Townsend breakdown, and extinction. The framing rate used in this work is up to 420 kHz giving a temporal resolution up to 2.1 μs, which essentially freezes the motion of the plasma column and resolves the changes of the emission intensities originating from the AC driving

power varying at 31.25 kHz (i.e., the half cycle duration is 16 μs). Distributions of ground-state OH radials generated in the plasma column are visualized.

### 3.2. Experimental methods

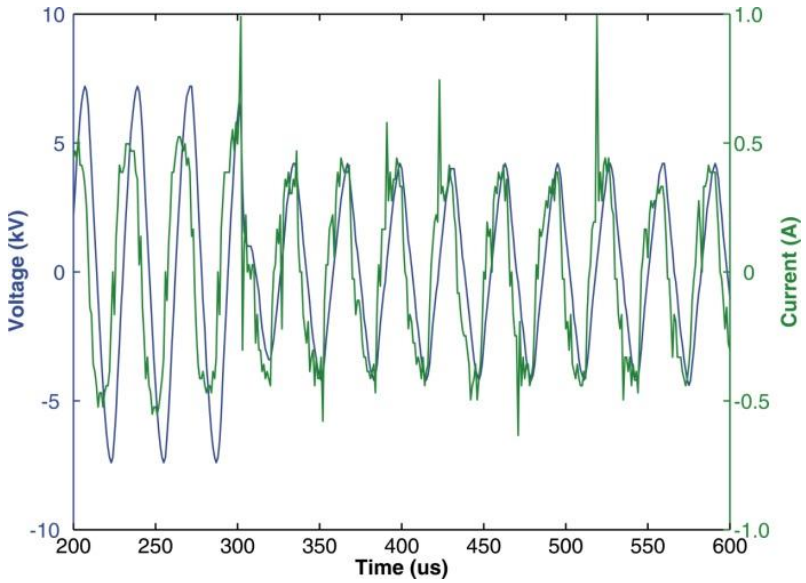


Figure 3.2. Typical voltage (blue) and current (green) waveforms recorded by the oscilloscope.

The air flowrate was fixed at 17.5 SLM unless otherwise stated. The air velocity was calculated to be about 40 m $s^{-1}$ at the nozzle exit providing turbulent flows with a Reynolds number of about Re = 8000. GA-IV was driven by an AC power supply at a frequency of 31.25 kHz. The input power to GA-IV was approximately 800 W. Typical waveforms of the voltage and the current are presented in Figure 3.2. The current follows the voltage, but the current spikes were occasionally observed.
A high-speed camera was used to capture ignition, propagation and extinction of GA-IV.
Planar laser-induced fluorescence (PLIF) was employed to investigate the distribution of the ground-state OH radicals. The laser beam was shaped into a thin laser sheet to enable a two-dimensional measurement of OH with high resolution in time and space. The ICCD camera was synchronized with the pumping laser, and the fluorescence was collected perpendicular to the laser sheet with an exposure time of 30 ns. The plasma column was also directly imaged using the ICCD camera through filters (UG5 + WG295) in order to investigate the spatial distribution. The OH-PLIF signal and the spontaneous plasma emission can be simultaneously collected using the ICCD with an exposure time of 2 μs.

### 3.3. Results and discussion

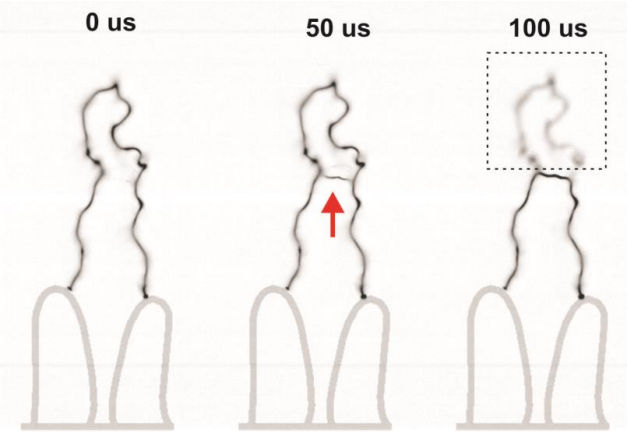


Figure 3.3. An example of a short-cutting event recorded at 20 kHz framing rate using an exposure time of 13.9 μs. The short-cut current path is indicated by the red arrow at 50 μs where a gas breakdown occurs between the two legs of the plasma column, forming a new current path.

The motion of GA-IV was recorded with the high-speed camera and the motion of the plasma column was captured at high temporal resolution to reveal detailed information on ignition, evolution, short-cutting, pulsation and extinction. An example of the short-cutting events captured is shown in Figure 3.3. As shown in the frame for t = 50 μs, the short-cut current path (indicated by the red arrow) exists simultaneously with the previous, longer current path. After the new current path is formed, photoemission is still observed (in the dashed box).

Figure 3.4 shows three typical frames of single-shot superimposed OH-PLIF distributions and photoemission at flowrates of 17.5 SLM and 42 SLM, respectively. An exposure time of 2 μs was used in order to simultaneously record OH distributions and plasma column photoemission. The conductive plasma column, illustrated as a bright string in Figure 3.4, is a 3D thin wrinkling channel that connects the two electrodes. The 100 μm thick laser sheet crossed the plasma column vertically and illuminated only part of the plasma column, where OH distributions in the thin cross-section were illustrated in the collected PLIF images. However, the simultaneously recorded bright string of the hot core was the projection of the whole plasma column. From the simultaneously recorded plasma emission and the OH-PLIF, one can see the hollow-shaped OH distribution around the plasma column. The thickness of the hollow structure is much wider (up to 0.9 cm) than the plasma column (about 0.1 cm) at low flowrates, while decreases to about 0.3 cm at high flowrates.

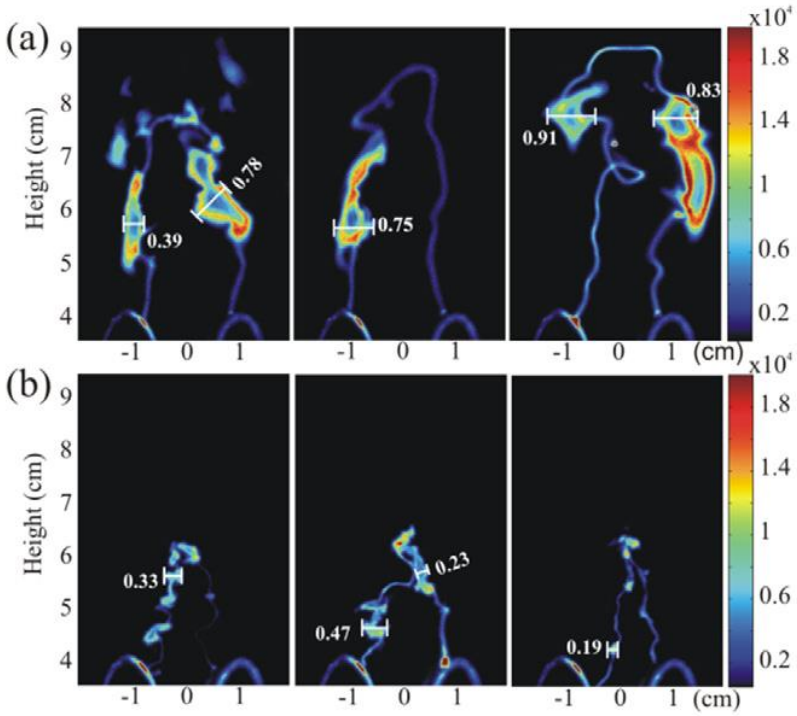


Figure 3.4. Three typical single-shot OH-PLIF images for 2 μs exposure, showing the OH distributions and plasma-column photoemission at two flowrates (a) 17.5 SLM, and (b) 42 SLM. The typical thickness of the OH distribution is labelled in the images with unit of centimetres. The colour bar is in arbitrary units of photoemission intensity.

## 3.4. Summary

The evolution of a gliding arc discharge has been investigated using the high speed camera and PLIF. Short-cutting events in the plasma column were observed as well as the re-ignition of the discharges in the closest gap between the electrodes. This type of short-cutting events reduces the re-ignition of the gliding arc, hence improves the efficiency of the production of non-equilibrium plasma generation. Townsend discharges were observed at the beginning of the short-cutting events. It was found that the re-ignitions between the electrodes occur while the previous plasma column still exists. After formation of the new plasma column, the previous plasma column decays. PLIF was applied to reveal the distribution of the ground-state OH. A hollow structure was found in the single-shot images of OH, which might be explained by the ground-state OH formation from the decay of excited OH.

## 4. Stability of AC gliding arcs [A10]

### 4.1. Introduction

A gliding arc is often operated using DC [19, 21], but AC can also be used [48]. The performance of a gliding arc is studied in terms of energy balance [46], force balance [49], and electric circuits [19, 50].
It is desirable in many applications that a gliding arc is not blown away in a short time but stays in a same location for the efficient use of energy introduced to the plasma. Stability of a DC gliding arc and its implication of the transition from thermal to non-thermal discharge have previously been discussed using a circuit theory [19]. It is assumed that a specific power dissipated from the discharge per unit length, $W$, is constant at a fixed gas flowrate. Experimental data supports this assumption [51]. Neglecting a self-inductance, Ohm's law can be written in the form [19]

$$V = RJ + \frac{Wl}{J} \tag{1}$$

and thus

$$J = \frac{V \pm \sqrt{V^2 - 4WlR}}{2R}. \tag{2}$$

Here, $V$ is the voltage applied from the power supply, $R$ is the serial resistance, $J$ is the current, and $l$ is the length along the DC gliding arc discharge column, which is different from the extension length from the edge of the electrodes. Electrode fall voltages can be up to approximately 300 V [52], and is thus assumed to be negligible. When the length of the discharge column $l$ increases and the discriminant of Eq. (2) reaches zero, the discharge evolution in equilibrium is terminated. This occurs at a critical length $l_{crit\_dc}$,

$$l \le l_{crit\_dc} = \frac{V^2}{4WR}. \tag{3}$$

Here, the critical length $l_{crit\_dc}$ is in inverse proportion to the energy dissipation $W$. If the length of the DC gliding arc discharge column exceeds the critical value of Eq. (3) (critical length in the thermal regime), a fast transition from thermal to non-equilibrium state with different discharge parameters takes place [19]. After the transition, the gas in the DC gliding arc rapidly cools while the electron temperature increases due to the increase of the electric field strength (non-thermal regime). This post-transition period after quenching, corresponding to a non-equilibrium state, is potentially useful, since only in this period the gas temperature is low enough so as to be applicable in a variety of general material processing. It is reported that after the transition, the critical length in the non-thermal regime can be approximately three times larger than the critical length in the thermal regime before the transition, since the energy dissipation from the DC gliding arc $W$ can be approximately three times smaller due to the lower gas temperature after the transition [19]. However, this post-transition period could constitute only a small portion of the total DC gliding arc cycle time, limiting the practical application of DC gliding arc discharges.
On the other hand, introduction of a self-inductance of the circuit $L$ into the DC gliding circuit decelerates the rate of current decrease and prolongs the evolution time of the non-equilibrium DC gliding arc [19]. Equation (1) is replaced with

$$V = RJ + \frac{Wl}{J} + L\frac{dJ}{dt}. \tag{4}$$

The influence on the critical length of the AC gliding arc has not been studied yet. In this chapter, this simple nonlinear model (Eq. (4)) is used to study the stability and critical length of an AC gliding arc in a non-thermal regime. The AC gliding arc presented here is characterized by the length of the plasma column of approximately 20 – 30 cm. It does not extinguish each half period but can survive over hundreds of AC periods after which the discharge is terminated by a new ignition at the closest gap between the electrodes (Chapter 3). This AC gliding arc is unique and significantly useful for surface modification, since three-dimensionally shaped bulky structures can be easily treated, and the energy consumption of the plasma is mainly used for sustaining a non-equilibrium plasma instead of arc ignition. As shown in Figure 3.2, the current waveform can be approximated by a sinusoidal form, which allows detailed analytical study of the model.

## 4.2. Stability analysis of an AC gliding arc

In Chapters 2 and 3 it is indicated that the AC gliding arcs (GA-III and GA-IV) driven at a high frequency (30-40 kHz) can be stably extended from the edges of the electrodes up to several centimetres in the post-transition period. In this chapter, GA-III and GA-IV were used. The closest gap between the blade-shaped pieces of GA-III is variable from 2 to 8 mm. GA-III and GA-IV were operated at a frequency of 31.25 kHz. Other conditions are similar to Chapters 2 and 3.

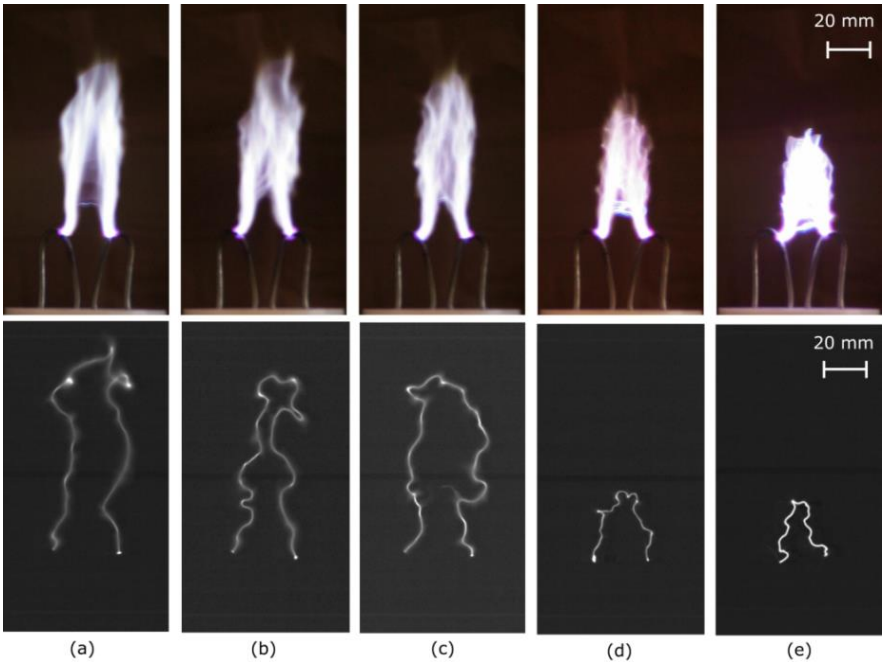


Figure 4.1. Photos of the AC GA-IV at different gas flowrates: (a) 14 SLM, (b) 17.5 SLM, (c) 21 SLM, (d) 31.5 SLM and (e) 42 SLM. The upper images are acquired by a normal camera using an automatic exposure time, showing how humans perceive the gliding arc. The lower images are captured by a high-speed camera using an exposure time of 13.9 μs and reveal the plasma column just before extinction.

It is observed that the behaviour of the gliding arc is affected by the movement of the gas around the discharge and that the plasma column tends to be longest when blown upwards in the direction of buoyancy for heated gas. When it is blown downwards against the direction of buoyancy, mixing of the gas and subsequent cooling of the plasma are enhanced and thus the plasma column would be shorter. In this chapter, the gas flow is kept upward. The behaviour of the gliding arc is also affected by the gas flow. Photos of GA-IV at various gas flowrates are shown in Figure 4.1. The upper photos were taken by a normal video camera with an automatic exposure time, corresponding to apparent visual images of a bulky plasma. However, the real dynamics of the gliding arc can be captured by a high speed camera, represented by a thin plasma column of the lower row of photos in Figure 4.1. The photos in the lower row are the last acquired images before extinction of the discharge column. As the framing rate was 20 kHz, the discharge extinguishes 50 μs after the time of these images or shorter. As the movement of the plasma column is negligible within this timeframe, these images show the maximum achievable length of the plasma column at each flowrate. It is seen that the maximum achievable length of the discharge column tends to decrease as the gas flowrate increases.

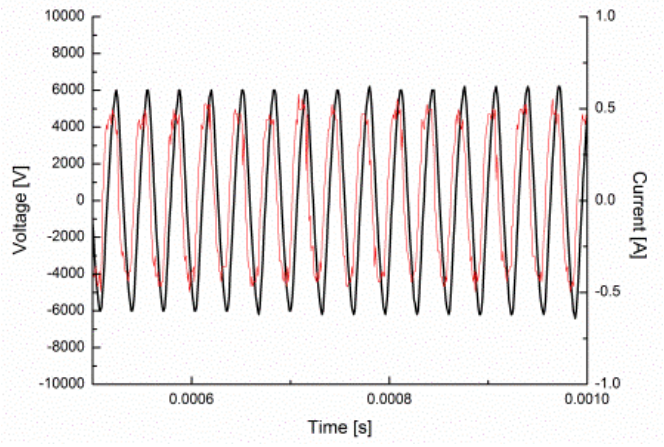


(a)

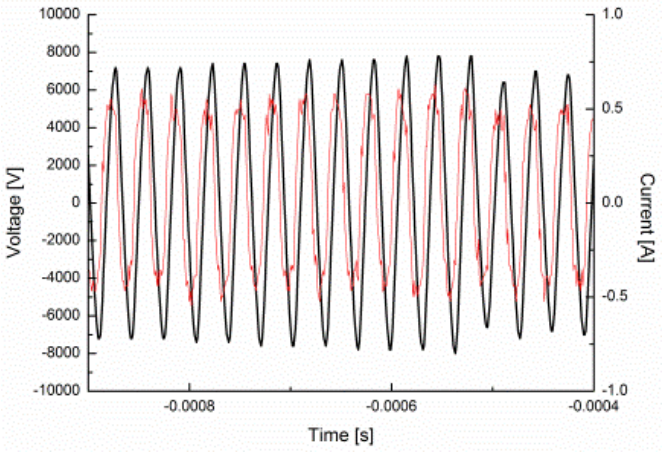


(b)

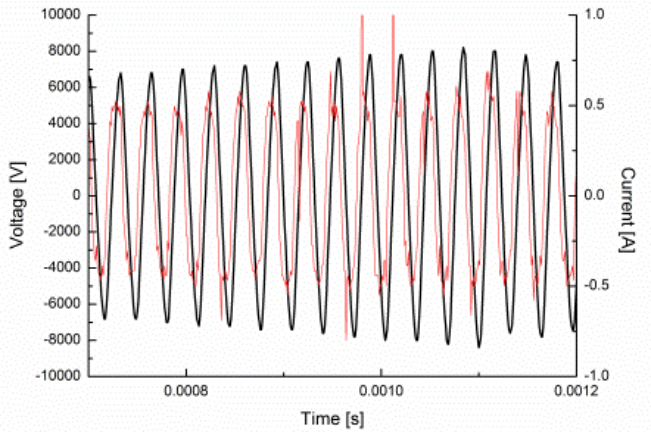


(c)

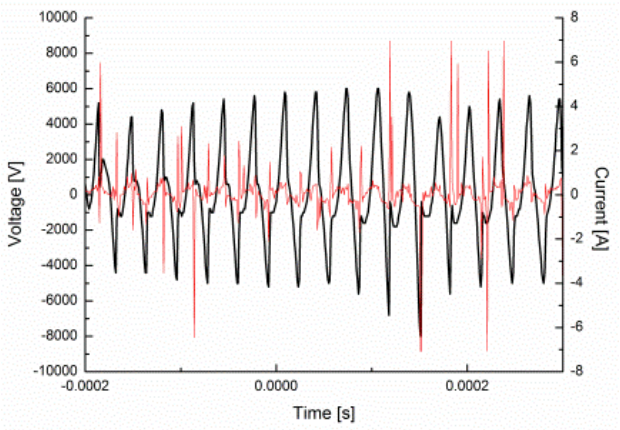


(d)

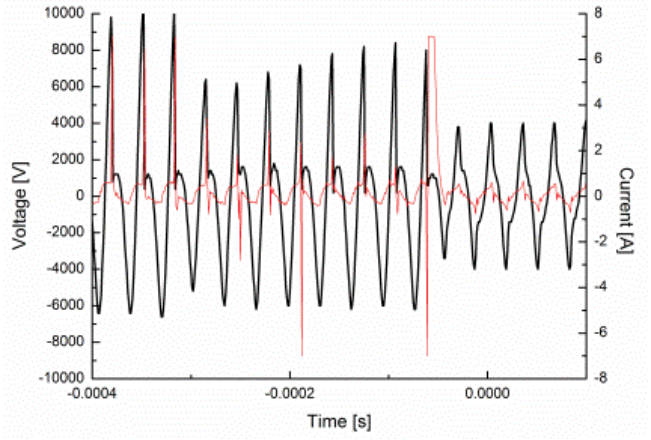


(e)

Figure 4.2. Typical voltage (black line) and current (red line) waveforms of the GA-IV at different gas flowrates: (a) 14 SLM, (b) 17.5 SLM, (c) 21 SLM, (d) 31.5 SLM and (e) 42 SLM.

When the gliding arc is generated with an AC power supply at an angular frequency $\omega$ = 2π × 31.25 kHz, the measured photoemission intensity from the gliding arc oscillates at the angular frequency $2\omega$ [A8], because the energy dissipated from the discharge reaches its maximum in each half period.
Figure 4.2 shows typical voltage and current waveforms of the AC driven GA-IV at different gas flowrates. At the gas flowrates between 17.5 SLM and 21 SLM, they approximately follow sinusoidal forms apart from occasional small spiky currents which correspond to arc ignitions or short cutting events. A phase-shift $\delta$ of the current from the voltage is seen in Figure 4.2. The current waveform indicates that the spiky current does not appear every half period and that the gliding arc discharge survives over several hundreds of periods at the lower gas flowrates. This indication was supported by the observations of the evolution of the discharge columns in Chapter 3. On the other hand, at the gas flowrates of 31.5 SLM and 42 SLM, the current waveforms involve sinusoidal-like waveform and frequent intense spiky current. Due to the intense spiky current, the voltage waveforms are also deformed. It is indicated that at higher flowrates, the discharge modes tend to fluctuate more frequently, since the electrical impedance differs significantly at different discharge modes primarily due to the change of the specific power dissipated from the discharge per unit length, *W*.
An electrical scheme of the AC gliding arc is shown in Figure 4.3. It is assumed that the self-inductance of the circuit *L* is dominated by that of the discharge column due to the long extension and significant fluctuation of the discharge column. It is also assumed that voltage and current waveforms are sinusoidal at the angular frequency $\omega$. The deviation from the sinusoidal waveform at higher gas flowrates will be discussed later. Since the measured photoemission intensity from the gliding arc oscillates at the angular frequency $2\omega$ [A8], it is realistic to assume that the specific power dissipated from the discharge per unit length *W* of the AC gliding arc is not constant but oscillates at the angular frequency of $2\omega$.

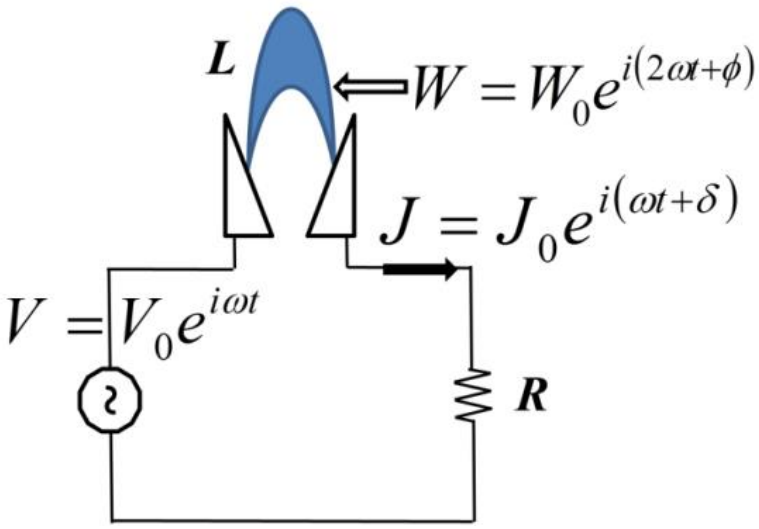


Figure 4.3. Electrical scheme of the AC gliding arc.

The supply voltage $V$ at the powered electrode, the current $J$ and the specific power $W$ dissipated from the discharge per unit length in Eq. (4) can be replaced with

$$V = V_0 e^{i\omega t}, \tag{5}$$

$$J = J_0 e^{i(\omega t+\delta)}, \tag{6}$$

$$W = W_0 e^{i(2\omega t+\phi)}, \tag{7}$$

where $V_0$, $J_0$ and $W_0$ are amplitudes and $\delta$ ( $|\delta| < \pi/2$, and thus $\cos\delta > 0$) and $\phi$ are phase shifts. Substitution of Eqs. (5-7) into Eq. (4) yields

$$V_0 = RJ_0 e^{i\delta} + \frac{W_0 l}{J_0} e^{i(\phi-\delta)} + i\omega L J_o e^{i\delta}. \tag{8}$$

Hence the phase shift $\phi$ of the specific power dissipated from the discharge per unit length is obtained:

$$\tan\phi = \frac{\frac{V_0}{J_0}\sin\delta - R\sin 2\delta - \omega L\cos 2\delta}{\frac{V_0}{J_0}\cos\delta - R\cos 2\delta + \omega L\sin 2\delta}. \tag{9}$$

The real part of Eq. (8) is

$$V_0 = RJ_0\cos\delta + \frac{W_0 l}{J_0}\cos(\phi-\delta) - \omega L J_o \sin\delta. \tag{10}$$

The general solutions of Eq. (10) are

$$J_0 = \frac{-V_0 \pm \sqrt{V_0^{\,2} + 4\omega L W_0 l\cos\delta\cdot\left(\tan\delta - \frac{R}{\omega L}\right)\cdot\cos(\phi-\delta)}}{2\omega L\cos\delta\cdot\left(\tan\delta - \frac{R}{\omega L}\right)}. \tag{11}$$

For real solutions, the discriminant must be positive or zero. In addition, the amplitude of the current $J_o$ must be positive.

Three different cases are discussed that depend on the relative values of $\tan\delta$ and the ratio of the characteristic time of the AC power supply $\omega^{-1}$ and that of the electrical circuit $L/R$. Namely $\tan\delta$ can be equal to, larger than or smaller than $R/\omega L$.

(i).

If

$$\tan\delta = \frac{R}{\omega L}, \tag{12}$$

Eq. (10) can be reduced to

$$\cos(\phi-\delta) = \frac{V_0 J_0}{W_0 l}. \tag{13}$$

After some calculations,

$$\tan\phi = \frac{\frac{\omega L}{R} + \left\{\frac{\omega^2 L^2}{R^2} + \frac{V_0^{\,2} J_0^{\,2}}{W_0^{\,2} l^2}\left(\frac{\omega^2 L^2}{R^2}+1\right) - 1\right\}^{\frac{1}{2}}}{\frac{V_0^{\,2} J_0^{\,2}}{W_0^{\,2} l^2}\left(\frac{\omega^2 L^2}{R^2}+1\right) - 1}. \tag{14}$$

(ii).
Further, if

$$\tan\delta > \frac{R}{\omega L}, \tag{15}$$

namely if the ratio of the characteristic time of the AC power supply $\omega^{-1}$ to that of the electrical circuit $L/R$ is smaller than tan $\delta$, then

$$\cos(\phi-\delta) > 0 \tag{16}$$

in order to have a positive solution in Eq. (11). In this case, the discriminant is always positive, and there exists the following positive solution for $J_0$

$$J_0 = \frac{-V_0 + \sqrt{V_0^{\,2} + 4\omega L W_0 l \cos\delta \cdot \left(\tan\delta - \frac{R}{\omega L}\right)\cdot\cos(\phi-\delta)}}{2\omega L\cos\delta\cdot\left(\tan\delta - \frac{R}{\omega L}\right)}. \tag{17}$$

Therefore, a critical length does not exist under condition (15).

(iii).
In the last case, if

$$\tan\delta < \frac{R}{\omega L}, \tag{18}$$

at least one positive solution exists in Eq. (11) as long as the discriminant is positive or zero.
When

$$\cos(\phi-\delta) \le 0, \tag{19}$$

the discriminant is always positive, and there would again be no critical length.
When

$$\cos(\phi-\delta) > 0, \tag{20}$$

$$l \le \frac{V_0^{\,2}}{4\omega L W_0 \cos\delta\cdot\left(\frac{R}{\omega L} - \tan\delta\right)\cdot\cos(\phi-\delta)} = l_{crit} \tag{21}$$

or

$$W_0 = \frac{V_0^{\,2}}{l_{crit}}\frac{1}{4\cos\delta\cdot(R-\omega L\tan\delta)\cdot\cos(\phi-\delta)}. \tag{22}$$

A critical length exists under this condition. If the voltage $V_0$ increases or the resistance $R$ decreases, the critical length will increase. In addition, as the angular frequency $\omega$ increases, the critical length steadily increases as long as condition (18) is still valid.
The specific power dissipated from the discharge per unit length $W_0$ will increase when the gas flowrate increases. It is thus predicted from Eqs. (21) and (22) that if the gas flowrate increases, the critical length will decrease. The maximum projected length of the gliding arc discharge column $l_{max}$ was obtained from the two-dimensional photos of the gliding arc discharge. This projected length in the two-dimensional photo plane is always shorter than the actual length in three dimensions. Nevertheless, it is reasonable to use the projected length as experimentally accessible measure as it should be roughly proportional to the actual length. The supply voltage $V_0$ was measured at the fixed resistance $R$ (1.45 Ω). The maximum projected length of

the gliding arc discharge column $l_{max}$ and $V_0^2/l_{max}$ at different air flowrates at a fixed frequency (31.25 kHz) is shown in Figure 4.4. Here Eq. (22) indicates that $V_0^2/l_{max}$ is proportional to $W_0$. Assuming that the maximum projected length of the discharge column is proportional to a critical length, the measured results suggest that the critical length tends to decrease and $W_0$ to increase with increasing gas flowrates in accordance with the predictions based on Eqs. (21) and (22).

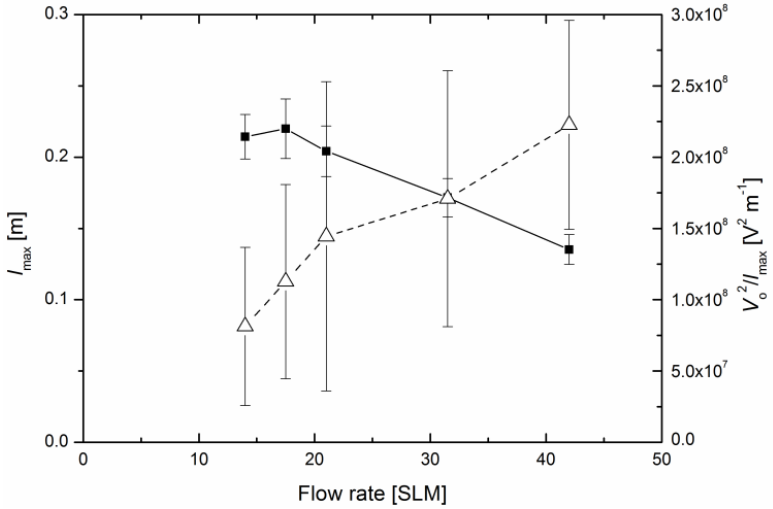


Figure 4.4. The maximum projected length of the gliding arc discharge column $l_{max}$ (solid square) and $V_0^2/l_{max}$ (open triangle) at different air flowrates. For a visual aid, they are connected by a solid line and a broken line, respectively.

Taking the ratio of $l_{crit}$ in Eq. (21) to $l_{crit\_dc}$ in Eq. (3) and assuming that $V$ and $W$ in Eq. (3) are equal to $V_0$ and $W_0$ in Eq. (21),

$$\frac{l_{crit}}{l_{crit\_dc}} = \frac{1}{\cos\delta \cdot \left(1 - \frac{\omega L}{R}\tan\delta\right) \cdot \cos(\phi - \delta)} > 1. \qquad (23)$$

Under these assumptions, if a critical length exists for the AC driven gliding arc, it is always longer than that of a corresponding DC driven gliding arc. This result is supported by the fact that the DC gliding arcs reported in the literature typically have shorter extension lengths than the AC gliding arcs [19, 46, 47, B22-B26].
It is observed that the length of the gliding arc is limited by two mechanisms: either the plasma current suddenly finds a shorter path in short-cutting events (Chapter 3) or the next discharge ignites at the closest gap $g$ of the electrodes. It is observed that the magnitude of the voltage $V_0$ increases as the length of the discharge column $l$ increases [53]. Once the voltage reaches the value at which the next gas breakdown occurs at the closest gap, the extended gliding arc will be extinguished [54]. It is therefore possible that the measured maximum length might be shorter than the achievable length predicted by Eq. (21). If the width of the closest gap increases at a fixed gas flowrate, the model suggests that the ignition voltage also increases so that the gliding arc can be further extended. However, depending on a specification of a high voltage power supply, there is a limitation of achievable maximum voltage at or

below which initial gas breakdown should occur in order to generate a gliding arc. Therefore an optimum gap $g_{opt}$ exists practically. If $g > g_{opt}$, the initial gas breakdown cannot occur. If $g < g_{opt}$, arc discharge can be more easily ignited at the closest gap so that the extended gliding arc can be extinguished. By tuning the width of the closest gap, the discharge length $l$ might be further increased. In order to verify the concept of the optimum gap experimentally, the gap between the electrodes of GA-III was varied from 2 to 8 mm. Figure 4.5 shows photos of GA-III taken by the normal video camera with an exposure time of 33.3 ms. The driving frequency was 31.25 kHz, the gas flowrate was 14 SLM, and power was approximately 800 W.

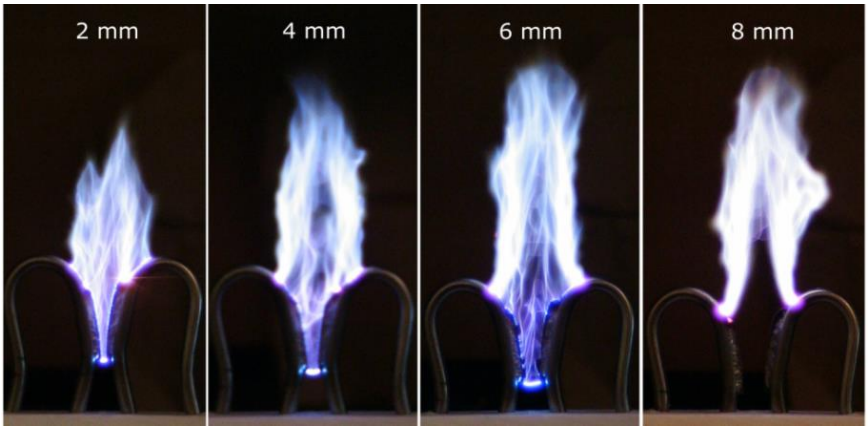


Figure 4.5. Photos of GA-III for the gaps of 2, 4, 6 and 8 mm taken by the normal video camera with an automatic exposure time. Frequency: 31.25 kHz, gas flowrate: 14 SLM, power: approximately 800 W.

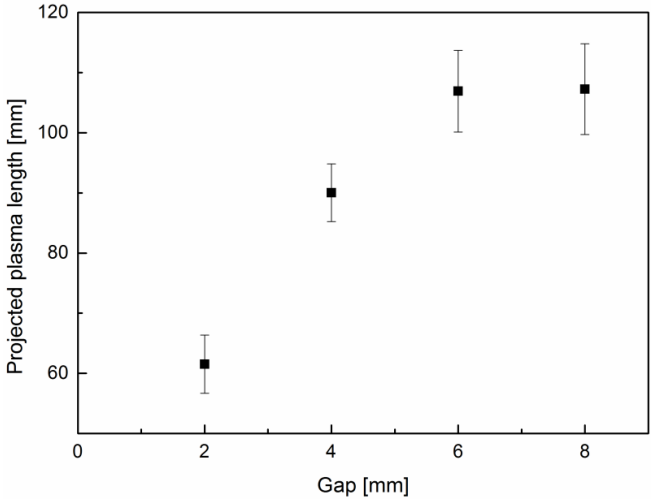


Figure 4.6. Measured projected length of the plasma column for the electrode gaps of 2, 4, 6 and 8 mm. The projected length is measured using the images taken by a normal video camera.

The projected length of the discharge column at different gaps was measured using the images taken by the normal video camera, as shown in Figure 4.6. As the gap increases, the gliding arc tends to be longer and the projected length approaches to a saturated value of approximately 110 mm, while the photoemission decreases in the region between the electrodes.

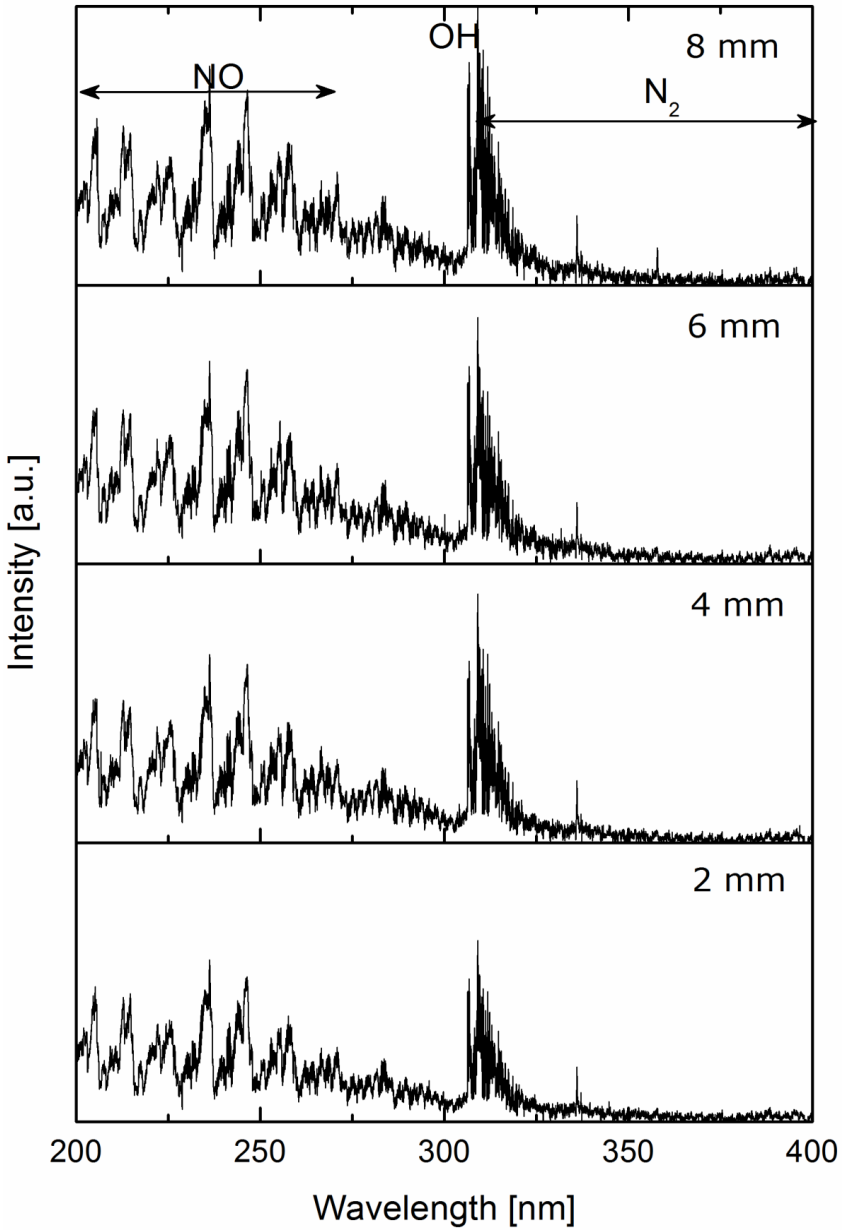


Figure 4.7. OES of GA-III for the gaps of 2, 4, 6 and 8 mm.

Measurements of OES were performed using an optical fibre, a spectrometer and a CCD. The photoemission of the GA-III at several cm above the edge of the electrodes was collected as shown in Figure 4.7. The OES includes NO, OH and $N_2$ bands. The photoemission intensity increases as the gap increases, whereas the relative intensities of the emission from these different bands are approximately the same. The chemical composition of the photo-emitting species is therefore independent of the gap width. These results in Figures 4.5, 4.6 and 4.7 mean that smaller gaps favour arc ignition but suppress extension of the plasma column. On the other hand, when the gap is too large, the discharge would not ignite. It is therefore experimentally concluded that an optimal gap exists to efficiently extend the gliding arc.

## 4.3. Summary

A stability analysis of the AC driven GA-III and GA-IV was carried out. The condition of the critical length of the gliding arc can be discriminated by the relation between the phase shift of the discharge current to the ratio of the characteristic time of the AC power supply to that of the electrical circuit. The calculation indicates that the AC gliding arcs can be preferably extended when the AC frequency increases, the serial resistance decreases and the gas flowrate is lowered. The suggested dependence of the maximum achievable discharge extension on the flowrate is demonstrated experimentally. Furthermore it is found that the critical length of an AC gliding arc would be longer than that of a corresponding DC gliding arc. It is indicated that the length of the gliding arc can be further extended by tuning the gas breakdown condition at the closest gap between the electrodes.
In order to fully determine the difference between the critical length and the maximum length of the gliding arc before extinction, parameters such as gas flow dynamics, gas temperature, geometrical aspects, and electrode materials need to be further considered.

## 5. Development of ultrasound enhanced plasma processing [A11-A16]

### 5.1 Introduction

In this chapter, the concept of the ultrasound enhanced plasma is introduced, and the application to surface modification is presented using a DBD.
Atmospheric pressure plasma surface modification is generally performed by feeding a process gas into the plasma. A boundary gas layer normally sticks at the material surface through which reactive species generated in the plasma are diffused for reaction with the surface. Due to the short lifetime of these species, only a small fraction of them can reach the surface. It is reported that ultrasonic waves with a sound power level (SPL) above 140 dB can reduce the thickness of the boundary gas layer [55]. It is therefore interesting to combine the techniques of plasma processing with ultrasound to reduce thickness of the boundary gas layer and to increase a probability of accessing generated reactive species toward material surfaces. Combinations of a plasma and ultrasonic waves have been investigated for understanding the interaction between plasma and ultrasound [56], electrical discharge machining [57], plasma etching [58], ozone generation [59], decomposition of volatile organic compounds [60], and improvement of charging performance of corona chargers [61]. Ultrasonic waves at a material surface are often generated by vibrating the material using a piezoelectric or other solid state electro-acoustic transducer. However, due to the significant difference in acoustic impedances between a solid and a gas, that is, acoustic impedance mismatch, most of the generated acoustic power by such a transducer cannot be emitted into the surrounding gas. Subsequently it is converted into thermal energy to heat materials. Therefore, ultrasound generated by such a transducer cannot efficiently reduce the thickness of the boundary gas layer at a material surface. On the other hand, a high-power gas-jet ultrasonic generator generates acoustic waves directly in a gas without acoustic impedance mismatch [55].
In this chapter, first, enhanced treatment effect for GFRP plates is demonstrated in a helium DBD driven at a frequency of 12 kHz and ca. 40 kHz with ultrasonic irradiation (*Section 5.3.1*). However, 50/60 Hz operation of a DBD is advantageous due to its simplicity and avoiding a radiation hazard related with high frequency operation, and 50 Hz plasma processing at atmospheric pressure is extensively investigated [13,62]. *Section 5.3.1* also presents a 50 Hz helium DBD with ultrasonic irradiation. However, as the use of helium gas is costly, it is of great interest to use air as a process gas. GFRP plates were also treated using a DBD in air with and without ultrasonic irradiation (*Section 5.3.2*). Furthermore, CNF coatings were treated using a helium DBD with and without ultrasonic irradiation (*Section 5.3.3*).

### 5.2 Experimental methods

Commercially available 2-mm thick GFRP plates were used as specimens (it is referred to as GFRP-II). They were cleaned and degreased with acetone and methanol. CNF coatings were prepared in a same manner as presented in *Section 2.2.2*.
The DBD was generated between two parallel plane electrodes (50 mm × 50 mm, gap: 5 mm) and driven by AC power supplies at frequencies of between 30 kHz and ca. 40 kHz, 12 kHz, and 50 Hz. When the DBD was generated at a frequency of 50 Hz with a step-up transformer, the peak-to-peak voltage was set to 30 kV, and the power measured in this way was lower than 0.5 W. It is distinctly different from a normal

DBD operated at a frequency of several kHz or higher, where the input power can be typically 100-1000 times higher. Figure 5.1 shows a schematic diagram of the DBD setup. Voltage and current were measured similarly to the previous chapters. A high-power gas-jet ultrasonic generator was placed near the top of the waveguide which is connected to the powered mesh electrode.

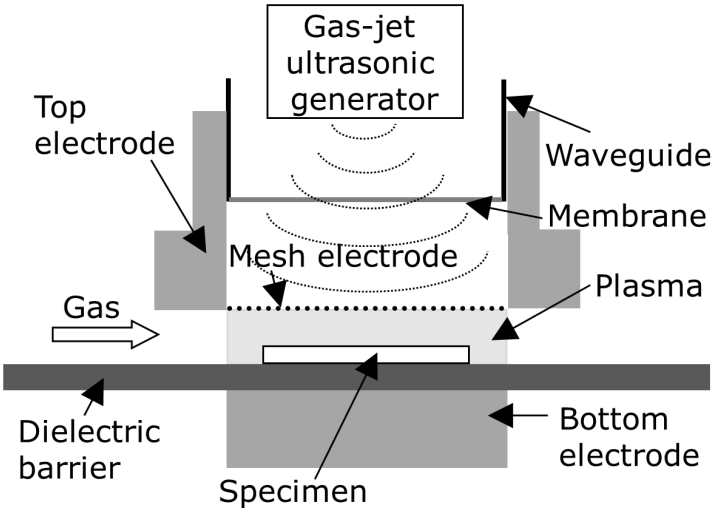


Figure 5.1. Diagram of the DBD setup with a high-power gas-jet ultrasonic generator.

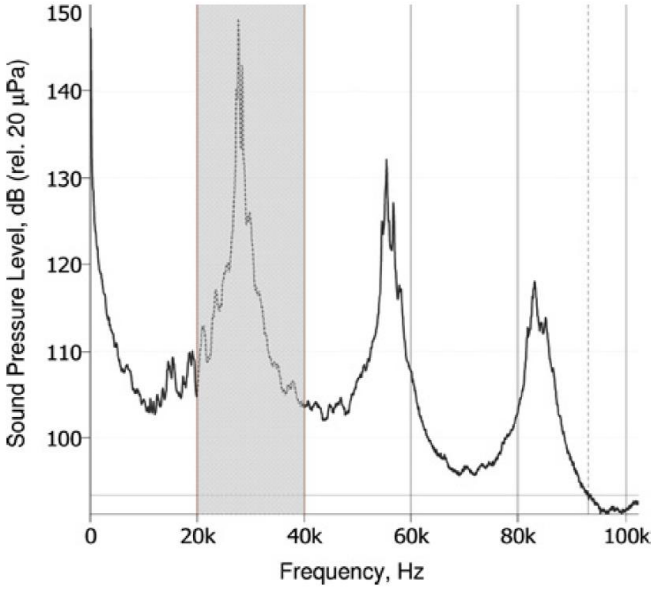


Figure 5.2. The acoustic spectrum transmitted through the mesh electrode.

The frequency range of the ultrasound was between 20 kHz and 40 kHz, and the SPL was approximately 150 dB at a material surface. Figure 5.2 shows an acoustic spectrum from the ultrasonic generator transmitted through the mesh electrode measured using a capacitive microphone and a sound analyzing system. The spectral band between 20 kHz and 40 kHz highlighted with the grey bar in Figure 5.2 was used for the calculation of the SPL by the acoustic generator. This band carries about 75% of total emitted acoustic energy and the corresponding SPL is approximately 154 dB relative to 20 μPa reference level. The plasma gas and ambient air were separated using a thin polyethylene film clamped in the waveguide. Helium or air was fed into the plasma at a flowrate of 3 SLM.
OES measurements were performed using an optical fibre and a 0.75 m spectrometer similarly to Chapters 2 and 4. Contact angles and XPS were measured similarly to Chapter 2. AFM was used to observe the surface and evaluate the roughness.

## 5.3 Results and discussion

### *5.3.1. Helium DBD*

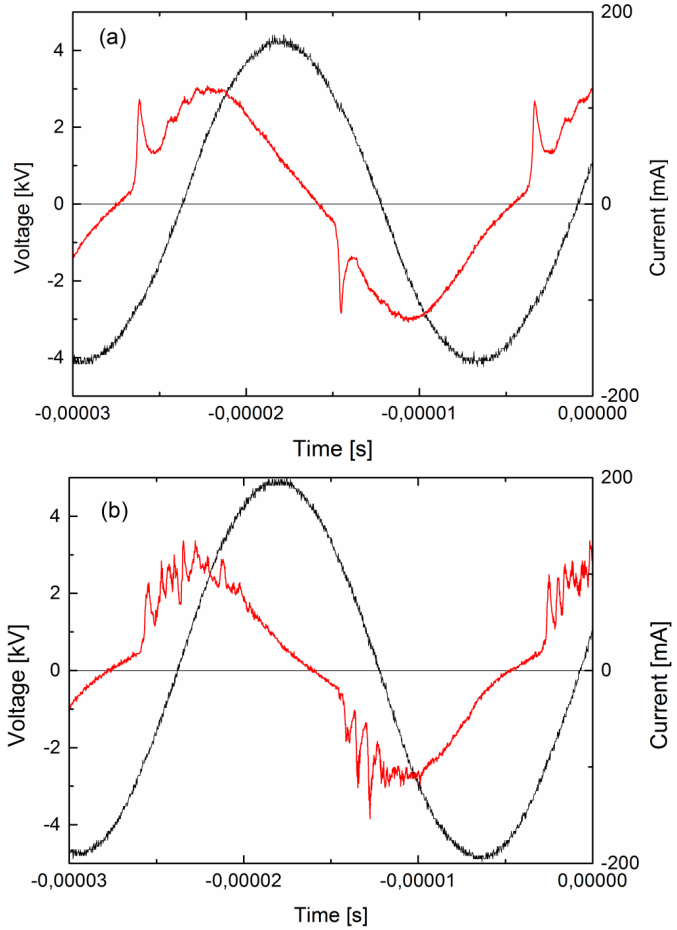


Figure 5.3. Voltage (black) and current (red) waveforms for a helium DBD operated at ca. 40 kHz at 100 W without (a) and with (b) ultrasonic irradiation.

The waveforms of voltage and current in the helium DBD without ultrasonic irradiation are shown in Figure 5.3 (a). The current waveform shows a few narrow spikes in each excitation, indicating that a homogeneous glow discharge was generated [B18]. When the ultrasound was irradiated to the DBD, a higher voltage was required to sustain the plasma at the same power than the plasma without ultrasonic irradiation. In addition, a filamentary micro-discharge was formed with ultrasonic irradiation, identified with complex spiky current waveforms of micro-discharges as shown in Figure 5.3 (b).
The current waveform at 50 Hz generally looks rather spiky due to the significant difference between the current pulse width and a period of the sinusoidal voltage waveform as shown in Figure 5.4 (a). The current pulse width of the helium DBD at 50 Hz without ultrasonic irradiation was approximately 1 μs (Figure 5.4 (a)). Ultrasonic irradiation decreases the current pulse width strongly, while it increases the height of the current several times as shown in Figure 5.4 (b). This result corresponds to the fact that the current waveform of the helium DBD driven at ca. 40 kHz changed from glow to filamentary with ultrasonic irradiation.

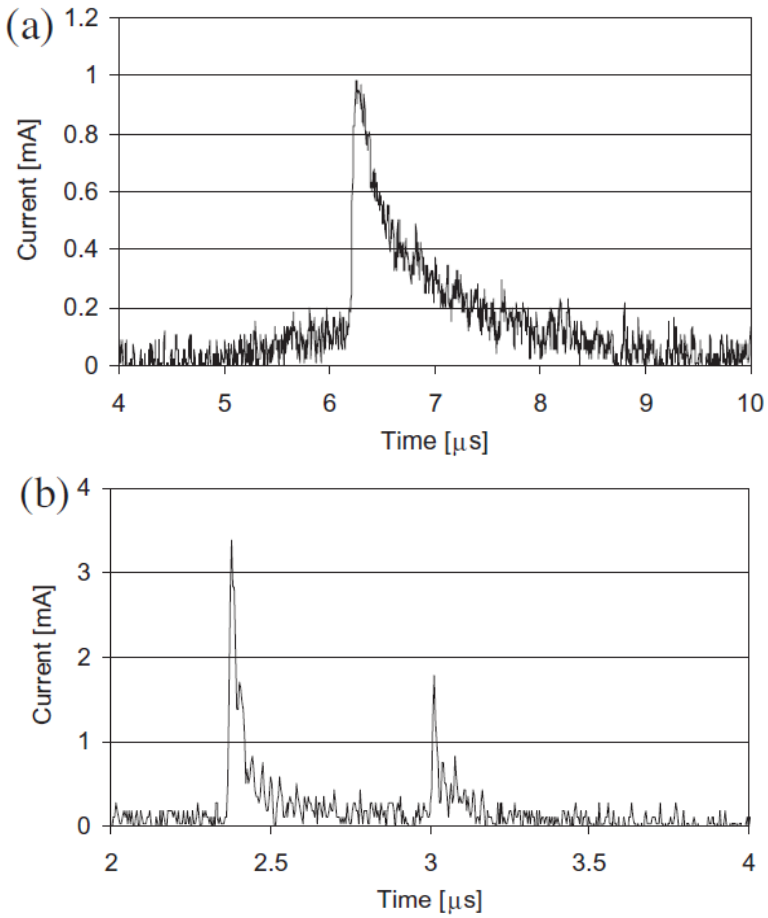


Figure 5.4. Typical current waveforms of the DBD. Without (a) and with (b) ultrasonic irradiation.

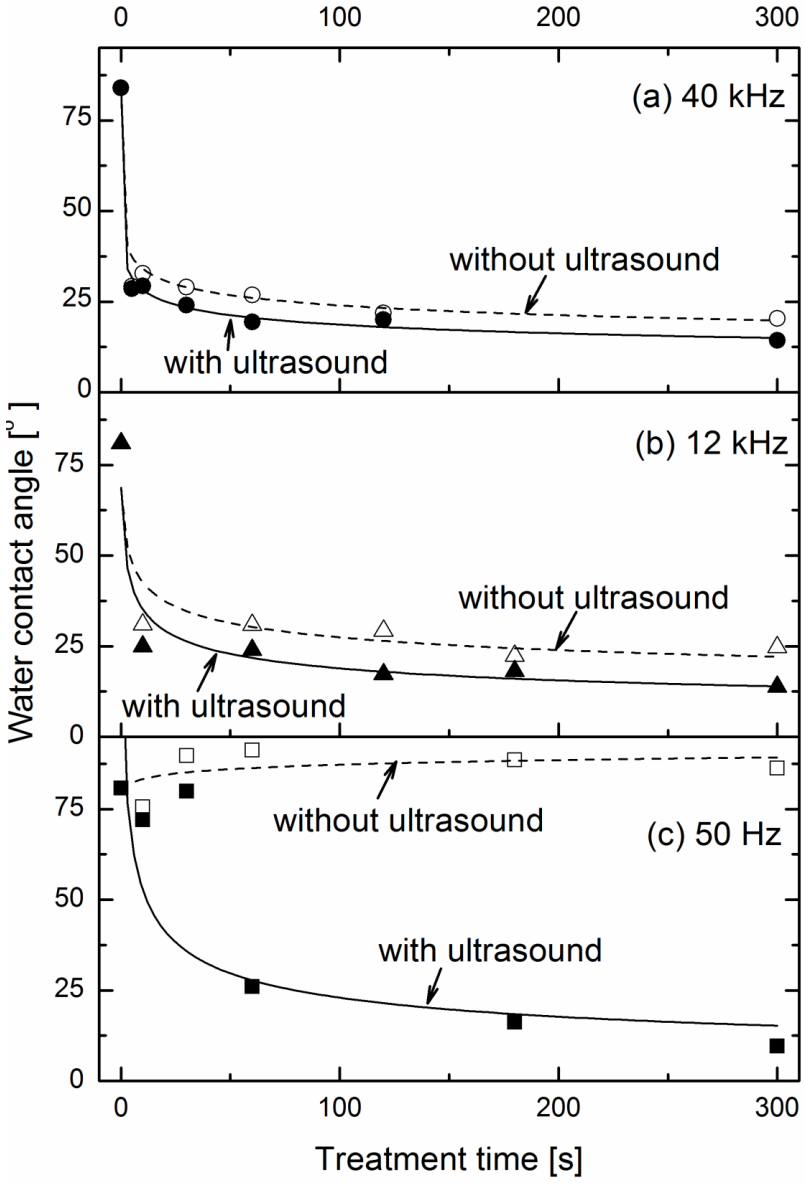


Figure 5.5. Water contact angle before and after DBD treatment operated at ca. 40 kHz (a), 12 kHz (b) and 50 Hz (c) with (solid) and without (open) ultrasonic irradiation.

Water contact angles of the GFRP-II plates were measured before and after the atmospheric pressure DBD treatment in helium at different frequencies (ca. 40 kHz, 12 kHz and 50 Hz) with and without ultrasonic irradiation. The results are shown in Figure 5.5. When the helium DBD was operated at ca. 40 kHz or 12 kHz, the water

contact angle dropped and the wettability improved significantly after the treatment for 10 s without ultrasonic irradiation, and longer treatment moderately improved the wettability. The ultrasonic irradiation consistently and moderately decreased the contact angle and improved the wettability as shown in Figure 5.5 (a) and Figure 5.5 (b). It is a significant contrast from the 50 Hz DBD treatment as shown in Figure 5.5 (c). The treatment did not significantly change the wettability even when they were treated for up to five minutes. It can be attributed to the low input energy introduced to the 50 Hz DBD in the present study. However, when the ultrasound was irradiated to the 50 Hz DBD, water contact angles markedly decreased.
AFM was used to measure the surface roughness of the GFRP-II plates before and after helium DBD treatment at ca. 40 kHz with and without ultrasonic irradiation, taking a fixed area of 2 μm × 2 μm. The average roughness of the untreated surface was approximately 1.7 – 4 nm. The GFRP-II plates were treated with the helium DBD at ca. 40 kHz with and without ultrasonic irradiation for 30 s. The roughness slightly increased to approximately 2 – 7 nm and 2 – 10 nm after the DBD treatment at ca. 40 kHz with and without ultrasonic irradiation, respectively. It is therefore unlikely that ultrasonic irradiation significantly enhances surface roughening during the helium DBD treatment at ca. 40 kHz.
On the other hand, after helium DBD treatment at 50 Hz with and without ultrasonic irradiation, no significant difference in roughness was observed. It is possibly because the energy applied to the DBD was too low for the efficient surface roughening.

Table 5.1. Elemental composition [at. %] and O/C ratio at the GFRP-II surfaces characterized by XPS. Treatment times for DBD at ca. 40 kHz and 50 Hz are 30 and 60 s, respectively.

| | treatment | untreated | DBD | | untreated | DBD | |
|---|---|---|---|---|---|---|---|
| | Frequency | - | 40 kHz | | - | 50 Hz | |
| | ultrasound | - | - | √ | - | - | √ |
| Elemental composition [at.%] | C | 76.5 | 71.5 | 68.3 | 81.1 | 81.8 | 79.8 |
| | O | 22.6 | 27.5 | 30.5 | 18.5 | 17.9 | 19.9 |
| | N | 0.6 | 0.5 | 0.2 | 0.4 | 0.3 | 0.3 |
| O/C ratio | | 0.30 | 0.39 | 0.45 | 0.23 | 0.22 | 0.25 |

The results of the XPS analysis are summarized in Table 5.1. After the DBD treatment at 40 kHz without ultrasonic irradiation, the O/C ratio increased by 0.09, indicating the introduction of oxygen containing polar functional groups on the surfaces. Ultrasonic irradiation further enhanced oxidation at the surface. The result agrees with the water contact angles shown in Figure 5.5 (a).
On the other hand, the O/C ratio remained almost unchanged after the DBD treatment at 50 Hz without ultrasonic irradiation, while it slightly increased from 0.23 to 0.25 after the plasma treatment with ultrasonic irradiation. An increase in the O/C ratio indicates that oxygen-containing polar functional groups are introduced at the surfaces, improving the wettability. This result shows an agreement with that of the contact angles in Figure 5.5 (c). No clear change was seen in the nitrogen content before/after the helium DBD treatment at 50 Hz with/without ultrasonic irradiation.
Figure 5.6 shows TOF-SIMS ion images of the surfaces before and after the 50 Hz DBD treatments with and without ultrasonic irradiation. Oxygen containing species were homogeneously distributed in all cases. The homogeneous distribution of

nitrogen species was observed only on the specimen surface after the 50 Hz DBD treatment with ultrasonic irradiation. It is suggested that nitrogen from ambient air reacted with the sample surfaces during the plasma treatment with ultrasonic irradiation. XPS detects similar amounts of traces of nitrogen on all the surfaces, while TOF-SIMS detects more intense nitrogen species on the surfaces treated with ultrasonic irradiation. This difference can be explained from the fact that TOF-SIMS is more surface sensitive (~1 nm) compared to XPS (5–10 nm).

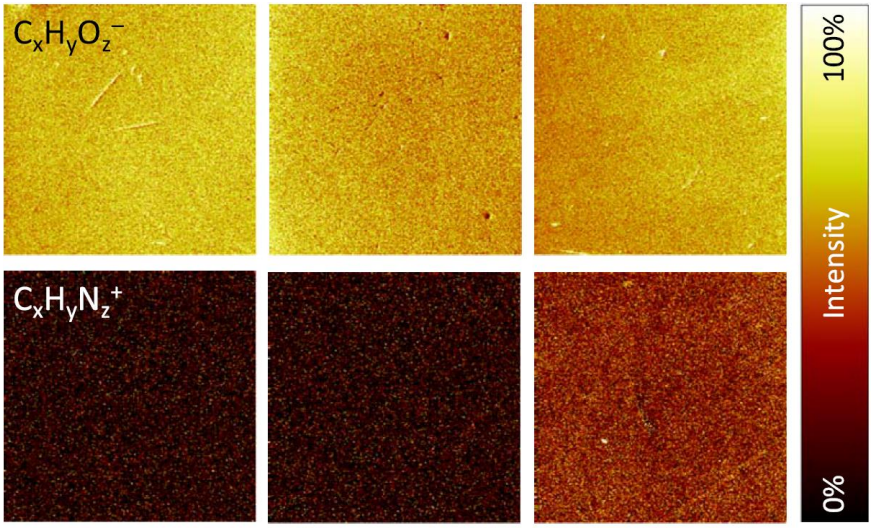


Figure 5.6. TOF-SIMS ion images (500 µm × 500 µm) showing the intensity distribution of $C_xH_yO_z$ and $C_xH_yN_z$ markers on the GFRP-II surfaces, corresponding to oxygen- and nitrogen-containing functional groups, respectively: (a) untreated, (b) DBD treated at 50 Hz for 60 s, and (c) DBD treated at 50 Hz for 60 s with ultrasonic irradiation. Brown corresponds to no intensity and white to 100% intensity.

*5.3.2. Air DBD*

It is presented that the helium DBD changed from a homogeneous glow discharge to filamentary micro-discharges with ultrasonic irradiation in *Section 5.3.1* accompanied with a change of current waveforms as shown in Figure 5.3. However, air DBD without ultrasonic irradiation is filamentary, identified from the presence of complex spiky current waveforms of micro-discharges as shown in Figure 5.7 (a). Ultrasonic irradiation does not change the complex spiky current waveforms of the air DBD as shown in Figure 5.7 (b).

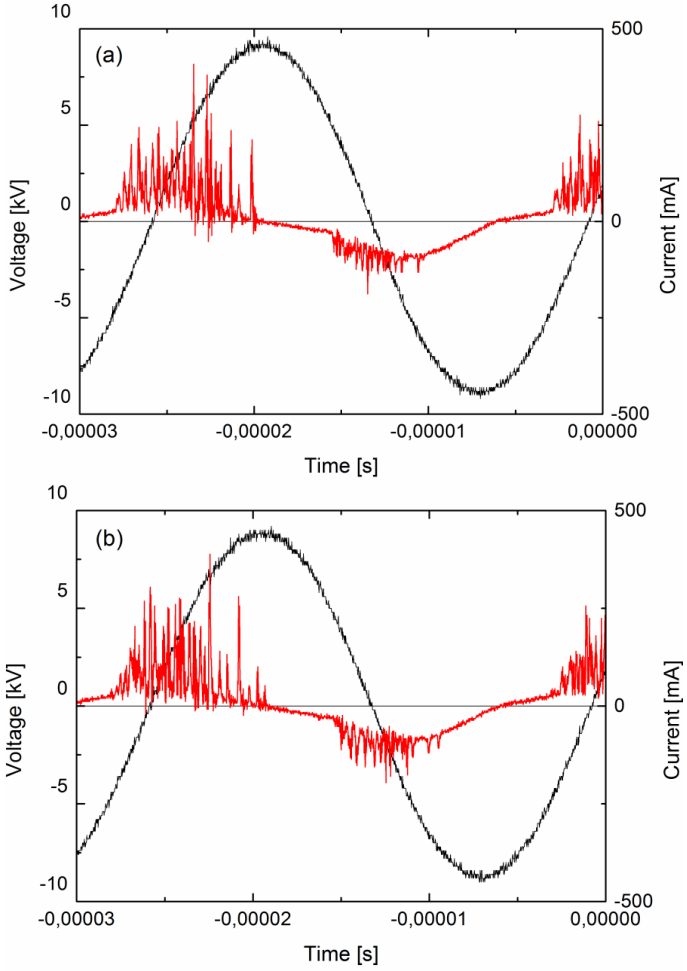


Figure 5.7. Voltage (black) and current (red) waveforms for an air DBD operated at ca. 40 kHz at 100 W without (a) and with (b) ultrasonic irradiation.

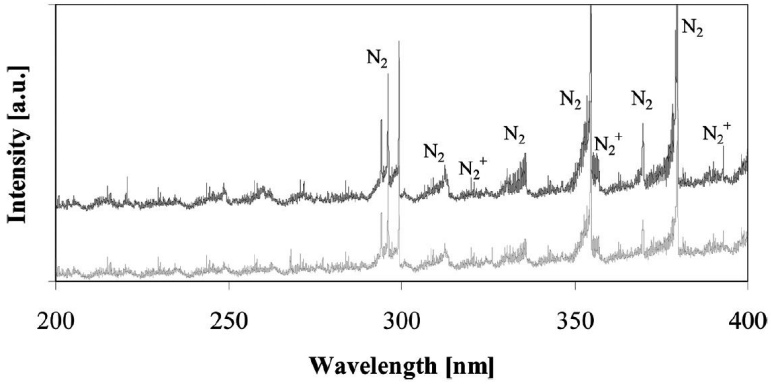


Figure 5.8. OES of the air DBD with (above) and without (below) ultrasonic irradiation.

OES was measured to identify excited species in the DBD. Figure 5.8 shows OES of the air DBD with and without ultrasonic irradiation, including $N_2$ and $N_2^+$ bands [37]. Ultrasonic irradiation did not change the OES significantly.

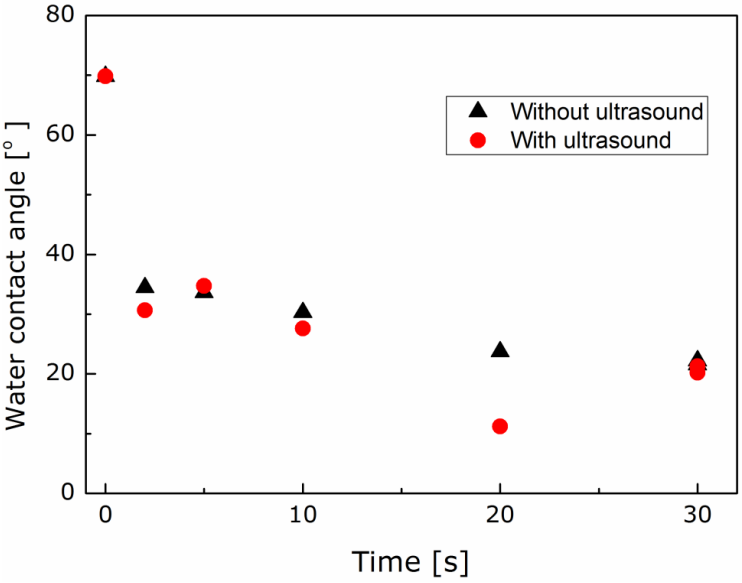


Figure 5.9. Water contact angle before and after plasma treatment with (circle) and without (triangle) ultrasonic irradiation.

The treatment drastically changed the GFRP-II surface wettability. The water contact angle on the GFRP-II plate was ~84° before the air DBD treatment, dropped markedly to around 35° after 2-s treatment without ultrasonic irradiation, and further decreased after longer treatments as shown in Figure 5.9. Ultrasonic irradiation during the air DBD treatment tended to decrease the contact angle moderately.

XPS survey analysis was carried out in order to analyze the elemental composition of the GFRP-II surfaces before and after the treatments for 5 and 30 s with and without ultrasonic irradiation. The results are summarized in Table 5.2. After the treatment for 5 s without ultrasonic irradiation, the O/C ratio increased from 0.23 to 0.29. The O/C ratio further increased after the treatment for 30 s. An increase in the O/C ratio indicates that oxygen containing polar functional groups are introduced onto the surfaces. Ultrasonic irradiation further enhanced oxidation at the surface. No clear change was seen in the nitrogen content before/after the treatments.

Table 5.2 also summarizes de-convolution of C1s spectra of the GFRP-II surfaces before and after the treatments for 30 s with and without ultrasonic irradiation. Peaks at approximately 285.0 eV, 286.5 eV, 288.0 eV, and 289.5 eV can be assigned to C-H/C-C, C-O-C/C-OH, C=O (carbonyl), and COO (carboxyl), respectively. The C1s component peak of (carboxyl) increased after longer treatment or with ultrasonic irradiation.

Table 5.2. Elemental composition [at. %], O/C ratio, and C1s peak components of the GFRP-II surfaces before and after the treatments characterized by XPS.

| | | Untreated | Air DBD | | | |
|---|---|---|---|---|---|---|
| | Time [s] | - | 5 | 30 | 5 | 30 |
| | Ultrasound | - | - | - | √ | √ |
| Elemental composition [at.%] | C | 81.0 | 77.1 | 72.2 | 70.7 | 70.8 |
| | O | 18.5 | 22.5 | 27.3 | 28.4 | 28.7 |
| | N | 0.4 | 0.4 | 0.5 | 0.9 | 0.5 |
| O/C ratio | | 0.23 | 0.29 | 0.38 | 0.40 | 0.41 |
| Deconvolution of C1s [%] | C-C, C-H (285.0 eV) | 59 | 54 | 52 | 46 | 50 |
| | C-O (286.5 eV) | 24 | 27 | 22 | 29 | 21 |
| | C=O (288.0 eV) | 7 | 11 | 15 | 11 | 15 |
| | COO (289.5 eV) | 10 | 8 | 10 | 14 | 14 |

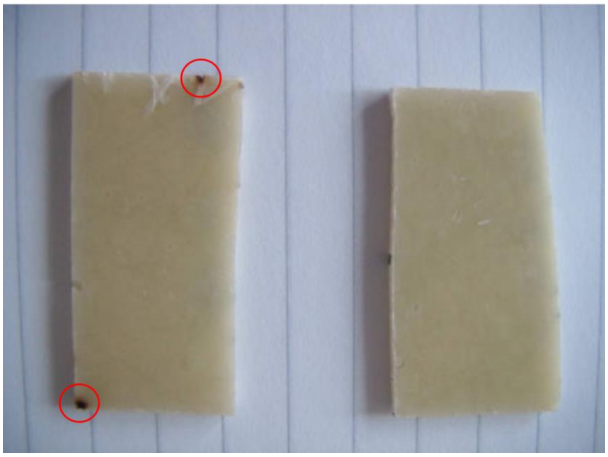

Figure 5.10. GFRP-II plates (ca. 18 mm × 40 mm) treated by the air DBD with (right) and without (left) ultrasonic irradiation [B27]. The damaged locations are indicated by red circles.

During the DBD treatment in air without ultrasonic irradiation, occasional arcing was observed. Consequently, the GFRP-II plate surface was partly damaged, as shown in Figure 5.10 (left). It was found that the arc ignition was suppressed during the air DBD treatment by the ultrasonic irradiation, preventing the GFRP-II plate from damaging (Figure 5.10 right).
Randomly distributed oxidized spots were observed in the TOF-SIMS ion image at the GFRP-II plate surface after the air DBD treatment without ultrasonic irradiation as shown in Figure 5.11 (b). Such spots were not seen at the surface after the air DBD treatment with ultrasonic irradiation (Figure 5.11 (c)). This indicates that ultrasonic irradiation can not only suppress arcing but also improve uniformity of the treatment. The homogeneous distribution of nitrogen species on only the treated sample surfaces suggests that nitrogen from ambient air reacted with the sample surfaces during treatment with/without ultrasonic irradiation.

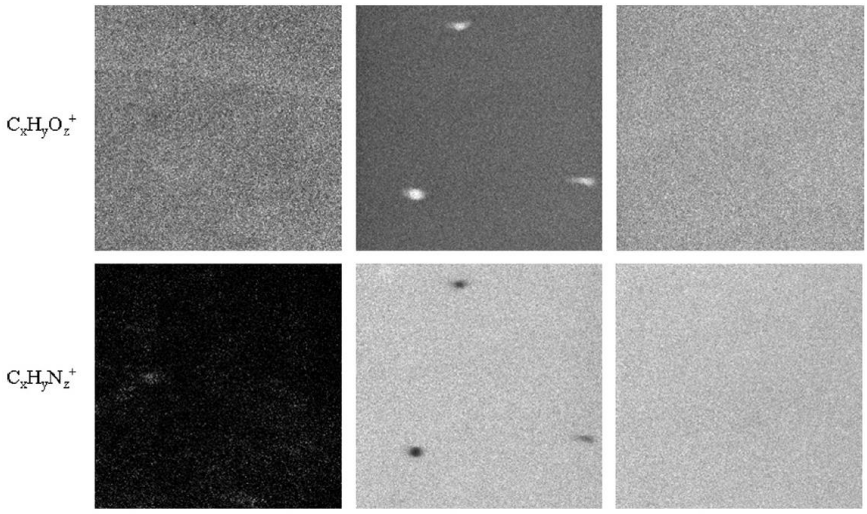


Figure 5.11. TOF-SIMS ion images (500 μm × 500 μm) showing the lateral intensity distribution of $C_xH_yO_z^+$ and $C_xH_yN_z^+$ markers corresponding to oxygen- and nitrogen-containing functional groups, respectively, on the GFRP-II surfaces: (a) untreated, (b) 30-s plasma treated, and (c) 30-s plasma treated with ultrasonic irradiation. Black corresponds to no intensity, grey to some intensity, and white to 100 % intensity.

AFM was used to measure the surface roughness of the GFRP-II plates. The average surface roughness of the untreated surface was 1.6 ± 0.2 nm. The GFRP-II plates were treated with the air DBD with and without ultrasonic irradiation for 30 s. The roughness increased to 3.3 ± 0.4 nm and 3.6 ± 0.6 nm after the plasma treatment with and without ultrasonic irradiation, respectively. It is therefore concluded that air DBD treatment significantly increase the surface roughness, but additional ultrasonic irradiation do not change the surface roughness to any detectable degree.

*5.3.3. Treatment of CNF coatings*

Deionized water and glycerol were used as test liquids for the contact angle measurement. Values of contact angles were scattered substantially, and thus the measurements were repeated for some treatment conditions. Possible causes of the scatter include uniformity and reproducibility of the CNF coating and the DBD treatment. Difference of the contact angles for the untreated CNF coatings was observed between two sets of the measurements as shown in Figure 5.12 (solid square), and thus influence of the specimen uniformity is not negligible. On the other hand, using the same setup of the DBD with and without ultrasonic irradiation for treating GFRP-II plates, less significant scatters of the contact angles were presented in *Sections 5.3.1-5.3.2*. A major cause of the significant deviation of the measured contact angles might be the process of coating application.

The water contact angle before the plasma treatment was typically 20º - 25º, and decreased to 12º-20º after the plasma treatment as shown in Figure 5.12 (a). Ultrasonic irradiation during the plasma treatment further decreased the water contact angle to below 10°. With ultrasonic irradiation, the reactive species in a plasma can approach the material surface more frequently, thereby enhancing the plasma

treatment effect. However, it can be seen that increasing the plasma power does not affect the water contact angle significantly especially without ultrasonic irradiation. It is reported that plasma treatment could often introduce polar functional groups on the surfaces in a short time, while the surface roughness could gradually increase as the increase in the treatment time [B6]. Therefore, at a fixed treatment time, higher plasma power would be needed for significant etching. Figure 5.12 (a) shows that the water contact angle further decreased at the power of 100 W when ultrasound was irradiated, indicating that ultrasonic irradiation would efficiently improve etching.

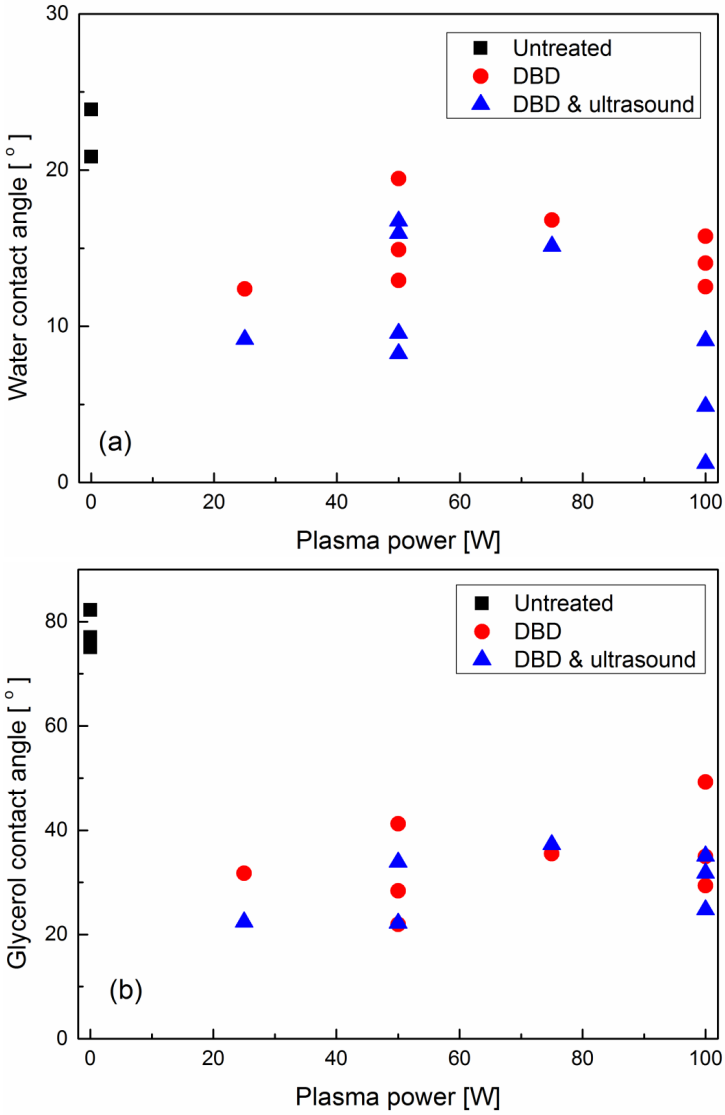


Figure 5.12. Contact angles of CNF coatings before and after helium DBD treatment for 30 s with varying plasma power, and with and without ultrasonic irradiation. Test liquids: (a) deionized water and (b) glycerol.

In the case of glycerol, as shown in Figure 5.12 (b), the contact angle before the plasma treatment was 75º-85º, which then markedly decreased to 20º - 50º after the plasma treatment. Ultrasonic irradiation further lowered the contact angle, while the influence of increasing plasma power was insignificant. The enhancement in glycerol wetting through the plasma treatment is beneficial since CNFs are usually dispersed in an organic solvent before being mixed into an organic polymer matrix during the composite manufacturing. The enhancement in glycerol wetting will thus potentially improve the processability and mechanical properties of the CNF composites.

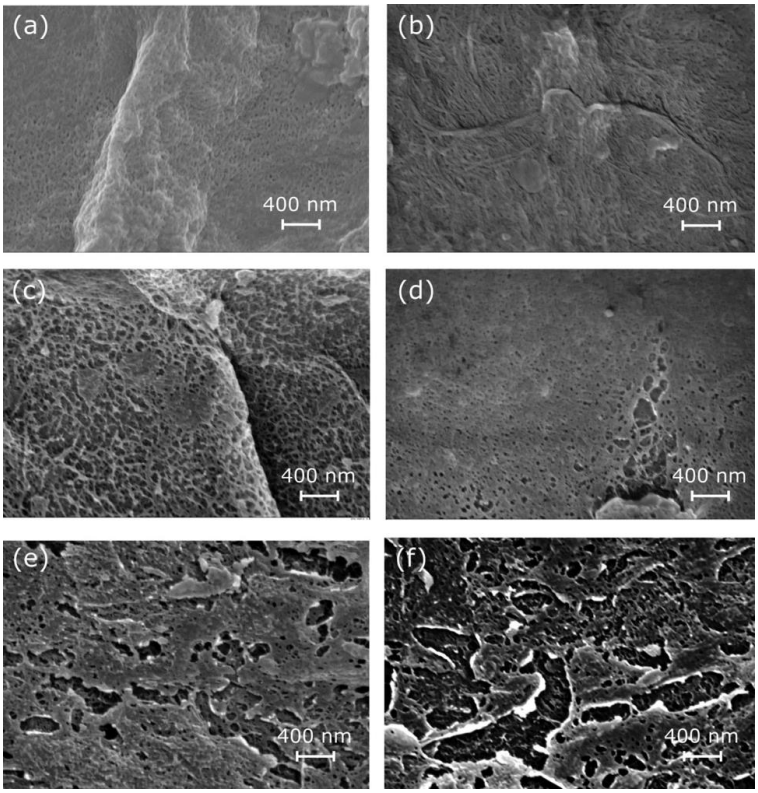


Figure 5.13. FE-SEM images of CNF coatings: (a,b) untreated, (c,d) plasma treated (100 W, 30 s), and (e, f) plasma treated (100 W, 30 s) with ultrasonic irradiation.

Figure 5.13 shows the FE-SEM images of the CNF coatings before and after the DBD treatment. Before the DBD treatment, the CNF coatings had a relatively smooth surface, seen in Figure 5.13 (a and b). Figure 5.13 (c) shows that the CNF surface became rougher following the DBD treatment, as indicated by the appearance of skeleton-like structures. This type of surface roughening is caused by selective plasma-chemical etching of weaker domains such as low-molecular weight domains and amorphous phases. As shown in Figure 5.13 (d), which is a different location on the same specimen as was used for Figure 5.13 (c), the majority of the surface area is less severely etched. This indicates that the plasma treatment etches the surface unevenly, as observed at micrometre scale. On the other hand, as shown in Figure

5.13 (e and f), when ultrasonic irradiation was combined with the DBD treatment, the surfaces were uniformly modified, and the nanoscale skeleton-like structures seen in Figure 5.13 (c) were hardly seen. *Section 5.3.2* presented that uniformity of DBD treatment was improved by ultrasonic irradiation; however, it was at a different length scale than it is in this section. Highly oxidized spots were randomly distributed on a polyester surface at a sub-millimetre range by DBD treatment in air, whilst the surface was uniformly oxidized without such spots under ultrasonic irradiation as discussed in *Section 5.3.2*. The results of this section indicate that the DBD treatment can roughen the CNF surface by selective etching of weaker domains, while ultrasonic irradiation can improve the uniformity of the roughening at micrometre level. From the perspective of CNF composites, an increased roughness indicates a larger surface area of the CNFs, which increases its interaction with the polymer matrix through a possibly improved physical interlocking at the fibre/matrix interface.

Table 5.3. Elemental composition and curve-fitted spectral data of C1s of the CNF coatings before and after plasma treatment (100 W, 30 s).

| | | Untreated | DBD | DBD & ultrasound |
|---|---|---|---|---|
| Elemental composition [at.%] | C | 60.1 | 49.7 | 47.3 |
| | O | 36.9 | 43.3 | 45.6 |
| | N | 0.9 | 1.5 | 0.9 |
| | Ca | 1.5 | 4.8 | 5.1 |
| Deconvolution of C1s [%] | C-C, C-H (285.0 eV) | 36 | 27 | 18 |
| | C-O (286.5 eV) | 48 | 44 | 40 |
| | C=O (288.0 eV) | 16 | 21 | 25 |
| | COO (289.5 eV) | 0 | 8 | 17 |

XPS measurements were carried out to analyze the elemental composition of the CNF coatings, summarized in Table 5.3. The oxygen content increased from 37 at.% (O/C ratio: 0.61) to 43 at.% (O/C ratio: 0.87) due to the DBD treatment, while the calcium content increased from 1.5 at.% to 4.8 at.%. The increase in the calcium content can be interpreted as preferential etching of the organic components. Furthermore, ultrasonic irradiation enhanced the oxidation (O/C ratio: 0.96). The trends of the XPS survey analysis correspond to those of the contact angle measurements.
Deconvolution of C1s spectra was performed to study the functional groups on the CNF coatings, as shown in Table 5.3. C-C, C-H and C-O (single bond) contents decreased, while C=O (carbonyl) and COO (carboxyl) contents increased following the DBD treatment. Ultrasonic irradiation further enhanced these effects. The increase in C=O and COO contents on the CNFs surfaces can improve its compatibility with organic solvents of medium polarity such as acetone, which is a commonly used solvent for dispersion of CNFs. In addition, increase in C=O and COO contents can improve the interaction of CNF with polymer matrix during processing. It is therefore indicated that the DBD treatment and the simultaneous ultrasonic irradiation can improve the dispersion level of CNFs, and their adhesion with the matrix.

It has been reported that the O/C ratio of the cellulose fibres before processing is approximately 0.66, as characterized by XPS [63], which is in good agreement with that of the untreated CNFs in the present study (Table 5.3). Corona treatment oxidized the cellulose fibre surfaces, but the reported achievable COO content of less than 7 % is significantly lower than that achieved in the present study (17 %).
A similar assessment on CNFs was carried out using GA-IV plasma at atmospheric pressure in *Section 2.3.3*. GA-IV treatment enhanced the oxidation and roughness of the CNF surface; however, longer treatment time weakened these effects. In addition, the level of oxidation of the GA-IV treated CNFs based on XPS C1s analysis (*Section 2.3.3*) was comparable to that of the corona treated cellulose [63]. It is therefore concluded that the atmospheric pressure DBD treatment with ultrasonic irradiation can oxidize the cellulose surfaces more efficiently than corona or GA-IV treatment.

## 5.4. Summary

A helium DBD in a glow mode changed to a filamentary discharge by the ultrasonic irradiation. Plasma treatment of the GFRP-II surfaces improved the wettability, and increased the roughness. The principal effect of ultrasonic irradiation can be attributed to enhanced surface oxidation during plasma treatment.
A 50-Hz DBD plasma treatment can be an economical method for surface modification, but without ultrasonic irradiation it did not change the surface properties of the GFRP-II plates significantly under the present tested conditions. The surface roughness remained almost unchanged after the plasma treatments with and without ultrasonic irradiation. Ultrasonic irradiation to the 50-Hz DBD enhanced the treatment efficiency markedly so that a certain amount of polar functional groups were introduced at the GFRP-II surfaces. This is in marked contrast to the 40-kHz DBD where the ultrasonic irradiation enhanced treatment efficiency only moderately.
A DBD in air was also used to treat GFRP-II surfaces. Ultrasonic irradiation during the plasma treatment suppressed arcing, but did not change the OES significantly. The polar component of the surface energy, the oxygen content, and the content of carboxyl group at the GFRP-II surface increased markedly after plasma treatment. Longer treatment or adding ultrasonic irradiation during the treatment tended to increase them furthermore. Oxygen and nitrogen containing functional groups were uniformly attached at the surfaces by the treatment with ultrasonic irradiation. On the other hand, randomly distributed oxidized spots were found at the surfaces after the treatment without ultrasonic irradiation, possibly with relevance to occasional arcing. The principal effect of ultrasonic irradiation on the surface can be again attributed to enhanced surface oxidation during plasma treatment.
DBD treatment of CNF coatings enhances the wettability by water and glycerol. The DBD treatment oxidized the coating surface and etched it unevenly. Ultrasonic irradiation enhanced the oxidation of the coating and the uniformity of the treatment. The said modifications are advantageous in enhancing the interaction of CNFs with a general organic solvent to improve their dispersion, and to ameliorate their adhesion with the polymer matrix during the manufacturing of CNF polymer composites. It is thus demonstrated that a DBD plasma treatment with ultrasonic irradiation is a promising technique to modify GFRP and CNF surfaces before composite processing.

## 6. Ultrasound enhanced gliding arcs [A17, A18]

### 6.1. Introduction

It is demonstrated in Chapter 5 that effects of DBD can be enhanced by the ultrasonic irradiation. In this chapter, gliding arcs are chosen as plasma sources and effects of ultrasonic irradiation are investigated. GFRP-II plates are treated with the gliding arc with and without ultrasonic irradiation. OES was used for plasma diagnostics. The treated surfaces are characterized using contact angle measurement, XPS, TOF-SIMS and AFM. In addition, a gliding arc (GA-IV) with and without ultrasonic irradiation is observed by using a high-speed camera.

### 6.2. Experimental methods

Commercially available 2-mm thick GFRP-II plates were used as specimens. They were cleaned and degreased with acetone and methanol.
GA-II and GA-IV were used in this chapter. The air flowrates of GA-II and GA-IV were 20 and 17.5 SLM, respectively. For the observation of the gliding arc with a high-speed camera, GA-IV was used. For the treatment of GFRP-II plate surface, GA-II was used. The operation conditions are similar to those presented in Chapters 1-4, except that they were tilted at a grazing angle of approximately 30º. Figure 6.1 shows a schematic diagram of a side view of the setup. Figure 6.2 shows photos of GA-II with/without ultrasonic irradiation. A specimen was fixed on a holder which moved forward and back at a speed of 180 mm $s^{-1}$, similarly to the treatment in Chapter 2. Ultrasonic waves were introduced to the gliding arc similarly to Chapter 5. The OES measurements were performed using an optical fibre. XPS and TOF-SIMS analyses were carried out and AFM imaging of GFRP-II plates was performed. The GFRP-II plates for TOF-SÌMS and AFM were treated using GA-II at 490 and 540 W with and without ultrasonic irradiation, respectively.

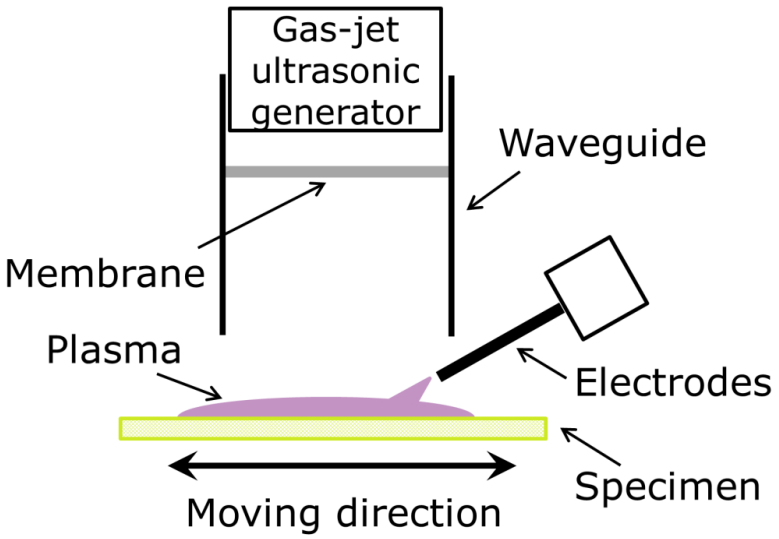


Figure 6.1. A side view of the gliding arc setup with a high-power gas-jet ultrasonic generator.

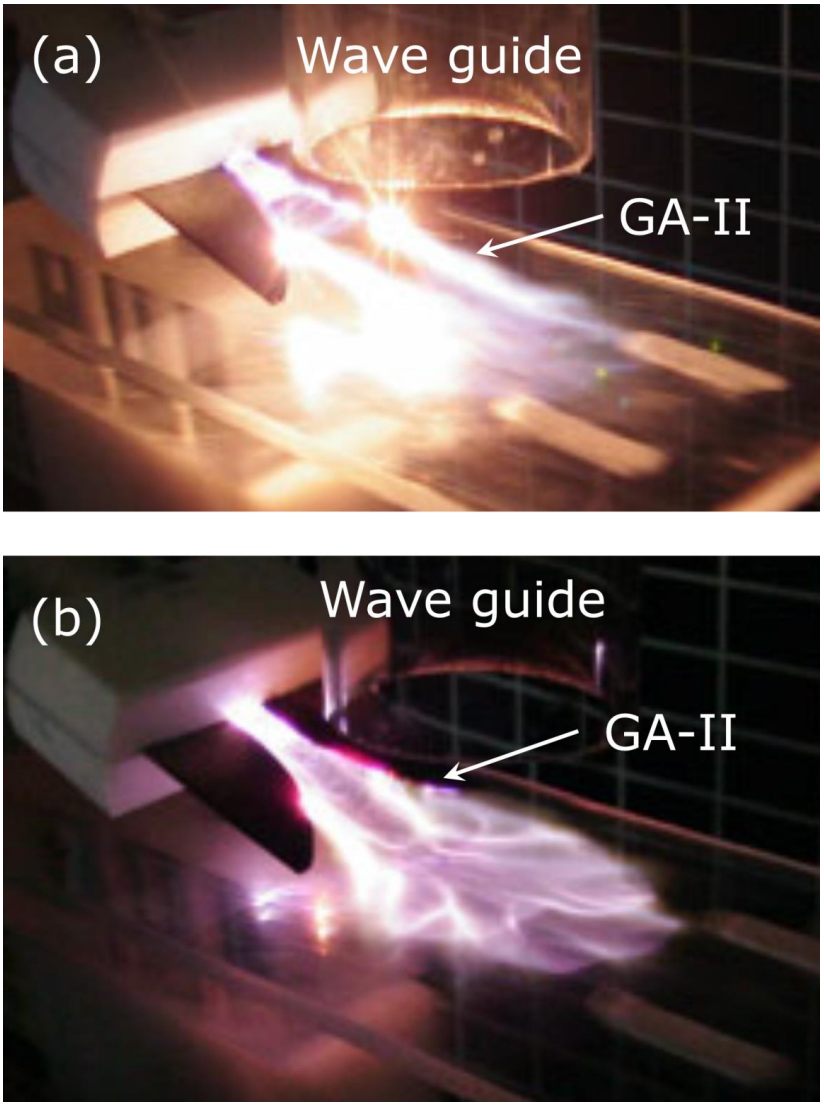


Figure 6.2. GA-II (a) without and (b) with ultrasonic irradiation [B27].

## 6.3. Results and discussion

The performance of GA-IV surface treatment was investigated using a high speed camera. Ultrasonic irradiation to GA-IV reduced the thickness of the boundary gas layer, as shown in Figure 6.3, indicating improvement of surface treatment effect. The OES of GA-II was measured to identify excited species in the discharge and to evaluate the rotational temperature. A typical OES includes the emissions from $N_2$, $N_2^+$, NO, OH. The OH comes from ambient air humidity. The intensity of optical emission, including OH, NO, $N_2$ and $N_2^+$ bands, significantly decreased with

ultrasonic irradiation. The rotational temperatures in the discharge with and without ultrasonic irradiation were 3200 and 3500 K, respectively. The difference in the rotational temperatures of a plasma with and without ultrasound was discussed in [64]. It is reported that an increase in the acoustic wave intensity can lead to a growth in the plasma column diameter and the generation of a uniform non-contracted discharge at high gas pressures. Consequently, an acoustic wave can reduce the gas temperature of a plasma at high pressure. This can be a reason of slightly reduced temperature of the gliding arc with ultrasonic irradiation compared to the gliding arc without ultrasound.

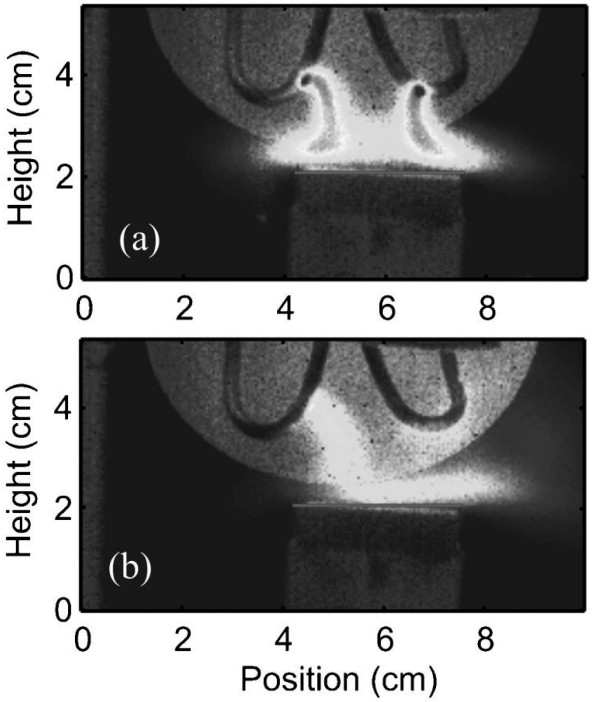


Figure 6.3. Average of 10 000 images of tilted GA-IV at gas flow-rate of 17.5 SLM (b) with and (a) without ultrasonic irradiation.

GA-II treatment drastically changed the GFRP-II surface wettability. The water contact angle on GFRP-II plate was approximately 72° before the treatment, dropped markedly to below 20° and tended to be lowered at high power to the plasma or with ultrasonic irradiation as shown in Figure 6.4.
XPS analysis was carried out to compare the elemental composition of the GFRP-II surfaces before and after the treatment. Carbon, oxygen and a small amount of nitrogen were detected. The nitrogen content was 0.4 at. % before treatment, and from 1 to 2 at. % after the treatment. Figure 6.4 shows the O/C ratio at GFRP-II surfaces before and after the treatment with and without ultrasonic irradiation. After the treatment without ultrasonic irradiation, the O/C ratio increased from 0.23 to approximately 0.36. When the input power was 370 W or higher with ultrasonic irradiation, the O/C ratio was as high as approximately 0.4. The results indicate that

ultrasonic irradiation can enhance oxidation at the GFRP-II surfaces. On the other hand, the O/C ratio was only 0.35 at the surface treated at the input power of 260 W with ultrasonic irradiation. A possible explanation of this rather low O/C ratio is that the input power might not be high enough to sustain a stable discharge, since ultrasonic irradiation enhances observed fluctuations of the discharge.

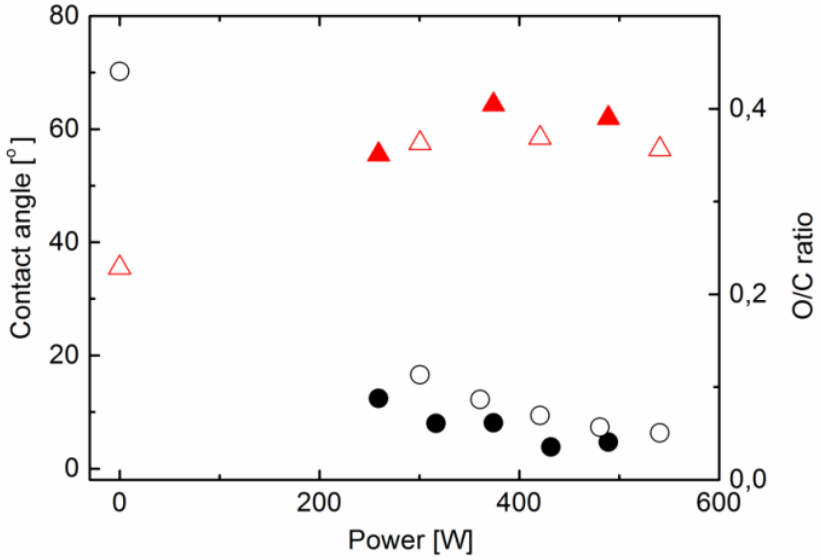


Figure 6.4. Water contact angle (scircle) and O/C ratio (triangle) of GFRP-II before and after GA-II treatment with (solid) and without (open) ultrasonic irradiation.

Table 6.1. C1s peak components of the GFRP surfaces before and after the treatments characterized by XPS.

| | | Untreated | GA-II | | | | | |
|---|---|---|---|---|---|---|---|---|
| | Power [W] | - | 300 | 420 | 540 | 260 | 374 | 489 |
| | Ultrasound | - | - | - | - | √ | √ | √ |
| De-convolution of C1s [%] | C-C, C-H (285.0 eV) | 59 | 50 | 48 | 46 | 51 | 47 | 46 |
| | C-O (286.5 eV) | 24 | 29 | 27 | 31 | 24 | 31 | 28 |
| | C=O (288.0 eV) | 10 | 9 | 12 | 12 | 13 | 11 | 10 |
| | COO (289.5 eV) | 8 | 12 | 13 | 12 | 13 | 12 | 15 |

The deconvolution of C1s spectra of the GFRP-II surfaces before and after the treatment with and without ultrasonic irradiation is summarized in Table 6.1. The C1s component peaks of C-O-C/C-OH, C=O (carbonyl), COO (carboxyl), increased after GA-II treatment with and without ultrasonic irradiation. The C1 peak of carboxyl group seems to increase slightly with ultrasonic irradiation.

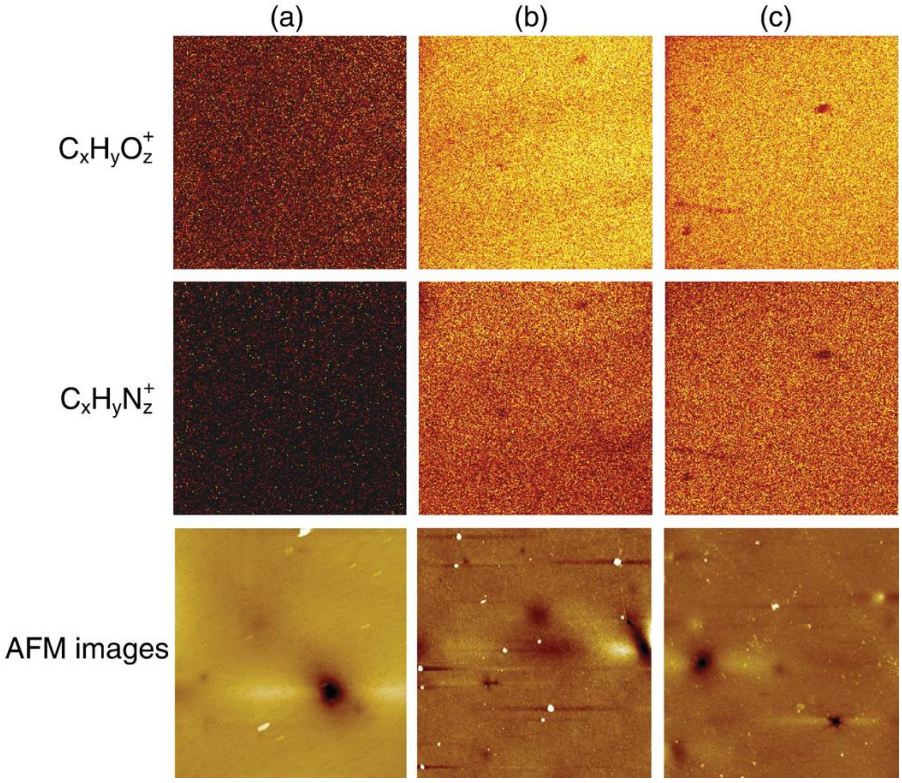


Figure 6.5. TOF-SIMS ion images (500 μm ×500 μm) showing the lateral intensity distribution of $C_xH_yO_z^+$ (upper images) and $C_xH_yN_z^+$ (middle images) markers, and AFM images (10 μm ×10 μm) (lower images) of the GFRP-II surfaces: (a) untreated, (b) GA-II treated without ultrasonic irradiation, and (c) GA-II treated with ultrasonic irradiation. Black corresponds to no intensity, brown to some intensity, and white to 100% intensity in the TOF-SIMS ion images.

Figure 6.5 (upper and middle images) shows TOF-SIMS ion images (500 μm × 500 μm) of the GFRP-II surfaces before and after the treatments. Both oxygen and nitrogen are homogeneously distributed after GA-II treatment with and without ultrasonic irradiation. These results contrast to that of DBD treatment in air in *Section 5.3.2*, where significantly oxidized spots were randomly created without ultrasonic irradiation, while uniformly treated with ultrasonic irradiation. These results indicate that a gliding arc can treat surfaces uniformly even without ultrasonic irradiation. Surface roughening is also useful for adhesion improvement because of the increased surface area and mechanical interaction with the adhesive. AFM was used to measure the surface roughness of the GFRP-II plates over 10 μm × 10 μm surface areas. Figure 6.5 (lower images) shows the AFM images of the GFRP-II plates before the treatment, and after GA-II treatment with/without ultrasonic irradiation. The average surface roughness of the untreated surface was 1.2 ± 0.2 nm (Figure 6.5 (a) (lower image)). The roughness increased to 1.9 ± 0.2 nm (Figure 6.5 (b) (lower image)) and 2.3 ± 0.6 nm (Figure 6.5 (c)) (lower image)) after GA-II treatment without and with

ultrasonic irradiation, respectively. It is therefore concluded that the treatment increases the surface roughness, but ultrasonic irradiation does not change the surface roughness to any detectable degree.

## 6.4. Summary

Observation using a high speed camera indicated that ultrasonic irradiation to GA-IV reduced the thickness of the boundary gas layer, indicating improvement of surface treatment effect. It is noted that the effect of the thickness reduction by the ultrasonic irradiation, which has been predicted in Chapter 5, was directly observed.
GFRP-II plates were treated by GA-II with and without ultrasonic irradiation. Ultrasonic irradiation reduced the rotational temperature of the discharge. The O/C ratio at the GFRP-II surface increased markedly after GA-II treatment without ultrasonic irradiation. Ultrasonic irradiation during the treatment tended to increase them furthermore. Oxygen and nitrogen containing functional groups were uniformly attached at the surfaces by the treatment with and without ultrasonic irradiation. The surfaces were roughened by the treatments, but the simultaneous ultrasonic irradiation did not significantly improve surface roughening.

## 7. Perspectives of future developments

### 7.1. Theoretical understandings of the plasma processes

There are already several reports on theoretical studies of gliding arcs as discussed in Chapter 4. They are however devoted to the conventional gliding arcs that are characterized by their short lifetimes in the non-equilibrium state. Chapter 4 initiated a theoretical study based on a simple analytical model, proposing possible approaches in further extending the length of the plasma column. This study does not include a turbulent flow and chemistry in the theory. In particular, gas phase reactions and interactions of the plasma column and the surrounding gas are interesting topics that can clarify the reaction mechanisms of the gliding arc. Furthermore, the gliding arc in the thesis focuses on air as a feeding gas. Other gases, such as inert gases for studying ignition and propagation of discharges, methane for natural gas conversion, ammonia and volatile organic compounds for toxic gas removal, can be investigated for deeper understanding of the gliding arc and exploring broader scopes of applications.

Ultrasound enhanced plasma processing using a gas-jet ultrasonic generator has been studied experimentally, and there are no theoretical studies attempted. There are two issues in the theoretical study to start with. One is the thickness-reduction mechanism of the boundary gas layer with ultrasonic irradiation. This includes aerodynamic modelling of the gas flow, combined with molecular reactions in the plasma and its surroundings. The other is surface-modification studies linked to the above model. It has been believed that the occurrence of the filamentary micro-discharge would be the cause of the uneven spotty treatment in an air DBD [9]. The phenomenon was also observed in Chapter 5. However, with ultrasonic irradiation, polymer surfaces were uniformly treated even though the discharge remained filamentary. This finding presented in Chapter 5 contradicts with the generally observed uneven spotty treatment in literature [9]. Therefore, the theoretical study of plasma surface modification mechanisms with ultrasonic irradiation will likely trigger a new concept of the uniform plasma surface treatment.

### 7.2. Applications

Composites constitute a polymer matrix with fibres. Design of interfaces between dissimilar materials significantly affects the mechanical performance of the composites. Therefore, there are potentially many applications of plasma processing, including adhesion improvement, surface cleaning, surface activation, chemical etching and coatings.

As the application of the gliding arc, adhesion improvement is promising, especially with experimental evidences of the gliding arcs presented in Chapter 2. It can be used for pre-treatment of fibre reinforced composites before assembly or application of coating, such as manufacture and repair of blades. For a practical use of the gliding arc, cost reduction is a crucial issue. Cost estimation, which is not included in the thesis, indicates that the investment for a plasma generator (power supply) dominates the expense, based on a simple assumption that a commercially available plasma generator which is not specifically designed for the developed gliding arc would be used per one gliding arc. In addition, commercially available plasma generators are usually sensitive to relatively high current pulses, recognize them as arcs and tend to

block the electrical power, with subsequent extinction of the gliding arc discharge. This limits efficient extension of the plasma column and shortens the lifetime of the discharge. It is therefore suggested that development of an economical, robust plasma generator which is optimized for the developed gliding arc and can operate a plurality of gliding arcs simultaneously would be advantageous.

Ultrasound enhanced plasma processing can potentially open new areas of materials processing and materials synthesis. For example, atmospheric pressure plasmas are believed to be rather unsuitable for synthesis of protective coatings which typically require ion bombardment at low gas pressure for achieving sufficient mechanical strength of the coatings. However, ultrasonic irradiation might enable new reaction paths and additional excitation at material surfaces so as to synthesize new materials. Potential applications include leading edge protection for wind turbine blades and gas barrier coatings.

Treatment of fibres and powders is also an interesting application. It is expected that ultrasonic irradiation can induce vibration and oscillation of fine filaments of fibres and fine particles so that a probability of surface exposure in a plasma can be increased. The technique can be applied for pre-treatment of fibres or powders as reinforcement, and subsequent manufacture of composites.

Plasma gases investigated in the thesis include helium, argon, and air. However, recent investigation using ammonia or oxygen ($O_2$) confirms that plasma treatment effect can be improved by ultrasonic irradiation, indicating that ultrasonic irradiation can enhance a variety of plasma treatments [B28-B30]. That is, existing plasma processing has a potential to improve its performance by ultrasonic irradiation.

One interesting observation is the demonstration of surface modification with ultrasonic irradiation at significantly low plasma power as presented in Chapter 5. It is particularly useful for applications in which low electrical power is demanded. Examples include “plasma medicine” for therapy where damage to human bodies should be avoided, and outdoor use where strictly safe operation is needed, such as repair of wind turbine blades onsite.

## 8. Summary

This chapter summarizes the major contents and results of the present thesis, following the order of the chapters.

### 8.1. Adhesion and atmospheric pressure plasmas

- Fundamental concepts of polymer adhesion and its improvement are presented.
- The state of art of the atmospheric pressure plasma processing is presented.
- Importance of plasma processing such as hybrid plasmas and ultrasound enhanced plasmas are noted.
- Objectives of the thesis are defined.

### 8.2. AC gliding arcs for materials processing

- Scheme for designing gliding arcs is proposed in terms of high input power, suitable gas glow, and cooling electrodes.
- The gliding arcs were designed and constructed, showing stable operation with high treatment efficiency.
- Highly oxidative agents, ground-state and excited OH (hydroxyl) radicals, were generated by the gliding arcs.
- OH radicals were detected up to approximately 6 cm away from the edge of the electrodes in the air.
- GFRP plates and CNF coatings were treated by the gliding arcs, indicating oxidation and roughening of the surfaces.
- DCB specimens of GFRP/(vinylester resin)/GFRP were manufactured.
- DCB specimens comprising the GFRP plates treated by the gliding arcs showed higher fracture energy than those with a conventional mechanical treatment.
- Alanine dosimeter films (fluoropolymer coated alanine (FCA) films) were used for investigating treatment effects of the gliding arc, a DBD, and gamma irradiation on surfaces and bulks of materials.
- After each treatment, the fluorine content decreased and the oxygen content increased at the FCA surface, while the alkyl free radicals were created in the bulk alanine.
- The bulk modification by the gliding arc and DBD treatments can be attributed to UV radiation during the treatments.
- In the selected conditions, the gliding arc treatment modified the surface more, and the bulk less than the DBD treatment.

### 8.3. Diagnostics of AC gliding arc

- Electrical measurements and optical diagnostics were carried out to study the gliding arc.
- In optimized conditions, the plasma column extends ca. 20 cm in length (total length of the plasma column), corresponding to approximately 6 cm extension of the gliding arc from the edges of the electrodes, and does not extinguish over a plurality of the AC period.

- After the re-ignition occurs in the nearest gap between the electrodes, the existing plasma column starts to decay for extinction.
- Short-cutting events in the plasma column occurred more often than the re-ignition.
- A hollow structure of the ground state OH radicals around the plasma column was formed, probably as a result of the decay of excited OH radicals generated in the plasma column.

## 8.4. Stability of AC gliding arcs

- A non-linear analytical model was proposed to study a stability of AC gliding arcs.
- The model indicates that the phase shift of the current waveform from the voltage waveform is independent of the plasma column length, and the specific power dissipated from the discharge per unit length.
- The condition of the critical length can be discriminated by the relation between the phase shift to the ratio of the characteristic time of the AC power supply to that of the electrical circuit.
- The theory predicts that AC gliding arcs can be preferably extended when the AC frequency increases, the serial resistance decreases and the gas flowrate is lowered.
- The suggested dependence of the maximum achievable discharge extension on the flowrate is demonstrated experimentally.
- The critical length of an AC gliding arc would be longer than that of a corresponding DC gliding arc.
- The length of the gliding arc discharge can be further extended by tuning the gas breakdown condition at the closest gap between the electrodes.

## 8.5. Development of ultrasound enhanced plasma processing

- A device of the ultrasound enhanced plasma processing was designed and constructed, combining a DBD and a high power gas-jet ultrasonic generator.
- A glow type helium DBD changed to a filamentary discharge by the ultrasonic irradiation.
- DBD treatment of GFRP in helium or air increased oxidation of specimen surfaces, and ultrasonic irradiation enhanced the effects.
- Ultrasonic irradiation during the air DBD treatment suppressed arcing.
- The air DBD treatment without ultrasound created randomly distributed oxidized spots (in millimetre scale or smaller) at the surfaces.
- Oxygen and nitrogen containing functional groups were uniformly attached at the surfaces by the air DBD treatment with ultrasonic irradiation.
- A 50-Hz DBD treatment without ultrasonic irradiation did not change the GFRP surface properties significantly under the tested conditions.
- Ultrasonic irradiation to the 50-Hz DBD enhanced the treatment effect markedly.
- Helium DBD treatment oxidized and roughened the CNF coating surfaces unevenly, and enhanced the wettability by deionized water and glycerol.
- Ultrasonic irradiation enhanced the oxidation of the coating and the uniformity of the treatment (sub-micro scale).

## 8.6. Ultrasound enhanced gliding arcs

- The gliding arcs presented in Chapters 1 to 4 were tilted to the material surface, enabling an introduction of ultrasound perpendicular to the surface.
- GFRP plates were treated by GA-II with and without ultrasonic irradiation.
- The oxygen content at the GFRP surface increased markedly after GA-II treatment, and ultrasonic irradiation increased the effect furthermore, similarly to the DBD treatment with and without ultrasonic irradiation.
- Observation using a high speed camera indicated that ultrasonic irradiation reduced the thickness of the boundary gas layer, indicating improvement of surface treatment effect.

## 9. Conclusions

1. Novel plasma processing of gliding arcs and ultrasound enhanced plasmas was proposed, and developed.

2. Various characterization techniques were employed to study the plasma, plasma treated surfaces and bulks, and mechanical properties of composites comprising the plasma treated substances.

3. Plasma treatment increased wettability and roughness of the treated surfaces, and subsequently increased interfacial fracture energy when assembled as composites.

4. Plasma treatment can affect not only material surfaces but also bulks, attributed to UV irradiation from the plasma.

5. Theoretical approach for the gliding arc indicates that the plasma column can be further prolonged.

6. Ultrasonic irradiation to the plasma enhances the plasma treatment effects, and can suppress arcing and improve treatment uniformity in millimetre- and sub-micrometre-scales.

## References

***Author's selected references that are attached in the Appendices***


[A1] **Y. Kusano** "Atmospheric pressure plasma processing for polymer adhesion – a review" *J. Adhesion* 90(9) (2014) 755-777.

[A2] **Y. Kusano** "Plasma surface modification at atmospheric pressure" *Surf. Eng.* 25(6) (2009) 415-416 (Editorial).

[A3] **Y. Kusano** "An apparatus for treating a surface with at least one gliding arc source" European patent No. 2,514,280 B1 (2014). There is a variation that has been granted in the US (U.S. patent No. 9,420,680 B2 (2016)).

[A4] **Y. Kusano**, B.F. Sørensen, T.L. Andersen, F. Leipold "Adhesion improvement of glass-fibre-reinforced polyester composites by gliding arc discharge treatment" *J. Adhesion* 89(6) (2013) 433-459.

[A5] **Y. Kusano**, B.F. Sørensen, T.L. Andersen, H.L. Toftegaard, F. Leipold, M. Salewski, Z.W. Sun, J.J. Zhu, Z.S. Li, M. Aldén "Water-cooled non-thermal gliding arc for adhesion improvement of glass-fibre-reinforced polyester" *J. Phys. D: Appl. Phys*. 46(13) (2013) 135203.

[A6] **Y. Kusano**, L. Berglund, Y. Aitomäki, K. Oksman, B. Madsen "Gliding arc surface modification of carrot nanofibre coating – perspective for composite processing" *Mater. Sci. Eng*. 139(1) (2016) 012027.

[A7] **Y. Kusano**, A. Bardenshtein, P. Morgen "Fluoropolymer coated alanine films treated by atmospheric pressure plasmas – in comparison with gamma irradiation" *Plasma Proc. Polym*. 15(3) (2018) 1700131.

[A8] Z.W. Sun, J.J. Zhu, Z.S. Li, M. Aldén, F. Leipold, M. Salewski, **Y. Kusano** "Optical diagnostics of a gliding arc" *Optics Express* 21(5) (2013) 6028-6044.

[A9] J.J. Zhu, Z.W. Sun, Z.S. Li, A. Ehn, M, Aldén, M. Salewski, F. Leipold, **Y. Kusano** "Dynamics, OH distributions and UV emission of a gliding arc at various flow-rates investigated by optical measurements" *J. Phys. D: Appl. Phys*. 47 (2014) 295203.

[A10] **Y. Kusano**, M. Salewski, F. Leipold, J.J. Zhu, A. Ehn, Z.S. Li, M. Aldén "Stability of alternating current gliding arcs" *Eur. Phys. J. D* 68 (2014) 319.

[A11] N. Krebs, A. Bardenshtein, **Y. Kusano**, H. Bindslev, H.J. Mortensen "Enhancing plasma surface modification using high intensity and high power ultrasonic acoustic wave" US patent No. 8,399,795 B2 (2013). There is a variation that has been granted in China (Chinese patent No. 101,743,785 B (2012)).

[A12] **Y. Kusano**, S.V. Singh, A. Bardenshtein, N. Krebs, N. Rozlosnik "Plasma surface modification of glass fibre reinforced polyester enhanced by ultrasonic irradiation" *J. Adhesion Sci. Technol*. 24 (2010) 1831-1839.

[A13] **Y. Kusano**, T.L. Andersen, H.L. Toftegaard, F. Leipold, A. Bardenshtein, N. Krebs "Plasma treatment of carbon fibres and glass-fibre-reinforced polyesters at atmospheric pressure for adhesion improvement" *Int. J. Mater. Eng. Innovation* 5(2) (2014) 122-137.

[A14] **Y. Kusano**, K. Norrman, S.V. Singh, F. Leipold, P. Morgen, A. Bardenshtein, N. Krebs "Ultrasound enhanced 50 Hz plasma treatment of glass-fiber-reinforced polyester at atmospheric pressure" *J. Adhesion Sci. Technol.* 27(7) (2013) 825-833.

[A15] **Y. Kusano**, S.V. Singh, K. Norrman, F. Leipold, J. Drews, P. Morgen, A. Bardenshtein, N. Krebs "Ultrasound enhanced plasma treatment of glass-fibre-

reinforced polyester in atmospheric pressure air for adhesion improvement" *J. Adhesion* 87 (2011) 720-731.

[A16] **Y. Kusano**, B. Madsen, L. Berglund, Y. Aitomäki, K. Oksman "Dielectric barrier discharge plasma treatment of cellulose nanofibre surfaces" *Surf. Eng.* 34(11) (2018) 825-831.

[A17] **Y. Kusano**, K. Norrman, J. Drews, F. Leipold, S.V. Singh, P. Morgen, A. Bardenshtein, N. Krebs "Gliding arc surface treatment of glass fiber reinforced polyester enhanced by ultrasonic irradiation" *Surf. Coat. Technol*. 205 (2011) S490-S494.

[A18] **Y. Kusano**, J.J. Zhu, A. Ehn, Z.S. Li, M. Aldén, M. Salewski, F. Leipold, A. Bardenshtein, N. Krebs "Observation of gliding arc surface treatment" *Surf. Eng.* 31(4) (2015) 282-288.

***Other related references by the author (not included in the thesis)***

[B1] S.V. Singh, **Y. Kusano**, P. Morgen, P.K. Michelsen "Surface charging, discharging and chemical modification at a sliding contact" *J. Appl. Phys*. 111 (2012) 083501.

[B2] **Y. Kusano**, H. Mortensen, S. Teodoru, J.M. Drews, T.L. Andersen, B.F. Sørensen, N. Rozlosnik, S. Goutianos, P. Kingshott, S. Mitra, F. Leipold, K. Almdal, P.K. Michelsen, H. Bindslev "Plasma surface modification of glassy carbon plates, carbon fibres and UHMWPE fibres for adhesion improvement" in "Fiber-reinforced composites" Nova Sci. Publishers, Inc. (2012) 251-296.

[B3] **Y. Kusano**, H. Mortensen, B. Stenum, S. Goutianos, B. Mitra, A. Ghanbari-Siahkali, P. Kingshott, B.F. Sørensen, H. Bindslev "Atmospheric pressure plasma treatment of glassy carbon for adhesion improvement" *Int. J. Adhesion Adhesives* 27(5) (2007) 402-408.

[B4] **Y. Kusano**, T.L. Andersen, P.K. Michelsen "Atmospheric pressure plasma surface modification of carbon fibres" *J. Phys. Conf. Series* 100 (2008) 012002.

[B5] **Y. Kusano**, S. Teodoru, C.M. Hansen "The physical and chemical properties of plasma treated ultra-high-molecular-weight polyethylene fibers" *Surf. Coat. Technol*. 205 (2011) 2793-2798.

[B6] S. Teodoru, **Y. Kusano**, N. Rozlosnik, P.K. Michelsen "Continuous plasma treatment of ultra high molecular weight polyethylene (UHMWPE) fibres for adhesion improvement" *Plasma Proc. Polym*. 6 (2009) S375-S381.

[B7] **Y. Kusano**, T.L. Andersen, B.F. Sørensen, N. Rozlosnik, H. Mortensen, S. Teodoru, P. Kingshott, F. Leipold, S.V. Singh, J. Bilde-Sørensen, P. Brøndsted, P.K. Michelsen, H. Bindslev, A. Bardenshtein, N. Krebs "Adhesion improvement of glass fibre reinforced polyester composite by atmospheric pressure plasma treatment" in "Fiber-reinforced composites" Nova Sci. Publishers, Inc. (2012) 297-318.

[B8] **Y. Kusano**, H. Mortensen, B. Stenum, P. Kingshott, T.L. Andersen, P. Brøndsted, J.B. Bilde-Sørensen, B.F. Sørensen, H. Bindslev "Atmospheric pressure plasma treatment of glass fibre composite for adhesion improvement" *Plasma Proc. Polym.* 4(S1) (2007) S455-S459.

[B9] I. Siró, **Y. Kusano**, K. Norrman, S. Goutianos, D. Plackett "Surface modification of nanofibrillated cellulose films by atmospheric pressure dielectric barrier discharge" *J. Adhesion Sci. Technol*. 27(3) (2013) 294-308.

[B10] S. Teodoru, **Y. Kusano**, A. Bogaerts "The effect of $O_2$ in a humid $O_2/N_2/NO_x$ gas mixture on $NO_x$ and $N_2O$ remediation by an atmospheric pressure dielectric barrier discharge" *Plasma Proc. Polym.* 9 (2012) 652-689.

[B11] **Y. Kusano**, F. Leipold, A. Fateev, B. Stenum, and H. Bindslev "Production of ammonia-derived radicals in a dielectric barrier discharge and their injection for denitrification" *Surf. Coat. Technol*. 200 (2005) 846-849.

[B12] **Y. Kusano**, F. Leipold, A. Fateev, H. Bindslev "NO reduction in the flue gas by reaction with $N_2$- and ammonia-derived radicals" in "Flue gases: Research, Technology and Economics" Nova Sci. Publishers, Inc. (2009) 328-345.

[B13] F. Leipold, N. Schultz-Jensen, **Y. Kusano**, H. Bindslev, T. Jacobsen "Decontamination of objects in a sealed container by means of atmospheric pressure plasmas" *Food Control* 22(8) (2011) 1296-1301.

[B14] F. Leipold, **Y. Kusano**, F. Hansen, T. Jacobsen "Decontamination of a rotating cutting tool during operation by means of atmospheric pressure plasmas" *Food Control* 21 (2010) 1194-1198.

[B15] F. Leipold, A. Fateev, **Y. Kusano**, B. Stenum, H. Bindslev "Reduction of NO in the exhaust gas by reaction with N radicals" *Fuel* 85 (2006) 1383-1388.

[B16] A. Fateev, F. Leipold, **Y. Kusano**, B. Stenum, E. Tsakadze, H. Bindslev "Plasma chemistry in an atmospheric pressure $Ar/NH_3$ dielectric barrier discharge" *Plasma Proc. Polym.* 2 (2005) 193-200.

[B17] M. Yoshikawa, **Y. Kusano**, S. Akiyama, K. Naito, S. Okazaki, M. Kogoma "Method and apparatus for surface treatment" *US Patent* No. 5,316,739 (1994).

[B18] M. Kogoma, M. Kusano, **Y. Kusano** (Ed.) "Generation and applications of atmospheric pressure plasmas" Nova Sci. Publishers, Inc. (2011).

[B19] H. Mortensen, **Y. Kusano**, F. Leipold, N. Rozlosnik, P. Kingshott, B.F. Sørensen, B. Stenum, H. Bindslev "Modification of glassy carbon surfaces by an atmospheric pressure cold plasma torch" *Jpn. J. Appl. Phys*. 45(10B) (2006) 8506-8511.

[B20] B.J. Lee, **Y. Kusano**, N Kato, K. Naito, T. Horiuchi, H. Koinuma "Oxygen plasma treatment of rubber surface by the atmospheric pressure cold plasma torch" *Jpn. J. Appl. Phys.* Pt. 1, 36 (1997) 2888-2891.

[B21] **Y. Kusano**, S. Teodoru, F. Leipold, T.L. Andersen, B.F. Sørensen, N. Rozlosnik, P.K. Michelsen "Gliding arc discharge – application for adhesion improvement of fibre reinforced polyester composites" *Surf. Coat. Technol*. 202 (2008) 5579-5582.

[B22] J.J. Zhu, **Y. Kusano**, ZS Li "Optical diagnostics of a gliding arc discharge at atmospheric pressure" in Atmospheric pressure plasmas" Nova Sci. Publishers, Inc. (2016) 19-51.

[B23] J.J. Zhu, J.L. Gao, Z.S. Li, A. Ehn, M, Aldén, A. Larsson, **Y. Kusano** "Sustained diffusive alternating current gliding arc discharge in atmospheric pressure air" *Appl. Phys. Let*. 105 (2014) 234102.

[B24] J.J. Zhu, J.L. Gao, A. Ehn, M, Aldén, Z.S. Li, D. Moseev, **Y. Kusano**, M. Salewski, A. Alpers, P. Gritzmann, M. Schwenk "Measurements of 3D slip velocities and plasma column lengths of a gliding arc discharge" *Appl. Phys. Let*. 106 (2015) 044101.

[B25] J.J. Zhu, J.L. Gao, A. Ehn, M, Aldén, Z.S. Li, A. Larsson, **Y. Kusano** "Spatiotemporally resolved characteristics of a gliding arc discharge in a turbulent air flow at atmospheric pressure" *Phys. Plasmas* 24 (2017) 013515.

[B26] J.J. Zhu, A. Ehn, J.L. Gao, C.D. Kong, M Aldén, A. Larsson, M. Salewski, F. Leipold, **Y. Kusano**, Z.S. Li "Translational, rotational, vibrational and electron temperatures of a gliding arc discharge" *Optics Express* 25(17) (2017) 20243-20257.

[B27] **Y. Kusano**, S.V. Singh, K. Norrman, J. Drews, F. Leipold, N. Rozlosnik, A. Bardenshtein, N. Krebs "Ultrasound enhanced plasma surface modification at atmospheric pressure" *Surf. Eng*. 28(6) (2012) 453-457.

[B28] J. Drews, **Y. Kusano**, F. Leipold, A. Bardenshtein, N. Krebs "Ozone production in a dielectric barrier discharge with ultrasonic irradiation" *Ozone: Sci. Eng*. 33 (2011) 483-488.

[B29] **Y. Kusano**, A. Bardenshtein, H. Bindslev, N. Krebs "使用高强度和高功率超声波在等离子体中增强气相反应" Chinese patent No. 101,731,025 B (2012).

[B30] **Y. Kusano**, J. Drews, F. Leipold, A. Fateev, A Bardenshtein, N. Krebs "Influence of ultrasonic irradiation on ozone production in a dielectric barrier discharge" *J. Phys. Conf. Series* 406 (2012) 012006.

***Other references***

[1] K.L. Mittal "The role of the interface in adhesion phenomena" *Polym. Eng. Sci.* 17(7) (1977) 467-473.

[2] T. Steiner "The hydrogen bond in the solid state" *Angew. Chem. Int. Ed.* 41(1) (2002) 49-76.

[3] A. Fridman, L.A. Kennedy "Plasma Physics and Engineering" Taylor & Francis, NY (2004).

[4] M.M. Kekez, M.R. Barrault, J.D. Craggs "Spark channel formation" *J. Phys. D: Appl. Phys*. 3 (1970) 1886–1896.

[5] E.M. Liston, L. Martinu, M.R. Wertheimer "Plasma surface modification of polymers for improved adhesion: a critical review" *J. Adhesion Sci. Technol*. 7 (1993) 1091–1127.

[6] H. Yasuda "Plasma Polymerization" Academic Press, Florida, Gainesville, FL (1986).

[7] S. Goutianos, B.F. Sørensen "The application of J integral to measure cohesive laws under large-scale yielding" *Eng. Fracture Mech*. 155 (2016) 145-165.

[8] Y.P. Raizer "Gas Discharge Physics" Springer-Verlag, Berlin (1991).

[9] U. Kogelschatz "Dielectric-Barrier Discharges: Their History, Discharge Physics, and Industrial Applications" *Plasma Chem. Plasma Proc*. 23 (2003) 1–46.

[10] V.I. Gibalov, G.J. Pietsch "The development of dielectric barrier discharges in gas gaps and on surfaces" *J. Phys. D: Appl. Phys*. 33 (2000) 2618–2636.

[11] V.I. Gibalov, G.J. Pietsch "Dynamics of dielectric barrier discharges in coplanar arrangements" *J. Phys. D: Appl. Phys*. 37 (2004) 2082–2092.

[12] Y. Babukutty, R. Prat, K. Endo, M. Kogoma, S. Okazaki, M. Kodama "Poly(vinyl chloride) Surface Modification Using Tetrafluoroethylene in Atmospheric Pressure Glow Discharge" *Langmuir* 15 (1999) 7055–7062.

[13] S. Okazaki, M. Kogoma, M. Uehara, Y. Kimura "Appearance of stable glow discharge in air, argon, oxygen and nitrogen at atmospheric pressure using a 50 Hz source" *J. Phys. D: Appl. Phys*. 26 (1993) 889–892.

[14] T. Yokoyama, M. Kogoma, T. Moriwaki, S. Okazaki “The mechanism of the stabilisation of glow plasma at atmospheric pressure” *J. Phys. D: Appl. Phys.* 23 (1990) 1125–1128.
[15] N. Balcon, A. Aanesland, R. Boswell “Pulsed RF discharges, glow and filamentary mode at atmospheric pressure in argon” *Plasma Sources Sci. Technol.* 16 (2007) 217-225.
[16] A. Schütze, J.Y. Jeong, S.E. Babayan, J. Park, G.S. Selwyn, R.F. Hicks “The atmospheric-pressure plasma jet: a review and comparison to other plasma sources” *IEEE Trans. Plasma Sci*. 26 (1998) 1685–1694.
[17] M.I. Boulos “The inductively coupled radio frequency plasma” *High Temp. Mater. Process*. 1 (1997) 17-39.
[18] J. Schäfer, P. Vasina, J. Hnilica, R. Foest, V. Kudrle, K.-D. Weltmann “Visualization of Revolving Modes in RF and MW Nonthermal Atmospheric Pressure Plasma Jets” *IEEE Trans. Plasma Sci*. 39 (2011) 2350–2351.
[19] A. Fridman, S. Nester, L.A. Kennedy, A. Saveliev, O. Mutaf-Yardimci “Gliding arc gas discharge” *Progress Energy Combustion Sci.* 25 (1999) 211–231.
[20] A. Czernichowski “Gliding arc: Applications to engineering and environment control” *Pure Appl. Chem.* 66 (1994) 1301–1310.
[21] J. Janča, A. Czernichowski “Wool treatment in the gas flow from gliding discharge plasma at atmospheric pressure” *Surf. Coat. Technol*. 98 (1998) 1112–1115.
[22] Operation instruction. Corona Station CKG-3*20 with generator V06. Treatment of metallic or non-conductive substrates with the plasma of indirect corona discharges. Manual for AB3353 Corona Station CKG-3*20. TIGRES Dr. Gerstenberg GmbH
[23] U. Lommatzsch, D. Pasedag, A. Baalmann, G. Ellinghorst, H.-E. Wagner “Atmospheric Pressure Plasma Jet Treatment of Polyethylene Surfaces for Adhesion Improvement” *Plasma Proc. Polym.* 4 (2007) S1041–S1045.
[24] J. Toshifuji, T. Katsumata, H. Takikawa, T. Sakakibara, I. Shimizu, “Cold arc-plasma jet under atmospheric pressure for surface modification” *Surf. Coat. Technol.* 202 (2008) 5579-5582.
[25] D.H. Kaelble “Dispersion-Polar Surface Tension Properties of Organic Solids” *J. Adhesion* 2 (1970) 66-81.
[26] M. Strobel, C.S. Lyons “An Essay on Contact Angle Measurements” *Plasma Proc. Polym.* 8 (2011) 8-13.
[27] C.M. Hansen “Hansen Solubility Parameters. A User’s Handbook” 2nd ed., Taylor & Francis, Florida (2007).
[28] F. Richard, J.M. Cormier, S. Pellerin, J. Chapelle “Gliding arcs fluctuations and arc root displacement” *High Temp. Mater. Proc*. 1 (1997) 239–248.
[29] R.D. Adams, R.W. Atkins, A. Harris, A.J. Kinloch “Stress Analysis and Failure Properties of Carbon-Fibre-Reinforced-Plastic/Steel Double-Lap Joints” *J. Adhesion* 20 (1986) 29-53.
[30] B.L. Peng, N. Dhar, H.L. Liu, K.C. Tam ”Chemistry and applications of nanocrystalline cellulose and its derivatives: a nanotechnology perspective” *Canadian J. Chem. Eng*. 89(5) (2011) 1191-1206.
[31] C.J. Chirayil, L. Mathew, S. Thomas “Review of recent research in nano cellulose preparation from different lignocellulosic fibers” *Rev. Adv. Mater.* 37 (2014) 20-28.

[32] A.N. Nakagaito, H. Yano “Novel high-strength biocomposites based on microfibrillated cellulose having nano-order-unit web-like network structure” *Appl. Phys. A* 80(1) (2005)155–159.
[33] M. Kuzuya, K. Kamiya, Y. Yanagihara, Y. Matsuno “Nature of plasma-induced free-radical formation of several fibrous polypeptides” *Plasma Sources Sci. Technol.* 2 (1993) 51-57.
[34] S.F. Sadova “The use of low-temperature plasmas in wool finishing” *High Energy Chem.* 40 (2006) 57-69.
[35] K.-D. Weltmann, T. von Woedtke “Plasma medicine—current state of research and medical application” *Plasma Phys. Control. Fusion* 59 (2017) 014031.
[36] Q. Bénard, M. Fois, M. Grisel “Peel ply surface treatment for composite assemblies: Chemistry and morphology effects” *Composites A* 36 (2005) 1562–1568.
[37] C.O. Laux, T.G. Spence, C.H. Kruger, R.N. Zare “Optical diagnostics of atmospheric pressure air plasmas” *Plasma Source Sci. Technol.* 12 (2003) 125-138.
[38] B.F. Sørensen, K. Jørgensen, T.K. Jacobsen, R.C. Østergaard ” DCB-specimen Loaded with Uneven Bending Moments” *Int. J. Fract.* 141 (2006) 163–176.
[39] K.M. Leichti, Y.-S. Chai “Asymmetric shielding in internal fracture under in-plane shear” *J. Appl. Mech.* 59 (1992) 295-304.
[40] R.E.J. Nicklin, A. Cornish, A. Shavorskiy, S. Baldanza, K. Schulte, Z. Liu, R.A. Bennett, G. Held “Surface Chemistry of Alanine on Ni{111}” *J. Phys. Chem. C* 119 (47) (2015) 26566-26574.
[41] J. Helt-Hansen, F. Rosendal, I.M. Kofoed, C.E. Andersen “Medical reference dosimetry using EPR measurements of alanine: development of an improved method for clinical dose levels” *Acta Oncologica* 48 (2009) 216-222.
[42] S.S. Sackey, M.K. Vowotor, A. Owusu, P. Mensah-Amoah, E.T. Tachie, B. Sefa-Ntiri, C.O. Hood, S.M. Atiemo “Spectroscopic Study of UV Transparency of Some Materials” *Environ. Pollut.* 4(4) (2015) 1-17.
[43] M.K. Yang, R.H. French, E.W. Tokarsky “Optical properties of Teflon® AF amorphous fluoropolymers” *J. Micro/Nanolith. MEMS MOEMS* 7(3) (2008) 033010.
[44] R. Abu-Eittah, A. Obaid, S. Basahl, E. Diefallah “Molecular orbital treatment of some amino acids” *Bull. Chem. Soc. Jpn.* 61 (1988) 2609-2613.
[45] V. Poenariu, M.R. Wertheimer, R. Bartnikas “Spectroscopic Diagnostics of Atmospheric Pressure Helium Dielectric Barrier Discharges in Divergent Fields” *Plasma Proc. Polym.* 3 (2006) 17-29.
[46] F. Richard, J.M. Cormier, S. Pellerin, J. Chapelle “Physical study of a gliding arc discharge” *J. Appl. Phys.* 79(5) (1996) 2245–2250.
[47] B. Benstaali, P. Boubert, B.G. Cheron, A. Addou, J.L. Brisset “Density and rotational temperature measurements of the OH degrees and NO degrees radicals produced by a gliding arc in humid air” *Plasma Chem. Plasma Proc.* 22(4) (2002) 553–571.
[48] V. Dalaine, J.M. Cormier, S. Pellerin, P. Lefaucheux “$H_2S$ destruction in 50 Hz and 25 kHz gliding arc reactors” *J. Appl. Phys.* 84 (1998) 1215-1221.
[49] A. Fridman, A, Gutsol, S. Gangoli, Y. Ju, T. Ombrello “Characteristics of Gliding Arc and Its Application in Combustion Enhancement” *J. Propuls. Power* 24 (2008) 1216-1228.

[50] S. Pellerin, J. Chapelle, F. Richard, K. Musiol, J. Chapelle "Determination of the electrical parameters of a bi-dimensional d.c. Glidarc" *J. Phys. D: Appl. Phys.* 32 (1999) 891-897.
[51] S. Pellerin, F. Richard, J. Chapelle, J.M. Cormier, K. Musiol "Heat string model of bi-dimensional dc Glidarc" *J. Phys. D: Appl. Phys.* 33 (2000) 2407-2419.
[52] J. Heberlein, J. Mentel, E. Pfender "The anode region of electric arcs: a survey" *J. Phys. D: Appl. Phys.* 43 (2010) 02301.
[53] I.V. Kuznetsova, N.Y. Kalashnikov, A.F. Gutsol, A.A. Fridman, L.A. Kennedy "Effect of "overshooting'' in the transitional regimes of the low-current gliding arc discharge" *J. Appl. Phys*. 92 (2002) 4231-4237.
[54] J.M. Meek, J.D. Craggs "Electrical Breakdown of Gases" (Oxford University Press, Oxford, 1953)
[55] N. Krebs, C. Langklær "Method and system for enhanced high intensity acoustic waves application" *EU patent* No. EP 2,037,766 B1 (2011).
[56] T. Nakane, T. Miyajima, T. Otsuka "Current Waveforms of Electric Discharge in Air under High-Intensity Acoustic Standing Wave Field" *Jpn. J. Appl. Phys*. 43 (2004) 2852-2856.
[57] Q.H. Zhang, R. Du, J.H. Zhang, Q.B. Zhang "An investigation of ultrasonic-assisted electrical discharge machining in gas" *Int. J. Machine Tools Manuf.* 46 (2006) 1582-1588.
[58] T. Hatsuzawa, M. Hayase, T. Oguchi "Mechanical vibration assisted plasma etching for etch rate and anisotropy improvement" *Precision Eng*. 26 (2002) 442-447.
[59] R. Bálek, S. Pekárek, Z. Bartáková "Ultrasonic resonator with electrical discharge cell for ozone generation" *Ultrasonics* 46 (2007) 227-234.
[60] S. Pekárek, R. Bálek, J. Kuhn, M. Pospl "Effect of ultrasound waves on a hollow needle to plate electrical discharge in air or mixture of air with VOCs" *Czech. J. Phys. Suppl. B* 56 (2006) B982-B989.
[61] K.-S. Choi, S. Nakamura, Y. Murata "Improvement of Charging Performance of Corona Charger in Electrophotography by Irradiating Ultrasonic Wave to Surrounding Region of Corona Electrode" *Jpn. J. Appl. Phys*. 44 (2005) 3248-3252.
[62] A.A. Garamoon, D.M. El-zeer "Atmospheric pressure glow discharge plasma in air at frequency 50 Hz" *Plasma Sources Sci. Technol*. 18(4) (2009) 045006.
[63] M.N. Belgacem, G. Czeremuszkin, S. Sapieha "Surface characterization of cellulose fibres by XPS and inverse gas chromatography" *Cellulose* 2 (1995) 145–157.
[64] G. A. Galechyan "Acoustic waves in plasma" *Phys.-Uspekhi* 238(12) (1995) 1309-1330.

# [Appendix A1]

Y. Kusano

## “Atmospheric pressure plasma processing for polymer adhesion : a review”

*The Journal of Adhesion* 90(9) (2014) 755-777.

*The Journal of Adhesion*, 90:755–777, 2014

ISSN: 0021-8464 print/1545-5823 online
DOI: 10.1080/00218464.2013.804407

Taylor & Francis
Taylor & Francis Group

# Atmospheric Pressure Plasma Processing for Polymer Adhesion: A Review

YUKIHIRO KUSANO

*Department of Wind Energy, Section of Composites and Materials Mechanics, Technical University of Denmark, Roskilde, Denmark*

*Atmospheric pressure plasma processing has attracted significant interests over decades due to its usefulness and a variety of applications. Adhesion improvement of polymer surfaces is among the most important applications of atmospheric pressure plasma treatment. Reflecting recent significant development of the atmospheric pressure plasma processing, this work presents its fundamental aspects, applications, and characterization techniques relevant to adhesion.*

*KEYWORDS Plasma; Polymers; Substrates and surfaces; Surface treatment by exited gases (e.g., flame, corona, plasma)*



## 1. INTRODUCTION

Polymeric materials exhibit various useful properties so that they are widely used in engineering and industrial applications. They are generally selected according to their bulk properties for their specific uses. They are often used as components of composites and laminates, as well as substrates of printings, paintings, and coatings. They usually demonstrate best performances when their adhesion with other materials is good enough. However, most polymer surfaces are chemically inert and difficult to adhere with other materials, and thus proper surface modification is desirable before joining. Plasma treatment is attractive for this application because it is a environmental-friendly process and highly reactive to the material surface

Received 8 April 2013; in final form 8 May 2013.

Address correspondence to Yukihiro Kusano, Department of Wind Energy, Section of Composites and Materials Mechanics, Technical University of Denmark, Risø Campus, Frederiksborgvej 399, DK-4000 Roskilde, Denmark. E-mail: yuki@dtu.dk

Color versions of one or more of the figures in the article can be found online at www.tandfonline.com/gadh.

to be treated while retaining the bulk properties of the material [1]. Plasma treatment is widely used for adhesion improvement of polymers, and its equipment are commercially available. The relevant techniques are reviewed and studied for example among

- Polymer surface modification techniques for adhesion improvement (not necessarily using plasma processing) [2–4]
- Plasma surface modification techniques of polymers (not necessarily for adhesion) [5–7]
- Exclusively plasma surface modification for adhesion improvement of polymers (low-pressure plasmas) [8–11]

Plasma processing is often performed at low pressures, and review articles often refer to low-pressure plasma processing only. The plasma treatments at low pressures, however, require expensive vacuum systems, and methods are well-developed only for batch or semi-batch treatments. However, plasmas can also be generated at atmospheric pressure [12], obviating vacuum equipment and permitting the treatment of large objects [13–15] and continuous treatment [16,17]. It has been shown that a variety of surface treatment methods performed in low-pressure plasmas are achievable at atmospheric pressure [12,18]. Reflecting recent significant interests and development of atmospheric pressure plasma processing, several important review articles are published [12,19–28]. In this paper, atmospheric pressure plasma processing for adhesion improvement of polymers is critically reviewed in terms of plasma sources, applications, and surface characterization techniques after the plasma treatment. Since there are too many publications in the relevant areas, this review will not try to cover everything, but will attempt to present updated, useful, and practical information for researchers working in adhesion, as well as atmospheric pressure plasma processing.



## 2. PLASMA AND SURFACE MODIFICATION EFFECTS

A plasma is a fully or partially ionized gas, containing electrons, ions, high-energy neutrals and radicals. It usually accompanies ultraviolet (UV) photoemission. At low-gas pressures, non-thermal plasmas, or a cold plasma, can be easily generated where the electron temperature is approximately 1 eV (ca. 10,000 K) or more, while gas temperatures can be as low as room temperature. Therefore, it is reasonable to call it a non-equilibrium plasma, but it is often conventionally called a non-thermal plasma or a cold plasma. Such kinds of non-thermal plasmas are useful especially for polymer surface processing since high electron temperature ensures production of highly reactive species, which support the main function of the plasma for its use

while avoiding damage of bulk properties due to low-gas temperature. At low-gas pressures, free electrons in a plasma can be efficiently accelerated and heated in an electric field without frequent collisions. If the gas pressure increases, however, the inelastic collision frequency of gas molecules with electron increases and gas temperature subsequently increases. As collision ionization by electron avalanche sustains the plasma, the input energy must be increased at a higher pressure. Consequently, the discharge is ready to be a thermal plasma or an arc at the equilibrium state. Figure 1 gives an idea of the evolution of a gas discharge. A timescale of each step highly depends on a plasma condition such as gas species and pressure [29]. It is indicated in Fig. 1 that in order to avoid generation of a thermal plasma the current should be blocked before the discharge becomes an arc. Different types of atmospheric pressure non-thermal plasmas will be discussed in the later sections referring to Fig. 1.

During plasma treatment of polymer surfaces, physical and chemical etching, and surface-chemistry modification are observed. Depending on the materials and conditions, one of them may be dominated, but in principle all these processes occur simultaneously.

- Etching
  Since atmospheric pressure non-thermal plasmas are only weakly ionized, chemical etching by neutral species is usually pronounced compared with physical etching. In other words, if effects of ions are desired in a process, atmospheric pressure non-thermal plasma may not be a good choice. Etching includes surface cleaning (removing organic contamination) and ablation. They are both governed by chemically preferential etching and subsequent gasification of contaminants and weak domains. Here, the weak domains include amorphous and low-molecular-weight domains, as well as organic domains compared with inorganic ones [30]. Cleaning is primarily important for adhesion improvement and is often considered to be one of the major reasons of improved bonding after plasma



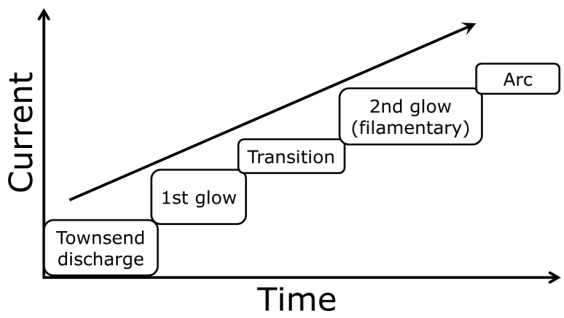


**FIGURE 1** Evolution of a gas discharge.

treatment [8]. Ablation, however, is also important in eliminating weak domains and increasing surface roughness [31].

- Surface-chemistry modification
  There are two major effects observed. First, to cut C–C and C–H bonds of polymer surfaces by attachment of electrically excited atoms and molecules, UV emission [8], and creation of free radicals at the surfaces. If there is flexibility in the polymer chains, or if the created radicals would migrate on the chains, there can be recombination, unsaturation, branching, or cross-linking. The cross-linking may improve the cohesive strength of the surfaces so that the resulting bond strength can be increased. It is known that helium or argon plasma can enhance this effect as long as the plasma gas does not contain certain contaminations. If a concentration of the contamination is high, other effects may dominate. However, special care should be taken for the effect of bond secession since breaking such bonds may result in creation of lower weight molecules (oligomers) so that weak domains may be created instead. An elastomer is a good example (see Section 4.4).



The second chemical effect is functionalization. It can be categorized according to the functions (*e.g.*, hydrophilization, hydrophobization, adhesability, printability, and paintability) and the chemistry of the process (*e.g.*, oxidation, nitration, and fluorination). They are realized by feeding a specific gas into the plasma volume.

If a film-forming gas (precursor) is introduced into a plasma volume, a coating can be synthesised on a polymer surface. This process is called plasma polymerization [32]. It is believed that adhesion of plasma-polymerized coating to polymeric material surfaces is generally good since the above-mentioned effects of etching and functionalization are expected at the beginning of the process. Plasma-polymerized coatings can be relevant to the adhesion improvement in two different manners. First, the plasma-polymerized coating serves as a final surface finish. Second, the coating serves as the glue or improves adhesion properties. The advantage of plasma polymerization is that suitable materials can be synthesised whose properties can be independent of the polymeric materials on which the coating is deposited. However, the plasma polymerization process is more complicated than non-film-forming plasma treatment. In addition, since the coating can be deposited not only on the polymeric material surfaces but also electrodes and walls of the process chamber, frequent cleaning of the system is necessary, limiting this process to be industrialized.

## 3. ATMOSPHERIC PRESSURE PLASMA SOURCES

A variety of atmospheric pressure plasma sources are developed for surface processing, including a corona discharge, a dielectric barrier discharge (DBD), a cold plasma torch, and a gliding arc.

### 3.1. Corona Discharge

Corona discharges can be generated when the electric field is significantly non-uniform [33]. They usually appear in a vicinity of sharp edges and thin wires of electrodes at atmospheric pressure. They are weakly luminous and essentially non-uniform [33]. A general configuration of the corona discharge is schematically illustrated in Fig. 2. After ignition near a sharp or thin electrode, a corona discharge extends to the remaining gap of the electrodes between which high voltage is applied and then transfers to a thermal plasma (arc discharge) as shown in Fig. 1. In order to achieve a continuous corona discharge, the discharge current must be somehow limited, resulting in low speed of the processing. It is overcome by applying pulsed high voltages so that the discharge is ignited at the onset of the high-voltage pulse and extinguished before arcing. The corona discharge is widely used for polymer surface treatment [34–38].

### 3.2. Dielectric Barrier Discharge (DBD)

Another solution for avoiding arcing is to insert at least one insulator (dielectric) between the electrodes, and block a direct current. It is called a dielectric barrier discharge (DBD) or a silent discharge, often operated at atmospheric pressure. The DBD is generated between electrodes covered with dielectrics by applying an alternating current (AC) high voltage [39–51]. DBDs have been widely used for adhesion improvement of materials [3,16,17,30,31,52–76]. In many cases, commercially available 'corona' discharge setups are in fact DBDs [5]. This misuse of the technical term may be due to the fact that the name 'corona' is believed to be more appealing to customers than 'DBD'. Since the term 'corona' is widely misused even in journal papers, one has to pay an attention when the difference of these discharges is important.

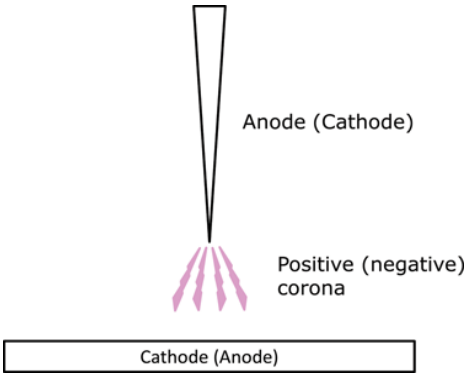


**FIGURE 2** A typical configuration of a corona discharge.

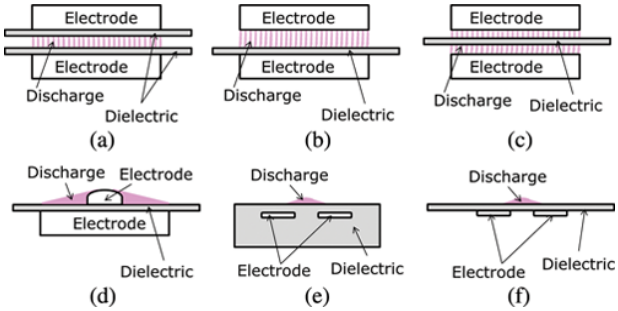


**FIGURE 3** Various types of DBDs: volume discharges (a)–(c) and surface discharges (d)–(f).

There are two types of basic configuration of DBDs, as shown in Fig. 3; the first is a volume discharge where the plasma is generated at the gap between the electrodes (Fig. 3(a)–(c)). For the plasma surface modification, a specimen is usually placed between the gap and the surface is directly exposed to the DBD. In order to ensure stable DBD operation of the volume discharge scheme, however, the gap between the electrodes is typically limited to several millimetres, which restricts the size and shape of the specimens to be treated. The second is a surface discharge [77]. A typical configuration of the surface discharge is a dielectric with an electrode on one side of the dielectric surface and another electrode on its reverse side [78,79] (Fig. 3(d)) or all electrodes embedded in the dielectric [80–83] (Fig. 3(e)). Another case is that both electrodes are attached on one side of the dielectric material and the surface discharge is preferably generated on its reverse side [84] (Fig. 3(f)). This is achieved by feeding specific gas such as helium or argon near the reverse side.

The frequency for operating a DBD is typically chosen between 500 Hz and 500 kHz [12], but DBDs driven at 50 or 60 Hz are reported [85]. As the frequency is lowered, the capacitance decreases at a fixed gap and the applicable power is lowered. Therefore, in general, higher frequency is preferred for high-speed processing. However, as the investment cost for the power supply often dominates the total cost of atmospheric pressure plasma processing, it is attractive to try the low-frequency regime at 50 or 60 Hz by using grid-connected power.

In most cases, DBDs are non-uniform and consist of numerous filamentary micro-discharges distributed in the discharge gap. This is called a filamentary mode. Subsequently, the plasma surface treatment is not uniform due to heavily treated regions by the individual filamentary micro-discharge [39]. In some conditions, however, uniform DBDs can be generated stably. This is often called a homogeneous or glow mode, and such a discharge is often called atmospheric pressure glow discharge [18,86–91]. It is indicated that in order to generate a glow discharge at atmospheric pressure, the

plasma gas should be diluted with helium in a DBD [92]. One explanation of the effect of helium gas is that helium has the metastable state with an extraordinary long lifetime and thus a long timescale of a glow phase in Fig. 1. Later, various different approaches are reported to realize the atmospheric pressure glow discharge plasmas. One example is to use ketone diluted with argon gas [93] that can reduce the cost since argon gas is much cheaper than helium. It is indicated in Fig. 1 that filamentary discharge can be avoided even without using noble gas if plasma is operated at high frequency (as high as radio frequencies (RFs)), or very short pulses. If the frequency is as high as RF or more, or if the pulse width is short enough, in fact, dielectric may not be necessary [94–97] when the power is not very high. However, the RF discharge transfers to the $\gamma$ mode at high power, and it is difficult to sustain a uniform discharge between the gap of the uncovered electrodes [98–100]. In addition, RF operation requires a matching network in order to deliver RF energy to the plasma efficiently, usually limiting high-voltage outputs. Accordingly, the gap of the electrodes should be significantly close enough for stable ignition of the discharge. Consequently, introduction of a specimen between the gap significantly affects the impedance between the gap due to the high capacitance and frequency, and the discharge can be unstable. Therefore, atmospheric pressure RF plasma is rather preferably investigated and developed for cold plasma torches (Section 3.3).

In many cases, the DBD is operated at the first or second glow mode in Fig. 1, but another approach is to block the current at the Townsend discharge mode [101]. Although Townsend discharge is not spatially uniformly distributed, it can avoid the filamentary phase. It is thus suggested that the specimen is moved for uniform treatment.

## 3.3. Cold Plasma Torches, Plasma Jets, and Plasma Pens

Plasma torches that can be extended in the ambient air have been developed for thermal processing, and the plasma in such a case is usually in an equilibrium state (thermal plasma). A plasma spray is a good example. It is widely used for materials synthesis, relying on a thermal process by heating in a plasma with a high current, and melting and spraying materials for deposition. However, followed by the recent developments of atmospheric pressure plasma processing, a variety of non-thermal atmospheric pressure plasma jets (cold plasma torches) have been developed [25,94,102,103]. It is reported that a cold plasma torch can be operated at a high- or radio frequency based on the DBD configuration [94,104–106]. With a high speed flow of argon gas, the plasma is extended to the ambient air. It is also demonstrated that a cold plasma torch can be generated without covering electrodes with the dielectrics [98–100]. Many different types of atmospheric pressure cold plasma torches have been developed [107–116]. Figure 4 shows an example of cold plasma torches based on a DBD configuration reported in the 1990s [105].

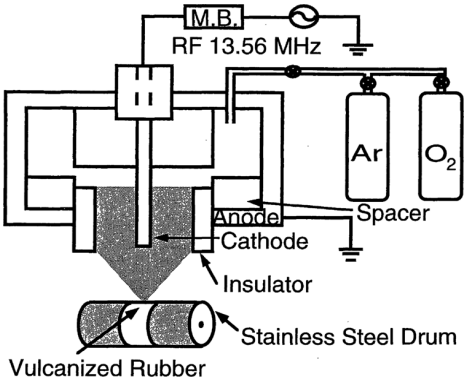


**FIGURE 4** A cold plasma torch based on a DBD configuration [105].



Since they typically use noble gases such as helium and argon, the operation cost must be a certain concern for practical applications. In addition, the extension length in the ambient air must be further elongated to treat 3D-shaped bulky materials in order to obtain further attention from different industrial sectors.

Inductively coupled RF plasma torch has been intensively used for gas analysis, but it is not intensively applied to adhesion improvement.

Atmospheric pressure plasmas can also be generated at microwave and extended as a plasma jet by a gas flow [117]. The plasma properties of the atmospheric pressure microwave plasma jet are similar to those of the atmospheric pressure gliding arcs (see Section 3.4), namely, the plasma is first significantly heated and subsequently cooled down by the gas flow to be a non-thermal plasma.

## 3.4. Gliding Arcs

One of the challenges of atmospheric pressure plasma processing is to achieve a hybrid condition with high reactivity and efficient productivity [118]. Here, the reactivity of a plasma corresponds to the non-equilibrium condition, while the efficient productivity relates to high-energy density. It is noted that general non-thermal (non-equilibrium) plasmas as well as thermal (equilibrium) plasmas cannot provide them simultaneously. However, a gliding arc can potentially achieve a hybrid condition [118]. A gliding arc is a discharge plasma generated between diverging electrodes and extended and quenched by a gas flow [118,119]. It is sometimes known in the industry as 'corona' or alike and not 'gliding arc'. Such a misuse should be avoided since they are completely different types of discharges.

A fast transition into a non-equilibrium state occurs once heat losses from the discharge column exceed the supplied energy. The gliding arc

combines a number of industrially attractive features of plasma-based surface treatment: it is an environmentally clean process, it operates well in air at atmospheric pressure with low costs, it can treat surfaces of bulky objects, and it allows fast processing. It is indicated that the gliding arc setup is more economical than microwave plasma [118]. They are useful for adhesion improvement of materials in industrial and engineering processing [120–122]. However, the treatment effects of commercially available gliding arcs are often disappointing, possibly due to the fact that the conditions of the non-equilibrium state and high-energy density are not taken into account properly. In fact, it is reported that gliding arcs are generally extinguished almost immediately after transition to the non-equilibrium state [118], suggesting that achieving hybrid condition may be practically difficult.

It is however reported that an AC gliding arc discharge can be extended in the ambient air for several centimetres stably and useful for surface treatment of bulky materials [13–15,123–125]. Figure 5 shows a photo of the gliding arc discharge elongated in the ambient air. This unique gliding arc is characterized by the long lifetime of the discharge over several AC periods without extinction [124,125]. It is suggested based on an analytical calculation that in order to realize such a condition, it should be driven at high AC power, serial low resistance should be connected, and the gas flow should be low [125]. Recently detailed optical diagnostics is performed to understand the physics and chemistry of the gliding arc discharges, indicating that OH excited state radicals exists up to approximately 60 mm from the edge of the electrodes [124,125] and that OH ground state radicals are detected in the vicinity of the discharge column [124].

Plasma processing, called open air technology 'Plasmatreat®', is also a plasma generated as an arc and extended and quenched by a gas flow, and can also be regarded as a hybrid plasma. Since high-voltage electrode is surrounded and shielded by a cylindrical ground electrode, both conductive and insulating materials can be treated [126–134]. The discharge can be extended up to 1–2 cm in the ambient air [135]. Optical emission

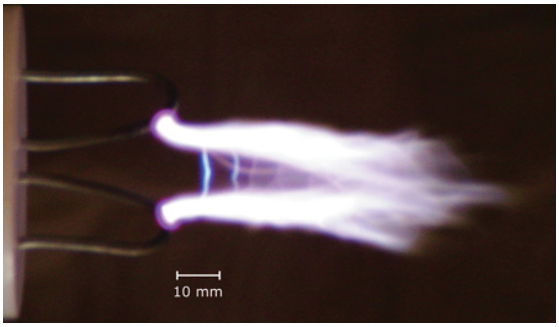


**FIGURE 5** A photo of an AC gliding arc discharge.

spectroscopy indicates that major photoemission lines are assigned to $NO_x$ and $N_2$ [135].

## 3.5. Ultrasound Processing

Atmospheric pressure plasma surface modification is generally performed by feeding a process gas into the plasma. A boundary gas layer normally sticks at the material surface through which reactive species generated in the plasma are diffused for reaction with the surface. Due to the short lifetime of these species, only a small fraction of them can reach the surface. It is reported that powerful ultrasonic waves with a sound power level (SPL) above approximately 140 dB can reduce the thickness of the boundary gas layer. It is also demonstrated that the treatment efficiency of atmospheric pressure plasma can be highly enhanced by simultaneous high-power ultrasonic irradiation onto the treating surface [136–142]. Figure 6 shows a schematic diagram of an ultrasound enhanced DBD.

It is found that ultrasonic irradiation can also prevent arcing and improve uniformity of the DBD treatment in air [139]. Figure 7 shows ion images of time-of-flight secondary ion mass spectrometry (TOF-SIMS) of glass fiber-reinforced polyester (GFRP) surfaces before and after atmospheric pressure DBD treatment in air. The existence of $C_xH_yO_z^+$ markers indicates oxygen-containing functional groups at the GFRP surfaces. It is seen that oxygen uniformly distributes at the untreated GFRP surface (left panel). After the plasma treatment without ultrasonic irradiation, heavily oxidized spots are randomly distributed all over the surface (central panel). However, after

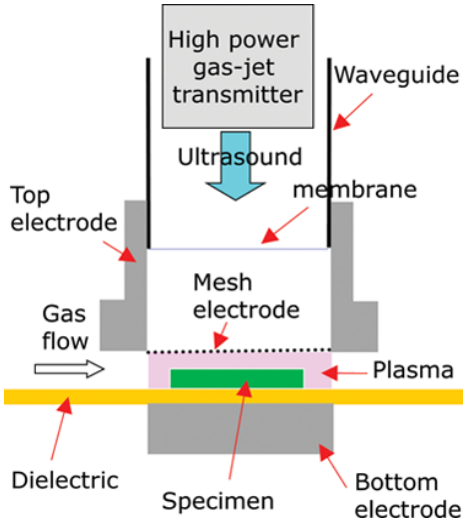


**FIGURE 6** A schematic diagram of the ultrasound enhanced DBD.

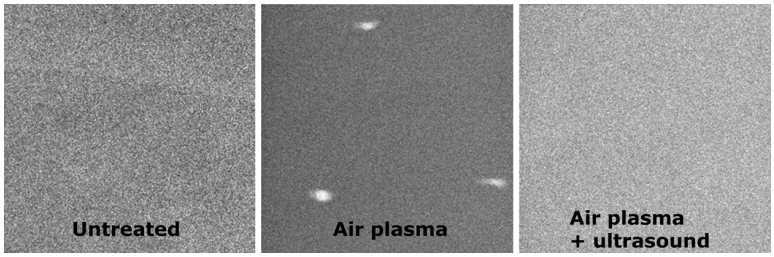


**FIGURE 7** TOF-SIMS ion images (500 μm × 500 μm) showing the lateral intensity distribution of $C_xH_yO_z^+$ markers on the GFRP surfaces: untreated, 30-s air-plasma treated, and 30-s air-plasma treated with ultrasonic irradiation. Black corresponds to no intensity, grey to some intensity, and white to 100% intensity [139].

the plasma treatment with ultrasonic irradiation, the GFRP surface gets uniformly oxidized (right panel).

The improvement by ultrasonic irradiation is rather moderate when plasma is driven at approximately 12 and 40 kHz but is significantly pronounced at 50 Hz [141,142]. In addition to the improvement of plasma treatment efficiency, gas phase reactions can also be enhanced by ultrasonic irradiation [143,144].

### 3.6. Triboplasma

A triboplasma is a gas discharge induced by tribological stimulation [145]. A triboplasma induced by triboelectrification has been experimentally detected around a sliding contact [146]. The detailed mechanism in triboelectrification is unknown, but empirical 'triboelectric series' and Cohen's law [147] can be helpful in predicting the ordering of the tendency for charge acquisition in rubbing. Like other discharge plasmas, a triboplasma can be potentially useful for surface modification such as adhesion improvement of certain surfaces [148]. The method is potentially attractive since the generation of a triboplasma is simple, its treatment effect is expected to be similar to that of normal process plasmas, and simultaneous mechanical rubbing can enhance the treatment effect.

## 4. APPLICATIONS

### 4.1. Treatment of Films, Textiles, and Thin Plates

Films, textiles, and thin plates can be easily treated by atmospheric pressure plasmas in order to improve bondability, printability, dyeability, and paintability, which are relevant to adhesion improvement. The DBDs are the most commonly used atmospheric pressure plasma processing for these

applications [3,12,16,17,20,22,30,31,51–76,85,93]. In most cases, oxygen-containing polar functional groups are introduced by the plasma treatment so that the adhesive properties of the surfaces are improved. However, when the glue has low-surface energy, it is important to reduce the surface energy to achieve a high degree of interaction with the glue [52].

The DBD setup can be easily integrated for continuous treatment of large surfaces, and commercial DBD systems are already available [12,39]. Cold plasma torches are also used for adhesion improvement of thin plates. Recent literature using cold plasma torches is often devoted to the fundamental study of adhesion, but industrially available setups also exist [94].

## 4.2. Treatment of Bulky Materials

When a bulky material is plasma-treated for adhesion improvement, it is often potentially aimed at the construction of mechanical structures [113–115]. DBDs are used to demonstrate adhesion improvement of fiber-reinforced polymers [30]. However, since the gap of the electrodes of the DBD is typically limited within at most several centimetres, the application of the DBD for the treatment of bulky substances is not practical. Instead, it has been recently reported that gliding arcs can efficiently improve the adhesion of FRPs [13–15]. The gliding arc treatment increased the density of oxygen-containing polar functional groups at the surfaces and bond strength with the vinyl ester adhesive. At optimized conditions, the gliding arc discharge can be elongated to the ambient air several centimetres stably so that 3D-shaped bulky structures can be readily treated.

## 4.3. Treatment of Fibers and Powders

One of the obvious advantages of the atmospheric pressure plasma processing is that air-to-air continuous treatment system can be easily designed and constructed. However, the first report to treat carbon fiber by atmospheric pressure plasma is not a continuous processing [3]. On the other hand, the continuous surface treatment by a helium DBD shows that adhesion with epoxy can be significantly improved in a short time, as short as 1–2 s [16]. Since the number of functional groups introduced onto the fiber surfaces by the conventional electrochemical oxidation is too small to have a significant effect [149], plasma treatment is very attractive for this application. In a same way, continuous DBD treatment of ultra-high-molecular-weight polyethylene (UHMWPE) fibers is also demonstrated [17].

Plasma processing is often used for the production of fine powers, but is rarely used for the surface treatment of powders since it is difficult to carry out. Although low-pressure plasmas can easily extend their volumes so that large surface areas of the powder can be potentially treated, the powders can be easily transported to the downstream and can seriously contaminate the

vacuum system. The use of atmospheric pressure would reduce this problem to some extent. Kogoma et al. invented a setup with which fine powders can be circulated through the plasma volume at atmospheric pressure, and their surfaces can be treated without serious segregations [12,150].

### 4.4. Treatment of Elastomers

It is known that plasma treatment might create low-molecular-weight oligomers at an elastomer surface. This is one of the possible reasons why adhesive properties may not always improve after plasma treatment.

Atmospheric pressure plasma has been performed for treating elastomers [105,151–153]. One attempt is to use halogen-containing gases in the atmospheric pressure plasma so as to heavily oxidize and halogenate the elastomer surfaces. It is reported that the adhesive properties of rubber compounds consisting of styrene-butadiene rubber (SBR) and natural rubber (NR) are significantly improved by DBD treatment in He, $O_2$, and halogen-containing gases [154].

### 4.5. Bio-Applications

'Plasma medicine' is a new area of research and development relevant to atmospheric pressure plasma processing [155,156]. This can be divided into three topics:

- Atmospheric pressure plasma for medical therapy
- Plasma-assisted modification of bio-relevant surfaces
- Plasma-based bio-decontamination and sterilization

Among these topics, the second topic of the plasma treatment of bio-relevant surfaces is relevant to adhesion improvement [157,158] since improved attachment of cells after treatment is expected by the plasma treatment.

## 5. SURFACE CHARACTERIZATION

Surface characterization is vitally important to understand the surface modification effects and to optimize the processes. Surface characterization is also performed for fractured parts of composites materials in order to investigate the interfaces and failure mechanisms. Commonly used techniques include contact angle measurement, Fourier transform infrared (FTIR) spectroscopy, x-ray photoelectron spectroscopy (XPS), energy dispersive x-ray spectrometry (EDS), and TOF-SIMS for surface chemistry analyses, and atomic force microscopy (AFM), optical microscopy, and scanning electron microscopy (SEM) for morphological analyses.

The contact angle measurement appears to be the simplest method to characterize the surfaces [159–163]. The measurement relies on the observation of the angle formed by a liquid at the three-phase boundary where the liquid, gas (usually air), and solid intersect. It can be performed immediately after the treatment. It is noted that the technique detects the topmost surface property with the analysis depth of approximately 1 nm or less and is extremely sensitive against its changes. One drawback of the contact angle measurement method is that if highly wetting weak domains exist at the material surface, high wettability may not necessarily result in strong adhesion since the weak domains might be easily separated from the material. Ageing of plasma-treated surfaces is often monitored by the contact angle measurement. Here, the ageing mechanisms include migration of polar functional groups into the material due to rotation of polymer main chains, removal of the polar functional groups, and deposition of contaminations. These changes are detectable by the contact angle measurement, but not necessarily by many other much more sophisticated and expensive methods. However, it is recommended that an adhesion test is performed for the confirmation after ageing of plasma-treated surfaces. It is because even if the surface wettability is reduced by the migration or the deposition, applying uncured adhesive might induce the recovery of the polar functional groups that were migrated beneath the material surfaces or the removal of the contamination by its diffusion into the adhesive, and thus wetting may not directly indicate adhesion properties. There are two types of contact angles reported in the literature. The static contact angle is measured by the sessile drop technique while the dynamic contact angle involves both advancing and receding contact angles. The advancing angle is measured when the liquid is advanced to an unwetted solid surface while the receding angle is measured when the liquid is retracted from a previously wetted surface. The problems of the static contact angle are seriously discussed [164–166], but the sessile drop technique is widely used in research works and process monitoring in the industry due to the simplicity and flexibility of the measurement.

FTIR spectroscopy is also a relatively simple technique, usually operated at atmospheric pressure. Photoabsorption in the infrared range is used to identify chemical functional groups. Many important functional groups created by plasma treatment are infrared-active. Attenuated total reflection FTIR (ATR-FTIR) is often used especially when a material to be analyzed has strong infrared absorption that disturbs reliable analysis. However, even ATR-FTIR detects the bulk information of some micrometres from the surface. Plasma surface treatment generally changes the top layer up to 10 nm or less, and so plasma-treated surfaces are usually insensitive against the FTIR measurement [30]. On the other hand, if the surface is heavily modified or if the surface volume ratio is significantly high (such as thin fibers or fine powders), the plasma modification effect can be clearly detected [17].

XPS, or electron spectroscopy for chemical analysis (ESCA), has appeared to be a powerful tool for surface characterization of polymeric materials surfaces after plasma treatment. XPS uses a soft x-ray source for electron emission from the surface at low-gas pressure. The energies of the emitted electrons are measured, and the binding energies of these electrons are obtained. The surface sensitivity of XPS is governed by the attenuation length of the emitted electrons, and XPS typically measures the average surface chemistry up to a depth of approximately 5 nm. Therefore, XPS is less surface sensitive than the contact angle measurement. It can quantitatively measure the elemental composition, atomic concentration, and chemical states of elements at a surface. It can also give localized information, depending on instrumentation and spatial resolutions, and maps by multiple measurements.

EDS also provides information of elemental composition at the surface. A focused electron beam bombards a specimen surface to emit an x-ray that can be used for the analysis. Since EDS is often attached in SEM, they are often performed at the same locations of the specimen. In many cases, however, EDS is not equipped for light elements that are important for polymer surface analysis.

TOF-SIMS uses a short-pulsed ion beam directing the specimen surface causing secondary ions emission. As all the secondary ions are accelerated to the same kinetic energy, their time-of-flight for the determined path provides their masses. TOF-SIMS is destructive but demonstrates high sensitivity (detection limit ppm–ppb, detection depth $< 1$ nm). For example, uniform distribution of nitrogen-containing functional groups after plasma treatment is detected by TOF-SIMS, as shown in Fig. 7 [139], but it is below the detection limit for XPS. Since TOF-SIMS measure masses only, a good understanding of the surface chemistry is necessary for the reasonable characterization.

A morphological property of the surface also significantly affects the adhesion property. AFM, SEM, and optical microscopy are commonly used for the observation of the surface morphology.

In addition to the above-mentioned surface characterization techniques, it is reported that Hansen solubility (cohesive energy) parameter (HSP) can be preferably used for characterizing the thermodynamic properties of plasma-treated surfaces [167,168]. It is particularly useful for characterizing specimens with high surface volume ratios such as thin fibers and fine particles. The HSP quantitatively describes the physical interactions among molecules. Similar HSP means solubility, permeation, chemical attack, adsorption leading to suspension or slow sedimentation of particulates, or other forms of what might be called positive affinity. Lack of similarity means perhaps only swelling or no physical effect at all, chemical resistance, good barrier properties, and rejection from surfaces such as dewetting, high contact angles, and rapid sedimentation of particulates. The noticeable disadvantage of the XPS is that it is a localized analysis and does not give information on the

uniformity and the overall character of the surfaces by a single measurement. XPS cannot tell exactly where the analysis took place, and in order to obtain full understanding, one has to repeat the expensive and time-consuming analyses and then rely on statistical methods. The advantage of the HSP method is that it can characterize the surface and give the macroscopic information. The HSP measurement was tested for characterizing UHMWPE fibers before and after atmospheric pressure DBD treatment [168]. Since matching the HSP of fibers and matrix polymer optimizes physical adhesion, it is important to know the HSP of the oxygenated surfaces of the UHMWPE fibers. HSP correlations of the interaction of solvents with untreated and plasma-treated UHMWPE fibers have shown that there are two types of surfaces. The first is found in both untreated and treated samples and is typical of polyethylene (PE) and is characteristic of aromatic solvents. The second type of surface is the result of oxygenated species. Matching these HSP with the HSP of a matrix polymer, or some entity connected with the matrix polymer, such as a tie polymer or suitable segment thereof, will optimize physical adhesion. HSP is found to be useful for characterizing plasma-treated polymer surfaces since a variety of functional groups introduced by the treatment sensitively affects HSP [168].



## 5. CONCLUSIONS

Atmospheric pressure plasma appears to be useful for adhesion improvement of polymer surfaces. In addition to the conventional atmospheric pressure plasma sources such as the corona discharge and the DBD, various types of plasma sources have been developed, showing their promising future in this application. In particular, plasmas that can be extended into the ambient air are attractive due to their applicability to practical industrial and engineering processing. Ultrasound-assisted plasma processing can stimulate additional future development and applications since efficiencies of the processing can be enhanced. Development of a triboplasma is interesting as potentially economical processing. Various different applications are listed in this paper as examples that might inspire further development of atmospheric pressure plasma processing.

## REFERENCES

[1] Cognard, J., *C. R. Chimie* **9**, 13–24 (2006).
[2] Chan, C.-M., Ko, T.-M., and Hirokawa, H., *Surf. Sci. Reports* **24**, 1–54 (1996).
[3] Mittal, K. L. (Ed.), *Polymer Surface Modification: Relevance to Adhesion, Volume 3* (VSP, The Netherlands, 2004).
[4] Luo, S. and van Ooij, W. J., *J. Adhes. Sci. Technol.* **16**, 1715–1735 (2002).
[5] Grace, J. M. and Gerenser, L. J., *J. Dispersion Sci. Technol.* **24**, 305–341 (2003).

[6] Arefi-Khonsari, F., Tatoulian, M., Bretagnol, F., Bouloussa, O., and Rondelez, F., *Surf. Coat. Technol.* **200**, 14–20 (2005).
[7] Biederman, H. and Osada, Y., *Polym. Phys. Adv. Polym. Sci.* **95**, 57–109 (1990).
[8] Liston, E. M., Martinu, L., and Wertheimer, M. R., *J. Adhes. Sci. Technol.* **7**, 1091–1127 (1993).
[9] Liston, E. M., *J. Adhes.* **30**, 199–218 (1989).
[10] Leahy, W., Barron, V., Buggy, M., Young, T., Mas, A., Schue, F., McCabe, T., and Bridge, M., *J. Adhes.* **77**, 215–249 (2001).
[11] Hall, J. R., Westerdahl, C. A. L., Devine, A. T., and Bodnar, M. J., *J. Appl. Polym. Sci.* **13**, 2085–2096 (1969).
[12] Kogoma, M., Kusano, M., and Kusano, Y. (Eds.), *Generation and Applications of Atmospheric Pressure Plasmas*, (NOVA Publishers Inc., New York, 2011).
[13] Kusano, Y., Teodoru, S., Leipold, F., Andersen, T. L., Sørensen, B. F., Rozlosnik, N., and Michelsen, P. K., *Surf. Coat. Technol.* **202**, 5579–5582 (2008).
[14] Kusano, Y., Sørensen, B. F., Andersen, T. L., and Leipold, F., *J. Adhes.* **89** (6), 433–459 (2013).
[15] Kusano, Y., Sørensen, B. F., Andersen, T. L., Toftegaard, H. L., Leipold, F., Salewski, M., Sun, Z.-W., Zhu, J., Li, Z., and Adén, M., *J. Phys. D: Appl. Phys.* **46**(13), 135203 (7 pp.) (2013).
[16] Kusano, Y., Andersen, T. L., and Michelsen, P. K., *J. Phys. Conf. Series* **100**, 012002 (2008).
[17] Teodoru, S., Kusano, Y., Rozlosnik, N., and Michelsen, P. K., *Plasm. Proc. Polym.* **6**, S375–S381 (2009).
[18] Kanazawa, S., Kogoma, M., Moriwaki, T., and Okazaki, S., *J. Phys. D: Appl. Phys.* **21**, 838–840 (1988).
[19] Wolf, R. A., *Atmospheric Pressure Plasma for Surface Modification*, (John Willey & Sons, New York, 2012).
[20] Tendero, C., Tixier, C., Tristant, P., Desmaison, J., and Leprince, P., *Spectrochimica Acta B* **61**, 2–30 (2006).
[21] Fridman, A., Chirokov, A., and Gutsol, A., *J. Phys. D: Appl. Phys.* **38**, R1–R24 (2005).
[22] Bogaerts, A., Neyts, E., Gijbels, R., and van der Mullen, J., *Spectrochimica Acta B* **57**, 609–658 (2002).
[23] Napartovich, A. P., *Plasmas Polym.* **6**, 1–14 (2001).
[24] Conrads, H. and Schmidt, M., *Plasma Sources Sci. Technol.* **9**, 441–454 (2000).
[25] Kunhardt, E. E., *IEEE Trans. Plasma Sci.* **28**, 189–200 (2000).
[26] Nehra, V., Kumar, A., and Dwivedi, H. K., *Int. J. Eng.* **2**, 53–61 (2008).
[27] Pochner, K., Neff, W., and Lebert, R., *Surf. Coat. Technol.* **74–75**, 394–398 (1995).
[28] Roth, J. R., Nourgoster, S., and Bonds, T. A., *IEEE Trans. Plasma Sci.* **35**, 233–250 (2007).
[29] Kekez, M. M., Barrault, M. R., and Craggs, J. D., *J. Phys. D: Appl. Phys.* **3**, 1886–1896 (1970).
[30] Kusano, Y., Mortensen, H., Stenum, B., Kingshott, P., Andersen, T. L., Brøndsted, P., Bilde-Sørensen, J. B., Sørensen, B. F., and Bindslev, H., *Plasma Proc. Polym.* **4** (S1), S455–S459 (2007).

[31] Kusano, Y., Mortensen, H., Stenum, B., Goutianos, S., Mitra, B., Ghanbari-Siahkali, A., Kingshott, P., Sørensen, B. F., and Bindslev, H., *Int. J. Adhes. Adhes.* **27** (5), 402–408 (2007).
[32] Yasuda, H., *Plasma Polymerization*, (Academic Press, Florida, Gainesville, FL, 1986).
[33] Raizer, Y. P., *Gas Discharge Physics*, (Springer-Verlag, Berlin, 1991).
[34] Yamamoto, T., Newsome, J. R., and Ensor, D. S., *IEEE Trans. Ind. Appl.* **31**, 494–499 (1995).
[35] Temmerman, E. and Leys, C., *Surf. Coat. Technol.* **200**, 686–689 (2005).
[36] Akishev, Y., Grushin, M., Napartovich, A., and Trushkin, N., *Plasmas Polym.* **7**, 261–289 (2002).
[37] Akishev, Y. S., Grushin, M. E., Monich, A. E., Napartovich, A. P., and Trushkin, N. I., *High Energy Chem.* **37**, 330–335 (2003).
[38] Temmerman, E., Akishev, Y., Trushkin, N., Leys, C., and Verschuren, J., *J. Phys. D: Appl. Phys.* **38**, 505–509 (2005).
[39] Kogelschatz, U., *Plasma Chem. Plasma Proc.* **23**, 1–46 (2003).
[40] Kogelschatz, U., *IEEE Trans. Plasma Sci.* **30** (4), 1400–1408 (2002).
[41] Kogelschatz, U., Eliasson, B., and Egli, W., *J. Phys. IV France C4* **7**, 47–66 (1997).
[42] Borcia, G., Anderson, C. A., and Brown, N. M. D., *Plasma Source Sci. Technol.* **12**, 335–344 (2003).
[43] Fateev, A., Leipold, F., Kusano, Y., Stenum, B., Tsakadze, E., and Bindslev, H., *Plasma Proc. Polym.* **2**, 193–200 (2005).
[44] Leipold, F., Fateev, A., Kusano, Y., Stenum, B., and Bindslev, H., *Fuel* **85**, 1383–1388 (2006).
[45] Leipold, F., Kusano, Y., Hansen, F., and Jacobsen, T., *Food Control* **21**, 1194–1198 (2010).
[46] Leipold, F., Schultz-Jensen, N., Kusano, Y., Bindslev, H., and Jacobsen, T., *Food Control* **22** (8), 1296–1301 (2011).
[47] Teodoru, S., Kusano, Y., and Bogaerts, A., *Plasma Proc. Polym.* **9**, 654–689 (2012).
[48] Kusano, Y., Leipold, F., Fateev, A., Stenum, B., and Bindslev, H., *Surf. Coat. Technol.* **200**, 846–849 (2005).
[49] Massines, F., Gouda, G., Gherardi, N., Duran, M., and Croquesel, E., *Plasma Polym.* **6**, 35–49 (2001).
[50] Wang, C. and He, X., *Surf. Coat. Technol.* **210**, 3377–3384 (2006).
[51] Wagner, H.-E., Brandenburg, R., Kozlov, K. V., Sonnenfeld, A., Michel, P., and Behnke, J. F., *Vacuum* **71**, 417–436 (2003).
[52] Siró, I., Kusano, Y., Norrman, K., Goutianos, S., and Plackett, D., *J. Adhes. Sci. Technol.* **27** (3), 294–308 (2013).
[53] Hwang, Y. J., Qiu, Y., Zhang, C., Jarrard, B., Stedeford, R., Tsai, J., Park, Y. C., and McCord, M., *J. Adhes. Sci. Technol.* **17**, 847–860 (2003).
[54] Chirokov, A., Gutsol, A., and Fridman, A., *Pure Appl. Chem.* **77**, 487–495 (2005).
[55] Borcia, G., Dumitrascu, N., and Popa, G., *Surf. Coat. Technol.* **197**, 316–321 (2005).
[56] Borcia, G., Anderson, C. A., and Brown, N. M. D., *Appl. Surf. Sci.* **221**, 203–214 (2004).

[57] Dumitrascu, N., Topala, I., and Popa, G., *IEEE Trans. Plasma Sci.* **33**, 1710–1714 (2005).
[58] Seeböck, R., Esrom, H., Charbonnier, M., and Romand, M., *Plasmas Polym.* **5**, 103–118 (2000).
[59] Kostov, K. G., des Santos, A. L. R., Hopnda, R. Y., Nascente, P. A. P., Kayama, M. E., Algatti, M. A., and Mota, R. P., *Surf. Coat. Technol.* **204**, 3064–3068 (2010).
[60] Dorai, R. and Kushner, M. J., *J. Phys. D: Appl. Phys.* **36**, 666–685 (2003).
[61] Goosens, O., Dekempeneer, E., Vangeneugden, D., Van de Leest, R., and Leys, C., *Surf. Coat. Technol.* **142–144**, 474–481 (2001).
[62] Geßner, C., Bartels, V., Betker, T., Matucha, U., Penache, C., and Klages, C.-P., *Thin Solid Films* **459**, 118–121 (2004).
[63] Šíra, M., Trunec, D., Stahel, P., Buršíková, V., Navrátil, Z., and Buršík, J., *J. Phys. D: Appl. Phys.* **38**, 621–627 (2005).
[64] De Geyter, N., Morent, R., Leys, C., Gengembre, L., Payen, E., Van Vlierberghe, S., and Schacht, E., *Surf. Coat. Technol.* **202**, 3000–3010 (2008).
[65] Prat, R., Suwa, T., Kogoma, M., and Okazaki, S., *J. Adhes.* **66**, 163–181 (1998).
[66] Senthilkumar, P., Janarthanan, M., and Krishna Prasad, G., *IE(I) J. TX* **88**, 9–12 (2008).
[67] Scott, C., Figgures, C. C., and Dixon, D. G., *Plasma Sources Sci. Technol.* **13**, 461–465 (2004).
[68] Cui, N.-Y., Upadhyay, D. J., Anderson, C. A., Meenan, B. J., and Brown, N. M. D., *Appl. Surf. Sci.* **253**, 3865–3871 (2007).
[69] Hwang, Y. J., Matthews, S., McCord, M., and Bourham, M., *J. Electrochem. Soc.* **151**, C495-C-501 (2004).
[70] Novák, I., Pollák, V., and Chodák, I., *Plasma Proc. Polym.* **3**, 335–364 (2006).
[71] Tanaka, K., Inomata, T., and Kogoma, M., *Thin Solid Films* **386**, 217–221 (2001).
[72] Zhang, Q., Wang, C., Babukutty, Y., Ohyama, T., and Kogoma, M., *J. Biomed. Mater. Res.* **60**, 502–509 (2002).
[73] Ogawa, T., Baba, S., and Fujii, Y., *J. Appl. Polym. Sci.* **100**, 3403–3408 (2006).
[74] Roth, J. R., *Phys Plasmas* **12**, 057103-1-057103-9 (2005).
[75] Esena, P., Riccardi, C., Zanini, S., Tontini, M., Poletti, G., and Orsini, F., *Surf. Coat. Technol.* **200**, 664–667 (2005).
[76] Vander Wielen, L. C., Östenson, M., Gatenholm, P., and Ragauskas, A. J., *Carbohydr. Polym.* **65**, 179–184 (2006).
[77] Gibalov, V. I. and Pietsch, G. J., *J. Phys. D: Appl. Phys.* **33**, 2618–2636 (2000).
[78] Yoshikawa, M., Kusano, Y., Akiyama, S., Naito, K., Okazaki, S., and Kogoma, M., US Patent No. 5,316,739 (1994).
[79] Zhang, R., Zhan, R.-J., Wen, X.-H., and Wang, L., *Plasma Sources Sci. Technol.* **12**, 590–596 (2003).
[80] Šimor, M., Ráhel, J., Vojtek, P., Černák, M., and Brablec, A., *Appl. Phys. Let.* **81**, 2716–2718 (2002).
[81] Štefečka, M., Kando, M., Černák, M., Korzec, D., Finantu-Dinu, E. G., Dinu, G. L., and Engemann, J., *Surf. Coat. Technol.* **174–175**, 553–558 (2003).
[82] Korzec, D., Finantu-Dinu, E. G., Schabedissen, A., Engemann, J., Ráhel, J., Štefečka, M., Imahori, Y., and Kando, M., *Surf. Coat. Technol.* **169–170**, 228–232 (2003).

[83] Gibalov, V. I. and Pietsch, G. J., *J. Phys. D: Appl. Phys.* **37**, 2082–2092 (2004).
[84] Babukutty, Y., Prat, R., Endo, K., Kogoma, M., Okazaki, S., and Kodama, M., *Langmuir* **15**, 7055–7062 (1999).
[85] Okazaki, S., Kogoma, M., Uehara, M., and Kimura, Y., *J. Phys. D: Appl. Phys.* **26**, 889–892 (1993).
[86] Massines, F., Rabehi, A., Decomps, P., Gadri, R. B., Ségur, P., and Mayoux, C., *J. Appl. Phys.* **83**, 2950–2957 (1998).
[87] Golubovskii, Y. B., Maiorov, V. A., Behnke, J., and Behnke, J. F., *Plasma Proc. Polym.* **2**, 188–192 (2005).
[88] Golubovskii, Y. B., Maiorov, V. A., Behnke, J., and Behnke, J. F., *J. Phys. D: Appl. Phys.* **36**, 39–49 (2003).
[89] Mangolini, L., Anderson, C., Heberlein, J., and Kortshagen, U., *J. Phys. D: Appl. Phys.* **37**, 1021–1030 (2004).
[90] Massines, F., Ségur, P., Gherardi, N., Khamphan, C., and Ricard, A., *Surf. Coat. Technol.* **174–175**, 8–14 (2003).
[91] Wang, X., Li, C., Lu, M., and Pu, Y., *Plasma Sources Sci. Technol.* **12**, 358–361 (2003). *Plasma Sources Sci. Technol.* **12**, 358-361 (2003).
[92] Yokoyama, T., Kogoma, M., Moriwaki, T., and Okazaki, S., *J. Phys. D: Appl. Phys.* **23**, 1125–1128 (1990).
[93] Okazaki, S., Kogoma, M., and Uchiyama, H., Proc. 3rd Int. Symp. High Pressure Low Temp. Plasma Chem. HAKONE III, Strasbourg, 101–106 (1991).
[94] Schütze, A., Jeong, J. Y., Babayan, S. E., Park, J., Selwyn, G. S., and Hicks, R. F., *IEEE Trans. Plasma Sci.* **26**, 1685–1694 (1998).
[95] Ráhel, J., Černák, M., Hudec, I., Štefečka, M., Kando, M., and Chodák, I., *Plasmas Polym.* **5**, 119–127 (2000).
[96] Cheng, S. Y., Yuen, C. W. M., Kan, C. W., Cheuk, K. K. L., Daud, W. A., Lam, P. L., and Tsoi, W. Y. I., *Vacuum* **84**, 1466–1470 (2010).
[97] Jaššo, M., Hudec, I., Alexy, P., Kováčik, D., and Krump, H., *Int. J. Adhes. Adhes.* **26**, 274–284 (2006).
[98] Laimer, J., Haslinger, S., Meissl, W., Hell, J., and Störi, H., *Vacuum* **79**, 209–214 (2005).
[99] Shi, J. J. and Kong, M. G., *Appl. Phys. Let.* **90**, 101502-1-101502-3 (2007).
[100] Yang, X., Moravej, M., Nowling, G. R., Babayan, S. E., Panelon, J., Chang, J. P., and Hicks, R. F., *Plasma Sources Sci. Technol.* **14**, 314–320 (2005).
[101] Aldea, E., Peeters, P., De Vries, H., Van De Sanden, M. C. M., *Surf. Coat. Technol.* **200**, 46–50 (2005).
[102] Laroussi, M. and Akan, T., *Plasma Proc. Polym.* **4**, 777–788 (2007).
[103] Laimer, J. and Störi, H., *Plasma Proc. Polym.* **4**, 266–274 (2007).
[104] Inomata, K., Ha, H., Chaudhary, K. A., and Koinuma, H., *Appl. Phys. Let.* **64**, 46–48 (1994).
[105] Lee, B. J., Kusano, Y., Nato, N., Naito, K., Horiuchi, T., and Koinuma, H., *Jpn. J. Appl. Phys. Pt.* 1, **36**, 2888–2891 (1997).
[106] Mortensen, H., Kusano, Y., Leipold, F., Rozlosnik, N., Kingshott, P., Sørensen, B. F., Stenum, B., and Bindslev, H., *Jpn. J. Appl. Phys.* **45** (10B), 8506–8511 (2006).
[107] Foest, R., Kindel, E., Ohl, A., Stieber, M., and Weltmann, K.-D., *Plasma Phys. Contr. Fusion* **47**, B525–B536 (2005).

[108] Kaemling, C., Kaemling, A., Tümmel, S., and Viöl, W., *Surf. Coat. Technol.* **200**, 668–671 (2005).
[109] Gesche, R., Kovacs, R., and Scherer, J., *Surf. Coat. Technol.* **200**, 544–547 (2005).
[110] Toshifuji, J., Tatsumata, T., Kakikawa, H., Sakakibara, T., and Shimizu, I., *Surf. Coat. Technol.* **171**, 302–306 (2003).
[111] Xie, J., Xin, D., Cao, H., Wang, C., Zhao, Y., Yao, L., Ji, F., and Qiu, Y., *Surf. Coat. Technol.* **206**, 191–201 (2011).
[112] Friedrich, J. F., Rohrer, P., Saur, W., Gross, T., Lippitz, A., and Unger, W., *Surf. Coat. Technol.* **59**, 371–378 (1993).
[113] Park, S.-J. and Lee, H.-Y., *J. Colloid Interf. Sci.* **285**, 267–272 (2005).
[114] Sladek, R. E. J., Baede, T. A., and Stoffels, E., *IEEE Trans. Plasma Sci.* **34**, 1325–1330 (2006).
[115] Cheng, C., Liye, Z., and Zhan, R.-J., *Surf. Coat. Technol.* **200**, 6659–6665 (2006).
[116] Zhang, J., Sun, J., Wang, D., and Wang, X., *Thin Solid Films* **506–507**, 404–408 (2006).
[117] Schäfer, J., Vašina, P., Hnilica, J., Foest, R., Kudrle, V., and Weltmann, K.-D., *IEEE Trans. Plasma Sci.* **39**, 2350–2351 (2011).
[118] Fridman, A., Nester, S., Kennedy, L. A., Saveliev, A., and Mutaf-Yardimci, O., *Progress Energy Combustion Sci.* **25**, 211–231 (1999).
[119] Czernichowski, A., *Pure Appl. Chem.* **66**, 1301–1310 (1994).
[120] Janča, J. and Czernichowski, A., *Surf. Coat. Technol.* **98**, 1112–1115 (1998).
[121] Oosterom, R., Ahmed, T. J., Poulis, J. A., and Bersee, H. E. N., *Med. Eng. Phys.* **28**, 323–330 (2006).
[122] Stewart, R., Goodship, V., Guild, F., Green, M., and Farrow, J., *Int. J. Adhes. Adhes.* **25**, 93–99 (2005).
[123] Kusano, Y., International Patent Application No. WO 2011 073170 A1 (2011).
[124] Sun, Z. W., Zhu, J. J., Li, Z. S., Aldén, M., Leipold, F., Salewski, M., and Kusano, Y., *Optics Express* **21** (5), 6028–6044 (2013).
[125] Kusano, Y., Salewski, M., Leipold, F., Zhu, J. J., Ehn, A., Li, Z. S., and Aldén, M., *J. Appl. Phys.* Submitted.
[126] Lommatzsch, U., Pasedag, D., Baalmann, A., Ellinghorst, G., and Wagner, H.-E., *Plasma Proc. Polym.* **4**, S1041–S1045 (2007).
[127] Martín-Martínez, J. M. and Romero-Sánchez, M. D., *Eur. Phys. J. Appl. Phys.* **34**, 125–138 (2006).
[128] Encinas, N., Díaz-Benito, B., Abenojar, J., and Martínez, M. A., *Surf. Coat. Technol.* **205**, 396–402 (2010).
[129] Encinas, N., Pantoja, M., Torres-Remiro, M., and Martínez, M. A., *J. Adhes.* **87** (7–8), 709–719 (2011).
[130] Encinas, N., Abenojar, J., and Martínez, M. A., *Int. J. Adhes. Adhes.* **33**, 1–6 (2012).
[131] Encinas, N., Dillingham, R. G., Oakley, B. R., Abenojar, J., Martínez, M. A., and Pantoja, M., *J. Adhes.* **88** (4–6), 321–336 (2012).
[132] Noeske, M., Degenhardt, J., Strudthoff, S., and Lommatzsch, U., *Int. J. Adhes. Adhes.* **24**, 171–177 (2004).
[133] Pombuena, V., Balart, J., Boronat, T., Sánchez-Nácher, L., and Garcia-Sanoguera, D., *Mater. Design* **47**, 49–56 (2013).

[134] Iqbal, H. M. S., Bhowmik, S., and Benedictus, R., *Int. J. Adhes. Adhes.* **30**, 418–424 (2010).
[135] Dowling, D. P., O'Neill, F. T., Langlais, S. J., and Law, V. J., *Plasma Polym. Proc.* **8**, 718–727 (2011).
[136] Kusano, Y., *Surf. Eng.* **25** (6), 415–416 (2009).
[137] Kusano, Y., Singh, S. V., Bardenshtein, A., Krebs, N., and Rozlosnik, N., *J. Adhes. Sci. Technol.* **24**, 1831–1839 (2010).
[138] Kusano, Y., Norrman, K., Drews, J., Morgen, P., Leipold, F., Singh, S. V., Bardenshtein, A., and Krebs, N., *Surf. Coat. Technol.* **205**, S490–S494 (2011).
[139] Kusano, Y., Singh, S. V., Norrman, K., Leipold, F., Drews, J., Morgen, P., Bardenshtein, A., and Krebs, N., *J. Adhes.* **87**, 720–731 (2011).
[140] Kusano, Y., Singh, S. V., Norrman, K., Drews, J., Leipold, F., Rozlosnik, N., Bardenshtein, A., and Krebs, N., *Surf. Eng.* **28** (6), 453–457 (2012).
[141] Kusano, Y., Norrman, K., Singh, S. V., Leipold, F., Morgen, P., Bardenshtein, A., and Krebs, N., *J. Adhes. Sci. Technol.* **27** (7), 825–833 (2013).
[142] Kusano, Y., Andersen, T. L., Toftegaard, H. L., Leipold, F., Bardenshtein, A., and Krebs, N., *Int. J. Mater. Eng. Innov.* In press.
[143] Drews, J., Kusano, Y., Leipold, F., Bardenshtein, A., and Krebs, N., *Ozone: Sci. Eng.* **33**, 783–788 (2011).
[144] Kusano, Y., Drews, J., Leipold, F., Fateev, A., Bardenshtein, A., and Krebs, N., *J. Phys. Conf. Series.* **406**, 012006 (2012).
[145] Heinicke, G., *Tribochemistry*, (Carl Hanser Verlag, Germany, 1984).
[146] Daly, J. H., Hayward, D., and R. A. Pethrick, R. A., *J. Phys. D: Appl. Phys.* **19**, 885–896 (1986).
[147] Nakayama, K. and Nevshupa, R. A., *J. Phys. D: Appl. Phys.* **35**, L53–L56 (2002).
[148] Singh, S. V., Kusano, Y., Morgen, P., and Michelsen, P. K., *J. Appl. Phys.* **111**, 083501 (2012).
[149] Farrow, G. J., Atkinson, K. E., Fluck, N., and Jones, C., *Surf. Interface Anal.* **23**, 313–318 (1995).
[150] Mori, T., Tanaka, K., Inomata, T., Takeda, A., and Kogoma, M., *Thin Solid Films* **316**, 89–92 (1998).
[151] Romero-Sánchez, M. D., Martín-Martínez, J. M., *Int. J. Adhes. Adhes.* **26**, 345–354 (2006).
[152] Tyczkowski, J., Zieliński, J., Kopa, A., Krawczyk, I., and Woźniak, B., *Plasma Proc. Polym.* **6**, S419–S424 (2009).
[153] Moreno-Couranjou, M., Choquet, P., Guillot, J., and Migeon, H.-N., *Plasma Proc. Polym.* **6**, S397–S400 (2009).
[154] Kusano, Y., Inagaki, T., Yoshikawa, M., and Akiyama, S., EU Patent No. EP 0,606,014 B1 (1999).
[155] Laroussi, M. and Fridman, A., *Plasma Proc. Polym.* **5**, 501 (2008).
[156] Lloyd, G., Friedman, G., Jafri, S., Schultz, G., Fridman, A., and Harding, K., *Plasma Proc. Polym.* **7**, 194–211 (2010).
[157] Brewis, D. M. and Critchlow, G. W., *J. Adhes.* **54**, 175–199 (1995).
[158] Girard-Lauriault, P.-L., Mwale, F., Iordanva, M., Demers, C., Desjardins, P., and Wertheimer, M. R., *Plasma Proc. Polym.* **2**, 263–270 (2005).
[159] Kaelble, D. H., *J. Adhes.* **2**, 66–81 (1970).
[160] Linford, R. G., *Chem. Soc. Rev.* **1**, 445–464 (1972).

[161] Good, R. J., *J. Adhes. Sci. Technol.* **6**, 1269–1302 (1992).
[162] Jacobasch, H.-J., Grundke, K., Mäder, G. E., Freitag, K.-H., and Panzer, U., *J. Adhes. Sci. Technol.* **6**, 1381–1396 (1992).
[163] Kwok, D. Y., Lam, C. N. C., Li, A., Leung, A., Wu, R., Mok, E., and Neumann, A. W., *Colloids Surf. A: Physicochem. Eng. Aspects* **142**, 219–235 (1998).
[164] Strobel, M. and Lyons, C. S., *Plasma Proc. Polym.* **8**, 8–13 (2011).
[165] Mundo, R. D. and Palumbo, F., *Plasma Proc. Polym.* **8**, 14–18 (2011).
[166] Müller, M. and Oehr, C., *Plasma Proc. Polym.* **8**, 19–24 (2011).
[167] Hansen, C. M. *Hansen Solubility Parameters. A User's Handbook*, 2nd ed., (Taylor & Francis, Florida, 2007).
[168] Kusano, Y., Teodoru, S., and Hansen, C. M., *Surf. Coat. Technol.* **205**, 2793–2798 (2011).

# [Appendix A2]

Y. Kusano

## “Plasma surface modification at atmospheric pressure”

*Surface Engineering* 25(6) (2009) 415-416 (Editorial).

# Technology vision

Yukihiro Kusano

## Plasma surface modification at atmospheric pressure

A plasma is an ionized gas. Ions, electrons, high-energy neutrals, radicals and ultra violet photons are generated in a plasma and these high-energy species can be used for modification of material surfaces. Surface modifications with non-thermal plasmas are attractive because of environmental compatibility, high treatment efficiency due to the non-equilibrium state at high electron temperature, and retained bulk properties of materials. They are often employed at low gas pressures, but require expensive vacuum systems, and are well-developed only for batch or semi-batch treatments. To overcome these drawbacks, plasma processing at atmospheric pressure has been developed,[1] obviating vacuum equipment and permitting the treatment of large objects and continuous treatment.[2] For example, a corona discharge and a dielectric barrier discharge (DBD) at atmospheric pressure have long been used for treatment of film surfaces. As they are temporally and spatially inhomogeneous at low electron temperatures, they were often thought to be unsuitable for efficient surface treatments or thin film synthesis. Therefore low pressure plasmas have commonly been used in such cases despite their drawbacks. However, Okazaki, Kogoma and their group in Sophia University reported at the 8th International Symposium on Plasma Chemistry (ISPC-8) in 1987 that even at atmospheric pressure a defusing glow discharge plasma, which is similar to a discharge obtainable at low pressures, can be generated by pulse excitation in a DBD of a noble gas such as helium.[3] It has subsequently been shown that a variety of surface treatments performed in low pressure plasmas are achievable at atmospheric pressure.[4,5] This technique has already been commercially applied. Some examples include surface treatment of plastic films for adhesion improvement, surface cleaning, and treatment of powders.

There are several review articles available in the topic.[6–9] Among them ref.[9] is a first review book focusing on recent development of atmospheric pressure plasmas. The book deals with generation and applications of atmospheric pressure plasmas, including the basics of the technique, and uses in electronics, surface cleaning, improvement of wetting, adhesion improvement, micro-plasmas, etching of Si and $SiO_2$, sterilization, and plasma enhanced chemical vapour deposition for synthesis of carbon nano-tubes, amorphous carbons, a-Si and oxides, surface modification and synthesis of powders, and ultra-precision machining. This book is written in Japanese, and the English version is now under preparation.

One of the challenges for atmospheric pressure plasma processing is to achieve high chemical selectivity and efficient productivity simultaneously. Selective chemical processes can be expected with a high non-equilibrium state in plasma so as to influence chemical bonding of the molecules in the plasma and/or at the material surfaces to be treated, and efficient productivity of plasma reactors can be demonstrated with high energy densities. However, general non-thermal plasmas as well as thermal plasmas cannot provide high non-equilibrium states and high energy densities simultaneously. In the present article, two possible approaches to overcome this issue are suggested: development of a hybrid plasma with a high energy density at a highly non-equilibrium state, and plasma processing assisted by external energy input.

The use of the transient type of $\gamma$- and arc discharges can be a promising route to create a hybrid plasma. A $\gamma$-discharge is a discharge sustained by secondary electron emission from electrode surfaces,[10] created by the breakdown of a low energy density discharge which is sustained by bulk ionization. Due to its low impedance a high energy density can be achieved in a $\gamma$-discharge. The problem of a $\gamma$-discharge is its poor controllability,[11] preventing it from practical use. In order to


Published by Maney on behalf of the Institute
DOI 10.1179/174329409X389281

avoid uncontrollability and instability of the discharge, plasma torches with high energy densities are usually operated at low pressures.[12] However, development of hybrid plasma sources with a controllable $\gamma$-discharge at atmospheric pressure would significantly impact plasma-chemical applications, considering optimized electrodes and efficient transition to non-equilibrium states. Another example of a hybrid plasma is a gliding arc generated between diverging electrodes in a fast gas flow. A fast transition into a non-equilibrium state occurs once heat losses from the discharge column exceed the supplied energy. Up to 80 % of the electrical energy may be directly absorbed by endothermic chemical reactions.[7] Although a similar effect is expected for microwave plasmas, a gliding arc system is less expensive than microwave plasma devices.[13] It is indicated that a gliding arc can be preferably applied in large scale exhaust gas cleaning, pollution control, fuel conversion, hydrogen production and surface modification. In particular, the gliding arc combines a number of industrially attractive features of plasma based surface treatments: it is environmentally much cleaner than mechanical or wet chemical processes, it operates well in air at atmospheric pressure with low costs; being a torch-like plasma source, it can treat surfaces of bulky objects, and it allows fast processing. Therefore it is useful in many industrial applications that involve coating, painting, printing, dying, and adhesion.[14] However, gliding arcs often degenerate heat sensitive materials by thermal irradiation from the electrodes. In addition, commercially available gliding arcs often result in poor performance due to insufficient non-equilibrium conditions and/or low input energy density applied practically.[15] Therefore it is of great interest to develop advanced gliding arcs with a higher level of non-equilibrium states and higher energy densities.

Plasma processing can be also improved by additional energy input in to plasma. Among possible techniques, ultrasound irradiation is attractive due to its simple setup, easy up-scaling, and high efficiency. During plasma surface modification, reactive species of ions, electrons, high-energy neutrals and radicals are generated in a plasma, diffuse through a boundary gas layer between the plasma and a material surface, and subsequently react with the surface. Due to the short lifetimes of these reactive species, only a small amount of them can reach the surface, limiting efficient, high speed treatment. Since ultrasonic waves can efficiently reduce the thickness of the boundary gas layer, surface modification efficiency can be enhanced by ultrasonic irradiation onto the surfaces during plasma treatment.[16]

It is concluded that plasma surface modification at atmospheric pressure is useful and already applied industrially, and can be improved by further development of the processing.

## References:


1. G. Borcia, C. A. Anderson and N. M. D. Brown: *Appl. Surf. Sci.,* 2004, **221**, 203–214
2. Y. Kusano, T. L. Andersen and P. K. Michelsen: *J. Phys. Conf. Series.*, 2008, **100**, 012002
3. S. Kanazawa, M. Kogoma, T. Moriwaki and S. Okazaki: *S. Proc. Int. Symp. Plasma Chem. (ISPC-8 (Tokyo))*. 1987, **3**, 1839–1844
4. K. Tanaka, T. Inomata and M. Kogoma: *Plasma and Polym.*, 1999, **4**, 269–281
5. Y. Sawada, S. Ogawa and M. Kogoma: *J. Phys. D App. Phys.*, 1995, **28**, 1661–1669
6. A. Bogaerts, E. Neyts, R. Gijbels and J. van der Mullen: *Spectrochimica,* 2002, **B 57**, 609–658
7. A. Fridman, A. Chirokov and A. Gutsol, *J. Phys. D Appl. Phys.,* 2005, **38**, R1–R24
8. C. Tendero, C. Tixier, P. Tristant, J. Desmaison and P. Leprince: *Spectrochimica,* 2006, **B 61**, 2–30
9. '大気圧プラズマの生成制御と応用技術 (Taikiatsu plasma no seisei seigyo to ouyou gijutsu – Generation and application of atmospheric pressure plasmas)' ed. M. Kogoma, 2006, Science & Technology
10. X. Yang, M. Moravej, G. R. Nowling, S. E. Babayan, J. Panelon, J. P. Chang and R. F. Hicks: *Plasm. Sources. Sci. Technol.* 2005, **14**, 314–320
11. J. Laimer, S. Haslinger, W. Meissl, J. Hell and H. Störi: *Vacuum,* 2005, **79**, 209–214
12. G. Dinescu, E. R. Ionita, I. Luciu, C. Grisolia and JET EFDA contributors: *Fusion Eng. Design,* 2007, **82**, 2311–2317
13. A. Fridman, S. Nester, L. A. Kennedy, A. Saveliev and O. Mutaf-Yardimci: *Prog. Energy and Combustion Sci.,* 1999, **25**, 211–231
14. Y. Kusano, S. Teodoru, F. Leipold, T. L. Andersen, B. F. Sørensen, N. Rozlosnik and P. K. Michelsen: *Surf. Coat. Technol.* 2008, **202**, 5579–5582
15. Y. Kusano: private communication
16. N. Krebs, A. Bardenshtein, Y. Kusano, H. Bindslev and H. J. Mortensen: *Int. Patent* WO2008-138901 A1



**Yukihiro Kusano**
**Senior Scientist**
*Risø National Laboratory for Sustainable Energy, Technical University of Denmark*
*PO Box 49, DK-4000 Roskilde, Denmark*
*yuki@risoe.dtu.dk*

# [Appendix A3]

Y. Kusano

## “An apparatus for treating a surface with at least one gliding arc source”

European patent No. 2,514,280 B1 (2014).

There is a variation that has been granted in the US (U.S. patent No. 9,420,680 B2 (2016)).

(19) Europäisches Patentamt
European Patent Office
Office européen des brevets

(11) **EP 2 514 280 B1**

(12) **EUROPEAN PATENT SPECIFICATION**

(45) Date of publication and mention of the grant of the patent:
**18.06.2014 Bulletin 2014/25**

(21) Application number: **10790447.6**

(22) Date of filing: **14.12.2010**

(51) Int Cl.:
***H05H 1/48*** *(2006.01)*

(86) International application number:
**PCT/EP2010/069587**

(87) International publication number:
**WO 2011/073170 (23.06.2011 Gazette 2011/25)**

(54) **AN APPARATUS FOR TREATING A SURFACE WITH AT LEAST ONE GLIDING ARC SOURCE**

Vorrichtung zur Behandlung einer Oberfläche mit mindestens einer Gleitlichtbogen-Quelle

Appareil pour traiter une surface avec au moins une source à arc glissant

(84) Designated Contracting States:
**AL AT BE BG CH CY CZ DE DK EE ES FI FR GB GR HR HU IE IS IT LI LT LU LV MC MK MT NL NO PL PT RO RS SE SI SK SM TR**

(30) Priority: **15.12.2009 EP 09179277**
**15.12.2009 US 286570 P**

(43) Date of publication of application:
**24.10.2012 Bulletin 2012/43**

(73) Proprietor: **Danmarks Tekniske Universitet**
**2800 Kgs. Lyngby (DK)**

(72) Inventor: **KUSANO, Yukihiro**
**DK-4000 Roskilde (DK)**

(74) Representative: **Zacco Denmark A/S**
**Hans Bekkevolds Allé 7**
**2900 Hellerup (DK)**

(56) References cited:
**US-B1- 6 236 013**

- **KUSANO Y ET AL: "Gliding arc discharge: application for adhesion improvement of fibre reinforced polyester composites", SURFACE & COATINGS TECHNOLOGY ELSEVIER SCIENCE S.A. SWITZERLAND LNKD- DOI: 10.1016/J.SURFCOAT.2008.06.076, vol. 202, no. 22-23, 30 August 2008 (2008-08-30), pages 5579-5582, XP002582085, ISSN: 0257-8972**
- **PRYSIAZHNEVYCH ET AL.: "Study of non-isothermality of atmospheric plasma in transverse arc discharge", UKR. JOURNAL OF PHYSICS, vol. 52, no. 11, 2007, pages 1061-1067, XP002582086, ISSN: 0503-1265**
- **PELLERIN ET AL.: "Heat string model of bi-dimensional DC Glidarc", JOURNAL OF PHYSICS D (APPLIED PHYSICS), vol. 33, no. 19, 7 October 2000 (2000-10-07), pages 2407-2419, XP002636296, UK ISSN: 0022-3727**
- **TOSHIFUJI ET AL.: "Cold arc-plasma jet under atmospheric pressure for surface modification", SURFACE & COATINGS TECHNOLOGY, vol. 171, no. 1-3, 1 July 2003 (2003-07-01), pages 302-306, XP002636297, Switzerland ISSN: 0257-8972**

EP 2 514 280 B1

## Description

### Field of the invention

**[0001]** The invention relates to an apparatus for treating a surface with at least one gliding arc source. The invention further relates to a corresponding method and system.

### Background of the invention

**[0002]** Non-equilibrium plasmas are preferably used for surface treatment in industry. In order to increase efficiency of the surface treatment, a gliding arc may be utilized whereby the power of the plasma may be increased by keeping the non-equilibrium condition, see e,g. A. Fridman et al., "Gliding arc discharge", Progress in Energy and Combustion Science 25, (1999), pages 211 - 231, or Kusano et al.: "Gliding are discharge: application for adhesion improvement of fibre reinforced polyester composites", Surface and Coatings Technology, vol, 202, 22-23 (2008), pages 5579-5582.

**[0003]** Existing gliding arcs yield a problem that the advantages of gliding arcs are not effectively used, and thereby the resulting surface treatment effect is insufficient. For example, the extension (or length) of the discharge of prior art gliding arcs is very limited which reduces their applicability for the object with a variety of sizes and shapes.

### Summary of the invention

**[0004]** According to one aspect, disclosed herein is an apparatus for treating a surface with at least one gliding arc source comprising

- at least one gas flow controlling unit and a set of electrodes for providing a plasma;
- a cooling unit for providing a cooling fluid, and
- a high voltage power supply for generating a discharge;

wherein at least one of the electrodes comprises a tubular portion fluidly coupled to the cooling unit, and wherein the tubular portion comprises, at least along a portion of its outer surface, a protrusion configured to lower the voltage applied to the electrodes required to ignite the plasma.

**[0005]** Hence, an efficient cooling of the electrodes is provided while ensuring an efficient plasma generation.

**[0006]** Alternatively or additionally to provide a protrusion, at least one of the electrodes may comprise a tubular portion fluidly coupled to the cooling unit 201, wherein the electrode further comprises an outer surface comprising at least one portion facing the other one of the electrodes; wherein an intersection of said at least one portion of the outer surface of the electrode with a plane normal to a longitudinal direction of the electrode has a curvature with a radius of curvature less than 3mm. For example, the tubular portion may define said longitudinal direction. Said portion of the outer surface may thus be curved in a plane normal to said longitudinal direction and have a radius of curvature smaller than 3mm, preferably smaller than 2mm.

**[0007]** For example the electrode may be formed as a tube having a radius no larger than 3mm. Alternatively, the electrode may comprise a tubular portion, e.g. a tubular portion with a radius no less than 3mm, and a protrusion extending radially from the tubular portion where the protrusion has a radially outward edge portion. The edge portion may be curved in a plane normal to said longitudinal direction and have a radius of curvature smaller than 3mm, preferably smaller than 2mm.

**[0008]** According to another aspect, disclosed herein is an apparatus for treating a surface with at least one gliding arc source comprising

- at least one gas flow controlling unit and a set of electrodes for providing a plasma;
- a cooling unit for supplying a cooling fluid;
- a high voltage power supply for generating a discharge
- a control unit adapted to control at least the cooling unit;
- a sensor adapted to measure a parameter indicative of the resistance of at least one of the electrodes,
- a computational unit communicatively coupled to the sensor;

wherein the computational unit is adapted to calculate a feedback signal based on the measured parameter; and wherein the control unit is adapted to control the power supply and/or the cooling unit responsive to the calculated feed back signal. The computational unit may be an integral part of the control unit or it may be embodied as a separate unit. Accordingly, the computational unit may be communicatively coupled to the control unit, e.g. via an internal communication such as a bus of the control unit and/or via an external communications interface between the computational unit and the control unit. In some embodiments, the computational unit and/or the control unit may further be communicatively coupled to the power supply. It will generally be appreciated that some or all of the various units of the apparatus described herein, e.g. the control unit, the computational unit, the sensor, the gas flow controlling unit, the cooling unit, etc. may be integrated into a single unit, suitably communicatively interconnected by internal communications means of the integrated unit.

**[0009]** Hence, an efficient control of the electrodes is provided while ensuring an efficient plasma generation.

**[0010]** According to yet another aspect, disclosed herein is an apparatus for treating a surface with at least one gliding arc source comprising at least one gas flow controlling unit for each gliding arc source; and a set of electrodes; wherein the at least one gas flow controlling

unit and the set of electrodes are controlled to provide a plasma comprising a rotational temperature at the point of arc ignition above approximately 2000K and more preferably above 3000K.

**[0011]** Thereby is achieved a plasma with an optimal or substantially optimal plasma for treating surfaces of samples.

**[0012]** Embodiments of the present invention also relates to a method corresponding to embodiments of the device.

**[0013]** More specifically, according to one aspect, the invention relates to a method of treating a surface with at least one gliding arc source comprising controlling at least one gas flow controlling unit and controlling a set of electrodes; and providing a plasma via the at least one gas flow controlling unit and the set of electrodes; and controlling the plasma to comprise a rotational temperature at the point of arc ignition above approximately 2000K and more preferably 3000K.

**[0014]** The method and embodiments thereof correspond to the device and embodiments thereof and have the same advantages for the same reasons.

**[0015]** Embodiments of the present invention also relate to a system corresponding to embodiments of the device.

**[0016]** More specifically, the invention relates to a system for treating a surface with at least one gliding arc source comprising an apparatus according to an embodiment of the invention and a sample, wherein the apparatus is adapted to provide a plasma to treat the sample surface.

**[0017]** In some embodiments, at least one of the electrodes comprises a tube having a first end and a second end wherein the tube is configured to receive, during operation a coolant at said first end and discharge the coolant at said second end, wherein the centre of the cross-section of the tube at the first end is displaced relative to the centre of the cross-section of the tube at the second end.

**[0018]** The cross section of the tube may have any shape such as round or rectangular. The cross section of the tube may have a width between 1 mm and 50 cm, between 0.5 cm and 20 cm, between 1 cm and 10 cm or between 2 cm and 8 cm. The cross section of the tube includes a portion facing the other electrode and the plasma. At least a part of this portion may be curved with a radius of curvature less than 3mm, e.g. les than 2mm. Both electrodes may comprise a tube.

**[0019]** The tube may have approximately a U shape where the first end and the second end are positioned at the upper part of the U approximately at the same height.

**[0020]** Consequently, an electrode is provided capable of being efficiently cooled by circulating coolant. The flow resistance is lowered allowing an even better cooling by designing the electrode as a tube with a larger inner diameter.

**[0021]** In some embodiments, at least one of the electrodes comprises a tubular portion wherein the tubular portion, at least along a portion of its outer surface, comprises a protrusion configured to lower the needed voltage applied to the electrodes to ignite the plasma, relatively to the needed voltage when the at least one electrode does not comprise said protrusion.

**[0022]** The protrusion may be an elongated, flat, e.g. blade-shaped, element elongated along the longitudinal direction of the electrode and having a width at an end distal to the electrode, which width is smaller than its longitudinal dimension and smaller than the height of the protrusion. Generally, the protrusion may extend along at least a portion of the outer surface of the tubular portion. The protrusion may project from the outer surface of the tubular portion towards the other electrode and the plasma, thus defining at least one edge portion facing the other electrode. The edge portion may be round and have a radius of curvature less than 3mm, e.g. less than 2mm. The radius of curvature may be measured in an intersection of the protrusion with a cross-sectional plane of the electrode normal to the longitudinal direction of the electrode.

**[0023]** The electrode protrusion e.g. electrode attachment, may protrude in a direction approximately towards the other electrode. The electrode protrusion may protrude with a height of at least 1 mm, 2 mm, 5 mm, 1 cm, 2 cm, 5 cm, or 10 cm. The electrode attachment may protrude with a height no more than 20 cm, 10 cm, 5 cm, 2 cm, 1 cm, or 5 mm.

**[0024]** The electrode protrusion may have a shape such that the intensity of the electric field around the part of the electrode comprising the protrusion is increased relatively to the intensity of electrical field of the same part of the electrode if the protrusion where removed, when a voltage is applied, whereby the voltage needed to ignite the plasma is lowered.

**[0025]** The electrode protrusion may be attached to the tubular portion after the tubular portion is formed or the tubular portion and the attachment may be formed as an integral body. It will further be appreciated that more than one protrusion, e.g. more than one attachment, may be provided at each electrode.

**[0026]** In some embodiments, the attachment, the blades and/or the protrusion may be directly cooled by circulating fluid.

In some embodiments, a cross section of the tubular portion being perpendicular to the longitudinal direction of the tubular portion, comprising a part of the electrode protrusion, may have a shape such that a first surface area defined between a first line and a second line originating in the centre of said cross section is at least a factor A larger than a second surface area defined between said second line and a third line originating in said centre, wherein the angle between said first and said second line, and said second line and said third line is B, wherein the first and the second line is positioned so that the first surface area comprises the electrode protrusion, and the third line is positioned so that the first surface area and the second surface area do not overlap.

**[0027]** A may be chosen from approximately 1.1, 1.5, 2, 3, 4, 5, or 10, and B may be chosen from approximately 180 degrees, 135 degrees, 90 degrees, 45 degrees, 30 degrees, 20, degrees, 10 degrees, or 5 degrees.

**[0028]** In some embodiments, the apparatus further comprises a computational unit communicatively coupled to the control unit via a first communication link and to a sensor via a second communication link, wherein said sensor is adapted to measure a parameter indicative of the resistance of at least one of the electrodes, and where the computational unit is adapted to calculate a feedback signal based on the measured parameter wherein the computational unit is further adapted to transmit the feedback signal to the control unit wherein the control unit is adapted to control the cooling unit responsive to the received feed back signal such that the cooling unit is controllable via a feedback loop. Additionally or alternatively, the computational unit may be adapted to calculate a feedback signal based on the measured parameter wherein the computational unit is further adapted to feed the feedback signal to the control unit wherein the control unit is adapted to control the power supply responsive to the received feedback signal such that the power supply is controllable via a feedback loop.

**[0029]** The parameter may be the temperature of the electrode, or the resistance of the electrode. The temperature of the electrode may be measured by attaching a temperature sensor to the electrode and/or measuring the Infra red and/or visible radiation from the electrode. The temperature of the electrodes may also be estimated by the temperatures of the fluid (coolant) before and after cooling the electrodes, or by measuring the temperature of the sample 112. The feedback signal may be generated securing that the resistance of the electrode is maintained below a predetermined value e.g. two or three times larger resistance than the resistance at room temperature, if the temperature of the electrode increases the feedback signal may secure that cooling unit cools the electrode more e.g. by increasing the flow rate of the coolant and/or decreasing the temperature of the coolant. Correspondingly, if the temperature of electrode decreases the feedback signal may cause the cooling unit to cool the electrode less e.g. by decreasing the flow rate of the coolant and/or increasing the temperature of the coolant. As the resistance and the temperature of an electrode normally have an approximately linear relationship the feedback signal may be generated securing that the temperature of the bulk part of the electrode is not raised with more than $3/\alpha$ from room temperature (e.g. from 20 degrees Celsius), where $\alpha$ is the temperature coefficient of the linear relationship between the resistance and temperature. For copper and aluminium $3/\alpha$ is approximately 769 degrees Celsius, and for tungsten it is 667 degrees Celsius. The feedback signal may be generated securing that the temperature of the electrode is not raised with more than $2/\alpha$ from room temperature, where $\alpha$ is the temperature coefficient of the linear relationship between the resistance and temperature. For copper and aluminium $2/\alpha$ is approximately 513 degrees Celsius, for tungsten it is 444 degrees Celsius, and for stainless steel it is 2000 degrees Celsius. The feedback signal may be generated securing that the temperature of the electrode is not raised with more than $1/\alpha$ from room temperature, where $\alpha$ is the temperature coefficient of the linear relationship between the resistance and temperature. For copper and aluminium $1/\alpha$ is approximately 256 degrees Celsius, for tungsten it is 222 degrees Celsius, and for stainless steel it is 1000 degrees Celsius.

**Brief description of the drawings**

**[0030]**

Figure 1 shows an embodiment of a device for generating at least one gliding arc plasma.

Figure 2 shows an embodiment of a device for generating at least one gliding arc plasma and comprising a cooling unit.

Figure 3 shows an embodiment of a device for generating at least one gliding arc plasma comprising a control unit.

Figure 4 shows an embodiment of a set of electrodes in which the electrodes are formed as hollow tubes.

Figure 5 shows an embodiment of a set of electrodes comprising hollow tube electrodes with blades.

Figure 6 shows the O/C ratio at the surface of a polyester sample after plasma treatment for a number of devices.

Figure 7 shows how parameters controlled by the device affect parameters of the plasma and a sample treated by the plasma.

Figure 8 shows an embodiment of a device 600 comprising a feedback loop for optimizing control of a plasma 107.

Figure 9 shows the polar component of the surface energy of a polyester sample versus the flow rate of the gas (air) supplied by the device to the plasma.

Figure 10 shows a definition of axial and circumferential curvatures.

Figure 11a-b shows a set of electrodes comprising electrode protrusions.

Figure 12a-d shows different tube and electrode protrusion designs.

Figure 13 shows an electrode comprising a tube hav-

ing and electrode protrusion.

Figure 14 shows a part of an apparatus for treating a surface with a gliding arc according to an embodiment of the present invention.

Figure 15 shows an embodiment of a device for generating at least one gliding arc plasma.

**Detailed description of the drawings**

**[0031]** Figure 1 shows an embodiment of a device 100 for generating at least one gliding arc plasma 107 such as one gliding arc plasma or a plurality of gliding arc plasmas. The device 100 may comprise a gas flow controlling unit 104, a set of electrodes 102 and a power supply 101.

**[0032]** The gas flow controlling unit 104 may be exemplified as a needle valve, which is able to regulate the flow, or a float type flow meter, which is able to regulate the flow and measure the flow, or a mass flow controller, which is able to regulate the flow via an external electric signal and to measure the flow.

**[0033]** In an embodiment, the gas flow controlling unit 104 may comprise a plurality of flow meters such as a flow meter for each gas component in a multiple component gas mixture. For example, the gas flow controlling unit 104 may comprise two flow meters when providing a two component gas mixture to the plasma 107, one flow meter for each component in a two component gas mixture.

**[0034]** The gas flow controlling unit and the power supply may be electrically coupled to the electric grid e.g. via respective electric wires. Thereby the electric grid may provide power to the gas flow controlling unit and to the power supply 101.

**[0035]** The power supply 101 may be electrically connected to the set of electrodes 102 e.g. via electrical wires 113. Generally, the voltage required may depend on e.g. the gap between the electrodes. If the gap is smaller, the ignition voltage is also smaller. In some embodiments the power supply may be configured to supply a voltage between 300 V and 40 kV. The operation of the arc requires normally requires much lower voltages than the ignition of the plasma.

**[0036]** Via the electrical wires 113, the power supply 101 may provide (electric) energy to the set of electrodes 102. For example, the power supply 101 may be connected to the electrical grid from where the power supply 101 may receive electric energy. Additionally, the power supply 101 may transform the power, e.g. alternating current, received from the electric grid into a format suitable for the set of electrodes, e.g. direct current or alternating current. Thereby, the set of electrodes 102 may generate a gliding arc using either direct current (DC) or alternating current (AC). The driving frequency of the alternating current may be between 5 Hz and 2 MHz, preferably between 50 Hz and 500 kHz.

**[0037]** The power supply 101 may additionally control the surface temperature of a sample 112 to be treated by the at least one gliding arc plasma 107. By increasing the power from the power supply 101 to the set of electrodes 102, the surface temperature of the sample may be increased.

**[0038]** The gas flow controlling unit 104 may inject gas into a plasma 107 contained in a volume. Alternatively, a plasma may be created in the volume. In the above and below, a plasma 107 may be characterized as a partially ionized gas, in which a certain proportion of electrons are free rather than being bound to an atom or a molecule in the gas. The ability of positive and negative charges to move somewhat independently makes the plasma electrically conductive so that it responds strongly to electromagnetic fields. Examples of suitable gases to be fed to the discharge for use in embodiments of an apparatus described herein include air, $N_2$, $O_2$, Ar, He, Ne, $CO_2$, $H_2O$, hydro-carbons (such as methane, ethane, propane, butane, alcohols, etc.), etc. or mixtures of the above.

**[0039]** For example, the gas flow controlling unit 104 may inject a gas into the plasma as indicated by the arrow 194. The volume containing the plasma may be partly or wholly expanded by the set of electrodes 102 and the gas flow 194.

**[0040]** The gas flow controlling unit 104 may be controlled manually by a person setting the flow rate of the gas injected into the plasma 107.

**[0041]** The set of electrodes 102 may, for example, comprise two electrodes having a radius of axial curvature. For example, the radius of axial curvature 901 may be at least approximately 20 mm (more preferably > 40 mm). Alternatively, the set of electrodes may comprise two straight electrodes. Further, the two electrodes may be positioned with a distance between approximately 0.2 mm and 20 mm (preferably 0.2 mm and 10 mm) between them at the point of minimal distance. Generally, the point of minimum distance between the electrodes corresponds to the point of ignition. However, if there is a sharply edged part of the electrode with a slightly larger gap, this may be the point of ignition. The ignition generally occurs only if the electric field is strong enough, i.e. the point of ignition is generally a location along the electrode where the electrical field between the electrodes is sufficiently strong.

**[0042]** In an embodiment, the set of electrodes 102 may comprise more than two electrodes e.g. three or four electrodes.

**[0043]** Large voltage differences (e.g.1-40 kV) between the electrodes induce ignition of an arc discharge. The arc discharge is extended by a high speed gas flow from the gas flow controlling unit 104. The input power, provided by the power supply 101, of the arc can be high e.g. in the order of 0,2 - 5 kW per one gliding arc. Thereby, the input power to the at least one gliding arc plasma may be controlled such that electrons in the at least one gliding arc have high temperature, e.g. above 0.5 eV.

**[0044]** Figure 2 shows an embodiment of a device 200

for generating at least one gliding arc plasma 107 such as one gliding arc plasma or a plurality of gliding arc plasmas. The device 200 may comprise the technical features of figure 1.

**[0045]** In the device 200, each electrode in the set of electrodes may be hollow enabling passage of a fluid through the set of electrodes.

**[0046]** Additionally, the device 200 may comprise a cooling unit 201. The cooling unit may be fluidly coupled to the set of electrodes 102 e.g. via a tube 202 or the like. Thereby, the cooling unit 201 may cool the set of electrodes 102 e.g. by pumping a coolant through the set of electrodes 102 via the tube 202.

**[0047]** The cooling unit 201 may be electrically coupled to the power supply 101 via an electric wire 204 or to an electric grid (not shown).

**[0048]** In an embodiment, the device 200 may further comprise an actuator 110 adapted to translate a sample 112 through the plasma 107. For example, the actuator 110 may comprise an X-Y-table. The actuator 110 may be controlled manually by an operator.

**[0049]** Optionally, the X-Y-table of the actuator 110 may be hollow enabling a fluid to pass through the actuator 110. In this case, the cooling unit 201 may be fluidly coupled to the actuator 110 e.g. via a tube 203 or the like. Thereby, the cooling unit 201 is able to cool the actuator 110 by pumping a coolant such as water through the actuator 110.

**[0050]** As in figure 1, the device 200 is able to generate a plasma 107 and to surface treat a sample 112.

**[0051]** Figure 3 shows an embodiment of a device 300 for generating at least one gliding arc plasma 107 such as one gliding arc plasma or a plurality of gliding arc plasmas. The device 300 may comprise a power supply 101, a control unit 103, at least one gas flow controlling unit 104 (e.g. one gas flow controlling unit) and a set of electrodes 102.

**[0052]** The power supply 101 may be electrically communicated with the control unit 103 e.g. via an electrical wire 105, such that the control unit 103 may control the power supply 101.

**[0053]** The control unit 103 may control the power provided to the at least one gas flow controlling unit 104 e.g. via electric wire 113.

**[0054]** For example, the set of electrodes 102 may be electrically coupled to the power supply 101 via e.g. an electric wire 106, and communicatively coupled to the control unit 103 via a wireless and/or wired communication link 106. The communication link may be established via e.g. an electrical wire and/or Bluetooth. Thereby, via the electric wire 105, the control unit 103 may control the frequency and/or the amplitude of the power supplied to the set of electrodes 102, and via the electric wire 106, the power supply may provide power to the set of electrodes 102.

**[0055]** Additionally, the control unit 103 may control the at least one gas flow controlling unit 104. The at least one gas flow controlling unit 104 may be communicatively coupled to the control unit 103 e.g. by a wireless and/or wired communication link 113. The communication link may be established via an electrical wire and/or Bluetooth. Thereby, the control unit 103 may control the amount of gas and/or the flow rate of gas injected by the at least one gas flow controlling unit 104. Thereby, the control unit 103 may comprise controlling flow of the gas used in the plasma 107 and thus, for example, the gas in the plasma may be cooled while the electron temperature is substantially maintained e.g. within +/- 30 %.

**[0056]** The at least one gas flow controlling unit 104 may inject gas into a plasma 107 contained in a volume via the set of electrodes 102. Alternatively, a plasma may be created in the volume. In the above and below, a plasma 107 may be characterized as a partially ionized gas, in which a certain proportion of electrons are free rather than being bound to an atom or a molecule in the gas. The ability of positive and negative charges to move somewhat independently makes the plasma electrically conductive so that it responds strongly to electromagnetic fields.

**[0057]** The set of electrodes 102 may, for example, comprise two or more electrodes having a radius of axial curvature. For example, the radius of axial curvature (see 901 in figure 10 for a definition of axial curvature) may be approximately more than 20mm (preferably > 40 mm). Alternatively, the set of electrodes may comprise two straight electrodes. Further, the two electrodes may be positioned with a distance between approximately 0,2 mm and 20 mm (preferably 0.2 mm and 10 mm) between them at the point of minimal distance.

**[0058]** Large voltage differences (e.g. 1-40 kV) between the electrodes induces ignition of an arc discharge. The arc discharge is extended by a high speed gas flow. The input power of the arc can be high e.g. in the order of 0,2 - 5 kW per one gliding arc. Thereby, the input power to the at least one gliding arc plasma may be controlled such that electrons in the at least one gliding arc have high temperature, e.g. above 0,5 eV. Thereby, the control unit 103 may be adapted to control the input power to the at least one gliding arc plasma via the set of electrodes 102 such that electrons in the at least one gliding arc have high temperature, e.g. above 0,5 eV, and such that the energy density in the at least one gliding arc is high (typically at least 200 W, preferably at least 400 W).

**[0059]** In an embodiment, the device 300 may further comprise a cooling unit 201 which may be controlled by the control unit 103. For example, the cooling unit 201 may be communicatively coupled to the control unit 103 e.g. by a wireless and/or wired communication link 109 such as an electrical wire and/or Bluetooth.

**[0060]** The cooling unit 201 may be fluidly connected to the set of electrodes 102 via e.g. a tube 202 or the like. The electrodes 102 may be hollow to enable a fluid to pass through them. Thereby, the cooling unit 201 may be adapted to provide a coolant to the set of electrodes 102. The coolant may, for example, be water, oil or air. Generally, the coolant may be an insulating fluid and/or

a fluid with high resistance. Generally, in some embodiments a gas may be fed through the tubes of the electrodes for cooling, and all or a part of the gas may subsequently be fed to the plasma.

**[0061]** The cooling unit 201 may optionally be fluidly connected to the X-Y table 110 via a tube 203.

**[0062]** In an embodiment, the device 300 may further comprise an actuator 110 adapted to translate a sample 112 through the plasma 107. For example, the actuator 110 may comprise an X-Y-table. The actuator 110 may be communicatively coupled to the control unit 103 e.g. by a wireless and/or wired communication link 111 such as an electrical wire and/or Bluetooth. Thereby, the control unit 103 is adapted to control the actuator 110 such as for example the speed by which the sample 112 is translated through the plasma 107.

**[0063]** Figure 4 shows an embodiment of a set of electrodes 102 in which the electrodes 102 are formed as hollow tubes enabling a fluid to circulate within them. The hollow electrodes 102 may be fluidly connected to the cooling unit 201 so as to enable the coolant to be circulated in the electrodes 102. Thereby, the control unit 103 of figure 3 may be adapted to control the temperature of the electrodes by circulating the coolant in the hollow set of electrodes 102.

**[0064]** In an embodiment, the hollow tubes of the electrodes 102 may be thin, for example having an outer diameter of 3 mm and an inner diameter of 2 mm. Thin electrodes may provide a more efficient use of the power supplied from the power supply 101 to the electrodes because if the point of arc ignition is sharply edged, the intensity of the electric field generated by the electrodes is higher, and a discharge, ignited by the electrodes, is ignited with a lower voltage. Generally the radius of curvature of the portion of the surface (measured in a plane normal to the longitudinal direction of the electrode, also referred to as circumferential curvature) at the point of arc ignition should be no more than 3mm.

**[0065]** Alternatively or additionally, if the circumferential curvature (see 902 in figure 10 for a definition of circumferential curvature) of the electrodes is small, the intensity of the electric field generated by the electrodes is also higher, and the discharge, ignited by the electrodes, is ignited with a lower voltage.

**[0066]** Generally, a power supply 101 may provide a higher power if the required voltage is lower. Therefore, by using thin electrodes, a given power supply 101 may provide a higher power than if thick electrodes are used.

**[0067]** Additionally, as the cost of a power supply 101 increases with the maximum deliverable power in the specification, it may be desirable to reduce the required voltage which may be achieved using thin electrodes.

**[0068]** In an embodiment, the hollow tubes of the electrodes 102 may be thick, for example having an outer diameter of 6 mm and an inner diameter of 4 mm. Increasing the inner diameter of the hollow set of electrodes 102 may enable more efficient cooling due to the possibility of using a higher coolant flow rate in a tube with a larger inner diameter. More efficient cooling enables a higher electric energy to be delivered to the plasma than the thinner electrodes because the resistance of the electrodes increases with temperature, and thus the resistance of the thick electrodes, which are better cooled, is smaller than the thin electrodes. When the resistance is higher, more electrical energy is consumed for heating. Thereby, a higher plasma energy may be achieved which may result in better surface treatment.

**[0069]** In an embodiment, one electrode may be thick and one electrode may be thin.

**[0070]** Figure 5 shows an embodiment of a set of electrodes 102 comprising attachments 301. The attachments 301 may, for example, be blade-shaped. By including attachments 301 in the electrodes 102, the voltage required for generating the plasma may be reduced as disclosed above under thin electrodes. Thus, the voltage required for generating a plasma using thick electrodes may be lowered by including attachments 301.

**[0071]** In an embodiment, the attachments are rigidly coupled to the electrodes e.g. via welding or the like.

**[0072]** The blades 301 may be made of the same material as the electrodes 102 e.g. copper or aluminum, stainless steel, tungsten or the like. The blades 401 may be welded to the electrodes 102 or the electrodes 102 and blades 301 may be cast into a single piece. Alternatively, the blades may be made of a different material than the electrodes.

**[0073]** In an embodiment, the blades 301 may be included in a hollow set of electrodes i.e. electrodes through which the coolant may be circulated. Optionally, the blades 301 may also be hollow and fluidly connected to the hollow set of electrodes 102, e.g. via one or more holes, thereby enabling coolant to circulate through the blades and thus enabling cooling of the blades 301.

**[0074]** Generally, the blades 301 may be designed such that they enable a lowering of the ignition voltage for the plasma, whereby a condition comprising a high electron temperature (e.g. greater than 0,5 eV) and a high input power to at least one gliding arc (e.g. greater than 0,2 kW and below 5 kW) may be established. The design of the attachments may include using sharp edged blades and/or blades with a small radius of curvature (i.e. small diameter no more than 4 mm (if radius no more than 2 mm)) so that high electric field can be generated at the electrodes 301.

**[0075]** Additionally or alternatively, the electrodes may be designed to include sharp edged and/or a small radius of curvature (i.e. small diameter) so that a high electric field can be generated at the electrodes 102.

**[0076]** The sharp edges of the attachments 301 and/or the electrodes may ensure a low ignition voltage, thereby enabling a high energy input to the plasma 107.

**[0077]** Figure 6 shows the atomic composition at the surface of a polyester sample 112 after treatment with a prior art device represented by solid diamonds, a device according to Figure 4 comprising thin tubes (in order to achieve a low ignition voltage) represented by open

squares, and a device according to figure 4, thick tubes and blades (in order to achieve a low ignition voltage and a low resistance in the electrodes) represented by solid triangles, measured by means of x-ray photoelectron spectroscopy. When the oxygen to carbon ratio (O/C ratio) increases, it is an indication of better performance of a device due to more oxygen from the plasma having reacted with the plastic of the sample 112. Thus, from figure 6 it is seen that the gliding arc plasma system with blades is most efficient in oxidizing the polyester surfaces of the plastic sample 112. Further, it is seen that the gliding arc plasma system comprising cooled electrodes is more efficient than the prior art device.

**[0078]** Figure 7 shows how parameters controlled by the device 100, 200, 300 affects parameters of the plasma 107 and a sample 112 treated by the plasma.

**[0079]** For example, if the control unit 103 increases the power applied to the electrodes 102, then the energy density of the plasma 107 increases and therefore, the device 100, 200, 300 is able to increase the speed of translating the sample 112 through the plasma 107 in order to treat the sample 112.

**[0080]** Further, increasing the power applied to the electrodes 102 provides for a higher electron temperature in the plasma and higher plasma density and thereby a faster treatment of the sample 112 surface.

**[0081]** If the at least one gas flow controlling unit 104 is able to provide a suitable gas flow to the plasma 107, the device 100, 200, 300 may provide a higher electron temperature and a lower gas temperature in the plasma 107. When the flow rate is increased, the gas and electrons are cooled more at and around the arc ignition point e.g. within a perimeter of e.g. a radius of 20 mm around the arc ignition point. The electron temperature may remain substantially (e.g. within 30 %) unchanged beyond this perimeter, while the gas temperature decreases furthermore beyond the perimeter.

**[0082]** Additionally, by having the at least one gas flow controlling unit 104 providing a suitable gas flow, the device 100, 200, 300 may increase the discharge length of the plasma. If the flow rate is too low, it cannot extend (blow out) the discharge well and thus the extension of the discharge is short. If the flow rate is too high, the plasma (gas and electrons) are cooled down too much to extend the discharge. Therefore, a suitable gas flow exists which may provide a discharge length of an appropriate size.

**[0083]** The gas flow rate has to be low enough to sustain a high temperature of the arc discharge. Further, by providing a high gas flow, corrosion of the electrodes may be impeded or prevented.

**[0084]** If the cooling unit 201 increases cooling of the electrodes 102, then the electrical resistance of the electrodes decreases. Thereby is achieved that a higher power may be applied to the electrodes 102 without risking damaging the electrodes 102. Further, lower resistance results in lower power loss.

**[0085]** Further, by cooling the electrodes 102, the surface temperature of the sample 112 may be controlled. By cooling the electrodes 102, low thermal damage to the sample 112 being treated is achieved because thermal radiation from the electrodes to the sample 112 is reduced.

**[0086]** The actuator 110 may control the surface temperature of the sample 112. If the actuator 110 increases the speed of the sample 112 through the plasma 107, low thermal damage to the sample 112 may be achieved because an irradiated part of the sample 112 may cool down while another part of the sample 112 subsequently becomes irradiated.

**[0087]** The surface temperature of the sample 112 may be controlled by changing the distance between the sample and the at least one gliding arc source.

**[0088]** The temperature of the sample 112 may be decreased by placing the sample on a cooled sample holder.

**[0089]** Figure 8 shows an embodiment of a device 600 comprising a feedback loop for optimizing control of a plasma 107.

**[0090]** The temperature of the gas in the plasma 107 may be estimated using the rotational temperature obtained from optical emission (e.g. OH emission) in the gas e.g. as disclosed in C. O. Laux, T. G. Spence, C. H. Kruger, and R. N. Zare, "Optical diagnostics of atmospheric pressure air plasmas", Plasm. Source Sci. Technol. 12 (2003), p 125-138.

**[0091]** The rotational temperature may be detected by an optical detector 602 by observing the optical emission from the plasma 107.

**[0092]** In an embodiment, the device 600 comprises a computational unit 605 adapted to analyze the rotational spectrum.

**[0093]** The computational unit 605 may be communicatively connected to the optical detector 602 and the control unit 103 of the device 200 via respective wired and/or wireless communication links 606, 607 such as electrical wires and/or Bluetooth communication links.

**[0094]** The computational unit 605 may receive a rotational spectrum from the optical detector 602 via connection 606, e.g. via an electrical wire. Based on the rotational spectrum received, the computational unit 605 may estimate a rotational temperature.

**[0095]** The rotational temperature may be representative of the molecule/gas temperature in the plasma 107, and thus, the computational unit 605 may be adapted to determine a temperature of the gas (ions and/or molecules) in the plasma based on the rotational temperature.

**[0096]** Based on the estimated gas temperature in the plasma, the computational unit 605 may be adapted to transmit a feedback signal to the control unit 103 of the device 200 via communication link 607 in order to e.g. have the control unit 103 to increase the gas flow to the plasma 107 via the at least one gas flow controlling unit 104 and/or to increase the electric current in the electrodes, etc., in order to optimize the plasma 107 according to predetermined plasma values stored in the com-

putational unit 107 e.g. a rotational temperature of 2000K at a flow rate of 30 L/min (corresponding to a gas velocity of 81 m/s +/-10%).

**[0097]** Further, the rotational temperature may be representative of the electron temperature at the arc of the electrodes and therefore, the computational unit 605 may be adapted to determine the electron temperature at the arc of the electrodes based on the rotational temperature.

**[0098]** Figure 9 shows the surface energy of a sample 112 versus the flow rate of the gas supplied by the device 200, 600 to the plasma 107. In figure 9, the distance between the sample and the location of the arc ignition was 65 mm. The higher the polar component of the surface energy of the sample 112 the better for adhesion, because more amounts of polar functional groups are created, which efficiently interact with adhesives. Thus, from figure 9 it is seen that a flow-rate of approximately 20 - 25 L/min (corresponding to a gas velocity of approximately 58 - 68 m/s +/-10%) is optimal for this type of device. A flow-rate of 15 - 30 L/min (corresponding to a gas velocity of approximately 41 - 81 m/s +/- 10%) corresponds to a rotational temperature of 2000 - 5000K, and therefore such a rotational temperature may be optimal. Therefore, a rotational temperature above approximately 2000K (i.e. 3000K +/ 10%), corresponding to a flow rate below 30 L/min (corresponding to a gas velocity of approximately 81 m/s +/- 10%), may be seen as optimal. Further, it is noted that a flow rate of approximately 40 L/min (corresponding to a gas velocity of approximately 108 m/s +/-10%) corresponds to a rotational temperature of approximately 1800K.

**[0099]** Besides the flow rate, other parameters which may be controlled are the input power to the gliding arc and temperature of the set of electrodes. These parameters (flow rate, input power and temperature) may affect the parameters shown in figure 6. Examples of values of the controlled parameters may be input power above 0.4 kW, flow rate/gas velocity lower than 81 m/s +/-10 %. Additionally, the temperature of the bulk part of the electrode may be defined using the temperature coefficient $\alpha$ of the electrode material, Assuming that maximum acceptable resistance of the bulk part of the electrodes is 2 times that of room temperature, the maximum acceptable temperature is approximately $1/\alpha$ degree. For example, if the electrode is made of copper, $\alpha$ = 0.393 % per degree C and thus the maximum acceptable temperature is approximately 254 degree C.

**[0100]** In an embodiment, the gliding arc may be perpendicular to the sample surface to be treated.

**[0101]** In an embodiment, the gliding arc generated by the electrodes 102 may be tilted with respect to the sample surface such that the gliding arc plasma is at a non-perpendicular angle to the sample 112. For example, the gliding arc plasma 107 may be tilted an angle between 0 and 90° (preferably no less than 5 °) with respect to the sample 112 surface to be treated. This may for example be achieved by angling the set of electrodes with respect to the sample 112 surface to be treated. Thereby, the sample surface area treated increases thus increasing effectiveness of the device 100, 200, 300.

**[0102]** In general, any of the technical features and/or embodiments described above and/or below may be combined into one embodiment. Alternatively or additionally any of the technical features and/or embodiments described above and/or below may be in separate embodiments. Alternatively or additionally any of the technical features and/or embodiments described above and/or below may be combined with any number of other technical features and/or embodiments described above and/or below to yield any number of embodiments.

**[0103]** Figure 11a-b shows a set of electrodes comprising electrode protrusions. Each electrode 1101 1102 comprises a tube having an approximately U shape. Each tube comprises a first end 1107 1109 where a coolant enters the electrode and a second end 1108 1110 where the cooling exits the electrode, where the centre of the cross section at the first end is displaced relative to the centre of the cross section at the second end. Each electrode comprises an electrode protrusion 1103 1104 protruding from the surface of the tubes. Each electrode protrusion 1103 1104 protrudes approximately towards the other electrode and/or towards the other electrode protrusion. Fig 11b shows a cross-section of the electrode 1102 at the plane 1105. The electrode 1102 comprises a circular tube having an inner shape 1106 and an outer shape 1102. The electrode protrusion 1103 is blade shaped. The electrode protrusion 1103 protrudes with a height H in the direction towards the other electrode 1101. The electrode protrusion 1103 has a width W in the direction perpendicular to the height in the cross section 1105. In fig. 11 b the protrusion has two rounded edges each having a radius of curvature of less than 3mm.

**[0104]** The electrode protrusion e.g. electrode attachment, may protrude with a height of at least 1 mm, 2 mm, 5 mm, 1 cm, 2 cm or 5 cm. The electrode attachment may protrude with a height no more than 10 cm, 5 cm, 2 cm, 1 cm, or 5 mm.

**[0105]** The electrode protrusion e.g. electrode attachment, may have a width of at least 0.1 mm, 0.2 mm, 0.5 mm, 1 mm, 1 cm or 2 cm. The electrode protrusion may have a width of no more than 10 cm, 5 cm, 2 cm, 1 cm, 5 mm, 2 mm, or 1 mm.

**[0106]** Figure 12a-d shows different tube and electrode protrusion designs.

**[0107]** Figure 13 shows an electrode comprising a tube having and electrode protrusion. Shown is a cross section of the tube being perpendicular to the longitudinal direction of the tube, at a part of the tube comprising the electrode protrusion, where the electrode protrusion has a shape such that a first surface area defined between a first line 1303 and a second line 1304 originating in the centre 1308 of said cross section is at least a factor A larger than a second surface area defined between said second line 1304 and a third line 1305 originating in said centre 1308 , wherein the angle 1306 between said first

and said second line 1303 1304, and said second line 1304 and said third line 1305 is B, wherein the first and the second lines 1303 1304 are positioned so that the first surface area comprises the electrode protrusion 1302, and the third line 1305 is positioned so that the first surface area and the second surface area does not overlap.

**[0108]** A may be chosen from approximately 1.1, 1.5, 2, 3, 4, 5, or 10, and B may be chosen from approximately 180 degrees, 135 degrees, 90 degrees, 45 degrees, 30 degrees, 20, degrees, 10 degrees, or 5 degrees.

**[0109]** Figure 14 shows a part of an apparatus for treating a surface with a gliding arc according to an embodiment of the present invention. The apparatus comprises a computational unit 1401 communicatively coupled to the control unit 1403 via a first communication link 1406 and to a sensor 1402 via a second communication link 1405, wherein said sensor 1402 is adapted to measure a parameter indicative of the resistance of at least one of the electrodes, and where the computational unit 1401 is adapted to calculate a feedback signal based on the measured parameter wherein the computational unit 1401 is further adapted to transmit the feedback signal to the control unit 1403 wherein the control unit 1403 is adapted to control the cooling unit 1404 responsive to the received feed back signal such that the cooling unit 1404 is controllable via a feedback loop.

**[0110]** Fig. 15 illustrates operation of an embodiment of a device for generating at least one gliding arc plasma.The shape and size of the electrodes 1502 facing the plasma are interesting features of the apparatus. At the point of discharge ignition 1508, the electrodes 1502 should, at least at their side facing the respective other electrode, be thin enough and/or have a radius of curvature (in a plane normal to the longitudinal direction of the electrode) small enough, and the gap between the electrodes should be small enough to ignite a discharge with low voltage. In the region 1509 different from the ignition region 1508 (also referred to as region of discharge extension), the gap between the electrodes gradually increases. As long as the discharge bridges the electrodes, the current flows in the plasma, which increases the energy. As the gap size increases with increasing distance from the point of ignition, when a certain gap size is reached, the discharge cannot sustain the arc (equilibrium) condition and changes to a non-equilibrium plasma 1511, which is used for the processing.

**[0111]** Fig. 16 illustrates a different embodiment of a device for generating at least one gliding arc plasma with electrodes 1602 having a convex shape.

**[0112]** It will be appreciated that, in some embodiments of the apparatus described herein, the properties and/or the shape of the gliding arc plasma may be further modified by applying magnetic field and/or any other known technologies for any specific applications.

**[0113]** Although some embodiments have been described and shown in detail, the invention is not restricted to them, but may also be embodied in other ways within the scope of the subject matter defined in the following claims. In particular, it is to be understood that other embodiments may be utilised and structural and functional modifications may be made without departing from the scope of the present invention.

**[0114]** In device claims enumerating several means, several of these means can be embodied by one and the same item of hardware. The mere fact that certain measures are recited in mutually different dependent claims or described in different embodiments does not indicate that a combination of these measures cannot be used to advantage.

**[0115]** It should be emphasized that the term "comprises/comprising" when used in this specification is taken to specify the presence of stated features, integers, steps or components but does not preclude the presence or addition of one or more other features, integers, steps, components or groups thereof.

## Claims

1. An apparatus for treating a surface with a at least one gliding arc source comprising

   - a at least one gas flow controlling unit (104) and a set of elongated electrodes (102) for providing a plasma;
   - a cooling unit (201) for providing a cooling fluid, and
   - a high voltage power supply (101) for generating a discharge

   wherein at least one of the electrodes (102) comprises a tubular portion fluidly coupled to the cooling unit (201) wherein the tubular portion defines a longitudinal direction of the electrode, wherein the electrode (102) further comprises an outer surface comprising a portion facing the other one of the electrodes (102) said portion of the outer surface being curved in a plane normal to said longitudinal direction.

2. An apparatus according to claim 1, wherein said portion of the outer surface being curved in a plane normal to said longitudinal direction is having a radius of curvature less than 3mm.

3. An apparatus according to claim 1 or 2, wherein the tubular portion comprises, at least along a portion of its outer surface, a protrusion configured to lower the voltage applied to the electrodes (102) required to ignite the plasma, said protrusion comprising said portion of the outer surface.

4. An apparatus according to claim 3, wherein each electrode of the set of electrodes (102) comprises a protrusion.

5. An apparatus according to claim 3 or 4, wherein the protrusion is blade-shaped.

6. An apparatus according to anyone of claims 3 to 5, wherein the protrusion is hollow and fluidly coupled to the cooling unit (201) via the said tubular portion.

7. An apparatus according to anyone of claims 1 to 6, wherein at least one of the electrodes (102) comprises a tubular portion having a first end and a second end wherein the tubular portion is configured to receive, during operation, a coolant at said first end and discharge the coolant at said second end, wherein the centre of the cross-section of the tube at the first end is displaced relative to the centre of the cross-section of the tube at the second end.

8. An apparatus according to anyone of claims 1 to 7, further comprising a control unit (103) adapted to control at least the cooling unit.

9. An apparatus according to claim 8, wherein the apparatus further comprises a computational unit communicatively coupled to the control unit and to a sensor, wherein said sensor is adapted to measure a parameter indicative of the resistance of at least one of the electrodes, and where the computational unit is adapted to calculate a feedback signal based on the measured parameter; and wherein the control unit is adapted to control the cooling unit responsive to the calculated feed back signal.

10. An apparatus according to claim 1, further comprising

- a control unit (103) adapted to control at least the cooling unit (201),
- a sensor (1402) adapted to measure a parameter indicative of the resistance of at least one of the electrodes (102),
- a computational unit communicatively coupled to the control unit (103) and to the sensor;

wherein the computational unit is adapted to calculate a feedback signal based on the measured parameter; and wherein the control unit (103) is adapted to control the cooling unit responsive to the calculated feed back signal.

11. An apparatus according to claim 10, wherein the computational unit is adapted to calculate the feedback signal so as to control a maximum temperature of a bulk part of the electrodes (102) to not exceed a room temperature by more than a predetermined multiple of an inverse of a temperature coefficient indicative of a linear relationship between the resistance of the electrode (102) and the temperature.

12. An apparatus according to any one of the preceding claims, wherein the at least one gas flow controlling unit (104) and the set of electrodes (102) are controllable to provide a plasma comprising a rotational temperature at the point of arc ignition above approximately 2000 K.

13. An apparatus according to any one of claims 6 through 12, wherein the control unit (103) is communicatively coupled to the gas flow controlling unit (104) and to the set of electrodes (102) via respective communication links (106, 113) such that the control unit (103) is adapted to control the gas flow controlling unit (104) and the set of electrodes (102) via said respective communication links.

14. An apparatus according to anyone of the preceding claims wherein the cooling unit (201) is communicatively coupled to the control unit (103) via a communication link (109) such that the control unit (103) is adapted to control the cooling unit (201).

**Patentansprüche**

1. Vorrichtung zur Behandlung einer Oberfläche mit mindestens einer Gleitlichtbogen-Quelle, umfassend

- mindestens eine Gasströmungssteuereinheit (104) und einen Satz von länglichen Elektroden (102) zum Bereitstellen eines Plasmas;
- eine Kühleinheit (201) zum Bereitstellen einer Kühlflüssigkeit und
- eine Hochspannungsstromversorgung (101) zum Erzeugen einer Entladung,

wobei mindestens eine der Elektroden (102) einen rohrförmigen mit der Kühleinheit (201) in einer flüssigen Verbindung stehenden Teil umfasst, wobei der rohrförmige Teil eine Längsrichtung der Elektrode definiert, wobei die Elektrode (102) zusätzlich eine Außenfläche umfasst, umfassend einen der anderen der Elektroden (102) zugewandten Teil, wobei der Teil der Außenfläche in einer Ebene senkrecht zur Längsrichtung gekrümmt ist.

2. Vorrichtung nach Anspruch 1, wobei der Teil der Außenfläche, der in einer Ebene senkrecht zur Längsrichtung gekrümmt ist, einen Krümmungsradius weniger als 3 mm aufweist.

3. Vorrichtung nach Anspruch 1 oder 2, wobei der rohrförmige Teil, mindestens entlang eines Teils seiner Außenfläche, einen Vorsprung umfasst, der dazu ausgelegt ist, die Spannung zu mindern, die an die Elektroden (102) angelegt wird, welche für das Zünden des Plasmas notwendig sind, wobei der Vor-

sprung den Teil der Außenfläche umfasst.

**4.** Vorrichtung nach Anspruch 3, wobei jede Elektrode des Satzes von Elektroden (102) einen Vorsprung umfasst.

**5.** Vorrichtung nach Anspruch 3 oder 4, wobei der Vorsprung klingenförmig ist.

**6.** Vorrichtung nach irgendeinem der Ansprüche 3 bis 5, wobei der Vorsprung hohl ist und über den rohrförmigen Teil mit der Kühleinheit (201) in flüssiger Verbindung steht.

**7.** Vorrichtung nach irgendeinem der Ansprüche 1 bis 6, wobei mindestens eine der Elektroden (102) einen rohrförmigen Teil mit einem ersten Ende und einem zweiten Ende umfasst, wobei der rohrförmige Teil dazu ausgelegt ist, während des Betriebs ein Kühlmittel am ersten Ende zu erhalten, und das Kühlmittel am zweiten Ende auszutragen, wobei die Mitte des Querschnitts des Rohrs am ersten Ende im Verhältnis zur Mitte des Querschnitts des Rohrs am zweiten Ende versetzt ist.

**8.** Vorrichtung nach irgendeinem der Ansprüche 1 bis 7, zusätzlich umfassend eine Steuereinheit (103), die dazu eingerichtet ist, mindestens die Kühleinheit zu steuern.

**9.** Vorrichtung nach Anspruch 8, wobei die Vorrichtung zusätzlich eine mit der Steuereinheit und mit einem Sensor kommunikativ gekoppelte Recheneinheit umfasst, wobei der Sensor dazu eingerichtet ist, einen den Widerstand mindestens einer der Elektroden anzeigenden Parameter zu messen, und wobei die Recheneinheit dazu eingerichtet ist, beruhend auf dem gemessenen Parameter ein Rückführsignal zu berechnen; und wobei die Steuereinheit dazu eingerichtet ist, als Antwort auf das berechnete Rückführsignal die Kühleinheit zu steuern.

**10.** Vorrichtung nach Anspruch 1, zusätzlich umfassend

- eine Steuereinheit (103), die dazu eingerichtet ist, mindestens die Kühleinheit (201) zu steuern;
- einen Sensor (1402), der dazu eingerichtet ist, einen den Widerstand mindestens einer der Elektroden (102) anzeigenden Parameter zu messen,
- eine mit der Steuereinheit (103) und mit dem Sensor kommunikativ gekoppelte Recheneinheit;

wobei die Recheneinheit dazu eingerichtet ist, beruhend auf dem gemessenen Parameter ein Rückführsignal zu berechnen; und wobei die Steuereinheit (103) dazu eingerichtet ist, als Antwort auf das berechnete Rückführsignal die Kühleinheit zu steuern.

**11.** Vorrichtung nach Anspruch 10, wobei die Recheneinheit dazu eingerichtet ist, das Rückführsignal zu berechnen, um ein Maximaltemperatur eines Mengenteils der Elektroden (102) zu steuern, damit sie eine Raumtemperatur nicht um mehr als ein vorbestimmtes Mehrfache einer Inverse eines Temperaturkoeffizienten übersteigt, der eine lineare Beziehung zwischen dem Widerstand der Elektrode (102) und der Temperatur anzeigt.

**12.** Vorrichtung nach irgendeinem der vorhergehenden Ansprüche, wobei die mindestens eine Gasströmungssteuereinheit (104) und der Satz von Elektroden (102) steuerbar sind, um ein Plasma bereitzustellen, umfassend eine Rotationstemperatur am Zeitpunkt der Lichtbogenzündung oberhalb von etwa 2000 K.

**13.** Vorrichtung nach irgendeinem der Ansprüche 6 bis 12, wobei die Steuereinheit (103) über jeweilige Kommunikationsverbindungen (106, 113) mit der Gasströmungssteuereinheit (104) und mit dem Satz von Elektroden (102) kommunikativ gekoppelt ist, so dass die Steuereinheit (103) dazu eingerichtet ist, über die jeweiligen Kommunikationsverbindungen die Gasströmungssteuereinheit (104) und den Satz von Elektroden (102) zu steuern.

**14.** Vorrichtung nach irgendeinem der vorhergehenden Ansprüche, wobei die Kühleinheit (201) über eine Kommunikationsverbindung (109) mit der Steuereinheit (103) kommunikativ verbunden ist, so dass die Steuereinheit (103) dazu eingerichtet ist, die Kühleinheit (201) zu steuern.

**Revendications**

**1.** Appareil pour traiter une surface avec au moins une source à arc glissant, comprenant

- au moins une unité de commande d'écoulement gazeux (104) et un ensemble d'électrodes allongées (102) pour fournir un plasma;
- une unité de refroidissement (201) pour fournir un fluide de refroidissement, et
- une alimentation d'électricité à haute tension (101) pour générer une décharge

au moins l'une des électrodes (102) comprenant une partie tubulaire en liaison fluidique avec l'unité de refroidissement (201), la partie tubulaire définissant une direction longitudinale de l'électrode, l'électrode (102) comprenant en outre une surface extérieure comprenant une portion faisant face à l'autre des

électrodes (102), ladite portion de la surface extérieure étant courbée dans un plan normal à ladite direction longitudinale.

**2.** Appareil selon la revendication 1, dans lequel ladite portion de la surface extérieure étant courbée dans un plan normal à ladite direction longitudinale présente un rayon de courbure inférieur à 3 mm.

**3.** Appareil selon la revendication 1 ou 2, dans lequel ladite partie tubulaire comprend, au moins au long d'une portion de sa surface extérieure, une protubérance configurée pour abaisser la tension appliquée aux électrodes (102) nécessaires pour allumer le plasma, ladite protubérance comprenant ladite portion de la surface extérieure.

**4.** Appareil selon la revendication 3, dans lequel chaque électrode de l'ensemble d'électrodes (102) comprend une protubérance.

**5.** Appareil selon la revendication 3 ou 4, dans lequel la protubérance est en forme de lame.

**6.** Appareil selon l'une quelconque des revendications 3 à 5, dans lequel la protubérance est creuse et en liaison fluidique avec l'unité de refroidissement (201) par l'intermédiaire de ladite partie tubulaire.

**7.** Appareil selon l'une quelconque des revendications 1 à 6, dans lequel au moins l'une des électrodes (102) comprend une partie tubulaire ayant une première extrémité et une deuxième extrémité, la partie tubulaire étant configurée à recevoir, pendant le fonctionnement, un fluide de refroidissement au niveau de ladite première extrémité et à décharger le fluide de refroidissement au niveau de ladite deuxième extrémité, le centre de la section transversale du tube au niveau de la première extrémité étant déplacé par rapport au centre de la section transversale du tube au niveau de la deuxième extrémité.

**8.** Appareil selon l'une quelconque des revendications 1 à 7, comprenant en outre une unité de commande (103) adaptée à commander au moins l'unité de commande.

**9.** Appareil selon la revendication 8, dans lequel l'appareil en outre comprend une unité computationnelle couplée de manière communicative à l'unité de commande et à un capteur, ledit capteur étant adapté pour mesurer un paramètre indicatif de la résistance d'au moins l'une des électrodes, et l'unité computationnelle étant adaptée pour calculer un signal de rétroaction sur la base du paramètre mesuré; et l'unité de commande étant adaptée pour commander l'unité de refroidissement en réponse au signal de rétroaction calculé.

**10.** Appareil selon la revendication 1, comprenant en outre

- une unité de commande (103) adaptée pour commander au moins l'unité de refroidissement (201);
- un capteur (1402) adapté pour mesurer un paramètre indicatif de la résistance d'au moins l'une des électrodes (102),
- une unité computationnelle couplée de manière communicative à l'unité de commande (103) et au capteur;

l'unité computationnelle étant adaptée pour calculer un signal de rétroaction sur la base du paramètre mesuré; et l'unité de commande (103) étant adaptée pour commander l'unité de refroidissement en réponse au signal de rétroaction calculé.

**11.** Appareil selon la revendication 10, dans lequel l'unité computationnelle est adaptée pour calculer le signal de rétroaction en vue de commander une température maximale d'une majeure partie des électrodes (102) de ne pas dépasser une température ambiante de plus d'un multiple prédéterminé d'un inverse d'un coefficient de température indicatif d'un rapport linéaire entre la résistance de l'électrode (102) et la température.

**12.** Appareil selon l'une quelconque des revendications précédentes, dans lequel l'au moins une unité de commande d'écoulement gazeux (104) et l'ensemble d'électrodes (102) peuvent être commandés pour fournir un plasma comprenant une température de rotation au point d'allumage d'arc supérieure à environ 2000 K.

**13.** Appareil selon l'une quelconque des revendications 6 à 12, dans lequel l'unité de commande (103) est couplée de manière communicative à l'unité de commande d'écoulement gazeux (104) et à l'ensemble d'électrodes (102) par l'intermédiaire de liaisons de communication respectives (106, 113) si bien que l'unité de commande (103) est adaptée pour commander l'unité de commande d'écoulement gazeux (104) et l'ensemble d'électrodes (102) par l'intermédiaire desdites liaisons de communication respectives.

**14.** Appareil selon l'une quelconque des revendications précédentes, dans lequel l'unité de refroidissement (201) est couplée de manière communicative à l'unité de commande (103) par l'intermédiaire d'une liaison de communication (109) si bien que l'unité de commande (103) est adaptée pour commander l'unité de refroidissement (201).

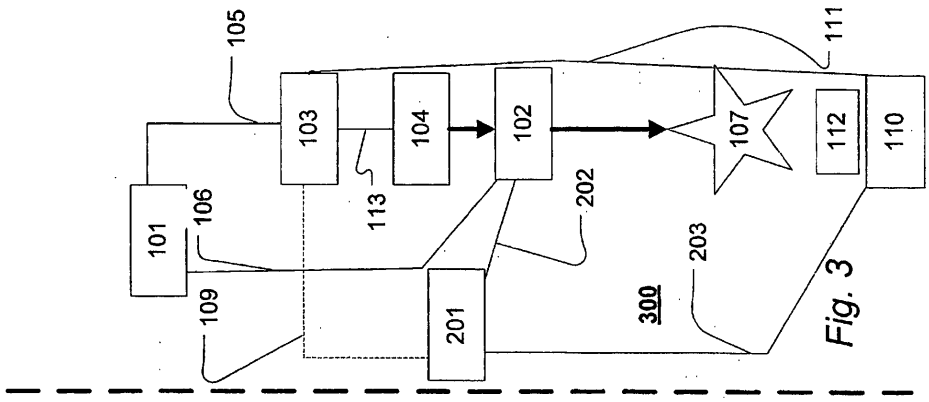


Fig. 3

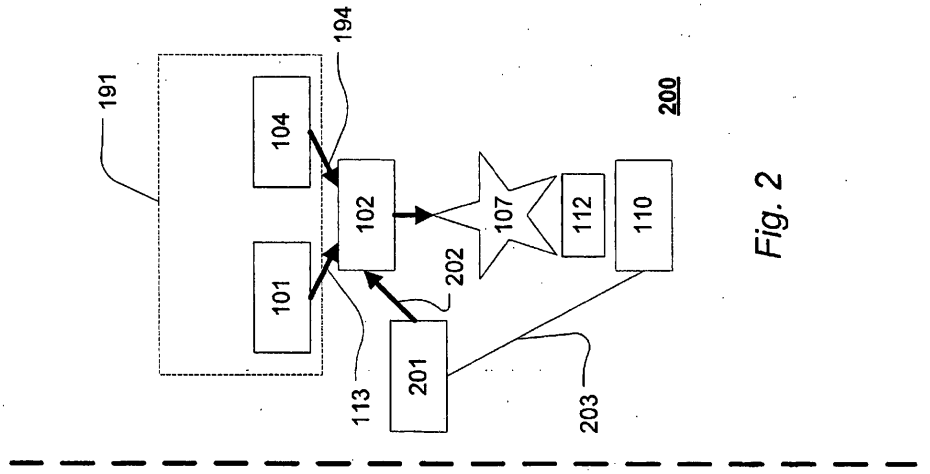


Fig. 2

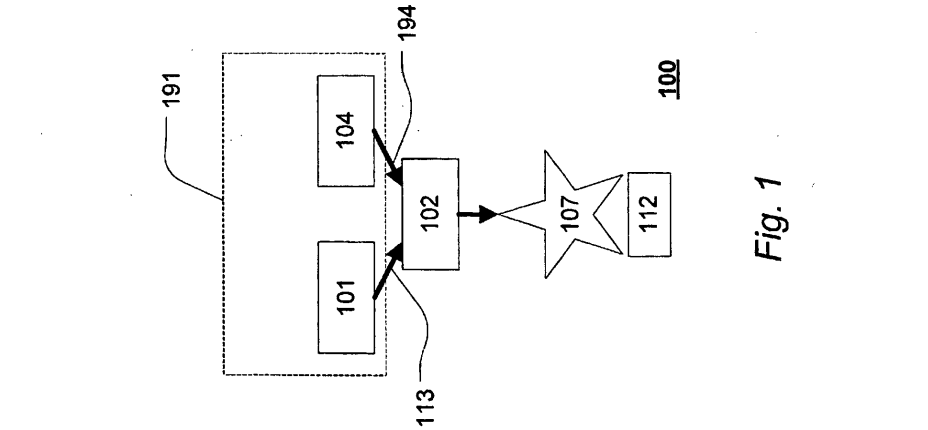


Fig. 1

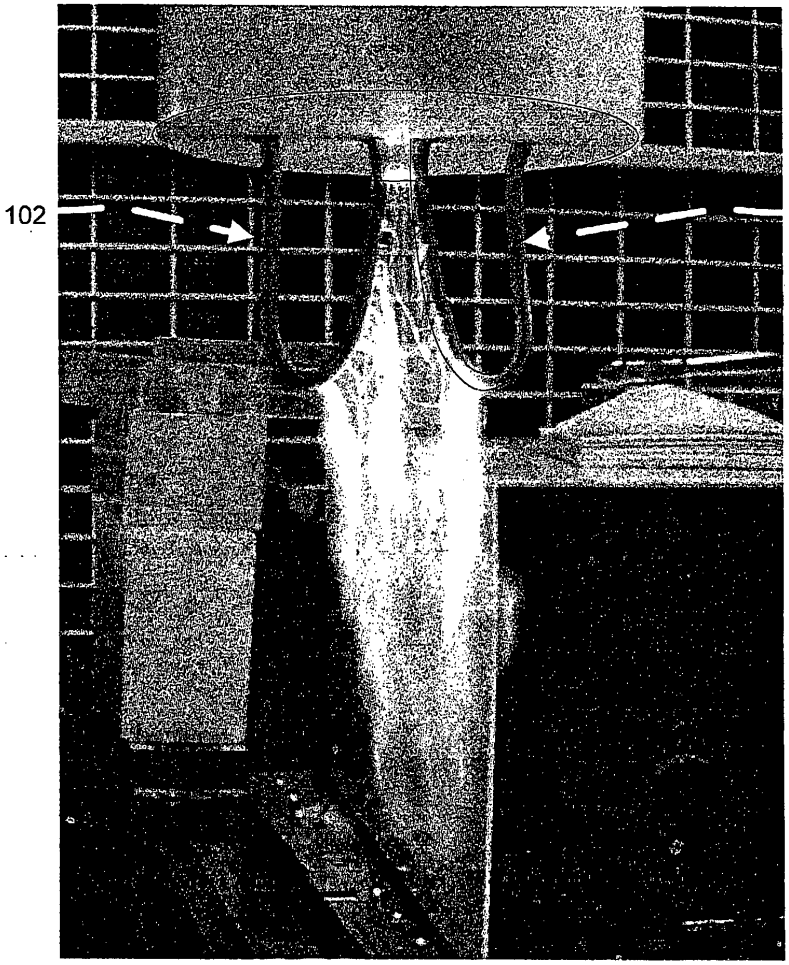


*Fig. 4*

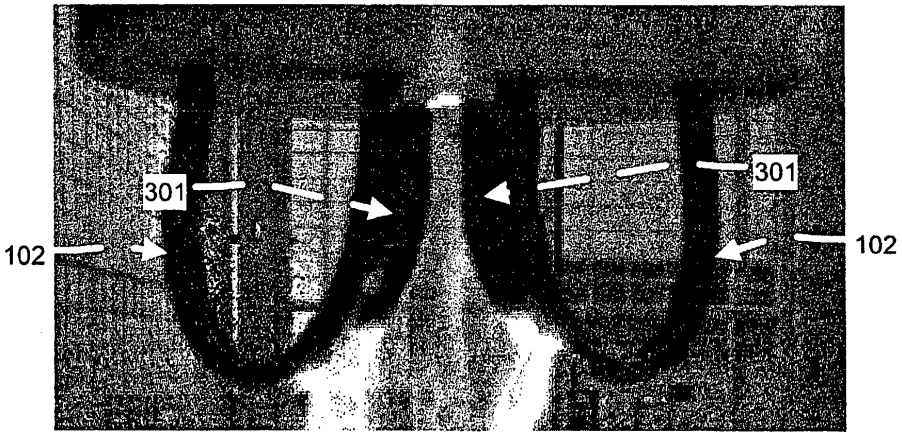
301
301
102
102

*Fig. 5*

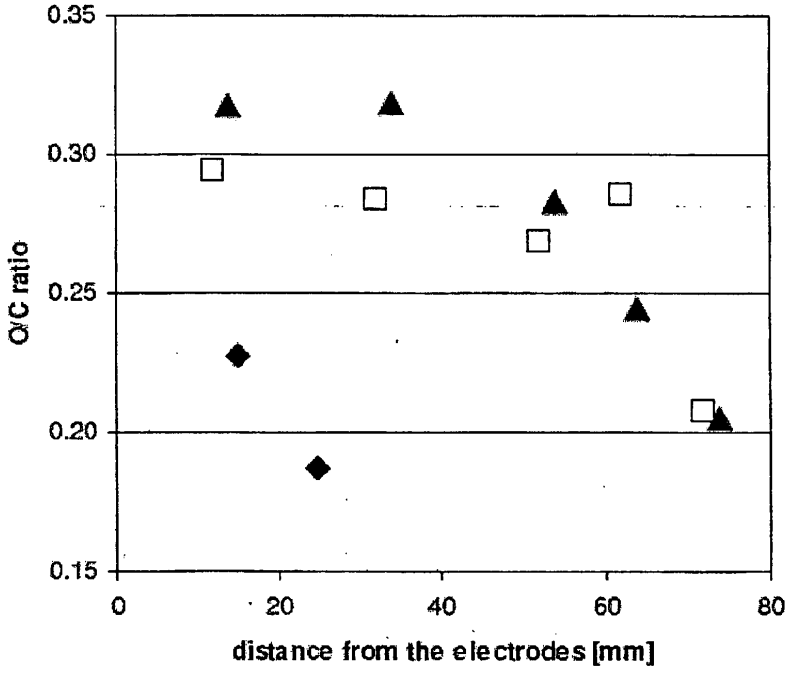
0.35
0.30
0.25
0.20
0.15
O/C ratio
0
20
40
60
80
distance from the electrodes [mm]

*Fig. 6*

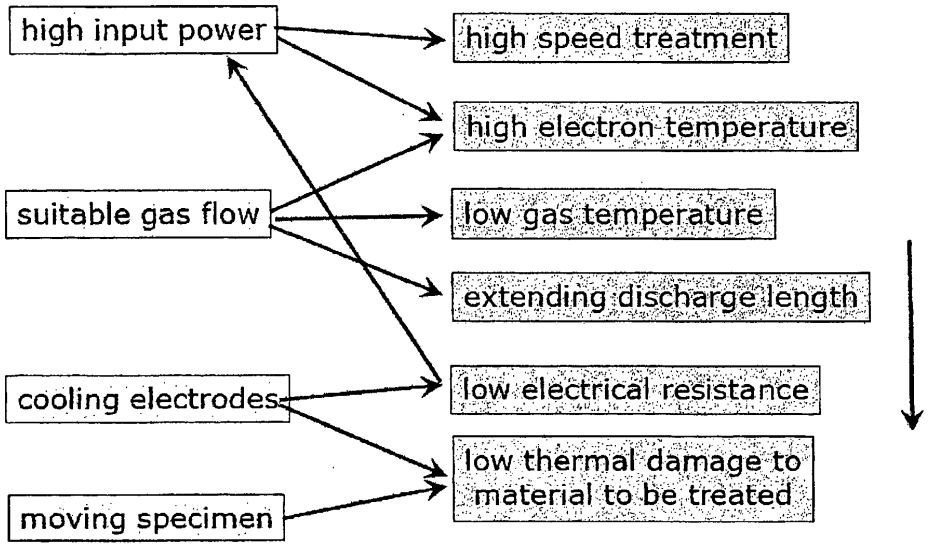
high input power
suitable gas flow
cooling electrodes
moving specimen
high speed treatment
high electron temperature
low gas temperature
extending discharge length
low electrical resistance
low thermal damage to material to be treated

*Fig. 7*

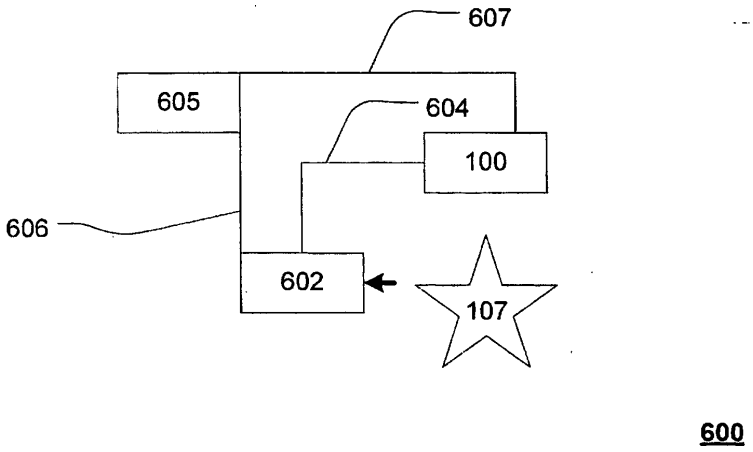
607
605
604
100
606
602
107
600

*Fig. 8*

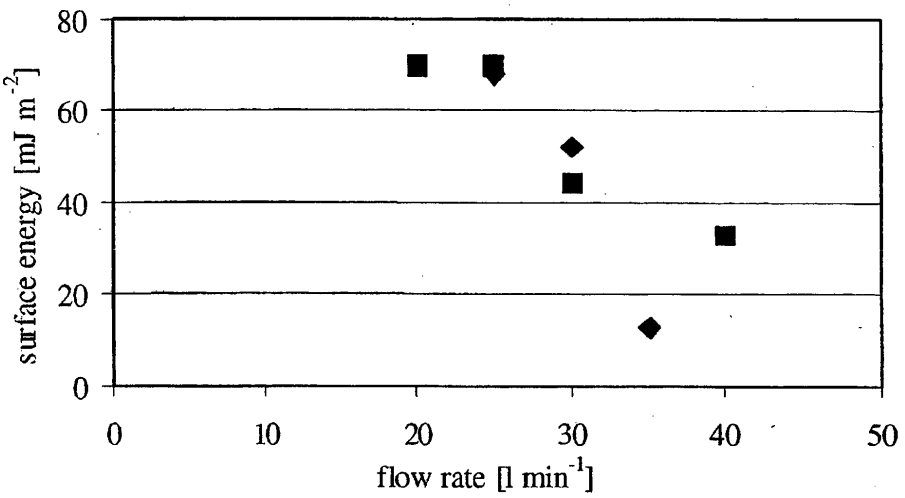
80
60
40
20
0
surface energy [mJ m-2]
0
10
20
30
40
50
flow rate [l min-1]

Fig. 9

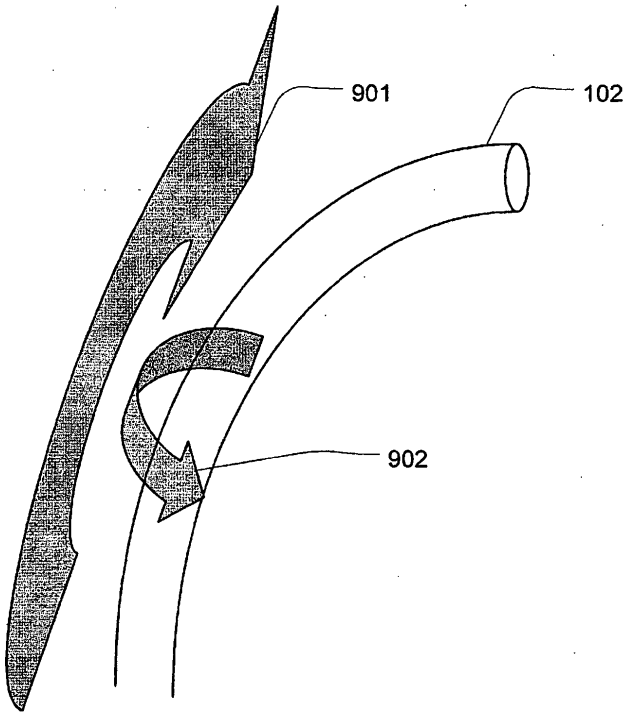
901
102
902

Fig. 10

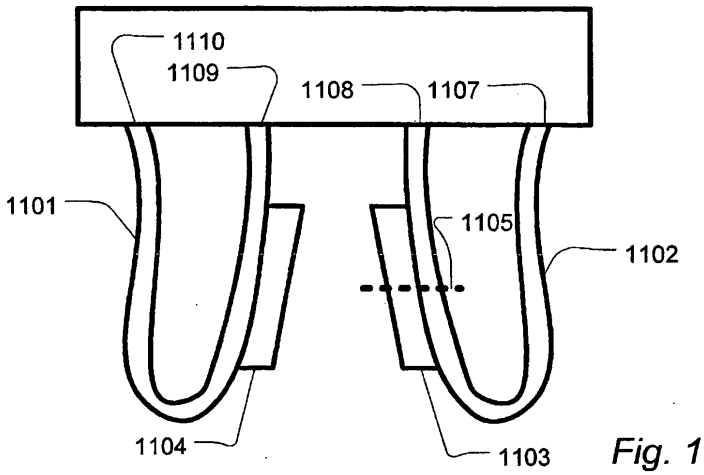


Fig. 11a

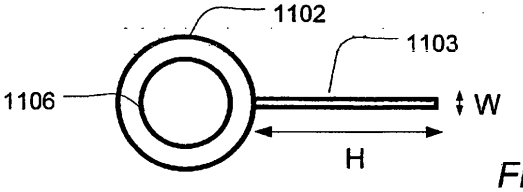


Fig. 11b

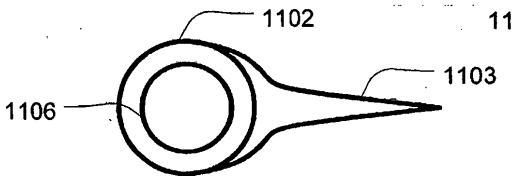


Fig. 12b

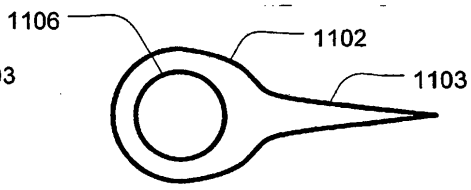


Fig. 12a

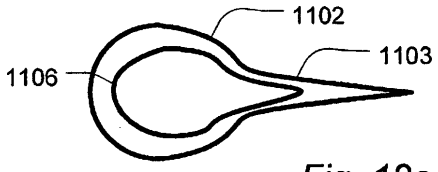


Fig. 12c

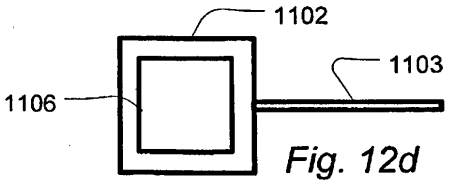


Fig. 12d

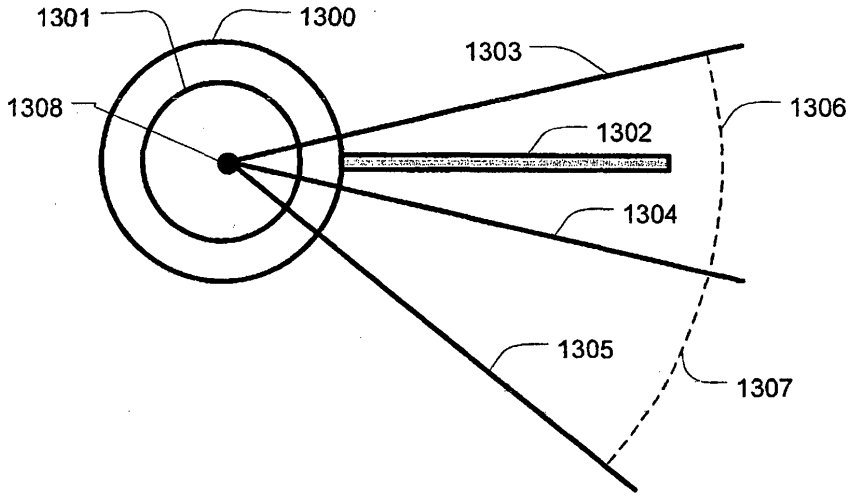
1301
1300
1303
1308
1306
1302
1304
1305
1307

Fig. 13

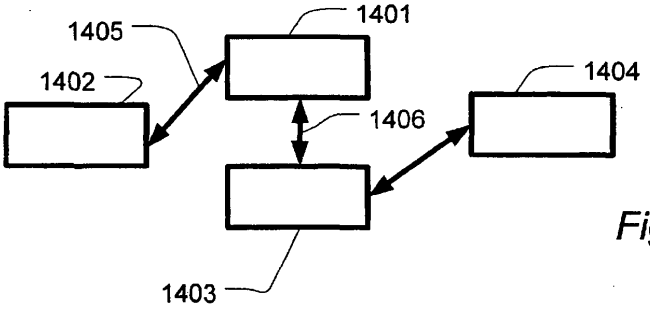
1401
1405
1402
1404
1406
1403

Fig. 14

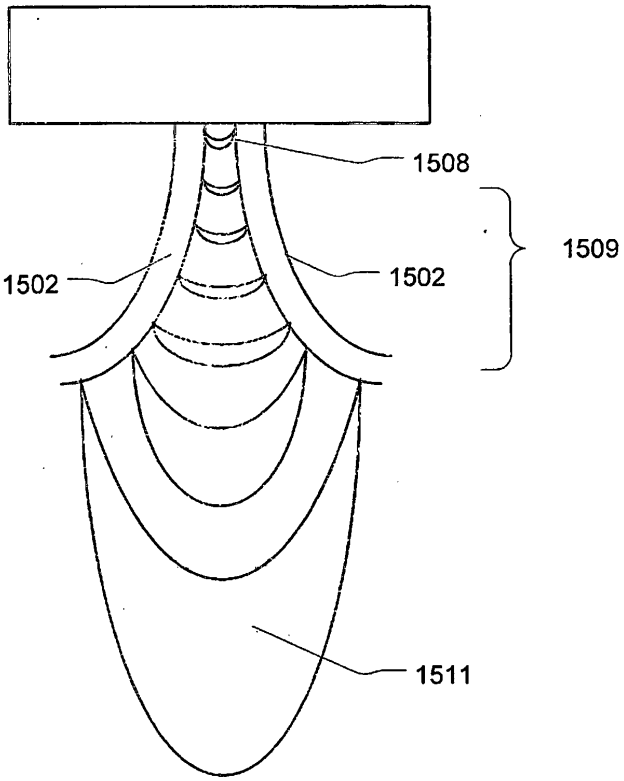


Fig. 15

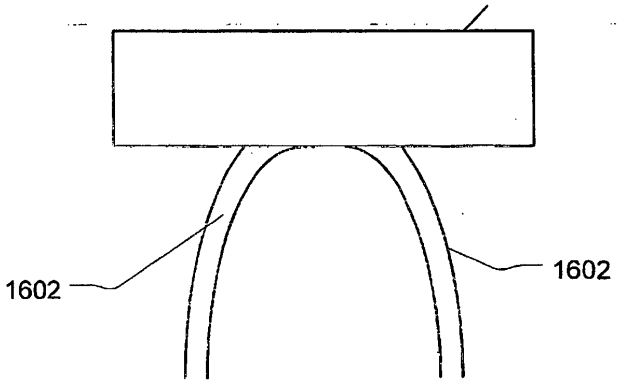


Fig. 16

## REFERENCES CITED IN THE DESCRIPTION

*This list of references cited by the applicant is for the reader's convenience only. It does not form part of the European patent document. Even though great care has been taken in compiling the references, errors or omissions cannot be excluded and the EPO disclaims all liability in this regard.*

### Non-patent literature cited in the description


- **A. FRIDMAN et al.** Gliding arc discharge. *Progress in Energy and Combustion Science,* 1999, vol. 25, 211-231 **[0002]**
- **KUSANO et al.** Gliding are discharge: application for adhesion improvement of fibre reinforced polyester composites. *Surface and Coatings Technology,* 2008, vol. 202 (22-23), 22-23 **[0002]**
- **C. O. LAUX ; T. G. SPENCE ; C. H. KRUGER ; R. N. ZARE.** Optical diagnostics of atmospheric pressure air plasmas. *Plasm. Source Sci. Technol.,* 2003, vol. 12, 125-138 **[0090]**

# [Appendix A4]

Y. Kusano, B.F. Sørensen, T.L. Andersen, F. Leipold

## “Adhesion improvement of glass-fibre-reinforced polyester composites by gliding arc discharge treatment”

*The Journal of Adhesion* 89(6) (2013) 433-459.

*The Journal of Adhesion*, 89:433–459, 2013

ISSN: 0021-8464 print/1545-5823 online
DOI: 10.1080/00218464.2013.759063

Taylor & Francis
Taylor & Francis Group

# Adhesion Improvement of Glass-Fibre-Reinforced Polyester Composites by Gliding Arc Discharge Treatment

YUKIHIRO KUSANO[1], BENT F. SØRENSEN[1], TOM L. ANDERSEN[1], and FRANK LEIPOLD[2]

[1]*Department of Wind Energy, Section of Composites and Materials Mechanics, Technical University of Denmark, Risø Campus, Roskilde, Denmark*
[2]*Department of Physics, Technical University of Denmark, Roskilde, Denmark*



*A gliding arc is a plasma that can be operated at atmospheric pressure and applied for plasma surface treatment for adhesion improvement. In the present work, glass-fibre-reinforced polyester plates were treated using an atmospheric pressure gliding arc discharge with an air flow to improve adhesion with a vinylester adhesive. The treatment improved wettability and increased the polar component of the surface energy and the density of oxygen-containing polar functional groups at the surfaces. Double cantilever beam specimens were prepared for fracture mechanics characterisation (fracture resistance as a function of nominal mode mixity) of the laminate adhesive interface. It was found that gliding arc treatment significantly increases the interfacial fracture energy and fracture resistance in comparison with a standard peel ply treatment, although the mixed mode fracture energy of the gliding arc treated specimen was not as high as that of the laminate itself.*

*KEYWORDS Adhesion; Fibre-reinforced polyester; Fracture energy; Gliding arc; Plasma treatment; Vinylester*

Received 7 July 2012; in final form 7 November 2012.

Address correspondence to Yukihiro Kusano, Department of Wind Energy, Section of Composites and Materials Mechanics, Technical Unviersity of Denmark, Risø Campus, Frederiksborgvej 399, Roskilde, DK 4000, Denmark. E-mail: yuki@dtu.dk

## 1 INTRODUCTION

Fibre-reinforced polymer (FRP) materials have high strength-to-weight ratios and corrosion resistance and are, therefore, used for a variety of applications in civil engineering, wind energy, the ship, aerospace, and automobile industries [1–5]. Adhesives are often required for joining these materials to components fabricated from similar FRPs or other types of materials. FRPs usually have smooth surfaces that mainly consist of the polymer matrix materials with low surface energies. In addition, they often have a wide range of contaminants on the surfaces, that can form a weak boundary layer in an adhesive bond [6]. Therefore, an adhesive joint usually requires careful surface preparation. In the case of conventional FRPs based on thermoplastic polymeric matrices a treatment employing abrasion followed by solvent cleaning is inadequate to obtain high joint strength [7]. Examples of thermoplastic polymeric matrices include poly(ether-ether ketone) (PEEK), polyamide copolymer, poly(ether imide), polyimide, and poly(phenylene sulphide). Instead of abrasion, various surface treatment techniques have been investigated, including flame treatment [8], corona treatment [8–12], plasma treatment [8,9], excimer laser treatment [8], acid etching [8,11,12], and primer treatment [8]. On the other hand, in the case of thermosetting composites such as unsaturated polyester, vinylester, and epoxy resins, mechanical treatment has been applied for surface preparation [13,14]. Peel plying is a prime example of a mechanical treatment used for adhesion improvement [15] since it provides a ready-to-bond surface that may not require further surface cleaning before bonding. Another example is mechanical roughening that needs laborious abrasion followed by solvent cleaning before adhesive bonding in order to achieve high joint strength [13].

Plasma treatment is attractive for this application due to its environmental friendliness and high reactivity to the surface to be bonded while retaining the bulk properties of the material [16]. During the plasma treatment, polymer surfaces interact with radicals, ions, and electrons, and are irradiated with ultraviolet light [17]. Plasma processing is often performed at low pressures. The plasma treatments at low pressures, however, require expensive vacuum systems, and methods are well-developed only for batch or semi-batch treatments. On the other hand, an atmospheric pressure plasma treatment can not only avoid the need for vacuum equipment but also permit both the treatment of large objects and continuous treatment on production lines [18–26]. A dielectric barrier discharge (DBD) is often operated at atmospheric pressure, generated between electrodes covered with dielectrics by applying a time-varying voltage [27–34]. DBDs have been used for adhesion improvement of FRPs [35–39]. In order to ensure stable DBD operation, however, the gap between the electrodes is limited to a few millimetres, which restricts the size and shape of the specimens to be treated.

Gliding arc discharges can also be generated at atmospheric pressure. They can potentially provide a high degree of non-equilibrium, high electron temperature, and high electron density simultaneously and thus enable high reactivity with high productivity [40–42]. They are generated between divergent electrodes and are extended by a gas flow. A fast transition into a non-equilibrium state occurs once heat losses from the discharge column exceed the supplied energy. The gliding arc combines a number of industrially attractive features of plasma based surface treatment [43]: it is environmentally much cleaner than mechanical or wet chemical processes; it operates well in air at atmospheric pressure with low costs; being a torch-like plasma source, it can treat surfaces of bulky objects; and it allows fast processing. Therefore, it is useful in many industrial applications that involve coating, painting, printing, dyeing, and adhesion. It has recently been reported that gliding arcs can efficiently improve adhesion of FRPs [44–46]. The gliding arc treatment increased the polar component of the surface energy, the density of oxygen-containing polar functional groups at the surfaces, and bond strength with the vinylester adhesive.

The mechanical strength of adhesive joints can be characterised in terms of the fracture energy of an interface crack. Crack growth along an interface between two dissimilar materials always occurs in mixed mode [47]. Experiments have shown that the fracture energy of interface cracks depends on the mode mixity: the fracture energy is usually lowest in peel (Mode I) and increases with increasing amount of shear (Mode II) [48,49]. The increase in the macroscopic fracture energy has been attributed to a frictional contact between crack faces at the crack tip and to different development of the crack tip plastic zone.

In the present work, glass-fibre-reinforced polyester (GFRP) laminates are surface-treated with a gliding arc in air at atmospheric pressure for adhesion improvement for adhesive bonding by a vinylester adhesive. Optical emission spectra (OES) are measured to estimate the rotational temperature in the discharge [50]. The treated surfaces are characterised using contact angle measurement and x-ray photoelectron spectroscopy (XPS). The properties of the laminate/adhesive interface are characterised in terms of the fracture energy as a function of mode mixity. The interfacial fracture energy of the plasma treated interface is compared with two other relevant fracture energies: that of adhesive joints made by the use of a standard peel ply and that of the glass fibre laminate itself undergoing delamination. These comparisons are relevant since adhesive bonds created by applying the adhesive directly to freshly created peel-ply surfaces are considered to give sufficiently strong adhesive joints [15]. Thus, the fracture energy of an adhesive joint made from a peel ply represents an acceptable minimum value for the interfacial fracture energy. Furthermore, the laminate itself is expected to have a higher fracture energy. If the adhesive and the adhesive/laminate

interface possess a fracture energy that is higher than that of the laminate, fracture is likely to occur within the laminate. Thus, the fracture energy of the adhesive joint made from plasma-treated surfaces should surpass that of the peel ply interface but not necessarily the fracture energy of the laminate itself. The fracture energy of the laminate thus usually represents an upper limit for fracture energy of the adhesive joint.

## 2. EXPERIMENTAL METHODS

Four different types of double cantilever beam (DCB) test specimens were used in the present work as listed in Table 1. Typically "peel ply," "gliding arc" plasma-treated, and "crack in glue" test specimens were all based on two bonded rods cut from manufactured GFRP panels each having a thickness of 8 mm. For testing of the laminate fracture energy, "crack in laminate," a 16-mm thick laminate with crack initiation in the middle was manufactured.

GFRP panels ($600 \times 600 \times 8$ mm) were manufactured by resin infusion. The symmetric and almost unidirectional fibre lay-up was established using ten layers of fabric. The first and last layers in the lay-up were a biaxial ($\pm 45°$) 450-g/m$^2$ layer (DB 450-E05, Devold AMT, Langevåg, Norway). The middle eight layers were a mat (L1200/G50-E07, Devold AMT, Langevåg, Norway) containing 1152-g/m$^2$ unidirectional (0°), 52-g/m$^2$ transverse (90°), and 50-g/m$^2$ chopped strand glass. The orthophthalic polyester matrix was a mixture of Polylite® 413-575 resin and 2-wt% Norpol Peroxide™ 19 (Reichhold Danmark A/S, Kolding, Denmark). The support materials used for the vacuum bagging and resin infusion were a peel ply layer (Stitch PLY A™, AIRTECH Europe Saarl, Differdange, Luxembourg) directly on top of the lay-up, followed by a perforated release foil (Halar®, Aerovac Systems, Keighley, UK), distribution net (Green Flow 75, AIRTECH Europe Saarl, Differdange, Luxembourg), 6-mm diameter inlet and 10-mm diameter outlet tubes, tape for fixation of lay-up and support materials (Micropore, 3-M™, Copenhagen, Denmark), vacuum bag (WC8500, AIRTECH Europe Saarl, Differdange, Luxembourg), and a sealant tape (GS 43 MR, AIRTECH Europe Saarl, Differdange, Luxembourg).

Panels were cured at room temperature for 16 h and post-cured at 60°C for 24 h. After post-curing, rods ($290 \times 30 \times 8$ mm) were cut from the GFRP

**TABLE 1** Specimens and Types of the Adhesion Test

| Type of test specimen | Adhesive | Type of test |
|---|---|---|
| Peel ply | Vinylester | Mode I and mixed mode |
| Gliding arc | Vinylester | Mode I and mixed mode |
| Crack in glue | Vinylester | Mode I |
| Crack in laminate | None | Mode I and mixed mode |

laminate panel with the main fibre orientation parallel to the long side of the rods. Two countersunk nuts (M5 BN224, Bossard, Skovlunde, Denmark), for later screwing of specially formed tabs allowing pure moment loading at the specimens, were mounted in one end of each rod. Nuts were fixed with rapid curing glue (Scotch Weld™ DP100, 3 M, Copenhagen, Denmark). The advantage of using the nuts is the possibility of removing and reusing the specially formed tabs. Peel-ply was not removed from the laminate during the cutting and mounting of nuts in order to be able to maintain a clean surface before gliding arc treatment. Just before the plasma treatment, the peel-ply was unwrapped and subsequently the surfaces were gently cleaned and degreased with methanol and acetone in order to ensure a reproducible surface condition.

Specimens for surface characterization were further cut into smaller pieces for easier handling. For XPS analysis, specimens were ultrasonically cleaned in acetone (purity >99%) for 5 minutes twice and in methanol (purity >99.5%) for 5 minutes before gliding arc treatment. It is assumed that this solvent pre-treatment does not affect the adhesive property of the GFRP surface significantly. In fact, a preliminary experiment indicated that the plasma-treated GFRP beams demonstrated similar fracture characteristics in an adhesion test independently of the solvent pre-treatment or lack thereof.

The gliding arc was generated between two diverging stainless steel tubular electrodes as shown in Fig. 1 [46]. Cooling water was fed through the 6-mm diameter tubular electrodes during operation. Blade-shaped stainless steel pieces were welded on the tubular electrodes, facing each other. The arc discharge was ignited between these blade-shaped pieces. A similar configuration is presented in detail in [44]. Air flow was fed between the electrodes to extend the discharge. It was driven by an alternating current (AC) power supply at a frequency of approximately 30 kHz (Generator 6030, SOFTAL Electronic GmbH, Hamburg, Germany). The average power input was obtained by measuring voltage and current with a high-voltage probe and a current viewing resistor, respectively. In order to treat a GFRP rod surface, the rod was fixed on a holder which moved forward and back at a speed of 180 mm/s. The distance between the specimen surface exposed to the discharge and the edge of the electrode was fixed during the treatment. The air flow rate was 20 L/min, the distance between the specimen surface and the edge of the electrode was 15 mm, and the number of exposures was four, unless mentioned otherwise. The input power to the gliding arc was fixed at 720 W.

OES measurements of the gliding arc were performed without the GFRP rod using an optical fibre and a 0.75-m spectrometer equipped with a grating with 3600 grooves/mm and a charge-coupled device (CCD) camera (PI-MA × 1024, Princeton Instruments, Uppsala, Sweden). The OES of the discharge approximately 55 mm below the arc ignition point was measured using the optical fibre. The three nearest points approximation method

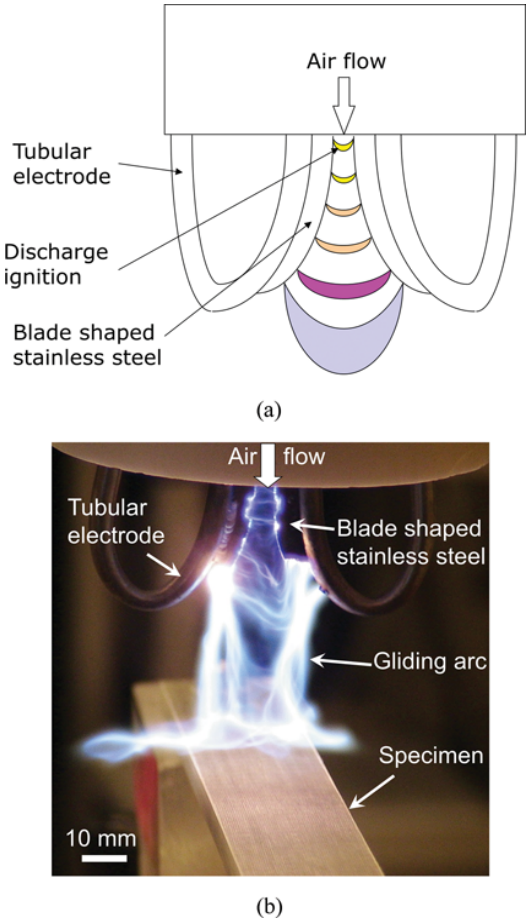


**FIGURE 1** Setup of the gliding arc discharge. (a) Schematic diagram, and (b) a photo image showing the gliding arc treatment of GFRP (color figure available online).



was applied for smoothing the OES. The rotational temperature, $T_{rot}$, which is assumed to be close to the gas temperature, was evaluated by the relative intensity of two groups of rotational OES lines corresponding to the R and P branches of the OH A-X (0,0) vibrational band [44]. The OH molecules come from ambient air humidity. The relation between the rotational temperature, $T_{rot}$, and the relative intensity of the R and P branches is given in [50].

The contact angles for deionized water and glycerol on the GFRP surfaces were measured in air at room temperature for calculation of the estimated surface energy using a contact angle measurement system (CAM 100, Crelab Instruments AB, Billdal, Sweden). The polar component of the surface energy of the GFRP plates was obtained by the two-liquid geometric

method [31]. The standard deviations of the measured contact angle and the polar component of surface energy were typically less than approximately 5° and 15 $mJ/m^2$, respectively.

XPS (Sage 100, SPECS, Berlin, Germany) was employed to study the changes of the elemental composition at the GFRP surfaces. Atomic concentrations of each element were calculated by determining the relevant integral peak intensities using a linear background [35], and the O/C ratio was obtained.

DCB specimens for crack in laminate measurements were cut directly from the cured laminate manufactured from 20 layers of fabric. The crack initiation was established using a 12.7-μm thin E-CTFE film (WL4900, AIRTECH Europe Saarl, Differdange, Luxembourg) between the middle two fabric layers. Tabs were mounted with both screws and glue (Scotch Weld DP360, 3 M, Copenhagen, Denmark). Overall geometry of the DCB test specimens used and a close up of the three different crack initiations used are shown in Fig. 2.

For crack initiation in the interface between glue and laminate, used for peel-ply and gliding arc test specimens, a 51-μm thin polytetrafluoroethylene (PTFE) release tape (Teflease MG2, AIRTECH Europe Saarl, Differdange, Luxembourg) was mounted on the laminate surface in a position of 70 mm from the tab-end of the rod, as illustrated in Fig. 2. On top of the release tape was a 2-mm thick PTFE chamfered spacer placed close to the tip of the crack initiation. Another 2-mm thick spacer was mounted in the other end of the rod ensuring a uniform glue thickness, $h$. Crack initiation in the centre of the glue line was established using two 1-mm thick chamfered PTFE spacers and in between a thin release film to make the crack tip as thin and sharp as possible. The release film was the 51-μm PTFE tape (Teflease MGZ). During application of the bonding paste, special attention was paid to the release film, which should not be bent accidentally, and the crack initiation position at 70 mm from the rod end was obtained. The GFRP rods were bonded using a vinylester adhesive (0555 Oldopal® VE Bonding paste, Monofiber A/S, Herlev, Denmark) [44]. Excess paste was removed from the edge of the DCB specimen. The bonded specimens were cured at 40°C for 16 h. Holes for mounting of steel pins facilitating the mounting of an extensometer were drilled in the laminate at the crack initiation position at 70 mm from the rod end. Extensometers measured the crack opening during the test.

The adhesion test was performed by applying uneven pure bending moments to the DCB-specimens [51,52]. The DCB loaded by uneven bending moments (DCB-UBM) test configuration provides stable crack growth for materials having a constant (or rising) fracture resistance and enables the testing of the whole mode mixity range from Mode I ($\psi = 0°$) to Mode II ($\psi = 90°$) ($\psi$ being the mode mixity, defined as the phase angle of the complex stress intensity factor, see [53]). In the present study, the fracture resistance and mode mixity were calculated without accounting for the stiffness

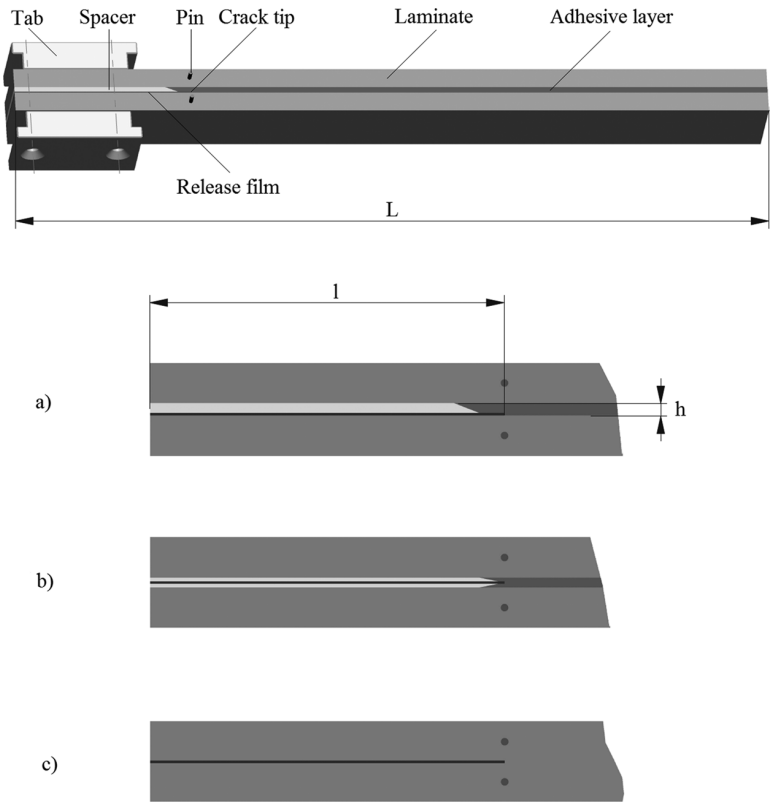


**FIGURE 2** Overall geometry of the 290-mm long (L) DCB test specimens illustrated with mounted tabs and 2-mm (h) glue thickness. Crack initiation (l) starts 70 mm from the specimen end where also the pins for mounting of extensometers are positioned. A close-up of the three different crack initiation types: a) interface between glue, and laminate, b) center of glue, and c) in the middle of the laminate. The crack initiation is established with a thin release film and chamfered spacers support the release film and control the glue thickness.



and thickness of the adhesive layer, *i.e.*, analysing the specimens as being a homogeneous laminate. The mode mixity, $\psi$, calculated in this manner is therefore a nominal mode mixity, $\psi_{nom}$. Table 1 shows the types of the specimens used and types of the tests applied in the present work.

The fracture experiments were conducted using a special test configuration based on wires and rollers. The test configuration of the fracture experiments is described elsewhere [52]. The experiments were conducted at a constant displacement rate of 10 mm/min. The load was measured using two 5-kN static load cells. The DCB specimens were instrumented with an extensometer to record the end-opening, $\delta^*$, at the tip of the crack initiation.

Fracture mechanical characterisation was conducted for four different nominal mode mixities. For the Mode I experiment a small mode mixity

(nominal Mode I: $\psi_{nom} = 0.3°$) was used in order to prevent the crack from kinking into the mid-plane of the specimen, *i.e.*, inside the middle of the adhesive layer (thus leaving the adhesive/laminate interface). The other mode mixity values were chosen to be $\psi_{nom} = 41°$, 58°, and 83°. The latter is close to Mode II. Mode II was avoided in order to minimize effects of crack face friction possibly evolving if crack faces were in sliding contact. Six DCB specimens were tested for each loading configuration. An acoustic emission (AE) sensor (PAC DiSP-16, Physical Acoustics Ltd., Cambridgeshire, UK) was mounted at the specimen to assist in the detection of crack growth.

The fracture resistance was calculated from a J integral analysis for the isotropic DCB-UBM [50] (plane stress):

$$J = \frac{21\left(M_1^2 + M_2^2\right) - 6M_1M_2}{4B^2H^3E} \qquad |M_1| < M_2, \tag{1}$$

where $M_1$ and $M_2$ are the two applied moments, $B$ is the specimen width, $H$ the specimen height, and $E$ is the Young's modulus. The nominal mode mixity, $\psi_{nom}$ can be obtained as [52]

$$\psi_{nom} = \tan^{-1}\left(\frac{\sqrt{3}}{2}\frac{M_1 + M_2}{M_2 - M_1}\right) \qquad |M_1| < M_2. \tag{2}$$

The fracture resistance, $J_R$, was calculated for the homogenous DCB specimen using the elastic properties of the glass/polyester composite (Young's modulus $E = 37$ GPa).

## 3. RESULTS

### 3.1. Rotational Temperature and Surface Characterization

$T_{rot}$ was estimated to be 3800 K at a flow rate of 20 L/min and decreased as the flow rate increased. Figure 3 shows the rotational temperature at different flow rates.

The contact angles and the polar component of the surface energy after the gliding arc treatment at different air flow rates are shown in Fig. 4. It is seen that the wettability markedly dropped down at the flow rate of 30 L/min. At this flow rate, the excess cooling reduced the rotational temperature as low as approximately 2000 K (see Figure 3), resulting in an insufficient treatment effect. The tendency of the wettability and the rotational temperature shows good agreement with earlier results [44].

In the following experiment the air flow rate was fixed at 20 L/min in order to demonstrate efficient adhesion improvement. The contact angle and the polar component of surface energy of the GFRP plate surfaces, measured before and after the gliding arc treatment at different numbers of

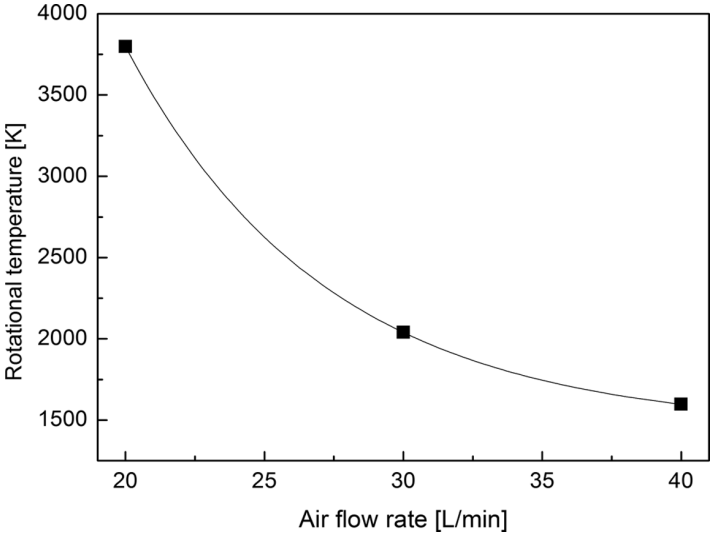


**FIGURE 3** Rotational temperature of the gliding arc at different air flow rates and fixed power (720 W).

exposure, are shown in Fig. 5. The water contact angles dropped to approximately 20° and the polar component of the surface energy increased to approximately 80 mJ/m$^2$ when the specimen surface was exposed in the gliding arc four times or more.

The XPS analysis indicated that the GFRP surfaces were mostly dominated by oxygen (O) and carbon (C) atoms. The O/C ratio of the GFRP

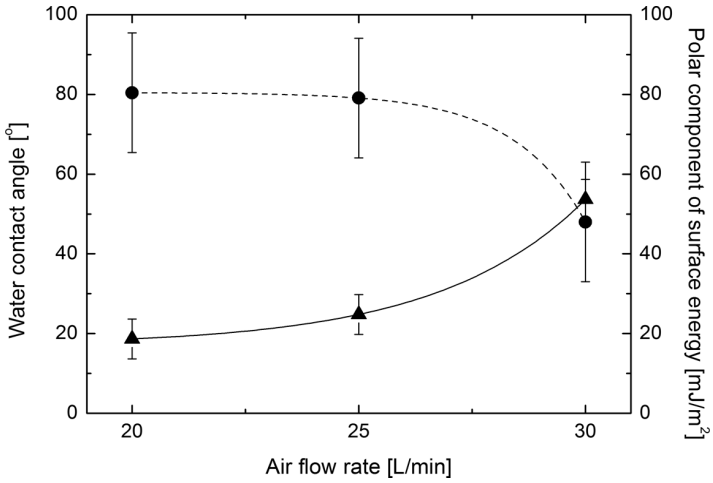


**FIGURE 4** Water contact angle (▲) and the polar component of surface energy (●) of the GFRP plates after the gliding arc treatment at different air flow rates and fixed power (720 W).

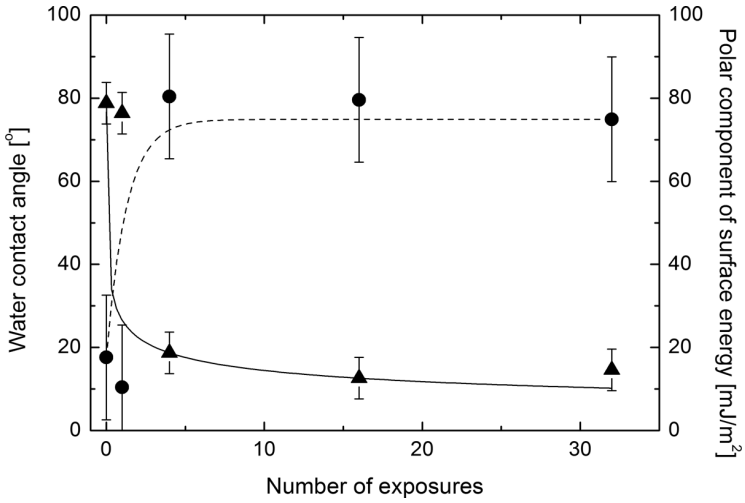


**FIGURE 5** Water contact angle (▲) and the polar component of surface energy (●) of the GFRP plates after the gliding arc treatment at different number of exposures at fixed air flow rate (20 L/min) and fixed power (720 W).

surfaces before and after the treatment was compared as shown in Fig. 6. The oxygen content increased more after the longer treatment, approaching approximately 0.42.

Since the gliding arc discharge can be extended into the ambient air up to several centimeters, it is interesting to investigate an effective distance of the treatment. Contact angles were measured after the gliding arc treatment at different distances from the edges of the electrodes to the GFRP plate surface. The water contact angle and the polar component of surface energy and O/C ratio at the GFRP plate surface after the gliding arc treatment are shown in Figs. 7 and 8, respectively. The results indicate that the GFRP plate surface can be efficiently oxidized when the distance between the edges of the electrodes and the GFRP surface was up to approximately 6 cm.

## 3.2. Fracture Properties of Peel Ply Joints

During the Mode I fracture mechanical tests of the DCB specimens prepared from peel ply only (*i.e.*, no plasma treatment), crack propagation occurred smoothly along the laminate/adhesive interface with no visible fibre bridging, see Fig. 9.

Measured fracture resistance data, the fracture resistance (the value of the J integral during crack propagation) as a function of end-opening, are shown in Fig. 10. No or very little opening occurs before the initiation of crack growth, which takes place at a fracture resistance value of around

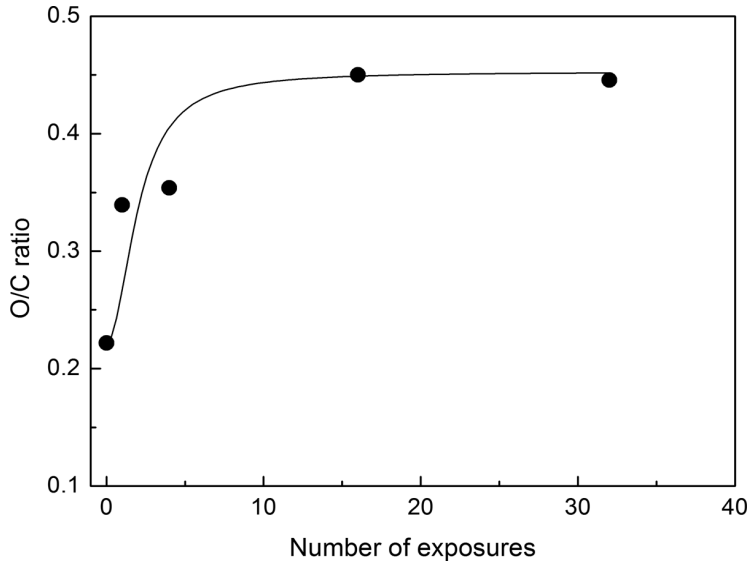


**FIGURE 6** O/C ratio of the GFRP plates after the gliding arc treatment at different number of exposures at fixed air flow rate (20 L/min) and fixed power (720 W).

140–160 J/m$^2$. Thereafter, as the crack propagates, the end-opening increases. The crack propagation occurs at a near-constant, but slightly lower, fracture resistance value (110–140 J/m$^2$).

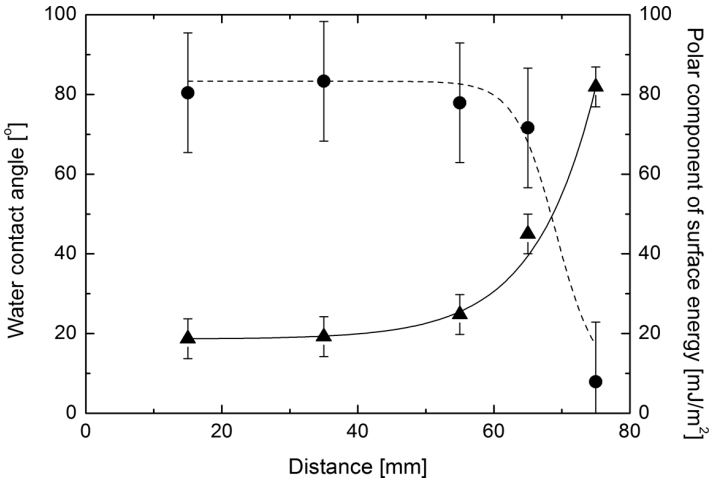


**FIGURE 7** Water contact angle (▲) and the polar component of surface energy (●) of the GFRP plates after the gliding arc treatment at different distances from the edges of the electrodes to the GFRP plate surface at fixed air flow rate (20 L/min), fixed power (720 W), and fixed number of exposures to the gliding arc (four times).

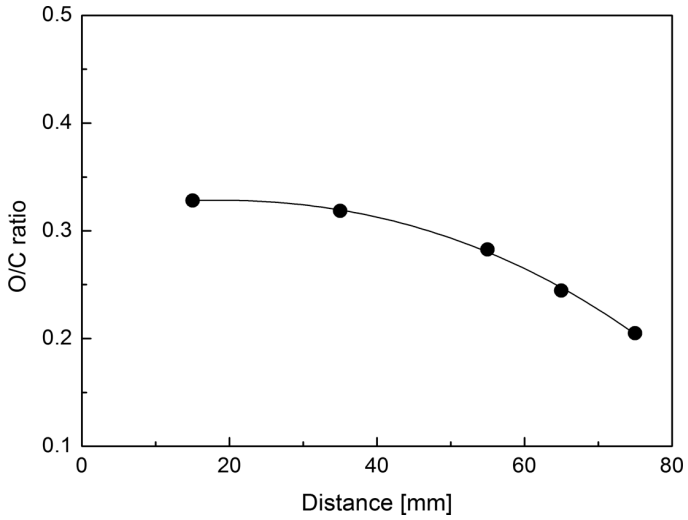


**FIGURE 8** O/C ratio of the GFRP plates after the gliding arc treatment at different distances from the edges of the electrodes to the GFRP surface at fixed air flow rate (20 L/min), fixed power (720 W), and fixed number of exposures to the gliding arc (four times).

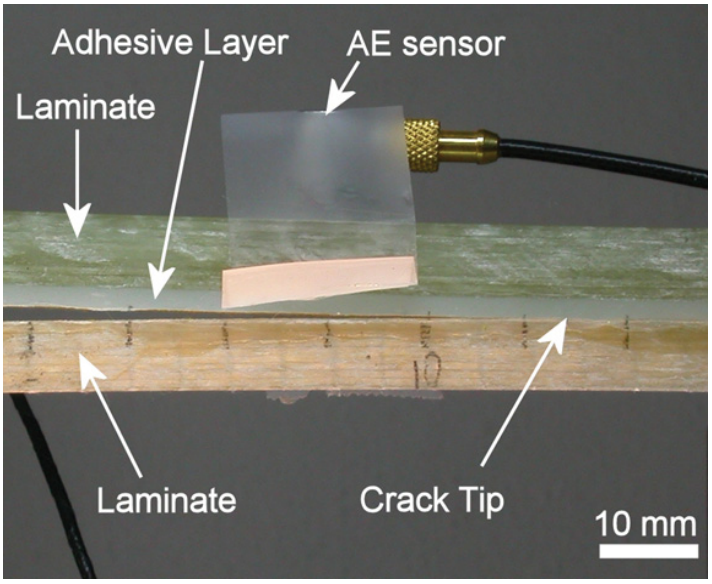


**FIGURE 9** Example of crack growth along the laminate/adhesive interface for nominal Mode I ($\psi_{nom} = 0.3°$) for standard peel ply without plasma treatment (color figure available online).

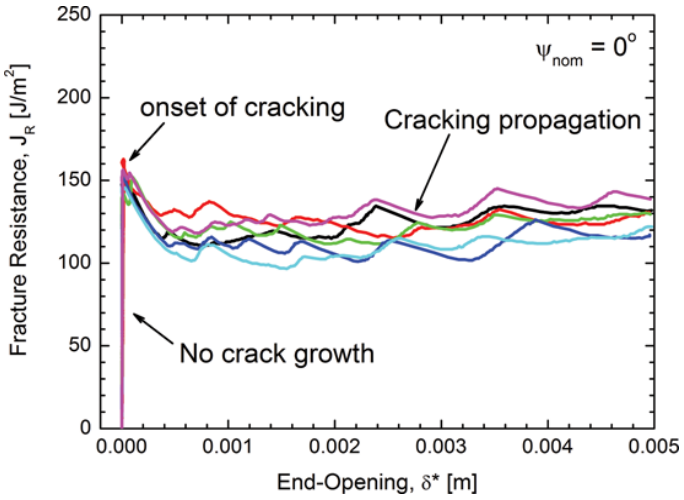


**FIGURE 10** Measured nominal Mode I ($\psi_{nom} = 0.3°$) fracture resistance curves (the fracture resistance as a function of the end-opening) for standard peel ply (no treatment) (color figure available online).

For standard peel ply specimens tested under $\psi_{nom} = 41°$ and 58°, cracking also occurred along the adhesive/laminate interface without fibre bridging. However, for dominant Mode II ($\psi_{nom} = 83°$), most specimens experienced cracking smoothly along the adhesive/laminate interface, but one DCB specimen showed some fibre bridging. Furthermore, for most specimens, a few shear cracks were observed to develop in the adhesive layer, see Fig. 11.

Fracture resistance data for $\psi_{nom} = 83°$ are shown in Fig. 12. The value of fracture resistance corresponding to initiation of crack growth is in the range of 520–620 J/m$^2$. The fracture resistance corresponding to crack propagation is approximately constant for each specimen, but there is a large specimen-to-specimen variation. Thus, for $\psi_{\text{nom}} = 83°$, the fracture energy associated with crack propagation is in the range of 320–660 J/m$^2$.

Average values of the fracture energies of the various mode mixities were calculated from the fracture resistance data for $1\,\text{mm} < \delta^* < 5\,\text{mm}$, $1\,\text{mm} < \delta^* < 3\,\text{mm}$, $1\,\text{mm} < \delta^* < 3\,\text{mm}$, and $0.5\,\text{mm} < \delta^* < 1.5\,\text{mm}$ for $\psi_{\text{nom}} =$ 0°, 41°, 58°, and 83°, respectively, and summarized in Section 4.2. Only values from specimens showing smooth interface fracture were included, and, thus, the effect of fibre bridging is excluded.

## 3.3. Fracture Properties of Plasma Treated Joints

The fracture resistance behaviour of plasma treated specimens is now described. For some specimens tested under nominal Mode I ($\psi_{nom} = 0.3°$),

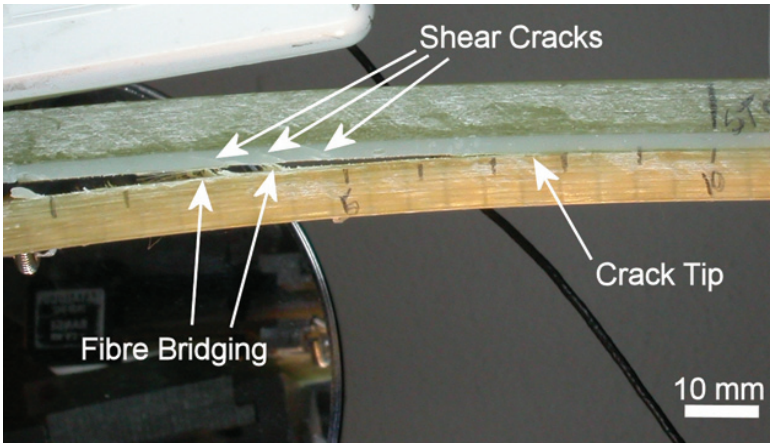


**FIGURE 11** Example of crack growth along laminate/adhesive interface for dominant Mode II ($\psi_{nom} = 83°$) for standard peel ply (no treatment). A few shear cracks can be seen in the adhesive layer (color figure available online).

the cracking occurred cleanly along the interface without fibre bridging (*e.g.*, #02 and #04), one specimen showed a little bit of crack bridging (#03), one some bridging (#04), while for others (specimens #01 and #06) the fracture process zone consisted of cracking that had occurred along two layers, one inside the laminate (the leading crack tip) and one along the adhesive/laminate interface. Both cracking planes exhibited fibre bridging, see Fig. 13.

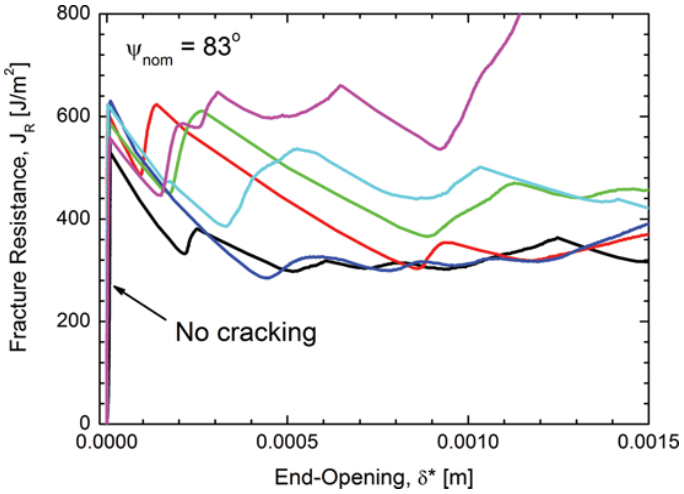


**FIGURE 12** Fracture resistance curves for standard peel ply (no treatment) subjected to $\psi_{nom} = 83°$ (color figure available online).

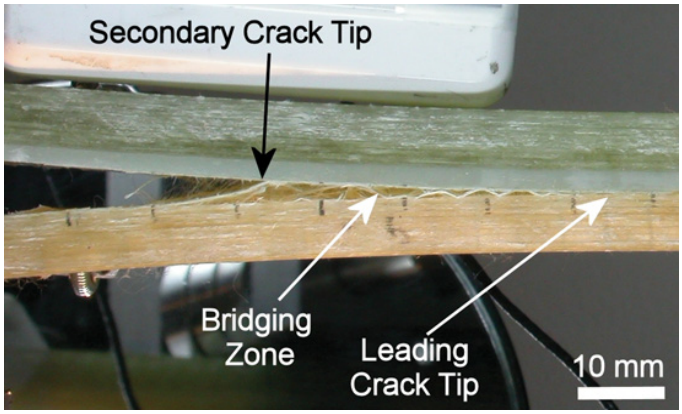


**FIGURE 13** Example of crack growth along laminate/adhesive interface for nominal Mode I ($\psi_{nom} = 0.3°$) for plasma treatment. This specimen shows smooth crack propagation (close to the slip foil) and the formation of a large-scale fracture process zone in the form of two parallel cracks (one inside the laminate, running further down along the laminate than the one that runs along the laminate/adhesive interface) (color figure available online).



The associated fracture resistance data for $\psi_{nom} = 0.3°$ are shown in Fig. 14. As for the failure modes described above, there is a large specimen-to-specimen variation in the fracture resistance. Initiation of cracking occurs at a $J_R$ value of about 210–345 J/m$^2$. For some specimens (#02 and #04)—the ones that did not show crack bridging—the fracture resistance remains at that level with further crack propagation. For the other specimens

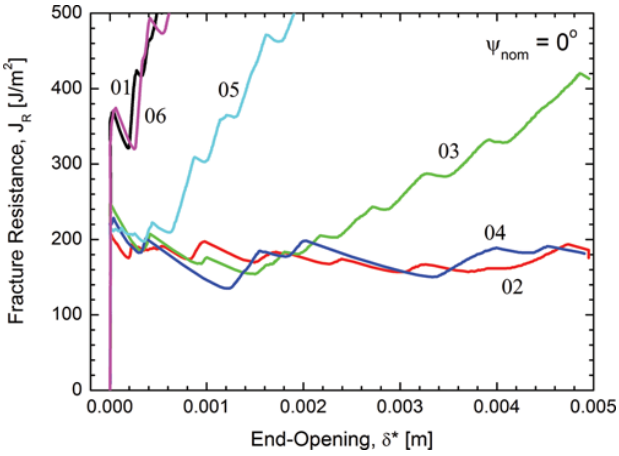


**FIGURE 14** Measured nominal Mode I ($\psi_{nom} = 0.3°$), fracture resistance curves (the fracture resistance as a function of the end-opening) for plasma treatment. The steeply rising fracture resistance is associated with fibre bridging (color figure available online).

(#01, #05, and #06), the fracture resistance increases sharply with increasing end-opening. One specimen (#03) shows a mixed behaviour, having initially a near-constant fracture energy until an end-opening of about 2 mm. For larger opening, the fracture resistance of that specimen increases sharply.

Figure 15 shows the fracture process zone of plasma-treated specimens under dominant Mode II ($\psi_{nom} = 83°$). The fracture process zone is long (larger than 5 cm) and consists of two parallel cracks: one of the cracks extends inside the laminate and the other (the shorter one) extends along the laminate/adhesive interface. Both cracking planes experience crack bridging by fibres.

The fracture resistance of the adhesive joints prepared with plasma treatment is shown as a function of the end-opening in Fig. 16. Crack initiation occurs at a J value of about 650–900 J/m$^2$, rising rapidly to an approximately maximum (not quite steady-state) value of 1.8–2.2 kJ/m$^2$ for an end-opening of about 3 mm.

## 3.4. Fracture Properties of Laminate

Figure 17 shows a pure laminate subjected to pure Mode I testing. A (~4 cm) long crack bridging zone has formed between the slip foil (initial crack tip position) and the actual crack tip. The associated fracture resistance is shown as a function of the end-opening in Fig. 18. Initiation of crack growth takes place at a J value of about 125–150 J/m$^2$. With increasing end-opening (increasing crack length and, thus, increasing the bridging zone) the fracture resistance increases rather smoothly to a steady-state value of 850–1050 J/m$^2$. Note that the specimen-to-specimen variation is rather small.

Figure 19 shows a laminate subjected to dominant Mode II loading ($\psi_{nom} = 83°$). The crack seems to be closed the first few centimetres from

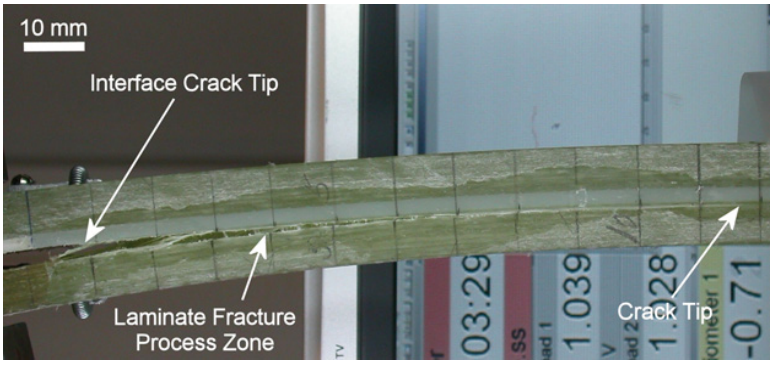


**FIGURE 15** Development of the fracture process zone under dominant Mode II ($\psi_{nom} = 83°$) for plasma treatment. Note the development of two cracking planes: one inside the laminate (the leading crack tip) and one along the laminate/adhesive interface (color figure available online).

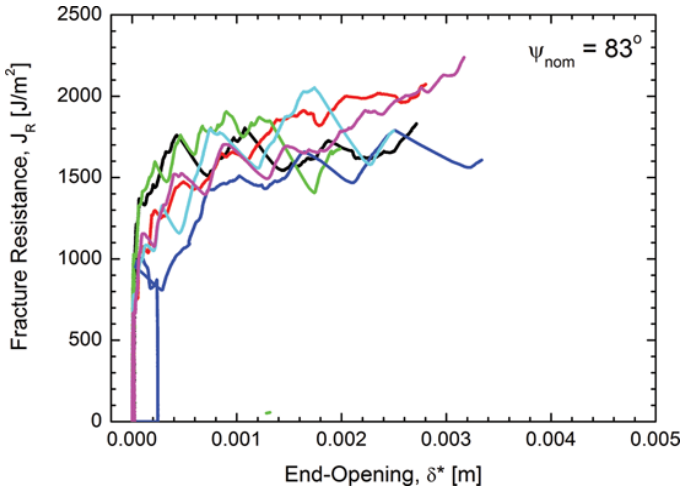


**FIGURE 16** Measured dominant Mode II ($\psi_{nom} = 83°$) fracture resistance curves (the fracture resistance as a function of the end-opening) for plasma treatment (color figure available online).

the crack tip (*i.e.*, undergoing predominantly tangential crack face displacements) but shows an increasing normal opening further away from the crack tip. There appears to be crack bridging along most of the crack.

The associated fracture resistance data are shown in Fig. 20. Initiation of cracking takes place at a fracture resistance value of about 1.1–1.3 kJ/m$^2$. Within an increasing end-opening of 0.2 mm, the fracture resistance increases to a near-constant value of 1.6–2.0 kJ/m$^2$.

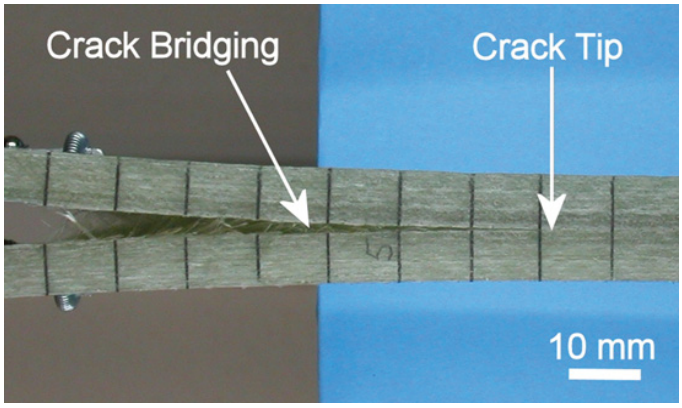


**FIGURE 17** Example of crack growth for nominal Mode I ($\psi_{nom} = 0.3°$) for the laminates. Note the presence of a large-scale crack bridging zone (color figure available online).

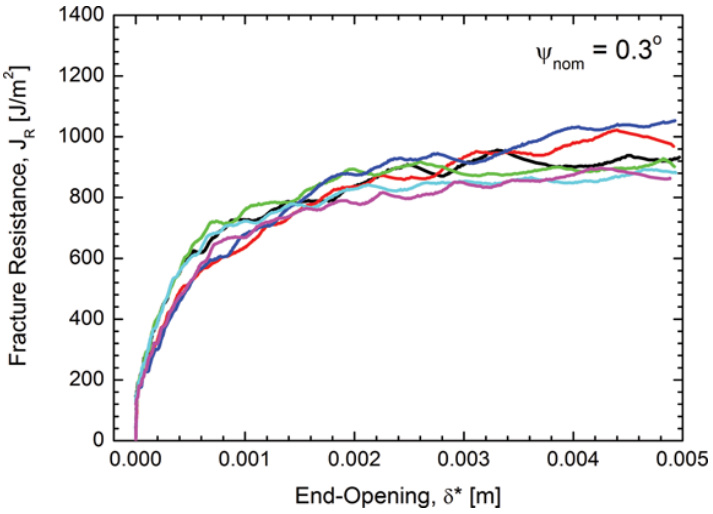


**FIGURE 18** Measured nominal Mode I ($\psi_{nom} = 0.3°$) fracture resistance curves (the fracture resistance as a function of the end-opening) for the laminate (color figure available online).

## 3.5. Fracture Properties of the Adhesive

Each specimen having an adhesive layer subjected to pure Mode I loading ($\psi_{nom} = 0°$) developed crack propagation along the specimen mid-plane, *i.e.*, within the adhesive layer. The value of J at the initiation of crack growth was 450–500 J/m$^2$. Once crack growth has initiated, the crack grew unstably. It was, thus, not possible to determine a fracture energy corresponding to stable crack growth.

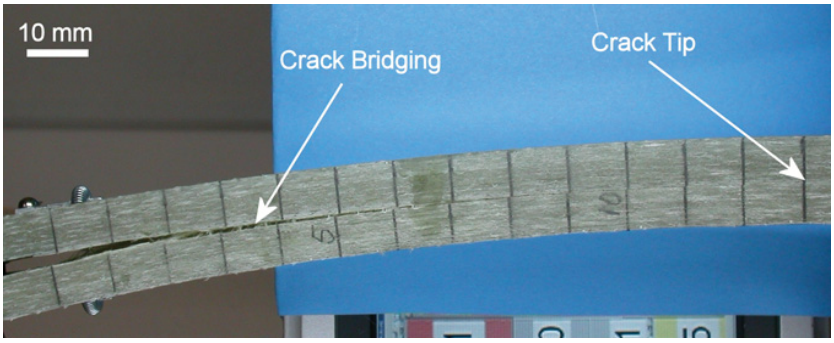


**FIGURE 19** Laminate undergoing delamination due to dominant Mode II loading ($\psi_{nom} = 83°$) (color figure available online).

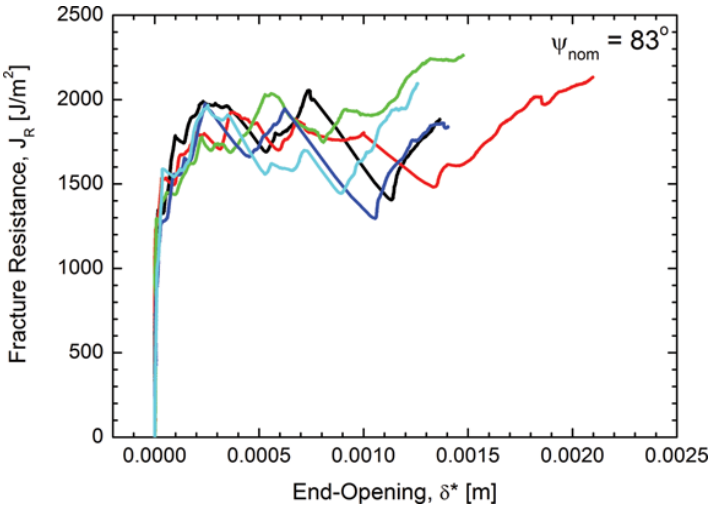


**FIGURE 20** Measured dominant Mode II ($\psi_{nom} = 83°$) fracture resistance curves (the fracture resistance as a function of the end-opening) for the laminates (color figure available online).

## 4. DISCUSSION

### 4.1. Plasma Surface Modification by the Gliding Arc Treatment

It is shown in the present work (Figs. 4–8) that the gliding arc treatment can improve wettability and increase the polar component of the surface energy, the oxygen content at the GFRP surface and, subsequently, bond strength with a vinylester adhesive. Since the major bond mechanism with vinylester adhesive is non-specific interaction [54], the effect of the gliding arc treatment can be primarily attributed to the introduction of a certain amount of polar functional groups at the surfaces and better wetting by the uncured liquid vinylester adhesive prior to hardening. Namely, these polar functional groups can preferably interact with the vinylester adhesive that contains similar polar functional groups. In addition, gliding arc treatment can create reactive free radicals at the GFRP surface. There is a chance that these radicals can directly react with the reactive sites of the vinylester resin, forming covalent bonds and further improving bond strength.

### 4.2. Comparison of Fracture Energies

Figure 21 shows the initiation fracture energy as a function of mode mixity for crack growth of the peel ply specimens, the plasma-treated specimens, and crack growth in the laminate (delamination). The value of Mode I cracking growth initiation within the adhesive is also included.

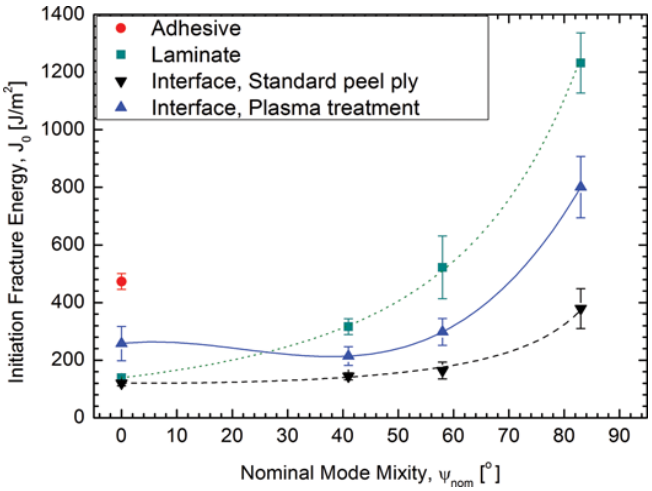


**FIGURE 21** Mixed mode interfacial fracture energy shown as a function of the mode mixity (color figure available online).



First, the general trend observed in Fig. 21 is that the fracture energy increases with increasing mode mixity. Such trends are in good agreement with results of earlier studies of mixed mode interface fracture [48,49].

Next, for nominal Mode I ($\psi_{nom} = 0.3°$), the fracture initiation values of the laminate and the peel ply specimens are comparable, while the fracture initiation values of the plasma-treated specimens are higher than those of the laminates and the peel ply specimens but lower than those within the adhesive layer. For higher values of $\psi_{nom}$, the results associated with the peel ply specimen, the plasma-treated specimens and the laminates are clearly different. This suggests that Mode I testing only may not be sufficient for screening and selecting interface treatments.

The most important result from Fig. 21 is that the fracture energy data associated with the plasma-treated specimens are significantly higher than those of the peel ply specimens. Thus, the plasma treatment results in a significant increase in the fracture energy of the adhesive joint. The mixed mode fracture energy is, however, not as high as the mixed mode fracture energy of the pure laminate, *i.e.*, specimens having no adhesive layer.

If we assume that each carbon atom could bond at most one oxygen atom, the O/C ratio can represent a ratio of carbon atoms that directly bond oxygen atoms. They can induce ionic or hydrogen-bond interactions with the adhesive. The O/C ratio of the untreated specimen is approximately 0.23, while it increased $1.6 - 2$ times after the plasma treatment as shown in Fig. 6. It is, therefore, roughly estimated that the plasma treatment may increase the adhesive strength at the interface upto a factor of two. Although

this estimation is based on the simplified assumption, it shows good agreement with the initiation fracture energy at the mixed modes in Fig. 21.

## 4.3. Fracture Resistance and Failure/Cracking Modes

As noted in Section 3.5, crack growth within the adhesive layer in Mode I occurred unstably. This suggests that the fracture resistance of the adhesive depends on the crack growth velocity. Such a phenomenon, denoted slip-stick behaviour, is not uncommon for adhesives [55].

It is interesting to note that shear cracks were observed in the adhesive layer for the peel ply specimens under dominant Mode II loading ($\psi_{nom} = 83°$), Fig. 11, but not for the plasma-treated specimens tested under the same loading condition ($\psi_{nom} = 83°$) (Fig. 15), even though the latter show a much higher fracture resistance during crack propagation (Fig. 16). A major difference in the cracking mode of the two series is that for the peel ply specimens, the crack propagates as a single crack tip, whereas the plasma-treated specimens develop a fracture process zone consisting of two crack tips and two long crack bridging zones. Apparently, a single sharp crack tip causes a higher stress in the adhesive layer than the longer fracture process zone, causing the development of shear cracks.

As observed for the plasma-treated specimens subjected to Mode I ($\psi_{nom} = 0.3°$, Fig. 13), the fracture resistance of adhesive joints depends strongly on the exact cracking modes. Cracking by an unbridged crack propagating along the adhesive/laminate interface resulted in a fracture resistance value of the order of $200\,J/m^2$ while the development of a fracture process zone with two bridged cracks resulted in a significant increase in the fracture resistance with increasing end-opening. There is, thus, a consistent relationship between constant fracture resistance and growth of an unbridged crack and increasing fracture resistance in connection with the formation of a large-scale crack bridging zone. This observation confirms earlier work on toughening by crack bridging [52,56].

## 4.4. Origin of Increase in Fracture Resistance from Plasma Treatment

A modern view of fracture is to consider fracture properties in terms of cohesive laws [57]. That is, a fracture process zone—being small (*e.g.*, in the case of failure by a single sharp crack) or being large (*e.g.*, in the case of a large scale bridging zone)—can be represented by a traction-separation law that possesses both a peak traction value, $\hat{\sigma}$ (strength), and the work of separation, $J_{ss}$ (fracture energy), see Fig. 22a. Now consider the situation encountered in the present study. Fracture can occur along two planes: along the adhesive/laminate interface and/or along a plane just a small distance within the laminate below the surface layer (delamination). Now imagine

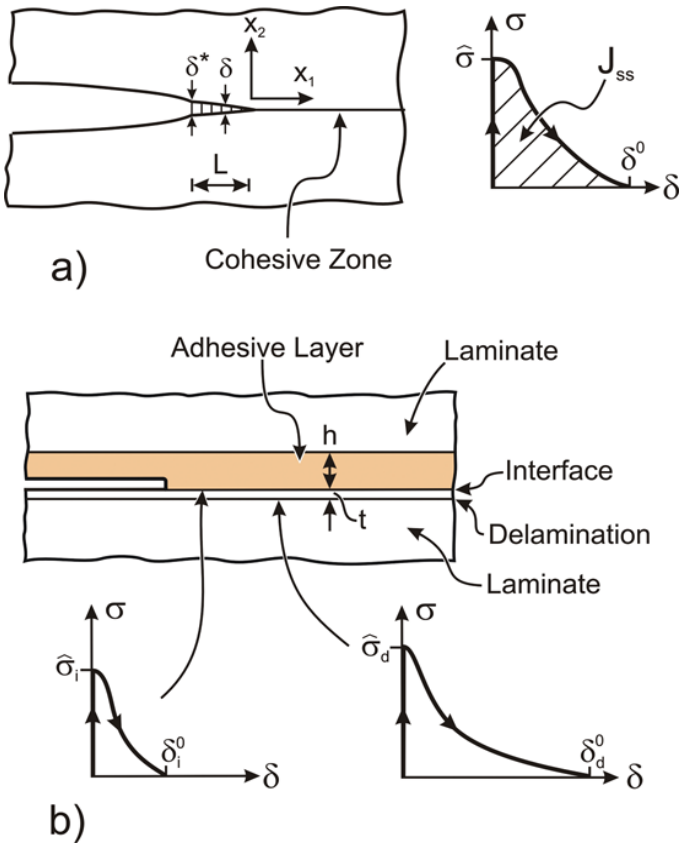


**FIGURE 22** a) Representation of a fracture process zone in terms of a cohesive law (traction-separation relationship) that possesses a strength, $\hat{\sigma}$, and a fracture energy, $J_{ss}$. b) The cohesive law of the adhesive/laminate interface is assumed to be different from the cohesive law associated with cracking inside the laminate (delamination) (color figure available online).

that fracture of each potential cracking plane is represented by a cohesive law. As indicated in Fig. 22b, the cohesive laws of the two different cracking planes are different, since the mechanical properties of the two cracking planes differ. If the thickness that separates the two cracking planes, t, is small, the stresses cannot be redistributed much so that the stresses in the two fracture process zones must be the same. Consequently, the separation will occur along the plane that possesses the lower peak traction value. If the strength of the adhesive/laminate interface, $\hat{\sigma}_i$, is lower than that of the laminate, $\hat{\sigma}_d$, cracking will occur along the adhesive/laminate interface. Conversely, if $\hat{\sigma}_i$ is raised so that $\hat{\sigma}_i > \hat{\sigma}_d$, cracking will occur as delamination in the laminate. Returning to the experimental results, we then conclude that for the peel ply specimens—that fail by the propagation of a single crack

along the adhesive/laminate interface—the peak traction value of the cohesive law of the adhesive/laminate interface, $\hat{\sigma}_i$, must be lower than that of the laminate, $\hat{\sigma}_d$, $(\hat{\sigma}_i < \hat{\sigma}_d)$ However, for the plasma treated specimens—for which the primary cracking occurred by crack propagation within the laminate—the peak traction of the cohesive law of the adhesive/laminate interface must be higher than the peak traction value of the laminate $(\hat{\sigma}_i > \hat{\sigma}_d)$. It is reasonable to assume that the cohesive laws (and thus $\hat{\sigma}_d$) of the laminates are identical, since the plasma treatment affects only the very surface layers. This hypothesis, thus, suggests that the plasma treatment increases the strength of the adhesive/laminate interface $\hat{\sigma}_i$. However, for nominal Mode I ($\psi_{nom} = 0.3°$), it is seen that the fracture initiation values of the plasma-treated specimens are higher than those of the laminates. Further investigation will be necessary for deep understanding of this phenomenon.



## 5. CONCLUSION

Gliding arc treatment of laminate surfaces of glass-fibre-reinforced polymers (GFRP) increased wettability, the polar component of the surface energy, and the oxygen content at the GFRP surfaces. The fracture energy of an interface between laminates and a vinylester adhesive was significantly higher than that from interfaces made by conventional peel plying. The increased mixed mode fracture resistance was attributed to the formation of two cracking planes (one along the adhesive/laminate interface and another within the laminate) both displaying crack bridging. The change in failure mechanism (the formation of the crack within the laminate) was most likely induced by a plasma treatment enhancement of the cohesive strength of the adhesive/laminate interface.

## ACKNOWLEDGMENTS

This work was partly sponsored by the Ministry of Science, Technology and Innovation through the National Danish Proof of Concept Funding Scheme (grant number: 09-076196). Bent F. Sørensen was partially supported by the Danish Centre for Composite Structures and Materials for Wind Energy (DCCSM) from the Danish Research Council for Strategic Research (grant number: 09-067212). Mirko Salewski is acknowledged for his fruitful suggestions. Søren Nimb is acknowledged for the design and construction of the gliding arc sources. Christian Hjelm Madsen is acknowledged for the manufacturing of GFRP laminate and the DCB test specimens. Erik Vogeley is acknowledged for his assistance in the fracture mechanical testing and Ulrich Mortensen for drawings of the different types of DCB specimens.

## REFERENCES


[1] Davis, P., Cantwell, W. J., Jar, P. Y., Bourban, P. E., Zysman, V., and Kausch, H. H., *Composites* **22** (6), 425–431 (1991).
[2] Wade, G. A., Cantwell, W. J., and Pond, R. C., *Interf. Sci.* **8**, 363–373 (2000).
[3] Dagher, H. J., Iqbal, A., and Bogner, B., *Polym. Polym. Composites* **12** (3), 169–182 (2004).
[4] Kaiser, H. and Karbhari, V. M., *Int. J. Mater. Product Technol.* **21** (5), 349–384 (2004).
[5] Bakis, C. E., Bank, L. C., Brown, V. L., Cosenza, E., Davalos, J. F., Lesko, J. J., Machida, A., Rizkalla, S. H., and Triantafillou, T. C., *J. Composites for Construction* **6** (2), 73–87 (2002).
[6] Shenton, J., Lovell-Hoare, M. C., and Stevens, G. C., *J. Phys. D Appl. Phys.* **34**, 2761–2768 (2001).
[7] Kinloch, A. J. and Taig, C. M., *J. Adhes.* **21**, 291–302 (1987).
[8] Wingfield, J. R. J., *Int. J. Adhes. Adhes.* **13** (3), 151–156 (1993).
[9] Blackman, B. R. K., Kinloch, A. J., and Watts, J. F., *Composites* **25** (5), 332–341 (1994).
[10] Kinloch, A. J., Kodokian, G. K. A., and Watts, J. F., *Phil. Trans. R. Soc. Lond. A* **338**, 83–112 (1992).
[11] Kodokian, G. K. A. and Kinloch, A. J., *J. Mater. Sci. Let.* **7**, 625–627 (1988).
[12] Kodokian, G. K. A. and Kinloch, A. J., *J. Adhes.* **29**, 193–218 (1989).
[13] Adams, R. D., Atkins, R. W., Harris, A., and Kinloch, A. J., *J. Adhes.* **20**, 29–53 (1986).
[14] Pocius, A. V. and Wenz, R. P., *SAMPLE J.* **20** (5), 50–58 (1985).
[15] Bénard, Q., Fois, M., and Grisel, M., *Composites A* **36**, 1562–1568 (2005).
[16] Cognard, J., *C. R. Chimie* **9**, 13–24 (2006).
[17] Hegemann, D., Brunner, H., and Oehr, C., *Nucl. Insum. Methods Phys. Res. B* **208**, 281–286 (2003).
[18] Kogoma, M., Kusano, M., and Kusano, Y.,(Eds.) *Generation and Applications of Atmospheric Pressure Plasmas*, (NOVA Publishers Inc., New York, 2011).
[19] Kanazawa, S., Kogoma, M., Moriwaki, T., and Okazaki, S., *J. Phys. D Appl. Phys.* **21**, 838–840 (1988).
[20] Tendero, C., Tixier, C., Tristant, P., Desmaison, J., and Leprince, P., *Spectrochimica Acta B* **61**, 2–30 (2006).
[21] Teodoru, S., Kusano, Y., Rozlosnik, N., and Michelsen, P. K., *Plasm. Proc. Polym.* **6**, S375–S381 (2009).
[22] Kusano, Y., Teodoru, S., and Hansen, C. M., *Surf. Coat. Technol.* **205**, 2793–2798 (2011).
[23] Kusano, Y., Andersen, T. L., and Michelsen, P. K., *J. Phys. Conf. Series* **100**, 012002 (2008).
[24] Lee, B. J., Kusano, Y., Nato, N., Naito, K., Horiuchi, T., and Koinuma, H., *Jpn. J. Appl. Phys. Pt. 1* **36**, 2888–2891 (1997).
[25] Mortensen, H., Kusano, Y., Leipold, F., Rozlosnik, N., Kingshott, P., Sørensen, B. F., Stenum, B., and Bindslev, H., *Jpn. J. Appl. Phys.* **45** (10B), 8506–8511 (2006).
[26] Singh, S. V., Kusano, Y., Morgen, P., and Michelsen, P. K., *J. Appl. Phys.* **111**, 083501 (2012).

[27] Kogelschatz, U., *Plasm. Chem. Plasm. Proc.* **23**, 1–46 (2003).
[28] Fateev, A., Leipold, F., Kusano, Y., Stenum, B., Tsakadze, E., and Bindslev, H., *Plasm. Proc. Polym.* **2**, 193–200 (2005).
[29] Leipold, F., Fateev, A., Kusano, Y., Stenum, B., and Bindslev, H., *Fuel* **85**, 1383–1388 (2006).
[30] Kusano, Y., Leipold, F., Fateev, A., Stenum, B., and Bindslev, H., *Surf. Coat. Technol.* **200**, 846–849 (2005).
[31] Kusano, Y., Mortensen, H., Stenum, B., Goutianos, S., Mitra, B., Ghanbari-Siahkali, A., Kingshott, P., Sørensen, B. F., and Bindslev, H., *Int. J. Adhes. Adhes.* **27** (5), 402–408 (2007).
[32] Leipold, F., Kusano, Y., Hansen, F., and Jacobsen, T., *Food Control* **21**, 1194–1198 (2010).
[33] Leipold, F., Schultz-Jensen, N., Kusano, Y., Bindslev, H., and Jacobsen, T., *Food Control* **22** (8), 1296–1301 (2011).
[34] Drews, J., Kusano, Y., Leipold, F., Bardenshtein, A., and Krebs, N., *Ozone: Sci. Eng.* **33**, 783–788 (2011).
[35] Kusano, Y., Mortensen, H., Stenum, B., Kingshott, P., Andersen, T. L., Brøndsted, P., Bilde-Sørensen, J. B., Sørensen, B. F., and Bindslev, H., *Plasm. Proc. Polym.* **4** (S1), S455–S459 (2007).
[36] Kusano, Y., Singh, S. V., Bardenshtein, A., Krebs, N., and Rozlosnik, N., *J. Adhes. Sci. Technol.* **24**, 1831–1839 (2010).
[37] Kusano, Y., Singh, S. V., Norrman, K., Leipold, F., Drews, J., Morgen, P., Bardenshtein, A., and Krebs, N., *J. Adhes.* **87**, 720–731 (2011).
[38] Kusano, Y., Singh, S. V., Norrman, K., Drews, J., Leipold, F., Rozlosnik, N., Bardenshtein, A., and Krebs, N., *Surf. Eng.* **28** (6), 453–457 (2012).
[39] Kusano, Y., Norrman, K., Leipold, F., Singh, S. V., Morgen, P., Bardenshtein, A., and Krebs, N., *J. Adhes. Sci. Technol.* Published online DOI: 10.1080/01694243.2012.727156 (2012).
[40] Fridman, A., Chirokov, A., and Gutsol, A., *J. Phys. D Appl. Phys.* **38**, R1–R24 (2005).
[41] Fridman, A., Nester, S., Kennedy, L. A., Saveliev, A., and Mutaf-Yardimci, O., *Progress in Energy and Combustion Sci.* **25**, 211–231 (1999).
[42] Janča, J. and Czernichowski, A., *Surf. Coat. Technol.* **98**, 1112–1115 (1998).
[43] Kusano, Y., *Surf. Eng.* **25** (6), 415–416 (2009).
[44] Kusano, Y., Teodoru, S., Leipold, F., Andersen, T. L., Sørensen, B. F., Rozlosnik, N., and Michelsen, P. K., *Surf. Coat. Technol.* **202**, 5579–5582 (2008).
[45] Kusano, Y., Norrman, K., Drews, J., Morgen, P., Leipold, F., Singh, S. V., Bardenshtein, A., and Krebs, N., *Surf. Coat. Technol.* **205**, S490–S494 (2011).
[46] Kusano, Y., "An apparatus and a method and a system for treating a surface with at least one gliding arc source," *International patent application* No. WO 2011 073170 A1 (2011).
[47] Rice, J. R., *J. Appl. Mech.* **55**, 98–103 (1988).
[48] Cao, H. C. and Evans, A. G., *Mech. Mater.* **7**, 295–304 (1989).
[49] Liechti, K. M. and Chai, Y.-S., *J. Appl. Mech.* **59**, 295–304 (1992).
[50] Laux, C. O., Spence, T. G., Kruger, C. H., and Zare, R. N., *Plasm. Source Sci. Technol.* **12**, 125–138 (2003).
[51] Plausinis, D. and Spelt, J. K., *Int. J. Adhes. Adhes.* **15**, 225–232 (1995).

[52] Sørensen, B. F., Jørgensen, K., Jacobsen, T. K., and Østergaard, R. C., *Int. J. Fract.* **141**, 159–172 (2006).
[53] Hutchinson, J. W. and Suo, Z., Mixed Mode Cracking in Layered Materials, in *Advances in Applied Mechanics*, J. W. Hutchinson, and T. Y. Wu (Eds.) (Academic Press Inc., Boston, 1992), Vol. 29, pp. 63–191.
[54] Brown, J. R. and Mathys, Z., *J. Mater. Sci.* **32**, 2599–2604 (1997).
[55] Webb, T. E. and Aifantis, E. C., *Int. J. Solids Structures* **32**, 2725–2743 (1995).
[56] Spearing, S. M. and Evans, A. G., *Acta Metall. Mater.* **40**, 2191–2199 (1992).
[57] Hutchinson, J. W. and Evans, A. G., *Acta Materialia* **48**, 125–135 (2000).

# [Appendix A5]

Y. Kusano, B.F. Sørensen, T.L. Andersen, H.L. Toftegaard, F. Leipold, M. Salewski, Z.W. Sun, J.J. Zhu, Z.S. Li, M. Aldén

## "Water-cooled non-thermal gliding arc for adhesion improvement of glass-fibre-reinforced polyester"

*Journal of Physics D: Applied Physics* 46(13) (2013) 135203.

IOP PUBLISHING JOURNAL OF PHYSICS D: APPLIED PHYSICS
J. Phys. D: Appl. Phys. **46** (2013) 135203 (7pp) doi:10.1088/0022-3727/46/13/135203

# Water-cooled non-thermal gliding arc for adhesion improvement of glass-fibre-reinforced polyester

**Yukihiro Kusano[1], Bent F Sørensen[1], Tom L Andersen[1], Helmuth L Toftegaard[1], Frank Leipold[2], Mirko Salewski[2], Zhiwei Sun[3], Jiajian Zhu[3], Zhongshan Li[3] and Marcus Alden[3]**

[1] Department of Wind Energy, Section of Composites and Materials Mechanics, Technical University of Denmark, Risø Campus, Frederiksborgvej 399, DK-4000 Roskilde, Denmark
[2] Department of Physics, Technical University of Denmark, Risø Campus, Frederiksborgvej 399, DK-4000 Roskilde, Denmark
[3] Department of Physics, Combustion Physics Division, Lund University, PO Box 118, S-221 00 Lund, Sweden

E-mail: yuki@dtu.dk

Received 21 December 2012, in final form 28 January 2013
Published 28 February 2013
Online at stacks.iop.org/JPhysD/46/135203

**Abstract**
A non-equilibrium quenched plasma is prepared using a gliding-arc discharge generated between diverging electrodes and extended by a gas flow. It can be operated at atmospheric pressure and applied to plasma surface treatment to improve adhesion properties of material surfaces. In this work, glass-fibre-reinforced polyester plates were treated using an atmospheric pressure gliding-arc discharge with air flow to improve adhesion with a vinylester adhesive. The electrodes were water-cooled so as to operate the gliding arc continually. The treatment improved wettability and increased the density of oxygen-containing polar functional groups on the surfaces. Double cantilever beam specimens were prepared for fracture mechanic characterization of the laminate adhesive interface. It was found that gliding-arc treatment significantly increases the fracture resistance in comparison with a standard peel-ply treatment.

(Some figures may appear in colour only in the online journal)

## 1. Introduction

Plasma treatment is useful for adhesion improvement of material surfaces, because it readily improves the surfaces to be bonded due the high chemical reactivity of the plasma, while it retains the bulk properties of the material and it is an environmentally friendly process. Plasma processing is generally performed at low gas pressures, but often atmospheric pressure would be preferable [1]. A gliding arc is a plasma generated between diverging electrodes and extended and quenched by a gas flow [2, 3]. Gliding arcs can be operated in air at atmospheric pressure and thus advantageously and economically used for large-scale processing. They can treat surfaces of bulky objects and are useful for adhesion improvement of materials in industrial processing [4–7]. They can potentially provide a high degree of non-equilibrium at high electron temperature and at quasi-ambient gas temperature and a high energy density simultaneously and thus enable high reactivity with high productivity. However, the treatment effects of commercially available gliding arcs are often disappointing, possibly due to the fact that the conditions of the non-equilibrium state and high energy density are not taken into account properly.

In order to achieve the condition of the high energy density, high power must be introduced to the discharge, which inevitably leads to heating up the electrodes. Subsequently, the resistance of the electrodes increases and Joule heating of the electrodes is enhanced. This is not only energy-inefficient, but it also induces unstable operation of the gliding arc due to the changing electrical impedance of the electrodes.

 

Furthermore, excess heat irradiation may damage the setup and materials to be treated. Therefore, it is desirable to cool the electrode efficiently. One common and efficient way of cooling electrodes in other applications than the gliding arc is internal cooling by flowing coolants, usually water, through the hollow electrodes. Interestingly, electrodes of gliding arcs are rarely water-cooled, probably because surface erosion of the water-cooled electrodes has been observed [8]. However, in the same work it is reported that the lifetime of the electrodes is not affected by the water cooling.

Glass-fibre-reinforced polymer (GFRP) materials exhibit high strength-to-weight ratios and corrosion resistance and are therefore used for a variety of applications in wind energy, ship, aerospace and automobile industry [9–13]. These GFRP materials are usually assembled together with other materials and jointed using adhesives. Such adhesive joints require careful surface preparation of GFRPs. When a thermosetting polymer such as unsaturated polyester, vinylester and an epoxy resin is used as a matrix of composites, mechanical treatment has been applied for the surface preparation [14, 15]. Peel-plying is a prime example of mechanical treatment used for adhesion improvement [16] since it provides a ready-to-bond surface that may not require further surface cleaning before bonding. Another example is mechanical roughening that needs laborious abrasion followed by solvent cleaning before adhesive bonding for achieving high joint strength [14]. Plasma treatment has also been investigated to improve adhesive bonding of GFRPs [4–6, 17–22]. It generally increases the polar component of the surface energy, the density of oxygen-containing polar functional groups at the GFRP surfaces, and bond strength with the vinylester adhesive.

In this work, GFRP laminates are treated with a gliding arc in air at atmospheric pressure to improve the adhesive bonding by a vinylester adhesive. Tubular electrodes with an external diameter of 3 mm are water-cooled so that the gliding arc can be operated continuously and stably. Optical emission spectroscopy (OES) is used for plasma diagnostics at different locations of the gliding arc. The treated surfaces are characterized using contact angle measurements and x-ray photoelectron spectroscopy (XPS). The mechanical properties of the laminate/adhesive interface are characterized in terms of the fracture energy. The interfacial fracture energy of the gliding-arc treated interface is compared with that of adhesive joints made by a standard peel-ply. This comparison is relevant since adhesive bonds created by applying the adhesive directly to freshly created peel-ply surfaces are considered to give sufficiently strong adhesive joints [16]. The fracture energy of an adhesive joint made from a peel-ply thus represents an acceptable minimum value for the interfacial fracture energy.

## 2. Experimental methods

Two types of double cantilever beam (DCB) specimens [22] were tested in this work. Peel-ply and gliding-arc plasma treated test specimens were based on two bonded beams cut from manufactured 8 mm thick GFRP panels. GFRP panels (600 mm × 600 mm × 8 mm) were manufactured by resin infusion. The symmetric and almost unidirectional fibre lay-up was established using ten layers of fabric. The first and last layers in the lay-up were biaxial (±45°) 450 g m$^{-2}$ layers (DB 450-E05, Devold AMT, Norway). The middle eight layers comprised a mat (L1200/G50-E07, Devold AMT, Norway) containing 1152 g m$^{-2}$ unidirectional (0°), 52 g m$^{-2}$ transverse (90°) and 50 g m$^{-2}$ chopped strand glass. The orthophalic polyester matrix was a mixture of Polylite 413-575 resin and 2 wt% Norpol Peroxide 19 (Reichold Danmark A/S, Denmark). The support materials used for the vacuum bagging and resin infusion were a peel-ply layer (Stitch PLY A, AIRTECH Europe, Luxembourg) directly on top of the lay-up; a perforated release foil (Halar, Aerovac Systems, UK); distribution net (Green Flow 75, AIRTECH Europe, Luxembourg); 6 mm diameter inlet and 10 mm diameter outlet tubes; a tape for fixation of lay-up and support materials (Micropore, 3M, Denmark); a vacuum bag (WC8500, AIRTECH Europe, Luxembourg); and a sealant tape (GS 43 MR, AIRTECH Europe, Luxembourg) [22].

Panels were cured at room temperature for 16 h and post-cured at 60 °C for 24 h. After post-curing, beams (290 mm × 30 mm × 8 mm) were cut from the GFRP laminate panel with the main fibre orientation parallel to the long side of the beams. Two countersunk nuts (M5 BN224, Bossard, Denmark), for later screwing of specially formed tabs allowing pure moment loading at the specimens, were mounted at one end of each beam. Nuts were fixed with rapid curing glue (Scotch Weld DP100, 3M, Denmark). Using the nuts enables removal and reuse of the specially formed tabs. Peel-ply was not removed from the laminate during the cutting and mounting of nuts in order to maintain a clean surface before gliding-arc treatment. Just before the gliding-arc treatment, the peel-ply was unwrapped and subsequently the surfaces were gently cleaned and degreased with methanol and acetone in order to ensure a reproducible surface condition.

Specimens for surface characterization were further cut into smaller pieces for easier handling. For the XPS analysis, specimens were ultrasonically cleaned in acetone for 2 × 5 min and in methanol for 5 min before gliding-arc treatment. It is assumed that this solvent pre-treatment does not affect the adhesive property of the GFRP surface significantly. In fact a preliminary experiment indicated that the gliding-arc treated GFRP beams demonstrated similar fracture characteristics in an adhesion test independently of the solvent pre-treatment or lack thereof.

The gliding arc was generated between two diverging stainless steel tubular electrodes as shown in figure 1. The outer diameter of the tubular electrodes is 3 mm. Cooling water was fed through the electrodes during operation. It is noted that without water cooling, the electrodes were heated up and subsequently the discharge became unstable in a few minutes. Similar configurations with blade-shaped electrodes are presented in detail in [5–7, 22]. Air flow was fed between the electrodes to extend the discharge. The gliding arc was driven by an alternating current (ac) power supply at a frequency of 31.25 kHz (Generator 6030, SOFTAL Electronic GmbH, Germany). The average power to the gliding arc was obtained by measuring voltage and current with a high-voltage

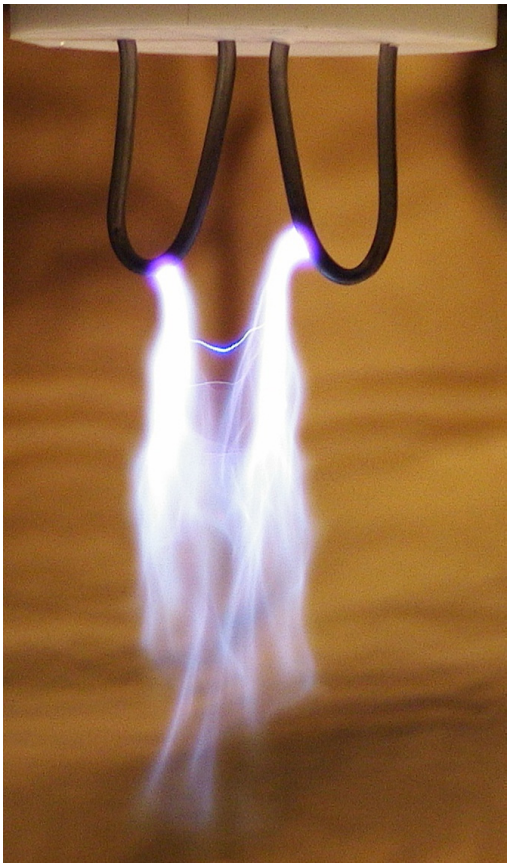

**Figure 1.** A photo of the gliding-arc discharge with water-cooled electrodes.

probe and resistors, respectively. In order to treat a GFRP plate surface without excess thermal damage from the gliding arc, the plate was fixed on a holder which moved forwards and backwards at a speed of 180 mm $s^{-1}$. Since the length of the GFRP plate is 290 mm, the residence time of a specimen is approximately 1.6 s per one exposure. The air humidity was not controlled during the treatment. The distance between the specimen surface exposed to the gliding arc and the edges of the electrodes was fixed at 15, 35, 55, 65 or 75 mm during the treatment.

OES measurements of the gliding arc were performed without the GFRP plate using an optical fibre and a spectrometer (USB2000, Ocean Optics, USA).

The contact angles for de-ionized water on the GFRP surfaces were measured in air at room temperature using a contact angle measurement system (CAM100. Crelab Instruments AB, Sweden). A typical drop size was 1 $\mu$l. The contact angle was measured within 5 s after the drop was attached onto the surface. The standard deviation of the measured contact angle was typically less than approximately 5°.

XPS data were collected using a micro-focused, monochromatic Al K$\alpha$ x-ray source (1486.6 eV) with a lateral resolution of 30 $\mu$m (K-alpha, ThermoFischer Scientific, UK) to study the changes of the elemental composition at the GFRP surfaces. Atomic concentrations of each element were calculated by determining the relevant integral peak intensities subtracting a linear background, and the O/C ratio was obtained.

For crack initiation at the interface between glue and laminate, a 51 $\mu$m thin polytetrafluoroethylene (PTFE) release tape (Teflease MG2, Air-Tech A/S, Denmark) was mounted on the laminate surface at a position of 70 mm from the tab-end of the beam. On top of the release tape was a 2 mm thick PTFE chamfered spacer placed close to the tip of the crack initiation. Another 2 mm thick spacer was mounted at the other end of the beam ensuring a uniform glue thickness. Crack initiation at the centre of the glue line was established using two 1 mm thick chamfered PTFE spacers and in between a thin release film to make the crack tip as thin and sharp as possible. The release film was the 51 $\mu$m PTFE tape (Teflease MG2, AIRTECH Europe, Luxembourg). During application of the bonding paste, special care was taken not to bend the release film accidentally and to obtain the crack initiation position at 70 mm from the beam end. The GFRP beams were bonded using a vinylester adhesive (0555 Oldopal® VE Bonding paste, Monofiber A/S, Denmark) [5]. Excess paste was removed from the edge of the DCB specimen. The bonded specimens were cured at 40 °C for 16 h. Holes for mounting of steel pins were drilled in the laminate at the crack initiation position at 70 mm from the tab-end of the beam. Extensometers mounted on the steel pine measured the crack opening during the test.

The adhesion test was performed by applying uneven pure bending moments to the DCB specimens [23, 24]. The DCB-loaded-by-uneven-bending-moments (DCB-UBM) test configuration provides stable crack growth for materials having a constant or rising fracture resistance. In this study, the fracture resistance was calculated without accounting for the stiffness and thickness of the adhesive layer, i.e. analysing the specimens as being homogeneous laminates. The fracture experiments were conducted using a special test configuration based on wires and rollers. The detailed test configuration of the fracture experiments is described elsewhere [24]. The experiments were conducted at a constant displacement rate of 10 mm $min^{-1}$. The load was measured using two 5 kN static load cells. As mentioned above, the DCB specimens were instrumented with an extensometer to record the end-opening, $\delta^*$, at the tip of the crack initiation.

## 3. Results

The water contact angles of the GFRP plate surfaces measured before and after the gliding-arc treatment at different number of exposures are shown in figure 2. The water contact angle before the gliding-arc treatment was approximately 80°. The water contact angle dropped to approximately 25° when the specimen surface was exposed in the gliding arc four times. When the surfaces were exposed more often, the water contact angles decreased only gradually.

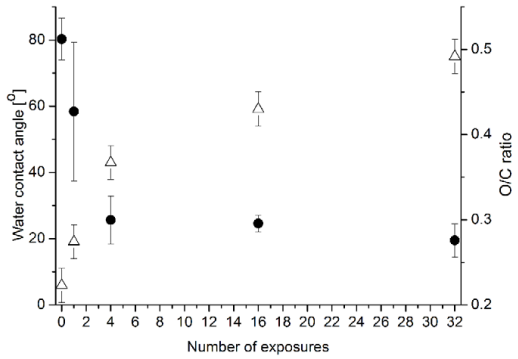


**Figure 2.** Water contact angle (solid circle) and O/C ratio (open triangle) of the GFRP plate surfaces before and after the gliding-arc treatment at different number of exposures at a fixed air flow rate (17.5 SLM), fixed power (800 W) and fixed distance between the specimen surface and the edge of the electrodes (15 mm).

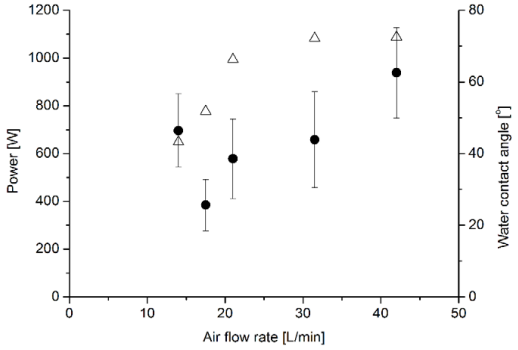


**Figure 3.** Input power to the gliding-arc discharge (open triangle) and water contact angle of the GFRP plates after the gliding-arc treatment (solid circle) at different flow rates. The distance between the specimen surface and the edges of the electrodes was 15 mm, and the specimen surface was exposed to the gliding arc four times.

The XPS analysis indicated that the GFRP surfaces were mostly dominated by oxygen (O) and carbon (C) atoms with less than a few per cent of nitrogen atoms. No noticable change in the nitrogen content was observed after the treatment. The O/C ratios of the GFRP surfaces before and after the gliding-arc treatment are compared in figure 2. The O/C ratio before the gliding-arc treatment was below 0.25, and increased with the number of exposures to the gliding arc, approaching approximately 0.5. It indicates that oxidizing effects are the major chemical reactions by the treatment.

The air flow rate plays an important role in the nature of the gliding arc. The input power and the water contact angle of GFRP plates after the gliding-arc treatment (4 times exposure) at different flow rates are shown in figure 3. As the flow rate increases, the input power increases and approaches approximately 1.1 kW. Although it is reported that higher power input to a plasma generally shows better plasma treatment effect [5, 25], a minimum water contact

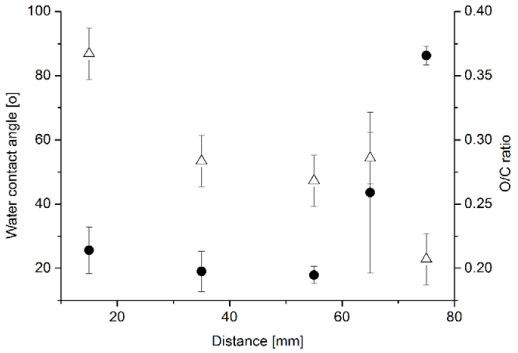


**Figure 4.** Water contact angle (solid circle) and the O/C ratio (open triangle) of the GFRP plates after the gliding-arc treatment at different distances from the edges of the electrodes to the GFRP plate surface at a fixed air flow rate (17.5 SLM), fixed power (800 W) and fixed number of exposures to the gliding arc (4 times).

angle was observed when the air flow rate was 17.5 SLM (standard litre per minute). In the following experiment the air flow rate was fixed at 17.5 SLM in order to demonstrate high treatment efficiency for adhesion improvement. When the water contact angle is lower, it is expected that the interaction between general adhesives and the surface increases and that the subsequent adhesion property increases.

Since the gliding-arc discharge can be extended into the ambient air up to several centimetres, it is interesting to investigate at what distances the gliding-arc treatment is effective. Water contact angles were measured after the gliding-arc treatment at different distances from the edges of the electrodes to the GFRP plate surface. The water contact angle and the O/C ratio at the GFRP plate surface after the gliding-arc treatment are shown in figure 4. The results indicate that the GFRP plate surface can be efficiently oxidized when the distance between the edges of the electrodes and the GFRP surface was up to approximately 60 mm.

Figure 5 shows OES of the gliding-arc discharge operated at the air flow rate of 17.5 SLM and the power of 800 W, including NO, $N_2$ and OH bands. In particular the emission from OH($A$–$X$) was detected up to a distance of 60 mm from the edges of the electrodes.

During the fracture tests of the DCB specimens prepared from peel-ply only (i.e. no gliding-arc treatment), crack propagation occurred smoothly along the laminate/adhesive interface with no visible fibre bridging [22]. Measured fracture resistance data, the fracture resistance (the value of the $J$ integral during crack propagation [24]) as a function of end-opening $\delta^*$, are shown in figure 6($a$). No or very little end-opening occurs before the initiation of crack growth, which took place at a fracture resistance value of around 140–160 J m$^{-2}$. Thereafter, as the crack propagates, the end-opening increases. The crack propagation occurs at a near-constant, but slightly lower fracture resistance value (110–140 J m$^{-2}$) than the fracture resistance value at the crack initiation.

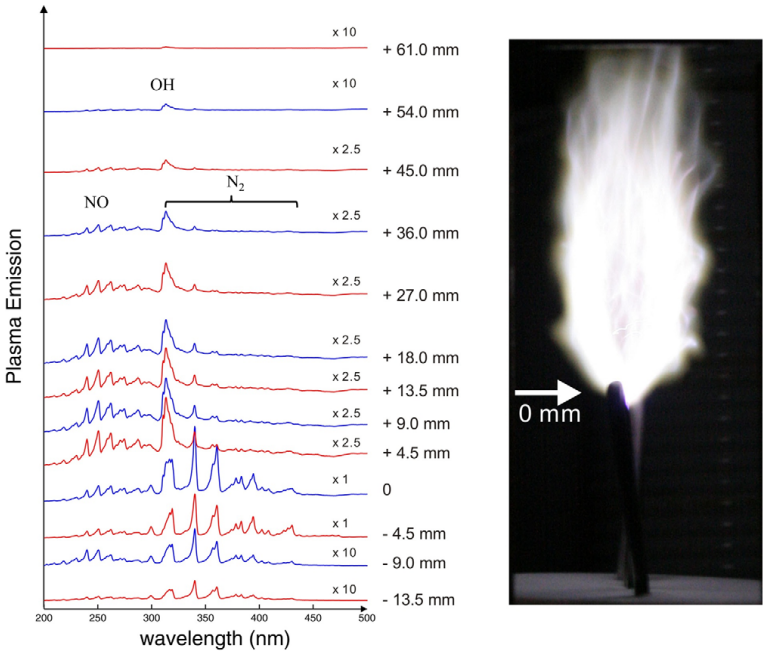


**Figure 5.** OES at different heights and a side-view of the gliding-arc discharge operated at an air flow rate of 17.5 SLM and a power of 800 W. The height of the image is approximately 12 cm.

The fracture resistance is increased with significantly larger variations after the gliding-arc treatment at a fixed air flow rate (17.5 SLM) and fixed power (800 W) as shown in figures 6(*b*)–(*e*). When the distance from the edges of the electrodes to the GFRP plate surface was 15 mm and the surface was exposed to the gliding arc once, the initial fracture took place at the fracture resistance value of around 150–250 J m$^{-2}$ in five cases, while the fracture resistance value almost steadily increased in one case as shown in figure 6(*b*). When the number of exposures was increased, the initial fracture resistance values were further increased to around 260–330 J m$^{-2}$ and around 220–490 J m$^{-2}$ at 4 and 32 exposures, respectively (figures 6(*c*) and (*d*)).

Figure 6(*e*) shows that the gliding-arc treatment is still effective even when the distance from the edges of the electrodes to the GFRP plate surface is 55 mm. After four exposures, the initial fracture resistance value was around 170–230 J m$^{-2}$ which is comparable to that of the GFRP plates treated with one exposure at a distance of 15 mm (figure 6(*b*)).

## 4. Discussion

It is shown in this work (figures 2–4 and 6) that the gliding-arc treatment can improve wettability and increase the oxygen content at the GFRP surface, and subsequently fracture energy with vinylester adhesive. When the flow rate increases, the discharge is cooled down more and becomes less reactive [5]. On the other hand, at the lowest flow rate of 14 SLM the fluctuation of the discharge was pronounced, and the GFRP surfaces were not appropriately exposed to the discharge. As a result the optimum flow rate of 17.5 SLM was observed in figure 3.

The uniformity of the treatment is the important issue for the industrial application. The measured contact angles scattered significantly when the surface was exposed twice (figure 2) and when the distance to the GFRP surface was 65 mm (figure 4), indicating poor uniformity of the treatment. It is therefore suggested that in order to ensure a certain uniformity of the treatment the surface should be exposed more than twice and the distance should be less than 65 mm.

Since the major bond mechanism with vinylester adhesive is a non-specific interaction [25], the effect of the gliding-arc treatment can be primarily attributed to the introduction of a certain amount of polar functional groups at the surfaces and better wetting with the uncured liquid vinylester adhesive prior to hardening. These polar functional groups can preferably interact with the vinylester adhesive which contains similar polar functional groups.

At a distance of 55 mm between the edges of the electrodes and the GFRP surface, the GFRP surface can be efficiently oxidized as shown in figure 4, OH emission is detected (figure 5), and the fracture energy is increased (figure 6(*e*)). It is noted that the intensity of the optical emission drops at a distance <40 mm, indicating low concentrations of excited OH radicals above this distance. However, the OES was performed on a freely developing gliding arc, whereas in the surface

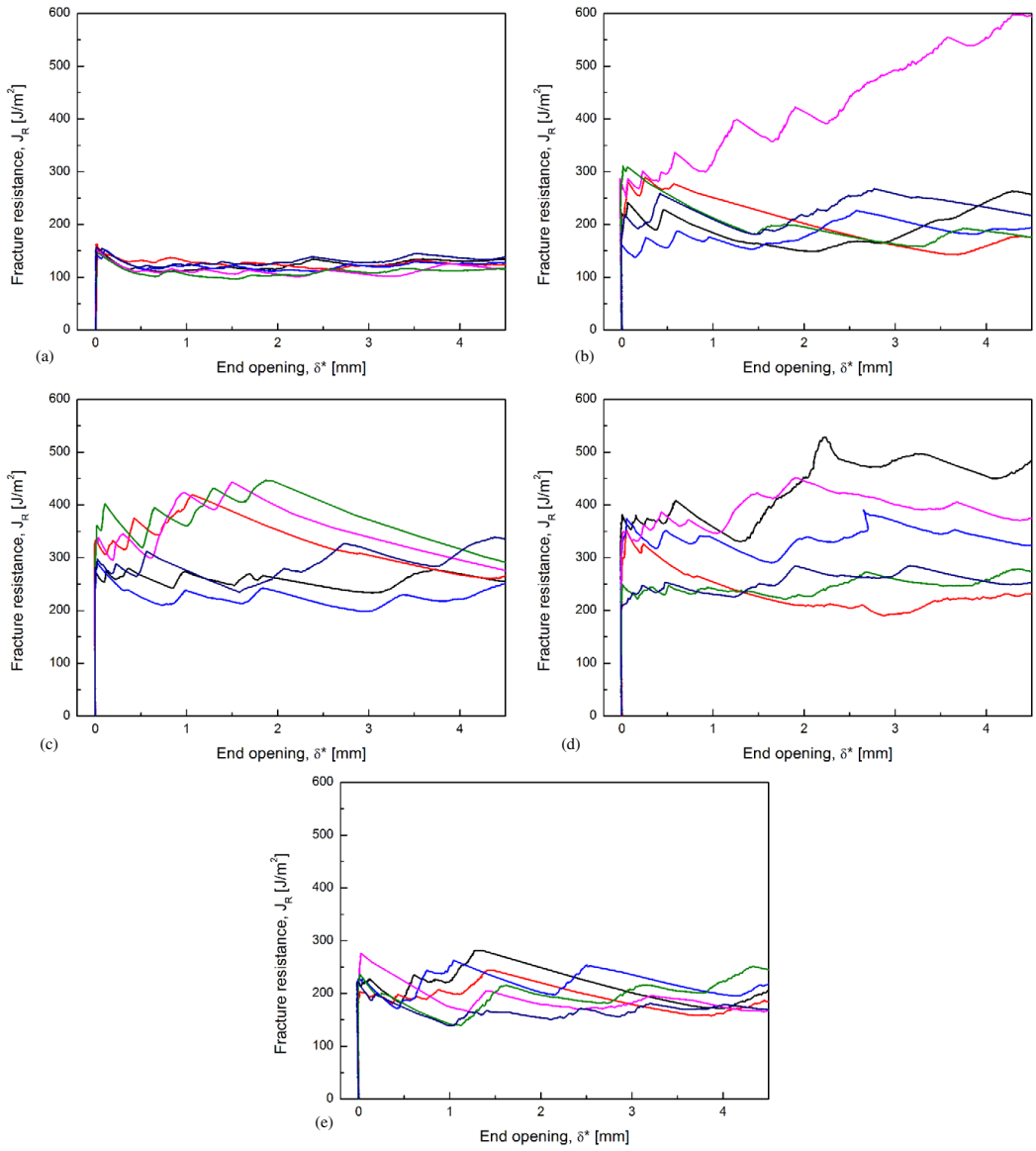


**Figure 6.** Measured fracture resistance curves (the fracture resistance as a function of the end-opening $\delta^*$) for standard peel-ply (*a*) and gliding-arc treatment (*b*)–(*e*) at a fixed air flow rate (17.5 SLM) and fixed power (800 W) but at varying distance from the edges of the electrodes to the GFRP plate surface and number of exposures. (*b*) 1 exposure at 15 mm distance; (*c*) 4 exposures at 15 mm distance; (*d*) 32 exposures at 15 mm distance; (*e*) 4 exposures at 55 mm distance.

treatment the discharge and the gas flow field are altered due to the presence of the GFRP surface. In particular, when the gas approaches the surface, it is slowed down, and this will increase the radical concentration. Furthermore, the ground state OH, that can also contribute to the surface treatment but cannot be detected by OES, would have much longer lifetime than the excited state OH. Hence the good performance of surface treatment and improvement of the fracture energy at distances as long as 55 mm are understandable.

Table 1 summarizes the O/C ratio of the GFRP plate surfaces and the typical fracture resistance values in figure 6. The O/C ratio of the untreated specimen is approximately

**Table 1.** Comparison of O/C ratio and fracture resistance values under various treatment conditions.

| Distance between the electrodes and the surface (mm) | Number of exposures | O/C ratio | Fracture resistance ($J\,m^{-2}$) |
|---|---|---|---|
| — | — | 0.22 | 110–140 |
| 15 | 1 | 0.27 | 150–250 |
| 15 | 4 | 0.37 | 260–330 |
| 15 | 32 | 0.49 | 220–490 |
| 55 | 4 | 0.27 | 170–230 |

0.22, while it increased after the gliding-arc treatment. If it is assumed that each carbon atom at the GFRP surface can bond at most one oxygen atom, the O/C ratio can represent a fraction of carbon atoms directly bonding oxygen atoms, because the number of oxygen atoms can be approximately equal to that of carbon atoms directly bonding oxygen atoms. They can induce ionic or hydrogen-bond interactions with the adhesive. Since the O/C ratio increases from 0.22 to 0.49 (table 1) and thus by a factor of up to 2–2.5, it is roughly estimated that the gliding-arc treatment may increase the adhesive strength at the interface by a factor of 2–2.5. This rough estimation shows good agreement with the measured values of the fracture energy in table 1.

## 5. Conclusions

The stable gliding-arc discharge was demonstrated by effective water cooling of the electrodes. Gliding-arc treatment of GFRP surfaces increased wettability and the oxygen content at the GFRP surfaces, and subsequently improved the fracture resistance at the adhesive joints. Since the gliding arc can efficiently oxidize the GFRP plate surfaces when the distance from the edge of the electrodes is up to approximately 6 cm in open air, it can be advantageously applied to plasma surface modification of bulky objects for adhesion improvement of materials in industrial processing.

## Acknowledgments

This work was financially supported by the Ministry of Science, Technology and Innovation through the National Danish Proof of Concept Funding Scheme (grant number: 09-076196) and by the Swedish Energy Agency through the CECOST and EFFECT project. MA and ZL would like to thank the Swedish Research Council for VR projects and the European Research Council for the Advanced Grant DALDECS.

## References

[1] Kogoma M 2011 *Generation and Applications of Atmospheric Pressure Plasmas* ed M Kogoma *et al* (New York: NOVA Publishers)
[2] Fridman A, Nester S, Kennedy L A, Saveliev A and Mutaf-Yardimci O 1998 *Prog. Energy Combust. Sci.* **25** 211–31
[3] Czernichowski A 1994 *Pure Appl. Chem.* **66** 1301–10
[4] Kusano Y 2009 *Surf. Eng.* **25** 415–6
[5] Kusano Y, Teodoru S, Leipold F, Andersen T L, Sørensen B F, Rozlosnik N and Michelsen P K 2008 *Surf. Coat. Technol.* **202** 5579–82
[6] Kusano Y, Norrman K, Drews J, Leipold F, Singh S V, Morgen P, Bardenshtein and Krebs N 2011 *Surf. Coat. Technol.* **205** S490–4
[7] Sun Z W, Zhu J J, Li Z S, Aldén M, Leipold F, Salewski M and Kusano Y 2013 submitted
[8] Richard F, Cormier J M, Pellerin S and Chapelle J 1997 *High Temp. Mater. Process.* **1** 239–48
[9] Davis P, Cantwell W J, Jar P Y, Bourban P E, Zysman V and Kausch H H 1991 *Composites* **22** 425–31
[10] Wade G A, Cantwell W J and Pond R C 2000 *Interface Sci.* **8** 363–73
[11] Dagher H J, Iqbal A and Bogner B 2004 *Polym. Polym. Compos.* **12** 169–82
[12] Kaiser H and Karbhari V M 2004 *Int. J. Mater. Product Technol.* **21** 349–84
[13] Bakis C E, Bank L C, Brown V L, Cosenza E, Davalos J F, Lesko J J, Machida A, Rizkalla S H and Triantafillou T C 2002 *J. Compos. Constr.* **6** 73–87
[14] Adams R D, Atkins R W, Harris A and Kinloch A J 1986 *J. Adhes.* **20** 29–53
[15] Pocius A V and Wenz R P 1985 *SAMPE J.* **21** 50–8
[16] Bénard Q, Fois M and Grisel M 2005 *Composites* A **36** 1562–8
[17] Kusano Y, Mortensen H, Stenum B, Kingshott P, Andersen T L, Brøndsted P, Bilde-Sørensen J B, Sørensen B F and Bindslev H 2007 *Plasma Process. Polym.* **4** S455–9
[18] Kusano Y, Singh S V, Bardenshtein A, Krebs N and Rozlosnik N 2010 *J. Adhes. Sci. Technol.* **24** 1831–9
[19] Kusano Y, Singh S V, Norrman K, Leipold F, Drews J, Morgen P, Bardenshtein A and Krebs N 2011 *J. Adhes.* **87** 720–31
[20] Kusano Y, Singh S V, Norrman K, Drews J, Leipold F, Rozlosnik N, Bardenshtein A and Krebs N 2012 *Surf. Eng.* **28** 453–7
[21] Kusano Y, Norrman K, Singh S V, Leipold F, Morgen P, Bardenshtein A and Krebs N 2012 *J. Adhes. Sci. Technol.* DOI:10.1080/01694243.2012.727156
[22] Kusano Y, Sørensen B F, Andersen T L and Leipold F *J. Adhes.* in press DOI:10.1080/00218464.2013.759063
[23] Plausinis D and Spelt J K 1995 *Int. J. Adhes. Adhes.* **15** 225–32
[24] Sørensen B F, Jørgensen K, Jacobsen T K and Østergaard R C 2006 *Int. J. Fract.* **141** 163–76
[25] Teodoru S, Kusano Y, Rozlosnik N and Michelsen P K 2009 *Plasma Process. Polym.* **6** S375–81

# [Appendix A6]

Y. Kusano, L. Berglund, Y. Aitomäki, K. Oksman, B. Madsen

## “Gliding arc surface modification of carrot nanofibre coating – perspective for composite processing”

*Materials Science and Engineering*
139(1) (2016) 012027.

IOP Conf. Series: Materials Science and Engineering **139** (2016) 012027 doi:10.1088/1757-899X/139/1/012027

# Gliding arc surface modification of carrot nanofibre coating – perspective for composite processing

**Y Kusano[1], L Berglund[2], Y Aitomäki[2], K Oksman[2] and B Madsen[1]**

[1]Department of Wind Energy, Section of Composites and Materials Mechanics, Technical University of Denmark, Risø Campus, DK-4000 Roskilde, Denmark
[2]Division of Materials Science, Composite Centre Sweden, Luleå University of Technology, SE-971 87 Luleå, Sweden

E-mail: yuki@dtu.dk

**Abstract**. Surfaces of carrot nanofibre coatings were modified by a gliding arc in atmospheric pressure air. The treatment strengthened wetting of deionized water and glycerol, increased an oxygen content, C-O and C=O, and moderately roughened the surfaces. In the perspective of composite materials, these changes to the nanofibres can potentially improve their processability when they are to be impregnated with a polymeric matrix. However, longer exposure to the gliding arc reduced oxidation and roughness of the surface, and thus there exists an optimum condition to achieve good wetting to solvents.

## 1. Introduction

Non-thermal plasma processing at atmospheric pressure is widely used for surface modification [1, 2]. Its applications include surface cleaning [3], decontamination and sterilization [4,5], deposition of functional coatings [6], and improvement of adhesion, wetting and paintability [7-15].

One of the challenges in non-thermal plasma processing at atmospheric pressure is to achieve high reactivity and high productivity simultaneously [16]. Here, high reactivity is ensured by a high electron temperature in a non-equilibrium plasma so as to change chemical bonding of molecules in the plasma or the plasma-treated surfaces. Meanwhile, high productivity can be demonstrated using high energy densities. However, most plasmas can hardly sustain a non-equilibrium state at high energy densities. One possible approach to overcome this issue is to develop a hybrid plasma with a high energy density in a non-equilibrium state.

A gliding arc is one of the hybrid plasmas [17], generated between diverging electrodes as a low-impedance thermal arc discharge, extended by a gas flow and quenched to a non-thermal condition [18]. It can be operated in atmospheric pressure air and thus advantageously used for large-scale processing [19-26]. An alternating current (AC) gliding arc has a long lifetime extending over hundreds of AC periods without extinction. The plasma column can be elongated to approximately 20 – 30 cm [21-29]. The AC gliding arc is useful for adhesion improvement of glass fibre reinforced polyesters (GFRPs) [22,23], efficiently oxidizing GFRP surfaces when the distance between the edge of the electrodes and the GFRP surface is up to 6 cm in open air. It is also demonstrated that optical techniques are promising for non-instructive diagnostics of the AC gliding arc [24-29]. In particular, the dynamics of the gliding arc is observed by using a high-speed camera. In addition, excited and ground-state hydroxyl radicals are observed in the plasma column and its vicinity, respectively. It is

noted that the hydroxyl radical has a high oxidation potential, next to fluorine and higher than ozone and chlorine. Therefore, the hydroxyl radicals generated by the gliding arc can play an important role in surface modification.

Cellulose is renewable, nontoxic, and biodegradable, and is known to be the most abundant biopolymer on earth [30]. It has been extensively studied in terms of biological, chemical, and mechanical properties. In particular, nano-celluloses (NCs) have attracted significant interests due to their high strength, high modulus, high surface area and unique optical properties. Typical lateral dimensions are approximately 5 – 20 nm, while longitudinal dimensions are from tens of nm to several μm [31]. Acid hydrolysis of cellulose will remove the amorphous part of cellulose and lead to highly crystalline and rigid nanoparticles called cellulose nanocrystals or cellulose nanowhiskers [32]. On the other hand, cellulose nanofibres (CNF) can be produced by ultrafine grinding, microfluidization or high pressure homogenization through delamination of fibre cell walls and subsequent liberation of nano-sized fibrils [33].

Promising application for demonstrating mechanical properties of NCs is to mix NCs to impregnate a nanofibre network with a polymer and create strong, light-weight and transparent composite [34]. Its application includes packaging [35,36], vehicles and aeronautical applications. For demonstrating the best performance of NC composites, it is important to achieve substantial dispersion of NCs and strong interfacial interaction between the NC and the polymer matrix. In this respect, surface modification of NCs has attracted significant interests [37,38].

However, surface modification of NCs is not an easy task even using a plasma. For example, when NC is dispersed in a liquid, a plasma as a gas phase does not have a direct contact with NC surfaces. On the other hand, when NCs are dried without a liquid, they are easily aggregated, disturbing uniform surface treatment. There are some studies presented in literature to solve or tackle with these handling problems [1].

In the present work, as a feasibility study, effects of plasma treatment on NC are investigated in a simplified form of NC so as to avoid the above handling problems. That is, nanofibre coatings are treated by a plasma not because of the application for coatings, but because of a simplified specimen feature. More specifically, nanofibres were separated from a carrot residue, dispersed in water, painted on a glass plate, and dried. The subsequent coating surfaces were treated using a gliding arc in atmospheric pressure air. The treated surfaces were characterized by means of contact angle measurements, x-ray photoelectron spectroscopy (XPS), and field emission scanning electron microscopy (FE-SEM) in order to investigate the treatment effect.

## 2. Experimental methods

### *2.1 Materials*

Carrot nanofibres were isolated from carrot residue supplied by Brämhults Juice AB, Sweden. This raw material is a by-product from carrot juice production. A chemical purification was carried out prior to the fibrillation following the procedure described by Siqueira et al. (2016) [31]. The residue was first washed with distilled water at 85°C, alkali-treated (2% NaOH) at 80°C for 2h, and subsequently bleached with $NaClO_2$ (1.7 %) in an acetic buffer (pH 4.5) at 80°C for 2h for lignin removal. Finally the material was washed until a neutral pH was reached.

This bleached residue was fibrillated by ultrafine grinding using a supermass colloider (MKZA10-20J, Masuko Sangyo, Japan), at consistency of 2%. Prior to the grinding, the suspension was dispersed using a shear mixer (Silverson L4RT Silverson Machine Ltd., England). The grinding was operated at a rotor speed of 1,500 rpm and the grinding stones were gradually adjusted to 100 μm (negative). The total processing time was 40 min. The obtained aqueous carrot nanofibre suspension (2wt% concentration) was used to prepare coatings on glass plates (CORNING® 2947-75x25), and dried at room temperature in atmospheric pressure air for a couple of days. The coating thickness was estimated to be approximately 6 μm.

*2.2 Plasma treatment*

The gliding arc was generated between two diverging stainless steel tubular electrodes as shown in Figure 1. The outer diameter of the tubular electrodes is 3 mm. Cooling water was fed through the electrodes during operation [22-29]. An air flow was fed between the electrodes with a flow rate of 17.5 standard litres per minutes (SLM). The gliding arc was driven by an AC power supply at a frequency of 31.25 kHz (Generator 6030, SOFTAL Electronic GmbH). The electric power applied to the gliding arc was approximately 700 W. In order to treat the nanofibre coating surface without excess thermal damage from the gliding arc, a poly(methyl-methacrylate) holder was moved forward and backward at a speed of 180 mm/s on which the coated glass plate was fixed. The angle between the gas flow direction and the specimen surface is approximately 90º when the surface is treated. The closest distance between the coating surface and the edges of the electrodes was 15 mm.

**Figure 1.** A photo of the gliding arc with water cooled electrodes.

*2.3 Surface characterization*

Surface characterization is vitally important to understand the surface modification effects and to optimize the process conditions.

Contact angles were measured with deionized water and glycerol in air at room temperature both before and after the gliding arc treatment using a contact angle measurement system (CAM100, Crelab Instruments AB, Sweden). A typical drop size was 1$\mu$L. The contact angle was measured within 5 s after the drop was attached onto the surface. Typically 10 measurements were made for each specimen, and their arithmetic mean was calculated.

XPS data were collected using a micro-focused, monochromatic Al K$\alpha$ X-ray source (1486.6 eV) with a lateral resolution of 30 μm (K-alpha, ThermoFischer Scientific, UK). Atomic concentrations of

all elements were calculated by determining the relevant integral peak intensities using the Shirley background. The K-alpha was also used for a high resolution analysis on the carbon 1s (C1s) spectra acquired over 30 scans. The binding energies were referred to the hydrocarbon component (C-H, C-C) at 285 eV. The spectra were de-convoluted through curve fitting, taking purely Gaussian components with linear background subtraction. The full-width at half-maximum (FWHM) for all peaks of C1s was constrained to 1.5 eV.

The surface morphology of the nanofibre coating was observed by using an FE-SEM (Zeiss SUPRA 35, Germany). The NFC surfaces were sputter-coated with approximately 15-nm thick Au before the observation.

## 3. Results and discussion

The contact angles of the nanofibre coating were measured before and after the gliding arc treatment. Typical images of the deionized water- and glycerol-drops on the nanofibre coatings are shown in Figure 2.

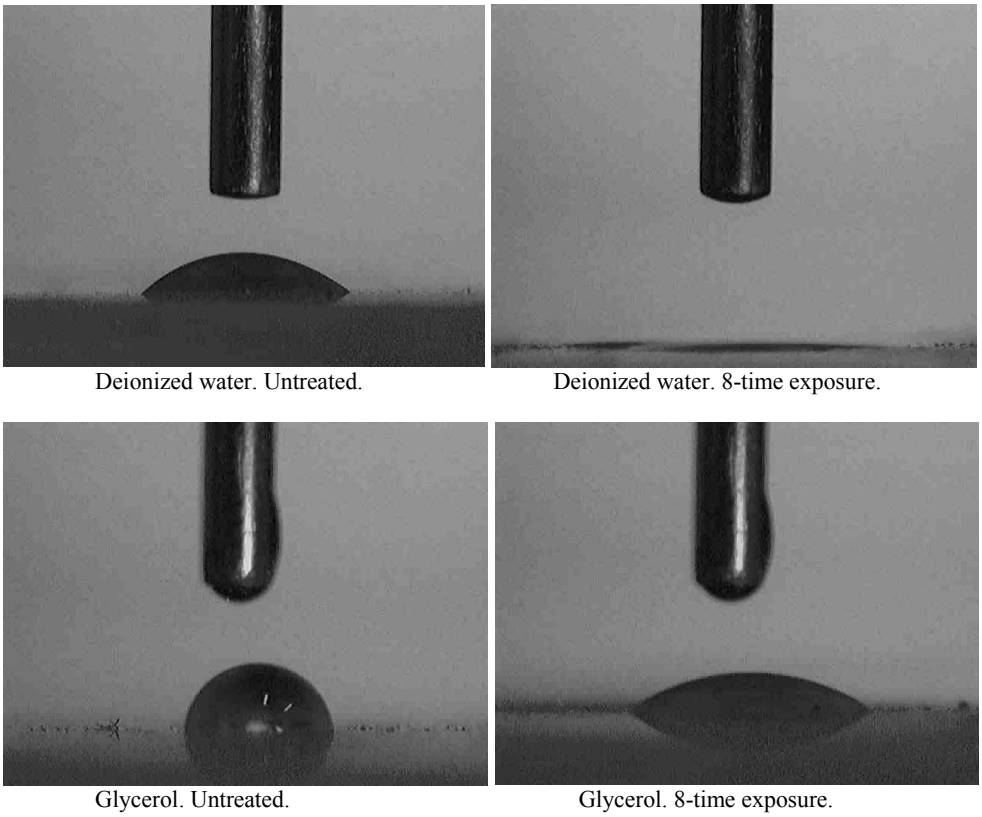


**Figure 2.** Typical photo images of deionized water-drops and glycerol-drops on the nanofibre coatings.

Figure 3 shows measured contact angles of deionized water and glycerol at different numbers of

exposure. The contact angles of deionized water and glycerol before the gliding arc treatment, corresponding to 0-time exposure, were typically between 20º - 35º and 70º - 80º, respectively. The deionized water contact angles tend to decrease as the number of exposure increases, approaching 0º. The glycerol contact angles also tend to decrease as the number of exposure increases, approaching approximately 30º. Enhancement of glycerol wetting is preferable when nanofibres are mixed in a composite, since nanofibres are usually dispersed in an organic solvent for mixing it into a polymeric matrix, potentially improving processability and mechanical properties of the composite. However, it is noted that after 16-time exposure, contact angles of deionized water and glycerol slightly increased.

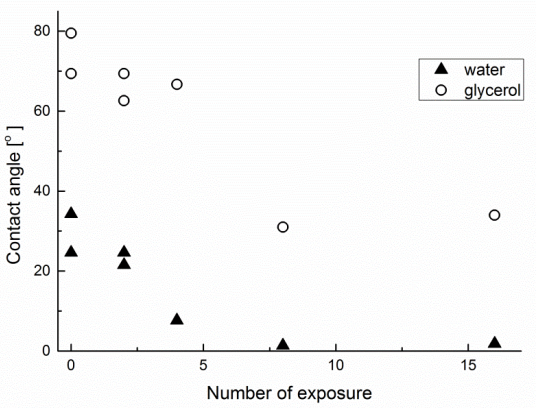


**Figure 3.** Contact angles of the nanofibre coatings at different times of exposure to the gliding arc. The numbers of exposure are 0 (corresponding to an untreated surface), 2, 4, 8 and 16. Solid triangle: deionized water. Open circle: glycerol.

XPS measurement was carried out to analyze the elemental composition of the nanofibre coatings before and after the gliding arc treatment. The nanofibre surfaces typically contain C, O, Ca, and low concentration impurities. The atomic ratios of O/C and Ca/C calculated using the XPS survey spectra are shown in Figure 4 (a). After 2-time exposure, the O/C ratio increased from 0.59 to approximately 0.72. The O/C ratio may not significantly increase by further exposure, and eventually decreased to approximately 0.64 after 16-time exposure. The Ca/C ratio also increased, after the gliding arc treatment, from 0.02 to 0.03-0.04. The increase in the calcium content can be interpreted as preferential etching of organic components in the coatings. It is indicated that the Ca/C ratio does not monotonically increase as the increase in the exposure to the gliding arc, and that the preferential etching of organic component is not a leading effect of the gliding arc treatment.

Deconvolution of the C1s spectra of the nanofibre coatings before and after the gliding arc treatment was carried out. The result is shown in Figure 4 (b). Peaks at approximately 285 eV, 286.8 eV, and 288.4 eV can be assigned to C-H/C-C, C-O, and C=O (carbonyl). A peak corresponding to carboxy group at approximately 289.5 eV was not detected. Since general plasma treatment can readily create carboxy group on polymer surfaces by oxidation [11], it is suggested that the gliding arc may result in moderate oxidation on polymer surfaces. After 2-time exposure, the peak corresponding to C-H/C-C decreased, while then peaks corresponding to C-O and C=O increased. Similar to the O/C ratio, they may not significantly change by further exposure, and after 16-time exposure, the peak of C-H/C-C increased and the peaks of C-O and C=O decreased.

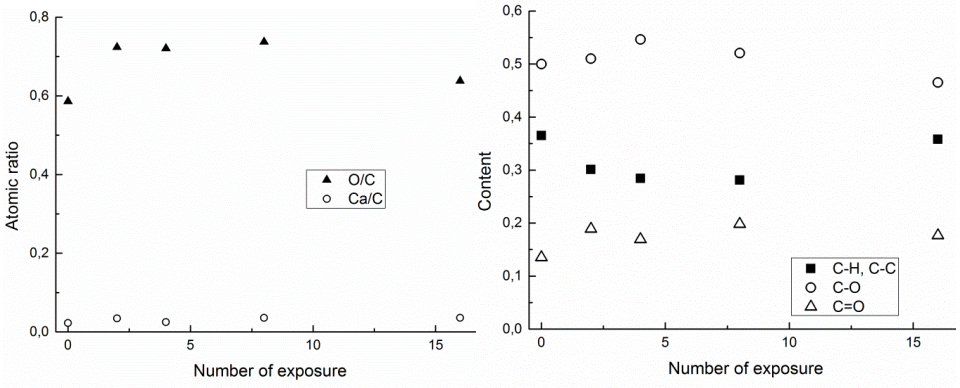


**Figure 4.** (a) O/C and Ca/C ratios of the nanofibre coating surfaces at different times of exposure to the gliding arc. (b) Contents of peaks obtained by curve-fitting of C1s spectra of the nanofibre coating surfaces at different times of exposure to the gliding arc.

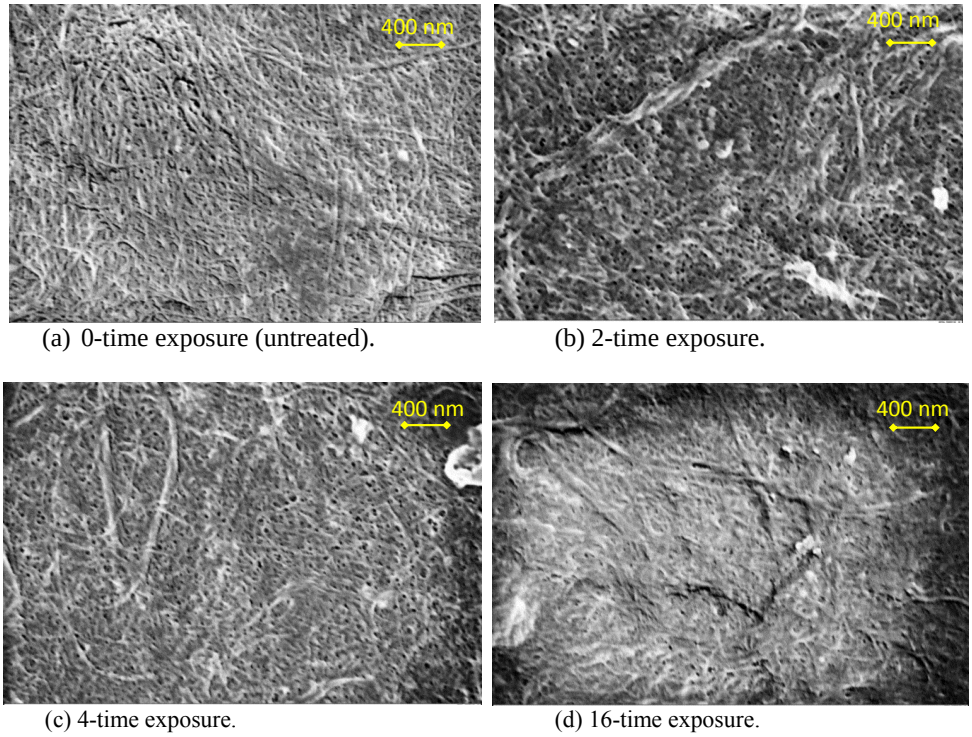


(a) 0-time exposure (untreated). (b) 2-time exposure.

(c) 4-time exposure. (d) 16-time exposure.

**Figure 5**. FE-SEM images of the nanofibre coating surfaces.

The morphological changes after the gliding arc treatment is possible only when nano-scale observation is performed, since plasma surface treatment generally changes the top layer up to 10 nm or less [11]. Figure 5 shows FE-SEM images before and after the gliding arc treatment. Figure 5 (a) indicates that the untreated nanofibre coating shows assemblies of nano-cellulose fibrils surrounded by an unstructured phase. 2-time exposure in Figure 5 (b) seems to roughen the surface, most likely due to the preferential etching of the surrounding phase, supported by the XPS result of the increase in the Ca/C ratio. However, further exposure may not significantly roughen the nanofibre coating surfaces in a nano-scale as shown in Figure 5 (c) and (d). Instead, these images indicate that the surface become smoother in nanoscale, while a larger scale deformation might occur (Figure (d)). A possible explanation of this morphological change by the gliding arc treatment is that the nanofibre coating surface could be etched and roughened moderately, and that longer exposure could result in microscale melting at the surface. A similar phenomenon was observed for the gliding arc treatment of glass-fibre reinforced polyester plates [19].

In next steps, treatment optimisation and treatment of larger amounts of nanofibres will be investigated so as to be feasible for production of carrot nanofibre composites with desired properties.

## 4. Conclusion

Gliding arc treatment can oxidize and roughen the carrot nanofibre surface and strengthen the wetting of deionized water and glycerol, and thus can be potentially useful for surface modification of the carrot nanofibres when they are mixed in a composite since the treatment can potentially improve processability and mechanical properties of the composite.

## Acknowledgement

This work was financially supported by the European Commission through the Framework VII programme, INCOM project, contract number 608746.

## References

[1] 2011 *Generation and applications of atmospheric pressure plasmas* ed M Kogoma, M Kusano and Y Kusano (New York: NOVA Science Publishers, Inc.) chapters 3-6 pp 45-100
[2] Kogelschatz U 2003 *Plasma Chem. Plasma Proc.* **23(1)** 1-46
[3] Yi CH, Lee YH and Yeom GY 2003 *Surf. Coat. Technol.* **171** 237-240
[4] Leipold F, Kusano Y, Hansen F and Jacobsen T 2010 *Food Control* **21(8)** 1194-1198
[5] Leipold F, Schultz-Jensen N, Kusano Y, Bindslev H and Jacobsen T 2011 *Food Control* **22(8)** 1296-1301
[6] Nwankire CE, Favaro G, Duong Q-H and Dowling DP 2011 *Plasma Proc. Polym.* **8** 305-315.
[7] 1994 *Plasma surface modification of polymers: relevance to adhesion* ed M Strobel, CS Lyons and KL Mittal (Utrecht, VSP)
[8] Kusano Y, Andersen TL and Michelsen PK 2008 *J. Phys. Conf. Series.* **100** 012002
[9] Kusano Y, Teodoru S and Hansen CM 2011 *Surf. Coat. Technol.* **205** 2793-2798
[10] Singh SV, Kusano Y, Morgen P and Michelsen PK 2012 *J. Appl. Phys.* **111** 083501
[11] Kusano Y 2014 *J. Adhesion* **90(9)** 755-777
[12] Teodoru S, Kusano Y, Rozlosnik N and Michelsen PK 2009 *Plasm. Proc. Polym.* **6** S375-S381
[13] Kusano Y, Mortensen H, Stenum B, Kingshott P, Andersen TL, Brøndsted P, Bilde-Sørensen JB, Sørensen BF and Bindslev H 2007 *Plasm. Proc. Polym.* **4(S1)** S455-S459
[14] Kusano Y, Mortensen H, Stenum B, Goutianos S, Mitra B, Ghanbari-Siahkali A, Kingshott P, Sørensen BF and Bindslev H 2007 *Int. J. Adhesion and Adhesives* **27(5)** 402-408
[15] Lee BJ, Kusano Y, Kato N, Naito K, Horiuchi T and Koinuma H 1997 *Jpn. J. Appl. Phys.* **Pt. 1, 36** 2888-2891
[16] Kusano Y 2009 *Surf. Eng.* **25(6)** 415-416
[17] Fridman A, Nester S, Kennedy LA, Saveliev A and Mutaf-Yardimci O 1999 *Prog. Energy*

*Combustion Sci*. **25** 211-231
[18] Czernichowski A 1994 *Pure Appl. Chem*. **66(6)** 1301-1310
[19] Kusano Y, Teodoru S, Leipold F, Andersen TL, Sørensen BF, Rozlosnik N and Michelsen PK 2008 *Surf. Coat. Technol*. **202** 5579-5582
[20] Kusano Y, Norrman K, Drews J, Morgen P, Leipold F, Singh SV, Bardenshtein A and Krebs N 2011 *Surf. Coat. Technol*. **205** S490-S494
[21] Kusano Y, Andersen TL, Toftegaard HL, Leipold F, Bardenshtein A and Krebs N 2014 *Int. J. Mater. Eng. Innovation* **5(2)** 122-137
[22] Kusano Y, Sørensen BF, Andersen TL and Leipold F 2013 *J. Adhesion* **89(6)** 433-459
[23] Kusano Y, Sørensen BF, Andersen TL, Toftegaard HL, Leipold F, Salewski M, Sun ZW, Zhu JJ, Li ZS and Aldén M 2013 *J. Phys. D Appl. Phys*. **46(13)** 135203
[24] Sun ZW, Zhu JJ, Li ZS, Aldén M, Leipold F, Salewski M and Kusano Y 2013 *Optics Express* **21(5)** 6028-6044
[25] Zhu JJ, Sun ZW, Li ZS, Ehn A, Aldén M, Salewski M, Leipold F and Kusano Y 2014 *J. Phys. D Appl. Phys*. **47**, 295203
[26] Kusano Y, Salewski M, Leipold F, Zhu JJ, Ehn A, Li ZS and Aldén M 2014 *Eur. Phys. J. D* **68** 319
[27] Kusano Y, Zhu JJ, Ehn A, Li ZS, Aldén M, Salewski M, and Leipold F 2015 *Surf. Eng*. **31(4)** 282-288
[28] Zhu JJ, Gao JL, Ehn A, Aldén M, Li ZS, Moseev D, Kusano Y, Salewski M, Alpers A, Gritzmann P and Schwenk M 2015 *Appl. Phys. Let.* **106** 044101
[29] Zhu JJ, Gao JL, Li ZS, Ehn A, Aldén M, Larsson A and Kusano Y 2014 *Appl. Phys. Let*. **105** 234102
[30] Peng BL, Dhar N, Liu HL and Tam KC 2011 *Canadian J. Chem. Eng*. **89(5)** 1191-1206
[31] Siqueira G, Tadokoro S K, Mathew AP and Oksman K 2016 *Comp. Sci. Technol*. **123** 49-56
[32] Bondeson D, Mathew AP and Oksman K 2006 *Cellulose* **13** 171-180
[33] Jonoobi M, Oladi R, Davoudpour Y, Oksman K, Dufresne A and Hamzeh Y 2015 *Cellulose* **22(2)** 935-969
[34] Nakagaito AN and Yano H 2005 *Appl. Phys. A* **80(1)** 155–159
[35] Herrera M, Mathew AP and Oksman K 2014 *Carbohydrate Polym*. **112** 494-501
[36] Herrera M, Sirviö J, Mathew A and Oksman K 2016 *Mater. Design* **93** 19-25
[37] Olsson RT, Azizi Samir MAS, Salazar-Alvarez G, Belova L, Ström V, Berglund LA, Ikkala O, Nogués J and Gedde UW 2010 *Nature Nanotechnol*. **5** 584-588
[38] Siró I, Kusano Y, Norrman K, Goutianos S and Plackett D 2013 *J. Adhesion Sci. Technol*. **27(3)** 294-308

# [Appendix A7]

Y. Kusano, A. Bardenshtein, P. Morgen

## “Fluoropolymer coated alanine films treated by atmospheric pressure plasmas – in comparison with gamma irradiation”

*Plasma Processes and Polymers* 15(3) (2018) 1700131.

The attached online version (DOI: 10.1002/ppap.201700131) is identical to the published one.

Received: 3 July 2017 | Revised: 4 September 2017 | Accepted: 25 September 2017
DOI: 10.1002/ppap.201700131

FULL PAPER

PLASMA PROCESSES AND POLYMERS

# Fluoropolymer coated alanine films treated by atmospheric pressure plasmas – In comparison with gamma irradiation

**Yukihiro Kusano**[1] | **Alexander Bardenshtein**[2] | **Per Morgen**[3]

[1] Department of Wind Energy, Section of Composites and Materials Mechanics, Technical University of Denmark, Risø Campus, 4000 Roskilde, Denmark

[2] Danish Technological Institute, Materials Division, Centre for Plastic and Packaging Technology, Gregersensvej 5, 2630 Taastrup, Denmark

[3] Department of Chemical Engineering, Biotechnology and Environmental Technology, Campusvej 55, University of Southern Denmark, 5230 Odense, Denmark

**Correspondence**
Yukihiro Kusano, Department of Wind Energy, Section of Composites and Materials Mechanics, Technical University of Denmark, Risø Campus, 4000 Roskilde, Denmark.
Email: yuki@dtu.dk

Fluoropolymer coated alanine films are treated by a dielectric barrier discharge and a gliding arc at atmospheric pressure as well as with gamma irradiation. The film surfaces and the underlying bulk materials are characterized before and after each treatment. The fluorine content decreases and the oxygen content increases at the fluoropolymer surfaces, while deposition of specific plasma energies in the alanine films is detected by electron paramagnetic resonance spectroscopy, indicating that not only the fluoropolymer surfaces but also the bulk alanine materials are modified. Differences of surface and bulk modification effects between the two plasma treatments are discussed in detail.

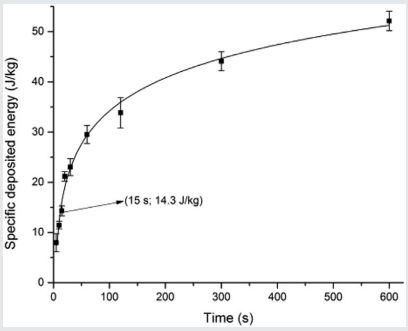


**KEYWORDS**
alanine, atmospheric pressure plasma, fluoropolymer, gamma irradiation, ion bombardment

## 1 | INTRODUCTION

Electron paramagnetic resonance (EPR, also called electron spin resonance [ESR]) spectroscopy is a method to study the presence and properties of unpaired electrons in atoms or molecules. In other words, EPR can detect radicals and electronic defects in a material. Alanine-EPR dosimetry for various kinds of ionizing radiation is well-documented and standardized.[1–3] Alanine is found to be a convenient material for establishing a quantitative link between an absorbed dose of radiation and DNA modification – or microbiological decontamination – caused by ionizing radiation, since the amination of an alanine molecule produces a stable alkyl free radical, $CH_3CHCOO^-$. For the application in radiation dosimetry, tablets or films of alanine-comprising compounds are used as calibrated witness dosimeters. Figure 1 shows examples of commercial alanine films laminated on paper strips used for Alanine-EPR dosimetry. They are typically coated with a fluoropolymer resin.

Calibrated gamma-cells with an established traceability to the international radiation dose standard are used for calibration of the alanine dosimeters. Specifically, the calibration procedure includes irradiation of alanine dosimeters in the gamma-cell by predetermined systematically increasing doses of gamma-radiation in a certain range of absorbed dose values. Here, the range is representative for further comparative experiments where alanine dosimeters from the same manufacturing batch are used. Thus, the main advantage of the gamma-calibrated alanine-EPR dosimetry is that it enables a very straightforward link between


**FIGURE 1** Alanine dosimeter films comprising composites laminated on the left (non-engraved-) side of the paper strips

concentration of radiation damages seen as concentrations of polar defects, radicals, and the like, and the amount of absorbed energy of radiation, or simply absorbed dose of radiation.

Non-thermal plasma processing is useful for surface modification of certain materials due to its environmental friendliness and high reactivity with the surface.[4,5] It is generally believed that plasma treatment can modify material surfaces while retaining bulk properties. High electron temperatures ensure efficient production of reactive species in a non-thermal plasma, which establishes the useful function of such a plasma in surface processing. Meanwhile a thermal plasma such as an arc at its equilibrium conditions should be avoided for surface processing to prevent the treated materials from thermal damages. It is indicated that to avoid generation of a thermal plasma the current should be blocked before the transition to an arc occurs.[6] This type of plasma processing is often employed at low pressures. Unfortunately, plasma treatments at low pressures require expensive vacuum systems, and suitable methods are generally only well-developed for batch or semi-batch treatments. However, useful plasmas can also be generated at atmospheric pressure,[7] obviating vacuum equipment and permitting the treatment of large objects[8–20] and continuous processing of surfaces.[21,22] It has been shown that in many cases surface treatment effects demonstrated with low-pressure plasmas are achievable at atmospheric pressure as well.[7]

A variety of atmospheric pressure plasma sources have been developed for surface processing, including a corona discharge, a dielectric barrier discharge (DBD), a cold plasma torch, and a gliding arc plasma.[6] DBDs or "silent" discharges are non-equilibrium gas discharges which can be operated at atmospheric pressure.[23] DBD processes demonstrate great flexibility with respect to geometry, working gas composition, and other operational parameters.[24–26] The DBD is also characterized by the presence of at least one insulating (dielectric) layer in the discharge gap between two metal electrodes. To ensure stable DBD operation, however, the gap between the electrodes is typically limited to a few millimeters, which restricts the size and shape of the active area on the specimens to be treated.

Gliding arc discharges can also be generated at atmospheric pressure. They are quenched plasmas, which can simultaneously provide a high degree of non-equilibrium, high electron temperature, and high electron density and thus enable high reactivity and high productivity.[8–19] They are generated between diverging electrodes and are extended by a gas flow. A fast transition into a non-equilibrium state occurs once heat losses from the discharge column exceed the supplied energy. The gliding arc combines a number of industrially attractive features of plasma based surface treatment: it is environmentally much cleaner than mechanical or wet chemical processes; it operates well in air at atmospheric pressure with low costs; being a torch-like plasma source, it can treat surfaces of bulky objects; and it allows fast processing. Therefore, it is useful in many automated industrial applications that involve coating, painting, printing, dyeing, and adhesion. It has recently been reported that gliding arcs can efficiently improve adhesion of fibre reinforced polymers.[6,11,13,16,19] It is demonstrated that the gliding arc treatment can improve surface wettability for polar liquids, and increase the density of oxygen-containing polar functional groups at the surfaces and the bond strength with adhesives.

EPR (ESR) has been used for characterization of polymeric materials after plasma processing.[27–32] Here, plasma modification effects are considered to happen at material surfaces[27,29] or within a thin surface layer of less than 1 μm depth.[32] However, in the present work, preliminary experiments for plasma treatment of the fluoropolymer coated alanine (FCA) films indicated that both fluoropolymer surfaces and the bulk alanine were modified after the treatment. When plasma processing is used for surface treatment, changes of bulk properties should be avoided. On the other hand, in some medical applications such as plasma medicine,[33,34] it is desirable that the bulk properties can also be affected by plasmas. Motivated by the above argumentations, FCA films were studied as treated by a DBD and a gliding arc at atmospheric pressure, and after gamma irradiation and ion bombardment. The treated specimens were characterized by surface analysis using X-ray photoelectron spectroscopy (XPS), and by the values of the absorbed doses for the bulk alanine. The treatment effects are compared and based on the comparison of the results, applications for plasma medicine are suggested.

## 2 | EXPERIMENTAL SECTION

FCA films (Figure 1) manufactured by Kodak in accordance with Bruker BioSpin Corporation Specifications, Reference Number ES-200-2112B 6140500, LOT#0311, CAT 8748220, were used in the experiment. The fluoropolymer coating has a porous structure with a thickness of approximately 20 μm.

An atmospheric pressure DBD was generated between two parallel plane water-cooled electrodes (50 mm × 50 mm)

and driven by an alternating current power supply at a frequency of 40 kHz (Generator 6030, SOFTAL Electronic GmbH, Germany). The water-cooled bottom electrode is grounded and covered with an alumina plate as a dielectric barrier. The distance between the upper powered electrode and the alumina plate was fixed at 5 mm. A similar setup was used and presented previously.[36–40] Helium was fed into the DBD at a flow rate of 3 L $min^{-1}$. The FCA film was placed on the alumina plate and exposed to the DBD at the power of 120 W. The average power to the DBD was obtained by measuring voltage and current with a high-voltage probe and resistors, respectively. The FCA films were treated for 2, 5, 10, 20, 30, 60, 120, 300, and 600 s.

The gliding arc was generated between two diverging stainless steel tubular electrodes. The outer diameter of the tubular electrodes is 3 mm. Cooling water was fed through the electrodes during operation. Similar configurations are presented in detail in Refs.[10–19] An air flow was fed between the electrodes to extend the discharge. The gliding arc was driven by an alternating current power supply at a frequency of 31.25 kHz at the power of 600 W (Generator 6030, SOFTAL). To treat an FCA film surface without excess thermal damage from the gliding arc, the plate was fixed on a holder which continuously moved forwards and backwards at a speed of approximately 180 mm $s^{-1}$. Since the length of the FCA film is 40 mm and the specimen was moved in the length direction, the residence time of a specimen is approximately 0.2 s per one exposure. The specimen surfaces were exposed to the discharge twice in 5 s, and the number of exposures was 2, 4, 10, 20, 30, and 40.

The treated surfaces were studied by XPS. Data were collected using a double anode (Mg $Al^{-1}$) source, and for the present measurements, the Mg Kα line with an energy of 1253.6 eV was used, with a lateral resolution of 2 mm diameter of the analyzed spot to study the changes in elemental compositions and the functional groups on the FCA surfaces. Atomic concentrations of all elements were estimated from the integral peak intensities subtracting a "smooth" type background from the wide-scan spectra, which were recorded at 50 eV pass energy, using the CasaXPS software. A higher-resolution study was performed of the carbon 1s (C1s) peak region (at a pass energy of 25 eV) acquired over three scans. These spectra were deconvoluted to study the bonding of carbon in the samples, also using the CasaXPS software and in this case with a Shirley type background for the peaks. An untreated sample was depth profiled with bombardment of 1 keV Ar ions, down to an estimated depth of about 40 nm, using wide scan recordings of the XPS spectra. As it turned out, this measurement revealed damage of the sample in combination with sputter etching.

The temperature of the specimen surface was measured immediately after plasma treatments by using a thermocouple.

FCA films were irradiated with gamma rays in a $^{60}Co$ Gammacell 220 Excel (MDS Nordion, Canada) at Risø High Dose Reference Laboratory of the Center for Nuclear Technologies of Technical University of Denmark, which delivered the absorbed dose rate of approximately 79 Gy $min^{-1}$. The expected range of absorbed dose for the calibration was chosen from 10 Gy to 250 Gy.

The application of the EPR for the plasma treated films is considered in the following way.

1. Irradiation of a set of virgin FCA films in a calibrated gamma-cell up to predetermined doses to prepare calibration films.
2. Measuring EPR spectra of the gamma-irradiated calibration films.
3. Plotting EPR alanine signal amplitudes (sweeps from main minimum to main maximum of the alanine spectra) vs. absorbed doses and fitting them with a calibration function.
4. Plasma treating another set of virgin FCA films as witnesses during plasma processing.
5. Measuring EPR spectra of the plasma treated FCA films.
6. Deriving "absorbed dose" of absorbed energy in the bulk alanine using the calibration function obtained from step 3, subtracting that of the virgin FCA film as a background.

## 3 | RESULTS AND DISCUSSION

A wide energy scan XPS spectrum of an untreated sample is shown in Figure 2. The surface is dominated by carbon, fluorine, oxygen and nitrogen atoms. An attempt to measure a depth profile of the untreated FCA film is shown in Figure 3. The bombardment of the surface with 1 keV Ar ions causes sputter etching of the surface, but also chemical decompositions due to the impact of the ion beam, which affects a depth of 2–3 nm below the surface. Thus, the obtained profile is a combination of these effects, and not just a picture of the in-depth composition of the sample. The sputter rate is estimated with the program SRIM for a Teflon sample, but does not take into account the chemical modifications of the surface under the Ar bombardment. The initial surface is dominated by substantially equal concentrations of carbon and fluorine atoms. The carbon content increases while the fluorine content decreases during continued bombardment. The concentration changes seen in Figure 3 are relatively well fitted with smooth sigmoidal functions, indicative of the dynamics of the effects of ion bombardment, and the control of the parameters in the sputtering process. The total sputter time for this experiment was 488 min.

Elemental compositions of FCA films deduced from the XPS results, before and after each treatment, are summarized in Table 1. Plasma treatment decreases the fluorine content and increases the oxygen content. For the present conditions, the gliding arc treatment shows a higher effect in decrease of

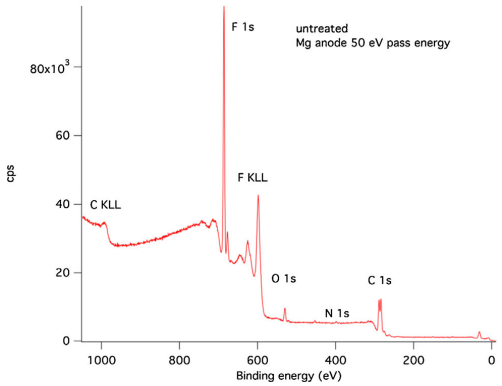


**FIGURE 2** XPS wide scan of the untreated FCA film

fluorine and increase of oxygen than the DBD treatment. Gamma radiation also decreases the fluorine content and increases the oxygen content, comparable to the gliding arc treatment.

Higher-resolution C 1s spectra are shown in Figure 4 with deconvolutions of the main peaks. Figure 4a–d shows the C1s spectral region of the FCA films before and after each treatment. Two major peaks are immediately identified in each spectrum, one corresponding to C—C and C—H bonds with an average central energy at 284 eV and the other for C—F related bonds at an average central energy of 289 eV. However, the C—C/C—H peak is clearly wider than the C—F peak. This indicates that there could be an additional C—O component in the wider peak, although it was not possible to get an acceptable fit with any additional

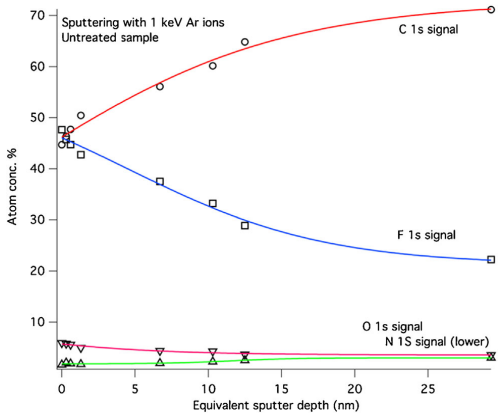


**FIGURE 3** Depth profile of an untreated FCA film measured by XPS

**TABLE 1** Elemental composition of FCA surfaces by XPS [%]

| Elements | C | F | O | N |
|---|---|---|---|---|
| Untreated | 48 | 48 | 4 | 0 |
| DBD, 15 s | 51 | 42 | 5 | 1 |
| Gliding arc, 2 exposures | 54 | 33 | 10 | 2 |
| Gamma-irradiated | 56 | 32 | 9 | 2 |

and smaller peak inside the wider peak, so the indication of the relative areas of these two peaks in the experiments could underestimate the number of C—F bonds in relation to the number of C—C and C—H bonds. Using the wide scan spectra as a guide, the C—C to C—F signals from the untreated sample is around 1:1, and the changes with the treatments seen in the C 1s spectra should be related to this ratio from the start. After each treatment, the number of C—F bonds has decreased. A similar effect was observed for thermal decomposition of alanine on a Ni (111) surface.[41] It is confirmed that the gliding arc treatment shows a higher effect of reducing fluorine (C—F) than the DBD treatment, as was found in the XPS survey analysis. In addition, gamma radiation decreases the number of C—F bonds, comparable to the gliding arc treatment. The results of the C 1s analysis are summarized in Table 2.

The results of temperature measurements at the FCA film surfaces are shown in Figure 5. As the exposure time or treatment time increases, heat was accumulated and the temperature increased. After 600 s treatment with the DBD, the temperature exceeded 80 °C. On the other hand, even after 40 exposures by the gliding arc, the temperature remained below 40 °C, indicating that the treatment process of the gliding arc in the present work can prevent the treated films from excess thermal damage.

The EPR spectra obtained from gamma irradiated and plasma treated FCA films with the use of Bruker EMS104 EPR spectrum analyzer are shown in Figure 6. Both waveforms shown in Figure 6 present typical ESR spectra of alanine radicals, as described in Refs.[1–3] Fluoropolymer as well as the untreated alanine does not have significant amounts of free radicals and thus the resultant EPR signal of fluoropolymer is weak. After each treatment, detectable amounts of the stable alkyl free radical in alanine are created, shown as a fingerprint in Figure 6.[1–3] On the other hand, XPS analysis shows that such an alkyl radical is not created on the FCA surfaces after each treatment. Other free radicals created by each treatment at the surfaces are, if any, typically unstable, and show different and weak EPR spectra. Examples of EPR spectra of untreated and irradiated fluoropolymer can be found in literature.[42] Since they are different and weak compared to the EPR of alanine, they do not disturb the dosimetry study using the FCA films.

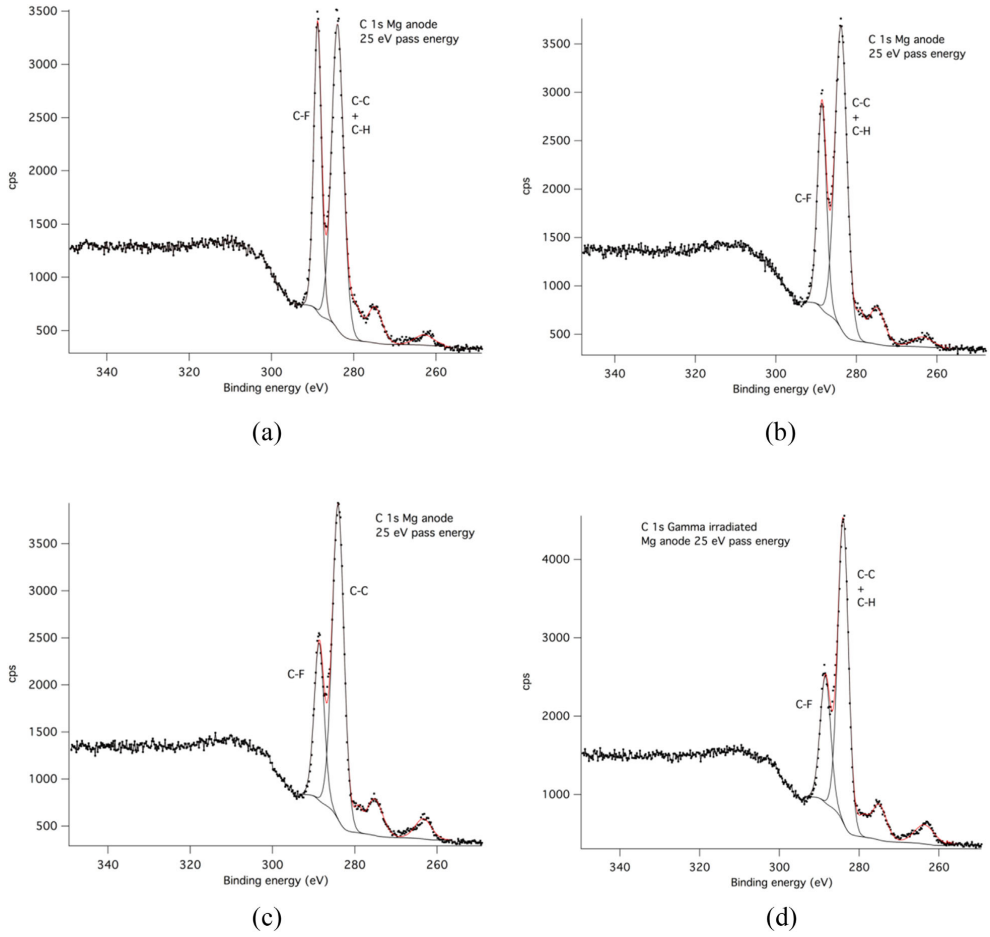


**FIGURE 4** C 1s spectra of the FCA films. Untreated (a), DBD for 15s (b), gliding arc 2 exposures (c), and after gamma irradiation

In other words, the films subjected to gamma irradiation and plasma treatment have indistinguishable EPR spectra if the absorbed dose of radiation and the plasma processing dose are chosen appropriately. Moreover, the preliminary experiment indicated that the plasma processing during reasonable time of a few minutes results in an alanine EPR response comparable to one caused by absorbed dose of ionizing radiation of 10–100 Gy (10–100 J $kg^{-1}$). Corresponding amplitudes of EPR waveforms are 5.6 a.u. for gamma irradiation and 5.3 a.u. for DBD processing in Figure 6. These are comparatively low doses resulting in low-amplitude EPR response that is difficult to measure using a relatively insensitive spectrometer as the Bruker EMS104 EPR. Thus, a more sensitive instrument, Bruker EMX-micro EPR, was used in the systematic experiments for the plasma treatments.

**TABLE 2** Relative compositions in C 1s spectra [%]

| Elements | C—C + C—H at 284 eV | C—F at 289 eV |
|---|---|---|
| Untreated | 62 | 48 |
| DBD, 15 s | 66 | 34 |
| Gliding arc, 2 exposures | 70 | 30 |
| Gamma-irradiated | 71 | 29 |

The basic calibration was carried out for a broad range of doses from 10 to 1000 Gy in ascending order, and the tri-serial irradiation for each absorbed dose value (i.e., each dose was deposited in three films simultaneously) was made. The EPR responses, each derived from the average values obtained from three films, were put versus pre-set doses in Figure 7. The data obtained from irradiation to doses from 100 to 1,000

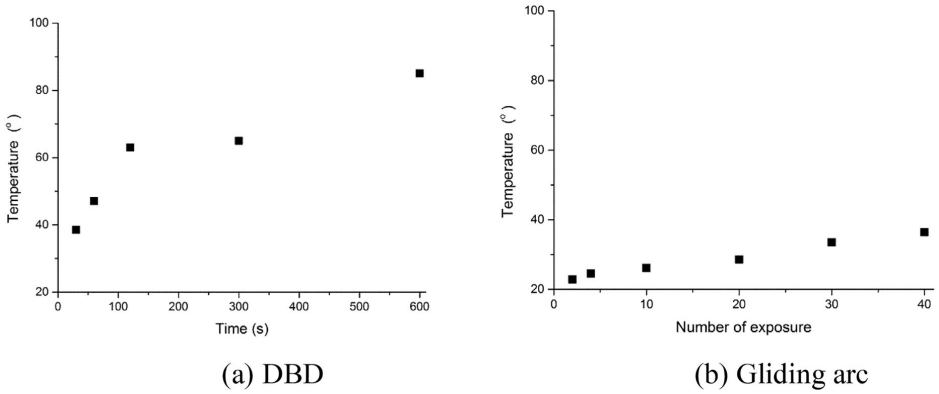


**FIGURE 5** Temperature of the FCA surface after the DBD treatment (a) and the gliding arc treatment (b)

Gy was processed in accordance with the standard.[1] They allowed a simple linear regression whose residuals in regard of the pre-set absorbed dose values were less than 2%, as shown in Figure 7 (right). The intercept of the fitted line in Figure 7 (left) is $1.7 \times 10^5$ which is close to the measured EPR response of the untreated film at $1.4 \times 10^5$. It is approximately 10 times smaller than the EPR values obtained for the irradiated FCA films, and thus the EPR signal of the untreated FCA film is weak, showing good agreements of the measured EPR signals of untreated alanine in literature.[3]

As for the low doses from 4 to 100 Gy, an improved method of processing alanine-EPR data proposed in Ref.[3] was used. This method enables measurements of low doses of 4–10 Gy with the uncertainty of 30 mGy. The procedure is based upon comparison of slopes of lines connecting main minima and maxima of the EPR spectra, resulting from irradiation by known (reference) and unknown (measured) doses of radiation. Typically, a higher dose response is chosen for deriving a reference slope to have a reasonably high signal-to-noise ratio. In these experiments, the reference slope was derived as an average of the slopes from EPR signals of three FCA films irradiated to 160 Gy. Example of an unknown EPR response versus the average response to 160 Gy within the magnetic field range from main maximum to main minimum of an EPR waveform is shown in Figure 8. The unknown dose is then found as a product of 160 Gy and the dimensionless slope of the linear approximation line in the graph in Figure 8. For example, if the slope is 0.1612, the unknown dose is 160 Gy · 0.1612 = 25.8 Gy.

Generation of free radicals (paramagnetic centers) in alanine is temperature dependent: the higher the temperature is, the easier it becomes to break molecular bonds and form radicals.[41] Results of alanine/EPR dosimetry are therefore dependent on the temperature and a correction of the alanine dosimeter response is necessary when the irradiation temperature is different from the calibration temperature. The implementation of the temperature correction is based on the experimentally-confirmed assumption about a linear dependence of the alanine/EPR dosimeter system response on the irradiation temperature.[35] The correction is therefore given by following expression

$$R_{\tau_i} = R[1 + \kappa_\tau(\tau_i - \tau_c)]$$

where $R$ is the measured EPR response of an alanine dosimeter, $R_{\tau_i}$ is the response value corrected to the processing temperature

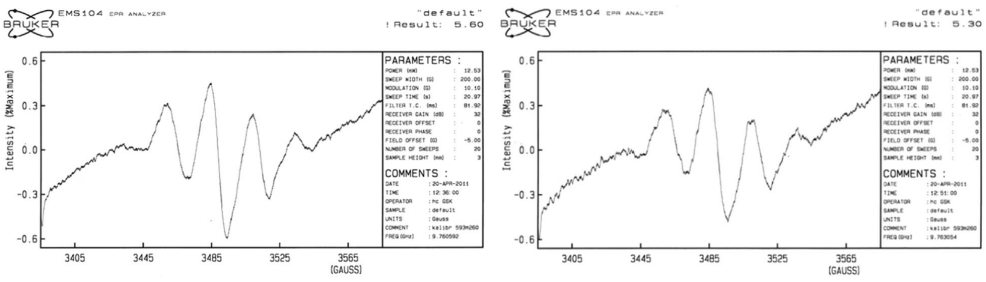


**FIGURE 6** EPR spectra of identical FCA films subjected to 80-Gy dose of gamma-radiation (left image) and DBD treatment for 600 s (right image). The background subtraction was not performed

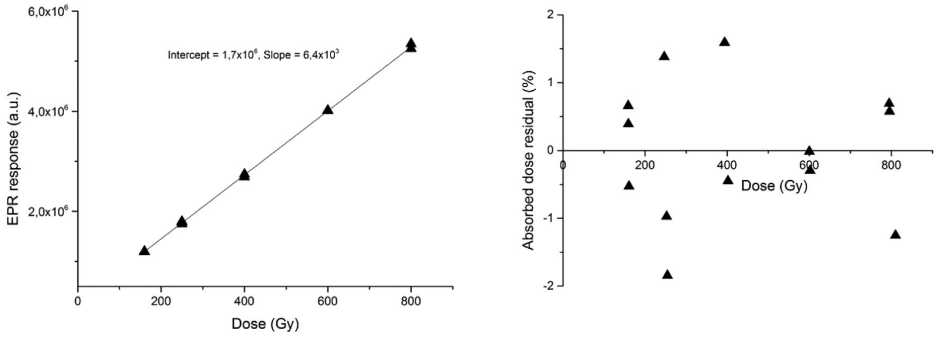


**FIGURE 7** Gamma-calibration of FCA films in the dose range from 100 to 1000 Gy: EMX-Micro EPR responses (ordinaltes, a.u.) (left graph), and the absorbed dose residuals (ordinates,%) (right graph). The background subtraction was not performed

$\tau_i$, and $\tau_c$ is the temperature of calibration of alanine dosimeters. The temperature coefficient $\kappa_\tau$ is determined for each new batch of alanine dosimeters. The dosimeters are usually calibrated at the temperature $\tau_c = 25$ °C. The temperature coefficient $\kappa_\tau$ for the films specified above was measured to be 0.0011 $°C^{-1}$. It was also shown that the temperature correction that takes into account maximum temperature achieved during the irradiation (processing) is the most reliable for alanine film dosimeters. Obviously, the maximum temperatures of FCA films were achieved in the end of the plasma treatments as shown in Figure 5.

Finally, the results of absorbed dose (specific deposited energy) measurements for DBD and gliding arc treatments of FCA films using EPR spectra processing with temperature corrections are shown in Figure 9. Here, gamma rays are known to be the most penetrating of the radiations and

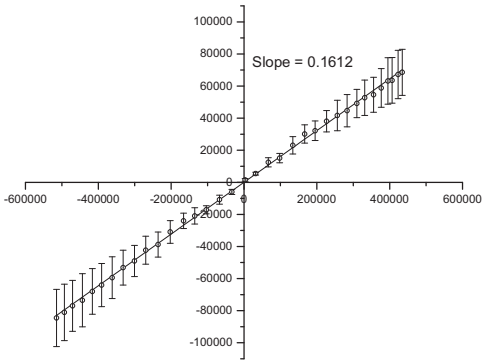


**FIGURE 8** Example of implementation of low-dose response measurements algorithm suggested in Ref.[3] The graph shows EPR response to unknown dose versus response to 160 Gy in the magnetic field range from ~3504 G to ~3512 G between main maximum and main minimum of the alanine response

can pass through the FCA film. If plasma treatment modifies only the surface layer of the materials[5] up to approximately 1 μm,[32] the bulk material properties of alanine would be retained due to the 20 μm thick fluoropolymer covering alanine. However, Figures 6 and 9 indicate that plasma treatments eventually modified the bulk alanine, and thus the plasma treatments affected not only surfaces but also bulk materials. Since increase in temperature by the treatment was moderate as shown in Figure 5, the bulk modification in the present study is probably caused by high energy photo-emission of the plasmas such as ultraviolet (UV) rays. Penetration depth of UV rays into polymeric materials depends on the materials themselves and the wavelength of UV.[43] Fluoropolymers are known to be substantially UV transparent even at short wavelengths,[44] while alanine absorbs a broad range of UV.[45] It is therefore likely that UV rays emitted from the plasma can pass through the fluoropolymer layer and easily be absorbed by alanine. This in turn indicates that the alanine dosimetry can be potentially used as a measure of bulk modification caused by the plasma treatment. For the general plasma treatment of materials, modification of bulk properties is unexpected and often undesirable, since the plasma treatment typically aims at modifying surface layers only. However, in some specific applications such as plasma medicine, the treatment eventually aims at modifying or affecting textures of bulk substances. In plasma medicine, a liquid phase reaction initiated by a plasma is thought to be the major mechanism for clinical effects.[34] On the other hand, the bulk modification in the present work does not include a liquid phase. It is therefore suggested that understanding of clinical effects in plasma medicine might be further matured by considering the bulk modification in a solid phase as well as a liquid phase.

It is interesting to compare the modification effects of the surfaces and the bulk for the two different plasma treatments.

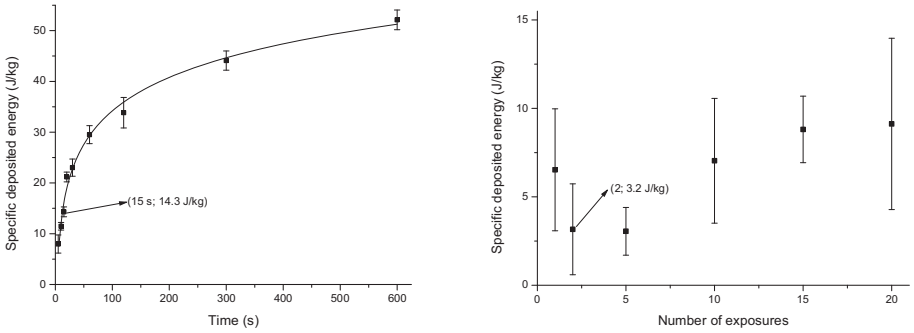


(a) DBD (b) Gliding arc

**FIGURE 9** Specific energy deposited in FCA films treated by the DBD (a) and the gliding arc (b)

The gliding arc treatment decreased the fluorine content and increased the oxygen content much more than the DBD treatment. On the other hand, the specific deposited energies of the films after the gliding arc and the DBD treatments whose C 1s spectra are shown in Figure 4b and c are approximately 3 and 14 J $kg^{-1}$, respectively, as shown in Figure 9. These results indicate that in the specific conditions, the gliding arc treatment can modify the material surface and retain the bulk properties more efficiently than the DBD treatment. In other words, the gliding arc treatment may be more appropriate for surface modification while the DBD treatment may be the choice for bulk modification in the application of, for example, plasma medicine.

UV emission of the gliding arc includes emissions from NO, OH, and $N_2$, and its intensity is lowered in an optimal condition for surface treatment,[46] corresponding to the condition of the present work. In addition, the intensity of the UV emission a few centimeters away from the electrodes, where the specimen can be exposed, is much weaker than that in the vicinity of the electrodes, characterized by less spiky UV lines with broad emission toward a visible range.[12] On the other hand, the helium DBD typically has strong UV emissions consisting of $N_2$, $N_2^+$, and NO.[47] The difference of the UV emission between the gliding arc and the helium DBD can be one of the reasons of the higher bulk modification effect of the DBD. However, further investigation will be necessary for better understanding of the observed phenomena.

## 4 | CONCLUSION

FCA films were treated by the DBD and the gliding arc at atmospheric pressure as well as gamma irradiation. Each treatment decreased fluorine contents and increased oxygen contents at the surfaces of the fluoropolymer coatings on the alanine films. On the other hand, each treatment also modified the bulk alanine films. It is indicated that the plasma treatments can affect bulk properties, and the changes can be detected by the EPR technique. In the selected conditions, the gliding arc treatment modified the surface more and the bulk less than the DBD treatment.

## ACKNOWLEDGEMENTS

Authors are grateful to Prof. Arne Miller of Risø High Dose Reference Laboratory of the Center for Nuclear Technologies of Technical University of Denmark for providing alanine films and granting access to the gamma-cell and the EPR spectrometers and to Dr. Shailendra V. Singh for his help in conducting experiments and XPS data analysis.

## ORCID

*Yukihiro Kusano* http://orcid.org/0000-0003-3928-8729

## REFERENCES

[1] ISO ASTM 51607 "Practice for use of the alanine-EPR dosimetry system".
[2] W. L. McLaughlin, *Radiat Protection Dosimetry* **1993**, *47*, 45.
[3] J. Helt-Hansen, F. Rosendal, I. M. Kofoed, C. E. Andersen, *Acta Oncol* **2009**, *48*, 216.
[4] J. Cognard, *JCR Chimie* **2006**, *9*, 13.
[5] Y. Qiu, X. Shao, C. Jensen, Y. J. Hwang, C. Zhang, M. G. McCord, *Polymer Surface Modification: Relevance to Adhesion* (Ed.: K.L. Mittal), VSP, The Netherlands **2004**, 3.
[6] Y. Kusano, *J Adhesion* **2014**, *90*, 755.
[7] M. Kogoma, *Generation and Applications of Atmospheric Pressure Plasmas* (Eds.: M. Kogoma, M. Kusano, Y. Kusano), NOVA Science Publishers, Inc, NY, USA **2011**, vii.
[8] A. Fridman, A. Chirokov, A. Gutsol, *J Phys D Appl Phys* **2005**, *38*, R1.
[9] A. Czernichowski, *Pure Appl Chem* **1994**, *66*, 1301.

[10] Y. Kusano, M. Salewski, F. Leipold, J. J. Zhu, A. Ehn, Z. S. Li, M. Aldén, *Eur Phys J D* **2014**, *68*, 319.
[11] Y. Kusano, B. F. Sørensen, T. L. Andersen, F. Leipold, *J Adhesion* **2013**, *89*, 433.
[12] Z. W. Sun, J. J. Zhu, Z. S. Li, M. Aldén, F. Leipold, M. Salewski, Y. Kusano, *Opt Express* **2013**, *21*, 6028.
[13] Y. Kusano, B. F. Sørensen, T. L. Andersen, H. L. Toftegaard, F. Leipold, M. Salewski, Z. W. Sun, J. J. Zhu, Z. S. Li, M. Aldén, *J Phys D Appl Phys* **2013**, *46*, 135203.
[14] J. J. Zhu, J. L. Gao, A. Ehn, M Aldén, Z. S. Li, A. Larsson, Y. Kusano, *Phys Plasmas* **2017**, *25*, 01351.
[15] Y. Kusano, L. Berglund, Y. Aitomäki, K. Oksman, B. Madsen, *Open Access J IOP Conf Series Mater Sci Eng* **2016**, *139*, 012027.
[16] Y. Kusano, J. J. Zhu, A. Ehn, Z. S. Li, M. Aldén, M. Salewski, F. Leipold, *Surf Eng* **2015**, *31*, 282.
[17] J. J. Zhu, J. L. Gao, A. Ehn, M Aldén, Z. S. Li, D. Moseev, Y. Kusano, M. Salewski, A. Alpers, P. Gritzmann, M. Schwenk, *Appl Phys Let* **2015**, *106*, 044101.
[18] J. J. Zhu, J. L. Gao, Z. S. Li, A. Ehn, M Aldén, A. Larsson, Y. Kusano, *Appl Phys Let* **2015**, *105*, 234102.
[19] Y. Kusano, S. Teodoru, F. Leipold, T. L. Andersen, B. F. Sørensen, N. Rozlosnik, P. K. Michelsen, *Surf Coat Technol* **2008**, *202*, 5579.
[20] O. V. Penkov, M. Khadem, W.-S. Lim, D.-E. Kim, *J Coat Technol Res* **2015**, *12*, 225.
[21] Y. Kusano, T. L. Andersen, P. K. Michelsen, *J Phys Conf Series* **2008**, *100*, 012002.
[22] S. Teodoru, Y. Kusano, N. Rozlosnik, P. K. Michelsen, *Plasm Proc Polym* **2009**, *6*, S375.
[23] U. Kogelschatz, *Plasma Chem Plasma Proc* **2003**, *23*, 1.
[24] F. Leipold, N. Schultz-Jensen, Y. Kusano, H. Bindslev, T. Jacobsen, *Food Control* **2011**, *22*, 1296.
[25] F. Leipold, Y. Kusano, F. Hansen, T. Jacobsen, *Food Control* **2010**, *21*, 1194.
[26] F. Leipold, A. Fateev, Y. Kusano, B. Stenum, H. Bindslev, *Fuel* **2006**, *85*, 1383.
[27] M. Kuzuya, K. Kamiya, Y. Yanagihara, Y. Matsuno, *Plasma Sources Sci Technol* **1993**, *2*, 51.
[28] M. Kuzuya, Y. Matsuno, T. Yamashiro, M. Tsuiki, *Plasma Polym* **1997**, *2*, 79.
[29] J. Janca, P. Stahel, J. Buchta, D. Subedi, F. Krcma, J. Pryckova, *Plasmas Polym* **2001**, *6*, 15.
[30] L. Song, Z.-Y. J. Sunc, K. E. Colemana, M. B. Zwickd, J. S. Gachd, J. Wangc, E. L. Reinherza, G. Wagnerc, M. Kimb, *PNAS* **2009**, *106*, 9057.
[31] G. Sun, B. X. Dong, M. H. Cao, B. Q. Wei, C. W. Hu, *Chem Mater* **2011**, *23*, 1587.
[32] S. F. Sadova, *High Energy Chem* **2006**, *40*, 83.
[33] J. Gay-Mimbrera, M. C. García, B. Isla-Tejera, A. Rodero-Serrano, A. V. García-Nieto, J. Ruano, *Adv Ther* **2016**, *33*, 894.
[34] K.-D. Weltmann, T. von Woedtke, *Plasma Phys Control Fusion* **2017**, *59*, 014031.
[35] M. A. Sharpe, M. D. Krzyaniak, S. J. Xu, J. McCracken, S. Ferguson-Miller, *Biochem* **2009**, *48*, 328.
[36] Y. Kusano, B. Madsen, L. Berglund, Y. Aitomäki, K. Oksman, *Surf Eng* **2017**, published online. https://doi.org/10.1080/02670844.2017.1334411
[37] Y. Kusano, K. Norrman, S. V. Singh, F. Leipold, P. Morgen, A. Bardenshtein, N. Krebs, *J Adhesion Sci Technol* **2013**, *27*, 825.
[38] Y. Kusano, S. V. Singh, K. Norrman, J. Drews, F. Leipold, N. Rozlosnik, A. Bardenshtein, N. Krebs, *Surf Eng* **2012**, *28*, 453.
[39] Y. Kusano, S. V. Singh, K. Norrman, F. Leipold, J. Drews, P. Morgen, A. Bardenshtein, N. Krebs, *J Adhesion* **2011**, *87*, 720.
[40] Y. Kusano, S. V. Singh, A. Bardenshtein, N. Krebs, N. Rozlosnik, *J Adhesion Sci Technol* **2010**, *24*, 1831.
[41] E. Richard, J. Nicklin, A. Cornish, A. Shavorskiy, S. Baldanza, K. Schulte, Z. Liu, R. A. Bennett, G. Held, *J Phys Chem C* **2015**, *119*, 26566.
[42] A. Oshima, T. Seguchi, Y. Tabata, *Radiat Phys Chem* **1997**, *50*, 601.
[43] S. S. Sackey, M. K. Vowotor, A. Owusu, P. Mensah-Amoah, E. T. Tachie, B. Sefa-Ntiri, C. O. Hood, S. M. Atiemo, *Environ Pollut* **2015**, *4*, published online. https://doi.org/10.5539/ep.v4n4p1
[44] M. K. Yang, E. W. Tokarsky, *J Micro/Nanolith MEMS MOEMS* **2008**, *7*, 033010.
[45] R. Abu-Eittah, A. Obaid, S. Basahl, E. Diefallah, *Bull Chem Soc Jpn* **1988**, *61*, 2609.
[46] J. J. Zhu, Z. W. Sun, Z. S. Li, A. Ehn, M. Aldén, M. Salewski, F. Leipold, Y. Kusano, *J Phys D Appl Phys* **2014**, *47*, 295203.
[47] V. Poenariu, M. R. Wertheimer, R. Bartnikas, *Plasm Proc Polym* **2006**, *3*, 17.

**Y. KUSANO** is Senior Scientist at Technical University of Denmark. He did his undergraduate study at the Department of Applied Physics, University of Tokyo. He was awarded PhD in King's College, Cambridge, UK. As a professional researcher, he had been Research Engineer at Bridgestone Co. Japan; Research Associate at the Department of Engineering, University of Cambridge, UK; and Scientist/Senior Scientist at Risø National Laboratory, and the Technical University of Denmark. His research experience includes surface engineering, plasma processing, adhesion, and tribology.

**A. BARDENSHTEIN** is R&D Product Manager at Danish Technological Institute. He studied applied physics at the Department of Electrophysics, Tomsk Polytechnic University and was awarded PhD in Tomsk State University, Russia. He did his postdoctoral studies in laser-generated ultrasound at Risø National Laboratory, Denmark. He had been Research Engineer at Tomsk Polytechnic University (Russia) and FORCE Technology (Denmark), Researcher and Senior Researcher at the Institute of High-Current Electronics (Russia) and Technical University of Denmark, and Senior Consultant at Danish Technological Institute. He has worked in radiation matter interaction, radiation dosimetry, non-destructive testing, ultrasound, plasma, and microwave processing applications.

**P. MORGEN** is professor emeritus at University of Southern Denmark, Odense. His studies were at Aarhus University and at The Niels Bohr Institute, at Risø, Denmark. PhD and DSc from Odense University, Denmark. He has been scientific assistant at Royal Veterinary and Agricultural University, Copenhagen, professor at University of Brasilia, Brazil, visiting professor at Stanford University, visiting scientist at The Technical University of Munich, Germany, Scientific Director of EuroPace, Paris, and visiting professor at the Indian Institute of Science, Bangalore India. Research in nuclear physics, functional nanostructured materials, semiconductor surface physics, plasmonic structures, plasma processing, and tribology.

**How to cite this article:** Kusano Y, Bardenshtein A, Morgen P. Fluoropolymer coated alanine films treated by atmospheric pressure plasmas – In comparison with gamma irradiation. *Plasma Process Polym*. 2017;e1700131, https://doi.org/10.1002/ppap.201700131

# [Appendix A8]

Z.W. Sun, J.J. Zhu, Z.S. Li, M. Aldén, F. Leipold, M. Salewski, Y. Kusano

## “Optical diagnostics of a gliding arc”

*Optics Express* 21(5) (2013) 6028-6044.

The attached accepted version is identical to the published one.

# Optical diagnostics of a gliding arc

**Z.W. Sun,[1] J. J. Zhu,[1] Z.S. Li,[1]* M. Aldén,[1] F. Leipold,[2] M. Salewski,[2] and Y. Kusano[3]**

[1]*Division of Combustion Physics, Lund University, P.O. Box 118, S-221 00 Lund, Sweden*

[2]*Department of Physics, Plasma Physics and Fusion Energy Section, Technical University of Denmark, DTU Risø Campus, Frederiksborgvej 399, DK-4000 Roskilde, Denmark*

[3]*Department of Wind Energy, Composites and Materials Mechanics Section, Technical University of Denmark, DTU Risø Campus, Frederiksborgvej 399, DK-4000 Roskilde, Denmark*

*zhongshan.li@forbrf.lth.se

**Abstract:** Dynamic processes in a gliding arc plasma generated between two diverging electrodes in ambient air driven by 31.25 kHz AC voltage were investigated using spatially and temporally resolved optical techniques. The life cycles of the gliding arc were tracked in fast movies using a high-speed camera with framing rates of tens to hundreds of kHz, showing details of ignition, motion, pulsation, short-cutting, and extinction of the plasma column. The ignition of a new discharge occurs before the extinction of the previous discharge. The developed, moving plasma column often short-cuts its current path triggered by Townsend breakdown between the two legs of the gliding arc. The emission from the plasma column is shown to pulsate at a frequency of 62.5 kHz, i.e., twice the frequency of the AC power supply. Optical emission spectra of the plasma radiation show the presence of excited $N_2$, NO and OH radicals generated in the plasma and the dependence of their relative intensities on both the distance relative to the electrodes and the phase of the driving AC power. Planar laser-induced fluorescence of the ground-state OH radicals shows high intensity outside the plasma column rather than in the center suggesting that ground-state OH is not formed in the plasma column but in its vicinity.



**OCIS codes:** (280.5395) Plasma diagnostics; (300.2140) Emission; (300.2530) Fluorescence, laser-induced; (300.6500) Spectroscopy, time-resolved.

## References and links

1. Y. Kusano, H. Mortensen, B. Stenum, S. Goutianos, S. Mitra, A. Ghanbari-Siahkali, P. Kingshott, B. F. Sorensen, and H. Bindslev, "Atmospheric pressure plasma treatment of glassy carbon for adhesion improvement," Int. J. Adhes. Adhes. **27**, 402-408 (2007).
2. Y. Kusano, S. V. Singh, A. Bardenshtein, N. Krebs, and N. Rozlosnik, "Plasma surface modification of glass-fibre-reinforced polyester enhanced by ultrasonic irradiation," J. Adhes. Sci. Technol. **24**, 1831-1839 (2010).
3. Y. Kusano, K. Norrman, J. Drews, F. Leipold, S. V. Singh, P. Morgen, A. Bardenshtein, and N. Krebs, "Gliding arc surface treatment of glass-fiber-reinforced polyester enhanced by ultrasonic irradiation," Surf. Coat. Tech. **205**, S490-S494 (2011).
4. W. Sun, M. Uddi, T. Ombrello, S. H. Won, C. Carter, and Y. Ju, "Effects of non-equilibrium plasma discharge on counterflow diffusion flame extinction," Proc. Combust. Inst. **33**, 3211-3218 (2011).
5. W. Sun, M. Uddi, S. H. Won, T. Ombrello, C. Carter, and Y. Ju, "Kinetic effects of non-equilibrium plasma-assisted methane oxidation on diffusion flame extinction limits," Combust. Flame **159**, 221-229 (2012).
6. A. Gutsol, A. Rabinovich, and A. Fridman, "Combustion-assisted plasma in fuel conversion," J. Phys. D: Appl. Phys. **44**, 274001 (2011).
7. A. Fridman, A. Gutsol, S. Gangoli, Y. Ju, and T. Ombrellol, "Characteristics of gliding arc and its application in combustion enhancement," J. Propul. Power **24**, 1216-1228 (2008).
8. T. Ombrello, Y. Ju, and A. Fridman, "Kinetic ignition enhancement of diffusion flames by nonequilibrium magnetic gliding arc plasma," AIAA J. **46**, 2424-2433 (2008).

9. T. Ombrello, X. Qin, Y. G. Ju, and C. Carter, "Combustion enhancement via stabilized piecewise nonequilibrium gliding arc plasma discharge," AIAA J. **44**, 142-150 (2006).
10. C. M. Du, J. Wang, L. Zhang, H. X. Li, H. Liu, and Y. Xiong, "The application of a non-thermal plasma generated by gas-liquid gliding arc discharge in sterilization," New J. Phys. **14**, 013010 (2012).
11. F. Leipold, Y. Kusano, F. Hansen, and T. Jacobsen, "Decontamination of a rotating cutting tool during operation by means of atmospheric pressure plasmas," Food Control **21**, 1194-1198 (2010).
12. F. Leipold, N. Schultz-Jensen, Y. Kusano, H. Bindslev, and T. Jacobsen, "Decontamination of objects in a sealed container by means of atmospheric pressure plasmas," Food Control **22**, 1296-1301 (2011).
13. M. Laroussi and F. Leipold, "Evaluation of the roles of reactive species, heat, and UV radiation in the inactivation of bacterial cells by air plasmas at atmospheric pressure," Int. J. Mass Spectrom. **233**, 81-86 (2004).
14. M. Moreau, N. Orange, and M. G. J. Feuilloley, "Non-thermal plasma technologies: New tools for bio-decontamination," Biotechnol. Adv. **26**, 610-617 (2008).
15. A. Fateev, F. Leipold, Y. Kusano, B. Stenum, E. Tsakadze, and H. Bindslev, "Plasma chemistry in an atmospheric pressure Ar/$NH_3$ dielectric barrier discharge," Plasma Process. Polym. **2**, 193-200 (2005).
16. Y. Kusano, F. Leipold, A. Fateev, B. Stenum, and H. Bindslev, "Production of ammonia-derived radicals in a dielectric barrier discharge and their injection for denitrification," Surf. Coat. Tech. **200**, 846-849 (2005).
17. F. Leipold, A. Fateev, Y. Kusano, B. Stenum, and H. Bindslev, "Reduction of NO in the exhaust gas by reaction with N radicals," Fuel **85**, 1383-1388 (2006).
18. A. Czernichowski, "Gliding arc - Applications to engineering and environment control," Pure Appl. Chem. **66**, 1301-1310 (1994).
19. A. Fridman, S. Nester, L. A. Kennedy, A. Saveliev, and O. Mutaf-Yardimci, "Gliding arc gas discharge," Prog. Energ. Combust. **25**, 211-231 (1999).
20. A. Bogaerts, E. Neyts, R. Gijbels, and J. van der Mullen, "Gas discharge plasmas and their applications," Spectrochim. Acta B. **57**, 609-658 (2002).
21. C. Tendero, C. Tixier, P. Tristant, J. Desmaison, and P. Leprince, "Atmospheric pressure plasmas: A review," Spectrochim. Acta B. **61**, 2-30 (2006).
22. O. Mutaf-Yardimci, A. V. Saveliev, A. A. Fridman, and L. A. Kennedy, "Thermal and nonthermal regimes of gliding arc discharge in air flow," J. Appl. Phys. **87**, 1632-1641 (2000).
23. Y. Kusano, "Plasma surface modification at atmospheric pressure," Surf. Eng. **25**, 415-416 (2009).
24. Y. D. Korolev, O. B. Frants, V. G. Geyman, N. V. Landl, and V. S. Kasyanov, "Low-current "gliding arc" in an air flow," IEEE T. Plasma Sci. **39**, 3319-3325 (2011).
25. P. Bruggeman and D. C. Schram, "On OH production in water containing atmospheric pressure plasmas," Plasma Sources Sci. T. **19**, 045025 (2010).
26. I. V. Kuznetsova, N. Y. Kalashnikov, A. F. Gutsol, A. A. Fridman, and L. A. Kennedy, "Effect of "overshooting" in the transitional regimes of the low-current gliding arc discharge," J. Appl. Phys. **92**, 4231-4237 (2002).
27. S. Pellerin, J. M. Cormier, F. Richard, K. Musiol, and J. Chapelle, "Determination of the electrical parameters of a bi-dimensional dc Glidarc," J. Phys. D: Appl. Phys. **32**, 891-897 (1999).
28. S. Pellerin, F. Richard, J. Chapelle, J. M. Cormier, and K. Musiol, "Heat string model of bi-dimensional dc Glidarc," J. Phys. D: Appl. Phys. **33**, 2407-2419 (2000).
29. F. Richard, J. M. Cormier, S. Pellerin, and J. Chapelle, "Physical study of a gliding arc discharge," J. Appl. Phys. **79**, 2245-2250 (1996).
30. B. Benstaali, P. Boubert, B. G. Cheron, A. Addou, and J. L. Brisset, "Density and rotational temperature measurements of the OH degrees and NO degrees radicals produced by a gliding arc in humid air," Plasma Chem. Plasma P. **22**, 553-571 (2002).
31. S. Pellerin, J. M. Cormier, K. Musiol, B. Pokrzywka, J. Koulidiati, F. Richard, and J. Chapelle, "Spatial fluctuations of 'gliding' arc," High Temp. Mater. P-US. **2**, 49-68 (1998).
32. X. Tu, H. J. Gallon, and J. C. Whitehead, "Dynamic behavior of an atmospheric argon gliding arc plasma," IEEE T. Plasma Sci. **39**, 2900-2901 (2011).
33. Y. Kusano, S. Teodoru, F. Leipold, T. L. Andersen, B. F. Sorensen, N. Rozlosnik, and P. K. Michelsen, "Gliding arc discharge - Application for adhesion improvement of fibre reinforced polyester composites," Surf. Coat. Tech. **202**, 5579-5582 (2008).
34. N. Balcon, N. Benard, P. Braud, A. Mizuno, G. Touchard, and E. Moreau, "Prospects of airflow control by a gliding arc in a static magnetic field," J. Phys. D: Appl. Phys. **41**, 205204 (2008).
35. S. P. Gangoli, A. F. Gutsol, and A. A. Fridman, "A non-equilibrium plasma source: magnetically stabilized gliding arc discharge: I. Design and diagnostics," Plasma Sources Sci. T. **19**, 065003 (2010).
36. S. P. Gangoli, A. F. Gutsol, and A. A. Fridman, "A non-equilibrium plasma source: magnetically stabilized gliding arc discharge: II. Electrical characterization," Plasma Sources Sci. T. **19**, 065004 (2010).
37. J. C. Sagas, A. Hadade Neto, A. C. Pereira Filho, H. S. Maciel, and P. T. Lacava, "Basic characteristics of gliding-arc discharges in air and natural gas," IEEE T. Plasma Sci. **39**, 775-780 (2011).

38. C. O. Laux, T. G. Spence, C. H. Kruger, and R. N. Zare, "Optical diagnostics of atmospheric pressure air plasmas," Plasma Sources Sci. T. **12**, 125-138 (2003).
39. R. K. Hanson, J. M. Seitzman, and P. H. Paul, "Planar laser fluorescence imaging of combustion gases," Appl. Phys. B-Photo. **50**, 441-454 (1990).
40. S. Hammack, X. Rao, T. Lee, and C. Carter, "Direct-coupled plasma-assisted combustion using a microwave waveguide torch," IEEE T. Plasma Sci. **39**, 3300-3306 (2011).
41. A. Fridman, A. Chirokov, and A. Gutsol, "Non-thermal atmospheric pressure discharges," J. Phys. D: Appl. Phys. **38**, R1-R24 (2005).
42. A. Lebouvier, C. Delalondre, F. Fresnet, F. Cauneau, and L. Fulcheri, "3D MHD modelling of low current-high voltage dc plasma torch under restrike mode," J. Phys. D: Appl. Phys. **45**, 025204 (2012).
43. S. Teodoru, Y. Kusano, and A. Bogaerts, "The effect of $O_2$ in a humid $O_2/N_2/NO_x$ gas mixture on $NO_x$ and $N_2O$ remediation by an atmospheric pressure dielectric barrier discharge," Plasma Process. Polym. **9**, 652-689 (2012).

## 1. Introduction

Atmospheric pressure non-equilibrium plasma has found many applications in different fields such as surface treatment [1-3], combustion enhancement [4-9], bacterial inactivation [10-14] and pollutant reduction [15-17]. Some other applications are reviewed in references [18-21]. As a non-equilibrium plasma generator, a gliding arc is technically of particular interest since it can be used to produce, with high efficiency, large plasma volumes at highly non-equilibrium conditions characterized by hot electrons and colder ions [18, 22, 23]. This opens up chemical pathways not available under equilibrium conditions [19]. A typical gliding arc is a plasma column that extends between two diverging electrodes in a turbulent gas flow. When applying high electric power in a gas flow, the generated gliding arc is visualized as a blurred glowing region, as shown in Fig. 1. The gliding arc reveals its true instantaneous structure in photographs with short exposure time as the ones shown in Fig. 2. The gliding arc is a thin, string-like plasma column that repeatedly ignites in the narrowest gap between the diverging electrodes, glides up along the electrodes, and extinguishes. The large-scale motion of the gliding arc is caused by convection in a turbulent free jet that stretches the cold plasma column to form an arc connecting the anchor points on the electrodes. The length of the plasma column increases until its extinction unless the plasma column short-cuts a long current path with a shorter one. Figure 2 shows an ignition event of a new plasma column between the electrodes. After the ignition of a new plasma column, the previous plasma column decays. At the ignition stage the plasma is hot but the ions are quickly cooled, creating non-equilibrium conditions that are attractive for industrial applications, as referred above.

In spite of the widely established applications, detailed mechanisms of plasma treatment especially with gliding arcs at atmospheric pressure are still unclear. Knowledge of the freely developing gliding arc discharge is a pre-requisite to understand more complicated practical situations, such as surface treatment where the gliding arc interacts with a surface. Free-developing gliding arcs, therefore, have been investigated in modeling [19, 22, 24-29] and in experiments [22, 24, 26-32]. Existing measurements of gliding arcs were usually done at temporal resolution that did not allow the fastest dynamic processes, such as ignition and small-scale movement, to be tracked. The temporal resolution of spontaneous emission measurements of species concentrations was typically longer than the period of the supplied voltage and hence dependences on the phase of the AC drive could not be demonstrated.


Fig. 1. Photograph of an ambient-air gliding arc discharge taken with a digital camera (Cannon 350D) using an exposure time of 33 ms.

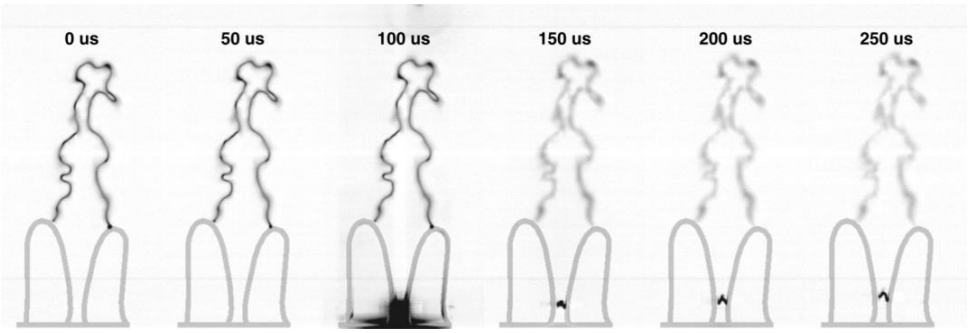


Fig. 2. Photographs of an ambient-air gliding arc discharge taken every 50 μs. The exposure time of the digital camera was 13.9 μs. A new plasma column ignites in the third frame after which the previous discharge extinguishes and the optical emissions decay.

Recent advances in optical diagnostic make it possible to do spectrally resolved measurements of the gliding arc discharge with unprecedented temporal and spatial resolution even simultaneously. In the present work, we seek an understanding of the dynamics and chemistry of a gliding arc discharge in ambient air, and this work is focused on the dynamics of the gliding arc discharge on time scales accessible with the new optical diagnostic equipment. High speed photography reveals the dynamic processes and tracks the position of the gliding arc in time including ignition, short-cutting events triggered by Townsend breakdown, and extinction. The framing rate used in this work is up to 420 kHz giving a temporal resolution up to 2.1 μs, which essentially freezes the motion of the plasma column and resolves the changes of the emission intensities originating from the alternating current (AC) driving power varying at 31.25 kHz (i.e., the half cycle duration is 16 μs). High-speed Schlieren photography is employed to visualize the flow fields and the temperature gradient generated by the gliding arc. Optical emission spectroscopy is utilized to characterize the chemical composition of the plasma column, demonstrating the spatial distribution of the dominant radiating species OH, NO and $N_2$ and the time-dependent emission during the AC voltage cycles. Instantaneous distributions of ground-state OH radials generated in the plasma column are visualized using planar laser-induced fluorescence (PLIF).

The setup of the gliding arc and the optical diagnostics techniques are described in section 2, measurement results are reported in section 3 and a summary and concluding remarks are given in section 4.

## 2. Experimental setup

### *2.1 Gliding arc discharge setup*

The gliding arc plasma is generated between two diverging electrodes constructed with stainless steel tubes with an outer diameter of 3 mm that are cooled internally with water. A similar configuration is presented in detail in [3, 33]. Air flow was fed in through a hole with 3 mm diameter between the electrodes (see Fig. 1) to convect the plasma column and create the gliding motion. The air flow rate can be adjusted, but in this work it was fixed at 17.5 standard liters per minute (SLM). The air velocity was calculated to be about 40 m/s at the nozzle exit providing turbulent flows with a Reynolds number of about Re = 8000. The plasma discharge was driven by an AC power supply at a frequency of 31.25 kHz (Generator 6030, SOFTAL Electronic GmbH, Germany). The electrical circuit driving the gliding arc plasma is presented in Fig. 3. The input power to the gliding arc was approximately 800 W. The average input power was monitored by measuring the voltage and current with a high-voltage probe and a resistor, respectively. Typical waveforms of the voltage and the current are presented in Fig. 4. Generally the current follows the voltage, but spikes in the current were occasionally observed. The gliding arc plasma was placed in a shielding metal box in order to reduce the electromagnetic noise radiated from the discharge and for safety reasons. The optical access was provided by three windows, one for the laser beam, one for the emission to the cameras or spectrometers, and the third for the Schlieren setup.

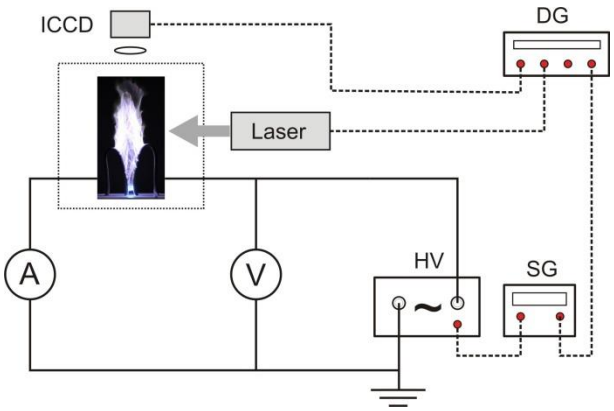


Fig. 3. The electrical scheme and the timing-controller system for the gliding arc discharge. HV, high-voltage power supply; SG, signal generator; DG, time delay generator and ICCD, intensified CCD camera. A digital oscilloscope was employed to monitor and record the current and voltage wave forms, the time-gating of the ICCD, laser pulses and the trigger signal from the SG.

The gliding arc investigated in this work can be run in two modes, i.e., the burst mode and the continuous mode. In most practical applications, the gliding arc was driven by a continuous AC voltage. However, in this mode it is difficult to synchronize the data acquisition with the plasma ignition events since they occur at seemingly random times. By programming the signal generator, the AC high voltage can be supplied to the electrodes with a predefined duration and repetition rates, like a burst. The gliding arc can be ignited and fully developed in each burst, provided the burst has a sufficiently long duration and the break time between consecutive bursts is enough to allow the plasma to extinguish fully. This arrangement gives the possibility to synchronize the optical detection system not only to the

selected phase of the AC driving power but also to the ignition process, so that the exact location of the plasma column during the time of data acquisition can be predicted approximately. In the burst mode, the data acquisition is triggered after the delay time TD+Td (see Fig. 5). TD is counted by the number of full periods of the 31.25 kHz AC voltage, which can be used to predict the position of the plasma column downstream from the ignition point. An additional delay time, Td, is added to lock the phase of the AC voltage for data acquisition. The timing relation between the gliding arc plasma and the detection system (TD and Td) is controlled by using a time delay generator (DG). The exposure time of the intensified CCD (ICDD) camera is Tg. The duration of the plasma discharge burst duration Tp was set to 20 ms. The timing relations are sketched in Fig. 5, and the timing relation between plasma and ICCD gate was monitored by a 200 MHz digital oscilloscope.

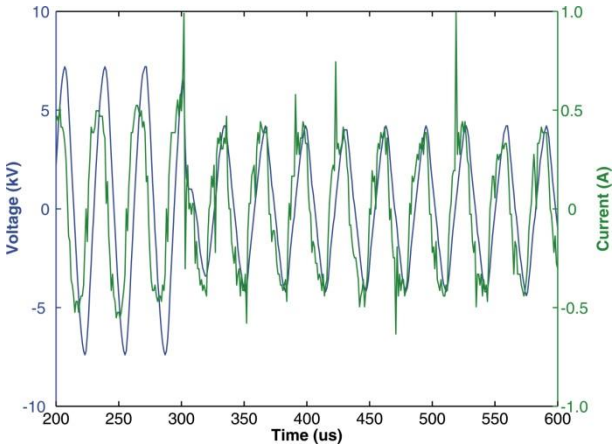


Fig. 4. Typical voltage and current waveforms recorded by the oscilloscope.

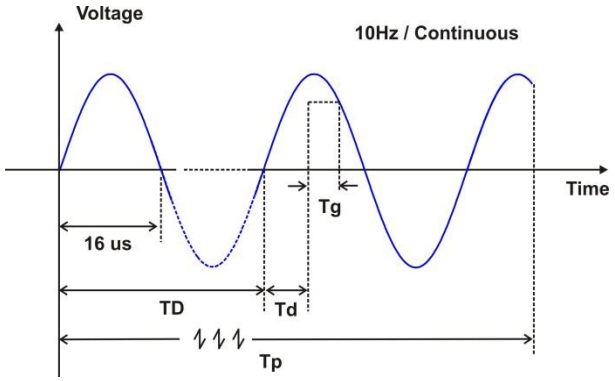


Fig. 5. Electronic waveform and timing notations. In the burst mode, the gliding arc was driven by a 10 Hz repetitive burst of 31.25 kHz AC powder with a burst duration Tp of 20 ms. TD: delay time to the desired half cycle in which data ass taken; Td: the phase delay time of data acquisition; Tg: the ICCD exposure or gate time. In the case of continuous mode, Td and Tg keep the same meaning as in the burst mode.

### *2.2. Optical measurements*

#### *2.2.1 High-speed photography*

High-speed photography has been applied to investigate gliding arc throughout recent years [22, 29, 32, 34, 35]. Usually the data acquisition was not synchronized with the plasma time-control in those works. Moreover, the relatively low framing rate adopted in the previous

results was not sufficient to fully reveal the details propagation of the gliding arc plasma column or the emission evolution in an electrical cycle. In the present work, a high-speed CMOS camera (Photron Fastcam SA5) was used to capture the ignition, propagation and extinction of the gliding arc. The high-speed camera was operated at 20, 50 and 420 kHz in measurements to meet different requirements. The camera was equipped with a Nikon lens (f = 50 mm, F/N = 1.2) collecting radiation from 380 nm to 980 nm. A high-speed movie showing the dynamics of the gliding arc discharge is attached in *Media 1* as supplementary material. Events captured in this movie will be discussed in section 3.1. Beside of direct view, Schlieren visualization of the propagating gliding arc was also captured using the same high-speed camera. Schlieren visualization is based on the deflection of light by a refractive index gradient. The plasma column has a higher temperature than the surroundings. Hence the flow field and the plasma column can be visualized by the Schlieren technique. An example Schlieren movie is shown in supplementary as *Media 2.*

*2.2.2 Optical emission spectroscopy*

Optical emission spectroscopy has been commonly used to find dominant excited species in gliding arcs [7, 25, 29, 30, 36, 37] and other plasmas [38]. Two different setups have been adopted in this work to monitor the optical emission. A fiber coupled spectrometer (OceanOptics, USB2000) was employed to collect the emission from the gliding arc plasma at different heights. A collimating lens (diameter = 5 mm) was installed before the fiber to enhance the signal collection. In the measurements, the gliding arc was imaged on the collimating lens which was adjusted vertically to achieve space-resolved measurements. For high temporal and spatial resolution, an ICCD based imaging spectrometer (SP-2300i) was employed to catch the plasma emission during its evolution in time and space. In this second setup, the input slit of the spectrometer was set parallel to the direction of the gas flow, and the spontaneous emission from plasma column can be time-resolved in a half cycle (16 μs). The position of the plasma column during the data acquisition could also be controlled as discussed in section 2.1. A 150 groves/mm grating was installed in the spectrometer and a spectral range of 170 nm was imaged by the ICCD camera. A Deuterium lamp was used to calibrate the spectral response of the system in the range of 220 – 390 nm.

*2.2.3 Planar laser-induced fluorescence*

Planar laser-induced fluorescence (PLIF) was employed to investigate the distribution of the ground-state OH radicals. PLIF is a common technique for OH detection in gas-phase environments like in combustion [39] and in plasma [7, 9, 40]. The laser beam was generally shaped into a thin laser sheet to enable a two-dimensional measurement of OH with high resolution in time and space. In this work, the $Q_2(5)$ line of the OH $X\ ^2\Pi - A\ ^2\Sigma^+$ (0, 1) band at 283.268 nm was excited using the second harmonic radiation from a dye laser (Continuum ND60, with Rhodamine 590 dye) pumped by a pulsed Nd:YAG (Brilliant B) laser. The fluorescence emission from the $X\ ^2\Pi - A\ ^2\Sigma^+$ (0, 0) and (1, 1) bands around 308 nm was collected by an ICCD camera through a filter combination (UG5 + WG295) that has a band-pass of 290 – 405 nm. The laser energy was around 8 mJ/pulse. The ICCD camera was synchronized with the pumping laser, and the fluorescence was collected perpendicular to the laser sheet with an exposure time of 30 ns.

The plasma column was also directly imaged using the ICCD camera through filters (UG5 + WG295) in order to investigate the spatial distribution of the plasma column. In this case, an exposure time of 2 μs was adopted. The OH-PLIF signal and the spontaneous plasma emission can be simultaneously collected using the ICCD with an exposure time of 2 μs.

## 3. Results

### *3.1 High-speed photography of the gliding arc*

The motion of the gliding arc plasma was recorded with the high-speed camera and the gliding motion of the plasma column was captured at high temporal resolution to reveal detailed information on ignition, evolution, short-cutting, pulsation and extinction. *Media 1* is a video image of the gliding arc plasma at 17.5 SLM air flow. The frame rate of the high-speed camera was 50,000 frames/s, and the exposure time was 16.3 μs. This movie covers 21 ms in real time, during this period the phenomena of an ignition of the gliding arc, the evolution in the convection flow and especially a short-cut of the plasma column can be observed. Note that the images shown in *Media 1* are line-of-sight signals. Phenomenologically, the following features can be observed:

1. At t = 1.74 ms, a new ignition is observed in the smallest gap between the two electrodes, where strong radiation is emitted. The emission from the previous plasma column is still visible for a short time (~ 500 μs). The plasma column is attached to both electrodes (bright points) and is convected in the gas flow while the anchor points of the plasma column glide up along the electrodes. Before t = 10 ms, the plasma column short-cuts several times leading to a sudden decrease of the plasma column length. Similar short-cut events were observed in [31]. At about 10 ms, the anchor points of plasma column become stationary on the electrodes (also see the photograph in Fig. 2). After t = 10 ms, the length of the plasma column increases while the anchor points remain approximately at the same locations.
2. At t = 12.64, 13.94 and 19.58 ms, short-cutting of the plasma column happens when suddenly a new, shorter current path forms after Townsend breakdown. Townsend breakdown is described for example in [41]. In every short-cutting process, before the real current path is formed, for example at t = 13.94 ms, a Townsend discharge is already evident at t = 13.68 ms.
3. When the plasma column is above the electrodes, there is a blurred emission signal around the plasma column. These emitting species help to form a new current path and then induce a short-cut event. (Especially see from t = 18 ms to 19.6 ms).

An example of the short-cut events captured in the fast movies is shown in Fig. 6. As shown in the frame for t = 50 μs, the short-cut current path (indicated by the red arrow) exists simultaneously with the previous, longer current path. After the new current path is formed, emission is still observed (in the dashed box). Its intensity slowly decays with time, as shown by the curve in Fig. 6. The decay time scale is on the order of 500 μs. The brightness of the plasma column seems homogeneous apart from strongly emitting regions appearing when the plasma column is oriented in the direction along the line-of-sight. It is notable that there is a blurred signal around the thin bright plasma column visible in Fig. 6.

Figure 7 shows the projected length of the plasma column in 10,000 continuous frames representing 200 ms recoding time. The number of CCD pixels illuminated by the plasma column was used to track the projected length of the plasma column. The shortest possible length of the plasma column is the gap width between the electrodes. This length is attained only at re-ignition which occurs three times in Fig. 7. The projected length of the plasma column generally increases with time but there are sudden drops at short-cutting events. In contrast to the re-ignition at the narrowest gap, the short-cutting events happen about 30 times. In other words, the period of new ignition was around tens to hundreds of milliseconds, while that of short-cutting events is less than 10 ms. The rates of new ignition and short-cutting events are strongly dependent on air flow rate, which will be reported elsewhere. It may be necessary to model short-cutting events if the ignition frequency of a gliding arc is to be predicted (e.g. [42]).

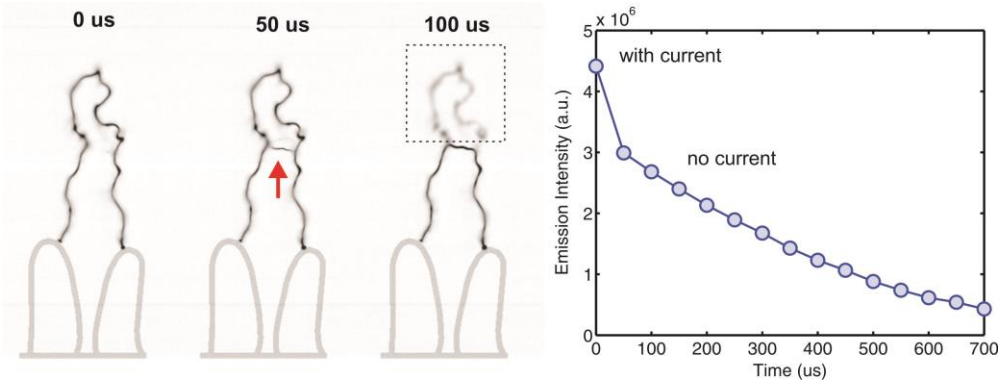


Fig. 6. An example of a short-cut event recorded at 20 kHz framing rate using an exposure time of 13.9 μs. The short-cut current path is indicated by the arrow in the frame of t = 50 μs where a Townsend breakdown occurs between the two legs of the plasma column, and a new current path forms. The integrated emission intensities of the plasma column (the part in the dashed box) are shown as a function of time to the right. A 50 kHz movie revealing the plasma evolution can be found in the supplements (*Media 1*).

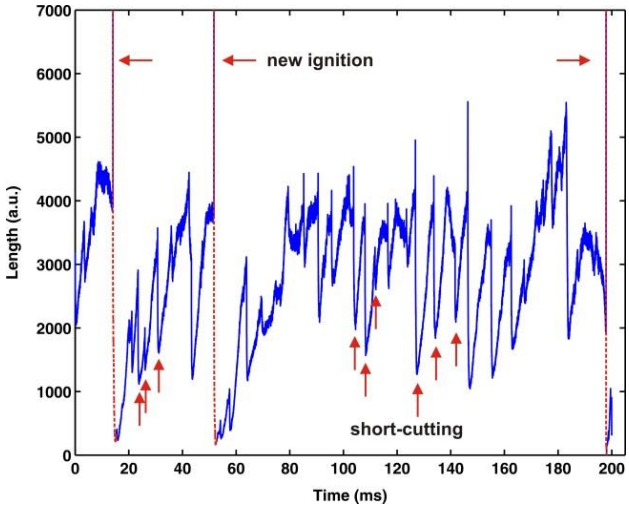


Fig. 7. The projected length of the plasma column in 10,000 continuously recorded frames. New ignition happened in tens to hundreds of ms while the time between two subsequent short-cutting events (only part of which were marked by the red arrow) was always less than 10 ms.

Figure 8 shows the integrated signal intensity (for wavelengths above 380 nm) as a function of the projected lengths reported in Fig. 7. The blue bar B denotes the shortest lengths of the plasma columns anchored at the top stationary points of the electrodes. The shorter lengths, i.e. to the left of the blue bar B, belong to plasma columns that glide up the electrodes from the ignition points to the stationary anchor points on the electrodes. The averaged emission intensity per unit length (proportional to the slope of every point with respect to the origin) varies with the length of the plasma column, and it decreases from *K1* to *K2* when the plasma column length increases. The emission per unit length shortly after the ignition (*K1*) was much stronger than that when the plasma column was well developed in non-equilibrium conditions. After the anchor points of the plasma column stabilized on the top of the electrodes, the unit length emission decreased much slower as the length of the plasma column increased compared with the region before bar B.

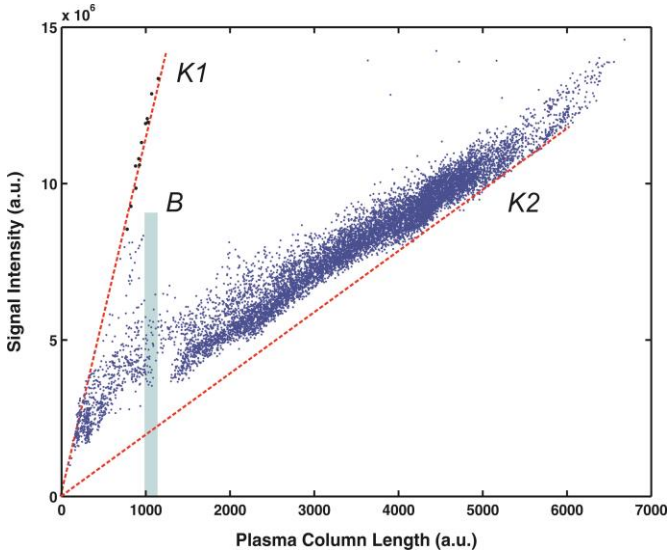


Fig. 8. The relation between integrated emission signal intensity and the projected length of the plasma column. Before the bar B, the anchor points of the plasma column were gliding up along the electrodes, and after that the anchor points were stationary on the top of the electrodes.

Using a framing rate of 420 kHz and an exposure time of 2.1 μs, the emission intensity variance in a half cycle of the 31.25 kHz power supply was temporally resolved. Fig. 9(a) shows sequential images of part of the plasma column. At the framing rate of 420 kHz, the camera observation region is limited to 64×128 pixels. Therefore only part of the plasma column was recorded. The emission intensity varied with time, i.e., with the supplied voltage within a half cycle while the shape of the plasma column was almost frozen during such a short period. The emission intensity of every frame as a function of time is shown in Fig. 9(b), where one can see a periodic change of the emission intensity with a quick increasing slope and a slower decaying slope. The intensity does not decay to zero, meaning the plasma column does always emit radiation. A Fourier transform of the emission intensity varied with time for 17,000 frames indicating that the dominant frequency was 62.5 kHz as the frequency of supplied power, i.e., twice the voltage driving frequency at 31.25 kHz. Since the high framing speed camera was not synchronized with the gliding arc timing system, the phase relation between the emission intensity and the supplied voltage was not measured.

The spatial location of the plasma column was investigated by statistically analyzing 17,000 images taken with 20 kHz framing rate. The plasma column position for every frame was obtained through image binary-conversion, and then the probability of spatial distribution was found by averaging all the frames, as shown in Fig. 10(a). The distribution probability is large near the top of the electrodes. The anchor points of the gliding arc on the electrodes move up to these positions and then stay there until the gliding arc extinguishes. Shown in Fig. 10(b) are examples of plasma column reaching this state in six consequent frames. The low part of the plasma column near the anchor points is rather stationary while the top part moves with the flow, which was also observed in the Schlieren movie, i.e., *Media 2*. Since sequential images of the plasma column were captured, projected velocities can be estimated. The velocity in the imaging plane was around 8 m/s for the top part of the plasma column, indicated by the red arrows, which is consistent with the nozzle exit velocity of about 40 m/s as the jet velocity has slowed down to such magnitudes at this location.

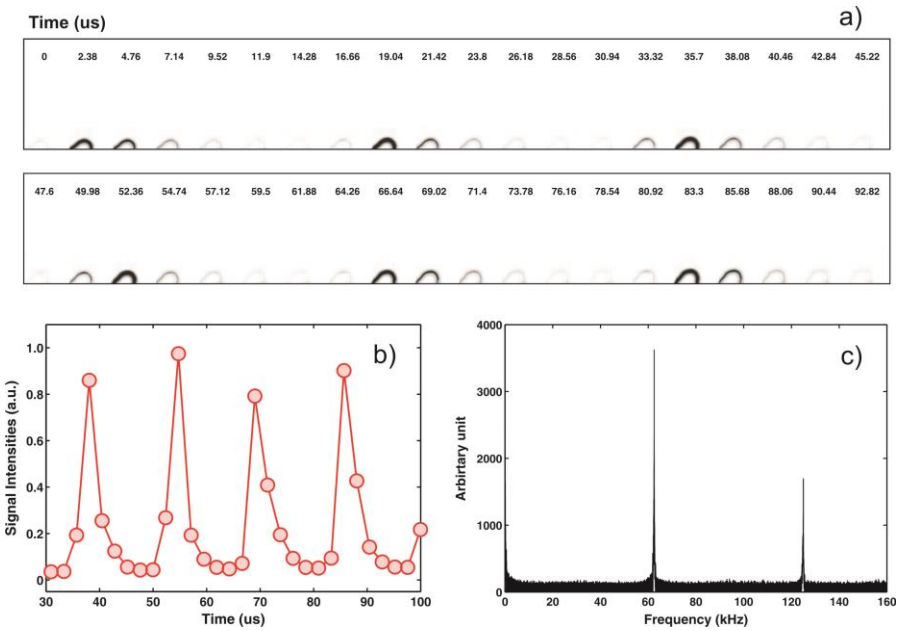


Fig. 9. (a) Sequential images of part of the plasma column. (b) The integrated emission intensity varying with time. (c) Fast Fourier transform for the curve in (b) for 17,000 frames.

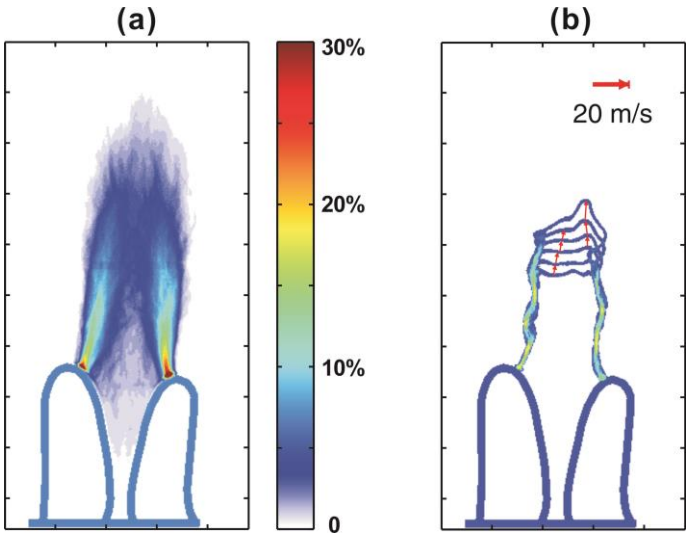


Fig. 10. (a) Distribution possibility of plasma column at 17.5 SLM air flow. (b) The estimated velocity of the plasma column using high frame rate images. The scaling velocity of 20 m/s is indicated showing that the upper part of the plasma column moves at about 8 m/s. High-speed Schlieren movie can be found in the supplements (*Media 2*).

High-speed Schlieren photography was intended for visualization of the flow fields and the temperature gradient generated by the gliding arc. The result is shown as *Media 2*. Compared with the thin and clearly structured filament in direct-view photographs (as shown in *Media 1* and Fig. 6), Schlieren photography did not show any sharp structure of the gliding arc column. This indicates that the ions are not much hotter than the surrounding air leading to small temperature gradients. The gas flow along the central axis moves fast while the outside part is rather stationary, which is consistent with the results shown in Fig. 10(b).

*3.2 Optical emission spectroscopy*

Spatially resolved emission spectra of the gliding arc running in continuous mode are shown in Fig. 11. The spectra were recorded by imaging different parts of the plasma plum to the input fiber tip of the spectrometer. The exposure time was 50 ms. The spectra at two different heights, *a* and *b*, are shown at the top of Fig. 11. Below H = 4.5 cm (the height of electrodes as shown in Fig. 1) $N_2$* rotational bands dominate the spectra, while above this position OH* rotational bands dominate and decrease at larger heights. NO emission exists at all heights, and the maximum intensity appears at around H = 5 cm. The OH bands belonging to the $X\ ^2\Pi$ – $A\ ^2\Sigma^+$ transition at around 308 nm are partially overlapped with some $N_2$* bands, which hinders the possibility of imaging the OH* spontaneous emission with spectral filters. Note that a broadband background appears above the electrodes. Two spectral structures at 592 nm and 780.5 nm were not identified, but will be investigated.

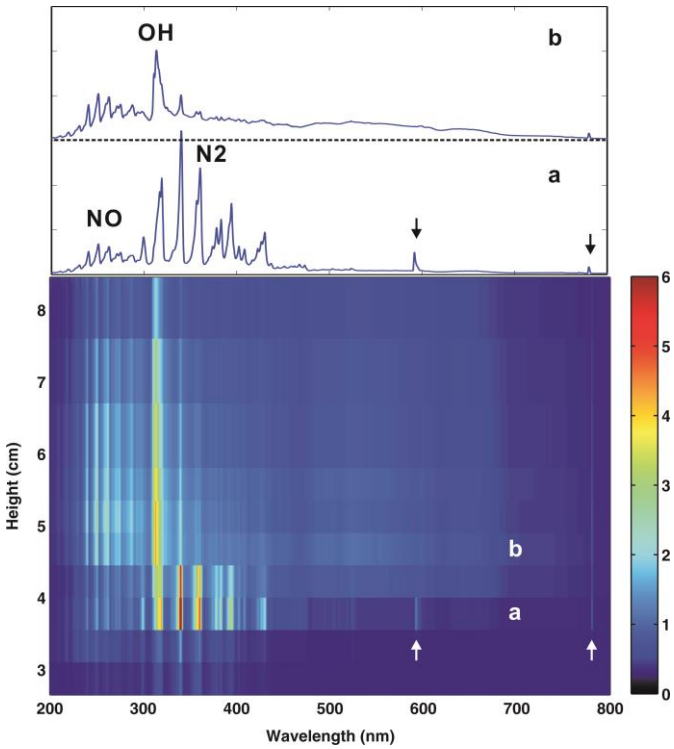


Fig. 11. Optical emission spectra of the gliding arc plasma recorded at different heights using a fiber-coupled spectrometer. The spectra at heights (a) and (b) are shown in curves to visualize the corresponding species.

Time-resolved optical emission spectra were recorded using the ICCD based imaging spectrometer. In this measurement, the gliding arc plasma was operated in the burst mode (10 Hz and Tp = 20 ms). The delay time between the gliding arc and the ICCD gate was adjusted using the time delay generator (for the cycle delay time TD) and the delay function in the ICCD software (for the phase delay time Td). The exposure time Tg of the ICCD was 5.3 µs enabling the resolve of a half period of the AC power. Figure 12 shows the emission spectra averaged over 100 frames at two different height ranges. The signals imaged on the ICCD were binned along the direction of the entrance slit. Therefore the two spectra shown in Fig. 12 were actually accumulated in the ranges of 0.4 – 1.8 cm (the middle height H = 1.1 cm) and 4.8 – 6.2 cm (the middle height H = 5.5 cm), respectively.

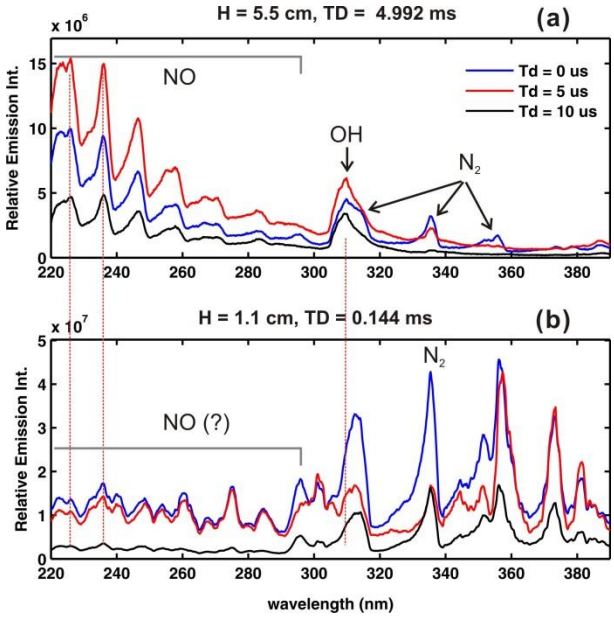


Fig. 12. Phase-resolved optical emission spectra of the plasma column at height ranges (a) 4.8 – 6.2 cm and (b) 0.4 -1.8 cm with the center at H = 5.5 cm and 1.1 cm, respectively. The gliding arc was operated in burst mode at 10 Hz. The camera exposure time was 5.3 μs and three Td values (0, 5, and 10 μs) were adopted, i.e., the emission in a half cycle was temporally resolved in a resolution of 5.3 μs. The spectra shown were averaged over 100 frames, and the intensity had been modified by the instrumental spectral response. Note the different intensity scales adopted in (a) and (b).

Figure 12 verifies the conclusion that emissions from NO*, OH* and $N_2$* vary with heights. $N_2$* bands dominate the emission source at lower positions (below the electrode top) while NO* and OH emissions dominate the positions above the electrodes. Besides the variation in space, the emission also varies within the voltage half cycle. In the newly ignited plasma column (TD = 0.144 ms, H=1.1 cm), OH* emission intensity decreased slightly with time as shown in the Fig. 12(b). Note that the magnitude and form of the line intensity variation depend on the particular band. The band emissions above 350 nm kept constant from Td = 0 μs to Td = 5 μs and decreased significantly from Td = 5 μs to Td = 10 μs. The band around 335 nm, however, acted in the opposite way. It might be explained by the changes of vibrational temperature of $N_2$ in a half cycle. The spectral structure below 290 nm in Fig. 12(b) could not be clearly assigned to any species. Nevertheless, two band peaks of NO* around 225 and 235 nm were identified.

When the plasma column moved up to H = 5.5 cm (above the electrodes) at TD = 4.992 ms, the OH and NO spectral structures were clearly identified besides that of $N_2$*. At this height, within half cycles the $N_2$* emission decreased with time while the emissions from NO* and OH* increased first and then decreased. The spectral structure of NO* did not vary with time indicating that the ambient temperature did not change much over the half cycles at this height where the plasma column is in a non-equilibrium condition.

The above results of phase-resolved emissions indicate that the characteristics of the plasma column vary within a half cycle, i.e., they follow the supplied AC voltage. Also the variance of the plasma column characteristics within every half cycle depends on the height of plasma column. Lastly, we note that these dependencies also greatly depend on the flow rate of air, which will be reported elsewhere.

*3.3 PLIF of ground-state OH radicals*

The ground-state OH radicals were measured using PLIF. The laser beam sheet was sent vertically through the two electrodes containing the central line of the jet and crossed the plane defined by the two electrodes at 45 degrees. The laser pulse duration was about 6 ns, and the effective OH fluorescence lifetime is less than a couple of nanoseconds, meaning most OH-PLIF signal was captured by the ICCD using a short gating time (30 ns in this work). Using a longer gating time (2 μs in this work) the OH-PLIF and the optical emission from the plasma column can be simultaneously captured. Note that, due to the filters (UG5 + WG295) installed in front of the ICCD objective, the emission from the plasma column comes from OH* and part of $N_2$* (see Fig. 11), which differs from the images recorded by the high-speed camera.

Figure 13 shows two PLIF images recorded at two different ICCD gate times, 30 ns and 2 μs, respectively. The OH-PLIF shows a hollow structure, indicating that ground-state OH surrounds the plasma column containing excited OH and $N_2$. This is verified in the image (the red arrow) recorded with 2 μs gating time in Fig. 13 where the plasma column was recorded as well by optical emissions. The ground-state OH is transported from the plasma column and its spatial structure is thicker than the plasma column. As shown by the white arrow in Fig. 13, OH radicals still survive even after local extinction of the plasma column (the current path) during short-cutting events. A zoom-in of the OH hollow structure is shown in Fig. 14. The thickness of ground-state OH layer was about 3 mm, and the hollow structure is clearly shown. At the *center* of the hollow structure, the PLIF signal intensity is almost at background level.

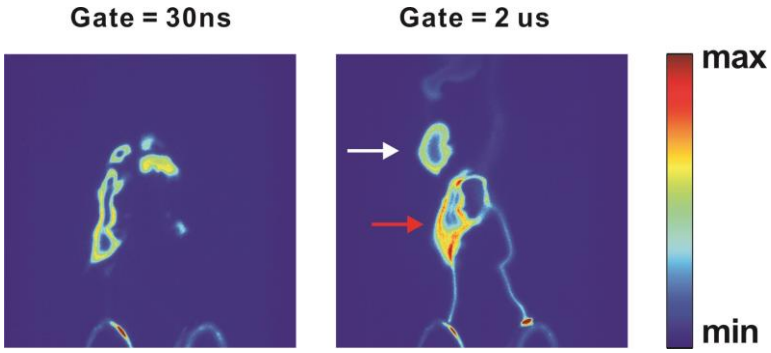


Fig. 13. Single-shot OH PLIF images captured using the ICCD with two gate times, (*left*) 30 ns for only capturing PLIF signal of ground-state OH and (*right*) 2 μs for capturing both OH-PLIF signal and plasma column emission. Ground-state OH is located around the plasma column (the red arrow), therefore a hollow structure appears in the OH-PLIF image to the right. Even when the current path is extinct, the ground-state OH still survives (the white arrow). The laser beam sheet contained the central line of the jet between the two electrodes and crossed the plane defined by the electrodes at an angle of 45 degrees.

One may speculate that the hollow structure in the OH PLIF was due to the high temperature in the center of the plasma column which caused the volume number density of OH to become too low to be imaged. This explanation would require hot ions on the order of 1eV, but the ions in our experiments were much colder. A reasonable explanation might be that the ground-state OH is formed from OH* by energy release and the formation happens during the species transport. In the single-shot spatially resolved spectra of the plasma column, as shown in Fig. 15, OH* is located in the inner part of the plasma column with a thickness of around 4 mm. It is very likely that the OH* is mainly generated by electron impact dissociation of $H_2O$ [43]. However, the reasons for OH hollow profile should be further investigated using a kinetic model.

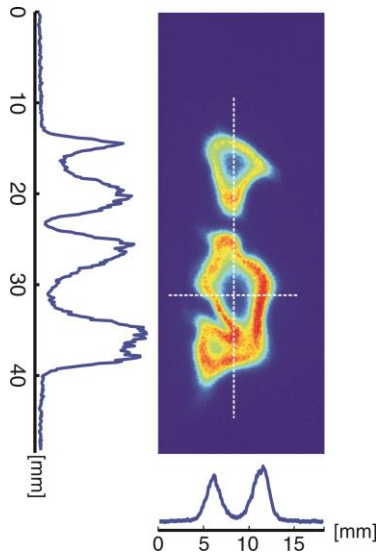


Fig. 14. OH PLIF image collected above the electrodes. The laser beam sheet contained the central line the jet between the two electrodes and perpendicularly crossed with the plane defined by the two electrodes. Vertical and horizontal cross sections of OH PLIF distribution show the thickness of OH radical in this case.

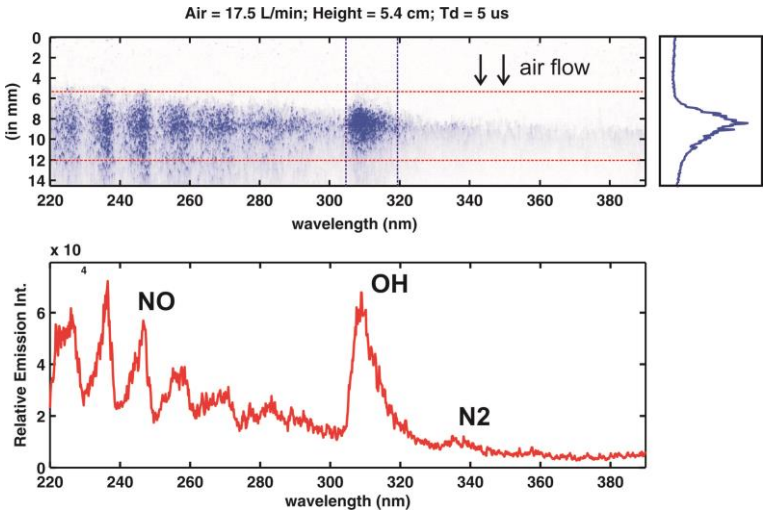


Fig. 15. (*upper*) Spectrally and spatially resolved, single-shot image of the plasma column in the VU spectral region recorded by an imaging spectrometer (gate time = 5.3 μs). (*upper right)* cross section in the area between two blue dash line. (*lower*) the spectra integrated in the area between two red dash lines.

Besides detailed structure investigation from single-shot OH PLIF, phase-averaged PLIF images can show ground-state OH global distribution in space and in time. The variance of OH PLIF signal intensity in a half cycle of the AC driving power was investigated when the gliding arc worked in continuous mode. The result based on the average of 100 frames is shown in Fig. 16(a). OH PLIF signal intensity is clearly independent of time and hence the supplied voltage. This is explained by the long lifetime of the ground-state OH radicals. After the ground-state OH radical is formed in the outer layer of plasma column, it survives more than a half cycle (16μs). Since the ambient temperature was relatively constant, Fig. 16(a) also indicates the concentration of OH is constant with time. Compared with PLIF signal, emission

intensities vary clearly with time, as shown in Fig. 16(b). Around the middle of the half cycle, i.e., at t = 8 μs, the emission intensity increases significantly which is consistent with Fig. 9(a). Note that emission from excited $N_2$ also contributed to the intensity level in Fig. 16(b).

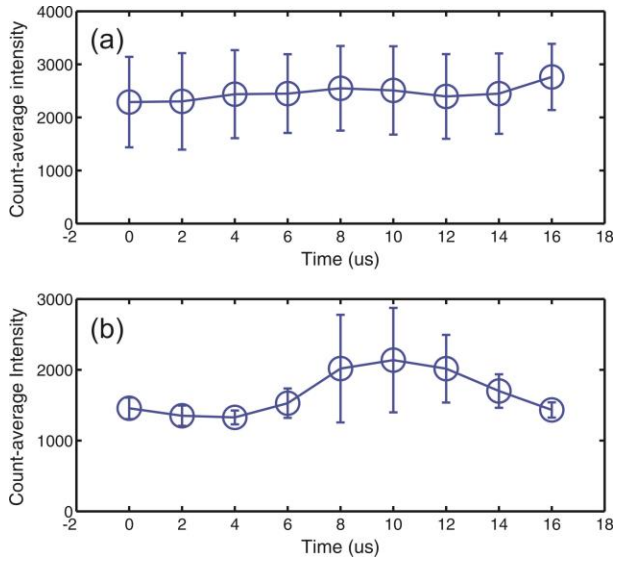


Fig. 16. (a) OH PLIF signal intensity as a function of time in a half cycle. (b) The emission intensity of plasma column (290 nm – 405 nm) in a half cycle. The averaged signals were based on 100 frames and the plasma column length had been counted. The zero point in the time scales indicated the beginning of a half cycle, when V(voltage) = 0. The gliding arc was synchronized with the laser and the ICCD camera.

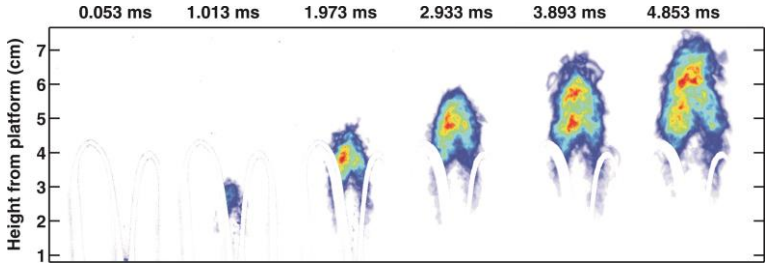


Fig. 17. The evolution of ground-state OH global distribution by accumulating 120 shots of OH-PLIF. The gliding arc discharge was run in the burst mode, and the phase delay time Td was kept at 8 μs. The plasma delay times TD are shown above the images.

The evolution of the ground-state OH global distribution was investigated by running the gliding arc plasma discharge in the burst mode. While keeping the phase delay time Td = 8 μs, the global distribution of OH radicals was captured by imaging accumulations, as shown in Fig. 17. Besides the expansion of OH distribution with the delay time TD, the signal intensity of OH PLIF also increased. The integrated OH PLIF signal intensity and the top height of the plasma column are plotted in Fig. 18 as a function of the delay time TD. It shows that with increase of the delay time, OH radicals distribute to a wider and higher region and the integrated signal intensity increased significantly. The velocity of the plasma column is estimated by the differentiation of the polynomial fit of plasma height, and the result of around 10 m/s above the electrodes (i.e. TD = 2.5 - 5 ms) is consistent with that shown in Fig. 10(b). In the early stage (i.e. for small TD values, 0 – 1 ms), the OH radical distribution changed with a high speed of around 25 m/s, which is consistent with the nozzle exit velocity of about 40 m/s.

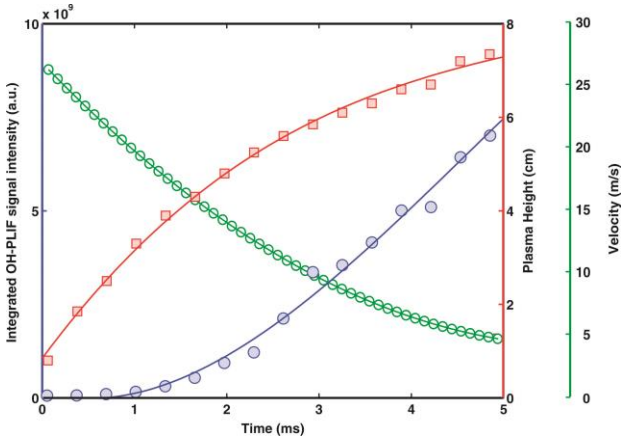


Fig. 18. Integrated signal intensity of OH PLIF and the height of the GA plasma column as a function of time TD shown as filled circles and squares, respectively, and the solid lines are the polynomial fits. The velocity of the gliding arc plasma evolution is estimated by differentiating the polynomial fit (the blue solid line) of plasma height.

## 4. Conclusions

The evolution of a gliding arc discharge has been investigated using multi-kHz high-speed movies and Schlieren images, spatial and temporally resolved optical emission spectroscopy, and PLIF. Short-cut events in the plasma column were tracked and shown to occur about ten times more often than the re-ignition of the discharges in the narrowest gap between the electrodes. This type of short-cut events reduces the re-ignition of the gliding arc, hence improves the efficiency of the production of non-equilibrium plasma generation. Townsend discharges were observed at the beginning of the short-cut events. It was found that the re-ignitions between the electrodes occur while the previous plasma column still exists. After formation of the new plasma column, the previous plasma column decays. In the direct optical emission measurements, it was found that excited $N_2$ dominated upstream near the electrodes whereas OH and NO were the main emitting species downstream. The emission intensity varied within a half cycle of the AC voltage (16 μs). Especially, $N_2$ emission had a different variance compared with NO and OH. The emission intensity per unit length of plasma column becomes weaker during the evolution of the gliding arc discharge, but the changes become smaller when the gliding arc develops. From high-speed images, the emission intensity variance of the plasma column within a half cycle was clearly observed with a time resolution of 2 μs. Moreover, PLIF was applied to reveal the distribution of the ground-state OH. A hollow structure was found in the single-shot images of OH, which might be explained by the ground-state OH formation from the decay of excited OH. The exploration of further details of the complicated processes in a gliding arc will challenge more advanced techniques such as quantitative PLIF measurements of key radicals with up to multi-kHz framing rate.

## Acknowledgment

This work was financially supported by the Swedish Energy Agency, CECOST (Center for Combustion Science and Technology), VR (Swedish Research Council) and European Research Council (Grant No. 246850). Financial support from the Ministry of Science, Technology and Innovation through the National Danish Proof of Concept Funding Scheme (grant number: 09-076196) was also acknowledged.

# [Appendix A9]

J.J. Zhu, Z.W. Sun, Z.S. Li, A. Ehn, M, Aldén, M. Salewski, F. Leipold, Y. Kusano

## "Dynamics, OH distributions and UV emission of a gliding arc at various flow-rates investigated by optical measurements"

*Journal of Physics D: Applied Physics* 47 (2014) 295203.

IOP Publishing
Journal of Physics D: Applied Physics
J. Phys. D: Appl. Phys. **47** (2014) 295203 (11pp)
doi:10.1088/0022-3727/47/29/295203

# Dynamics, OH distributions and UV emission of a gliding arc at various flow-rates investigated by optical measurements

**Jiajian Zhu[1], Zhiwei Sun[1], Zhongshan Li[1], Andreas Ehn[1], Marcus Aldén[1], Mirko Salewski[2], Frank Leipold[2] and Yukihiro Kusano[3]**

[1] Division of Combustion Physics, Lund University, P O Box 118, S-221 00 Lund, Sweden
[2] Department of Physics, Section for Plasma Physics and Fusion Energy, Technical University of Denmark, DK-2800 Kgs. Lyngby, Denmark
[3] Department of Wind Energy, Section for Composites and Materials Mechanics, Technical University of Denmark, Risø Campus, Frederiksborgvej 399, DK-4000 Roskilde, Denmark

E-mail: Zhongshan.li@forbrf.lth.se

Received 9 April 2014, revised 16 May 2014
Accepted for publication 4 June 2014
Published 26 June 2014

**Abstract**

We demonstrate a plasma discharge which is generated between two diverging electrodes and extended into a gliding arc in non-equilibrium condition by an air flow at atmospheric pressure. Effects of the air flow rates on the dynamics, ground-state OH distributions and spectral characterization of UV emission of the gliding arc were investigated by optical methods. High-speed photography was utilized to reveal flow-rate dependent dynamics such as ignitions, propagation, short-cutting events, extinctions and conversions of the discharge from glowtype to spark-type. Short-cutting events and ignitions occur more frequently at higher flow rates. The anchor points of the gliding arc are mostly steady at the top of the electrodes at lower flow rates whereas at higher flow rates they glide up along the electrodes most of the time. The afterglow of fully developed gliding arcs is observed to decay over hundreds of microseconds after being electronically short-cut by a newly ignited arc. The extinction time decreases with the increase of the flow rate. The frequency of the conversion of a discharge from glow-type to spark-type increases with the flow rate. Additionally, spatial distributions of ground-state OH were investigated using planar laser-induced fluorescence. The results show that the shape, height, intensity and thickness of ground-state OH distribution vary significantly with air flow rates. Finally, UV emission of the gliding arc is measured using optical emission spectroscopy and it is found that the emission intensity of NO $\gamma$ (A-X), OH (A-X) and $N_2$ (C-B) increase with the flow rates showing more characteristics of spark-type arcs. The observed phenomena indicate the significance of the interaction between local turbulence and the gliding arc.

Keywords: plasma diagnostics, gliding arc, nonthermal plasma

(Some figures may appear in colour only in the online journal)

## 1. Introduction

A gliding arc discharge can be an excellent source of non-equilibrium plasma. Driven by a high voltage, ionized gas initially forms a plasma column at the closest gap between two diverging electrodes. The plasma column is blown to glide along the electrodes by a gas flow to form a gliding arc [1]. Buoyant forces can also produce a gliding arc, but they are much smaller than the aerodynamic forces in the presence of a high flow rate gas jet [2]. A gliding arc is able to achieve a non-equilibrium state characterized by high electron temperature and low gas temperature [3, 4]. Furthermore, a gliding arc

 

potentially has high electron densities and can be operated at atmospheric pressure [5], which makes it stand out from most non-equilibrium plasmas, and widely usable in combustion enhancement [6, 7], surface treatment [8–13], airflow control [14], gas conversion and decontamination [15–18]. In these applications, it has been found that the gas flow rate is a crucial parameter affecting lifetimes of excited species [4], treatment efficiency for adhesion improvement [9] and conversion rates of foul gases [17]. Moreover, previous studies reported that flow rates primarily affected breakdown voltage [19] and transitions between thermal and non-thermal properties of a gliding arc [20]. However, in spite of the significant influence of flow rates on operating a gliding arc, there are few experimental results that have systematically investigated the effect of flow rates. This kind of experimental data is required for understanding the fundamental mechanisms of a gliding arc with effective turbulence–discharge interactions.

The experimental results recorded on different types of gliding arcs are often limited to electrical diagnostics, e.g. current–voltage characteristics [5, 19, 20], whereas optical diagnostics, especially laser-based diagnostics, have traditionally seldom been used to investigate gliding arcs. It has been shown that high-speed photography is an effective way to capture evolution processes of a gliding arc and to investigate the arc dynamics [21, 22]. Spectrally resolved emission spectra of excited species, e.g. $N_2^*$, OH* and NO*, provide the corresponding rotational and vibrational temperatures that reveal the thermal evolution of excited species [23, 24]. However, spontaneous emission was typically recorded with low temporal or spatial resolution. Furthermore, some reactive species may also be in the ground state and hence be invisible to optical emission spectroscopy. Planar laser-induced fluorescence (PLIF) is a powerful technique for visualization of the distribution of the ground-state species [25]. These three optical methods, i.e. high-speed photography, optical emission spectroscopy and OH-PLIF imaging have been successfully applied to characterize a gliding arc operated at a fixed gas flow rate in one of our previous works [26]. It was found that the flow rate strongly affects the performance of the gliding arc, which is also shown in figure 1.

Therefore, the present work focuses on the effects of the gas flow rate on the behaviour of the gliding arc using optical methods. High-speed photography was employed to investigate effects of flow rates on the dynamics of the gliding arc including ignitions, propagation, short-cutting events, extinctions and conversions. OH-PLIF was performed to measure spatial distributions of OH radicals in their ground-state. Optical emission spectroscopy was applied to study UV emission from the gliding arc.

## 2. Experimental setup

### 2.1. Gliding arc discharge system

The gliding arc discharge system established in open air consists of three primary components: electrodes, an air flow and a power supply. Since a similar system was used in our previous work [26], only a brief description of these components is given here. The electrodes are made of stainless steel and fixed on a Teflon plate (see figure 1). The hollow tubular electrodes with an outer diameter of 3 mm are internally water-cooled. One of the electrodes is connected to the high voltage power supply and acts as a powered electrode while the other serves as a ground electrode.

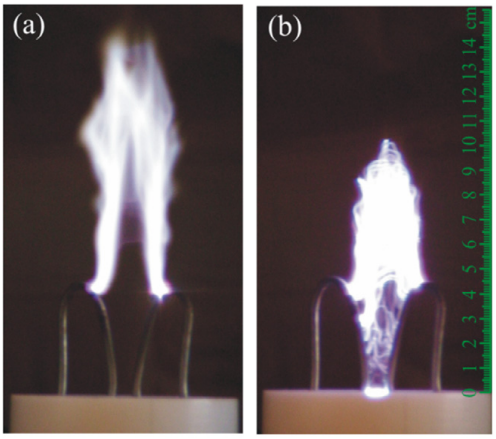


**Figure 1.** Photos of gliding arcs operated at flow rates of (*a*) 14 SLM (standard litres per minute) and (*b*) 42 SLM. The exposure time was 1/30 s.

**Table 1.** Experimental flow rates, exit velocities, Kolmogorov lengths, Reynolds numbers and ac input powers.

| Flow rate (SLM) | $V_{exit}$ (m s$^{-1}$) | $\eta$ ($\mu$m) | Re | Power (kW) |
|---|---|---|---|---|
| 14 | 33 | 1000 | 6400 | 0.65 |
| 17.5 | 41 | 851 | 8000 | 0.78 |
| 21 | 50 | 436 | 9600 | 0.98 |
| 31.5 | 74 | 97 | 14 400 | 1.08 |
| 42 | 99 | 60 | 19 200 | 1.10 |

The air flow from an air compressor was supplied through a 3 mm diameter hole in the Teflon plate between the two electrodes. The relative humidity of the compressed air was measured to be 36% using a humidity monitor and the amount of the water vapour was estimated to be 8 g m$^{-3}$. Flow rates used in the present experiments were controlled by a mass flow controller (MFC) and are summarized in table 1, where the corresponding exit velocities and Reynolds (Re) numbers at the different flow rates are also given. The Reynolds number can be written as $\mathrm{Re} = \rho v D \mu^{-1}$, where $\rho = 1.16\,\mathrm{kg\,m^{-3}}$ is the air density, $v$ is the exit velocity, $D = 3$ mm is the hole diameter in the Teflon plate, and $\mu = 1.8 \times 10^{-5}\,\mathrm{kg\,m^{-1}\,s^{-1}}$ is the dynamic viscosity of air. The Re numbers were larger than 6000 and hence the flows were turbulent at all flow rates. Based on the experimental data of jet flow velocity in the self-similar region [27], an estimation of the Kolmogorov length ($\eta$) is given in table 1, assuming that the translational gas temperature in the vicinity of the gliding arc is 1500 K [28]. The Kolmogorov length is the smallest size of turbulence

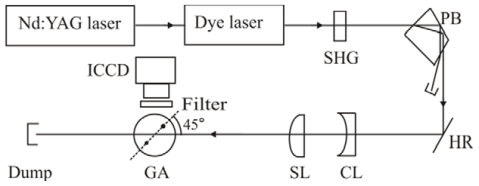


**Figure 2.** Experimental setup for OH-PLIF measurements. SHG, second harmonic generator; PB, Pellin-Broca prism; HR, high reflection mirror; CL, cylindrical lens; SL, spherical lens; GA, gliding arc. The two dots represent the electrodes seen from the top and the laser sheet passes through the middle between the electrodes and forms an angle of 45° with the plane containing the electrodes.

eddies, which can be expressed as $\eta = \left(\nu^3\epsilon^{-1}\right)^{0.25}$, where $\epsilon$ is the average dissipation rate of turbulent kinetic energy per unit mass, and $\nu$ is the kinematic viscosity of the fluid. The Kolmogorov length ranges from 1 mm (for the 14 SLM case) to 60 $\mu$m (for the 42 SLM case). Typical photos of gliding arcs operated at two different air flow rates are shown in figure 1.

The power of the discharge system is provided by a high voltage alternating current (ac) power supply (Generator 6030, SOFTAL Electronic GmbH, Germany). The ac power supply is operated at a frequency of 31.25 kHz and it delivers the input power to the gliding arc, which increases from 0.65 to 1.1 kW as the flow rates increases [9], as shown in table 1. The power supply can be operated both in a continuous or a burst mode by programming a signal generator [26]. In the burst mode, the gliding arc runs at a 10 Hz repetition rate with burst duration of 20 ms. The purpose of operating the gliding arc in the burst mode is to facilitate the synchronization of the ac voltage phase with the detection systems. The continuous mode was employed for diagnosing dynamics of the gliding arc and spatial distributions of ground-state OH radicals while the burst mode was employed in the spectroscopic study of the UV emission.

### *2.2. Optical diagnostic system*

A high-speed camera (Photron Fastcam SA5) with a frame rate of 20 kHz and an exposure time of 13.9 $\mu$s was employed to record instantaneous images of the gliding arc. The spatial resolution of the high-speed camera is about 0.2 mm. The emission of the gliding arc in the range 380–980 nm was collected with a Nikon glass lens ($f = 50$ mm).

The experimental setup of OH-PLIF imaging is illustrated in figure 2. A frequency-doubled Nd : YAG laser (Quantel, Brilliant B) providing a 532 nm beam was used to pump a dye laser (Continuum ND60). The dye laser, running with Rhodamine 590 as dye, was tuned to 566.536 nm and frequency-doubled using a second harmonic generation (SHG) crystal. The laser beam at 283.268 nm was separated from the fundamental wavelength in a Pellin-Broca (PB) prism and then directed into a cylindrical lens (CL, $f = -40$ mm) and spherical lens (SL, $f = 500$ mm) by a high reflection mirror (HR) and formed into a vertically oriented laser sheet. The laser sheet passed between the electrodes and cut the plane

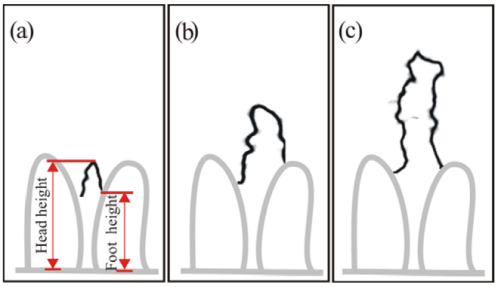


**Figure 3.** Propagation of a gliding arc at an air flow rate of 17.5 SLM revealed with instantaneous images recorded at (*a*) $\Delta t = 1$ ms, (*b*) $\Delta t = 2$ ms and (*c*) $\Delta t = 3$ ms after ignition. The exposure time of the camera was 13.9 $\mu$s. The definitions of head height and foot height are also shown.

containing the two electrodes at an angle of 45°. The laser sheet excited the OH transition and fluorescence at around 308 nm was detected by an intensified charge-coupled device (ICCD) camera (Princeton PI-MAX II). Filters (UG5+WG295) were placed in front of the ICCD camera to suppress scattered laser light. The transmittance curve of the filters was measured using a spectrophotometer (T60 UV/VIS) and is shown in the figure 14. Two different exposure times were adopted: 30 ns was used to reduce the spontaneous emission of the gliding arc and to capture the relatively pure ground-state OH PLIF signal; 2 $\mu$s was employed to record the spatial distributions of both the ground-state OH and the arc emission simultaneously.

An imaging spectrometer (SP-2300i, with a 150 groves/mm grating) equipped with an ICCD camera (Princeton PI-MAX III) was used to record the UV emission at 220–390 nm. The spectral response of the spectrometer was calibrated using a deuterium lamp. The slit of the spectrometer was vertically oriented, allowing the ICCD camera to observe a spatially resolved height range of 1.4 cm. Emission spectra centred at a height of 5.5 cm were acquired. The ICCD camera, with an exposure time of 5.3 $\mu$s, was synchronized precisely to the gliding arc in each burst of discharges, capturing spectra not only at the chosen phase of the ac driving power but also roughly in the same location in every cycle. The camera gate was set to acquire the initial stage of a half period (16 $\mu$s) of the ac driving voltage.

## 3. Results and discussion

### *3.1. Effects of flow rate on the gliding arc dynamics*

The gliding arc forms a conductive channel presented as a visible string connecting the two electrodes. Its dynamics include ignitions, propagation, short-cutting events, extinctions and conversions of the conductive, visible string.

*3.1.1. Propagation, short-cutting events and ignitions.* Propagation of the gliding arc is shown in figure 3, where the time delay between the sequential frames was 1 ms. The gliding arc generated between the electrodes propagated

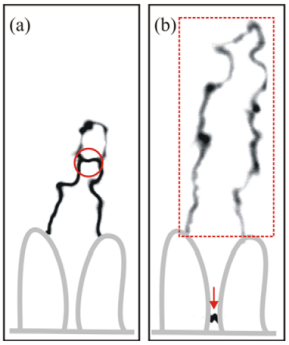


**Figure 4.** Typical images of the gliding arc taken by a high-speed camera showing (*a*) a short-cutting event (circle) and (*b*) an ignition (arrow) at an air flow rate of 17.5 SLM. Emission (marked by the rectangle) from the fully developed arc is still visible right after the ignition.

upwards with the gas flow. As illustrated in figure 3(*a*), the head height and foot height are defined as the distances from the top of the gliding arc and the anchor point on the electrode to the bottom, respectively. Both the head height and the foot height gradually increase as the gliding arc propagates, as shown in figures 3(*a*)–(*c*).

Apart from propagation of the gliding arc, short-cutting events and ignitions are also observed during the evolution of the gliding arc. Figure 4(*a*) shows a typical short-cutting event of the gliding arc, where a new current path forms (marked by a circle). When the short-cutting event takes place, the head height decreases, but the foot height is maintained. Figure 4(*b*) shows an ignition event of the gliding arc where a new arc is ignited at the smallest gap between the two electrodes (marked by an arrow). Compared to the short-cutting event, where only the head height is reduced, the ignition reduces both the head height and the foot height. Therefore, the head height and foot height can be used to identify the short-cutting events and ignitions in analyzing a large number of images taken by the high-speed camera. Short-cutting events and ignitions were also observed in [29, 30]. Additionally, figure 4(*b*) shows that emission (marked by a rectangle) from the fully developed arc is still visible right after the ignition. These dynamic processes are found to be strongly affected by flow rates, which will be discussed in the following sections.

As discussed earlier, a short-cutting event only decreases the head height of the gliding arc, while an ignition significantly reduces both the head height and the foot height. Statistics were performed based on 10 000 sequential images. Figure 5 shows the identified short-cutting events and ignitions by compiling statistics on the head height and the foot height at different air flow rates. In order to clearly show the fluctuations of the head height and the foot height, only 2000 sampling points covering a time interval of 100 ms are displayed in figures 5(*a*)–(*c*) and 400 sampling points covering a time interval of 20 ms are displayed in figures 5(*d*)–(*e*). The occurrences of typical short-cutting events and ignitions are marked in figure 5 by circles and arrows, respectively.

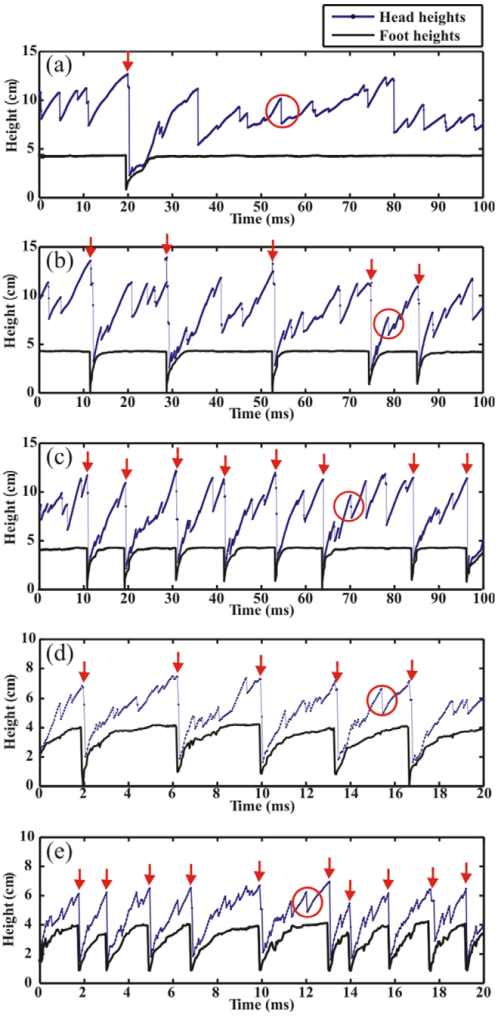


**Figure 5.** Identified short-cutting events and ignitions by statistical analysis of the head height and the foot height of the high-speed photography within 100 ms for flow rates at (*a*) 14 SLM; (*b*) 17.5 SLM; (*c*) 21 SLM; and within 20 ms for (*d*) 31.5 SLM; (*e*) 42 SLM. Ignitions are marked by arrows and a typical short-cutting event is marked by circle.

The short-cutting events and ignitions take place more frequently with increasing flow rates. Furthermore, a striking difference in the foot heights can be observed at different flow rates. For lower flow rates, e.g. 14, 17.5 and 21 SLM, the foot heights are almost constant at about 4 cm for a large fraction of the time. The head height often reaches approximately 11 cm. For higher flow rates, e.g. 31.5 and 42 SLM, the gliding arc spends most of the time gliding up the electrodes. When the foot height reaches the top position at 4 cm, the plasma column extinguishes rapidly and a new plasma column is formed at

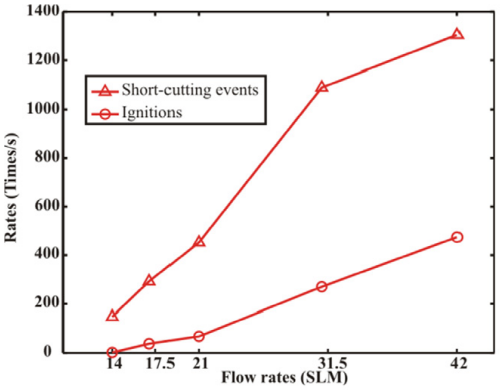


**Figure 6.** Rates of short-cutting events and ignitions at different air flow rates. Each data point is based on statistics from 10 000 images.

the closest gap between the electrodes, resulting in a short extension length of the plasma channel as observed in figure 1. These results partly explain the better performance observed at lower flow rates for surface treatment applications [9–11].

Figure 6 shows rates of the short-cutting events and the ignitions at different flow rates. The rate is defined as the number of short-cutting events or ignitions per second. The occurrence of short-cutting events and ignitions are identified using the ratio of head heights in two sequential images. Higher ratios (ratios $>$ 2.1) suggesting a significant height decrease of the gliding arc correspond to ignitions while lower ratios (2.1 $>$ ratios $>$ 1.05) suggesting a less significant height drop correspond to short-cutting events. The total number of ignitions and short-cutting events is recognized using the ratio method and then the corresponding rates are calculated. As shown in figure 6, an ignition of the gliding arc at a flow rate of 14 SLM takes place rarely, while the number of ignitions rises significantly with increasing gas flow rate. The number of short-cutting events also increases when air flow rates increase from 14 to 42 SLM. The increasing rate of short-cutting events at higher flow rates has also been observed for the gliding arc in helium and argon [30].

More frequently occurring ignitions at higher flow rates are due to the stronger turbulent convection cooling. At higher flow rates, a larger fraction of energy provided by a power generator will be transferred to heat loss due to stronger turbulent convection cooling, and then less electrical energy will be used to create ions and electrons. Therefore, the conductive channel at a higher flow rate is thinner and the corresponding resistance tends to be larger. The larger resistance of the conductive channel at a high flow rate easily promotes the increase of the voltage drop on the arc. When the voltage drop is as large as the breakdown voltage, a new ignition at the narrowest gap between the electrodes is more likely to occur. The higher rate of short-cutting events at higher flow rates can be explained by the stronger turbulence intensity. The turbulence intensities at different flow rates are characterized by the Re numbers, which are summarized in table 1. Higher gas flow rates generate stronger

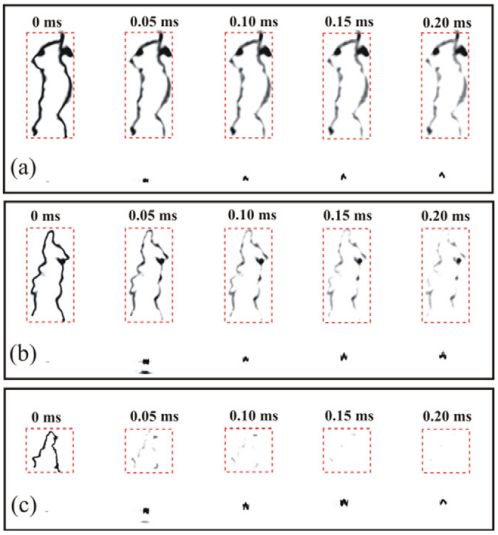


**Figure 7.** Extinction processes of a fully developed arc at different air flow rates (*a*) 14 SLM; (*b*) 21 SLM and (*c*) 42 SLM. The extinction process is shown in the dashed rectangles. At $t = 0$ ms, the gliding arc is fully developed, and then it gradually extinguishes in the following frames when a new arc ignites at the bottom. The emission taken by the high-speed camera is at a wavelength range of 380–980 nm.

turbulent eddies and vortices, which irregularly stretch the gliding arc and lead to more frequent short-cutting events of the gliding arc.

*3.1.2. Extinction time.* The emission intensity from a fully developed gliding arc is decaying exponentially in time after a new gliding arc is ignited. Figure 7 shows the extinction processes of the fully developed gliding arc within 0.2 ms after the ignition of a new gliding arc. At $t$ =0 ms, the gliding arc is fully developed and then a new ignition occurs in the next frame. After that, the emission of the fully developed gliding arc starts to gradually diminish. The diminishing gliding arc tends to fade more quickly with increased air flow rates, as illustrated in figure 7.

The intensity of the fading emission, as displayed in the dashed rectangle in figure 7, is integrated in each frame to provide a quantitative decay rate of the afterglow. These decay curves are normalized and displayed in figure 8. An exponential function $I = I_0 e^{-t/\tau}$ is used to fit the intensity–time dependence, and the extinction time is defined as the time when the ratio of the intensity is reduced to $e^{-1}$. It can be seen that the extinction time is significantly reduced with increasing air flow rates. Specifically, the gliding arc at 14 SLM has the longest extinction time of 0.9 ms while it falls to 0.5 ms at 21 SLM and further decreases to 0.15 ms at 42 SLM. The emission from the fading gliding arc can be attributed to the presence of residual excited species. Faster extinction time at higher flow rates is expected due to larger convective transport rates and subsequent dissipation of the excited species.

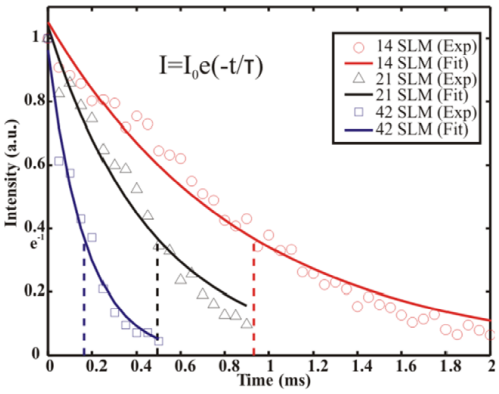


**Figure 8.** Extinction time of the fading gliding arcs at three different air flow rates. The circle, triangle and square markers show the experimental results while the solid lines indicate the corresponding fittings. The normalized average intensity is obtained by integrating the emission intensity of the fading gliding arc shown in each rectangle of figure 7.

*3.1.3. Glow-type to spark-type conversions.* Figure 9 shows statistics of the integrated arc emission intensity against projected arc length measured over 10 000 images for different flow rates. Each point represents an image taken by the high-speed camera where the lengths of the arc projections on the image plane are recorded. In figures 9(*a*)–(*c*), the gliding arcs at 14, 17.5 and 21 SLM can expand to a projected length of 16–18 cm while the gliding arcs at 31.5 and 42 SLM are limited to just 6–7 cm.

The brightness of the gliding arc can be regarded as the integrated arc emission intensity per unit length, and therefore the slope of the line connecting the point to the origin represents the brightness of the gliding arc. At a flow rate of 14 SLM and 17.5 SLM as shown in figures 9(*a*) and (*b*), most of the points follow the red lines with a slope of 1.81 and 1.44, respectively, indicating almost constant brightness of the plasma column while it becomes longer. However, for a flow rate of 21 SLM, as shown in figure 9(*c*), there are some points distributed far from the red line, showing stronger plasma column intensity and higher brightness. As the flow rate further increases, as shown in figures 9(*d*) and (*e*), the points with much higher brightness become more frequent or even dominate.

One can already find from photos shown in figure 1 that the gliding arc appears as a diffusive glow-type discharge for low flow rates and bright spark-type filaments for higher flow rates. Through analysing the instantaneous plasma column images shown in figure 10(*a*), one can find that some much brighter plasma columns exist among their neighbouring images, which might indicate a prompt conversion of glow-type discharge to spark-type discharge. A similar phenomenon has been previously observed and described in [31]. With increasing flow rate, turbulent convection causes intermittent energy dissipation from the plasma column and consequently a tendency toward conversions from glow-type discharge to spark-type. If the power supply could provide enough energy

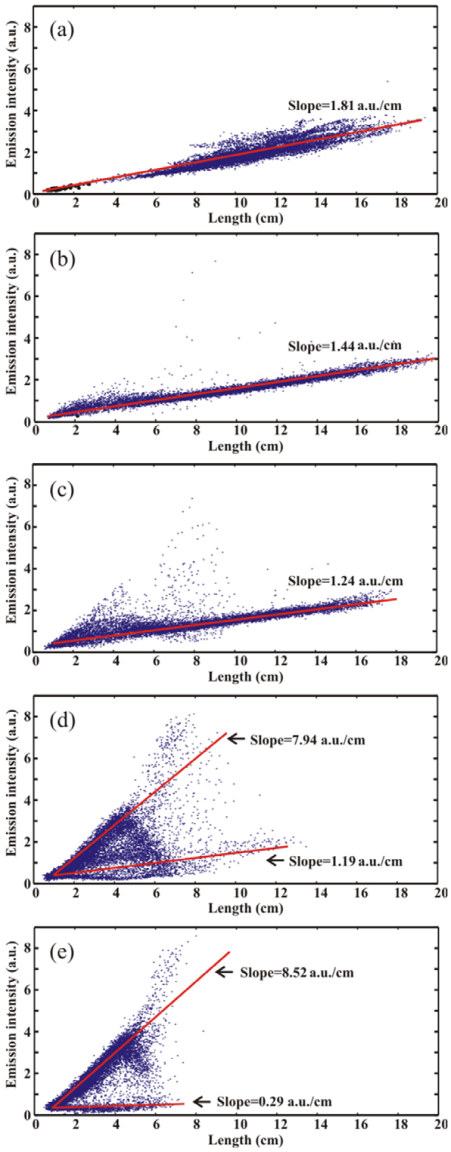


**Figure 9.** Statistics of the projected arc length and the integrated emission intensity for different flow rates: (*a*) 14 SLM; (*b*) 17.5 SLM; (*c*) 21 SLM; (*d*) 31.5 SLM and (*e*) 42 SLM. The brightness can be represented by the integrated emission intensity per unit length, i.e. the slope of the red lines.

[28], the spark-type discharge would become a stable arc discharge. However, the power limit in our system restricted further development of the spark-type discharge to only a short bright spark (as short as tens of nanoseconds as indicated by [31]). Figure 10(*b*) shows the full width at half maximum

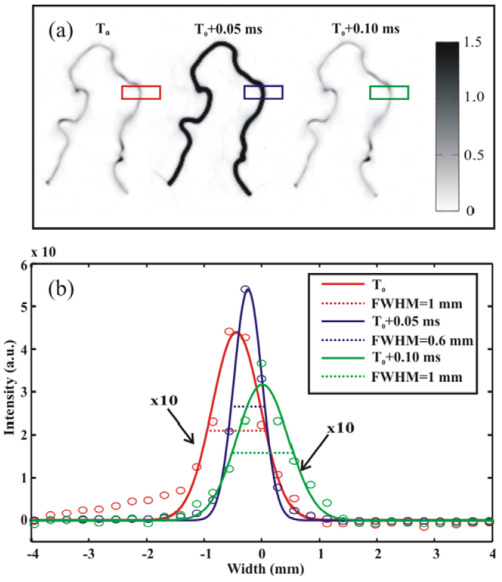


**Figure 10.** (*a*) Three sequential frames of gliding arc images recorded by the high-speed camera, showing the conversion from a glow-type discharge to a much brighter spark-type discharge. The frame rate was 20 kHz and the exposure time was 13.9 $\mu$s; (*b*) the full width at half maximum (FWHM) of the spark-type and glow-type discharge integrated in the region as marked in (*a*). The intensity of the glow-type discharge was multiplied by 10.

(FWHM) of the spark-type and glow-type discharge shown in figure 10(*a*). The cross-section of intensity marked by a rectangle in figure 10(*a*) was obtained and fitted by a Gaussian function. The FWHM of the spark-type discharge is about 0.6 mm while that of the glow-type discharge is about 1 mm. It is noted that only a few data points are available for the fitting limited by the spatial resolution of the high-speed camera (about 0.2 mm per pixel). In this case, the uncertainty of FWHM is believed to be at least the same order of magnitude of 0.2 mm.

This observation indicates that it is possible to manipulate the gliding arc conversion from glow-type to spark-type by controlling the local turbulence and a current restriction of the ac power supply.

### *3.2. Effects of flow rate on OH distributions*

OH is believed to be produced in the gliding arc primarily due to electron-induced dissociation of water vapour in the open air [32, 33].

$$H_2O + e \rightarrow OH + H + e$$

OH is one of the most important species for plasma chemistry due to its high reactivity [34, 35]. PLIF techniques can be applied to detect OH radicals in the ground-state that cannot be measured through optical emission spectroscopy. Figure 11

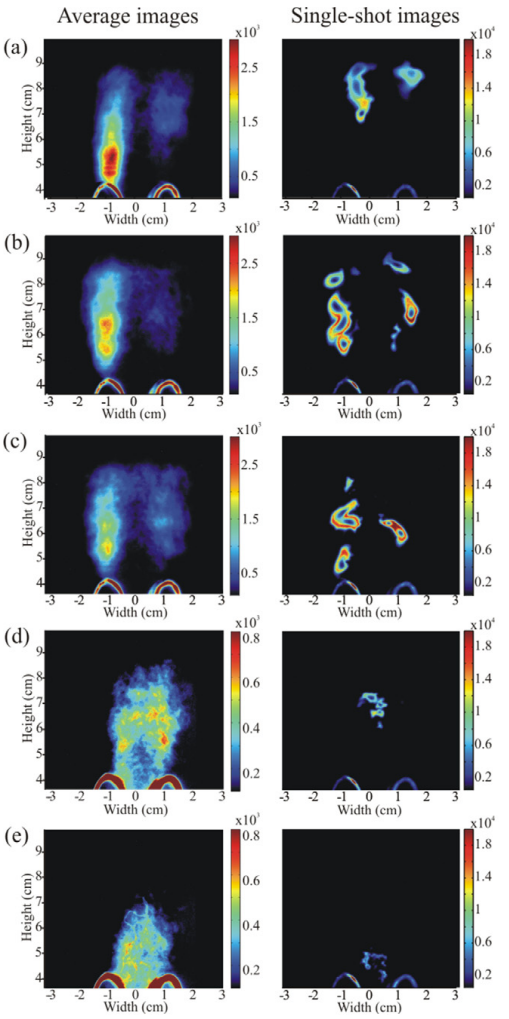


**Figure 11.** Average and single-shot OH-PLIF spatial distributions in the gliding arc at different air flow rates (*a*) 14 SLM; (*b*) 17.5 SLM; (*c*) 21 SLM; (*d*) 31.5 SLM and (*e*) 42 SLM. The left panel display average images while single-shot images are shown in the right panel. The single-shot images are obtained using an exposure time of 30 ns. The colour bar is in arbitrary units.

presents both average and single-shot PLIF images of ground-state OH recorded at five different air flow rates. The average images in the left panel are obtained by averaging 500 PLIF images for each case. The exposure time of the ICCD camera was set to 30 ns to suppress the gliding arc emission.

It is seen from the average images that the height, shape and intensity of the ground-state OH vary as the flow rate increases from 14 to 42 SLM. When the flow rate is lower than 21 SLM, ground-state OH can be detected in large quantities even at a height of about 9 cm. However, when the flow rate

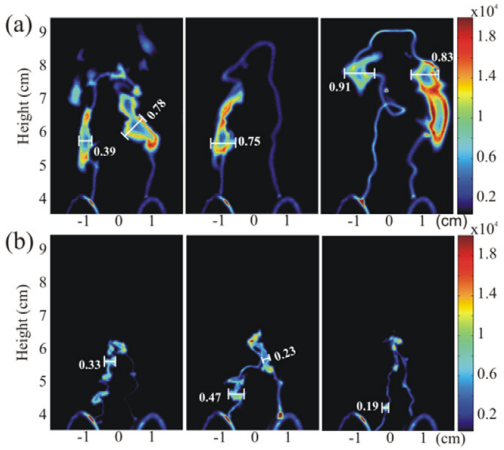


**Figure 12.** Three typical single-shot OH-PLIF images obtained using an exposure time of 2 $\mu$s, showing the OH distributions and arc emission at two flow rates (*a*) 17.5 SLM, (*b*) 42 SLM. The typical thickness of the OH distribution is labelled in the images with unit of centimetres. The colour bar is in arbitrary units.

is increased to 42 SLM, the OH PLIF signal is not present for heights above 7 cm. These OH distributions correlate well with the observed head heights of the plasma column shown in figure 5. Furthermore, the OH signal tends to have two separated maxima beside the central axis at lower flow rates. On the contrary, the intensity distribution has a single maximum on the central axis at 31.5 and 42 SLM. The shape of the OH distribution at 14 and 42 SLM agrees well with the emission shown in figure 1. The average ground-state OH signal is stronger at the top of one of the electrodes at lower flow-rates. The asymmetric intensity distribution in the average images is most likely a three-dimensional (3D) effect caused by a slight asymmetry in the propagation of the plasma column driven by the turbulent jet flow above the two electrodes, as indicated in the single-shot images in figure 11. The single-shot OH-PLIF images in figure 11 show a hollow structure of the distributions of ground-state OH radicals locating around the hot plasma column [26].

Figure 12 shows three typical frames of single-shot OH-PLIF distributions and arc emission at flow rates of 17.5 SLM and 42 SLM, respectively. An exposure time of 2 $\mu$s was used in order to simultaneously record OH distributions and arc emission. The conductive plasma column, illustrated as a bright string in figure 12, is a 3D thin wrinkling channel that connects the two electrodes. The 100 $\mu$m thick laser sheet crossed the plasma column vertically and illuminated only part of the plasma column, where OH distributions in the thin cross-section were illustrated in the collected PLIF images. However, the simultaneously recorded bright string of the hot core was the projection of the whole plasma column. From the simultaneously recorded plasma emission and the OH PLIF, one can see the OH distribution around the hot discharge core in the shape of a hollow tube.

The thickness of the discharge emission has the same order of magnitude (about 1 mm) as the FWHM shown in figure 10(*b*). The discharge emission primarily comes from the spontaneous emission of excited OH and $N_2$ since the filters (UG5 + WG295) with a transmittance curve shown in figure 14 were used. The ground state OH, distributed as a tube around the conductive filament, is much thicker than the excited OH signal from the plasma channel. The ground state OH thickness at 17.5 SLM is up to 0.9 cm while the OH thickness at 42 SLM is around 0.3 cm. Since the OH radical can only sustainably exist in air at temperature higher than 1000 K, the distribution of the observed OH agrees well with previous dc gliding arc measurements [5] and a prediction of the hot-wire modelling for a dc gliding arc [36].

Both figures 11 and 12 show that the OH intensity decreases at higher flow rates, e.g. 31.5 and 42 SLM, which may be due to the enhanced mass and heat transfer caused by the stronger local turbulence.

### *3.3. Effects of flow rate on UV emission*

The UV emission of the gliding arc was analysed using an ICCD based imaging spectrometer. The gliding arc was operated in burst mode with a 10 Hz repetition rate and 20 ms burst duration. The synchronization between the gliding arc and the ICCD camera enables the emission to be more frequently captured and still retain a short acquisition time, rendering high spatial resolution. The delay time between the driving signal of the gliding arc and the ICCD gate was mainly set by a pulse generator (DG535) and fine adjustments were made via a delay function in the ICCD camera software. An exposure time of 5.3 $\mu$s was adopted to acquire the initial stage of a half period (16 $\mu$s) of the ac driving voltage.

In order to obtain spatially resolved emission spectra of the highly dynamic plasma column, one hundred single-shot spectral images were recorded by the ICCD-based spectrometer setup. Emission was captured over a 1.4 cm distance along the centreline between the two electrodes. The heights of the gliding arc were significantly affected by the shorting-cutting and the ignition events. The plasma column could even be outside the field of view of the ICCD camera in some single-shot images. Therefore, each single-shot image was individually analysed to choose those properly caught for further evaluations. The central line of the discharge emission in the selected images was found, and the emission spectra near the central line were averaged. Figure 13 shows a single-shot spectral image of the gliding arc emission at 42 SLM. Emission within 2 mm from the central line was selected for averaging. The average optical emission spectra of the gliding arc are shown in figure 14, where spectral features of NO $\gamma$(A-X), OH (A-X) and $N_2$ (C-B) are presented at all investigated air flow rates. The intensities of NO $\gamma$(A-X), OH (A-X) and $N_2$ (C-B) are found to increase with the rising flow rates. Excited OH and NO are very reactive species. Furthermore, NO is responsible for the acid effects [37]. Hence, these two molecules are of great importance in gliding arc applications.

As previously mentioned, the plasma column appears brighter at high flow rates due to the glow-type to spark-type

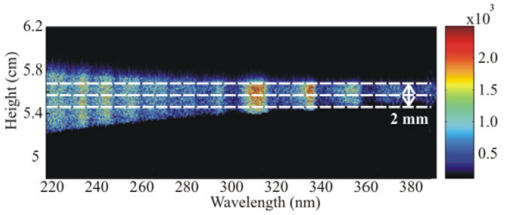


**Figure 13.** Single-shot UV emission spectrum of the gliding arc at 42 SLM. The arc emissions near the central line with a height of 2 mm were selected for averaging. The colour bar is in arbitrary units.

conversion of the gliding arc induced by turbulence. The spark-type gliding arc is hotter and closer to thermal equilibrium. The average UV emission from the gliding arc at high flow rates is dominated by the spark-type emission, while emission captured at low flow rates is predominantly the glow-type emission (as can be seen from figure 9). This is in agreement with the previous plasma temperature measurements [38], where $N_2$ lines are much stronger at high temperatures close to thermal equilibrium.

### *3.4. Effects of turbulence*

Some of the aforementioned experimental flow rate dependent observations can be explained by the interaction of the gliding arc and turbulence. A turbulent flow exhibits irregular and non-uniform flow motion, which convects the gliding arc in such a way that the conduction channel becomes rather twisted and wrinkled. As the Re number increases, the Kolmogorov length decreases and the wrinkling scales in the gliding arc become smaller. Furthermore, turbulent eddies enhance the transfer of heat and mass from the high temperature thin arc filament to the surrounding cold air. With higher Re numbers, the heat and mass transfer becomes stronger and the cooling of the gliding arc is increased. This has two consequences: first, the length of the gliding arc is kept short since the plasma column cannot survive for long periods in the strong turbulent environment, leading to quicker formation of new breakdowns at the narrowest gap, cf. figure 5; second, once a new gliding arc is formed the radicals and excited species, produced in vicinity of the new extinguishing plasma channel, are cooled and quenched more rapidly with high Re numbers, cf. figures 7 and 8. From table 1, it is seen that the two highest flow rate cases have a Kolmogorov eddy much smaller in length scale than the diameter of the plasma arc (which is around 1 mm for glow-type discharge and around 0.6 mm for spark-type discharge). It is expected that turbulence eddies can enter into the high temperature arc and effectively transfer the heat and mass between the high temperature region and the cold ambient air. This explains the high instability of the two high flow rate cases regarding their high frequency conversion between the glow-type to spark-type discharge. This also explains the rapid quenching of OH in the high flow rate case (figure 12), which is likely similar to the OH recombination reactions at low temperatures in a combustion system [39].

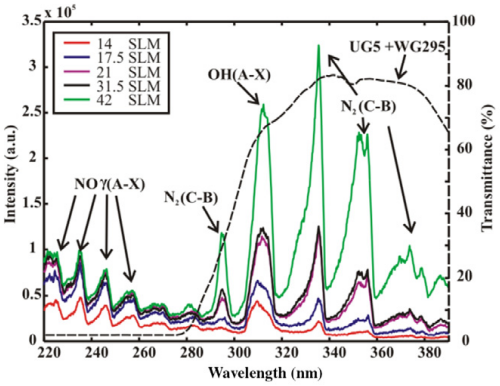


**Figure 14.** The average emission spectra of the gliding arc for different flow rates. The spectra were measured at 4.8–6.2 cm centred at 5.5 cm. The corresponding NO, OH and $N_2$ lines are labelled. The dashed line is the transmittance curve of the adopted filters (UG5 + WG295) for OH-PLIF measurement.

## 4. Summary

Optical methods were employed in the present work to experimentally investigate the effects of turbulent air flows with different Re numbers and Kolmogorov lengths on a high voltage ac gliding arc, which delivers a plume of cold plasma with an input power of up to 1 kW. The results show that both short-cutting events and ignitions take place more frequently at higher air flow rates due to larger turbulent convection cooling and stronger turbulent eddies and vortices.

Emission from a fully developed gliding arc and a newly ignited arc simultaneously exist for 0.2–0.9 ms depending on the flow rate. Conversions of glow-type to spark-type discharge with a much brighter plasma column are more frequent at the high flow rate.

Average PLIF results indicate that ground-state OH is distributed further downstream at the higher position with larger quantities at lower flow rates. Single-shot analysis shows that OH radicals are distributed around the hot plasma column like a hollow tube that is much wider (up to 0.9 cm) than the gliding arc (about 0.1 cm) at low flow rates, while the thickness of the OH distribution decreases to about 0.3 cm at high flow rates.

It was also found that the emission intensity of NO (A-X), OH (A-X) and $N_2$ (C-B) increases at high flow rates due to more frequent conversion to the thermal spark-type discharge. Excited NO and OH were observed in the emission spectra of the gliding arc at all flow rates, and therefore the gliding arc can have oxidizing and acidic effects.

All the experimental results direct to the conclusion that the interaction between the local turbulence and plasma column can be used to effectively manipulate the gliding arc operations of the present setup. A comprehensive computational fluid dynamics modelling would be very useful for a proper understanding and optimization of the performance of gliding arcs.

## Acknowledgments

This work was financially supported by the Swedish Energy Agency, Knut & Alice Wallenberg Foundation and European Research Council. The authors thank Professor Xuesong Bai (Lund University) and Professor Anders Larsson (FOI, Sweden) for fruitful discussions. J Z thanks the financial support from the China Scholarship Council.

## References

[1] Czernichowski A 1994 Gliding arc–applications to engineering and environment control *Pure Appl. Chem.* **66** 1301–10
[2] Šperka J, Souček P, Loon J W A, Dowson A, Schwarz C, Krause J, Kroesen G and Kudrle V 2013 Hypergravity effects on glide arc plasma *Eur. Phys. J.* D **67** 1–9
[3] Fridman A, Nester S, Kennedy L A, Saveliev A and Mutaf-Yardimci O 1998 Gliding arc gas discharge *Prog. Energy Combust. Sci.* **25** 211–31
[4] Fridman A, Gutsol A, Gangoli S, Ju Y G and Ombrellol T 2008 Characteristics of gliding arc and its application in combustion enhancement *J. Propulsion Power* **24** 1216–28
[5] Richard F, Cormier J M, Pellerin S and Chapelle J 1996 Physical study of a gliding arc discharge *J. Appl. Phys.* **79** 2245–50
[6] Ombrello T, Ju Y G and Fridman A 2008 Kinetic ignition enhancement of diffusion flames by nonequilibrium magnetic gliding arc plasma *AIAA J.* **46** 2424–33
[7] Ombrello T, Qin X, Ju Y, Gutsol A, Fridman A and Carter C 2006 Combustion enhancement via stabilized piecewise nonequilibrium gliding arc plasma discharge *AIAA J.* **44** 142–50
[8] Kusano Y, Teodoru S, Leipold F, Andersen T L, Sørensen B F, Rozlosnik N and Michelsen P K 2008 Gliding arc discharge–application for adhesion improvement of fibre reinforced polyester composites *Surf. Coat. Technol.* **202** 5579–82
[9] Kusano Y, Sorensen B F, Andersen T L, Toftegaard H L, Leipold F, Salewski M, Sun Z W, Zhu J J, Li Z S and Alden M 2013 Water-cooled non-thermal gliding arc for adhesion improvement of glass-fibre-reinforced polyester *J. Phys. D: Appl. Phys.* **46** 135203
[10] Kusano Y, Sorensen B F, Andersen T L and Leipold F 2013 Adhesion Improvement of glass-fibre-reinforced polyester composites by gliding arc discharge treatment *J. Adhes.* **89** 433–59
[11] Kusano Y, Norrman K, Drews J, Leipold F, Singh S V, Morgen P, Bardenshtein A and Krebs N 2011 Gliding arc surface treatment of glass-fiber-reinforced polyester enhanced by ultrasonic irradiation *Surf. Coat. Technol.* **205** (suppl. 2) S490–4
[12] Kusano Y 2014 Atmospheric pressure plasma processing for polymer adhesion–a review *J. Adhes.* **90** 755–77
[13] Janca J and Czernichowski A 1998 Wool treatment in the gas flow from gliding discharge plasma at atmospheric pressure *Surf. Coat. Technol.* **98** 1112–5
[14] Balcon N, Benard N, Braud P, Mizuno A, Touchard G and Moreau E 2008 Prospects of airflow control by a gliding arc in a static magnetic field *J. Phys. D: Appl. Phys.* **41** 205204
[15] Du C M, Yan J H, Li X D, Cheron B G, You X F, Chi Y, Ni M J and Cen K F 2006 Simultaneous removal of polycyclic aromatic hydrocarbons and soot particles from flue gas by gliding arc discharge treatment *Plasma Chem. Plasma Proces.* **26** 517–25
[16] Gallagher M J, Geiger R, Polevich A, Rabinovich A, Gutsol A and Fridman A 2010 On-board plasma-assisted conversion of heavy hydrocarbons into synthesis gas *Fuel* **89** 1187–92
[17] Dalaine V, Cormier J M, Pellerin S and Lefaucheux P 1998 H2S destruction in 50 Hz and 25 kHz gliding arc reactors *J. Appl. Phys.* **84** 1215–21
[18] Kalra C S, Gutsol A F and Fridman A A 2005 Gliding arc discharges as a source of intermediate plasma for methane partial oxidation *IEEE Trans. Plasma Sci.* **33** 32–41
[19] Sagas J C, Neto A H, Filho A C P, Maciel H S and Lacava P T 2011 Basic characteristics of gliding-arc discharges in air and natural gas *IEEE Trans. Plasma Sci.* **39** 775–80
[20] Mutaf-Yardimci O, Saveliev A V, Fridman A A and Kennedy L A 2000 Thermal and nonthermal regimes of gliding arc discharge in air flow *J. Appl. Phys.* **87** 1632–41
[21] Tu X, Yu L, Yan J H, Cen K F and Cheron B G 2009 Dynamic and spectroscopic characteristics of atmospheric gliding arc in gas–liquid two-phase flow *Phys. Plasmas* **16** 113506
[22] Xin T, Gallon H J and Whitehead J C 2011 Dynamic behavior of an atmospheric argon gliding arc plasma *IEEE Trans. Plasma Sci.* **39** 2900–1
[23] Zhao T L, Xu Y, Song Y H, Li X S, Liu J L, Liu J B and Zhu A M 2013 Determination of vibrational and rotational temperatures in a gliding arc discharge by using overlapped molecular emission spectra *J. Phys. D: Appl. Phys.* **46** 345201
[24] Benstaali B, Boubert P, Cheron B G, Addou A and Brisset J L 2002 Density and rotational temperature measurements of the OH degrees and NO degrees radicals produced by a gliding arc in humid air *Plasma Chem. Plasma Proces.* **22** 553–71
[25] Aldén M, Bood J, Li Z and Richter M 2011 Visualization and understanding of combustion processes using spatially and temporally resolved laser diagnostic techniques *Proc. Combust. Inst.* **33** 69–97
[26] Sun Z W, Zhu J J, Li Z S, Alden M, Leipold F, Salewski M and Kusano Y 2013 Optical diagnostics of a gliding arc *Opt. Express* **21** 6028–44
[27] Pope S B 2000 *Turbulent Flows* (Cambridge: Cambridge University Press)
[28] Korolev Y D, Frants O B, Geyman V G, Landl N V and Kasyanov V S 2011 Low-current 'gliding arc' in an air flow *IEEE Trans. Plasma Sci.* **39** 3319–25
[29] Kalra C S, Cho Y I, Gutsol A, Fridman A and Rufael T S 2005 Gliding arc in tornado using a reverse vortex flow *Rev. Sci. Instrum.* **76** 025110–7
[30] Mitsugi F, Furukawa J, Ohshima T, Kawasaki H, Kawasaki T, Aoqui S and Stryczewska H D 2013 Observation of dynamic behavior of gliding arc discharge *Eur. Phys. J.: Appl. Phys.* **61** 24308
[31] Zhang C, Shao T, Xu J Y, Ma H, Duan L W, Ren C Y and Yan P 2012 A gliding discharge in open air sustained by high-voltage resonant ac power supply *IEEE Trans. Plasma Sci.* **40** 2843–9
[32] Dolan T J 1993 Electron and ion collisions with water–vapor *J. Phys. D: Appl. Phys.* **26** 4–8
[33] Itikawa Y and Mason N 2005 Cross sections for electron collisions with water molecules *J. Phys. Chem. Ref. Data* **34** 1–22
[34] Ono R and Oda T 2001 OH radical measurement in a pulsed arc discharge plasma observed by a LIF method *IEEE Trans. Indust. Appl.* **37** 709–14
[35] Kanazawa S, Kawano H, Watanabe S, Furuki T, Akamine S, Ichiki R, Ohkubo T, Kocik M and Mizeraczyk J 2011 Observation of OH radicals produced by pulsed discharges on the surface of a liquid *Plasma Sources Sci. Technol.* **20** 034010
[36] Pellerin S, Richard F, Chapelle J, Cormier J M and Musiol K 2000 Heat string model of bi-dimensional dc Glidarc *J. Phys. D: Appl. Phys.* **33** 2407–19
[37] Brisset J L, Moussa D, Doubla A, Hnatiuc E, Hnatiuc B, Youbi G K, Herry J M, Naitali M and Bellon-Fontaine M N

2008 Chemical reactivity of discharges and temporal post-discharges in plasma treatment of aqueous media: examples of gliding discharge treated solutions *Indust. Eng. Chem. Res.* **47** 5761–81

[38] Laux C O, Spence T G, Kruger C H and Zare R N 2003 Optical diagnostics of atmospheric pressure air plasmas *Plasma Sources Sci. Technol.* **12** 125–38

[39] Kiefer J, Li Z S, Zetterberg J, Bai X S and Alden M 2008 Investigation of local flame structures and statistics in partially premixed turbulent jet flames using simultaneous single-shot CH and OH planar laser-induced fluorescence imaging *Combust. Flame* **154** 802–18

# [Appendix A10]

Y. Kusano, M. Salewski, F. Leipold, J.J. Zhu, A. Ehn, Z.S. Li, M. Aldén

## “Stability of alternating current gliding arcs”

*The European Physical Journal D* 68 (2014) 319.

Eur. Phys. J. D (2014) 68: 319
DOI: 10.1140/epjd/e2014-50343-8

THE EUROPEAN PHYSICAL JOURNAL D

Regular Article

# Stability of alternating current gliding arcs

Yukihiro Kusano[1,a], Mirko Salewski[2], Frank Leipold[2], Jiajian Zhu[3], Andreas Ehn[3], Zhongshan Li[3], and Marcus Aldén[3]

[1] Department of Wind Energy, Section of Composites and Materials Mechanics, Technical University of Denmark, DTU Risø Campus, Frederiksborgvej 399, 4000 Roskilde, Denmark
[2] Department of Physics, Technical University of Denmark, Fysikvej, 2800 Kgs. Lyngby, Denmark
[3] Division of Combustion Physics, Lund University, P.O. Box 118, 22100 Lund, Sweden

Received 30 April 2014 / Received in final form 4 August 2014
Published online 28 October 2014 – 

**Abstract.** A gliding arc is a quenched plasma that can be operated as a non-thermal plasma at atmospheric pressure and that is thus suitable for large-scale plasma surface treatment. For its practical industrial use the discharge should be extended stably in ambient air. A simple analytical calculation based on Ohm's law indicates that the critical length of alternating current (AC) gliding arc discharge columns can be larger than that of a corresponding direct current (DC) gliding arc. This finding is supported by previously published images of AC and DC gliding arcs. Furthermore, the analysis shows that the critical length can be increased by increasing the AC frequency, decreasing the serial resistance and lowering the gas flow rate. The predicted dependence of gas flow rate on the arc length is experimentally demonstrated. The gap width is varied to study an optimal electrode design, since the extended non-equilibrium discharge can be extinguished due to the ignition of an arc discharge at the closest electrode gap. It is experimentally found that as the gap is wider, the discharge column tends to be longer.

## 1 Introduction

Surface modification with a non-thermal plasma is useful for adhesion improvement of polymers, because it can simultaneously clean the surfaces, remove weak surface domains, roughen the surfaces, and introduce polar functional groups that can enhance wetting and interaction with adhesives [1]. Non-thermal plasmas are often generated at low pressures, but they can also be generated at atmospheric pressure [2], obviating vacuum equipment and permitting continuous treatment [3,4] and treatment of large objects [5–7]. It has been shown that a variety of surface treatment methods performed in low pressure plasmas are also achievable at atmospheric pressure [2].

A gliding arc is a quenched plasma that can be operated as a non-thermal plasma in air at atmospheric pressure and can thus be used advantageously and economically for large-scale plasma processing. It can treat surfaces of bulky objects and is useful for adhesion improvement of materials in industrial processing [5–10]. A gliding arc is ignited as a thermal arc discharge at the closest gap between diverging electrodes and is quickly quenched to non-thermal conditions while it is extended by a gas flow [11–16]. It is often operated using a direct current (DC) [12–16], but an alternating current (AC) can also be used for generating a gliding arc [5–7,17–21].

[a] e-mail: yuki@dtu.dk

The performance of a gliding arc is studied in terms of energy balance [13,22–24], force balance [25–27], and electric circuits [13,28].

The plasma string model [22,23] is based on an energy-balance equation at the equilibrium phase of a gliding arc [13], taking a small part of the discharge column and neglecting turbulent effects and radial convection for a steady state analysis. The simplified form of the governing equation corresponds to the Elenbass-Heller equation [29]. It is shown that physical parameters such as the electrical field, conductivity, temperature and radius of the gliding arc can be accurately described using simple assumptions and the simple physical model. Dalaine et al. [24] reports that at low flow rates the Elenbass-Heller equation can be used, but that quick variations of voltage should be taken into account at high flow rates.

It is desirable in many applications that a gliding arc is not blown away in a short time but stays in a same location for the efficient use of energy introduced to the plasma. The balance of forces acting on the plasma column has been studied, comparing the force due to the velocity difference between the plasma column and the surrounding gas to gravity [25] or the Lorentz force with the existence of a magnetic field [26,27].

Spatial fluctuation of gliding arcs is investigated experimentally [18,30,31]. It is challenging to study movement and spatial fluctuation of the gliding arc, considering the momentum balance in terms of fluid dynamics.

Due to the turbulent flow of the surrounding gas and nonlinear nature of the governing equations, the spatial fluctuation of a gliding arc is apparently random. In addition, even if a gliding arc fluctuates spatially, it can be stably sustained without extinction or fluctuation of discharge modes.

Stability of a DC gliding arc and its implication of the transition from thermal to non-thermal discharge have previously been discussed using a circuit theory [13–15]. It is assumed that a specific power dissipated from the discharge per unit length, $W$, is constant at a fixed gas flow rate [13–15]. Experimental data supports this assumption [22,23]. It can be said that the effect of the spatial fluctuation is indirectly included in this parameter. Neglecting a self-inductance, Ohm's law can be written in the form [13–15]

$$V = RJ + \frac{Wl}{J} \tag{1}$$

and thus

$$J = \frac{V \pm \sqrt{V^2 - 4WlR}}{2R}. \tag{2}$$

Here, $V$ is the voltage applied from the power supply, $R$ is the serial resistance, $J$ is the current, and $l$ is the length of the DC gliding arc discharge column [13–15]. Electrode fall voltages can be up to approximately 300 V [16,32,33] and are thus assumed to be negligible. The solution with $J > V/2R$ corresponds to the steady-state regime of the DC gliding arc whereas the solution with $J < V/2R$ has negative differential resistance of the circuit $dV/dJ$ and corresponds to the unstable regime [13,14]. When the length of the discharge column increases and the discriminant of equation (2) approaches zero, the discharge evolution in equilibrium is terminated. This occurs at a critical length $l_{crit\text{-}dc}$,

$$l \leqslant l_{crit\text{-}dc} = \frac{V^2}{4WR}. \tag{3}$$

It is reported that if the length of the DC gliding arc discharge column exceeds the critical value of equation (3) (critical length in the thermal regime), a fast transition from thermal to non-equilibrium state with different discharge parameters takes place [13,14]. Namely after the transition the gas in the DC gliding arc rapidly cools while the electron temperature increases due to the increase of the electric field strength (non-thermal regime). This post-transition period is potentially useful, since only in this period the gas temperature is low enough so as to be applicable in a variety of general material processing techniques. It is reported that after the transition, the critical length in the non-thermal regime can be approximately three times larger than the critical length in the thermal regime before the transition, since the energy dissipation from the DC gliding arc can be approximately three times smaller due to the lower gas temperature after the transition [13,14]. However, this post-transition period could constitute only a small portion of the total DC gliding arc cycle time [15], limiting the practical application of DC gliding arc discharges. It is reported that when the current is as low as 0.2 A, the specific power dissipated from the discharge per unit length may not be constant for a DC gliding arc, and that the discharge would be sustained by an electric field for ionization [16]. It is on the other hand reported that introduction of a self-inductance of the circuit $L$ into the DC gliding circuit decelerates the rate of current decrease and prolongs the evolution time of the non-equilibrium DC gliding arc [13,14]. Equation (1) is replaced with [13,14]

$$V = RJ + \frac{Wl}{J} + L\frac{dJ}{dt}. \tag{4}$$

The influence on the critical length of the DC gliding arc has not been studied until now.

In the present work, this simple nonlinear model (Eq. (4)) is used to study the stability and critical length of an AC gliding arc in a non-thermal regime analytically. While this model was exclusively used for a DC gliding arc [13,14], it has never been employed for AC gliding arcs. The AC gliding arc presented here is characterized by the long extension of the plasma column of approximately 20–30 cm. It does not extinguish each half period but can survive over hundreds of AC periods after which the discharge is terminated by a new ignition at the closest gap between the electrodes. Furthermore, it can be extended in any direction in ambient air, depending on the direction of the gas flow. Including the inductive term in equation (4) is appropriate so as to describe the sustainability of the AC gliding arc over AC periods. This AC gliding arc is unique and significantly useful for surface modification, since three-dimensionally shaped bulky structures can be easily treated, and the energy consumption of the plasma is mainly used for sustaining a non-equilibrium plasma instead of arc ignition. The current waveform can be approximated by a sinusoidal form [18], which allows detailed analytical study of the model for the first time. From this analysis, it is found that the performance of AC gliding arcs is significantly different from that of the DC gliding arcs, showing a good agreement with the observed difference of the general performance of the DC and AC gliding arcs.

## 2 Stability analysis of an AC gliding arc

Recent publications indicate that an AC gliding arc driven at a high frequency (30−40 kHz) can be stably extended from the edges of the electrodes up to several centimetres in the post-transition period [17–19]. The AC gliding arc reported in references [17–19] is characterized by a long lifetime of the elongated discharge column over several hundreds of sinusoidal AC periods between consecutive ignitions [18]. A typical achievable length of the AC gliding arc discharge column can be approximately 20−30 cm which is unique and practically useful for non-thermal plasma surface treatment of bulky substances [17–19]. In terms of AC gliding arcs, Dalaine et al. [20,21] also studied a pulsed or sinusoidal 50 Hz gliding arc [20,21] and a

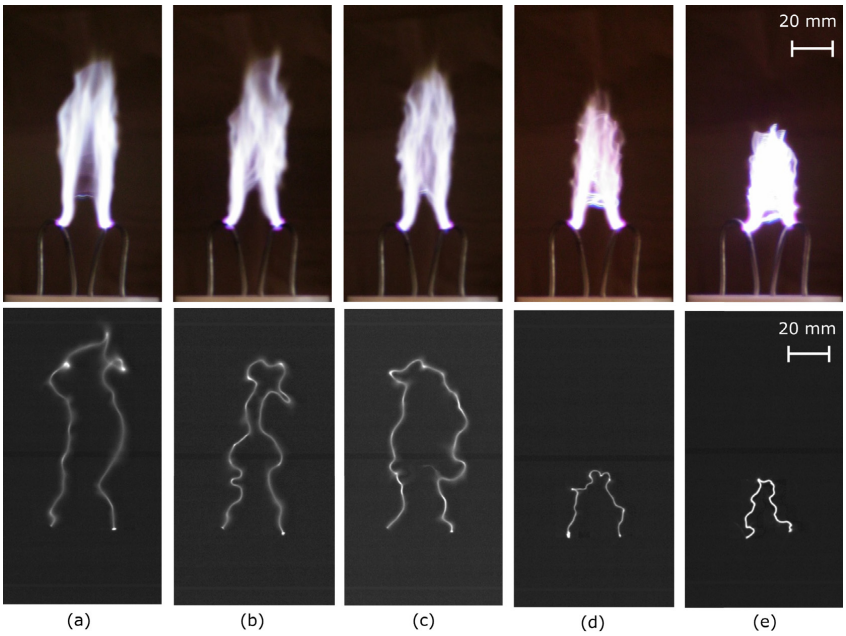


**Fig. 1.** Photos of the AC gliding arc I at different gas flow rates: (a) 14 standard litre per minute (SLM), (b) 17.5 SLM, (c) 21 SLM, (d) 31.5 SLM and (e) 42 SLM. The upper images are acquired by a normal camera using an automatic exposure time, showing how humans perceive the gliding arc. The lower images are captured by a high-speed camera using an exposure time of 13.9 $\mu$s and reveal the plasma column just before extinction.

square-wave 25 kHz gliding arc [21] for $H_2S$ destruction. Successive photographs of the moving 25 kHz gliding arc with a 5 ms interval, corresponding to 125 periods of the square wave, indicate that the gliding arc may not extinguish after every half period [21]. However, it is noted that the maximum length of the plasma column looks at least several times shorter than that of the AC gliding arcs in the present study, and thus the AC gliding arcs in references [20,21] cannot be efficiently used for the application of surface modification.

In the present work, the gliding arc was first generated between two diverging stainless steel tubular electrodes that were separated by approximately 5 mm at the closest gap between them (AC gliding arc I). The outer diameter of the tubular electrodes is 3 mm. The gliding arc was also generated between 6 mm outer-diameter stainless steel tubular electrodes on which blade-shaped stainless steel pieces were welded (AC gliding arc II) [17]. The closest gap between the blade-shaped pieces is variable from 2 to 8 mm. In both cases, the tubular electrodes were cooled internally by a water flow. Air flow was fed between the electrodes to cool and extend the discharge. The gliding arcs were driven by an AC power supply (Generator 6030, SOFTAL Electronic, GmbH) at a frequency of 31.25 kHz. The voltage and the current were measured with a high-voltage probe and a 1.45 Ω resistor ($R$), respectively. A detailed description of the experimental setup is presented elsewhere [17–19]. It is observed that the behaviour of the gliding arc is affected by the movement of the gas around the discharge and that the plasma column tends to be longest when blown upwards in the direction of buoyancy for heated gas. When it is blown downwards against the direction of buoyancy, mixing of the gas and subsequently cooling of the plasma are enhanced and thus the plasma column would be shorter. In the following experiment, the gas flow is kept upward. The behaviour of the gliding arc is also affected by the gas flow. Photos of the AC gliding arc I at various gas flow rates are shown in Figure 1. The upper photos were taken by a normal video camera (Canon. IXY DV M2) with an automatic exposure time, corresponding to apparent visual images of a bulky plasma. However, the real dynamics of the gliding arc can be captured by a high speed camera (Photron Fastcam SA5) [18], represented by a thin plasma column of the lower row of photos in Figure 1. The photos in the lower row are the last acquired images before extinction of the discharge column at different flow rates. As the framing rate was 20 kHz, the discharge extinguishes at most 50 $\mu$s after the time of these images. As the movement of the plasma column is negligible, within this timeframe, these images show the maximum achievable length of the plasma column at each flow rate. It is seen that the maximum achievable length of the discharge column tends to decrease as the gas flow rate increases.

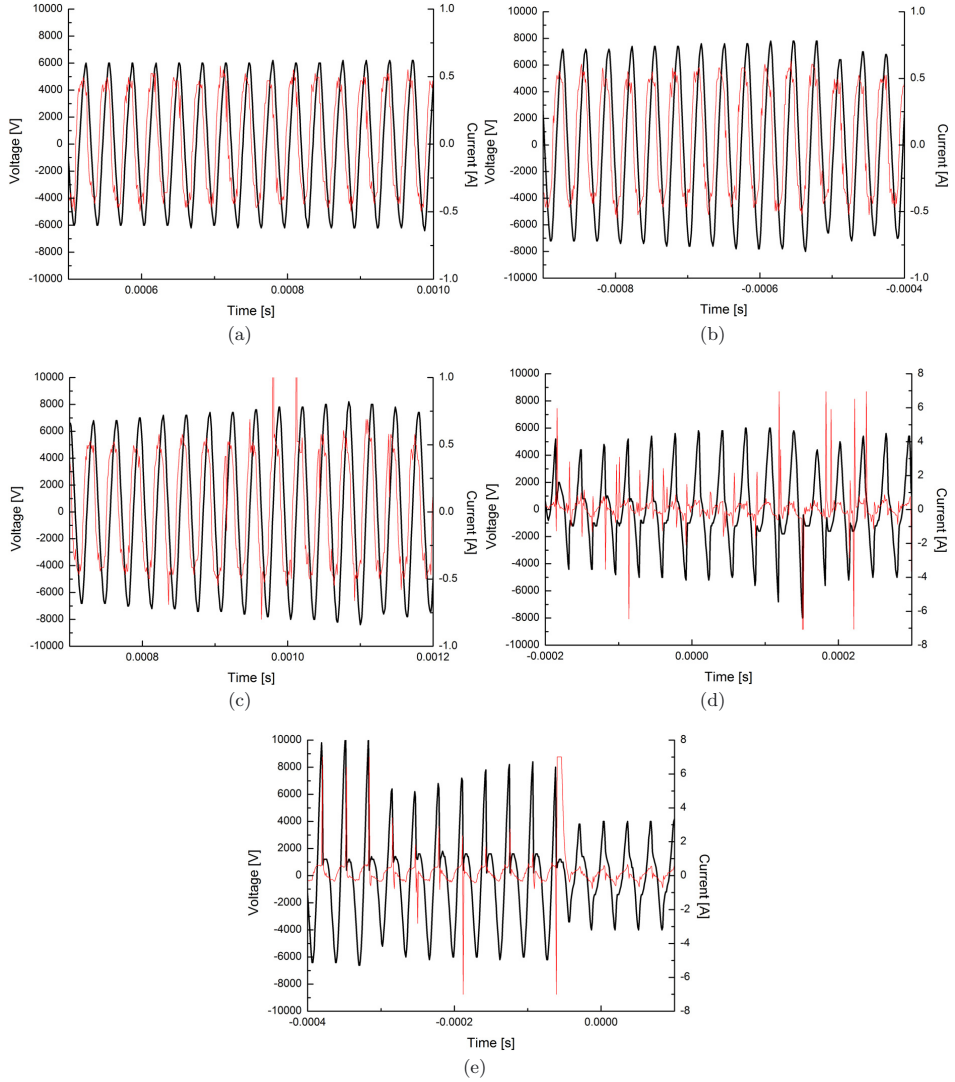


**Fig. 2.** Typical voltage (smooth and thick line) and current (rather irregular thin line) waveforms of the AC gliding arc I at different gas flow rates: (a) 14 SLM, (b) 17.5 SLM, (c) 21 SLM, (d) 31.5 SLM and (e) 42 SLM.

When the gliding arc I is generated with an AC power supply at an angular frequency $\omega = 2\pi \times 31.25$ kHz, the measured photoemission intensity from the gliding arc oscillates at the angular frequency $2\omega$ [18], because the energy dissipated from the discharge reaches its maximum in each half period.

Figure 2 shows typical voltage and current waveforms of the AC driven gliding arc I at different gas flow rates. At the gas flow rates between 14 and 21 SLM, they approximately follow sinusoidal forms apart from occasional small spiky currents which correspond to arc ignitions or short cutting events [18]. A phase-shift $\delta$ of the current from the voltage is seen. The current waveform indicates that the spiky current does not appear every half period and that the gliding arc discharge survives over several hundreds of periods at the lower gas flow rates. This indication was supported by the observations of the evolution of the discharge columns [18]. On the other hand,

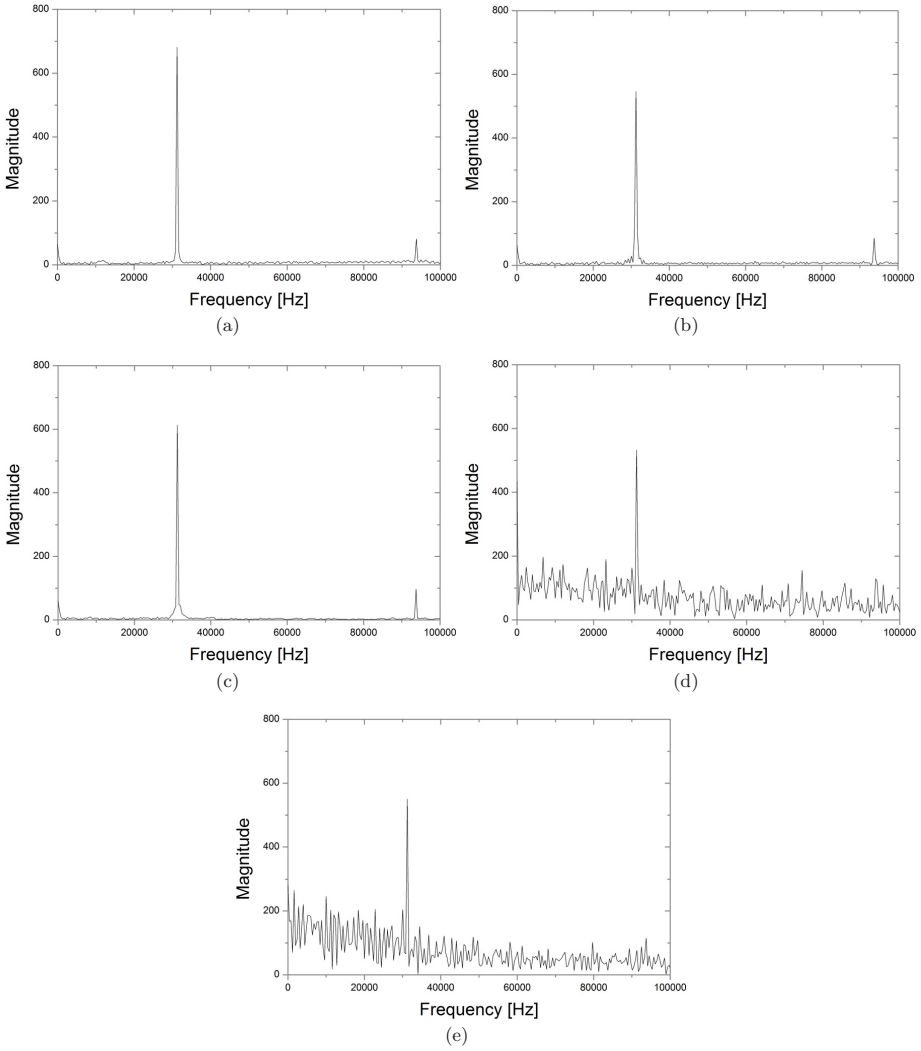


**Fig. 3.** Fourier transform spectra of the current of the gliding arc I at different gas flow rates: (a) 14 SLM, (b) 17.5 SLM, (c) 21 SLM, (d) 31.5 SLM and (e) 42 SLM.

at the gas flow rates of 31.5 and 42 SLM, the current waveforms involve sinusoidal-like waveform and frequent intense spiky current. Due to the intense spiky current, the voltage waveforms are also deformed.

These observations are clearly illustrated by Fourier transform spectra of the current at different gas flow rates as shown in Figure 3. At the lower gas flow rates, a dominant peak appears at the oscillation frequency of 31.25 kHz, whereas the frequency is less well defined at higher gas flow rates where the noisy background becomes significant. It is indicated that at higher flow rates, the discharge modes tend to fluctuate more frequently, since the electrical impedance differs significantly at different discharge modes primarily due to the change of the specific power dissipated from the discharge per unit length, $W$. This may be indirectly induced by the spatial fluctuation of the plasma column.

An electrical scheme of the AC gliding arc in the present work is shown in Figure 4. It is assumed that the self-inductance of the circuit is dominated by that of

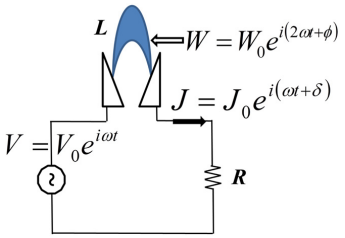


**Fig. 4.** Electrical scheme of the AC gliding arc.

the discharge column due to the long extension and significant fluctuation of the discharge column. It is also assumed that voltage and current waveforms are sinusoidal. The deviation from the sinusoidal waveform at higher gas flow rate will be discussed later. Since the measured photoemission intensity from the gliding arc oscillates at the angular frequency $2\omega$ [18], it is realistic to assume that the specific power dissipated from the discharge per unit length $W$ of the AC gliding arc is not constant but oscillates at the angular frequency of $2\omega$.

The supply voltage at the powered electrode $V$, the current $J$ and the specific power dissipated from the discharge per unit length $W$ in equation (4) can be replaced with

$$V = V_0 e^{i\omega t} \tag{5}$$

$$J = J_0 e^{i(\omega t+\delta)} \tag{6}$$

$$W = W_0 e^{i(2\omega t+\phi)} \tag{7}$$

where $V_0$, $J_0$ and $W_0$ are amplitudes and $\delta$ ($|\delta| < \pi/2$, and thus $\cos\delta > 0$) and $\phi$ are phase shifts. Substitution of equations (5)–(7) into equation (4) yields

$$V_0 = RJ_0 e^{i\delta} + \frac{W_0 l}{J_0} e^{i(\phi-\delta)} + i\omega L J_o e^{i\delta}. \tag{8}$$

Hence the phase shift of the specific power dissipated from the discharge per unit length is obtained:

$$\tan\phi = \frac{\frac{V_0}{J_0}\sin\delta - R\sin 2\delta - \omega L\cos 2\delta}{\frac{V_0}{J_0}\cos\delta - R\cos 2\delta + \omega L\sin 2\delta}. \tag{9}$$

Here it is noted from equation (9) that the phase shift of the specific power dissipated from the discharge is independent of the power dissipated from the discharge per unit length ($W$) and of the discharge length.

The real part of equation (8) is:

$$V_0 = RJ_0\cos\delta + \frac{W_0 l}{J_0}\cos(\phi-\delta) - \omega L J_o \sin\delta. \tag{10}$$

The general solutions of equation (10) are

$$J_0 = \frac{-V_0 \pm \sqrt{V_0^2 + 4\omega L W_0 l\cos\delta\left(\tan\delta - \frac{R}{\omega L}\right)\cos(\phi-\delta)}}{2\omega L\cos\delta\left(\tan\delta - \frac{R}{\omega L}\right)}. \tag{11}$$

For real solutions the discriminant must be positive or zero. In addition, the amplitude of the current $J_o$ must be positive.

Three different cases are discussed that depend on the relative values of $\tan\delta$ and the ratio of the characteristic time of the AC power supply $\omega^{-1}$ and that of the electrical circuit $L/R$. Namely $\tan\delta$ can be equal to, larger than or smaller than $R/\omega L$. If

$$\tan\delta = \frac{R}{\omega L}, \tag{12}$$

equation (10) can be reduced to:

$$\cos(\phi-\delta) = \frac{V_0 J_0}{W_0 l}. \tag{13}$$

After some calculations,

$$\tan\phi = \frac{\frac{\omega L}{R} + \left\{\frac{\omega^2 L^2}{R^2} + \frac{V_0^2 J_0^2}{W_0^2 l^2}\left(\frac{\omega^2 L^2}{R^2}+1\right) - 1\right\}^{\frac{1}{2}}}{\frac{V_0^2 J_0^2}{W_0^2 l^2}\left(\frac{\omega^2 L^2}{R^2}+1\right) - 1}. \tag{14}$$

Further, if

$$\tan\delta > \frac{R}{\omega L} \tag{15}$$

namely if the ratio of the characteristic time of the AC power supply $1/\omega$ to that of the electrical circuit $L/R$ is smaller than $\tan\delta$, then

$$\cos(\phi-\delta) > 0 \tag{16}$$

in order to have a positive solution in equation (11). In this case, the discriminant is always positive, and there exists the following positive solution for $J_0$

$$J_0 = \frac{-V_0 + \sqrt{V_0^2 + 4\omega L W_0 l\cos\delta\left(\tan\delta - \frac{R}{\omega L}\right)\cos(\phi-\delta)}}{2\omega L\cos\delta\left(\tan\delta - \frac{R}{\omega L}\right)}. \tag{17}$$

Therefore, a critical length does not exist under condition (15).

In the last case, if

$$\tan\delta < \frac{R}{\omega L}, \tag{18}$$

at least one positive solution exists in equation (11) as long as the discriminant is positive or zero.

When

$$\cos(\phi-\delta) \leqslant 0, \tag{19}$$

the discriminant is always positive, and there would again be no critical length. When

$$\cos(\phi-\delta) > 0 \tag{20}$$

$$l \leqslant \frac{V_0^2}{4\omega L W_0\cos\delta\left(\frac{R}{\omega L} - \tan\delta\right)\cos(\phi-\delta)} = l_{crit}, \tag{21}$$

or

$$W_0 = \frac{V_0^2}{l_{crit}} \frac{1}{4\cos\delta\,(R - \omega L\tan\delta)\cos(\phi - \delta)}. \quad (22)$$

A critical length exists under this condition. If the voltage $V_0$ increases or the resistance $R$ decreases, the critical length will increase. In addition, as the angular frequency $\omega$ increases, the critical length steadily increases as long as condition (18) is still valid.

Dalaine et al. compared 50 Hz and 25 kHz gliding arcs [21] and concluded that the discharge column is longer at a lower frequency, contradicting the present work. However, the voltage waveform, used by Dalaine et al., at 50 Hz was a pulsed wave whereas a square voltage waveform was used at 25 kHz. Therefore, results presented by Dalaine et al. cannot straightforwardly be compared to the current results since the present study assumes sinusoidal waves. Hence, the resulting current waveforms are distinctively different due to the different waveforms at the two different frequencies that were investigated by Dalaine et al. It is suggested that these differences affect the discharge elongation dynamics.

In the present work the gliding arc is generated with the approximately sinusoidal AC operation. The discharge column elongates most when its foot points are almost fixed at the electrodes [18], and the ratio of the discharge column length to the distance between the foot points can be up to approximately 10 (see Fig. 1), when the discharge column is blown into ambient air reaching far beyond the electrodes. On the other hand, the successive photos of the gliding arc presented by Dalaine et al. [21] show that the foot points of the discharge slide on the electrodes, the discharge column is always between the electrodes, and the ratio of the discharge column length to the distance never exceeds about 1−3. The much larger extension length of the AC gliding arc in the present work compared to that of Dalaine et al. [21] indicates that the discharge mechanisms between these two works might be significantly different, leading to difficulty in direct comparison of the results.

Meanwhile, it can be predicted that the specific power dissipated from the discharge per unit length $W_0$ will increase when the gas flow rate increases. It is thus predicted from equations (21) and (22) that if the gas flow rate increases, the critical length will decrease. The maximum projected length of the gliding arc discharge column $l_{\max}$ was obtained from the two-dimensional photos of the gliding arc discharge [18]. This projected length in the two-dimensional photo plane is always shorter than the actual length in three dimensions. Nevertheless, it is reasonable to use the projected length as experimentally accessible measure as it should be roughly proportional to the actual length. The supply voltage $V_0$ was measured at the fixed resistance $R$ (1.45 Ω). The maximum projected length of the gliding arc discharge column $l_{\max}$ and $V_0^2/l_{\max}$ at different air flow rates at a fixed frequency (31.25 kHz) is shown in Figure 5. Here equation (22) indicates that $V_0^2/l_{\max}$ is proportional to $W_0$. Assuming that the maximum projected length of the discharge column is proportional to a critical length, the measured results

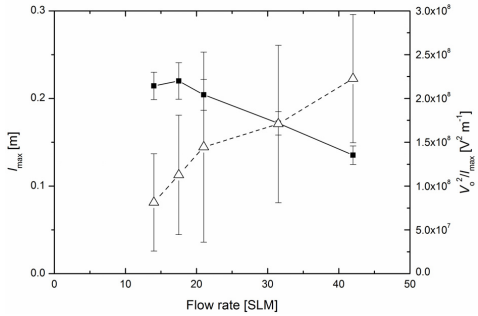


**Fig. 5.** The maximum projected length of the gliding arc discharge column $l_{\max}$ (solid square) and $V_0^2/l_{\max}$ (open triangle) at different air flow rates. For a visual aid, they are connected by a solid line and a broken line, respectively.

suggest that the critical length tends to decrease and $W_0$ to increase with increasing gas flow rates in accordance with the predictions based on equations (21) and (22).

Taking the ratio of $l_{crit}$ in equation (21) to $l_{crit\text{-}dc}$ in equation (3) and assuming that $V$ and $W$ in equation (3) are equal to $V_0$ and $W_0$ in equation (21),

$$\frac{l_{crit}}{l_{crit\_dc}} = \frac{1}{\cos\delta\left(1 - \frac{\omega L}{R}\tan\delta\right)\cos(\phi - \delta)} > 1. \quad (23)$$

Under these assumptions if a critical length exists for the AC driven gliding arc, it is always larger than that of a corresponding DC driven gliding arc. This result is supported by the fact that the DC gliding arcs reported in the literature typically have shorter extension lengths than the AC gliding arcs [5–7,17–19].

It is observed that the length of the gliding arc is limited by two mechanisms: either the plasma current suddenly finds a shorter path in short-cutting events [18] (also called back breakdown [30]) or the next discharge ignites at the closest gap $g$ of the electrodes. It is observed that the magnitude of the voltage $V_0$ increases as the length of the discharge column $l$ increases [15]. Once the voltage reaches the value at which the next gas breakdown occurs at the closest gap, the extended gliding arc will be extinguished [34]. It is therefore possible that the measured maximum length might be shorter than the achievable length predicted by equation (21). If the width of the closest gap increases at a fixed gas flow rate, the model suggests that the ignition voltage also increases so that the gliding arc can be further extended. However, depending on a specification of a high voltage power supply, there is a limitation of achievable maximum voltage at or below which initial gas breakdown should occur in order to generate a gliding arc. Therefore an optimum gap $g_{opt}$ exists practically. If $g > g_{opt}$, the initial gas breakdown cannot occur. If $g < g_{opt}$, arc discharge can be more easily ignited at the closest gap so that the extended gliding arc can be extinguished. By tuning the width of the closest gap, the discharge length $l$ might be further increased.

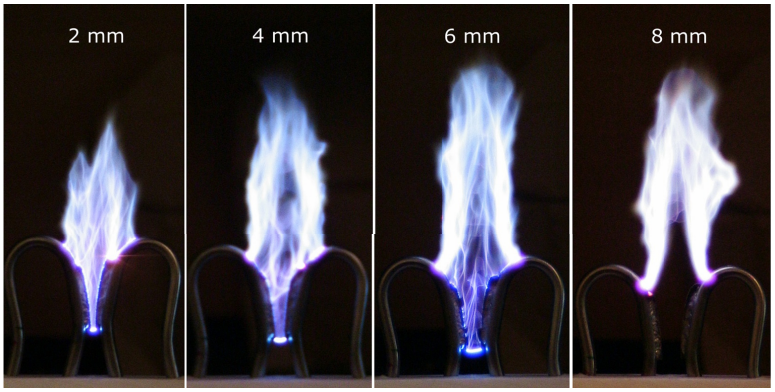


**Fig. 6.** Photos of the AC gliding arc II for the gaps of 2, 4, 6 and 8 mm taken by the normal video camera with an automatic exposure time. Frequency: 31.25 kHz, gas flow rate: 14 SLM, power: approximately 800 W.

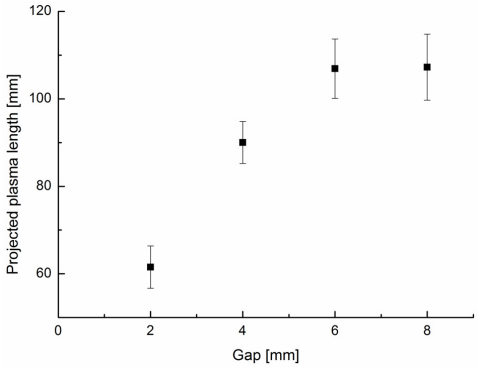


**Fig. 7.** Measured projected length of the plasma column for the electrode gaps of 2, 4, 6 and 8 mm. The projected length is measured using the images taken by a normal video camera.

In order to verify the concept of the optimum gap experimentally, the gap between the electrodes of the gliding arc II was varied from 2 mm to 8 mm. Figure 6 shows photos of the AC gliding arc II taken by the normal video camera with an exposure time of 33.3 ms. The driving frequency was 31.25 kHz, the gas flow rate was 14 SLM, and power was approximately 800 W. The projected length of the discharge column at different gaps was measured using the images taken by the normal video camera, as shown in in Figure 7. As the gap increases, the gliding arc tends to be longer and the projected length approaches to a saturated value of approximately 11 cm, while the photoemission decreases in the region between the electrodes. It is noted that the error bar of the projected length is much smaller compared with our previous work [31] due to different cameras used in the experiments.

Measurements of optical emission spectroscopy (OES) were performed using an optical fibre and a spectrometer equipped with a grating with 3600 grooves/mm and a CCD camera (PI-MAX 1024, Princeton Instruments). The photoemission of the gliding arc II at several cm above the edge of the electrodes was collected as shown in Figure 8. The OES includes NO, OH and $N_2$ bands. The photoemission intensity increases as the gap increases, whereas the relative intensities of the emission from these different bands are approximately the same. The chemical composition of the photo-emitting species is therefore independent of the gap width. These results in Figures 6–8 mean that smaller gaps favour arc ignition but suppress extension of the plasma column. On the other hand, when the gap is too large, the discharge would not ignite. It is therefore experimentally concluded that an optimal gap exists to efficiently extend the gliding arc discharge. In order to fully determine the difference between the critical length and the maximum length of the gliding arc before extinction, parameters such as gas flow dynamics, gas temperature, geometrical aspects, and electrode materials need to be further considered.

## 3 Conclusion

A stability analysis of the AC driven gliding arc discharges is carried out. It is indicated that the phase shift of the specific power dissipated from the discharge is independent of the discharge length and the power dissipated from the discharge per unit length. The condition of the critical length of the gliding arc can be discriminated by the relation between the phase shift of the discharge current to the ratio of the characteristic time of the AC power supply to that of the electrical circuit. The calculation indicates that the AC gliding arc discharges can be preferably extended when the AC frequency increases, the serial resistance decreases and the gas flow rate is lowered. The suggested dependence of the maximum achievable discharge extension on the mass flow rate is demonstrated experimentally. Furthermore it is found that the critical length of an AC

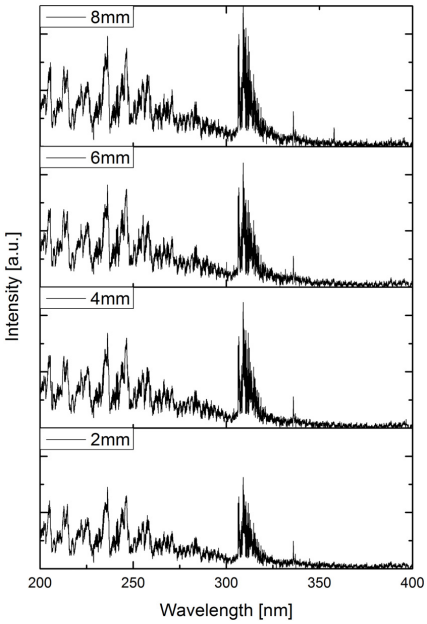


**Fig. 8.** OES of the gliding arc II for the gaps of 2, 4, 6 and 8 mm.

gliding arc would be longer than that of a corresponding DC gliding arc supported by a survey of previously published images of AC and DC gliding arcs in the literature. It is indicated that the length of the gliding arc discharge can be further extended by tuning the gas breakdown condition at the closest gap between the electrodes.

This work is financially supported by the Swedish Energy Agency and Knut Alice Wallenberg Foundation.

## References

1. K.L. Mittal, in *Polymer Surface Modification: Relevance to Adhesion* edited by K.L. Mittal (VSP, Utrecht, 2004), Vol. 3
2. M. Kogoma, in *Generation and Applications of Atmospheric Pressure Plasmas*, edited by M. Kogoma, M. Kusano, Y. Kusano (NOVA Publishers, New York, 2011)
3. Y. Kusano, T.L. Andersen, P.K. Michelsen, J. Phys. Conf. Ser. Surf. **100**, 012002 (2009)
4. S. Teodoru, Y. Kusano, N. Rozlosnik, P.K. Michelsen, Plasma Proc. Polym. **6**, S375 (2009)
5. Y. Kusano, S. Teodoru, F. Leipold, T.L. Andersen, B.F. Sørensen, N. Rozlosnik, P.K. Michelsen, Surf. Coat. Technol. **202**, 5579 (2008)
6. Y. Kusano, K. Norrman, J. Drews, F. Leipold, S.V. Singh, P. Morgen, A. Bardenshtein, N. Krebs, Surf. Coat. Technol. **205**, S490 (2011)
7. Y. Kusano, S.V. Singh, K. Norrman, J. Drews, F. Leipold, N. Rozlosnik, A. Bardenshtein, N. Krebs, Surf. Eng. **28**, 453 (2012)
8. J. Janča, A. Czernichowski, Surf. Coat. Technol. **98**, 1112 (1998)
9. Y. Kusano, J. Adhesion **90**, 755 (2013)
10. Y. Kusano, T.L. Andersen, H.L. Toftegaard, F. Leipold, A. Bardenshtein, N. Krebs, Int. J. Mater. Eng. Innovation, **5**, 122 (2014)
11. Y. Kusano, Surf. Eng. **25**, 415 (2009)
12. A. Czernichowski, Pure Appl. Chem. **66**, 1301 (1994)
13. A. Fridman, S. Nester, L.A. Kennedy, A. Saveliev, O. Mutaf-Yardimci, Prog. Energy Combust. Sci. **25**, 211 (1999)
14. A. Fridman, L.A. Kennedy, *Plasma Physics and Engineering* (Taylor & Francis, New York, 2004)
15. I.V. Kuznetsova, N.Y. Kalashnikov, A.F. Gutsol, A.A. Fridman, L.A. Kennedy, J. Appl. Phys. **92**, 4231 (2002)
16. Y.D. Korolev, O.B. Frants, V.G. Geyman, N.V. Landl, V.S. Kasyanov, IEEE Trans. Plasma Sci. **39**, 3319 (2011)
17. Y. Kusano, B.F. Sørensen, T.L. Andersen, F. Leipold, J. Adhesion **89**, 433 (2013)
18. Z.W. Sun, J.J. Zhu, Z.S. Li, M. Aldén, F. Leipold, M. Salewski, Y. Kusano, Optics Express **21**, 6028 (2013)
19. Y. Kusano, B.F. Sørensen, T.L. Andersen, H.L. Toftegaard, F. Leipold, M. Salewski, Z.W. Sun, J.J. Zhu, Z.S. Li, M. Aldén, J. Phys. D **46**, 135203 (2013)
20. V. Dalaine, J.M. Cormier, P. Lefaucheux, J. Appl. Phys. **83**, 2435 (1998)
21. V. Dalaine, J.M. Cormier, S. Pellerin, P. Lefaucheux, J. Appl. Phys. **84**, 1215 (1998)
22. F. Richard, J.M. Cormier, S. Pellerin, J. Chapelle, J. Appl. Phys. **79**, 2245 (1996)
23. S. Pellerin, F. Richard, J. Chapelle, J.M. Cormier, K. Musiol, J. Phys. D **33**, 2407 (2000)
24. V. Dalaine, J.M. Cormier, S. Pellerin, E. Hnatiuc, in *Proceedings of the 6th International Conference on Optimization of Electrical and Electronic Equipments (OPTIM '98)*, 1998, Vol. 1, p. 161
25. J. Špreka, P. Souček, J.J.W.A. Van Loon, A. Dowson, C. Schwarz, J. Krause, G. Kroesen, V. Kudrle, Eur. Phys. J. D **67**, 261 (2013)
26. A. Fridman, A, Gutsol, S. Gangoli, Y. Ju, T. Ombrello, J. Propuls. Power **24**, 1216 (2008)
27. H. Maecker, Z. Phys. **157**, 1 (1959)
28. S. Pellerin, J. Chapelle, F. Richard, K. Musiol, J. Chapelle, J. Phys. D **32**, 891 (1999)
29. T. Ombrello, X. Qin, Y. Ju, A. Gutsol, A. Fridman, C. Carter, AIAA J. **44**, 142 (2006)
30. S. Pellerin, J.M. Cormier, K. Musiol, B. Pokrzywka, J. Koulidiati, F. Richard, J. Chapelle, High Temp. Mater. Proc. **2**, 49 (1998)
31. J.J. Zhu, Z.W. Sun, Z.S. Li, A. Ehn, M, Aldén, M. Salewski, F. Leipold, Y. Kusano, J. Phys. D **47**, 295303 (2014)
32. R. Hemmi, Y. Yokomizu, T. Matsumura, J. Phys. D **36**, 1097 (2003)
33. J. Heberlein, J. Mentel, E. Pfender, J. Phys. D **43**, 02301 (2010)
34. J.M. Meek, J.D. Craggs, *Electrical Breakdown of Gases* (Oxford University Press, Oxford, 1953)

# [Appendix A11]

N. Krebs, A. Bardenshtein, Y. Kusano, H. Bindslev, H.J. Mortensen

## ”Enhancing plasma surface modification using high intensity and high power ultrasonic acoustic wave”

US patent No. 8,399,795 B2 (2013).

There is a variation that has been granted in China (Chinese patent No. 101,743,785 B (2012)).

US008399795B2

(12) **United States Patent**
**Krebs et al.**

(10) **Patent No.: US 8,399,795 B2**
(45) **Date of Patent: Mar. 19, 2013**

(54) **ENHANCING PLASMA SURFACE MODIFICATION USING HIGH INTENSITY AND HIGH POWER ULTRASONIC ACOUSTIC WAVES**

(75) Inventors: **Niels Krebs**, Hellerup (DK); **Alexander Bardenshtein**, Hedehusene (DK); **Yukihiro Kusano**, Roskilde (DK); **Henrik Bindslev**, Charlottenlund (DK); **Henrik Junge Mortensen**, Taastrup (DK)

(73) Assignees: **Force Technology**, Brondby (DK); **Technical University of Denmark**, Kgs. Lyngby (DK)

( * ) Notice: Subject to any disclaimer, the term of this patent is extended or adjusted under 35 U.S.C. 154(b) by 767 days.

(21) Appl. No.: **12/599,775**

(22) PCT Filed: **May 9, 2008**

(86) PCT No.: **PCT/EP2008/055773**

§ 371 (c)(1),
(2), (4) Date: **Nov. 11, 2009**

(87) PCT Pub. No.: **WO2008/138901**

PCT Pub. Date: **Nov. 20, 2008**

(65) **Prior Publication Data**

US 2010/0304146 A1 Dec. 2, 2010

(30) **Foreign Application Priority Data**

May 11, 2007 (DK) ..... 2007 00717

(51) **Int. Cl.**
***H05H 1/24*** (2006.01)
***B08B 6/00*** (2006.01)
***H05F 3/00*** (2006.01)
***A61F 2/00*** (2006.01)
***C23F 1/00*** (2006.01)

(52) **U.S. Cl.** ..... **219/121.36**; 216/67

(58) **Field of Classification Search** ..... 219/121.4, 219/121.43, 121.44; 315/111.21, 111.41, 315/111.51, 111.71; 204/298.38, 298.39; 216/67, 69; 156/345.41, 345.43, 345.48, 345.52; 118/723 R, 723 MW
See application file for complete search history.

(56) **References Cited**

U.S. PATENT DOCUMENTS

3,169,507 A * 2/1965 Rich ..... 116/137 R
5,367,139 A * 11/1994 Bennett et al. ..... 219/121.59
(Continued)

FOREIGN PATENT DOCUMENTS

JP 7060211 3/1995
JP 11335869 12/1999
(Continued)

OTHER PUBLICATIONS

Kwang-Seok Choi et al. "Improvement of Charging Performance of Corona Charger in Electrophotography by Irradiating Ultrasonic Wave to Surrounding Region of Corona Electrode", Japanese Journal of Applied Physics, vol. 44, No. 5A, 2005, pp. 3248-3252.

*Primary Examiner* — Long Tran
*Assistant Examiner* — Jordan Klein
(74) *Attorney, Agent, or Firm* — Morrison & Foerster LLP

(57) **ABSTRACT**

This invention relates to a plasma surface modification process (and a corresponding a system) of a solid object (**100**) comprising creating plasma (**104**) by a plasma source (**106**), application of the plasma (**104**) to at least a part of a surface (**314**) of the solid object (**100**), generating ultrasonic high intensity and high power acoustic waves (**102**) by at least one ultrasonic high intensity and high power acoustic wave generator (**101**), wherein the ultrasonic acoustic waves are directed to propagate towards said surface (**314**) of the object (**100**) so that a laminar boundary layer (**313**) of a gas or a mixture of gases (**500**) flow in contact with said solid object (**100**) is thinned or destructed for at least a part of said surface (**314**). In this way, the plasma can more efficiently access and influence the surface of the solid object to be treated by the plasma, which speeds the process time up significantly.

**29 Claims, 9 Drawing Sheets**

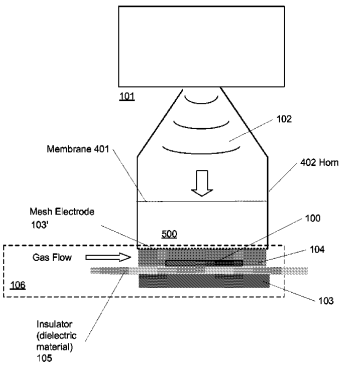

U.S. PATENT DOCUMENTS

| | | | | |
|---|---|---|---|---|
| 5,387,777 | A * | 2/1995 | Bennett et al. | 219/121.43 |
| 5,457,847 | A * | 10/1995 | Uzawa et al. | 15/345 |
| 6,261,373 | B1 * | 7/2001 | Grant | 118/725 |
| 6,383,301 | B1 * | 5/2002 | Bell et al. | 118/716 |
| 6,554,969 | B1 * | 4/2003 | Chong | 204/192.12 |
| 6,949,716 | B2 * | 9/2005 | Koulik et al. | 219/121.59 |
| 2001/0029964 | A1 * | 10/2001 | Fujii et al. | 134/1 |
| 2002/0182101 | A1 * | 12/2002 | Koulik et al. | 422/4 |
| 2003/0165636 | A1 * | 9/2003 | Koulik et al. | 427/569 |
| 2004/0105779 | A1 * | 6/2004 | Krebs | 422/26 |
| 2007/0065596 | A1 * | 3/2007 | Koulik et al. | 427/535 |
| 2009/0288910 | A1 * | 11/2009 | Krebs et al. | 181/175 |

FOREIGN PATENT DOCUMENTS

| | | |
|---|---|---|
| JP | 2000040689 | 2/2000 |
| JP | 2006013903 | 1/2006 |
| WO | 02078751 | 10/2002 |
| WO | 2008003324 | 1/2008 |

* cited by examiner

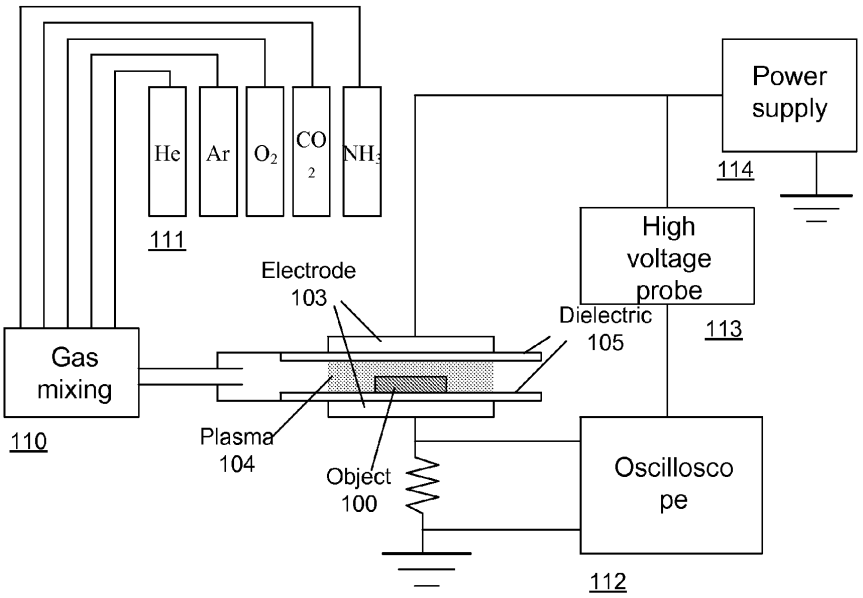


Figure 1

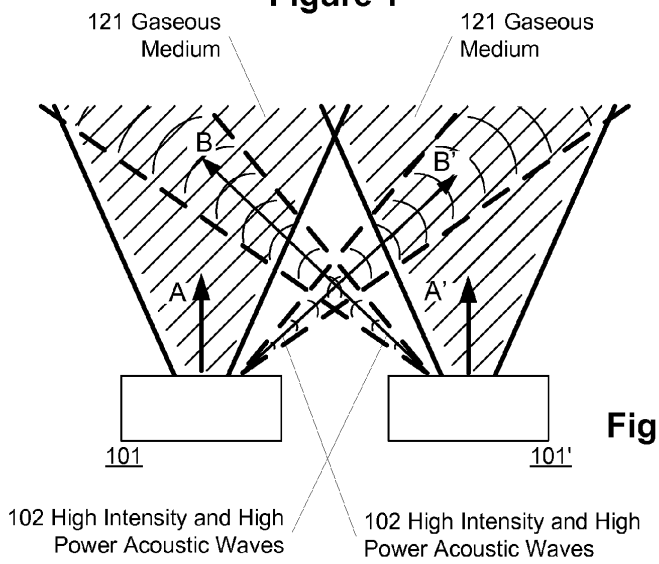


Figure 12

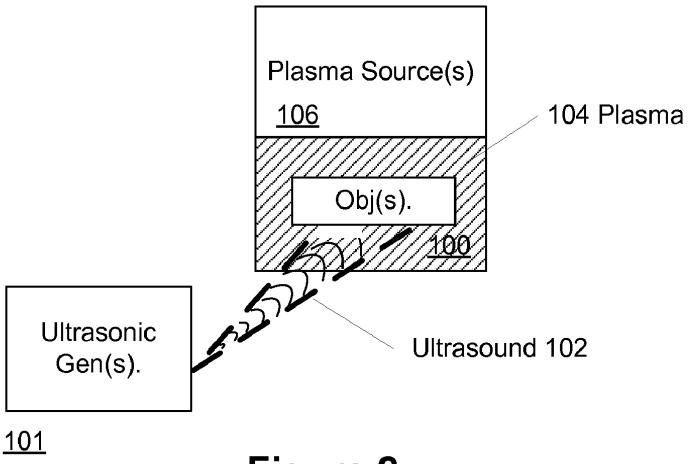


Figure 2

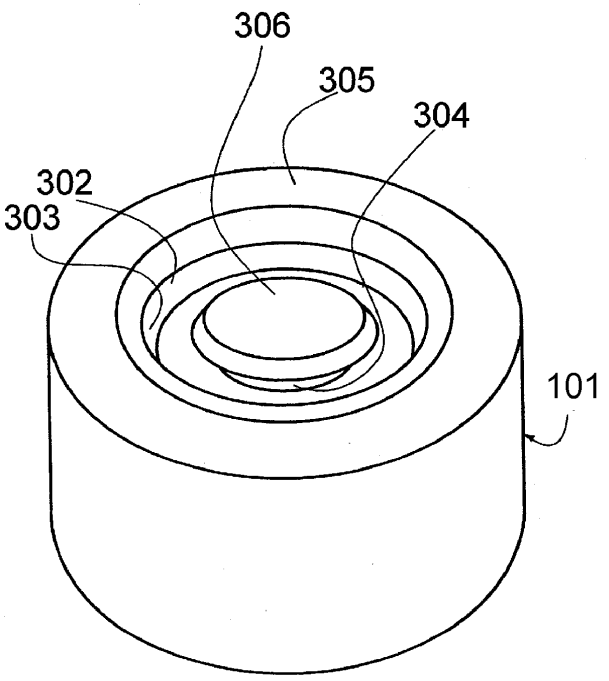


Figure 9

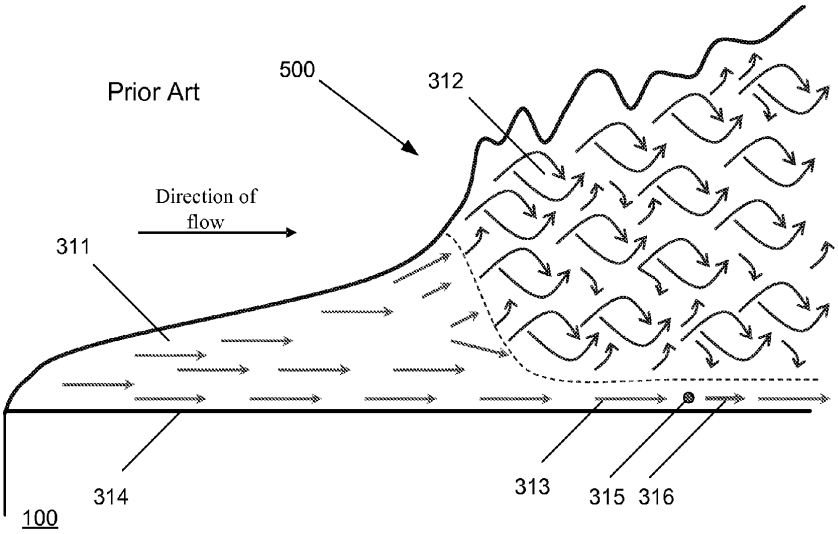


Figure 3a

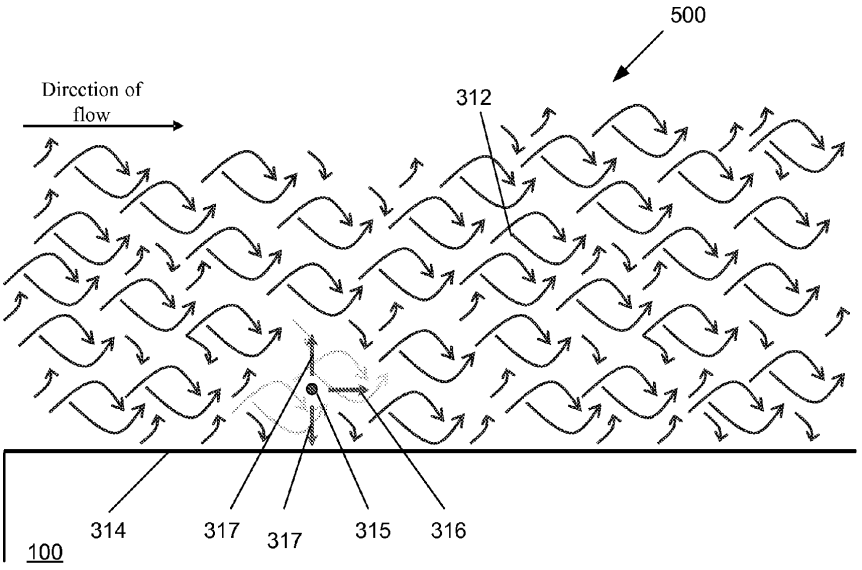


Figure 3b

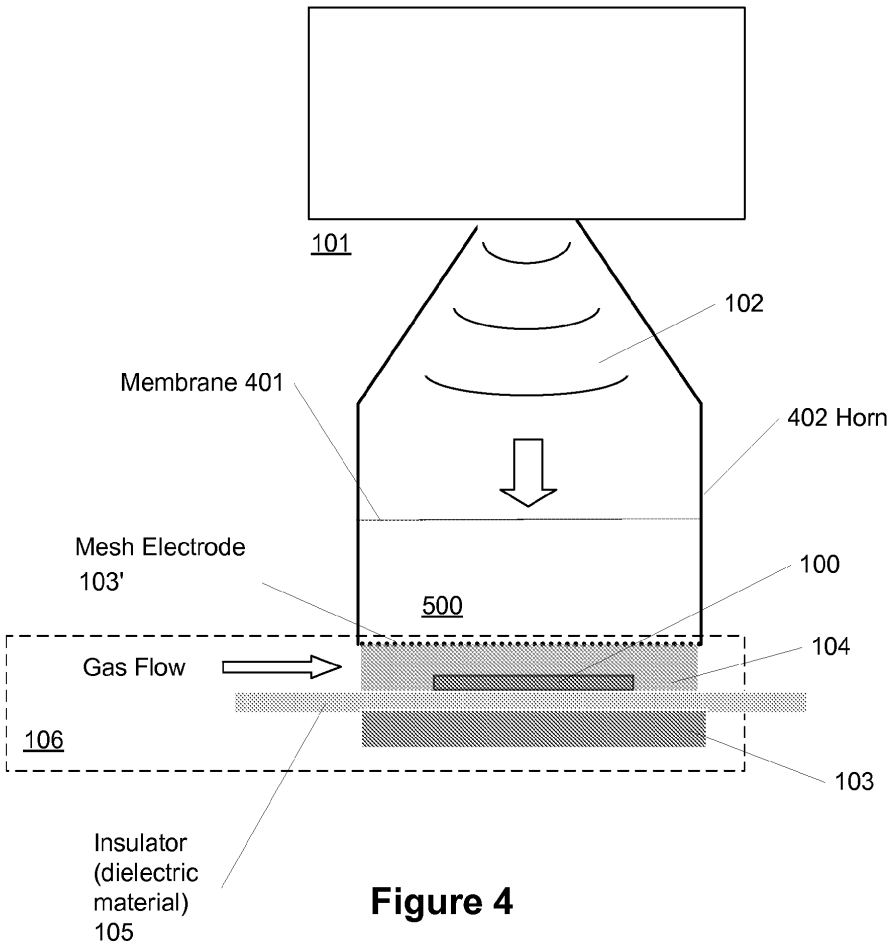
101
102
Membrane 401
402 Horn
Mesh Electrode
103'
500
100
104
Gas Flow
106
103
Insulator
(dielectric
material)
105

Figure 4

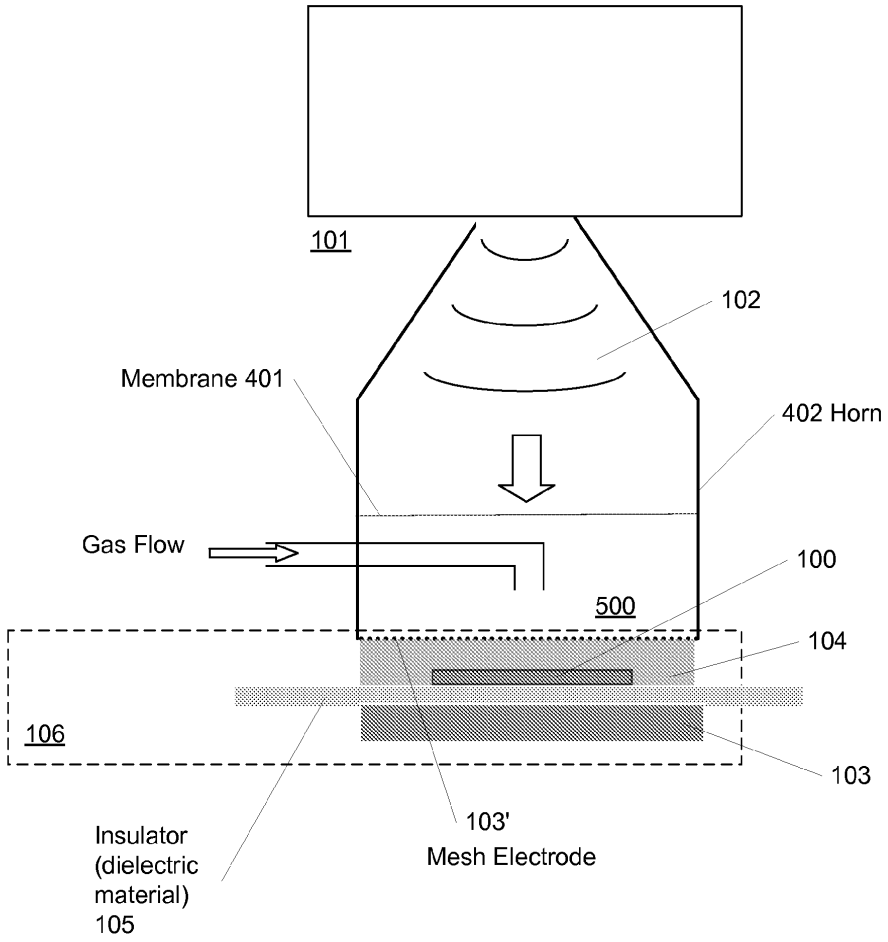
101
102
Membrane 401
402 Horn
Gas Flow
100
500
104
106
103
103'
Mesh Electrode
Insulator
(dielectric
material)
105

**Figure 5**

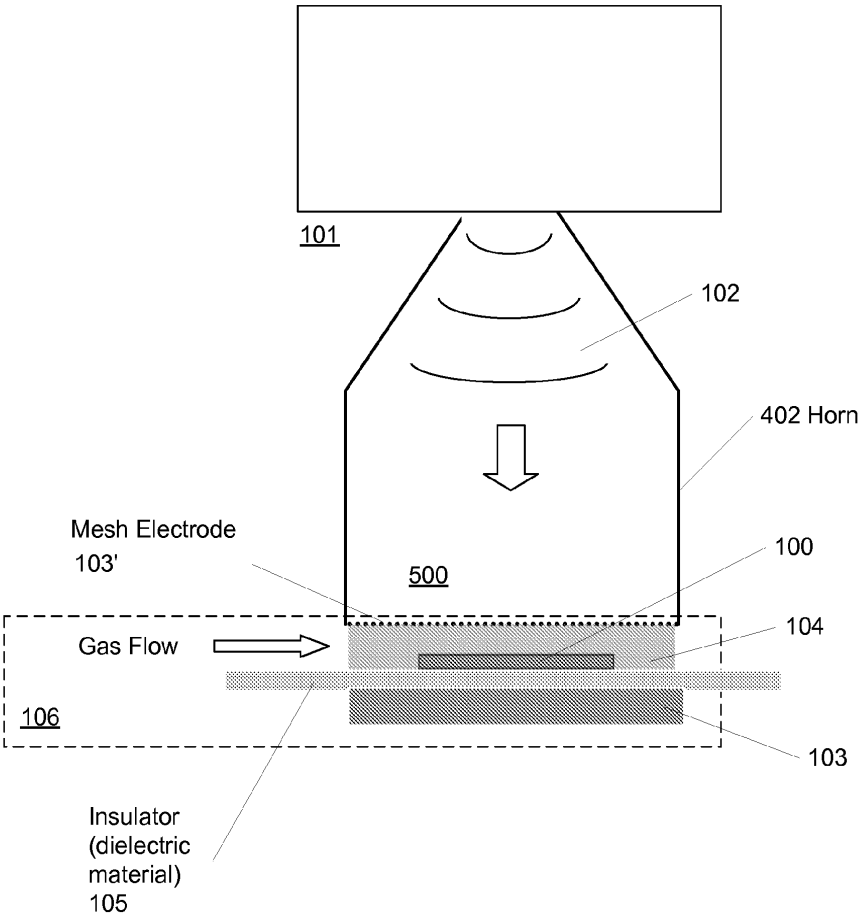
101
102
402 Horn
Mesh Electrode
103'
500
100
Gas Flow
104
106
103
Insulator
(dielectric
material)
105

Figure 6

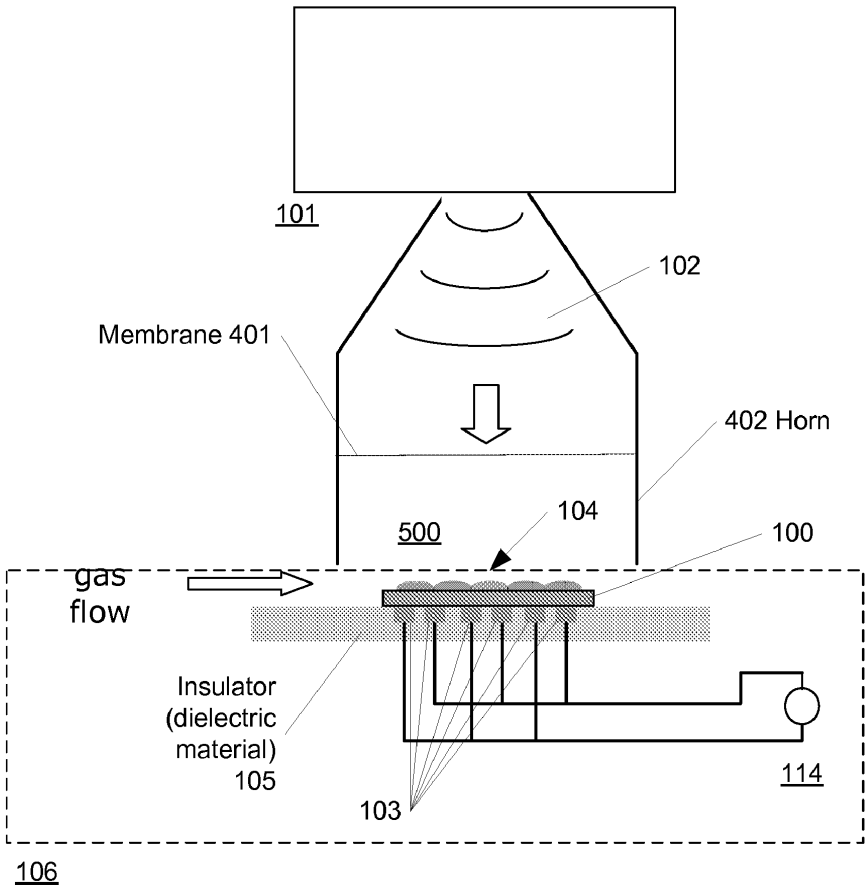
101
102
Membrane 401
402 Horn
104
500
100
gas
flow
Insulator
(dielectric
material)
105
114
103
106

Figure 7

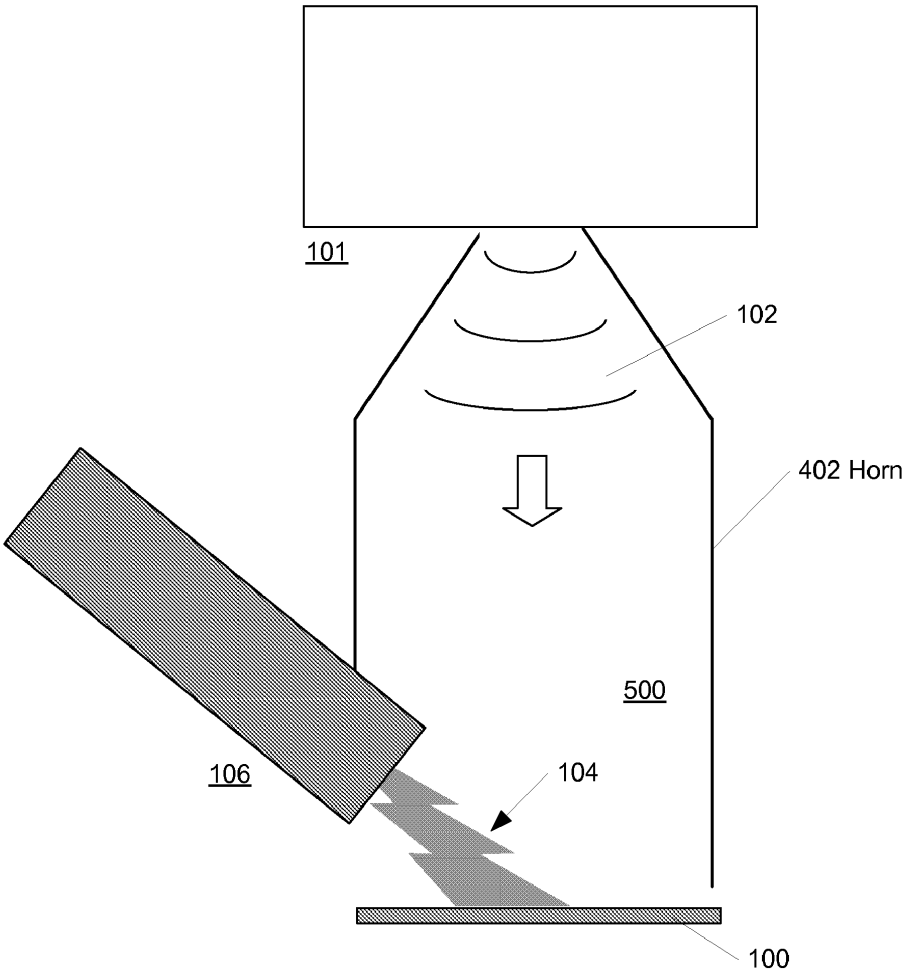


Figure 8

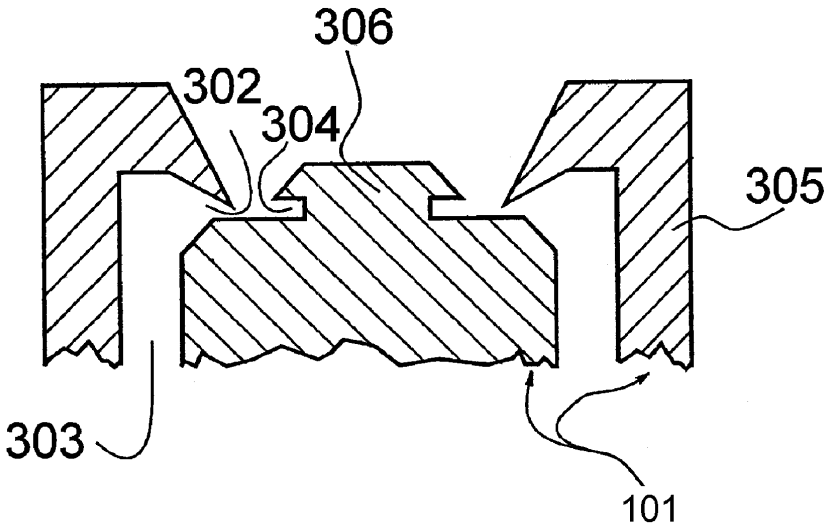


Figure 10

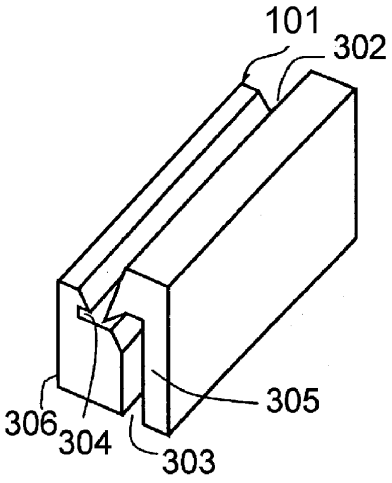


Figure 11

# ENHANCING PLASMA SURFACE MODIFICATION USING HIGH INTENSITY AND HIGH POWER ULTRASONIC ACOUSTIC WAVES

## FIELD OF THE INVENTION

The invention relates to a method of plasma surface modification of an object. The invention further relates to a system for plasma surface modification of an object and an object that has had its surface modified by plasma surface modification.

## BACKGROUND OF THE INVENTION

Plasma is an ionized gas. Active species of ions, electrons, high-energy neutrals, radicals as well as ultra-violet emission in plasmas can be used for modification of material surfaces such as surface activation/inactivation, adhesion improvement, wettability enhancement, printability improvement, surface cleaning, hardening, cross-linking, curing, polymer-chain secession, coloration, roughening, ashing, etching, sterilization, thin film deposition, material synthesis (particle formation at the surface etc.) etc.

Plasma surface modification can usually be divided into two categories with opposite effects, depending mainly on the process gas(es) used. The first one mainly ablates the surfaces, and is usually called "plasma treatment", "plasma surface modification", "plasma ablation" (R Li et al. Composites Pt.A 28A (1997) 73-86), or "non-polymer-forming plasma" (N Dilsiz J Adhesion Sci. Technol. 14(7) (2000) 975-987). The second one is usually called "plasma polymerization", "polymer-forming plasma" (N Dilsiz J Adhesion Sci. Technol. 14(7) (2000) 975-987) or plasma enhanced chemical vapour deposition (PECVD). In the following "plasma surface modification" is meant to cover both types while "plasma treatment" is used for the first one and "plasma polymerization" is used for the second one.

If the used gas(es) has high proportions of carbon and hydrogen atoms, double- or triple-bonds in its composition such as methane, ethylene, acetylene and ethanol, or if they are precursors such as metal-organic (organometallic) gas (es), the plasma often results in plasma polymerization or PECVD. Here, metal-organic gases are those which contain a metal, particularly compounds in which the metal atom has a direct bond with a carbon atom. Otherwise, the plasma will have a tendency of ablation (plasma treatment).

A variety of plasmas exists, including direct current plasmas, capacitively coupled plasmas, pulsed plasmas, magnetron plasmas, electron cyclotron resonance plasmas, inductively coupled plasmas, helicon plasmas, helical resonator plasmas, microwave plasmas, and plasma jets (see e.g. A Bogaerts et al. Spectrochimica Pt.B 57 (2002) 609-658.). Many of them are operated at low pressures, suffering from the drawbacks that they require expensive vacuum systems. Furthermore, methods are only well-developed for batch or semi-batch treatments. To overcome these drawbacks an atmospheric pressure plasma surface modification system can be used that not only avoids the need for vacuum equipment but also permits both the surface modification of large objects and production line continuous surface modification (see e.g. C Tendero et al. Spectrochimica Pt.B 61 (2006) 2-30.).

A prior art plasma application system is shown in FIG. **1** and is explained in more detail in the following. FIG. **1** illustrates an example of capacitively coupled plasma of the well-known so-called dielectric barrier discharge (DBD) type usable at atmospheric pressure.



Other types or variations of plasma sources include dielectric barrier discharges (DBDs) with a single dielectric barrier located substantially in the middle between the two electrodes or with a single dielectric barrier covering only one of the electrodes. Such plasma sources are typically also referred to as volume discharge (VD) sources where a micro-discharge can take place in thin channels generally randomly distributed over the electrode- and/or dielectric-surface. Other DBD plasma sources include so-called surface discharge (SD) plasma sources typically comprising a number of surface electrodes on a dielectric layer and a counter-electrode on the reverse side of the dielectric layer. Such SD plasma sources may include a so-called SPCP (Surface-discharge-induced Plasma Chemical Processing) discharge element or CDSD (Coplanar Diffuse Surface Discharge) element. In a SPCP, electrodes are attached on the dielectric(s) and in a CDSD the electrodes are embedded in the dielectric(s).

Other types of plasma sources are e.g. so-called plasma torches such as arc plasma torches, cold plasma torches (see e.g. H Mortensen et al. Jpn. J Appl. Phys. 45(10B) (2006) 8506-8511.), atmospheric pressure plasma jet (APPJ), pencil like torches, barrier torches, and microwave torches (see e.g. C Tendero et al. Spectrochimica Pt.B 61 (2006) 2-30.). Yet another type of plasma source is the so-called gliding arc (see for example A Fridman et al. J. Phys. D Appl. Phys. 38 (2005) R1-R24).

Additional types of plasma sources are low pressure plasmas, corona discharge (see e.g. A Bogaerts et al. Spectrochimica Pt.B 57 (2002) 609-658) and microplasmas (see e.g. V Karanassios Specrochimica Acta Pt.B 59 (2003) 909-928). See e.g. A Bogaerts et al. Spectrochimica Pt.B 57 (2002) 609-658, U Kogelschatz Plasma Chem. Plasma Proc. 23(1) (2003) 1-46, C Tendero et al. Spectrochimica Pt.B 61 (2006) 2-30 and A Fridman et al. J. Phys. D Appl. Phys. 38 (2005) R1-R24) for further details of plasmas and atmospheric pressure plasmas.

The two articles 'Ozone generation by hollow-needle to plate electrical in an ultrasound field', J. Phys. D: Appl. Phys. 37 (2004) 1214-1220 and 'Ultrasound and airflow induced thermal instability suppression of DC corona discharge: an experimental study', Plasma Sources Sci. Technol. 15 (2006) 52-58 by Stanislav Pekárek and Rudolf Bálek disclose suppression of DC corona discharge where ultrasound or ultrasound combined with an airflow is used in connection with a hollow needle-to-plate electrode system to activate the corona discharge for ozone production. The article 'Improvement of Charging Performance of Corona Charger in Electrophotography by Irradiating Ultrasonic Wave to Surrounding Region of Corona Electrode' (Kwang-Seok Choi, Satoshi Nakamura and Yuji Murata Jpn. J. Appl. Phys. 44(5A) (2005) 3248-3252.) discloses improvement of the charging speed of a corona charger in electrophotography using an ultrasonic wave where the ultrasonic wave increases the charge density on an insulator layer of a coated aluminum drum used instead of a photoreceptor drum used for printing. At least some of the findings in the articles have also been disclosed in patent application CZ 295687.

The ultrasonic generators disclosed in three above-mentioned articles are based on piezoelectric transducers. No mention is given of specific or preferred sound pressure levels of the emitted acoustic waves or ultrasonic waves or the advantages thereof.

Furthermore, the two first articles mention that the acoustic pressures developed by ultrasonic layouts are, respectively, of the order of 2 and 10 kPa near the emitting surface of the transducer at the frequency of generated ultrasound of 20.3

kHz. In the third article, the ultrasonic generator is a 28-kHz 50-mm-diam and 80-mm-height bolt-clamped Langevin-type piezoelectric transducer. The maximum input power is 50 W. These values give an estimation of the emitted acoustic pressure value to be approximately 2 kPa. The pressure values of 2 and 10 kPa correspond to very high sound pressure levels of 160 and 174 dB above the reference pressure of $2\times10^{-5}$ Pa. It can be estimated that the above-specified acoustic pressures at the above frequency correspond to ultrasound intensities of 4.4 and 20 kW/m$^2$ or the sound intensity levels of 156 and 163 dB above the reference intensity of 1 pW/m$^2$.

This characterizes the ultrasonic acoustic waves being applied in these three articles as high-intensity.

However, the acoustic power provided according to all three articles is in fact too low and too localized to allow for uniform minimization and/or elimination of a laminar boundary layer over a relatively substantial area of an object to have its surface modified by plasma.

The similar situation can be outlined regarding the patent specification U.S. Pat. No. 6,391,118. It discloses a method for removing particles from the surface of an article in an apparatus using corona discharge. The particles are supplied with an electric charge and subsequently an ultrasonic wave or gas stream is applied onto the surface of the article while an electric field is applied for driving away the electrically charged solid particles from the surface. The application of an ultrasonic wave and/or gas further facilitate the removal of the electrically charged solid particles. The variety of ultrasonic generators (oscillators) here includes a piezoelectric oscillator, a polymer piezoelectric membrane, an electrostrictive oscillator, a Langevin oscillator (that is as mentioned above just a special type of piezoelectric transducers), a magnetostrictive oscillator, an electrodynamic transformer, and a capacitor transformer. Use of such oscillators provides acoustic power that is low (no more than 50 W) and localized. It is too low and localized to allow for uniform minimization and/or elimination of a laminar boundary layer over a relatively substantial area of an object to have its surface modified by plasma. Moreover, no disclosure is given of a specific or preferred sound pressure level of the emitted ultrasonic waves or the advantages thereof. Furthermore, plasma surface modification is not addressed in this specification.

Additionally, no mention or discussion of a laminar boundary layer around the object to be modified is given. The presence of this boundary laminar layer hinders the excess of energetic plasma particles (and hence the mass and energy transfer) to the surface of the object and thereby reduces the efficiency of the plasma treatment. It is important to eliminate or reduce the laminar boundary layer substantially uniformly over a substantial area of the object to be modified by plasma.

Patent application US 2003/0165636 discloses a process for atmospheric pressure plasma surface modification of an object's surface where excitation of the surface to be treated is done so that it vibrates and undulates thereby activating the application of plasma. The energy for excitation of the surface may come from the process of creating the plasma, from an external source, or from a combination thereof. The energy for excitation of the surface may come from a vibration generator brought in contact with the object to be treated or by indirect contact from a vibration generator emitting acoustic waves, e.g. ultrasonic waves, to the object to be treated so that it provokes turbulent plasma. No disclosure is given of a specific or preferred sound pressure level of the acoustic waves or the ultrasonic waves or the advantages thereof. Therefore, exciting surface vibrations and undulations, or in other words, generation of guided and surface acoustic waves on the object is suggested in order to intensify a plasma treatment. Correspondingly, it is disclosed that the vibration of the surface to be treated can be the result of excitation at one or several eigenfrequencies and their harmonics associated with the body of the object to be treated. Thus, either the range of the characteristic dimension of the modified object (primarily its thickness) is strictly limited by the operating frequency of the used source of acoustic energy, or the said frequency is strictly determined by the dimension of the object. It is also disclosed that the vibration of the surface can also result from forced frequencies when an external generator of acoustic waves emits frequencies that are not harmonics of the eigenfrequencies of the object to be treated. This signifies generation of surface acoustic waves (primarily the Rayleigh surface waves).

The following procedures of transfer of acoustic power into ambient gas/plasma are mentioned:

1. External acoustic generator→Treated object surface vibration→Gas molecules (plasma particles) vibration.
2. Generation of the treated surface object vibration directly, for instance through a direct acoustic contact→Gas molecules (plasma particles) vibration.

Both procedures require acoustic waves to overpass the solid/gas interface at least once. However, due to more than four-orders-of-magnitude difference in acoustic impedance for a solid and a gas, most of generated acoustic power cannot be emitted (and especially re-emitted) into the gas atmosphere and remains in a solid being ultimately converted into thermal energy. Thus, it is not possible in this way to generate sound or ultrasound in the air with a power that would be enough to remove or reduce the laminar boundary layer on sufficiently large surfaces. Moreover, no mention or discussion of a laminar boundary layer near to the surface of the object to be modified is given. The presence of this boundary laminar layer hinders the access of energetic plasma particles (and hence the mass and energy transfer) to the surface of the object and thereby reduces the efficiency of the plasma treatment. Therefore, it is of prime importance not simply to "shake" the surface up and provoke uncontrolled turbulent plasma with unknown efficiency and spatial distribution in such a way, but rather to eliminate or reduce the boundary laminar layer directly, efficiently, and substantially uniformly over a substantial area of the object to be modified by plasma.

Patent specification CN 1560316 discloses a process for ultrasonic plasma-spraying for controlling coating porosity and improving coating bond strength where an ultrasonic excitation source is connected in parallel with an anode and a cathode of the spray gun of the plasma-spraying device and where the sprayed powder is heated and the ultrasound acts on the plasma and simultaneously on the melting sprayed powder. No mention or discussion of a boundary laminar layer over the surface of the object to be modified is given. The presence of this boundary laminar layer hinders the access of energetic plasma particles (and hence the mass and energy transfer) to the surface of the object and thereby reduces the efficiency of the plasma surface modification.

The generated acoustic power is relatively low (at any rate, below 100 W) because the power applied to the acoustic wave transmitter is actually 100 W, and the efficiency of sound generation in a gas atmosphere cannot exceed ~30% even for the most effective gas-jet ultrasonic transmitters, not to mention other methods. This is too low power to efficiently allow for substantial uniform minimization and/or elimination of the laminar boundary layer over a substantial area of an object to have its surface modified by plasma.

Patent application JP 11335869 A discloses a process for surface treatment and a device therefore where activated species in gas form is generated in a plasma and where the

activated species in gas form is subjected to ultrasound and brought in contact with a surface. So a surface treatment by a gas and not surface treatment by a plasma is disclosed.

A principal impediment to the transfer or transmission of energy and/or mass from a plasma to a solid surface is the laminar boundary layer between the plasma and the object to be treated, which adheres to the solid surface. Even when the motion of the gas is fully turbulent, a laminar boundary layer exists (as explained in greater detail in connection with FIGS. **3***a* and **3***b*) that obstructs mass transport and/or energy transfer. While various methods and types of apparatus have been suggested for overcoming the problem such as by means of driving the plasma with sonic waves and vibrating the solid object with external vibration generators, these methods while being effective to some extent, are inherently limited in their ability to generate an effective minimization of the laminar boundary layer and at the same time covering an area large enough to make the method efficient.

None of the mentioned prior art disclosures specify an acoustic power level sufficient to efficiently allow for substantial uniform minimization and/or elimination of the laminar boundary layer over a substantial area of an object to have its surface modified efficiently by plasma. Furthermore, the prior art involving piezoelectric transducers or other transducers involving a solid to transfer the energy, only provides the energy in a very localized fashion, e.g. very close to the piezoelectric transducer (or other solid transducer) and is therefore unsuitable for uniform surface modification.

## SUMMARY OF THE INVENTION

It is an object of the invention to provide a method of and a device for plasma surface modification that alleviates the above-mentioned shortcomings of prior art at least to an extent.

It is another object to enable enhancement of a plasma surface modification of a solid object or specimen.

It is yet another object to enable plasma to more efficiently immerse and influence a surface of a solid object or specimen.

An additional object is to speed the process of plasma surface modification of an object up.

These objectives are obtained at least to an extent by a method of plasma surface modification of a solid object comprising: creating plasma by at least one plasma source, and application of the plasma to at least a part of a surface of the solid object, wherein the method further comprises: generating ultrasonic high intensity and high power acoustic waves by at least one ultrasonic high intensity and high power gas-jet acoustic wave generator, where said ultrasonic high intensity and high power acoustic waves are directed to propagate towards said surface of the object so that a laminar boundary layer of a gas or a mixture of gases in contact with said solid object is removed or minimized for at least a part of said surface, and where a sound pressure level of said generated ultrasonic high intensity and high power acoustic waves is at least substantially 140 dB and where an acoustic power of said generated ultrasonic high intensity and high power acoustic waves is at least substantially 100 W.

In this way, a high sound intensity and power are obtained that efficiently allows for substantial uniform minimization and/or elimination over a substantial area of an object to have its surface modified by plasma, since a gas-jet acoustic wave generator is capable of delivering sufficiently high sound intensity and power.

As a comparison, the sound-emitting surface area of transducers, e.g. like the ones described in the previous mentioned prior art articles ('Ozone generation by hollow-needle to plate electrical in an ultrasound field'; 'Ultrasound and airflow induced thermal instability suppression of DC corona discharge: an experimental study'; and 'Improvement of Charging Performance of Corona Charger in Electrophotography by Irradiating Ultrasonic Wave to Surrounding Region of Corona Electrode') is of the order of $2\times10^{-3}$ $m^2$ and the emitted acoustic power is 10-40 W.

The acoustic power provided by a high-power gas-jet generator is capable of much higher acoustic power outputs along with the high sound pressure and intensity levels of 140 or 150 to 170 dB (see e.g. Y. Y. Borisov, Acoustic gas-jet generators of Hartmann type, in L. D. Rozenberg (ed.) Sources of High-Intensity Ultrasound (New York: Plenum: 1969) part I. and Levavasseur, R. High power generators of sound and ultrasound. US Patent, book 116-137, U.S. Pat. No. 2,755,767 (1956).).

It has been shown that an acoustic power of about 100 W or more enhances plasma surface modification of an object.

A high-power gas-jet generator is normally capable of an acoustic power of several hundreds watts (i.e. approximately one order of magnitude higher than the piezoelectric transducer acoustic power output) and typical SPL (sound pressure level) of 160 dB at 10 cm from the generator orifice at the frequency of 20-30 kHz. Even an acoustic power of 1-2 kW is attainable.

The main physical reason for such a dramatic difference in acoustic power outputs of piezoelectric (or other solid-state acoustic transducers) and gas-jet generators is that a piezoelectric transducer works by vibrating (using sound) a solid being in contact with a gas and thus transfers the vibrations to the gas. Due to the tremendous difference in acoustic impedance for a solid and a gas (a so-called acoustic impedance mismatch), most of generated acoustic power cannot be emitted in the ambient gas and remains in a solid. It is converted into thermal energy and results in a transducer warming-up.

Consequently, it is not possible in this way to generate sound or ultrasound in the gas with a power that would be enough to remove or reduce the laminar boundary layer of a plasma flow on sufficiently large surfaces. In fact, a single piezoelectric transducer provides the high-intensity ultrasound radiation only nearby its emitting surface and irradiates a limited surface area that is comparable with the area of its emitting surface. That is because of the acoustic wave diffraction, which is significant when the transducer diameter is comparable with the acoustic wavelength. Indeed, for ultrasound frequency of 20-30 kHz in the air the wavelength is about 10-20 mm that is of the order of the actual transducer diameter. In the case of gas-jet ultrasonic transmitters, a vibrating media is not a solid but a gas. It is clear that there is no any impedance mismatch and high enough acoustic power can be emitted in the ambient gas. Moreover, intensity and sound pressure levels of ultrasound radiation remain very high at several tens of centimeters from the gas-jet transmitter orifice while the acoustic wave front is broad (it is sometimes just a spherical wave front). In this way, it is possible to expose large surfaces to high-intensity ultrasound (sound intensity and sound pressure levels of substantially 140 dB and above at approximately 10 cm from the generator's orifice) and remove or reduce the laminar boundary layer of a gas or that of plasma flow over large surfaces efficiently thereby enhancing the plasma surface modification.

In this way, the ultrasonic high intensity and high power acoustic waves remove or minimize a laminar boundary layer surrounding the solid object as explained in greater detail in the following and in particular in connection with FIGS. **3***a*

and **3***b*. It has been shown that such a laminar boundary layer of a plasma flow also hinders plasma surface modification of a solid object.

The thinning or destruction of the laminar boundary layer enables the plasma particles to more efficiently be able to access and influence the surface of the solid object to be treated by the plasma.

This will allow for faster plasma surface modification processes.

Reducing the time needed for plasma surface modification of one or more objects reduces the cost of the process since the process is expensive and requires a lot of energy.

Furthermore, the shorter the time that an object is subjected to plasma surface modification, the lesser the risk is to spoil or degrade important physical or chemical characteristics (e.g. localized overheating and cracking, burnout, heat and electrical aging, discoloration etc.) of the treated object.

The use of a gas-jet generator also avoids that the surface of the object to be modified by plasma has its surface vibrated substantially.

In some embodiments, the solid object(s) may be covered (fully or partly) by a layer of a liquid or fluid during the plasma surface modification.

In one embodiment, the acoustic pressure level of said generated ultrasonic high intensity and high power acoustic waves is

at least substantially 150 dB,
at least substantially 160 dB,
at least substantially 170 dB,
at least substantially 180 dB,
at least substantially 190 dB, or
at least substantially 200 dB.

where the sound pressure level as they are at 10 cm from the generator orifice.

In one embodiment, the acoustic power of said generated ultrasonic high intensity and high power acoustic waves is

at least substantially 200 W,
at least substantially 300 W,
at least substantially 400 W,
about 400 W,
greater than substantially 400 W,
at least substantially 500 W,
at least substantially 1 kW, or
selected from about 1-2 kW.

It is to be understood, that if several acoustic generators are used even higher powers may be obtained.

In one embodiment, the plasma source comprises at least one source selected from a group of: a dielectric barrier discharge (DBD) plasma source, a surface discharge (SD) plasma source, a volume discharge (VD) plasma source, a plasma torch source, an arc plasma torch, a gliding arc plasma torch, a cold plasma torch, a pencil-like torch, a direct current plasma source, a capacitively coupled plasma source, a pulsed plasma source, a magnetron plasma source, an electron cyclotron resonance plasma source, an inductively coupled plasma source, a helicon plasma source, a helical resonator plasma source, a microwave plasma source, an atmospheric pressure plasma jet (APPJ) source, a barrier torch, an arc microwave torch, a corona discharge plasma source, a micro-plasma source, a low pressure plasma source, and a high pressure plasma source.

In one embodiment, a working gas pressure at an inlet of the at least one ultrasonic high intensity and high power gas-jet acoustic wave generator is between approximately 1.9 and approximately 5 bar.

In one embodiment, the plasma is created at atmospheric pressure.

In one embodiment, the plasma source comprises at least one electrode and wherein one electrode of said at least one electrode is a mesh type of electrode.

This allows the gas/energy to pass through the 'upper' electrode in a very simple and efficient way.

In one embodiment, the generated ultrasonic high intensity and high power acoustic waves are propagated towards a membrane so that any gases used by the at least one ultrasonic high intensity and high power acoustic wave generator is not mixed with one or more gases used by said plasma source to create said plasma.

In one embodiment, the generated ultrasonic high intensity and high power acoustic waves are generated using a gaseous medium and where the acoustic waves are directed towards said surface of the object and wherein said gaseous medium after exit of said at least one ultrasonic high intensity and high power gas-jet acoustic wave generator is directed away from said surface of the object.

In one embodiment, the generated ultrasonic high intensity and high power acoustic waves do not spatially overlap with the working gas flow outgoing from the generator orifice. Moreover, since the generated ultrasonic high intensity and high power acoustic waves are directed toward the treated surface and the gas outgoing from the ultrasonic high intensity and high power acoustic wave generator do not overlap in space, the said outgoing working gas is not mixed with one or more gases used by said plasma source to create said plasma.

In these ways, control of the gas environment for the plasma generation process is enabled.

In one embodiment, a gas mixture, that is used for creating the plasma, is supplied to at least one electrode of the plasma source substantially in a direction that said ultrasonic acoustic waves propagate towards said surface of the object.

In one embodiment, the at least one ultrasonic high intensity and high power gas-jet acoustic wave generator is selected from the group of:

- a Hartmann type gas-jet generator,
- a Levavasseur type gas-jet generator,
- a generator comprising an outer part and an inner part defining a passage, an opening, and a cavity provided in the inner part, where said ultrasonic high intensity and high power gas-jet acoustic wave generator is adapted to receive a pressurized gas and pass the pressurized gas to said opening, from which the pressurized gas is discharged in a jet towards the cavity,
- a generator of any of the above mentioned types, which includes any type of concentrators or reflectors of acoustic waves

In one embodiment, the solid object is food item, and the method further comprises applying steam to the food item so that the food item is subjected to steam and plasma causing a sterilization process of the food item.

In one embodiment, the generating ultrasonic high intensity and high power acoustic waves comprises:

- generating high intensity and high power acoustic waves by a first acoustic wave generator using a gaseous medium where the gaseous medium, after exit from the first acoustic wave generator, has a first principal direction that is different from a second principal direction of the high intensity and high power acoustic waves generated by the first acoustic wave generator,
- generating high intensity and high power acoustic waves by a second acoustic wave generator,
- where the first and second acoustic wave generators are located in relation to each other so that at least a part of the generated high intensity acoustic waves, being generated by said second acoustic wave generator, is

directed towards at least a part of the gaseous medium after exit from said first acoustic wave generator.

In one embodiment, the plasma surface modification of a solid object is selected from the group of:

surface activation and/or inactivation,
adhesion improvement,
wettability enhancement,
printability improvement,
surface cleaning,
hardening,
cross-linking,
curing,
polymer-chain secession,
coloration,
roughening,
ashing,
etching,
sterilization,
thin film deposition,
material synthesis, and
particle formation at the surface.

The present invention also relates to a system corresponding to the method of the present invention. More specifically, the invention relates to a system for plasma surface modification of a solid object comprising: at least one plasma source adapted to create plasma applied to at least a part of a surface of the solid object, wherein the system further comprises: at least one ultrasonic high intensity and high power gas-jet acoustic wave generator adapted to generate ultrasonic high intensity and high power acoustic waves being directed to propagate towards said surface of the solid object so that a laminar boundary layer of a gas or a mixture of gases in contact with said solid object is removed or minimized for at least a part of said surface, and where a sound pressure level of said generated ultrasonic high intensity and high power acoustic waves is at least substantially 140 dB and where an acoustic power of said generated ultrasonic high intensity and high power acoustic waves is at least 100 W.

The present invention also relates to a solid object having a surface being treated by plasma wherein the solid object have been treated with a method according to any embodiment of the present invention.

Advantageous embodiments of the system are defined in the sub-claims and are described in detail in the following. The embodiments of the system correspond to the embodiments of the method and have the same advantages for the same reasons.

## BRIEF DESCRIPTION OF THE DRAWINGS

These and other aspects of the invention will be apparent from and elucidated with reference to the illustrative embodiments shown in the drawings, in which:

FIG. **1** schematically illustrates a prior art plasma surface modification apparatus;

FIG. **2** schematically illustrates a block diagram of a plasma surface modification apparatus;

FIG. **3***a* schematically illustrates a (turbulent) flow over a surface of an object without application of ultrasonic high intensity and high power acoustic waves;

FIG. **3***b* schematically illustrates a flow over a surface of an object, where the effect of applying ultrasonic high intensity and high power acoustic waves to/in air/gas surrounding, or contacting a surface of an object;

FIG. **4** schematically illustrates one embodiment of an enhanced plasma surface modification apparatus;

FIG. **5** schematically illustrates an alternative embodiment of an enhanced plasma surface modification apparatus;

FIG. **6** schematically illustrates an alternative embodiment of an enhanced plasma surface modification apparatus;

FIG. **7** schematically illustrates an embodiment of an enhanced plasma surface modification apparatus where the plasma source is a surface discharge (SD) plasma source;

FIG. **8** schematically illustrates an embodiment of an enhanced plasma surface modification apparatus where the plasma source is a torch plasma source e.g. a gliding arc plasma source;

FIG. **9** schematically illustrates an embodiment of a high intensity and high power gas-jet acoustic wave generator wherein a converging supersonic gas jet outgoing a ring-shaped nozzle and braking in a mushroom resonator has the form of a disk (i.e. the so-called disk-jet Hartmann ultrasound generator);

FIG. **10** is a sectional view along the diameter of the high intensity and high power acoustic wave generator (**101**) in FIG. **9** illustrating the shape of an opening (**302**), a gas passage (**303**) and a cavity (**304**) more clearly;

FIG. **11** schematically illustrates another embodiment of a high intensity and high power acoustic generator in form of an elongated body; and

FIG. **12** schematically illustrates an embodiment of a high intensity and high power acoustic generator comprising two generators.

Throughout the figures, same reference numerals indicate similar or corresponding features.

## DESCRIPTION OF PREFERRED EMBODIMENTS

FIG. **1** schematically illustrates a prior art plasma surface modification apparatus. Shown is an example of a plasma generator or plasma source, i.e. any device or method capable of creating a plasma (forth only denoted plasma source) of the well-known so-called dielectric barrier discharge (DBD) type usable even at atmospheric pressure. Shown are a number of gases (**111**), such as He, Ar, $O_2$, $CO_2$, and $NH_3$ supplied to a gas mixing unit (**110**) mixing the gases into a proper composition for the given use or application. The selected gases for the plasma should be selected based on the type of surface modification and may be any gas, which is ordinarily used for known plasma surface modifications and/or the like. Specific and typical examples include He, Ar, Ne, Xe, air, $N_2$, $O_2$, $H_2O$, $CO_2$, halogen compound gases such as Freon gases ($CF_4$, $CHF_3$, $C_3F_6$, $C_4F_8$ etc.), halon gases, $NH_3$, $NF_3$, $SF_6$, organic compound gases ($CH_4$, $C_2H_6$, $C_2H_4$, $C_2H_2$, $C_6H_6$, $C_2H_5OH$, etc.), NOx, $SO_2$, silanes etc. and gas mixtures selected from them. In order to stabilize the plasma, the gas(es) can be diluted with He, Ar, see e.g. European patent EP 0508833 B1.

Further shown are two electrodes (**103**) placed apart with a discharge gap between them, where at least one of the electrodes (**103**) is adjoined or covered with an insulating or dielectric material (**105**) on a side of the electrode facing the other electrode in order to avoid arcing. In the figure, both electrodes (**103**) are adjoined or covered with dielectric material (**105**). One electrode (**103**) is connected to a suitable power supply (**114**) supplying AC high voltage, e.g. 0.1 kHz-500 kHz, between the electrodes (**103**).

Further, shown are a high voltage probe (**113**) connected to the power supply (**114**) and an oscilloscope connected to the high voltage probe (**113**). The high voltage probe is used for monitoring the applied voltage, but is not relevant for and does not influence the surface modification.

The gas mix is supplied from the gas-mixing unit (**110**) to the discharge area between the two electrodes (**103**) and, as a result, plasma (**104**) is created when voltage is applied to the electrodes (**103**). A specimen or object (**100**) is located in the plasma (**104**) for surface modification, treatment, processing, etc. (forth only denoted surface modification).

Typical examples of surface modifications are e.g. surface cleaning, etching, ashing, surface activation/inactivation, adhesion improvement, preparation of hydrophilic and hydrophobic surfaces, sterilization, thin film deposition, biocompatibility.

A surface modification of an object (**100**) can be enhanced as shown and explained in the following.

FIG. **2** schematically illustrates a block diagram of a plasma surface modification process/apparatus. Illustrated are one or more plasma sources (**106**) creating or supplying plasma (**104**) and one or more solid objects (**100**) located in or in contact with the plasma (**104**) whereby the plasma (**104**) will treat or modify the surface of the one or more solid objects (**100**).

Further illustrated are one or more ultrasonic high intensity and high power acoustic wave generators (**101**) generating high intensity and high power ultrasound (**102**). According to the present invention, the generated ultrasound (**102**) is applied to at least a part of the surface of the one or more solid objects (**100**).

Patent application WO 2006/015604 A1, by one of the applicants, discloses a method and device for enhancing a process involving a gas and a solid object where ultrasound is used to remove or minimize a boundary laminar layer. No disclosure of the process being a plasma surface modification, plasma-related process, or a surface treatment of an object is given.

However, it has surprisingly been shown that the application of high intensity and high power ultrasonic acoustic waves also work for enhancing a plasma surface modification of an object.

By applying high intensity and high power ultrasonic acoustic waves to one or more solid objects being subjected to plasma surface modification, the plasma surface modification of this or these objects is greatly enhanced, as explained in the following in connection with FIGS. **3***a* and **3***b*.

The working gas pressure at the inlet of the ultrasonic high intensity and high power acoustic wave generators (**101**) may be optimized so that high acoustic pressure can be generated. It is preferably between 1.9 and 5 bar or between 2.5 to 4 bar and will typically depend on the type generator used. The gas pressure at the outlet of the high-power gas-jet generators is lower than that at the inlet, and can be practically nearly equal to the gas pressure for the surface modification.

The air-pressure required for operation of gas-jet high-intensity and high-power ultrasonic generators is at least over 1.9 bar for operation under normal conditions and the pressure required for optimal operation providing stable generation of ultrasound with a SPL over 140 dB at 10 cm from the generator orifice is 2.5 to 4 bar depending on a generator type.

The one or more plasma sources (**106**) may be any plasma source suitable for surface modification of at least one object, e.g. such sources as explained earlier and in the following and/or combinations or such sources e.g. using one or more gases, as explained earlier, in creating the plasma. The plasma source(s) (**106**) can be chosen among any existing ones (both low and high pressure plasmas), and more specifically may be e.g. direct current plasmas, capacitively coupled plasmas, pulsed plasmas, magnetron plasmas, electron cyclotron resonance plasmas, inductively coupled plasmas, helicon plasmas, helical resonator plasmas, microwave plasmas, DBDs, SDs, plasma torches such as arc plasma torches, cold plasma torches, APPJs, pencil like torches, barrier torches, arc plasma torches, microwave torches, gliding arc, corona discharge, and microplasmas.

The gas pressure for the surface modification is preferably higher than 0.4 bar and may be around atmospheric pressure or more, so that the acoustic energy can be delivered efficiently. One the other hand, it is easier to generate plasmas at lower pressures. Therefore, the gas pressure for the surface modification is preferably more than 0.4 bar and less than the pressure at the inlet of the high-power gas-jet generators. More preferable plasma source may be DBDs, SDs, plasma torches such as arc plasma torches, cold plasma torches, APPJs, pencil like torches, barrier torches, microwave torches, gliding arc, corona discharge, and microplasmas, which can be operated at the pressures mentioned above.

The one or more ultrasonic high intensity and high power acoustic wave generator (**101**) is a gas-jet acoustic wave generator and may e.g. be one or more Hartmann type gas-jet generators, one or more Levavasseur type gas-jet generators, etc. or combinations thereof and as explained in the following and as shown in FIGS. **9-12**.

The use of a gas-jet acoustic wave generator has advantages like described earlier in terms of acoustic power, high intensity, acoustic impedance, etc.

If more than a single ultrasonic and high intensity and high power acoustic wave generator is used they need not be of the same type although they can be.

The surface modification may be e.g. surface cleaning, etching, ashing, surface activation/inactivation, adhesion improvement, wettability enhancement, printability improvement, hardening, cross-linking, curing, polymer-chain secession, coloration, roughening, preparation of hydrophilic and hydrophobic surfaces, sterilization, thin film deposition, biocompatibility and material synthesis (particle formation at the surface etc.) etc.

In one embodiment, the object to have its surface modified is a food item and steam and plasma is subjected to the food item in order to process the food item. This process will generated chemical radicals and sterilize the food item in a very efficient way.

In some embodiments, the solid object(s) (**100**) (e.g. metal plates) may be covered (fully or partly) with a layer of a liquid or fluid during the plasma surface modification. The liquid or fluid can be diminished or removed during the surface modification.

FIG. **3***a* schematically illustrates a (turbulent) flow over a surface of an object without application of ultrasonic high intensity and high power acoustic waves.

Shown is a surface (**314**) of a solid object (**100**) to have (at least a part of) its surface (**314**) modified by plasma where a gas or a mixture of gases (**500**) surrounds or contacts the surface (**314**) thereby preventing the plasma to approach and influence the surface efficiently.

Thermal energy can be transported through gas by conduction as well as by the movement of the gas from one region to another. This process of heat transfer associated with gas movement is usually referred to as convection. When the gas motion is caused only by buoyancy forces set up by temperature differences, the process is normally referred to as natural or free convection; but if the gas motion is caused by some other mechanism, it is usually referred to as forced convection. With a condition of forced convection, there will be a laminar boundary layer (**311**) near to the surface (**314**). The thickness of this layer is a decreasing function of the Reynolds number of the flow, so that at high flow velocities, the thickness of the laminar boundary layer (**311**) will decrease.

When the flow becomes turbulent the layer are divided into a turbulent boundary layer (**312**) and a laminar boundary layer (**313**). For nearly all practically occurring gas flows, the flow regime will be turbulent in the entirety of the streaming volume, except for the laminar boundary layer (**313**) covering the surface (**314**) wherein the flow regime is laminar. Considering a gas molecule or a particle (**315**) in the laminar boundary layer (**313**), the velocity (**316**) will be substantially parallel to the surface (**314**) and equal to the velocity of the laminar boundary layer (**313**). Heat transport across the laminar boundary layer will be by conduction or radiation, due to the nature of laminar flow.

Furthermore, mass transport across the laminar boundary layer will be solely by diffusion. The presence of the laminar boundary layer (**313**) does not provide optimal or efficient increased mass transport. Any mass transport across the boundary layer will be solely by diffusion, and therefore often be the final limiting factor in an overall mass transport.

The principal impediment to the transfer or transmission of energy and/or mass from a gas to a solid surface is the boundary layer of the gas, which adheres to the solid surface. Even when the motion of the gas is fully turbulent, the laminar boundary layer exists that obstructs mass transport and/or heat transfer. While various methods and types of apparatus have been suggested for overcoming the problem such as by means of driving the gas with sonic waves and vibrating the solid object (**100**) with external vibration generators, these methods while being effective to some extent, are inherently limited in their ability to generate an effective minimization of the laminar boundary layer and at the same time covering an area large enough to make the method efficient.

FIG. **3***b* schematically illustrates a flow over a surface of an object, where the effect of applying high intensity and high power ultrasonic acoustic waves to/in air/gas (**500**) surrounding or contacting a surface of an object is illustrated.

More specifically, FIG. **3***b* illustrates the conditions when the surface (**314**) of a solid object (**100**) is applied with high intensity and high power ultrasonic acoustic waves by a gas-jet acoustic wave generator (not shown; see e.g. **101** in other Figures). Again consider a gas molecule/particle (**315**) in the laminar layer; the velocity (**316**) will be substantially parallel to the surface (**314**) and equal to the velocity of the laminar layer prior applying ultrasound. In the direction of the emitted sound field to the surface (**314**) in FIG. **3***b*, the oscillating velocity of the molecule (**315**) has been increased significantly as indicated by arrows (**317**). As an example, a maximum velocity of v=4.5 m/sec and a displacement of +/−32 μm can be achieved where the frequency is f=22 kHz and the sound pressure level=160 dB. The corresponding (vertical) displacement in FIG. **3***a* is substantially zero since the molecule follows the laminar air stream along the surface. As a result, the acoustic waves will establish a forced heat flow and/or mass transport from the surface to surrounding gas/air (**500**) by increasing the conduction by minimizing the laminar boundary layer. The sound pressure level is in one embodiment substantially 140 dB or larger. Furthermore, the sound pressure level may be selected within the range of approximately 140-160 dB. The sound pressure level may be above substantially 150 dB, above substantially 160 dB, above substantially 170 dB, above substantially 180 dB, above substantially 190 dB or above substantially 200 dB.

The thinning or destruction of the laminar boundary layer has the effect that heat transfer and mass transport from the surface (**314**) to the surrounding or contacting gas (**500**) greatly is increased, as the presence or the reduced size of the laminar boundary layer no longer will hind heat transfer and/or mass transport to the surface of the solid object(s) (**100**) being subjected to plasma surface modification, i.e. the plasma will more efficiently influence the surface of the object.

Various embodiments are described in connection with the following figures.

FIG. **4** schematically illustrates one embodiment of an enhanced plasma surface modification apparatus.

Shown is at least one ultrasonic high intensity and high power acoustic wave is gas-jet generator (**101**) generating high intensity and high power ultrasonic acoustic waves (**102**) propagating towards and reaching a surface of at least one object (**100**) to be subjected to plasma surface modification.

The at least one object (**100**) to have its surface properties changed is immersed in or influenced by plasma (**104**) created by a plasma source (**106**) using the shown gas flow, the shown electrodes (**103**; **103'**), and an insulator or dielectric material (**105**) e.g. as explained in connection with FIG. **1**. The particular shown plasma source (**106**) is of the DBD type but could be of another type.

The at least one object (**100**) is in contact or surrounded by a gas or a gas mixture (**500**) that, even when turbulent, would comprise a laminar boundary layer or a non-reduced laminar boundary layer as shown and explained in connection with FIG. **3***a* when ultrasonic high intensity and high power acoustic waves (**102**) is not applied by a gas-jet generator (**101**).

The insulator or dielectric material (**105**) may e.g. comprise $Al_2O_3$ or in general material having a dielectric property or any kind of insulators such as ceramics, polymers and glasses. Ceramics and glasses are more durable against plasma since they have relatively high temperature resistance. They are often preferred, since they typically have high dielectric constants and thus plasma can be generated and sustained at lower AC voltages.

Further shown is a horn or the like (**402**) or sound guiding or directing means that ensures that the sound intensity and power is contained and focused towards the plasma/object.

In one embodiment, a membrane (**401**) or similar is located between the high intensity and high power ultrasonic acoustic wave generator (**102**) and the plasma. This enables control of the gas environment for the plasma generation process so that only the received gas flow is used in creating the plasma. This may be useful for gas driven generators (**102**) so that the gas from such generators do not interfere with the gas mix used for plasma creation. Other embodiments may exclude the membrane (**401**). The membrane (**401**) is preferably relatively thin and relatively transparent to ultrasound. The thickness, size, and/or shape of the membrane (**401**) and tension applied to it may be optimized for decreasing a loss of ultrasound.

In some embodiment, the membrane can be dispensed with even though it is not preferred that a mix of the gaseous medium used for generating the high intensity and high power ultrasonic acoustic waves and the gas(es) used for creating the plasma occurs. This can be achieved by having a high intensity and high power acoustic wave generator where the generated acoustic waves propagates generally in another direction than the general direction of the gaseous medium after exiting the acoustic wave generator.

In FIG. **12** is shown two such generators where the general direction of the generated acoustic waves are at an angle to the general direction of the gaseous medium after exit from the generator.

Generators can be designed so that the two directions are about opposite. For instance, stem-jet Hartmann generators radiating ultrasound in the so-called high-frequency regime allow such "natural" spatial separation of the ultrasound field and the outgoing gas flow (see e.g. Y. Y. Borisov, Acoustic

gas-jet generators of Hartmann type, in L. D. Rozenberg (ed.) Sources of High-Intensity Ultrasound (New York: Plenum: 1969) part I.). Such generators can be very useful in avoiding the use of a membrane as the gaseous medium may directed away from the plasma and the object that the plasma is to surface modify. In this way, no gas(es) used for generating the acoustic waves will influence the plasma gas(es). It is to be understood that even in such an arrangement a membrane may still be useful (although it may be of a different design) since it can contain the gas(es) used for creating the plasma contained so they do not diffuse into the surrounding environment, which may be useful since some have a significant cost.

Any kinds of membranes can be used, as long as there is neither significant loss of ultrasound nor significant gas leakage. As long as they can form thin films, their materials can be chosen from any thermoplastic and thermoset polymers such as polyesters, polyethylene terephthalate, polyolefins (low density (LD) polyethylene (PE), high density (HD) PE, ultra-high density PE, ultrahigh molecular weight PE, polypropylene, poly(vinyl chloride), poly(vinylidene chloride), polystyrene, polyimide, polyamide, poly(vinyl vinyl ether), polyisobutylene, polycarbonate, polystyrene, polyurethane, poly(vinyl acetate), poly-acrylonitrile, natural and synthetic rubbers, polymer alloys, copolymers, and their laminates. They can be coated with organic and/or inorganic materials using any existing techniques. Among them, lower density materials such as PE can be used. Furthermore, a metal foil may be used as a membrane. Other examples are metal coated (or material coated with inorganic material) or laminated polymer membranes.

As an alternative, the membrane may comprise or consist of Aerogel.

In one embodiment, the electrode located between the plasma (**104**) and the generator (**101**) is a mesh type of electrode (**103'**) or another type of perforated electrode. This enables the generated ultrasound to virtually pass unhindered to the object(s) (**100**) without loosing a significant amount of energy whereby as much energy as possible is present for influencing the laminar sub-layer around the object(s) (**100**). Other embodiments may exclude the mesh type/perforated electrode (**103'**).

The direction of outgoing gas/gas mixture, used for creating the plasma (**104**), and the ultrasound (**102**) is quite controllable and the angle between their principal directions may vary. In the shown embodiment, the angle is about 90°. But the angle may in principal be any angle. In FIG. **5** for example, the angle is about 0°.

The gas or gas mixture used for creating the plasma (**104**) may also be used for driving the gas-jet acoustic generator(s) (**101**). The plasma (**104**) may be generated before, in or after the acoustic generator (**101**).

FIG. **5** schematically illustrates an alternative embodiment of an enhanced plasma surface modification apparatus. This embodiment corresponds to the embodiment shown and explained in connection with FIG. **4** except that the gas for the plasma is not fed from the side but rather from the same direction as the high intensity and high power ultrasonic acoustic waves (**102**).

FIG. **6** schematically illustrates an alternative embodiment of an enhanced plasma surface modification apparatus. This embodiment corresponds to the embodiment shown and explained in connection with FIG. **4** except that it does not comprise a membrane. Such an embodiment is suitable for ambient or normal air plasma. In such an embodiment without a membrane, a high speed air flow used for the generation of high intensity and high power ultrasound can also be used as a process gas for the plasma.

FIG. **7** schematically illustrates an embodiment of an enhanced plasma surface modification apparatus where the plasma source is a surface discharge (SD) plasma source. The shown embodiment corresponds to the embodiment shown and explained in connection with FIG. **4** except that instead of a DBD plasma source it comprises a surface discharge (SD) plasma source (**106**) comprising a single insulator or dielectric material (**105**) and a number of electrodes (**103**) embedded in the insulator or the dielectric material (**105**). The shown SD plasma source is the so-called comprises a so-called CDSD discharge element. Alternatively, it could comprise a SPCP discharge element or by of another type of SD plasma source. As an alternative to the gas flow being received from the side, it could be supplied in the direction of the ultrasonic high intensity and high power acoustic waves e.g. as shown in FIG. **5** or in another way.

FIG. **8** schematically illustrates an embodiment of an enhanced plasma surface modification apparatus where the plasma source is a torch plasma source e.g. a gliding arc plasma source. The shown embodiment corresponds to the embodiment shown and explained in connection with FIG. **4** except that instead of a DBD plasma source it comprises a torch plasma source e.g. a gliding arc plasma source.

The torch plasma source could e.g. be a barrier torch design or cold plasma torch design as well-known in the art.

FIG. **9** schematically illustrates an embodiment of a high intensity and high power acoustic wave gas-jet generator in the form of a disk-shaped disk jet (i.e. a disk-jet Hartmann ultrasound generator). Shown is an embodiment of a high intensity ultrasound generator (**101**), in this example a so-called disk-jet. The generator (**101**) comprises a generally annular outer part (**305**) and a generally cylindrical inner part (**306**), in which an annular cavity (**304**) is recessed. Through an annular gas passage (**303**) gases may be diffused to the annular opening (**302**) from which it may be conveyed to the cavity (**304**). The outer part (**305**) may be adjustable in relation to the inner part (**306**), e.g. by providing a thread or another adjusting device (not shown) in the bottom of the outer part (**305**), which further may comprise fastening means (not shown) for locking the outer part (**305**) in relation to the inner part (**306**), when the desired interval there between has been obtained. Such an ultrasound device may generate a frequency of about 22 kHz at a gas pressure of 4 atmospheres. The molecules of the gas are thus able to migrate up to 33 μm about 22,000 times per second at a velocity of 4.5 m/s. These values are merely included to give an idea of the size and proportions of the ultrasound device and by no means limit of the shown embodiment.

FIG. **10** is a sectional view along the diameter of the high intensity and high power acoustic wave generator (**101**) in FIG. **9** illustrating the shape of an opening (**302**), a gas passage (**303**) and a cavity (**304**) more clearly. As mentioned in connection with FIG. **9** the opening (**302**) is generally annular.

The gas passage (**303**) and the opening (**302**) are defined by the substantially annular outer part (**305**) and the substantially cylindrical inner part (**306**) arranged therein. The gas jet discharged from the opening (**302**) hits the substantially circumferential cavity (**304**) formed in the inner part (**306**), and then exits the high intensity ultrasound generator (**101**). As previously mentioned the outer part (**305**) defines the exterior of the gas passage (**303**) and is further beveled at an angle of about 30° along the outer surface of its inner circumference forming the opening of the high intensity ultrasound generator, wherefrom the gas jet may expand when diffused. Jointly

with a corresponding beveling of about 60° on the inner surface of the inner circumference, the above beveling forms an acute-angled circumferential edge defining the opening (**302**) externally. The inner part (**306**) has a beveling of about 45° in its outer circumference facing the opening and internally defining the opening (**302**). The outer part (**305**) may be adjusted in relation to the inner part (**306**), whereby the pressure of the gas jet hitting the cavity (**304**) may be adjusted. The top of the inner part (**306**), in which the cavity (**304**) is recessed, is also beveled at an angle of about 45° to allow the oscillating gas jet to expand at the opening of the high intensity ultrasound generator.

FIG. **11** schematically illustrates another embodiment of a high intensity and high power acoustic wave generator in form of an elongated body. Shown is a high intensity and high power gas-jet acoustic wave generator (**101**) comprising an elongated substantially rail-shaped body, where the body is functionally equivalent with the embodiments shown in FIGS. **9** and **10**. In this embodiment the outer part comprises one rail-shaped portion (**305**), which jointly with a rail-shaped other part (**306**) forms an ultrasound device (**101**). A gas passage (**303**) is provided between the rail-shaped portion (**305**) and the rail-shaped other part (**306**). The gas passage has an opening (**302**) conveying emitted gas from the gas passage (**303**) to a cavity (**304**) provided in the rail-shaped other part (**306**). One advantage of this embodiment is that a rail-shaped body is able to coat a far larger surface area than a circular body. Another advantage of this embodiment is that the high intensity and high power acoustic wave generator may be made in an extruding process, whereby the cost of materials is reduced.

FIG. **12** schematically illustrates an embodiment of a high intensity and high power acoustic generator comprising two generators. Shown is an example of two gas-jet high intensity and high power acoustic wave generators (**101**; **101'**), a first (**101**) and a second (**101'**), where each generator (**101**; **101'**) generates high intensity and high power acoustic waves (**102**) using a gaseous medium (**121**). The gaseous medium (**121**) exits each generator (**101**) in a principal direction schematically indicated by arrow (A; A') in a cone-like shape, as represented by the hatched area, towards one or more solid objects (**100**) to have its surface modified by plasma.

The high intensity and high power acoustic waves (**102**) generated by the first generator (**101**) propagate in a principal direction as schematically indicated by arrows (B) that is different than the general direction of the gaseous medium (A) from the first generator (**101**) due to the design of the high power acoustic wave generator (**101**).

The high intensity and high power acoustic waves (**102**) generated by the second generator (**101'**) propagate in a general direction as schematically indicated by arrow (B').

One example of a high intensity and high power acoustic wave generator operating in a way like this is shown and explained in connection with FIG. **11**. This design generates high intensity and high power acoustic waves in a substantial line (seen from above), whereas the design of FIGS. **9** and **10** generates waves in a substantially circular way.

The first (**101**) and the second high power acoustic wave generator (**101**) are located in relation to each other so that at least a part of the generated high intensity and high power acoustic waves (**102**) from the second acoustic wave generator (**101'**) has a general direction (B') that is directed towards at least a part of the gaseous medium (**121**) from the first acoustic wave generator (**101**) and that at least a part of the generated high intensity and high power acoustic waves (**102**) from the first acoustic wave generator (**101**) has a general direction (B) that is directed towards at least a part of the gaseous medium (**121**) from the second acoustic wave generator (**101'**).

By directing high intensity and high power acoustic waves generated by the second generator (**101**) directly towards the gaseous medium (**121**) from the first generator (**101**), energy is supplied in as a direct way as possible so that it directly influences the gaseous medium (**121**) thereby increasing the efficiency or turbulence of the gaseous medium.

This gives a very compact and efficient setup as the gaseous medium of each generator is enhanced by the high intensity and high power acoustic waves of another generator using a total of only two generators.

If only a single generator (**101**) was used, the difference between the general directions of the high intensity and high power acoustic waves (B or B') and the general direction of the gaseous medium (A or A') for a single generator (**101**) would cause a loss in efficiency since the acoustic waves do not coincide with the gaseous medium (**121**).

The location of the generators (**101**; **101'**) in relation to each other may vary. One example is e.g. where the two generators are facing each other displaced or shifted but where the high intensity and high power acoustic waves still directly influences the gaseous medium of the other generator.

In the figure, the shown sizes, directions, etc. of the cones (**121**; **102**) do not relate to any specific physical properties like acoustic wave intensity, etc. but merely serve for illustrational purposes. The intensities and/or power of the two generators (**101**) may be equal or different (with either one being greater than the other is). Furthermore, the shapes, sizes, and directions may vary from application to application.

The specific location of one of the generator (**101**; **101'**) may also vary in relation to the other generator and may e.g. be placed above or higher than and/or e.g. facing, the other generator (**101**); as long as the acoustic waves (**102**) of one generator (**101**) directly influences the gaseous medium (**121**) of the other generator (**101**) and vice versa.

Although this particular example shows two generators it is to be understood that a given arrangement may comprises additional generators.

The gaseous medium (**102**) may in general be any gaseous medium. In one embodiment the gaseous medium (**102**) is steam. In an alternative embodiment the gaseous medium (**102**) comprises one or more gases used for creating the plasma to modify the surface of the solid object.

It is to be noted, that one or more of the acoustic generators shown in connection with FIG. **12** or any other Figure could comprise one or more reflectors e.g. of generally parabolic or elliptical shape for directing the acoustic energy to a preferred region or spot.

It should be emphasized that the term "comprises/comprising" when used in is this specification is taken to specify the presence of stated features, integers, steps or components but does not preclude the presence or addition of one or more other features, integers, steps, components and/or groups thereof.

In the claims, any reference signs placed between parentheses shall not be constructed as limiting the claim. The word "comprising" does not exclude the presence of elements or steps other than those listed in a claim. The word "a" or "an" preceding an element does not exclude the presence of a plurality of such elements.

The invention can be implemented by means of hardware comprising several distinct elements, and by means of a suitably programmed computer or processor. In the system and

device claims enumerating several means, several of these means can be embodied by one and the same item of hardware. The mere fact that certain measures are recited in mutually different dependent claims does not indicate that a combination of these measures cannot be used to advantage.

The invention claimed is:

**1**. A method of plasma surface modification of a solid object comprising:

creating plasma by at least one plasma source, and

application of the plasma to at least a part of a surface of the solid object, wherein the method further comprises:

generating ultrasonic high intensity and high power acoustic waves by at least one ultrasonic high intensity and high power gas-jet acoustic wave generator, where said ultrasonic high intensity and high power acoustic waves are directed to propagate towards said surface of the object so that a laminar boundary layer of a gas or a mixture of gases in contact with said solid object is removed or minimized for at least a part of said surface, and where a sound pressure level of said generated ultrasonic high intensity and high power acoustic waves is at least substantially 140 dB and where an acoustic power of said generated ultrasonic high intensity and high power acoustic waves is at least substantially 100 W.

**2**. A method according to claim **1**, wherein said sound pressure level of said generated ultrasonic high intensity and high power acoustic waves is

at least substantially 150 dB,

at least substantially 160 dB,

at least substantially 170 dB,

at least substantially 180 dB,

at least substantially 190 dB, or

at least substantially 200 dB.

**3**. A method according to claim **1**, wherein said acoustic power of said generated ultrasonic high intensity and high power acoustic waves is

at least substantially 200 W,

at least substantially 300 W,

at least substantially 400 W,

about 400 W,

greater than substantially 400 W,

at least substantially 500 W,

at least substantially 1 kW, or

selected from about 1-2 kW.

**4**. A method according to claim **1**, wherein said plasma source comprises at least one source selected from a group of: a dielectric barrier discharge (DBD) plasma source, a surface discharge (SD) plasma source, a volume discharge (VD) plasma source, a plasma torch source, an arc plasma torch, a gliding arc plasma torch, a cold plasma torch, a pencil-like torch, a direct current plasma source, a capacitively coupled plasma source, a pulsed plasma source, a magnetron plasma source, an electron cyclotron resonance plasma source, an inductively coupled plasma source, a helicon plasma source, a helical resonator plasma source, a microwave plasma source, an atmospheric pressure plasma jet (APPJ) source, a barrier torch, an arc microwave torch, a corona discharge plasma source, a micro-plasma source, a low pressure plasma source, and a high pressure plasma source.

**5**. A method according to claim **1**, wherein a working gas pressure at an inlet of said at least one ultrasonic high intensity and high power gas-jet acoustic wave generator is between approximately 1.9 and approximately 5 bar.

**6**. A method according to claim **1**, wherein said plasma is created at atmospheric pressure.

**7**. A method according to claim **1**, wherein said plasma source comprises at least one electrode and wherein one electrode of said at least one electrode is a mesh type of electrode.

**8**. A method according to claim **1**, wherein the generated ultrasonic high intensity and high power acoustic waves are propagated towards a membrane so that any gases used by the at least one ultrasonic high intensity and high power acoustic wave generator is not mixed with one or more gases used by said plasma source to create said plasma.

**9**. A method according to claim **1**, wherein the generated ultrasonic high intensity and high power acoustic waves are generated using a gaseous medium and where the acoustic waves are directed towards said surface of the object and wherein said gaseous medium after exit of said at least one ultrasonic high intensity and high power gas jet acoustic wave generator is directed away from said surface of the object.

**10**. A method according to claim **1**, wherein a gas mixture used for creating the plasma is supplied to at least one electrode of the plasma source substantially in a direction that said ultrasonic acoustic waves propagate towards said surface of the object.

**11**. A method according to claim **1**, wherein said at least one ultrasonic high intensity and high power gas-jet acoustic wave generator is selected from the group of:

a Hartmann type gas-jet generator,

a Levavasseur type gas-jet generator,

a generator comprising an outer part and an inner part defining a passage, an opening, and a cavity provided in the inner part, where said ultrasonic high intensity and high power gas-jet acoustic wave generator is adapted to receive a pressurized gas and pass the pressurized gas to said opening, from which the pressurized gas is discharged in a jet towards the cavity,

a generator of any of the above mentioned types, which includes any type of concentrators or reflectors of acoustic waves.

**12**. A method according to claim **1**, wherein said solid object is food item, and the method further comprises applying steam to the food item so that the food item is subjected to steam and plasma causing a sterilization process of the food item.

**13**. A method according to claim **1**, wherein said generating ultrasonic high intensity and high power acoustic waves comprises:

generating high intensity and high power acoustic waves by a first acoustic wave generator using a gaseous medium where the gaseous medium, after exit from the first acoustic wave generator, has a first principal direction (A) that is different from a second principal direction (B) of the high intensity and high power acoustic waves generated by the first acoustic wave generator,

generating high intensity and high power acoustic waves by a second acoustic wave generator,

where the first and second acoustic wave generators are located in relation to each other so that at least a part of the generated high intensity acoustic waves, being generated by said second acoustic wave generator, is directed towards at least a part of the gaseous medium after exit from said first acoustic wave generator.

**14**. A method according to claim **1**, wherein said plasma surface modification of a solid object is selected from the group of:

surface activation and/or inactivation,

adhesion improvement,

wettability enhancement,

printability improvement,

surface cleaning,
hardening,
cross-linking,
curing,
polymer-chain secession,
coloration,
roughening,
ashing,
etching,
sterilization,
thin film deposition,
material synthesis, and
particle formation at the surface.

**15**. A solid object having a surface being modified by plasma wherein the solid object have been modified with a method according to claim **1**.

**16**. A system for plasma surface modification of a solid object comprising:

at least one plasma source adapted to create plasma applied to at least a part of a surface of the solid object, wherein the system further comprises:

at least one ultrasonic high intensity and high power gas-jet acoustic wave generator adapted to generate ultrasonic high intensity and high power acoustic waves being directed to propagate towards said surface of the solid object so that a laminar boundary layer of a gas or a mixture of gases in contact with said solid object is removed or minimized for at least a part of said surface, and where a sound pressure level of said generated ultrasonic high intensity and high power acoustic waves is at least substantially 140 dB and where an acoustic power of said generated ultrasonic high intensity and high power acoustic waves is at least 100 W.

**17**. A system according to claim **16**, wherein the sound pressure level of said generated ultrasonic high intensity and high power acoustic waves is

at least substantially 150 dB,
at least substantially 160 dB,
at least substantially 170 dB,
at least substantially 180 dB,
at least substantially 190 dB, or
at least substantially 200 dB.

**18**. A system according to claim **16**, wherein said acoustic power of said generated ultrasonic high intensity and high power acoustic waves is

at least substantially 200 W,
at least substantially 300 W,
at least substantially 400 W,
about 400 W,
greater than substantially 400 W,
at least substantially 500 W,
at least substantially 1 kW, or
selected from about 1-2 kW.

**19**. A system according to claim **16**, wherein said plasma source comprises at least one source selected from a group of: a dielectric barrier discharge (DBD) plasma source, a surface discharge (SD) plasma source, a volume discharge (VD) plasma source, a plasma torch source, an arc plasma torch, a gliding arc plasma torch, a cold plasma torch, a pencil-like torch, a direct current plasma source, a capacitively coupled plasma source, a pulsed plasma source, a magnetron plasma source, an electron cyclotron resonance plasma source, an inductively coupled plasma source, a helicon plasma source, a helical resonator plasma source, a microwave plasma source, an atmospheric pressure plasma jet (APPJ) source, a barrier torch, an arc microwave torch, a corona discharge plasma source, a micro-plasma source, a low pressure plasma source, and a high pressure plasma source.

**20**. A system according to claim **16**, wherein a working gas pressure at an inlet of said at least one ultrasonic high intensity and high power gas-jet acoustic wave generator is between approximately 1.9 and approximately 5 bar.

**21**. A system according to claim **16**, wherein said plasma is created at atmospheric pressure.

**22**. A system according to claim **16**, wherein said plasma source comprises at least one electrode and wherein one electrode of said at least one electrode is a mesh type of electrode.

**23**. A system according to claim **16**, wherein said system further comprises a membrane and where the system is adapted to propagate the generated ultrasonic high intensity and high power acoustic waves towards the membrane so that any gases used by the at least one ultrasonic high intensity and high power acoustic wave generator is not mixed with one or more gases used by said plasma source to create said plasma.

**24**. A system according to claim **16**, wherein the generated ultrasonic high intensity and high power acoustic waves are generated using a gaseous medium and where the acoustic waves are directed towards said surface of the object and wherein said gaseous medium after exit of said at least one ultrasonic high intensity and high power gas-jet acoustic wave generator is directed away from said surface of the object.

**25**. A system according to claim **16**, said plasma source comprises at lease one electrode and wherein a gas mixture used for creating the plasma is supplied to the at least one electrode substantially in a direction that said ultrasonic acoustic waves propagates towards said surface of the object.

**26**. A system according to claim **16**, wherein said at least one ultrasonic high intensity and high power gas jet acoustic wave generator is selected from the group of:

a Hartmann type gas-jet generator,
a Levavasseur type gas-jet generator,
a generator comprising an outer part and an inner part defining a passage, an opening, and a cavity provided in the inner part, where said ultrasonic high intensity and high power gas-jet acoustic wave generator is adapted to receive a pressurized gas and pass the pressurized gas to said opening, from which the pressurized gas is discharged in a jet towards the cavity,
a generator of any of the above mentioned types, which includes any type of concentrators or reflectors of acoustic waves.

**27**. A system according to claim **16**, wherein said solid object is food item, and wherein said system further comprises means for applying steam to the food item so that the food item is subjected to steam and plasma causing a sterilization process of the food item.

**28**. A system according to claim **16**, wherein said at least one ultrasonic high intensity and high power gas-jet acoustic wave generator comprises

a first acoustic wave generator for generating high intensity acoustic waves using a gaseous medium where the gaseous medium after exit from said first acoustic wave generator has a first principal direction (A) that is different from a second principal direction (B) of generated high intensity acoustic waves being generated by said first acoustic wave generator, and
at least a second acoustic wave generator for generating high intensity acoustic waves,
where said first and second acoustic wave generators are located in relation to each other so that at least a part of the generated high intensity acoustic waves, being gen-

erated by one of said first and second acoustic wave generator, is directed towards at least a part of the gaseous medium after exit from the other of said first and said second acoustic wave generator.

**29**. A system according to claim **16**, wherein said plasma surface modification of a solid object is selected from the group of:

surface activation and/or inactivation,
adhesion improvement,
wettability enhancement,
printability improvement,
surface cleaning,
hardening,
cross-linking,
curing,
polymer-chain secession,
coloration,
roughening,
ashing,
etching,
sterilization,
thin film deposition,
material synthesis, and
particle formation at the surface.

* * * * *

# [Appendix A12]

Y. Kusano, S.V. Singh, A. Bardenshtein, N. Krebs, N. Rozlosnik

## “Plasma surface modification of glass fibre reinforced polyester enhanced by ultrasonic irradiation”

*Journal of Adhesion Science and Technology* 24 (2010) 1831-1839.

VSP

*Journal of Adhesion Science and Technology 24 (2010) 1831–1839*

Journal of ADHESION SCIENCE and TECHNOLOGY
brill.nl/jast

# Plasma Surface Modification of Glass-Fibre-Reinforced Polyester Enhanced by Ultrasonic Irradiation

**Yukihiro Kusano** [a,*], **Shailendra Vikram Singh** [a], **Alexander Bardenshtein** [b], **Niels Krebs** [b] **and Noemi Rozlosnik** [c]

[a] Plasma Physics and Technology Programme, Risø National Laboratory for Sustainable Energy, Technical University of Denmark, P.O. Box 49, 4000 Roskilde, Denmark

[b] FORCE Technology, 2605 Brøndby, Denmark

[c] Department of Micro- and Nanotechnology, Technical University of Denmark, 2800 Kongens Lyngby, Denmark

**Abstract**

During atmospheric pressure plasma treatment, reactive species generated in the plasma diffuse through a boundary gas layer which is adsorbed at the material surface. Many of the reactive species become inactivated before reaching the surface due to their short lifetime. The efficiency of plasma treatment can be highly enhanced by simultaneous high-power ultrasonic irradiation of the treating surface, because the delivered acoustic energy can reduce the thickness of the boundary gas layer. Here surfaces of glass-fibre-reinforced polyester (GFRP) plates were treated using an atmospheric pressure dielectric barrier discharge in helium with ultrasonic irradiation, particularly for the adhesion improvement. The ultrasound was irradiated through a powered mesh electrode using a high-power gas-jet ultrasonic generator. The discharge mode changed from glow to filamentary by the ultrasonic irradiation. The surface characterizations were performed using contact angle measurements, X-ray photoelectron spectroscopy (XPS) and atomic force mictroscopy (AFM). O/C ratios at the GFRP surfaces before the treatments, after 30-s plasma treatment, and after 30-s plasma treatment with ultrasonic irradiation were 0.295, 0.385 and 0.447, respectively. This indicated that the plasma treatment oxidized and roughened the GFRP surface, and the ultrasonic irradiation further enhanced the oxidation. It is concluded that plasma treatment efficiency for adhesion improvement of GFRPs is enhanced by the ultrasonic irradiation.


**Keywords**

Atmospheric pressure plasma, ultrasound, surface modification, glass-fibre-reinforced polyester

## 1. Introduction

Plasma surface modification is attractive because of its environmental compatibility and high treatment efficiency without affecting the textural characteristics of the

* To whom correspondence should be addressed. Tel.: +45 4677 4571; Fax: +45 4677 4565; e-mail: yuki@risoe.dtu.dk

 DOI:10.1163/016942410X507605

bulk materials [1]. This kind of plasma is generally obtained at low pressures. The plasma surface modification at a low pressure, however, suffers from the drawbacks that it requires expensive vacuum system, and is only well-developed for batch or semi-batch treatment. To overcome these drawbacks, plasma processing at atmospheric pressure can be used [2], avoiding the need for vacuum equipment, and permitting the treatment of large objects and continuous treatment on production lines [3–6]. In atmospheric pressure plasma sources, a dielectric barrier discharge (DBD) is generated between electrodes covered with dielectrics by applying a time varying voltage. Advantages of a DBD include its compactness, low-cost, and stable operation [7].

Atmospheric pressure plasma surface modification is generally performed by feeding a process gas into the plasma. However, even when the motion of gas is fully turbulent, a boundary gas layer sticks at a material surface. Reactive species such as ions, electrons, high-energy neutrals and radicals generated in the plasma diffuse through the boundary gas layer and activate, interact and/or react with the surface. Due to the short lifetime of these species, only a small fraction can reach the surface. It is reported that powerful ultrasonic waves with a sound power level (SPL) above approximately 140 dB can reduce the thickness of the boundary gas layer [8], and that the treatment efficiency of atmospheric pressure plasma can be highly enhanced by simultaneous high-power ultrasonic irradiation of the treating surface [9, 10]. It is because the acoustic energy can be delivered efficiently at high gas pressures which reduces the thickness of the boundary gas layer. As a result, more reactive species generated in the plasma can reach the surface before becoming inactivated, and can be utilized for surface modification efficiently.

Combinations of a plasma and ultrasonic waves have been investigated for understanding the interaction between plasma and ultrasound [11–16], electrical discharge machining [17], plasma etching [18], ozone generation [19, 20], decomposition of volatile organic compounds [21], improvement of charging performance of corona chargers [22], and surface modification [9, 23]. Electrical discharge machining is a manufacturing process with which a wanted shape of an object is obtained using electrical discharge plasmas. Ultrasonic waves at a material surface are often generated by vibrating the material using a piezoelectric or other solid state electro-acoustic transducer. However, due to the significant difference in acoustic impedances between a solid and a gas (acoustic impedance mismatch), most of the generated acoustic power by such a transducer cannot be transmitted into the surrounding gas, and is converted into thermal energy instead. Therefore, ultrasound generated by such a transducer cannot efficiently reduce the thickness of the boundary gas layer at a material surface. On the other hand, a high-power gas-jet ultrasonic generator excites acoustic waves directly in a gas without acoustic impedance mismatch. Furthermore, it can generate at least one order of magnitude higher acoustic power than any electro-acoustic transducer, and the powerful acoustic waves are capable of eliminating the boundary gas layer [8].

Glass-fibre-reinforced polyester (GFRP) materials, due to their high strength-to-weight ratios and corrosion resistance, are used for a variety of applications in civil engineering, aerospace and automobile industry [24], as well as medical and dental applications [25]. Adhesives are often required for joining these materials to components fabricated from similar GFRPs or other types of materials. GFRPs usually have smooth surfaces composed mainly of the polymeric matrix materials with low surface energies. Therefore, an adhesive joint usually requires careful surface preparation prior to adhesive bonding. Mechanical roughening has conventionally been applied for the surface preparation of GFRPs [26]. However, it needs laborious abrasion followed by solvent cleaning prior to adhesive bonding for achieving high joint strength. Thus plasma surface modification can be a good alternative for this application [27, 28]. It is reported that the adhesion strength of the surface after 2-s plasma treatment with vinylester resin was comparable to or higher than that achieved by the conventional mechanical abrasion method.

In the present preliminary work, the surfaces of GFRP plates are treated using an atmospheric pressure DBD in helium with and without ultrasonic irradiation for adhesion improvement. The treated surfaces are characterized using contact angle measurements, X-ray photoelectron spectroscopy (XPS) and atomic force microscopy (AFM).

## 2. Experimental Methods

GFRP plates were cut from a 2-mm thick commercial G-Etronax PM material which contains 35–40 wt% glass fibres (Elektro-Isola, Vejle, Denmark. http://www.elektro-isola.com/Products/sheets.htm). They were cleaned and degreased with acetone and methanol. However, for XPS analysis they were ultrasonically cleaned in acetone for $2 \times 5$ min and in methanol for 5 min before surface treatment. An atmospheric pressure DBD was used to treat the GFRP plates. The plasma was generated between two parallel plane electrodes and driven by an AC (approximately 40 kHz, 100 W) power supply (Generator 6030. SOFTAL Electronic GmbH, Germany). A schematic diagram of the setup is shown in Fig. 1. The discharge voltage and current were measured with a high voltage probe (PPE20kV, LeCroy) and a 50 Ω current-viewing resistor, respectively. The ground aluminium electrode (50 mm × 50 mm) was water cooled and covered with an alumina plate (100 mm × 100 mm × 3 mm), while the powered aluminium electrode (50 mm × 50 mm) had a 42 mm diameter perforated hole covered with a steel mesh. A 40 mm inner diameter poly(methyl methacrylate) (PMMA) waveguide was attached above the powered electrode for the introduction of ultrasound. A high-power gas-jet ultrasonic generator (SonoSteam®, FORCE Technology, Denmark) was placed near the top of the waveguide. The frequency diapason of the ultrasound ranged between 20 and 40 kHz, and the SPL was approximately 150 dB at the GFRP surface. The plasma gas and ambient air were separated using a thin polyethylene film clamped

in the waveguide. Helium gas was fed into the plasma at a flow rate of 3 l/min. Each GFRP plate was exposed to the DBD for 0, 5, 10, 30, 60, 120 or 300 s.

Contact angles were measured with deionized water and glycerol in air at room temperature both before and after the plasma treatment for evaluation of the surface energy using a contact angle measurement system (CAM100. Crelab Instruments AB, Sweden). The polar component of the solid surface energy of the GFRP plates was determined by the two-liquid geometric method [27, 29–32], namely by solving the simultaneous equations [33, 34]:

$$(1+\cos\theta_i)\cdot\gamma_{Li} = 2\left(\gamma_{Li}^{d}\cdot\gamma_{S}^{d}\right)^{1/2} + 2\left(\gamma_{Li}^{p}\cdot\gamma_{S}^{p}\right)^{1/2}, \quad i = 1, 2,$$

where $\theta$ is a measured contact angle, $\gamma_L^d$ and $\gamma_L^p$ are dispersion and polar components of the surface energy of test liquids, $\gamma_L$ is the surface energy of test liquids, and 1 and 2 denote deionized water and glycerol. $\gamma_L^d$ and $\gamma_L^p$ are 21.8 and 51 mJ/m$^2$ for deionized water [35], and 34 and 30 mJ/m$^2$ for glycerol [36].

XPS data were collected using a micro-focused, monochromatic Al $K_\alpha$ X-ray source (1486.6 eV) with a lateral resolution of 30 μm (K-alpha, ThermoFischer Scientific, UK) to study the changes in elemental compositions and the functional groups on the GFRP surfaces. Atomic concentrations of all elements were calculated by determining the relevant integral peak intensities using the Shirley background. A high resolution analysis was performed on the carbon 1s ($C_{1s}$) and oxygen 1s spectra (pass energy 25 eV) acquired over 30 scans. The binding energies were referred to the hydrocarbon component (C–C, C–H) at 285 eV. The spectra were deconvoluted through curve fitting, taking purely Gaussian components with linear background subtraction. The full-width at half-maximum (FWHM) for all peaks of $C_{1s}$ was constrained to 1.3 eV. The average roughness of the GFRP sur-

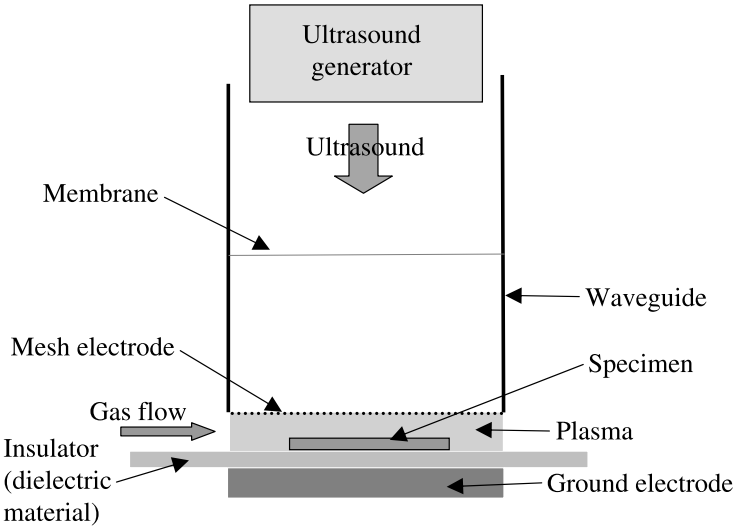


**Figure 1.** Diagram of the DBD setup with a high-power gas-jet ultrasonic generator.

faces was evaluated by AFM (XE-150, PSIA, USA) in Milli-Q water (Millipore Corp. USA) in the contact mode. It is defined as the arithmetic mean deviation of the surface heights from the mean line through the profile [37].

## 3. Results and Discussion

The waveforms of voltage and current in the helium DBD without ultrasonic irradiation are shown in Fig. 2(a). The current waveform shows a few narrow spikes in each excitation, indicating that a glow discharge was generated [38]. When the ultrasound was irradiated onto the DBD, a higher voltage was required to sustain the plasma at the same power than the plasma without ultrasonic irradiation. In addition, formation of a filamentary discharge was observed with ultrasonic irradiation. It can be identified with complex spiky current waveforms of micro-discharges as shown in Fig. 2(b).

The treatment drastically changed the GFRP surface wettability. The water contact angle on the GFRP plate was ∼84° before the treatment, dropped markedly to around 30° after 5-s plasma treatment without ultrasonic irradiation, and tended to decrease further after longer treatments as shown in Fig. 3. Ultrasonic irradiation during plasma treatment consistently improved the wettability. The treatment also changed the polar component of the surface energy. It was 12.1 mJ/m$^2$ before the treatment, between 58 and 67 mJ/m$^2$ after plasma treatment without ultrasonic

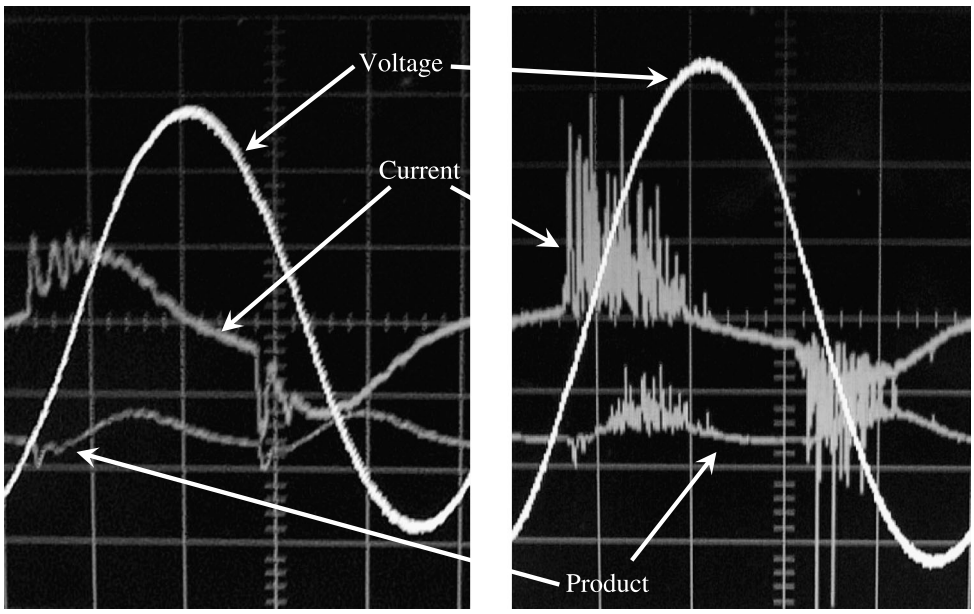


**Figure 2.** Voltage and current waveforms and their products for He DBD without (a) and with ultrasonic irradiation (b).

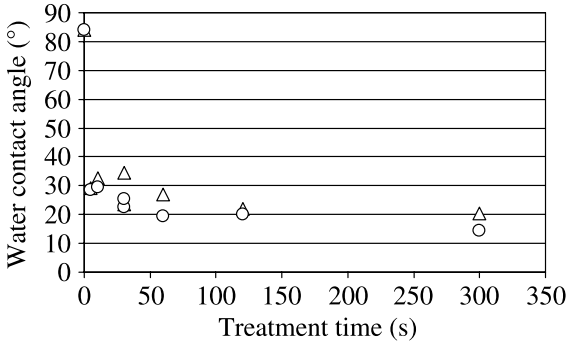


**Figure 3.** Water contact angle before and after plasma treatment with (circle) and without (triangle) ultrasonic irradiation.

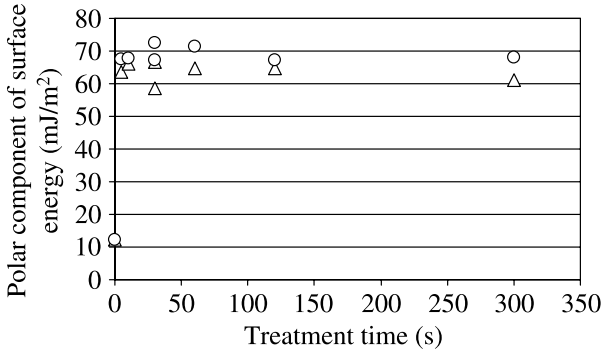


**Figure 4.** Polar component of surface energy before and after plasma treatment with (circle) and without (triangle) ultrasonic irradiation.

irradiation, and between 68 and 73 mJ/m$^2$ after plasma treatment with ultrasound irradiation as shown in Fig. 4. The polar component of the surface energy increased with ultrasonic irradiation, but it was insensitive to the treatment time. Similar result was reported for GFRP composites treated with atmospheric pressure dielectric barrier discharge [27].

XPS survey analysis was carried out to analyze the elemental composition of the GFRP surfaces before and after the 30-s treatments with and without ultrasonic irradiation. The results are summarized in Table 1. After the treatment without ultrasonic irradiation, the oxygen content increased approximately 5%, indicating the introduction of oxygen containing polar functional groups on the surfaces. Ultrasonic irradiation further enhanced oxidation at the surface. Although the mesh electrode was exposed to the plasma during treatment, contamination from the electrode is not apparent. Since Si contents at the treated and untreated surfaces were negligible, the surfaces of the GFRPs were almost covered with the polyester matrix and thus most of the glass fibre surfaces were not exposed to the plasma. It is, therefore, unlikely that the glass fibre surfaces were modified during the treatment.

**Table 1.**
Elemental composition (at%) and O/C ratio at the GFRP surfaces characterized by XPS

| Treatment | Elemental composition (at%) | | | | | O/C ratio |
|---|---|---|---|---|---|---|
| | C | O | N | Si | Ca, Cu, S, Na or Zn | |
| Untreated | 76.5 | 22.6 | 0.6 | 0.1 | 0.3 | 0.295 |
| Plasma, 30 s | 71.5 | 27.5 | 0.5 | 0.1 | 0.7 | 0.385 |
| Plasma + ultrasound, 30 s | 68.3 | 30.5 | 0.2 | 0.1 | 0.2 | 0.447 |

Figure 5 shows $C_{1s}$ spectra of the GFRP surfaces before and after 30-s plasma treatments with and without ultrasonic irradiation. Peaks at approximately 283, 284.4, 285, 286, 287, 288, 289 and >290 eV can be assigned to carbide, C=C, C–H/C–C, C–O–C, C–OH/O–C–O, epoxide, C=O (carbonyl), COO (carboxyl), and plasmon, respectively [5, 39]. On the other hand, the $O_{1s}$ spectrum is deconvoluted into three peaks: at approximately 532, 533 and 534 eV, assigned to O=C–O, O–C and O–C=O, respectively [40]. The $C_{1s}$ component peaks at approximately 284.4 eV (C=C), 287 eV (C–OH/O–C–O) and 289 eV (carboxyl), and all the $O_{1s}$ component peaks increased after plasma treatment without ultrasonic irradiation. It is also obvious that ultrasonic irradiation further increased the intensity of these component peaks, which demonstrates an enhanced oxidation at the surfaces during the plasma treatment due to ultrasonic irradiation. It is noted that introduction of these oxygen-containing polar functional groups on the surfaces increases the polar component of surface energy, and that the adhesion properties can be improved. However, further investigations are necessary for a deep understanding of the surface modification effect.

AFM was used to measure the surface roughness of the GFRP plates, taking a fixed area of $2 \times 2\ \mu m^2$. The average roughness ($r_a$) of the untreated surface was approximately 1.7–4 nm. The GFRP plates were treated with the helium DBD with and without ultrasonic irradiation for 30 s. The roughness slightly increased to approximately 2–7 nm and 2–10 nm after the plasma treatment with and without ultrasonic irradiation, respectively. It is, therefore, unlikely that ultrasonic irradiation further enhances surface roughening during the treatment.

## 4. Conclusions

An atmospheric pressure helium glow DBD changed to a filamentary discharge by the ultrasonic irradiation. Plasma treatment of the GFRP surfaces improved the wettability, increased the polar component of the surface energy, and increased the roughness. The ultrasonic irradiation during the plasma treatment further improved the wettability and the polar component of the surface energy. The principal effect of ultrasonic irradiation can be attributed to enhanced surface oxidation during plasma treatment.

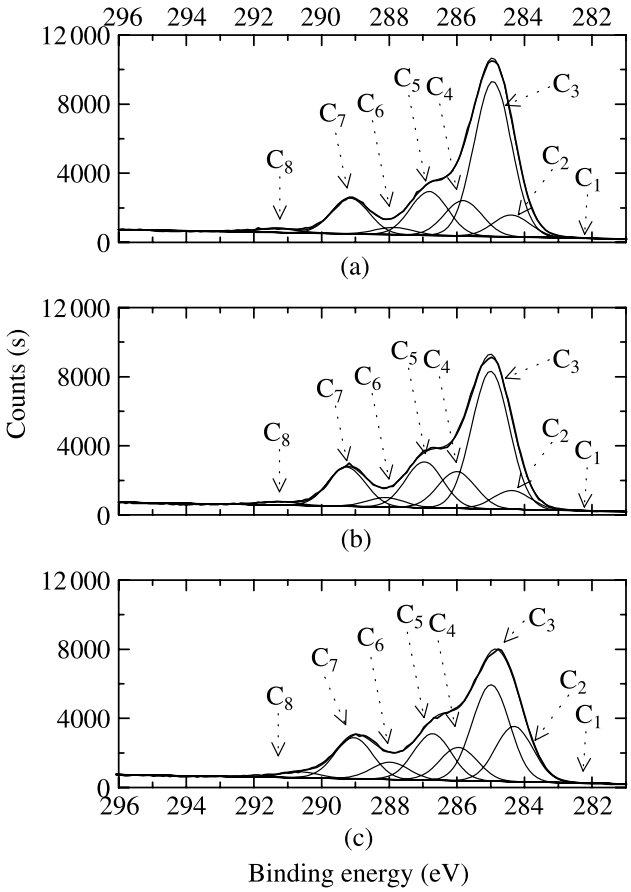


**Figure 5.** $C_{1s}$ spectra of the GFRP surfaces before and after the treatments. Untreated (a), plasma treated (30 s) (b) and plasma treated with ultrasonic irradiation (30 s) (c). Assignments correspond to $C_1$: carbide at 283 eV; $C_2$: C=C at 284.4 eV; $C_3$: C–H/C–C at 285 eV; $C_4$: C–O–C at 286 eV; $C_5$: C–OH/O–C–O and epoxide at 287 eV; $C_6$: carbonyl at 288 eV; $C_7$: carboxyl at 289 eV; and $C_8$: plasmon at >290 eV.

*Acknowledgements*

Lene Hubert is gratefully acknowledged for XPS measurements. This work is supported by a grant from the Proof of Concept Fund (07-017766).

## References

1. M. Strobel, C. S. Lyons and K. L. Mittal (Eds), *Plasma Surface Modification of Polymers: Relevance to Adhesion*. VSP, Utrecht (1994).
2. C. Tendero, C. Tixier, P. Tristant, J. Desmaison and P. Leprince, *Spectrochimica Acta B* **61**, 2 (2006).
3. Y. Kusano, T. L. Andersen and P. K. Michelsen, *J. Phys.: Conf. Series* **100**, 012002 (2008).

4. Y. Kusano, S. Teodoru, F. Leipold, T. L. Andersen, B. F. Sørensen, N. Rozlosnik and P. K. Michelsen, *Surf. Coat. Technol.* **202**, 5579 (2008).
5. S. Teodoru, Y. Kusano, N. Rozlosnik and P. K. Michelsen, *Plasma Polym. Proc.* **6**, 5375 (2009).
6. H. Mortensen, Y. Kusano, F. Leipold, N. Rozlosnik, P. Kingshott, B. F. Sørensen, B. Stenum and H. Bindslev, *Jpn. J. Appl. Phys.* **45B**, 8506 (2006).
7. U. Kogelschatz, *Plasma Chem. Plasma Proc.* **23**, 1 (2003).
8. N. Krebs, Int. Patent No. 2006 015,604 (2006).
9. N. Krebs, A. Bardenshtein, Y. Kusano, H. Bindslev and H. J. Mortensen, Int. Patent No. 2008 138,901 A1 (2008).
10. Y. Kusano, *Surf. Eng.* **25**, 415 (2009).
11. T. Nakane, T. Hirata and K. Seya, *Jpn. J. Appl. Phys.* **26** (Suppl.), 203 (1987).
12. T. Hirata, T. Nakane and K. Seya, *Jpn. J. Appl. Phys.* **30** (Suppl.), 54 (1991).
13. T. Kagiwada, T. Hirata, T. Nakane, T. Otsuka and K. Seya, in: *Proc. IEEE Ultrasonic Symp.*, p. 1015 (1991).
14. T. Otsuka, K. Teranishi and T. Nakane, *Jpn. J. Appl. Phys.* **40** (Pt. 1), 3797 (2001).
15. T. Nakane, T. Miyajima and T. Otsuka, *Jpn. J. Appl. Phys.* **43**, 2852 (2004).
16. R. Bálek, S. Pekárek and Z. Bartáková, *Ultrasonics* **44**, e549 (2006).
17. Q. H. Zhang, R. Du, J. H. Zhang and Q. B. Zhang, *Int. J. Machine Tools Manuf.* **46**, 1582 (2006).
18. T. Hatsuzawa, M. Hayase and T. Oguchi, *Precision Eng.* **26**, 442 (2002).
19. S. Pekárek and R. Bálek, *J. Phys. D: Appl. Phys.* **37**, 1214 (2004).
20. R. Bálek, S. Pekárek and Z. Bartáková, *Ultrasonics* **46**, 227 (2007).
21. S. Pekárek, R. Bálek, J. Kuhn and M. Pospl, *Czech. J. Phys. Suppl. B* **56**, B982 (2006).
22. K.-S. Choi, S. Nakamura and Y. Murata, *Jpn. J. Appl. Phys.* **44**, 3248 (2005).
23. P. Koulik, M. Samsonov, A. Cherepanov and E. Petrov, US Patent No. 2003 165,636 A1 (2003).
24. H. J. Dagher, A. Iqbal and B. Bogner, *Polym. Polym. Composites* **12**, 169 (2004).
25. M. Huttunen, N. Ashammakhi, P. Törmälä and M. Kellomäki, *Acta Biomaterialia* **2**, 575 (2006).
26. R. D. Adams, R. W. Atkins, A. Harris and A. J. Kinloch, *J. Adhesion* **20**, 29 (1986).
27. Y. Kusano, H. Mortensen, B. Stenum, P. Kingshott, T. L. Andersen, P. Brøndsted, J. B. Bilde-Sørensen, B. F. Sørensen and H. Bindslev, *Plasma Proc. Polym.* **4**, S455 (2007).
28. Y. Kusano, S. Teodoru, F. Leipold, T. L. Andersen, B. F. Sørensen, N. Rozlosnik and P. K. Michelsen, *Surf. Coat. Technol.* **202**, 5579 (2008).
29. K. Ma, T. S. Chung and R. J. Good, *J. Polym. Sci. B: Polym. Phys.* **36**, 2327 (1998).
30. D. K. Owens and R. C. Wendt, *J. Appl. Polym. Sci.* **13**, 1741 (1969).
31. D. H. Kaelble, *J. Adhesion* **2**, 66 (1970).
32. A. Schwarcz, *J. Polym. Sci. Pt. B Polym. Phys.* **12**, 1195 (1974).
33. D. M. Choi, C. K. Park, K. Cho and C. E. Park, *Polymer* **38**, 6243 (1997).
34. S. J. Park, M. H. Kim, J. R. Lee and S. Choi, *J. Colloid Interface Sci.* **228**, 287 (2000).
35. J. Cognard, *C. R. Chimie* **9**, 13 (2006).
36. N. Dilsiz and J. P. Wightman, *Colloids Surfaces* **164**, 325 (2000).
37. I. M. Hutchings, *Tribology*. Arnold, London, UK (1992).
38. T. Yokoyama, M. Kogoma, T. Moriwaki and S. Okazaki, *J. Phys. D: Appl. Phys.* **23**, 1125 (1990).
39. K. E. Mayerhofor and E. Neubauer, *Anal. Bioanal. Chem.* **374**, 602 (2002).
40. G. Beamson and D. Briggs, *High Resolution XPS of Organic Polymers, The Scienta ESCA300 Database*. Wiley, Chichester (1992).

# [Appendix A13]

Y. Kusano, K. Norrman, S.V. Singh, F. Leipold, P. Morgen, A. Bardenshtein, N. Krebs

## “Ultrasound enhanced 50 Hz plasma treatment of glass-fiber-reinforced polyester at atmospheric pressure“

*Journal of Adhesion Science and Technology* 27(7) (2013) 825-833.

*Journal of Adhesion Science and Technology*, 2013
Vol. 27, No. 7, 825–833, http://dx.doi.org/10.1080/01694243.2012.727156





# SHORT NOTE

## Ultrasound enhanced 50 Hz plasma treatment of glass-fiber-reinforced polyester at atmospheric pressure

Y. Kusano[a]*, K. Norrman[b], S.V. Singh[a], F. Leipold[c], P. Morgen[d], A. Bardenshtein[e] and N. Krebs[f]

[a]*Department of Wind Energy, Section of Composites and Materials Mechanics, Technical University of Denmark, Risø Campus, Frederiksborgvej 399, DK-4000 Roskilde, Denmark;* [b]*Department of Energy Conversion and Storage, Technical University of Denmark, Building 111, Frederiksborgvej 399, DK-4000 Roskilde, Denmark;* [c]*Department of Physics, Technical University of Denmark, Frederiksborgvej 399, DK-4000 Roskilde, Denmark;* [d]*Department of Physics, Chemistry and Pharmacy, University of Southern Denmark, Campusvej 55, DK-5230 Odense M, Denmark;* [e]*Danish Technological Institute, Gregersensvej 3, DK-2630 Taastrup, Denmark;* [f]*FORCE Technology, DK-2605 Brøndby, Denmark*

(*Received 29 January 2011; final version received 27 July 2012; accepted 28 July 2012*)

Glass-fiber-reinforced polyester (GFRP) plates are treated using a 50 Hz dielectric barrier discharge at a peak-to-peak voltage of 30 kV in helium at atmospheric pressure with and without ultrasonic irradiation to study adhesion improvement. The ultrasonic waves at the fundamental frequency of around 30 kHz with the sound pressure level of approximately 155 dB were introduced vertically to the GFRP surface through a cylindrical waveguide. The polar component of the surface energy was almost unchanged after the plasma treatment without ultrasonic irradiation, but drastically increased approximately from 20 up to 80 mJ $m^{-2}$ with ultrasonic irradiation. The plasma treatment with ultrasonic irradiation also introduced oxygen- and nitrogen-containing functional groups at the GFRP surface. These changes would improve the adhesion properties of the GFRP plates.

**Keywords:** dielectric barrier discharge; atmospheric pressure plasma; ultrasound; polyester; oxidation

### Introduction

Glass-fiber-reinforced polyester (GFRP) materials exhibit high strength-to-weight ratios and corrosion resistance and are therefore used for a variety of applications particularly in civil engineering. For such applications, GFRPs are often joined with similar or dissimilar materials using adhesives. However, they usually have smooth surfaces composed mainly of the polyester matrix materials with low surface energies. Therefore, the adhesive joint usually requires careful surface preparation. Mechanical roughening has been industrially applied for this purpose, but it needs laborious abrasion followed by solvent cleaning prior to adhesive bonding for achieving high joint strength. Plasma treatment is attractive for this application due to its environmental compatibility and high treatment efficiency without affecting the textural characteristics of the bulk material [1]. It is often employed at low pressure, but is possible and preferable at atmospheric pressure [2,3]. Among atmospheric pressure plasmas, a dielectric barrier discharge (DBD) is generated between electrodes covered with at least one dielectric

*Corresponding author. Email: yuki@dtu.dk

layer by applying AC voltage. Advantages of a DBD include: its compactness, low cost, and stable operation [4]. It is reported that the adhesion strength of the surface, after 2 s DBD treatment operated at a frequency of approximately 40 kHz, was comparable to or higher than that achieved by the conventional abrasion method [5]. A DBD is often operated at a frequency ranging between 50 Hz and 500 kHz [4–8]. A 50/60 Hz operation is advantageous due to its simplicity and avoiding a radiation hazard related with high-frequency operation. Consequently, 50 Hz plasma processing at atmospheric pressure is extensively investigated [9–12].

The efficiency of plasma processing can be further enhanced by external energy input [13]. Among possible techniques, ultrasonic irradiation by a high-power gas-jet ultrasound generator is attractive because of its simple setup and high efficiency of the generated acoustic energy transferring into a plasma [14–18]. It is further reported that simultaneous ultrasonic irradiation during the DBD treatment can enhance oxidation at the GFRP surfaces [15] and suppress arcing in air plasmas [16,17]. A gliding arc with and without ultrasonic irradiation was also used for the adhesion improvement of GFRP plates [19,20]. However, a 50 Hz DBD with ultrasonic irradiation is never attempted for plasma surface modification.

In the present work, GFRP plates are treated with the 50 Hz DBD with and without ultrasonic irradiation for the purpose of adhesion improvement. Optical emission spectroscopy (OES) is used for plasma diagnostics. The treated surfaces are characterized using contact angle measurement, X-ray photoelectron spectroscopy (XPS), time-of-flight secondary ion mass spectrometry (TOF-SIMS), and atomic force microscopy (AFM).



## Experimental methods

The 2 mm thick GFRP plates were used as specimens (G-Etronax PM. Elektro-Isola, Vejle, Denmark. http://www.elektro-isola.com/Products/sheets.htm). They contain 35–40 wt% glass fibers, and the surfaces are mostly covered with polyester matrix. They were cleaned and degreased with acetone and methanol. However, for XPS, TOF-SIMS, and AFM analyses, they were ultrasonically cleaned in deionized water for $2 \times 5$ min, acetone for $2 \times 5$ min, and in methanol for 5 min before the plasma treatment.

The DBD was generated between two parallel-plate electrodes (50 mm × 50 mm and gap: 3 mm) driven at a frequency of 50 Hz with a step up transformer. It is a modification of the DBDs introduced previously [6–8]. A 100 kΩ resistor was connected between the transformer and the powered electrode in order to avoid excess pulse current when a plasma was generated. The voltage and current were measured with a high voltage probe (PPE20 kV, LeCroy) and a 50 Ω current-viewing resistor, respectively. The peak-to-peak voltage was set to 30 kV. The average electrical power applied in the DBD was calculated by time integrating the product of the voltage and current over several periods and then dividing it by the time corresponding to that number of periods. The power measured in this way was less than 0.5 W. It is distinctly different from a normal DBD operated at a frequency of several kHz or more, where the input power can be typically 100–1000 times higher. The powered bottom aluminum electrode is covered with an alumina plate (100 mm × 100 mm × 3 mm), while the ground aluminum electrode has a 42 mm diameter perforated hole covered with a stainless steel mesh. A 40 mm inner diameter poly(methyl methacrylate) waveguide is attached above the ground electrode for the introduction of ultrasound. A high-power gas-jet air-operated ultrasonic generator (SonoSteam®, FORCE Technology, Denmark) is placed near the top of the waveguide. The fundamental frequency of the ultrasound is at around 30 kHz. The sound pressure level is approximately 155 dB at the discharge. The acoustic field in the DBD setup is probed using the capacitive microphone B&K Type 2670 and the signal is processed by means of the Portable Pulse Analyzer (Brüel & Kjær Sound and Vibrations, Denmark). The

DBD and ambient air are separated using a thin polyethylene membrane clamped between the outer wall of the waveguide and the upper part of the powered electrode. Helium gas was fed into the DBD at a flow rate of $3\,\mathrm{L\,min^{-1}}$. Each GFRP plate was exposed to the DBD for 0, 10, 30, 60, 180, or 300 s.

OES measurements were performed without a GFRP plate using an optical fiber and a 0.75 m spectrometer equipped with a grating with 3600 grooves/mm and a charge-coupled device (CCD) camera (PI-MAX 1024, Princeton Instruments, NJ, USA). The spectral resolution is 20 pm.

AFM imaging ($10\,\mu m \times 10\,\mu m$) was performed on an N8 NEOS (Bruker Nano GmbH, Herzogenrath, Germany) operating in an intermittent contact mode and using SSS-NCLR cantilevers (NANOSENSORS™, Neuchatel, Switzerland) for the GFRP plates before and after the plasma treatments for 60 s. Images were recorded at a scan speed of 0.5 lines $\mathrm{s^{-1}}$. A zero degree least mean squared (LMS) fit was used for the plane correction.

Contact angles were measured by the sessile drop method with deionized water and glycerol in air at room temperature both before and after the treatments for evaluation of the surface energy using a contact angle measurement system (CAM100. Crelab Instruments AB, Billdal, Sweden). A typical drop size was 1 μL. The contact angle was measured within 5 s after the drop was attached onto the surface. The polar component of the solid surface energy of the GFRP plates was determined by the two-liquid geometric method [21], namely by solving the simultaneous equations:

$$(1 + \cos\theta_i) \cdot \gamma_{Li} = 2(\gamma_{Li}^{d}\gamma_{S}^{d})^{1/2} + 2(\gamma_{Li}^{p}\gamma_{S}^{p})^{1/2} \qquad (i = 1, 2)$$

where $\theta$ is a measured contact angle, $\gamma_s^d$ and $\gamma_s^p$ are the dispersion and polar components of the surface energy of the solid, $\gamma_L^d$ and $\gamma_L^p$ are the dispersion and polar components of the surface energy of test liquids, $\gamma_L$ is the surface energy of test liquids, and 1 and 2 denote deionized water and glycerol. The $\gamma_L^d$ and $\gamma_L^p$ are 21.8 and $51\,\mathrm{mJ\,m^{-2}}$ for deionized water and 34 and $30\,\mathrm{mJ\,m^{-2}}$ for glycerol [15]. The problems of this method are discussed in [22]. However, this method was used in the present work in order to get an idea about the surface modification effect immediately after the plasma treatment.

XPS data were collected using a double anode (Mg/Al) source, and for the present measurements the Mg $K_\alpha$ line with an energy of 1253.6 eV was used, with a lateral resolution of 2 mm to study the changes in elemental compositions and the functional groups on the GFRP surfaces before and after the treatments for 60 s. XPS was operated at a pressure of $<10^{-5}$ Pa. Atomic concentrations of all elements were calculated by determining the relevant integral peak intensities subtracting a Shirley-type background. In addition, a high-resolution analysis was performed on the carbon 1s (C1s) peak (pass energy 25 eV) acquired over 3 scans. The binding energies were referred to the hydrocarbon component (C–C, C–H) at 285 eV. These spectra were curve fitted taking purely Gaussian components with linear background subtraction.

TOF-SIMS analyses were performed using a TOF-SIMS IV (ION-TOF GmbH, Münster, Germany). TOF-SIMS was acquired using 25 ns pulses of 25 keV $Bi^+$ that were bunched to form ion packets with a nominal temporal extent of <0.9 ns at a repetition rate of 10 kHz, yielding a target current of 1 pA. These primary ion conditions were used to acquire $500\,\mu m \times 500\,\mu m$ ion images of the sample surfaces with a lateral resolution of $\sim 2\,\mu m$.

## Results and discussion

The current wave formed at 50 Hz generally looks rather spiky due to the significant difference between the current pulse width and a period of the sinusoidal voltage waveform.

The current pulse width of the DBD was approximately 1 μs as shown in Figure 1(a) . A similar value is reported for a helium DBD at atmospheric pressure in the literature [23]. Ultrasonic irradiation decreases the current pulse width strongly, while it increases the height of the current several times as shown in Figure 1(b) . This result corresponds to the fact that the current waveform of the helium DBD driven at 40 kHz changed from glow to filamentary with ultrasonic irradiation [15,17].

OES was measured to identify excited species and estimate the gas temperature via the rotational temperature of $N_2$ in the DBD. Traces of nitrogen in the discharge originate from the surrounding air since the discharge was not completely gas tight. OES of the DBD with and without ultrasonic irradiation includes $N_2$ and $N_2^+$ bands. Ultrasonic irradiation reduced the optical emission intensity, but led to no detectable difference in the relative profile between the rotational spectra recorded with and without ultrasonic radiation. Figure 2 shows the measurement and simulation for the 0–0 transition of the 2nd positive system of nitrogen in the OES of the helium DBD without ultrasonic irradiation. The best fit was found for a rotational temperature of 300 K for the DBD with and without ultrasonic irradiation. It is therefore indicated that heating of the gas by ultrasonic irradiation was negligible.

Surface roughening is often useful for adhesion improvement because of the increased surface area and mechanical interaction with the adhesive. Six, three, and seven AFM images were obtained on the untreated specimen, the plasma-treated specimen, and the plasma-treated specimen with ultrasonic irradiation, respectively. Figure 3 shows some AFM images selected from all the acquired ones. The surface roughness values ($S_a$) were extracted from the AFM images, and summarized in Table 1. No significant difference in surface roughness is observed for the specimens before and after the treatments. It is possibly because the energy applied to the plasma was too low for the efficient surface roughening.

The wettability of the GFRP surface plays an important role for the adhesion improvement. However, helium DBD treatment without ultrasonic irradiation did not significantly improve the wetting as shown in Figures 4 and 5. This can again be attributed to the low energy input to the helium plasma. On the other hand, the water contact angle of the GFRP markedly decreased and the polar component of surface energy significantly increased when ultrasound was introduced. The longer treatment further improved the wetting of the GFRP surfaces. Accordingly, the polar component of the surface energy of the GFRP was increased by the plasma treatment with ultrasonic irradiation. It is a significant contrast from the atmospheric pressure plasma treatment driven at approximately 40 kHz AC voltage, where only moderate improvement of wettability was observed with ultrasonic irradiation [15–18, 20]. It is noted that the increasing wettability and the polar component of surface energy can most



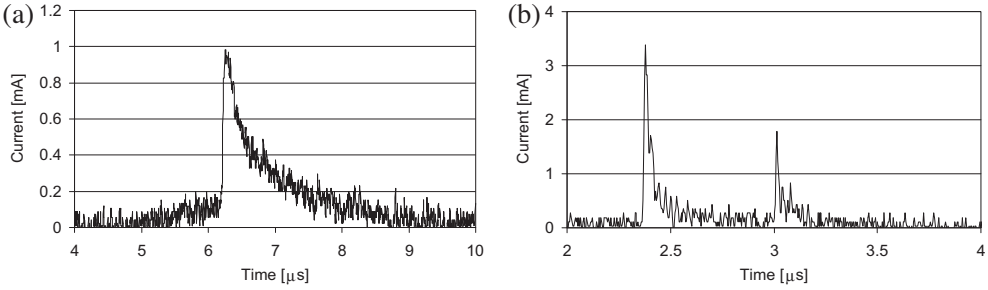


Figure 1. Typical current waveforms of the DBD. Without (a) and with (b) ultrasonic irradiation.

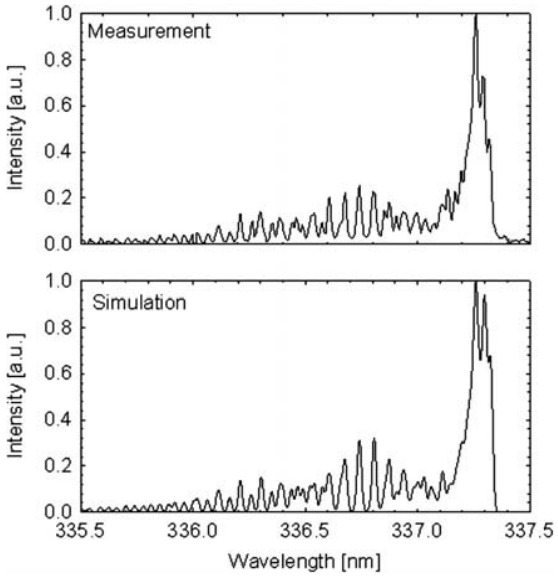


Figure 2. Measurement and simulation for the 0–0 transition of the 2nd positive system of nitrogen in the OES of the helium DBD with ultrasonic irradiation. The best fit was found for a rotational temperature of 300 K. The measured spectral resolution (FWHM) is 20 pm.

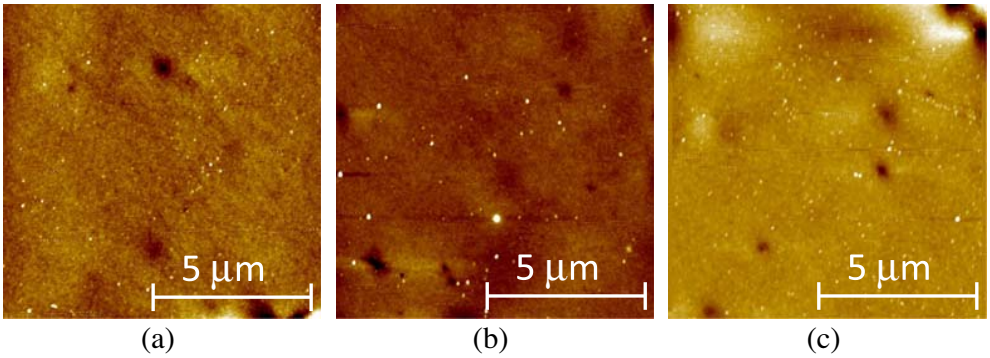


Figure 3. AFM images of GFRP surfaces (10 µm × 10 µm): (a) untreated, (b) 60 s plasma treated, and (c) 60 s plasma treated with ultrasonic irradiation.

Table 1. Surface roughness of the GFRP plates before and after the treatment.

| Specimen | Surface roughness (nm) |
|---|---|
| Untreated | 1.4 ± 0.2 |
| Plasma, 60 s | 1.3 ± 0.2 |
| Plasma + ultrasound, 60 s | 1.5 ± 0.2 |

likely improve adhesion properties of the GFRP surfaces because of strong interaction with general adhesives [19].

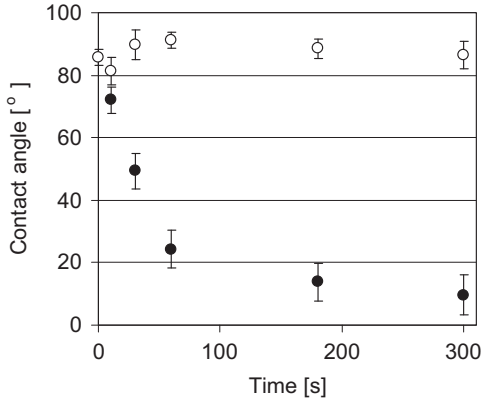


Figure 4. Water contact angle before and after plasma treatment with (filled circle) and without (open circle) ultrasonic irradiation.

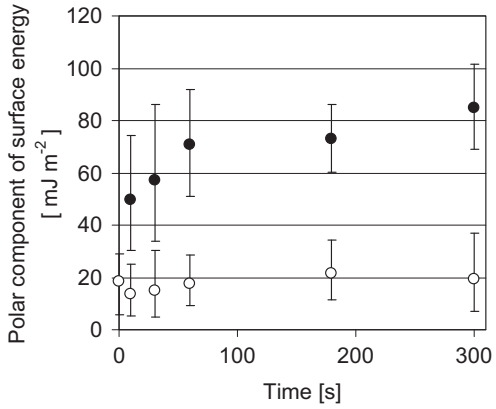


Figure 5. Polar component of surface energy before and after plasma treatment with (filled circle) and without (open circle) ultrasonic irradiation.



XPS survey analysis was carried out in order to analyze the elemental composition of the GFRP surfaces before and after the 60 s treatments with and without ultrasonic irradiation. The results are summarized in Table 2. The O/C ratio remained almost unchanged after the plasma treatment without ultrasonic irradiation, while it slightly increased from 0.23 to 0.25 after the plasma treatment with ultrasonic irradiation. An increase in the O/C ratio indicates

Table 2. Elemental composition (at.%) and O/C ratio of the GFRP surfaces characterized by XPS.

| | Elemental composition (at.%) | | | |
|---|---|---|---|---|
| Treatment | C1s | O1s | N1s | O/C ratio |
| Untreated | 81.1 | 18.5 | 0.4 | 0.23 |
| Plasma, 60 s | 81.8 | 17.9 | 0.3 | 0.22 |
| Plasma + ultrasound, 60 s | 79.8 | 19.9 | 0.3 | 0.25 |

Table 3. The result of curve fitting of C1s spectra of the GFRP surfaces characterized by XPS.

| | C1s (area%) | | | | |
|---|---|---|---|---|---|
| | C–H/C–C | C–O–C/C–OH | C = O | C(O)O– | Plasmon |
| Binding energy (eV) | 285 | 286.48 | 288.03 | 289.46 | >290 |
| Untreated | 57.2 | 23.2 | 8.9 | 7.6 | 3.1 |
| Plasma, 60 s | 58.0 | 24.1 | 9.2 | 7.5 | 1.2 |
| Plasma + ultrasound, 60 s | 56.6 | 24.4 | 9.1 | 7.9 | 2.0 |

that oxygen-containing polar functional groups are introduced at the surfaces, improving the wettability. This result shows an agreement with that of the contact angle measurement. On the other hand, no clear change was seen in the nitrogen content before/after the DBD treatment with/without ultrasonic irradiation.

Table 3 summarizes the result of the curve fitting of C1s spectra of the GFRP surfaces before and after 60 s plasma treatments with and without ultrasonic irradiation. Peaks at approximately 285 eV (A), 286.48 eV (B), 288.03 eV (C), 289.46 eV (D), and > 290 eV (E) can be assigned to C–H/C–C, C–O–C/C–OH, C = O (carbonyl), C(O)O– (carboxyl), and plasmon ($\pi^*$–$\pi$ shake-up), respectively [15,16,24]. Due to the existence of an aromatic ring structure in the polyester, the peak A at 285 eV should contain a lower energy peak (F) at approximately 284.5 eV. However, the curve fitting of the peak F was not attempted, since the peaks A and F are too close to offer a case of reliable curve fitting. No clear differences

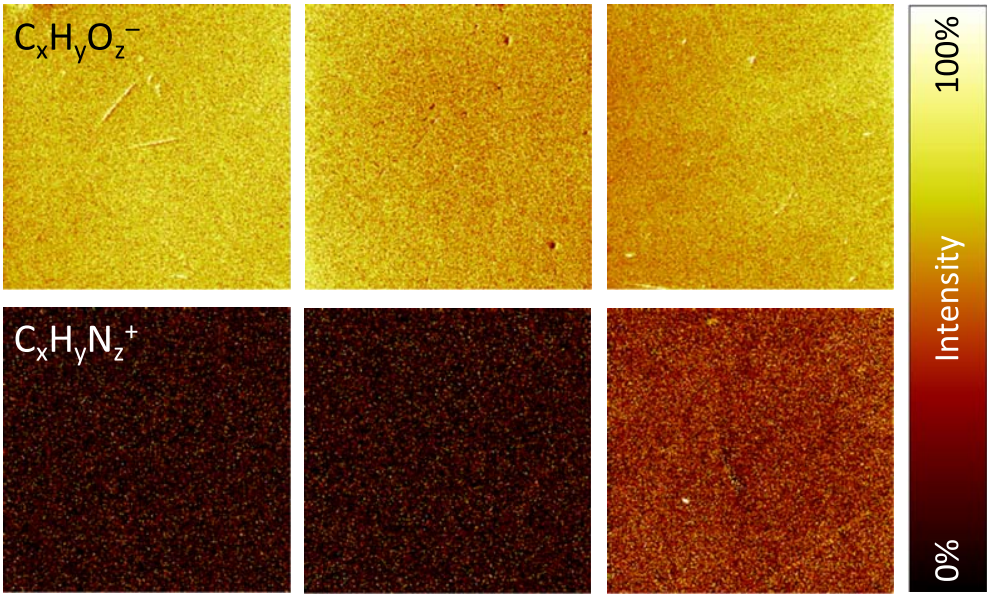


Figure 6. TOF-SIMS ion images (500 μm × 500 μm) showing the lateral intensity distribution of $C_xH_yO_z^-$ and $C_xH_yN_z^+$ markers on the GFRP surfaces: (a) untreated, (b) 60 s plasma treated, and (c) 60 s plasma treated with ultrasonic irradiation. Brown corresponds to no intensity and white to 100% intensity.

can be seen in the C1s spectra before/after the DBD treatment with/without ultrasonic irradiation.

Figure 6 shows TOF-SIMS ion images (500 μm × 500 μm) of the sample surfaces before and after the plasma treatments with and without ultrasonic irradiation. Oxygen-containing species were homogeneously distributed in all cases. The homogeneous distribution of nitrogen species was observed only on the specimen surface after the plasma treatment with ultrasonic irradiation. It is suggested that nitrogen from ambient air reacted with the sample surfaces during the plasma treatment with ultrasonic irradiation. XPS detects similar amounts of traces of nitrogen on all the surfaces, while TOF-SIMS detects more intense nitrogen species on the surfaces treated with ultrasonic irradiation. This difference can be explained from the fact that TOF-SIMS is more surface sensitive (∼1 nm) compared to XPS (5–10 nm).

It is reported that ozone production is pronounced with ultrasonic irradiation when an atmospheric pressure $O_2$ DBD is driven at a lower frequency [25]. This might explain the reason why in the present work the treatment efficiency of 50 Hz DBD was significantly improved by ultrasonic irradiation. However, further investigation is necessary for a deeper understanding of all the involved surface modification mechanisms.



## Conclusion

A 50 Hz DBD plasma treatment can be an economical method for surface modification, but without ultrasonic irradiation it did not change the surface properties of the GFRP plates significantly under the present tested conditions. The surface roughness remained almost unchanged after the plasma treatments with and without ultrasonic irradiation. It is found that ultrasonic irradiation to the 50 Hz DBD enhanced the treatment efficiency markedly, so that a certain amount of oxygen- and nitrogen-containing polar functional groups was introduced at the GFRP surfaces. This is in marked contrast to the 40 kHz DBD, where the ultrasonic irradiation enhanced treatment efficiency only moderately [15–18]. The attachment of these functional groups on the surfaces will contribute to the increase in the polar component of surface energy and potentially improve the adhesion properties of the surfaces [5,15–20].

## Acknowledgments

This work is supported by a grant from the Proof of Concept Fund (07-017766). Søren Nimb is gratefully acknowledged for the design and construction of the gliding arc source.

## References

[1] Strobel M, Lyons CS, Mittal KL, editors. Plasma surface modification of polymers: relevance to adhesion. Utrecht: VSP; 1994.
[2] Tendero C, Tixier C, Tristant P, Desmaison J, Leprince P. Atmospheric pressure plasmas: a review. Spectrochimica Acta B: Atomic Spectroscopy. 2006 Jan;61(1):2–30.
[3] Kogoma M, Kusano M, Kusano Y, editors. Generation and applications of atmospheric pressure plasmas. New York (NY): NOVA Science Publishers; 2011.
[4] Kogelschatz U. Dielectric-barrier discharges: their history, discharge physics, and industrial applications. Plasma Chemistry and Plasma Processing. 2003 Mar;23(1):1–46.
[5] Kusano Y, Mortensen H, Stenum B, Kingshott P, Andersen TL, Brøndsted P, Bilde-Sørensen JB, Sørensen BF, Bindslev H. Atmospheric pressure plasma treatment of glass fibre composite for adhesion improvement. Plasma Processes and Polymers. 2007 Apr;4(S1):S455–9.
[6] Kusano Y, Leipold F, Fateev A, Stenum B, Bindslev H. Production of ammonia-derived radicals in a dielectric barrier discharge and their injection for denitrification. Surface and Coatings Technology. 2005 Oct;200(1–4):846–9.

[7] Fateev A, Leipold F, Kusano Y, Stenum B, Tsakadze E, Bindslev H. Plasma chemistry in an atmospheric pressure Ar/$NH_3$ dielectric barrier discharge. Plasma Processes and Polymers. 2005 Mar;2 (3):193–200.
[8] Leipold F, Fateev A, Kusano Y, Stenum B, Bindslev H. Reduction of NO in the exhaust gas by reaction with N radicals. Fuel. 2006 Jul-Aug;85(10–11):1383–8.
[9] Okazaki S, Kogoma M, Uehara M, Kimura Y. Appearance of stable glow discharge in air, argon, oxygen and nitrogen at atmospheric pressure using a 50 Hz source. Journal of Physics D: Applied Physics. 1993 May;26(5):889–92.
[10] Golubovskii YuB, Maiorov VA, Behnke JF, Tepper J, Lindmayer M. Study of the homogeneous glow-like discharge in nitrogen at atmospheric pressure. Journal of Physics D: Applied Physics. 2004 May;37(9):1346–56.
[11] Bulina NV, Lopatin VA, Novikov PV, Vnukova NG, Churilov GN, Krätschmer W. Fullerene synthesis in helium flow at atmospheric pressure. In: Veziroglu TN, Zaginaichenko SY, Schur DV, Baranowski B, Shpak AP, Skorokhod VV, Kale A, editors. Hydrogen materials science and chemistry of carbon nanomaterials. Proceedings of the NATO Advanced Research Workshop on Hydrogen Materials Science and Chemistry of Carbon Nanomaterials (ICHMS'2005); 2005 Sept 5–11; Sevastopol, Crimea (Ukraine): Nato Security through Science Series A; 2007. p. 269–74.
[12] Garamoon AA, El-zeer DM. Atmospheric pressure glow discharge plasma in air at frequency 50 Hz. Plasma Sources Science and Technology. 2009 Nov;18(4):045006.
[13] Kusano Y. Plasma surface modification at atmospheric pressure. Surface Engineering. 2009 Aug;25 (6):415–6.
[14] Krebs N, Bardenshtein A, Kusano Y, Bindslev H, Mortensen HJ, inventors; Enhancing plasma surface modification using high intensity and high power ultrasonic acoustic waves. European patent EP 2,153,704 A1. 2010 Feb 17.
[15] Kusano Y, Singh SV, Bardenshtein A, Krebs N, Rozlosnik N. Plasma surface modification of glass-fibre-reinforced polyester enhanced by ultrasonic irradiation. Journal of Adhesion Science and Technology. 2010 Aug;24(11–12):1831–9.
[16] Kusano Y, Singh SV, Norrman K, Leipold F, Drews J, Morgen P, Bardenshtein A, Krebs N. Ultrasound enhanced plasma treatment of glass-fibre-reinforced polyester in atmospheric pressure air for adhesion improvement. Journal of Adhesion. 2011 Jul;87(7–8):720–31.
[17] Kusano Y, Singh SV, Norrman K, Drews J, Leipold F, Bardenshtein A, Krebs N. Ultrasound enhanced plasma surface modification at atmospheric pressure. Surface Engineering. 2012 Jun;28 (6):453–7.
[18] Kusano Y, Andersen TL, Sørensen BF, Rozlosnik N, Mortensen H, Teodoru S, Kingshott P, Leipold F, Singh SV, Bilde-Sørensen J, Brøndsted P, Michelsen PK, Bindslev H, Bardenshtein A, Krebs N. Adhesion improvement of glass fibre reinforced polyester composite by atmospheric pressure plasma treatment. Fiber-reinforced composites. In: Cheng Q, editor. Fiber-reinforced composites. New York (NY): NOVA Science Publishers; 2012. 297–318.
[19] Kusano Y, Teodoru S, Leipold F, Andersen TL, Sørensen BF, Rozlosnik N, Michelsen PK. Gliding arc discharge – application for adhesion improvement of fibre reinforced polyester composites. Surface and Coatings Technology. 2008 Aug;202(22–23):557982.
[20] Kusano Y, Norrman K, Drews J, Leipold F, Singh SV, Morgen P, Bardenshtein A, Krebs N. Gliding arc surface treatment of glass-fiber-reinforced polyester enhanced by ultrasonic irradiation. Surface and Coatings Technology. 2011 Jul;205(Supplement 2):S490–4.
[21] Kaelble DH. Dispersion-polar surface tension properties of organics solids. Journal of Adhesion. 1970 Jan;2:66–81.
[22] Strobel M, Lyons CS. An essay on contact angle measurements. Plasma Processes and Polymers. 2011 Jan;8(1):8–13.
[23] Tochikubo, F Chiba T, Watanabe T. Structure of low-frequency helium glow discharge at atmospheric pressure between parallel plate dielectric electrodes. Japanese Journal of Applied Physics, Part 1. 1999 Sep;38(9A):5244–50.
[24] Beamson G, Briggs D. High Resolution XPS of Organic Polymers, The Scienta ESCA300 Database. Chichester: Wiley; 1992.
[25] Drews J, Kusano Y, Leipold F, Bardenshtein A, Krebs N. Ultrasound enhanced plasma treatment of glass-fibre-reinforced polyester in atmospheric pressure air for adhesion improvement. Ozone: Science and Engineering. 2011 Nov–Dec;33(6):483–8.

# [Appendix A14]

Y. Kusano, T.L. Andersen, H.L. Toftegaard, F. Leipold, A. Bardenshtein, N. Krebs

## ”Plasma treatment of carbon fibres and glass-fibre-reinforced polyesters at atmospheric pressure for adhesion improvement”

*International Journal of Materials Engineering Innovation* 5(2) (2014) 122-137.

# Plasma treatment of carbon fibres and glass-fibre-reinforced polyesters at atmospheric pressure for adhesion improvement

Yukihiro Kusano*, Tom L. Andersen and Helmuth L. Toftegaard

Department of Wind Energy,
Section of Composites and Materials Mechanics,
Technical University of Denmark,
Risø Campus, DK-4000 Roskilde, Denmark
E-mail: yuki@dtu.dk
E-mail: toan@dtu.dk
E-mail: heto@dtu.dk
*Corresponding author

Frank Leipold

Department of Physics,
Technical University of Denmark,
Risø Campus, DK-4000 Roskilde, Denmark
E-mail: leip@fysik.dtu.dk

Alexander Bardenshtein

Danish Technological Institute,
Gregersensvej 3, DK-2630 Taastrup, Denmark
E-mail: alb@teknologisk.dk

Niels Krebs

FORCE Technology,
DK-2605 Brøndby, Denmark
E-mail: nk@force.dk

**Abstract:** Atmospheric pressure plasma treatment is useful for adhesion improvement, because cleaning, roughening and addition of polar functional groups can be expected at the surfaces. Its possible applications in the wind energy industry include plasma treatment of fibres and fibre-reinforced polymer composites before assembling them to build wind turbine blades. In the present work, unsized carbon fibres are continuously treated using a dielectric barrier discharge plasma in helium at atmospheric pressure, and carbon fibre reinforced epoxy composite plates are manufactured for the mechanical test. The plasma treatment improved fracture toughness, indicating that adhesion between the fibres and the epoxy was enhanced by the treatment. In addition, glass-fibre-reinforced polyester plates are treated using a gliding arc and an ultrasound enhanced dielectric barrier discharge, improving the wettability and/or the adhesive strength with a vinylester resin.

**Keywords:** carbon fibre; glass-fibre-reinforced polymer; epoxy; polyester; vinylester; adhesion; fracture resistance; plasma; atmospheric pressure; dielectric barrier discharge; DBD; gliding arc; ultrasound.

**Reference** to this paper should be made as follows: Kusano, Y., Andersen, T.L., Toftegaard, H.L., Leipold, F., Bardenshtein, A. and Krebs, N. (2014) 'Plasma treatment of carbon fibres and glass-fibre-reinforced polyesters at atmospheric pressure for adhesion improvement', *Int. J. Materials Engineering Innovation*, Vol. 5, No. 2, pp.122–137.

**Biographical notes:** Yukihiro Kusano is a Senior Scientist at the Department of Wind Energy, Technical University of Denmark. He was awarded the BEng at the Department of Applied Physics, University of Tokyo, Japan in 1986 and the PhD at King's College, Cambridge, UK (Materials Science) in 2000. He has worked in surface science/engineering, plasma processing, thin films, magnetron sputtering, adhesion and tribology at Bridgestone Co. Japan, the University of Cambridge, UK and the Technical University of Denmark. He is acting as an editor in *Surface Physics*, *Central European Journal of Physics*, and a member of the editorial board of the *Journal of Adhesion*, *Journal of Composites and Biodegradable Polymers*, and *ISRN Materials Science*.

Tom L. Andersen is a Senior Development Engineer at the Department of Wind Energy, Technical University of Denmark (DTU). He has worked in research and development of manufacturing technology for advanced fibre composites with a polymer matrix. He was honoured with DTU's Innovation price in 2008 for the work with new spin-off companies as well as the close collaboration with especially the windmill industry typically as confidential consultant work.

Helmuth Toftegaard is a Senior Scientist at the Department of Wind Energy, Technical University of Denmark. He was awarded the MSc in Mechanical Engineering at the Technical University of Denmark in 1979. He has worked in mechanical testing and modelling of composite materials.

Frank Leipold is a Senior Scientist at the Technical University of Denmark and responsible officer for the implementation of glow discharge cleaning systems in ITER (ITER Organisation, France). He worked in the field of plasma processing using atmospheric pressure discharges and RF and microwave engineering. He was Research Assistant Professor at the Old Dominion University, Norfolk, VA, USA until 2003. He worked on high resolution interferometry for electron density measurements in atmospheric pressure plasmas.

Alexander Bardenshtein is a Senior Consultant at the Materials Division, Danish Technological Institute. He was awarded the Eng. Phys. (MSc Eng. Phys.) at the Department of Electro-physics, Tomsk Polytechnic Institute, Russia in 1988 and the Cand. Phys. Math. Sci. (PhD) at Tomsk State University, Russia (Solid-State Physics) in 1996. He has worked in high-power radiation interaction with matter, non-destructive testing, ultrasonics and ultrasound-enhanced kinetic processes on solid-gas and solid-plasma interfaces as well as in industrial microwave heating applications.

Niels Krebs is the Vice President at SonoSteam, FORCE Technology, Denmark. He has been working with high-power acoustic energy since 1985. First at IPU, Technical University of Demark and since 1988 at FORCE Technology. His later years work has been focused on industrial applications based on the ability of high power ultrasound to disrupt the sublaminare boundary layer. He was awarded by the Danish Engineer Society in 1987 and achieved product awards in 2006 and 2007.

This paper is a revised and expanded version of a paper entitled 'Plasma surface treatment of fibres and fibre-reinforced polymers at atmospheric pressure for adhesion improvement' presented at International Conference on Wind Energy: Materials, Engineering and Policies (WEMEP-2012), BITS-Pilani Hyderabad Campus, Hyderabad, India, 22–23 November 2012.

## 1 Introduction

Fibre-reinforced polymer (FRP) materials have high strength-to-weight ratios and corrosion resistance. They are used as components of rotor blades for wind energy turbines among a variety of engineering and industrial applications (Davis et al., 1991; Dagher et al., 2004; Kaiser and Karbhari, 2004; Bakis et al., 2002). In order to ensure reliable behaviour of large wind turbine blades, it is necessary to design FRPs and their adhesive joints with high strength. More specifically, interface properties of fibre/matrix, FRPs/adhesives (adhesive joints), and sandwich structures of dissimilar FRPs must be designed properly.

Carbon fibres exhibit high strength, high toughness and light weight, and thus they are extensively used for improving the mechanical property and reducing the weight of FRPs. In order to achieve high mechanical strength of the FRPs, fibre distribution, alignment, fibre damage, and interface between fibre surfaces and a polymer matrix need to be considered. In particular, strong adhesion between the fibre surfaces and the polymer matrix is one of the key issues for improving the longitudinal tensile strength of FRPs (Dilsiz, 2000). However, due to the non-polar nature of carbon fibres, they are difficult to wet and almost impossible to chemically bond to general polymer matrices. Proper surface modification should be chosen so that carbon fibre surfaces can be wettable by the polymer matrix and bond to it tightly. It can be achieved by surface treatment of the carbon fibres, mainly by oxidation of the surfaces, introducing reactive polar functional groups onto the fibre surfaces.

Extensive research has been devoted to the surface modification of carbon fibres in order to improve their bonding to the polymer matrix. An epoxy resin is often preferred for the host matrix due to excellent electrical properties, high mechanical strength, high resistance against aging/hydrolysis, and high bond strength to many other polymer materials (Jones, 1991). It is noted that for adhesion improvement the chemical effect of oxygen containing polar functional groups such as –OH, =O, and –COOH at the carbon fibre surfaces is more important than the mechanical effect of rough surfaces (Fukunaga and Ueda, 2000). The methods of surface modification of carbon fibres include electrochemical oxidation (Bowling et al., 1989), non-thermal plasma treatment, polymer coatings, plasma polymerisation, and plasma enhanced chemical vapour deposition (PECVD) (Dilsiz, 2000; Fitzer and Weiß, 1981). The electrochemical oxidation method usually uses nitric acid. However, such a chemical method may be least preferable, although it is industrialised. For example, when the carbon fibres are oxidised in concentrated nitric acid, the equipment used must have good corrosion resistance and the acid adsorbed on the fibre surfaces must be properly removed by subsequent washing, which is time-consuming and inevitably damages and tangles the carbon fibres (Dilsiz, 2000). The chemical method can also produce environmental pollution.

FRPs are often joined to components fabricated from similar FRPs or other types of materials using adhesives for practical applications. However, FRPs usually have smooth surfaces that mainly consist of the polymer matrix materials with low surface energies. In addition, they often have a wide range of contaminants on the surfaces, which can form a weak boundary layer in an adhesive bond (Shenton et al., 2001). Therefore, an adhesive joint usually requires careful surface preparation. In the case of conventional FRPs based on thermosetting polymeric matrices such as unsaturated polyester, vinylester and epoxy resins, mechanical treatment has been applied for the surface preparation (Adams et al., 1986; Pocius and Wenz, 1985). Peel plying is a prime example of mechanical treatment used for adhesion improvement (Bénard et al., 2005) since it provides a ready-to-bond surface that may not require further surface cleaning before bonding. Another example is mechanical roughening that needs laborious abrasion followed by solvent cleaning before adhesive bonding for achieving high joint strength (Adams et al., 1986).

Non-thermal plasma treatment is attractive for the application to adhesion improvement due to its environmental friendliness and high reactivity to the surface to be bonded while retaining the bulk properties of the material (Cognard, 2006). High electron temperature ensures production of reactive species in a non-thermal plasma, which support the main function of the plasma for its use. Meanwhile a thermal plasma (arc) at an equilibrium state should be avoided in order to prevent the treated materials from thermal damages. Figure 1 shows the evolution of a gas discharge (Kusano, 2013). A timescale of each step depends on plasma conditions (Kekez et al., 1970). It is indicated that in order to avoid generation of a thermal plasma the current should be blocked before the transition to an arc occurs. Namely the evolution of the discharge should be terminated either at Townsend discharge, 1st glow discharge, its transition to the 2nd glow, or the 2nd glow discharge.

**Figure 1** Evolution of discharge current

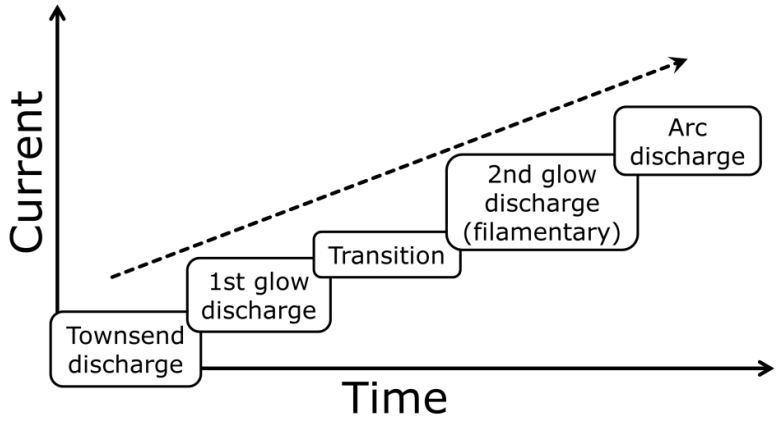


*Source:* Kusano (2013) reprinted by permission of the publisher (Tayler & Francis Ltd., http://www.tandf.co.uk/journals) and based on Kekez et al. (1970)

During the plasma treatment, surfaces interact with radicals, ions and electrons, and are irradiated with ultraviolet light (Hegemann et al., 2003). Plasma processing is often performed at low pressures. The plasma treatments at low pressures, however, require expensive vacuum systems, and methods are well-developed only for batch or semi-batch treatments. On the other hand, an atmospheric pressure plasma treatment can not only avoid the need for vacuum equipment but also permit simple setups (Kanazawa et al., 1988; Tendero et al., 2006; Singh et al., 2012; Kusano, 2013), treatment of large objects, and continuous treatment on production lines (Kogoma et al., 2011; Teodoru et al., 2009; Kusano et al., 2008a, 2008b; 2011a).

Among atmospheric pressure plasma sources, a dielectric barrier discharge (DBD) is generated between electrodes covered with dielectrics by applying a time varying voltage (Kogelschatz, 2003; Fateev et al., 2005; Leipold et al., 2006, 2010, 2011; Kusano et al., 2005; 2007a, 2007b; Teodoru et al., 2012; Siró et al., 2013). DBDs have been used for adhesion improvement of fibres (Kusano et al., 2008a, 2011a; Teodoru et al., 2009) and FRPs (Kusano et al., 2007b). In order to ensure stable DBD operation, however, the gap between the electrodes is limited to a few millimetres (Kogelschatz, 2003), which restrict the size of the specimens to be treated. In contrast to DBDs, with plasma torches, activated species generated in the plasmas are transported to the site of sample exposure by high speed gas flow. Atmospheric pressure plasma torches include inductively coupled plasmas, cold plasma torches (Lee et al., 1997; Mortensen et al., 2006). Gliding arcs are plasmas quenched from arc discharges and can also be extended to atmospheric pressure air for surface processing (Kusano et al., 2008b, 2013a, 2013b; Sun et al., 2013). They are applicable to treatment of bulky substrates and substrates with complicated structures. They can potentially provide a high degree of non-equilibrium, high electron temperature and high electron density simultaneously and thus enable high reactivity with high productivity (Czernichowski, 1994; Fridman et al., 1999, 2005; Janča and Czernichowski, 1998). They are generated between diverging electrodes and are extended by a gas flow. A fast transition into a non-equilibrium state occurs once heat losses from the discharge column exceed the supplied energy. The gliding arc combines a number of industrially attractive features of plasma based surface treatment (Kusano, 2009): it is environmentally much cleaner than mechanical or wet chemical processes; it operates well in air at atmospheric pressure with low costs; it can treat surfaces of bulky objects; and it allows fast processing. Therefore it is useful in many industrial applications that involve coating, painting, printing, dying, and adhesion. It has recently been reported that gliding arcs can efficiently improve adhesion of FRPs (Kusano et al., 2008b; 2011b). The gliding arc treatment increased the density of oxygen containing polar functional groups at the surfaces and bond strength with the vinylester adhesive.

Atmospheric pressure plasma surface modification is generally performed by feeding a process gas into the plasma. A boundary gas layer normally sticks at the material surface through which reactive species generated in the plasma are diffused for reaction with the surface. Due to the short lifetime of these species, only a small fraction of them can reach the surface. It is reported that powerful ultrasonic waves with a sound power level (SPL) above approximately 140 dB can reduce the thickness of the boundary gas layer (Kusano, 2009; Kusano et al., 2010; 2011b, 2011c; 2012a, 2012b; 2013c; Drews et al., 2011). In these works it is also demonstrated that the treatment efficiency of atmospheric pressure plasma can be highly enhanced by simultaneous high-power ultrasonic irradiation onto the treating surface.

In the present work carbon fibres are continuously treated by the DBD in a helium gas. The modified surfaces are characterised and the adhesive properties with an epoxy resin are evaluated. In addition, the surfaces of glass-fibre-reinforced polyester (GFRP) plates are treated using a DBD or a gliding arc at atmospheric pressure for adhesion improvement. The effect of ultrasonic irradiation during the DBD treatment is also investigated.

## 2 Experimental methods

### *2.1 DBD treatment of carbon fibres*

Poly(acrylonitrile) (PAN) based unsized electrochemically-treated carbon fibres (TOHO TENAX HTA5001, 800tex) were used for the DBD treatment at atmospheric pressure without pre-cleaning. Figure 2 shows an image of the experimental setup of the DBD with parallel plate water cooled aluminium electrodes (50 mm × 50 mm) covered with alumina plates (100 mm × 100 mm × 3 mm). The DBD was generated in helium gas by an alternating current (AC) (frequency: approximately 40 kHz, peak-to-peak voltage: 23 kV) power supply (generator 6030. SOFTAL Electronic GmbH). The average power input was calculated by measuring voltage and current with a high voltage probe and a 50 Ω resistor, respectively. The applied power to the discharge was 80–100 W. The flow rate of helium gas was 1 L/min. The treating times were 1 and 2 s, corresponding to the line speeds of 3.0 and 1.5 m/min, respectively.

**Figure 2** Continuous carbon fibre treatment with He DBD (see online version for colours)

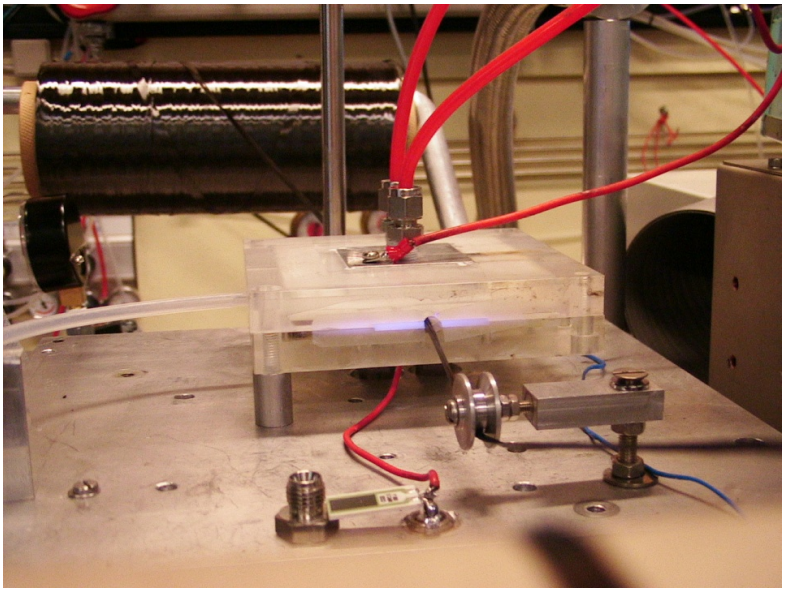

Plates for double cantilever beam (DCB) specimens were prepared for the adhesion test using both untreated, 1- and 2-s plasma-treated carbon fibres with an epoxy resin (epoxy resin [prime 20. SP systems] mixed with diethylenetriamine/polyoxypropylamine). Steel beams were glued to the outside of each composite plate with an epoxy adhesive (Scotch Weld) which was cured for 24 h at room temperature. The fracture mechanics test was performed by applying pure bending moments to the DCB specimens using a dedicated test machine (Sørensen et al., 2006). X-ray photoelectron spectroscopy (XPS) was performed for measuring elemental composition of carbon fibre surfaces using a SPECS Sage 100 instrument with a non-monochromatic Mg $K\alpha$ x-ray source.

### *2.2 Gliding arc treatment of GFRPs*

Two types of gliding arcs were used. In each case, the gliding arc was generated between two diverging stainless steel tubular electrodes through which cooling water was fed during operation. Figure 3(a) shows the first gliding arc (GA-I) with 6-mm outer diameter electrodes on each of which a blade-shaped stainless steel electrode is welded (Kusano et al., 2013b). The second gliding arc (GA-II) has 3-mm outer diameter electrodes as shown in Figure 3(b) (Kusano et al., 2013a). Air flow was fed between the electrodes to extend the discharge. The gliding arc was driven by an AC power supply at a frequency of 30–40 kHz (generator 6030, SOFTAL Electronic GmbH, Germany). The average power to the gliding arc was 700–800 W, obtained by measuring voltage and current with a high-voltage probe and resistors, respectively.

**Figure 3** Setups of the water cooled gliding arcs (a) GA-I with 6-mm diameter tubes with blade-shaped electrodes, (b) GA-II with 3-mm diameter electrodes (see online version for colours)

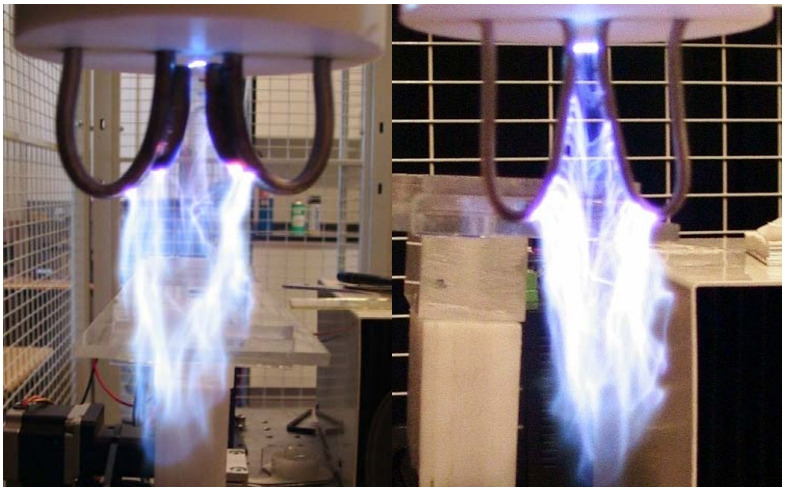

(a) (b)

GFRPs used are covered with the polyester matrix, and thus plasma treatment of the GFRP beam is essencially the trteatment of the polyester in the present work. Four types of DCB test specimens were compared. 'Crack in glue', 'peel ply', 'GA-I treated' and 'GA-II treated' specimens (290 mm × 30 mm × 8 mm) used two bonded beams cut from manufactured 8-mm thick GFRP-I panels. The peel ply was unwrapped just before the gliding arc treatment (GA-I or -II) or just before manufacturing of DCB specimens for the 'peel ply' condition. In order to treat a GFRP-I beam surface by GA-I or -II, the beam was fixed on a holder which moved forward and back at a speed of 180 mm/s and the surface was exposed to the plasma four times. The distance between the specimen surface exposed to the gliding arc and the edges of the electrodes was fixed at 15 mm during the treatment. The treated sides of the beams were faced and bonded using a vinylester adhesive. For crack initiation at the interface between the vinylester and the GFRP-I beam, a polytetrafluoroethylene (PTFE) release tape was mounted on the GFRP-I beam surface in the position of 70 mm from the tab-end of the beam. After curing, fracture energies of the DCB specimens were measured. In addition, 'crack in laminate', a 16-mm thick laminate with crack initiation at the middle was cut from the 16-mm thick GFRP-I panel, and the laminate fracture was measured. Detailed procedures of the specimen preparation are presented elsewhere (Kusano et al., 2013a, 2013b).

### *2.3 Ultrasound enhanced DBD treatment of GFRPs*

GFRP-II plates were cut from a 2-mm thick commercial G-Etronax PM material (Elektro-Isola, Vejle, Denmark). An atmospheric pressure DBD was generated between two parallel plate electrodes and driven at three different frequencies: approximately 40 kHz by an AC power supply (generator 6030. SOFTAL Electronic GmbH) (Kusano et al., 2010; 2011c; 2012a), 12 kHz by an AC power supply (MODEL 1140L, ENI) and 50 Hz by the grid-connected power (Kusano et al., 2013c). The 50 Hz operation is advantageous in that the system can be simple and that a radiation hazard at high frequencies is avoided. The power applied to the 40 kHz DBD or the 12 kHz DBD was approximately 100 W, while that of the 50 Hz plasma was less than 0.5 W. Different step-up transformers were used to obtain AC high voltages. In the case of 50 Hz DBD, a 100 kΩ resistor was connected between the transformer and the powered electrode, avoiding an excess pulse current. A schematic diagram and a photo of the setup are shown in Figure 4. The bottom electrode was covered with an aluminium plate (100 mm × 100 mm × 3 mm), while the upper electrode had a perforated hole covered with a stainless-steel mesh for the introduction of ultrasound. Detailed information is provided elsewhere (Drews et al., 2011; Kusano et al., 2010; 2011c; 2012a, 2012b). Helium, argon or synthetic air was fed to the DBD at the flow rate of 3 L $min^{-1}$.

The ultrasonic waves of the frequency range between 20 and 40 kHz at the SPL of approximately 150 dB can be introduced vertically to the GFRP surface through a 40 mm inner diameter cylindrical waveguide.

Contact angles were measured with deionised water in air at room temperature both before and after the plasma treatment for evaluation of the wettability using a static contact angle measurement system (CAM100, Crelab Instruments AB, Sweden).

XPS data were collected using a micro-focused, monochromatic Al $K\alpha$ X-ray source (1486.6 eV) with a lateral resolution of 30 μm (K-alpha, ThermoFischer Scientific, UK) for the untreated GFRP-II surfaces and those treated by helium or argon DBD, and a

double anode Mg source with a lateral resolution of 2 mm for those treated by air DBD to study the changes in elemental compositions at the GFRP-II surfaces.

**Figure 4** A schematic diagram (a) and a photo (b) of ultrasound enhanced DBD (see online version for colours)

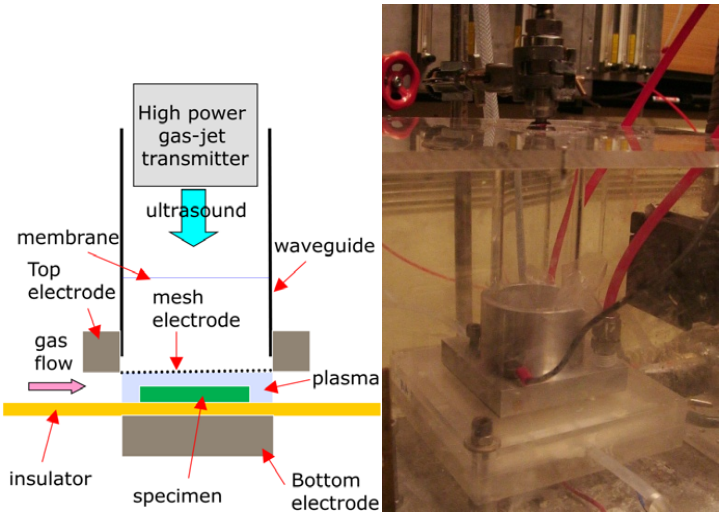


(a) (b)

## 3 Results and discussion

### *3.1 DBD treatment of carbon fibres*

The major effect of the conventional electrochemical treatments on carbon fibres for fibre/resin adhesion is believed to be the removal of weakly bound crystallites at the fibre surfaces. It is reported that the number of functional groups introduced onto the fibre surfaces by the conventional electrochemical oxidation is too small to have a significant effect (Farrow and Jones, 1994). They are less effective when they are applied to highly graphitised surfaces (Montes-Morán et al., 2001). It is therefore interesting to know whether the plasma treatment can effectively add oxidative functional groups onto the carbon fibre surfaces. The elemental composition of the carbon fibre surfaces before and after the plasma treatments was measured using XPS. The surfaces are dominated by carbon and oxygen with up to a few % of nitrogen. Table 1 summarises ratios of O/C for each specimen. It is found that He plasma treatment for 1 s resulted in significant oxidation, while the longer treatments for 2 s did not enhance oxidation. The level of the O/C ratio after plasma treatment in the present study is close to the maximum achievable O/C ratio of PAN carbon fibres excluding carbon fibres produced by Hercules (Kusano et al., 2008a). It is thus indicated that the oxidation of the He DBD treatment is efficient.

**Table 1** O/C ratio at the carbon fibre surfaces and fracture energy of the carbon fibre reinforced epoxy composites

| *Treatment time [s]* | *O/C ratio* | *Fracture energy [J m$^{-2}$]* | |
|---|---|---|---|
| | | *Crack initiation* | *Steady state* |
| 0 | 0.16 | 210 ± 50 | 1600 ± 200 |
| 1 | 0.18 | 220 ± 60 | 1950 ± 250 |
| 2 | 0.18 | 270 ± 40 | 2050 ± 250 (*) |

Note: (*) The fracture energy at the end-opening of approximately 5 mm.

*Source:* Partly based on Kusano et al. (2008a)

Untreated, 1 s and 2 s He plasma treated carbon fibres were used to prepare carbon fibre reinforced epoxy plates for the mechanical fracture tests. The measured result of the fracture energy is also summarised in Table 1. The observed fracture energy of the fibre composites with untreated and 1 s treated carbon fibres first increased as the end-opening increased, and approached to saturating steady state values (Kusano et al., 2012c). The fibre composites with 1 s treated one shows higher saturation values, indicating that the mechanical strength was improved even by the 1 s treatment. The fracture energy of the 2 s treated specimens steadily increased as the end-opening increased. It is therefore concluded that the plasma treatment improved the adhesion properties of the composites, and that the longer treatment further improved them. Since the O/C ratios at the surface after 1 and 2 s treatments were almost same, possible explanation of this improvement is increased roughness at the carbon fibre surfaces after longer treatment.

### *3.2 Gliding arc treatment of GFRPs*

The interfacial fracture energies of the GA-I and GA-II plasma treated specimens are compared with two other relevant fracture energies: That of adhesive joints made by the use of a standard peel ply and that of the glass fibre laminate itself. Here, adhesive bonds created by applying the adhesive directly to freshly created peel-ply surfaces are considered to give sufficiently strong adhesive joints (Bénard et al., 2005). Thus, the fracture energy of an adhesive joint made from a peel ply represents an acceptable minimum value for the interfacial fracture energy. Furthermore, the laminate itself is expected to have a higher fracture energy. If the adhesive and the adhesive/laminate interface possess a fracture energy that is higher than that of the laminate, fracture is likely to occur within the laminate. It is thus expected that the fracture energy of the adhesive joint made from plasma treated surfaces should surpass that of the peel ply interface but not necessarily the fracture energy of the laminate itself.

**Table 2** Comparison of crack initiation fracture resistance values

| *Specimen* | *Crack initiation fracture energy [J m$^{-2}$]* |
|---|---|
| Adhesive (cured vinylester resin) | 470 ± 30 |
| Laminate | 140 ± 15 |
| Peel ply | 120 ± 10 |
| Gliding arc (GA-I) | 260 ± 60 |
| Gliding arc (GA-II) | 295 ± 35 |

*Source:* Based on Kusano et al. (2013a, 2013b)

It is reported that the gliding arc discharge can be extended into the ambient air up to several centimetres and that the gliding arc treatment can improve wettability, increase the oxygen content and carbonyl groups at the GFRP surface, and subsequently enhance bond strength with the vinylester adhesive (Kusano et al., 2011b, 2013a, 2013b). Since the major bond mechanism with the vinylester adhesive is non-specific interaction, the effect of the gliding arc treatment can be primarily attributed to the introduction of a certain amount of polar functional groups at the surfaces and better wetting with the uncured vinylester adhesive prior to hardening. Table 2 summarises the typical crack initiation fracture energy values. The fracture initiation values for the 'laminate' and the 'peel ply' are comparable while those of the gliding arc treated ones are consistently higher than the 'laminate' and the 'peel ply'. It contradicts with the above mentioned expectation. One possible explanation is that the crack was forcefully initiated at the interface between the GFRP-I surface and the vinylester adhesive. However, further investigation will be necessary for deep understanding of this phenomenon.

### *3.3 Ultrasound enhanced DBD treatment of GFRPs*

It is known that adhesion of polymer surfaces can be improved by plasma treatment (Strobel et al., 1994). It is reported that atmospheric pressure plasma treatment of GFRP-II plates typically increases the density of oxygen containing polar functional groups at the surfaces and improves wettability (Kusano et al., 2007b, 2008b). It is also reported that ultrasonic irradiation to the plasma during surface treatment can enhance treatment efficiency (Kusano et al., 2010, 2011b, 2011c, 2012a, 2013c). These changes are very likely to improve adhesion properties of the surfaces. Water contact angles of the GFRP-II plates were measured before and after the atmospheric pressure DBD treatment in helium at different frequencies (approximately 40 kHz, 12 kHz and 50 Hz) with and without ultrasonic irradiation. The results are shown in Figure 5. When the He DBD was operated at approximately 40 or 12 kHz, the water contact angle dropped and the wettability improved significantly after 10 s treatment without ultrasonic irradiation, and longer treatment moderately improved the wettability. The ultrasonic irradiation consistently and moderately improved the wettability as shown in Figure 5(a) and Figure 5(b). It is a significant contrast from the 50 Hz DBD treatment as shown in Figure 5(c). The treatment did not significantly change the wettability of the GFRP-II surfaces even when they were treated for up to five minutes. It can be attributed to the low input energy introduced to the 50 Hz DBD in the present study. However, when the ultrasound was irradiated to the 50 Hz DBD, water contact angles markedly decreased. The longer treatment further decreased the contact angle (Kusano et al., 2013c).

Focusing on the DBD driven at approximately 40 kHz, XPS analysis was carried out to analyse the elemental composition of the GFRP-II surfaces before and after DBD treatments with and without ultrasonic irradiation. The surfaces were dominated by carbon and oxygen atoms. The results of measured O/C ratios are summarised in Table 3. After the treatment without ultrasonic irradiation, the O/C ratio increased by 0.07–0.09, indicating the introduction of oxygen containing polar functional groups on the surfaces. The ultrasonic irradiation further increased the O/C ratio. It is also reported that ultrasonic irradiation can suppress arcing and improve uniformity of the plasma treatment (Kusano et al., 2011c, 2012a), anticipating a variety of applications in addition to the adhesion improvement of bulky polymeric materials.

**Figure 5** Water contact angle after helium DBD treatment with (solid) and without (open) ultrasonic irradiation. The driving frequencies of DBD are approximately 40 kHz (a), 12 kHz (b), and 50 Hz (c).

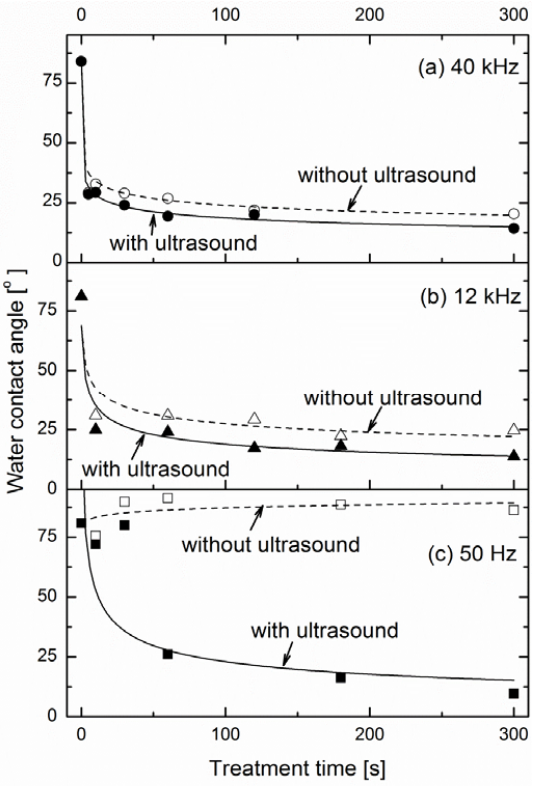


*Source:* Partly based on Kusano et al. (2011c, 2013c)

**Table 3** O/C ratio at the GFRP surfaces characterised by XPS.

| | *O/C Ratio* | |
|---|---|---|
| | - | *Ultrasonic irradiation* |
| Untreated | 0.30 | - |
| Helium DBD 30 s | 0.39 | 0.45 |
| Argon DBD 30 s | 0.37 | 0.44 |
| Air DBD 30 s | 0.38 | 0.41 |

*Source:* Based on Kusano et al. (2012a)

## 4 Conclusions

Non-thermal plasmas at atmospheric pressure can be generated by avoiding the transition to the arc. It is demonstrated that atmospheric pressure non-thermal plasma processing is useful for adhesion improvement of carbon fibres and GFRPs. The continuously treated carbon fibres were oxidised and demonstrated enhanced adhesion to the epoxy resin. Gliding arc discharges were obtained by quenching thermal (arc) discharges, and were extended to the ambient air for the surface processing. The DCB specimens consisting of the vinyl ester adhesive and the GFRP plates treated by two different gliding arcs showed higher initial fracture resistances than those of the laminates and the peel ply treated specimens. Ultrasonic irradiation to the atmospheric pressure plasmas consistently improves efficiency of the surface treatment. Its effects include enhancing oxidation, supressing arcing, and improving treatment uniformity.

## Acknowledgements

This work was supported by grants from the Ministry of Science, Technology and Innovation through the National Danish Proof of Concept Funding Scheme (grant numbers: 07-017766 and 09-076196) and the Danish Technical Research Council (grant number: 26-04-0251).

## References

Adams, R.D., Atkins, R.W., Harris, A. and Kinloch, A.J. (1986) 'Stress analysis and failure properties of carbon-fibre-reinforced-plastic/steel double-lap joints', *The Journal of Adhesion*, Vol. 20, No. 1, pp.29–53.

Bakis, C.E., Bank, L.C., Brown, V.L., Cosenza, E., Davalos, J.F., Lesko, J.J., Machida, A., Rizkalla, S.H. and Triantafillou, T.C. (2002) 'Fiber-reinforced polymer composites for construction – state-of-the-art review', *Journal of Composites for Construction*, Vol. 6, No. 2, pp.73–87.

Bénard, Q., Fois, M. and Grisel, M. (2005) 'Peel ply surface treatment for composite assemblies: chemistry and morphology effects', *Composites A*, Vol.36, No. 11, pp.1562–1568.

Bowling, R., Packard, R.T. and McCreery, R.L. (1989) 'Mechanism of electrochemical activation of carbon electrodes: role of graphite lattice defects', *Langmuir*, Vol. 5, No. 3, pp.683–688.

Cognard, J. (2006) 'Some recent progress in adhesion technology and science', *Comptes Rendus Chimie*, Vol. 9, No. 1, pp.13–24.

Czernichowski, A. (1994) 'Gliding arc: applications to engineering and environment control', *Pure and Applied Chemistry*, Vol. 66, No. 6, pp.1301–1310.

Dagher, H.J., Iqbal, A. and Bogner, B. (2004) 'Durability of isophthalic polyester composites used in civil engineering applications', *Polymers and Polymer Composites*, Vol. 12, No. 3, pp.169–182.

Davis, P., Cantwell, W.J., Jar, P.Y., Bourban, P.E., Zysman, V. and Kausch, H.H. (1991) 'Joining and repair of a carbon fiber-reinforced thermoplastic', *Composites*, Vol. 22, No. 6, pp.425–431.

Dilsiz, N. (2000) 'Plasma surface modification of carbon fibers: a review', *Journal of Adhesion Science and Technology*, Vol. 14, No. 7, pp.975–987.

Drews, J., Kusano, Y., Leipold, F., Bardenshtein, A. and Krebs, N. (2011) 'Ozone production in a dielectric barrier discharge with ultrasonic irradiation', *Ozone: Science & Engineering: The Journal of the International Ozone Association*, Vol. 33, No. 6, pp.483–488.

Farrow, G.J. and Jones, C. (1994) 'The effect of low power nitrogen plasma treatment of carbon fibres on the interfacial shear', *The Journal of Adhesion*, Vol. 45, Nos. 1–4, pp.29–42.

Fateev, A., Leipold, F., Kusano, Y., Stenum, B., Tsakadze, E. and Bindslev, H. (2005) 'Plasma chemistry in an atmospheric pressure Ar/$NH_3$ dielectric barrier discharge', *Plasma Processes and Polymers*, Vol. 2, No. 3, pp.193–200.

Fitzer, E. and Weiß, R. (1981) *Processing and Uses of Carbon Fibre Reinforced Plastics*, VDI-Verlag GmbH, Düsseldorf.

Fridman, A., Chirokov, A. and Gutsol, A., (2005) 'Topical review: non-thermal atmospheric pressure discharges', *Journal of Physics: D Applied Physics*, Vol. 38, No. 2, pp.R1–R24.

Fridman, A., Nester, S., Kennedy, L.A., Saveliev, A. and Mutaf-Yardimci, O. (1999) 'Gliding arc discharge', *Progress in Energy and Combustion Science*, Vol. 25, No. 2, pp.211–231.

Fukunaga, A. and Ueda, S. (2000) 'Anodic surface oxidation for pitch-based carbon fibers and the interfacial bond strengths in epoxy matrices', *Composites Science and Technology*, Vol. 60, No. 2, pp.249–254.

Hegemann, D., Brunner, H. and Oehr, C. (2003) 'Plasma treatment of polymers for surface and adhesion improvement', *Nuclear Instruments and Methods in Physics Research Section B*, August, Vol. 208, pp.281–286.

Janča, J. and Czernichowski, A. (1998) 'Wool treatment in the gas flow from gliding discharge plasma at atmospheric pressure', *Surface and Coatings Technology*, Vol. 98, Nos. 1–3, pp.1112–1115.

Jones, C. (1991) 'The chemistry of carbon-fiber surfaces and its effect on interfacial phenomena in fiber epoxy composites', *Composites Science and Technology*, Vol. 42, Nos. 1–3, pp.275–298.

Kaiser, H. and Karbhari, V.M. (2004) 'Non-destructive testing techniques for FRP rehabilitated concrete: I – a critical review', *International Journal of Materials and Product Technology*, Vol. 21, No. 5, pp.349–384.

Kanazawa, S., Kogoma, M., Moriwaki, T. and Okazaki, S. (1988) 'Stable glow plasma at atmospheric pressure', *Journal of Physics D: Applied Physics*, Vol. 21, No. 5, pp.838–840.

Kekez, M.M., Barrault, M.R. and Craggs, J.D. (1970) 'Spark channel formation', *Journal of Physics D: Applied Physics*, Vol. 3, No. 12, pp.1886–1896.

Kogelschatz, U. (2003) 'Dielectric-barrier discharges: their history, discharge physics, and industrial applications', *Plasma Chemistry and Plasma Processing*, Vol. 23, No. 1, pp.1–45.

Kogoma, M., Kusano, M. and Kusano, Y. (Eds.): (2011) *Generation and Applications of Atmospheric Pressure Plasmas*, NOVA Science Publishers, Inc., New York.

Kusano, Y. (2009) 'Plasma surface modification at atmospheric pressure', *Surface Engineering*, Vol. 25, No. 6, pp.415–416.

Kusano, Y. (2013) 'Atmospheric pressure plasma processing for polymer adhesion – a review', *The Journal of Adhesion* [online] http://www.tandfonline.com/doi/abs/10.1080/00218464.2013.804407.

Kusano, Y., Andersen, T.L. and Michelsen, P.K. (2008a) 'Atmospheric pressure plasma surface modification of carbon fibres', *Journal of Physics, Conference Series*, Vol. 100, Part 1, 012002.

Kusano, Y., Teodoru, S., Leipold, F., Andersen, T.L., Sørensen, B.F., Rozlosnik, N. and Michelsen, P.K. (2008b) 'Gliding arc discharge – application for adhesion improvement of fibre reinforced polyester composites', *Surface and Coatings Technology*, Vol. 202, Nos. 22–23, pp.5579–5582.

Kusano, Y., Singh, S.V., Norrman, K., Drews, J., Leipold, F., Rozlosnik, N., Bardenshtein, A. and Krebs, N. (2012a) 'Ultrasound enhanced plasma surface modification at atmospheric pressure', *Surface Engineering*, Vol. 28, No. 6, pp.453–457.

Kusano, Y., Drews, J., Leipold, F., Fateev, A., Bardenshtein, A. and Krebs, N. (2012b) 'Influence of ultrasonic irradiation on ozone production in a dielectric barrier discharge', *Journal of Physics, Conference Series*, conference 1, Vol. 406, 012006.

Kusano, Y., Mortensen, H., Teodoru, S., Drews, J.M., Andersen, T.L., Sørensen, B.F., Rozlosnik, N., Goutianos, S., Kingshott, P., Mirta, S., Leipold, F., Almdal, K., Michelsen, P.K. and Bindslev, H. (2012c) 'Plasma surface modification of glassy carbon plates, carbon fibres and UHMWPE fibres for adhesion improvement', in Cheng, Q. (Ed.): *Fiber-Reinforced Composites*, pp.251–295, NOVA Science Publishers, Inc., New York.

Kusano, Y., Leipold, F., Fateev, A., Stenum, B. and Bindslev, H. (2005) 'Production of ammonia-derived radicals in a dielectric barrier discharge and their injection for denitrification', *Surface and Coatings Technology*, Vol. 200, Nos. 1–4, pp.846–849.

Kusano, Y., Mortensen, H., Stenum, B., Goutianos, S., Mitra, B., Ghanbari-Siahkali, A., Kingshott, P., Sørensen, B.F., and Bindslev, H. (2007a) 'Atmospheric pressure plasma treatment of glassy carbon for adhesion improvement', *International Journal of Adhesion and Adhesives*, Vol. 27, No. 5, pp.402–408.

Kusano, Y., Mortensen, H., Stenum, B., Kingshott, P., Andersen, T.L., Brøndsted, P., Bilde-Sørensen, J.B., Sørensen, B.F. and Bindslev, H. (2007b) 'Atmospheric pressure plasma treatment of glass fibre composite for adhesion improvement', *Plasma Processes and Polymers*, Vol. 4, No. S1, pp.S455–S459.

Kusano, Y., Teodoru, S. and Hansen, C.M. (2011a) 'The physical and chemical properties of plasma treated ultra-high-molecular-weight polyethylene fibers', *Surface and Coatings Technology*, Vol. 205, Nos. 8–9, pp.2793–2798.

Kusano, Y., Norrman, K., Drews, J., Morgen, P., Leipold, F., Singh, S.V., Bardenshtein, A. and Krebs, N. (2011b) 'Gliding arc surface treatment of glass fiber reinforced polyester enhanced by ultrasonic irradiation', *Surface and Coatings Technology*, Vol. 205, Supplement 2, pp.S490–S494.

Kusano, Y., Singh, S.V., Norrman, K., Leipold, F., Drews, J., Morgen, P., Bardenshtein, A. and Krebs, N. (2011c) 'Ultrasound enhanced plasma treatment of glass-fibre-reinforced polyester in atmospheric pressure air for adhesion improvement', *The Journal of Adhesion*, Vol. 87, Nos. 7–8, pp.720–731.

Kusano, Y., Sørensen, B.F., Andersen, T.L., Toftegaard, H.L., Leipold, F., Salewski, M., Sun, Z.W., Zhu, J.J., Li, Z.S. and Aldén, M. (2013a) 'Water-cooled gliding arc source used for adhesion improvement of glass-fibre-reinforced polyester', *Journal of Physics: D Applied Physics*, Vol. 46, No. 13, pp.135–203.

Kusano, Y., Sørensen, B.F., Andersen, T.L. and Leipold, F. (2013b) 'Adhesion improvement of glass-fibre-reinforced polyester composites by gliding arc discharge treatment', *The Journal of Adhesion*, Vol. 89, No. 6, pp.433–459.

Kusano, Y., Norrman, K., Singh, S.V., Leipold, F., Morgen, P., Bardenshtein, A. and Krebs, N. (2013c) 'Ultrasound enhanced 50 Hz plasma treatment of glass-fiber-reinforced polyester at atmospheric pressure', *Journal of Adhesion Science and Technology*, Vol. 27, No. 7, pp.825–833.

Kusano, Y., Singh, S.V., Bardenshtein, A., Krebs, N. and Rozlosnik, N. (2010) 'Plasma surface modification of glass fibre reinforced polyester enhanced by ultrasonic irradiation', *Journal of Adhesion Science and Technology*, Vol. 24, Nos. 11–12, pp.1831–1839.

Lee, B.J., Kusano, Y., Kato, N., Naito, K., Horiuchi, T. and Koinuma, H. (1997) 'Oxygen plasma treatment of rubber surface by the atmospheric pressure cold plasma torch', *Japanese Journal of Applied Physics, Part 1*, Vol. 36, No. 5A, pp.2888–2891.

Leipold, F., Fateev, A., Kusano, Y., Stenum, B. and Bindslev, H. (2006) 'Reduction of NO in the exhaust gas by reaction with N radicals', *Fuel*, Vol. 85 , Nos. 10–11, pp.1383–1388.

Leipold, F., Kusano, Y., Hansen, F. and Jacobsen, T. (2010) 'Decontamination of a rotating cutting tool during operation by means of atmospheric pressure plasmas', *Food Control*, Vol. 21, No. 8, pp.1194–1198.

Leipold, F.,Schultz-Jensen, N., Kusano, Y., Bindslev, H. and Jacobsen, T. (2011) 'Decontamination of objects in a sealed container by means of atmospheric pressure plasmas', *Food Control*, Vol. 22, No. 8, pp.1296–1301.

Montes-Morán, M.A., Martínez-Alonso, A., Tascón, J.N.D. and Young, R.J. (2001) 'Effects of plasmaoxidation on thesurfaceandinterfacialproperties of ultra-high moduluscarbon fibres', *Composites A: Applied Science and Manufacturing*, Vol. 32, Nos. 3–4, pp.361–371.

Mortensen, H., Kusano, Y., Leipold, F., Rozlosnik, N., Kingshott, P., Sørensen, B.F. Stenum, B. and Bindslev, H. (2006) 'Modification of glassy carbon surfaces by an atmospheric pressure cold plasma torch', *Japanese Journal of Applied Physics*, Vol. 45, No. 10B, pp.8506–8511.

Pocius, A.V. and Wenz, R.P. (1985) 'Mechanical surface preparation of graphite-epoxy. Composite for adhesive bonding', *SAMPE J.*, Vol. 20, No. 5, pp.50–58.

Shenton, J., Lovell-Hoare, M.C. and Stevens, G.C. (2001) 'Surface modification of polymer surfaces: atmospheric plasma versus vacuum plasma treatments', *Journal of Physics: D Applied Physics*, Vol. 34, No. 18, pp.2761–2768.

Singh, S.V., Kusano, Y., Morgen, P. and Michelsen, P.K. (2012) 'Surface charging, discharging and chemical modification at a sliding contact', *Journal of Applied Physics*, Vol. 111, No. 8, pp.083–501.

Siró, I., Kusano, Y., Norrman, K., Goutianos, S. and Plackett, D. (2013) 'Surface modification of nanofibrillated cellulose films by atmospheric pressure dielectric barrier discharge', *Journal of Adhesion Science and Technology*, Vol. 27, No. 3, pp.294–308.

Sørensen, B.F., Jørgensen, K., Jacobsen, T.K. and Østergaard, R.C. (2006) 'DCB-specimen loaded with uneven bending moments', *International Journal of Fracture*, Vol. 141, Nos. 1–2, pp.163–176.

Strobel, M., Lyons, C.S. and Mittal, K.L. (Eds.) (1994) *Plasma Surface Modification of Polymers: Relevance to Adhesion*, VSP, Utrecht.

Sun, Z.W., Zhu, J.J., Li, Z.S., Aldén, M., Leipold, F., Salewski, M. and Kusano, Y. (2013) 'Optical diagnostics of a gliding arc', *Optics Express,* Vol. 21, No. 5, pp.6028–6044.

Tendero, C., Tixier, C., Tristant, P., Desmaison, J. and Leprince, P. (2006) 'Atmospheric pressure plasmas: a review', *SpectrochimicaActa B*, Vol. 61, No. 1, pp.2–30.

Teodoru, S., Kusano, Y. and Bogaerts, A. (2012) 'The effect of $O_2$ in a humid $O_2/N_2/NO_x$ gas mixture on $NO_x$ and $N_2O$ remediation by an atmospheric pressure dielectric barrier discharge', *Plasma Processes and Polymers*, Vol. 9, No. 7, pp.652–689.

Teodoru, S., Kusano, Y., Rozlosnik, N. and Michelsen, P.K. (2009) 'Continuous plasma treatment of ultra high molecular weight polyethylene (UHMWPE) fibres for adhesion improvement', *Plasma Processes and Polymers*, Vol. 6, No. S1, pp.S375–S381.

# [Appendix A15]

Y. Kusano, S.V. Singh, K. Norrman, F. Leipold, J. Drews, P. Morgen, A. Bardenshtein, N. Krebs

## "Ultrasound enhanced plasma treatment of glass-fibre-reinforced polyester in atmospheric pressure air for adhesion improvement"

*The Journal of Adhesion* 87 (2011) 720-731.

*The Journal of Adhesion*, 87:720–731, 2011

ISSN: 0021-8464 print/1545-5823 online
DOI: 10.1080/00218464.2011.596798

Taylor & Francis
Taylor & Francis Group



# Ultrasound Enhanced Plasma Treatment of Glass-Fibre-Reinforced Polyester in Atmospheric Pressure Air for Adhesion Improvement

**Yukihiro Kusano[1], Shailendra Vikram Singh[1], Kion Norrman[1], Frank Leipold[1], Joanna Drews[2], Per Morgen[2], Alexander Bardenshtein[3], and Niels Krebs[3]**

[1]Risø National Laboratory for Sustainable Energy, Technical University of Denmark, Roskilde, Denmark
[2]Department of Physics and Chemistry, University of Southern Denmark, Odense, Denmark
[3]FORCE Technology, Brøndby, Denmark

*A glass-fibre-reinforced polyester (GFRP) plate was treated with dielectric barrier discharge (DBD) at atmospheric pressure in air for adhesion improvement. The effects of ultrasonic irradiation using a high-power gas-jet generator during the treatment were investigated. The optical emission spectrum of the discharge remained almost unchanged by the ultrasonic irradiation, indicating that the bulk property of the discharge was not significantly influenced by the ultrasound. However, the ultrasonic irradiation during the plasma treatment suppressed occasional arcing in the DBD, preventing damage of the GFRP plates. The polar component of the surface energy of the polyester plate was 21 $mJ/m^2$ before the treatment, increased markedly to 52 $mJ/m^2$ after 2-s plasma treatment without ultrasonic irradiation, and further increased slightly after longer treatments. In addition, the polar component of the surface energy increased due to the simultaneous ultrasonic irradiation, indicating that the adhesive property would be further improved. This result shows a good agreement with surface characterization by X-ray photoelectron spectroscopy. Time-of-flight secondary ion mass spectrometry ion images show that nitrogen-containing functional groups were uniformly attached after the treatments. The roughness of the GFRP surfaces increased after the plasma treatment, but the ultrasonic irradiation did not enhance surface roughening.*

Received 8 June 2010; in final form 29 September 2010.

Presented in part at the 4th International Conference on Advanced Computational Engineering and Experimenting (ACE-X 2010), Paris, France, 8–9 July 2010.

Address correspondence to Yukihiro Kusano, Risø National Laboratory for Sustainable Energy, Technical University of Denmark, P. O. Box 49, 4000 Roskilde, Denmark. E-mail: yuki@risoe.dtu.dk

**Keywords:** Atmospheric pressure plasma; Glass fibre-reinforced polyester; Surface modification; Ultrasound



## 1. INTRODUCTION

Glass fibre-reinforced polyester (GFRP) materials are used in a variety of engineering and industrial applications owing to their high strength-to-weight ratios and corrosion resistance [1]. They are often joined to similar or other types of components using adhesives. Since most GFRP materials have smooth surfaces composed mainly of the polymeric matrices with low surface energies, careful surface preparation prior to adhesive bonding is usually required. Plasma surface modification is attractive for this purpose because of its environmental compatibility and high treatment efficiency with respect to retaining the textural characteristics of the bulk materials [2]. This kind of plasma can be generated even at atmospheric pressure without using expensive vacuum equipment [3]. Among atmospheric pressure plasma sources, a dielectric barrier discharge (DBD) is widely used because of its compactness, low-cost, and stable operation [4].

Atmospheric pressure plasma treatment is generally performed by feeding a process gas into the plasma. However, even when the motion of gas is fully turbulent, a boundary gas layer sticks at a material surface. Reactive species such as ions, electrons, high-energy neutrals, and radicals generated in a plasma are diffused through the boundary gas layer and activate, interact, and/or react with the surface. Due to the short lifetime of these species, only a small amount can reach the surface. It is reported that powerful ultrasonic waves with a sound power level (SPL) above approximately 140 dB can reduce the thickness of the boundary gas layer [5], and that the treatment efficiency of atmospheric pressure plasma can be highly enhanced by simultaneous high-power ultrasonic irradiation onto the treating surface. It is because the acoustic energy can be delivered efficiently at high gas pressures, that the thickness of the boundary gas layer is reduced, and thus more reactive species generated in the plasma can reach the surface before becoming inactivated, and be utilized efficiently for surface modification. It has been demonstrated that the efficiency of surface treatment in helium DBD at atmospheric pressure is enhanced by simultaneous ultrasonic irradiation onto the treating surface using a high-power gas-jet ultrasonic generator [6]. The ultrasonic irradiation changes the discharge mode from glow to filamentary. A brief review of research on combining plasma and ultrasonic waves is also presented in Ref [6].

As the use of helium gas is costly, it is of great interest to use air as a process gas. In the present work, the surfaces of GFRP plates are treated using an atmospheric pressure DBD in air with and without ultrasonic irradiation for adhesion improvement. Contact angle measurement, X-ray photoelectron spectroscopy (XPS), time-of-flight secondary ion mass spectrometry (TOF-SIMS), and atomic force microscopy (AFM) were used for surface characterization. On the other hand, optical emission spectra (OES) were measured for plasma diagnostics.

## 2. EXPERIMENTAL METHODS

2-mm thick GFRP plates were used as specimens (G-Etronax PM. Elektro-Isola, Vejle, Denmark; http://www.elektro-isola.com/Products/sheets.htm). They contain 35–40 wt% glass fibres, and the surfaces are mostly covered with polyester matrix. They were cleaned and degreased with acetone and methanol. However, for XPS, TOF-SIMS, and AFM analyses they were ultrasonically cleaned in deionized water for $2 \times 5$ minutes, in acetone for $2 \times 5$ minutes, and in methanol for 5 minutes before plasma treatment.

The used setup is described elsewhere in detail [6]. The DBD was generated between two parallel plane electrodes ($50 \times 50$ mm, gap: 5 mm) and driven by an AC power supply (Generator 6030, SOFTAL Corona & Plasma GmbH, Hamburg Germany) at a frequency of approximately 40 kHz. The average power input was obtained by measuring voltage and current with a high-voltage probe (PPE 20 kV, LeCroy, Chestnut Ridge, NY, USA) and a 50 Ω current viewing resistor, and was adjusted to be at 100 W. A high-power gas-jet ultrasonic generator (SonoSteam®, FORCE Technology, Brøndby, Denmark) was placed near the top of the waveguide which is connected to the powered mesh electrode. The frequency diapason of the ultrasound ranged between 20 and 40 kHz, and the sound pressure level (SPL) was approximately 150 dB at the GFRP surface. Figure 1 shows an acoustic spectrum from the ultrasonic generator transmitted through the mesh electrode measured using a capacitive microphone and a sound analyzing system (PULSE™; Brüel & Kjær, Nærum, Denmark). The spectral band between 20 and 40 kHz highlighted with the gray bar in Fig. 1 was used for the calculation of the SPL by a fundamental resonance of the acoustic generator. This band carries about 75% of total emitted acoustic energy and the corresponding SPL is approximately 154 dB relative to 20 μPa reference level. The plasma gas and ambient air were separated using a thin polyethylene film clamped in the waveguide. Air was fed into the plasma at a flow

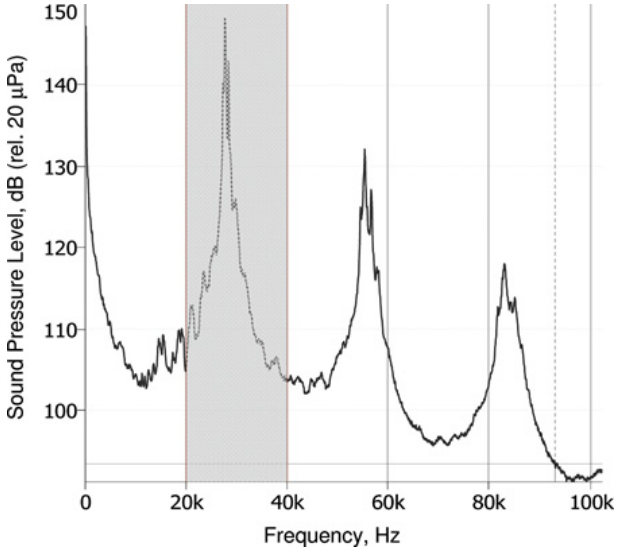


**FIGURE 1** The acoustic spectrum transmitted through the mesh electrode (color figure provided online).

rate of 3 L/min by a mass flow controller. Each GFRP plate was exposed to the DBD for 0, 2, 5, 10, 20, or 30 s.

The OES measurements were performed without a GFRP plate using an optical fibre and a 0.75 m spectrometer equipped with a grating with 3600 grooves/mm and a charge-coupled device (CCD) camera (PI-MAX 1024, Princeton Instruments, Acton, MA, USA).

Contact angles were measured with deionized water and glycerol in air at room temperature both before and after the plasma treatment for evaluation of the surface energy using a contact angle measurement system (CAM100, Crelab Instruments AB, Billdal, Sweden). The polar component of the solid surface energy of the GFRP plates was determined by the two-liquid geometric method [6–8].

XPS data were collected using a double anode (Mg/Al) source, and for the present measurements the Mg $K_\alpha$ line with an energy of 1253.6 eV was used, with a lateral resolution of 2 mm, to study the changes in elemental compositions and the functional groups on the GFRP surfaces. Atomic concentrations of all elements were calculated by determining the relevant integral peak intensities subtracting a Shirley-type background. A high-resolution analysis was performed on the carbon 1 s (C1 s) peak (pass energy 40 eV) acquired over three scans. The binding energies were referred to the hydrocarbon component (C-C, C-H) at 285 eV. The spectra were de-convoluted through

curve fitting, taking purely Gaussian components with linear background subtraction. The instrumental full-width at half-maximum (FWHM) for all peaks of C1 s was 1.6 eV, which is the resolution of the spectrometer as well as the X-ray source. The fitted components had larger widths than this. Some of the widening of the peaks are due to the measurement at the polymer surface.

TOF-SIMS analyses were performed using a TOF-SIMS IV (ION-TOF GmbH, Münster, Germany). TOF-SIMS were acquired using 25-ns pulses of 25 keV $Bi^+$ that were bunched to form ion packets with a nominal temporal extent of $< 0.9$ ns at a repetition rate of 10 kHz, yielding a target current of 1 pA. These primary ion conditions were used to acquire $500 \times 500\,\mu m^2$ ion images of the sample surfaces with a lateral resolution of $\sim 2\,\mu m$.

AFM imaging was performed on an N8 NEOS (Bruker Nano GmbH, Herzogenrath, Germany) operating in an intermittent contact mode and using SSS-NCLR cantilevers (NANOSENSORS$^{TM}$, Neuchatel, Switzerland). Images were recorded at a scan speed of 0.5 lines/min.

## 3. RESULTS AND DISCUSSION

It is reported that the current waveform of the helium DBD changed from glow to filamentary with ultrasonic irradiation [6]. When the ultrasound was irradiated to the helium DBD, a higher voltage was required to sustain the plasma at the same power as the DBD without ultrasonic irradiation. However, the current waveform of air DBD without ultrasonic irradiation is filamentary which is identified from the presence of complex spiky current waveforms of micro-discharges. With ultrasonic irradiation, the power remained unchanged without changing the voltage. In addition, the discharge mode and the current waveform did not change with ultrasonic irradiation. During the treatment of GFRP plates without ultrasonic irradiation, occasional arcing was observed. It was found that the arc ignition was suppressed during plasma treatment by the ultrasonic irradiation, preventing the GFRP plate from being damaged.

OES was measured to identify excited species in the DBD. Figure 2 shows OES of the air DBD with and without ultrasonic irradiation, including $N_2$ and $N_2^+$ bands [9,10]. Ultrasonic irradiation did not change the OES significantly.

The gas temperature in the discharge was determined by measuring the rotational band structure of the 0–0 transition of the second positive system of nitrogen, compared with simulated spectra at different temperatures. It is assumed that the rotational temperature is equal to the gas temperature. The best fit between measurement

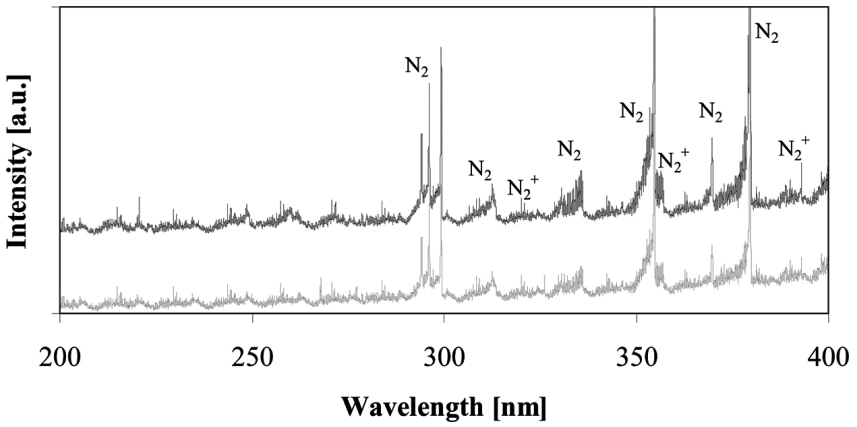


**FIGURE 2** OES of the DBD in air with (above) and without (below) ultrasonic irradiation.

and simulation was found for a rotational temperature of 650 K, as shown in Fig. 3.

The treatment drastically changed the GFRP surface wettability. The water contact angle on the GFRP plate was ~70° before the treatment, dropped markedly to around 35° after 2-s plasma treatment without ultrasonic irradiation, and further decreased after longer treatments, as shown in Fig. 4. Ultrasonic irradiation during plasma treatment tended to improve the wettability. The treatment also changed the polar component of the surface energy as shown in Fig. 5. The polar components were 21, 52, and 56 $mJ/m^2$ before the treatment, after 2-s plasma treatment without, and with ultrasonic irradiation, respectively. The longer treatment seemed to increase slightly the value of the polar component of the surface energy.

XPS survey analysis was carried out in order to analyze the elemental composition of the GFRP surfaces before and after the 5-s and 30-s treatments with and without ultrasonic irradiation. The results are summarized in Table 1. After the 5-s treatment without ultrasonic irradiation, the O/C ratio increased from 0.23 to 0.29. The O/C ratio further increased after 30-s treatment. An increase in the O/C ratio indicates that oxygen-containing polar functional groups are introduced onto the surfaces. Ultrasonic irradiation further enhanced oxidation at the surface. Although the mesh electrode was exposed to the plasma during treatment, contamination from the electrode is not apparent. No clear change was seen in the nitrogen content before/after the plasma treatment with/without ultrasonic irradiation.

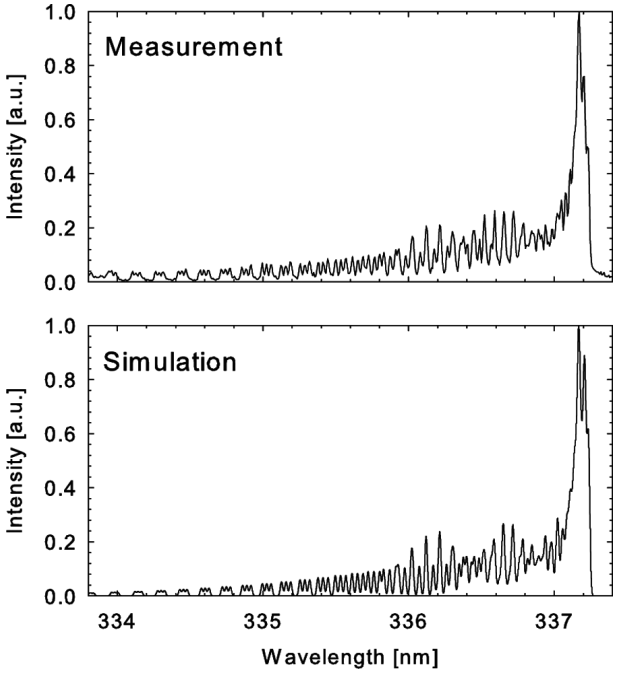


**FIGURE 3** Measurement and simulation for the 0-0 transition of the second positive system of nitrogen. The best fit was found for a rotational temperature of 650 K. The measured spectral resolution (FWHM) is 22 pm.

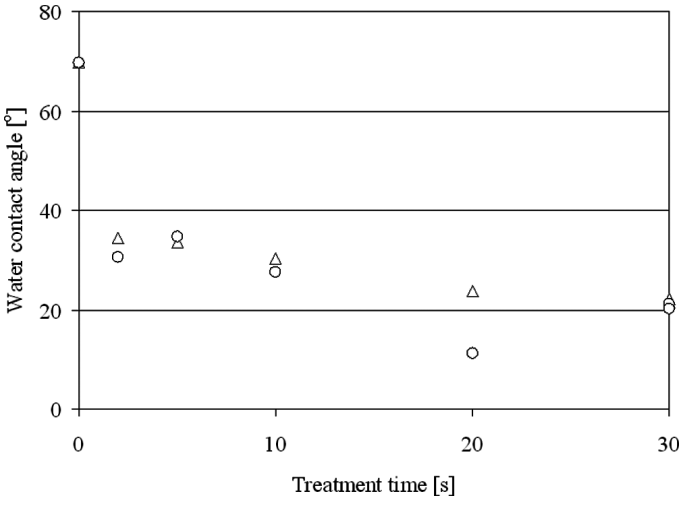


**FIGURE 4** Water contact angle before and after plasma treatment with (circle) and without (triangle) ultrasonic irradiation.

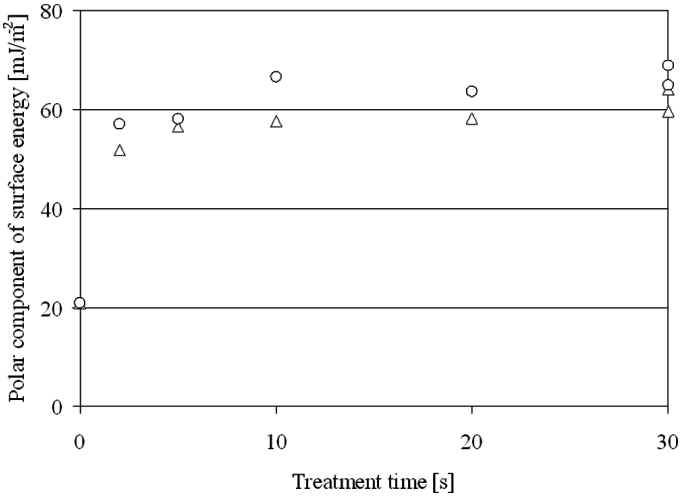


**FIGURE 5** Polar component of surface energy before and after plasma treatment with (circle) and without (triangle) ultrasonic irradiation.

Figure 6 summarizes de-convolution of C1 s spectra of the GFRP surfaces before and after 30-s plasma treatments with and without ultrasonic irradiation. Peaks at approximately (A) 285 eV, (B) 286.48 eV, (C) 288.03 eV, (D) 289.46 eVs, and (E) > 290 eV can be assigned to C-H/C-C, C-O-C/C-OH, C=O (carbonyl), C(O)O- (carboxyl), and Plasmon ($\pi^*$-$\pi$ shake-up), respectively [6,11,12]. Due to the existence of an aromatic ring structure in the polyester, the peak A at 285 eV should contain a lower energy peak (F) at approximately 284.5 eV. However, the de-convolution of the peak F was not attempted, since the peaks A and F are too close to have reliable de-convolution. The C1 s component peak of D (carboxyl) increased after longer treatment or with ultrasonic irradiation. It is noted that

**TABLE 1** Elemental Composition [at. %] and O/C Ratio at the GFRP Surfaces Characterized by XPS

| | Elemental composition [at. %] | | | |
|---|---|---|---|---|
| Treatment | C1 s | O1 s | N1 s | O/C ratio |
| Untreated | 81.0 | 18.5 | 0.4 | 0.23 |
| Plasma, 5 s | 77.1 | 22.5 | 0.4 | 0.29 |
| Plasma, 30 s | 72.2 | 27.3 | 0.5 | 0.38 |
| Plasma + ultrasound, 5 s | 70.7 | 28.4 | 0.9 | 0.40 |
| Plasma + ultrasound, 30 s | 70.8 | 28.7 | 0.5 | 0.41 |

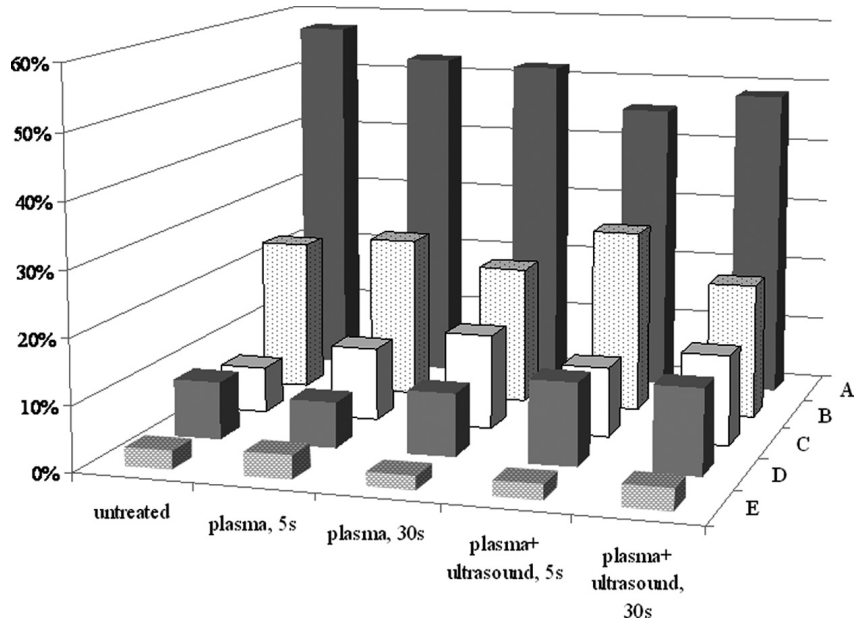


**FIGURE 6** C1 s peak components of the GFRP surfaces before and after the treatments. Assignments correspond to A: C-H/C-C at 285 eV; B: C-O-C/C-OH at 286.48 eV; C: carbonyl at 288.03 eV; D: carboxyl at 289.46 eV; E: Plasmon at > 290 eV.

introduction of the carboxyl group on the surfaces is usually the most important for improving the adhesion properties because of its strong interaction with general adhesives.

Figure 7 shows TOF-SIMS ion images ($500 \times 500\,\mu m^2$) of the sample surfaces before and after the treatments. The homogeneous distribution of nitrogen species on only the treated sample surfaces suggests that nitrogen from ambient air reacted with the sample surfaces during treatment with/without ultrasonic irradiation. XPS detects similar trace amounts of nitrogen on all the surfaces, while TOF-SIMS detects more intense nitrogen species on the treated surfaces. This difference can be explained from the fact that TOF-SIMS is more surface sensitive (~1 nm) compared with XPS (5–10 nm). The attachment of nitrogen-containing functional groups on the sample surfaces will most likely contribute to the increase in the polar component of surface energy and, thus, most likely improve the adhesion properties of the surfaces.

One interesting observation was made on the plasma treated surface without ultrasonic irradiation (Fig. 7b). The surface is covered

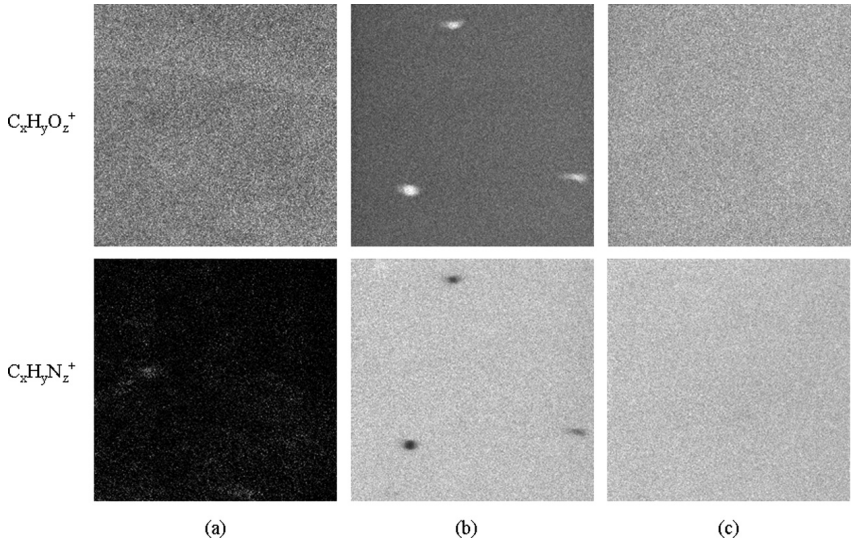


**FIGURE 7** TOF-SIMS ion images ($500 \times 500\,\mu m^2$) showing the lateral intensity distribution of $C_xH_yO_z^+$ and $C_xH_yN_z^+$ markers on the GFRP surfaces: (a) untreated, (b) 30-s plasma treated, and (c) 30-s plasma treated with ultrasonic irradiation. Black corresponds to no intensity, grey to some intensity, and white to 100% intensity.

with randomly distributed spots that, according to the mass spectral data, consist of more oxidized material. This is supported by the presence of more intense $C_xH_yO_z^+$ spots in Fig. 7b. One possible explanation for the presence of these oxidized spots could be the above-mentioned occasional arcing that is suppressed by the ultrasonic irradiation. It is noted that improving the treatment uniformity is important for achieving better wettability of the surfaces [13]. However, further investigation is necessary for the understanding of the adhesion mechanisms by performing adhesion tests.

Surface roughening is also useful for adhesion improvement because of the increased surface area and mechanical interaction with the adhesive. AFM was used to measure the surface roughness of the GFRP plates over $10 \times 10\,\mu m^2$ surface areas. Figure 8 shows the AFM images of the GFRP plates before the treatment, and after the treatment with/without ultrasonic irradiation. The average surface roughness ($S_a$) of the untreated surface was $1.6 \pm 0.2$ nm. The GFRP plates were treated with the air DBD with and without ultrasonic irradiation for 30 s. The roughness increased to $3.3 \pm 0.4$ nm and $3.6 \pm 0.6$ nm after the plasma treatment with and without ultrasonic irradiation, respectively. It is, therefore, concluded that plasma treatment


**FIGURE 8** AFM images of GFRP surfaces ($10 \times 10\,\mu m^2$): (a) untreated, (b) 30-s plasma treated, and (c) 30-s plasma treated with ultrasonic irradiation.

significantly increases the surface roughness, but additional ultrasonic irradiation does not change the surface roughness to any detectable degree.

## 4. CONCLUSIONS

An atmospheric pressure DBD in air was used to treat GFRP surfaces. Ultrasonic irradiation during the plasma treatment suppressed arcing, but did not change the OES significantly. The polar component of the surface energy, the oxygen content, and the content of carboxyl groups at the GGFRP surface increased markedly after plasma treatment without ultrasonic irradiation. Longer treatment or adding ultrasonic irradiation during the treatment tended to increase them further. Oxygen-and nitrogen-containing functional groups were uniformly attached at the surfaces by the treatment with ultrasonic irradiation. On the other hand, randomly distributed oxidized spots were found at the surfaces after the treatment without ultrasonic irradiation, possibly corresponding to occasional arcing. The surfaces were roughened by the treatments, but the simultaneous ultrasonic irradiation did not significantly improve surface roughening. The principal effect of ultrasonic irradiation on the surface can be attributed to enhanced surface oxidation during plasma treatment.

## ACKNOWLEDGMENTS

This work is supported by a grant from the Proof of Concept Fund (07-017766), Ministry of Science, Technology and Innovation, Copenhagen, Denmark.

## REFERENCES

[1] Dagher, H. J., Iqbal, A., and Bogner, B., *Polym. Polym. Composites* **12**, 169–182 (2004).
[2] Strobel, M., Lyons, C. S., and Mittal, K. L. (Eds.), *Plasma Surface Modification of Polymers: Relevance to Adhesion*, (VSP, Utrecht, 1994).
[3] Yokoyama, T., Kogoma, M., Moriwaki, T., and Okazaki, S., *J. Phys. D: Appl. Phys.* **23**, 1125–1128 (1990).
[4] Kogelschatz, U., *Plasma Chem. Plasma Proc.* **23**, 1–46 (2003).
[5] Krebs, N., "The method and device for enchancing a process involving a solid object and a gas," Int. Patent No. WO 2006 015,604 (2006).
[6] Kusano, Y., Singh, S. V., Bardenshtein, A., Krebs, N., and Rozlosnik, N., *J. Adhesion. Sci. Technol.* **24**, 1831–1839 (2010).
[7] Kusano, Y., Mortensen, H., Stenum, B., Kingshott, P., Andersen, T. L., Brøndsted, P., Bilde-Sørensen, J. B., Sørensen, B. F., and Bindslev, H., *Plasma Proc. Polym.* **4**, S455–S459 (2007).
[8] Kaelble, D. H., *J. Adhesion* **2**, 66–81 (1970).
[9] Laux, C. O., Spence, T. G., Kruger, C. H., and Zare, R. N., *Plasma Sources Sci. Technol.* **12**, 125–138 (2003).
[10] Kusano, Y., Teodoru, S., Leipold, F., Andersen, T. L., Sørensen, B. F., Rozlosnik, N., and Michelsen, P. K., *Surf. Coat. Technol.* **202**, 5579–5582 (2008).
[11] Teodoru, S., Kusano, Y., Rozlosnik, N., and Michelsen, P. K., *Plasma Proc. Polym.* **6**, S375–S381 (2009).
[12] Beamson, G. and Briggs, D., *High Resolution XPS of Organic Polymers, The Scienta ESCA300 Database*, (Wiley, Chichester, 1992).
[13] Massines, F., Messaoudi, R., and Mayoux, C., *Plasmas Polym.* **3**, 43–59 (1998).

# [Appendix A16]

Y. Kusano, B. Madsen, L. Berglund, Y. Aitomäki, K. Oksman

## “Dielectric barrier discharge plasma treatment of cellulose nanofibre surfaces”

*Surface Engineering* 34(11) (2018) 825-831.

SURFACE ENGINEERING
2018, VOL. 34, NO. 11, 825–831
https://doi.org/10.1080/02670844.2017.1334411

The Institute of Materials, Minerals and Mining
Taylor & Francis
Taylor & Francis Group



# Dielectric barrier discharge plasma treatment of cellulose nanofibre surfaces

Yukihiro Kusano [a], Bo Madsen[a], Linn Berglund [b], Yvonne Aitomäki [b] and Kristiina Oksman [b]

[a]Department of Wind Energy, Section of Composites and Materials Mechanics, Technical University of Denmark, Roskilde, Denmark; [b]Division of Materials Science, Composite Centre Sweden, Luleå University of Technology, Luleå, Sweden

**ABSTRACT**

Dielectric barrier discharge plasma treatment was applied to modify cellulose nanofibre (CNF) surfaces with and without ultrasonic irradiation. The plasma treatment improved the wetting by deionised water and glycerol, and increased the contents of oxygen, carbonyl group, and carboxyl group on the nanofibre surface. Ultrasonic irradiation further enhanced the wetting and oxidation of the nanofibre coating. Scanning electron microscopic observations showed skeleton-like features on the plasma-treated surface, indicating preferential etching of weaker domains, such as low-molecular weight domains and amorphous phases. Ultrasonic irradiation also improved the uniformity of the treatment. Altogether, it is demonstrated that atmospheric pressure plasma treatment is a promising technique to modify the CNF surface before composite processing.

**ARTICLE HISTORY**
Received 21 January 2017
Revised 25 April 2017
Accepted 11 May 2017

**KEYWORDS**
Cellulose; nanofibres; plasma treatment; ultrasound; surface modification; wetting; etching; uniformity

## Introduction

Cellulose, the most abundant biopolymer on earth, is characterised by its renewability, nontoxicity, and biodegradability. Intensive studies on cellulose nanofibres (CNFs) have been stimulated by their high strength, high modulus, high surface area, and unique optical properties [1]. Typical lateral dimensions of the nanofibres are approximately 5–20 nm, while the longitudinal dimensions are up to several micrometre [2]. CNFs can be produced by ultrafine grinding, micro-fluidisation, or high-pressure homogenisation through delamination of plant fibre cell walls and subsequent liberation of nano-sized cellulose fibrils [3].

The mechanical properties of CNFs can be effectively availed when the nanofibres are impregnated with a polymer to create strong and light-weight composite materials [3]. These materials find applications in packaging [4,5] and aeronautical industries [6]. CNF composites can exhibit optimum mechanical performance when the CNFs are substantially dispersed and when strong interfacial interactions exist between the CNFs and the polymer matrix. If these criteria are not met, interfacial defects are created which may result in non-uniform material properties. In this respect, enhancing the interfacial interaction by surface modification of CNFs is of great importance [7]. Among the reported surface treatment techniques, plasma treatment is attractive because it is solvent-free and environmentally compatible with high treatment efficiency [8]. Plasmas are easily generated at low pressure and could efficiently modify the CNF surface. However, there is a risk that the nanofibres will be a source of contamination for the low-pressure system due to transportation of nanofibres downstream with the gas flow. This can be resolved by using plasmas generated at the atmospheric pressure [9–11]. The use of atmospheric pressure plasmas avoids the need for a vacuum system, permit the treatment of larger objects, and continuous treatment on production lines [10–18]. Dielectric barrier discharge (DBD) plasma is the most widely used plasma operated at atmospheric pressure. It is generated between electrodes separated by dielectrics by applying an alternating current voltage [19]. However, the CNFs should be carefully handled during the plasma treatment, even when an atmospheric pressure plasma is used due to the easy aggregation of nano materials [10].

In the present work, the effect of plasma treatment on CNFs is studied by using them in the form of coatings to avoid the aggregation. In addition, this makes the process of treatment and subsequent characterisation significantly simpler. CNF coatings were treated using a DBD plasma in a helium gas with and without simultaneous ultrasonic irradiation. The treated CNF coatings were characterised by means of contact angle measurements, field emission scanning electron microscopy (FE-SEM), Fourier transform infrared (FTIR) spectroscopy, and X-ray photoelectron spectroscopy (XPS).

## Materials and methods

### Materials

CNFs were isolated from carrot residue supplied by Brämhults Juice AB, Brämhult, Sweden. This raw

**CONTACT** Yukihiro Kusano yuki@dtu.dk Department of Wind Energy, Section of Composites and Materials Mechanics, Technical University of Denmark, Risø Campus, Roskilde DK-4000, Denmark

material is a by-product of carrot juice production. Chemical purification was carried out prior to fibrillation following the procedure described in detail in a previous study [20]. The residue was first washed with distilled water at 85°C. Thereafter the pulp was alkali treated (2% NaOH) at 80°C for 2 h, and subsequently bleached with $NaClO_2$ (1.7%) in an acetic buffer (pH 4.5) at 80°C for 2 h for lignin removal. Finally, the material was washed until a neutral pH was reached.

The bleached residue was fibrillated at consistency of 2% by ultrafine grinding using a supermasscolloider (MKZA10–20J, Masuko Sangyo, Saitama, Japan). Prior to grinding, a shear mixer (Silverson L4RT Silverson Machine Ltd., Waterside, England) was used for dispersing the suspension. The grinding was operated at a rotor speed of 1500 rev $min^{-1}$ and the grinding stones were gradually adjusted to 100 µm contact grinding. The total processing time to obtain aqueous CNF suspension (2 wt-%) was 40 min.

To prepare the CNF coatings, a thin layer of nanofibre suspension was applied on a glass plate (dimensions of 25 mm × 75 mm × 1 mm, CORNING® 2947–75×25, Flintshire, England), and dried at room temperature under atmospheric pressure air for at least 2 days. The mass per unit area of the dried coating, measured by a precision balance, was approximately 10 g $m^{-2}$. Assuming that the density of the CNFs is 1.60 g $cm^{-3}$, considering the density of crystalline cellulose [21], the estimated coating thickness is approximately 5–10 µm.

## Surface treatment

An atmospheric pressure DBD plasma was generated between two parallel plane water-cooled electrodes as shown in Figure 1. It was driven by an alternating current (approximately 40–50 kHz) power supply (Generator 6030, SOFTAL Electronic GmbH, Hamburg, Germany). The water-cooled bottom electrode (50 mm × 50 mm) was grounded and covered with an alumina plate (100 mm × 100 mm × 3 mm) that acted as a dielectric barrier. The water-cooled top electrode was powered, and had a perforated central hole covered with a stainless-steel mesh for the introduction of ultrasound. Plasma power was obtained by measuring voltage- and current-waveforms with a high-voltage probe (PPE 20 kV, LeCroy, New York, USA) and a 50-Ω current viewing resistor, respectively, and integrating the product of the waveforms over a period. Helium was introduced in a 5-mm gap between the water-cooled top electrode and the alumina plate at a flow rate of 3 L $min^{-1}$. The CNF coated glass plate was placed on the alumina plate and exposed to the DBD plasma.

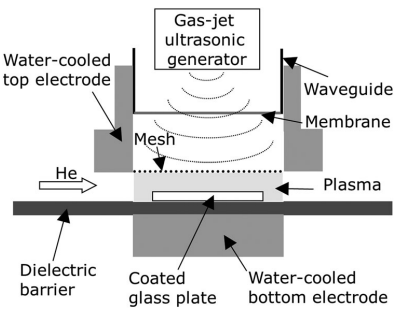


**Figure 1.** A schematic diagram of the experimental setup of DBD plasma treatment with ultrasonic irradiation.

The effects of atmospheric pressure plasma processing can be enhanced by simultaneous irradiation with ultrasonic waves. In the present work, acoustic waves were introduced vertically to the surface of the CNF coatings through a 42-mm inner diameter cylindrical poly(methyl methacrylate) waveguide using a high power gas jet ultrasonic generator (SonoSteam; FORCE Technology, Brøndby, Denmark) placed near the top of the waveguide. The dominant acoustic frequency range was between 20 and 40 kHz, and the measured sound pressure level was approximately 150 dB [22–28]. Plasma gas and ambient air were separated using a thin polyethylene film clamped in the waveguide.

More specifically, the plasma treatment was carried out as follows; the CNF coated glass plate was placed on the alumina plate, and He gas was introduced in the gap between the electrodes. The DBD plasma was ignited and then stabilised at a predetermined condition within a few second. If the ultrasonic irradiation was included in the treatment condition, it was applied just before the ignition of the DBD plasma and retained during the plasma treatment. After a predetermined treatment time, the plasma power was decreased to zero to extinguish the DBD plasma. Subsequently, the plasma-treated CNF coating was subjected to surface characterisations.

## Characterisation

The contact angles of the coatings were measured in ambient air at room temperature with deionised water and glycerol as the test liquids before and after the plasma treatment to evaluate the change in the surface wettability of the CNF coatings. A static contact angle measurement system (CAM100, Crelab Instruments AB, Billdal, Sweden) was used. The contact angle was measured within 5 s of placing a drop onto the surface. A typical drop size of 1 µL was used. For each specimen, 10 individual measurements were taken to obtain an average contact angle. Each point in Figure 3 corresponds to the average value of each specimen. For each treatment, 1–4 specimens were examined.

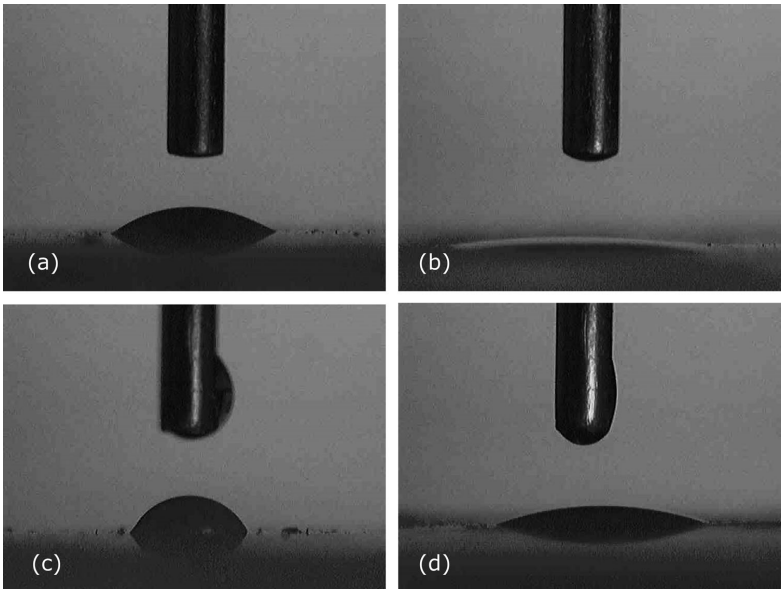


**Figure 2.** Typical photographs of deionised water-drops (a ,b) and glycerol-drops (c,d) on the CNF coatings. The untreated CNF coatings (a,c), and the CNF coatings after plasma treatment for 30 s at 100 W with ultrasonic irradiation (b, d).

The surface morphologies of the CNF coatings were observed using FE-SEM (SUPRA 35, Zeiss, Oberkochen, Germany). The CNF coatings were sputter-coated with Au to a thickness of approximately 15 nm to avoid charging.

Attenuated total reflectance (ATR) FTIR spectroscopy was employed to study the changes in the functional groups on the CNF coatings. FTIR measurements were performed using FTIR spectrometer (Spectrum One, Perkin Elmer, Waltham, MA, USA) with 32 scans and a resolution of 4 $cm^{-1}$.

XPS data was collected using a micro-focused, monochromatic Al Kα X-ray source (1486.6 eV) with a lateral resolution of 30 µm (K-Alpha, ThermoFisher Scientific, Hemel Hempstead, UK). The atomic concentrations of all the elements were calculated by determining the relevant integral peak intensities using Shirley background. The K-Alpha was also used for a high resolution analysis of the carbon 1s (C1s) spectra acquired over 30 scans. The binding energies were referred to the hydrocarbon component (C–C and C–H) at 285 eV. The spectra were de-convoluted through curve fitting, using purely Gaussian components with linear background subtraction. The full-width at half-maximum for all peaks of C1s was constrained to 1.5 eV.

## Results and discussion

During plasma treatment, physical and chemical etching, and surface-chemistry modification are generally observed due to generated reactive species and high energy photo-irradiation. Depending on materials to be treated and plasma conditions, one or more of them may be dominated, but all these processes occur simultaneously [11]. Figure 2 shows the typical images of contact angle measurements, i.e. droplets of deionised water and glycerol on the CNF coatings. The contact angles of the CNF coatings before and after the plasma treatment at various plasma powers are shown in Figure 3. Values of measured contact angles were scattered substantially, and thus the measurements were repeated for some treatment conditions. Possible causes of the scatter include uniformity and reproducibility of the CNF coating and the plasma treatment. Difference of the contact angles for the untreated CNF coatings was observed between two sets of the measurements as shown in Figure 3 (solid square), and thus influence of the specimen uniformity is not negligible. On the other hand, using the same setup of the DBD plasma with and without ultrasonic irradiation for treating glass fibre reinforced polyester plates, less significant scatters of the contact angles were reported [24–26,28]. Since the CNF suspension was carefully prepared as described in the section 'Materials and methods', a major cause of the significant deviation of the measured contact angles might be the process of coating application to the glass plates. Further investigation is necessary for better understandings of the scatter of the contact angles in the future work.

The water contact angle before the plasma treatment was typically 20–25°, and it decreased to 12–20° after

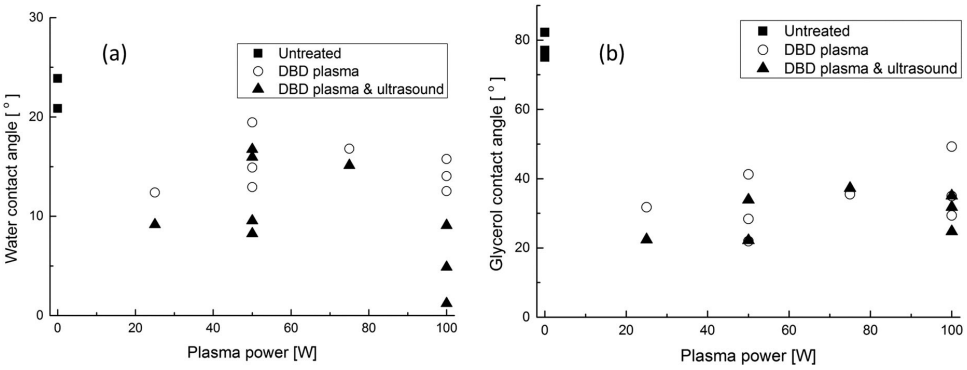


**Figure 3.** Contact angles of nanofibre coatings before and after plasma treatment for 30 s with varying plasma power, and with and without ultrasonic irradiation. Testing liquids: (a) deionised water and (b) glycerol.

the plasma treatment, as shown in Figure 3(a). Ultrasonic irradiation during the plasma treatment further decreased the water contact angle to below 10°. It has been reported that ultrasonic waves with sound power level above approximately 140 dB can reduce the thickness of the boundary gas layer on a material surface [22–28]. Therefore, the reactive species in a plasma can approach the material surface more frequently, thereby enhancing the plasma treatment effect. However, it can be seen that increasing the plasma power does not affect the water contact angle significantly especially without ultrasonic irradiation. It is reported that plasma treatment could often introduce polar functional groups on the surfaces in a short time, while the surface roughness could gradually increase as the increase in the treatment time [29]. Therefore, at a fixed treatment time, higher plasma power would be needed for significant etching. In the present study, the water contact angle further decreased at 100 W when ultrasound was irradiated, indicating that ultrasonic irradiation would efficiently improve etching.

In the case of glycerol, as shown in Figure 3(b), the contact angle before the plasma treatment was 75–85°, which then markedly decreased to 20–50° after the plasma treatment. Ultrasonic irradiation further lowered the contact angle, while the influence of increasing plasma power was insignificant. The enhancement in glycerol wetting through the plasma treatment is beneficial since CNFs are usually dispersed in an organic solvent before being mixed into an organic polymer matrix [30] during the composite manufacturing process. The enhancement in glycerol wetting will therefore potentially improve the processability and mechanical properties of the CNF composites.

Figure 4 shows the FE-SEM images of the CNF coatings before and after the plasma treatment. Before the plasma treatment, the CNF coatings had a relatively smooth surface, seen in Figure 4(a,b). Figure 4(c) shows that the CNF surface became rougher following the plasm treatment, as indicated by the appearance of skeleton-like structures. It is known that this type of surface roughening is caused by selective plasma-chemical etching of weaker domains, such as low-molecular weight domains and amorphous phases [31]. As shown in Figure 4(d), which is a different location on the same sample as was used for Figure 4(c), the majority of the surface area is less severely etched. This indicates that the plasma treatment etches the surface unevenly, as observed at micrometre scale. On the other hand, as shown in Figure 4(e,f), when ultrasonic irradiation was combined with the plasma treatment, the surfaces were uniformly modified, and the nanoscale skeleton-like structures seen in Figure 4(c) were hardly seen. A previous study observed that plasma treatment uniformity was improved by simultaneous ultrasonic irradiation; however, it was at a different length scale than it is in the present study. Highly oxidised spots were randomly distributed on a polyester surface at a sub-millimetre range by DBD plasma treatment in air, while the surface was uniformly oxidised without such spots under ultrasonic irradiation [25]. Altogether, the results of the present study indicate that the plasma treatment can roughen the CNF surface by selective etching of weaker domains, while ultrasonic irradiation can improve the uniformity of the roughening at micrometre level. From the perspective of CNF composites, an increased roughness indicates a larger surface area of the CNFs, which increases its interaction with the polymer matrix through a possibly improved physical interlocking at the fibre/matrix interface.

Figure 5 compares the ATR-FTIR spectra of the CNF coatings before and after the plasma treatment. The relative intensity of the broad band at around 3400 $cm^{-1}$ was adjusted to normalise the spectra, and the curves were vertically shifted appropriately in order to aid visual comparison of the spectra. Broad absorption bands were observed at around 3400,

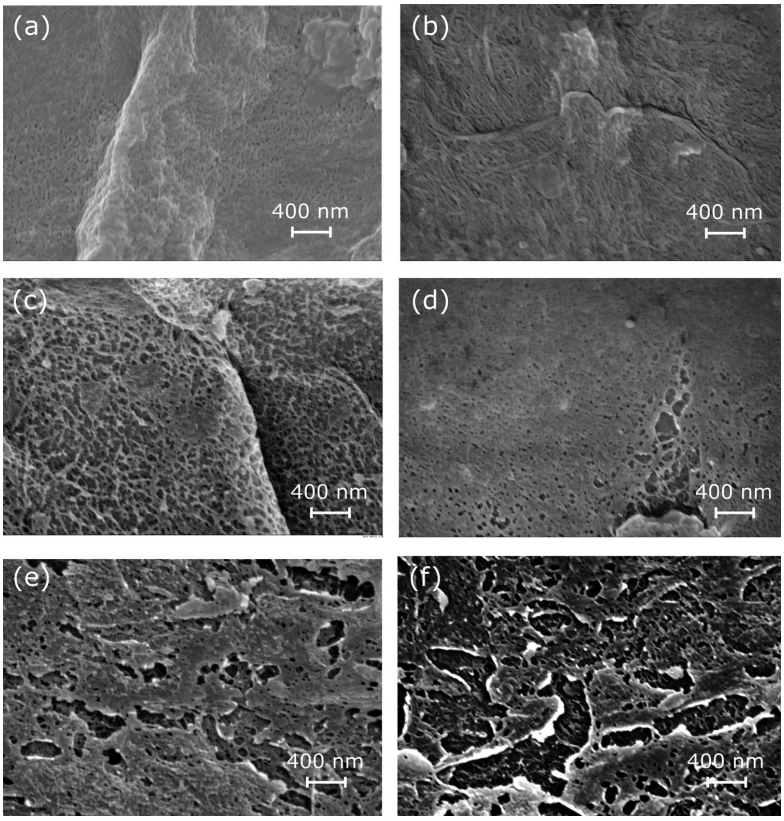


**Figure 4.** FE-SEM images of CNF coatings: (a,b) untreated, (c,d) plasma treated (100 W, 30 s), and (e, f) plasma treated (100 W, 30 s) with ultrasonic irradiation.

2900, and 1640 $cm^{-1}$, corresponding to the stretching vibrations of O–H, symmetric stretching vibrations of C–H, and stretching vibrations of C=O, respectively. Possible assignments for the bands in the region between 1500 and 800 $cm^{-1}$ are as follows: HCH and OCH in-plane bending vibrations at 1430 $cm^{-1}$; C–O–C asymmetrical stretching at around 1160 $cm^{-1}$; C–C, C–OH, and C–H ring and side group vibrations between 1100 and 1000 $cm^{-1}$; and COC, CCO, and CCH deformation and stretching vibrations between 1000 and 850 $cm^{-1}$ [32]. No significant differences could be discerned among the ATR-FTIR spectra of CNFs before and after the plasma treatment with and without ultrasonic irradiation, indicating that this technique may be insensitive in detecting the chemical changes on the surfaces of the CNF coatings.

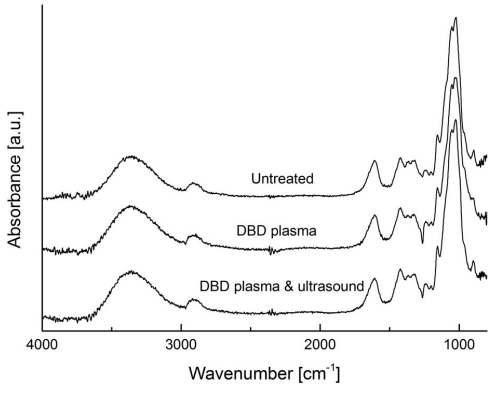


**Figure 5.** ATR-FTIR spectra of CNF coatings before and after plasma treatment (100 W, 30 s).

XPS measurements were carried out to analyse the elemental composition of the CNF coatings before and after the plasma treatment. The results of the XPS survey spectra are summarised in Table 1. The oxygen content increased from 37 at.-% (O/C ratio: 0.61) to 43 at.-% (O/C ratio: 0.87) due to the plasma treatment, while the calcium content increased from 1.5 to 4.8 at.-%. The increase in the calcium content can be interpreted as preferential etching of the organic components in the coatings. Furthermore, ultrasonic irradiation enhanced the oxidation (O/C ratio: 0.96) of the coating. The trends of the XPS survey analysis correspond to those of the contact angle measurements.

**Table 1.** Atomic composition and curve-fitted spectral data of C1s of the CNF coatings before and after plasma treatment (100 W, 30 s).

| | | Untreated | DBD plasma | DBD plasma and ultrasound |
|---|---|---|---|---|
| Atomic composition [%] | C | 60.1 | 49.7 | 47.3 |
| | O | 36.9 | 43.3 | 45.6 |
| | N | 0.9 | 1.5 | 0.9 |
| | Ca | 1.5 | 4.8 | 5.1 |
| Deconvolution of C1s [%] | C–C, C–H (285.0 eV) | 36 | 27 | 18 |
| | C–O (286.5 eV) | 48 | 44 | 40 |
| | C=O (288.0 eV) | 16 | 21 | 25 |
| | COO (289.5 eV) | 0 | 8 | 17 |

Deconvolution of C1s spectra was performed to study the functional groups on the CNF coatings, as shown in Table 1. It was observed that C–C, C–H, and C–O (single bond) contents decreased, while C=O (carbonyl) and COO (carboxyl) contents increased following the plasma treatment. Ultrasonic irradiation further enhanced these effects. The increase in C=O and COO contents on the CNFs surfaces can improve its compatibility with organic solvents of medium polarity, such as acetone, which is one of the commonly used solvents for dispersion of CNFs [30]. In addition, increase in the contents of C=O and COO can improve the interaction of CNF with polymer matrix during processing. It is therefore indicated that the plasma treatment and the simultaneous ultrasonic irradiation can improve the dispersion level of CNFs, and their adhesion with the matrix.

It has been reported that the O/C ratio of the cellulose fibres before processing is approximately 0.66, as characterised by XPS [33], which is in good agreement with that of the untreated CNFs in the present study (Table 1). Corona treatment oxidised the cellulose fibre surfaces [33], but the reported achievable COO content of less than 7% is significantly lower than that achieved in the present study (17%).

A similar assessment on CNFs was recently reported using a gliding arc plasma at atmospheric pressure [34]. The gliding arc treatment enhanced the oxidation and roughness of the CNF surface; however, longer treatment time weakened these effects. In addition, the level of oxidation of the gliding arc treated CNFs based on XPS C1s analysis [34] was comparable to that of the corona treated cellulose [33]. It is, therefore, concluded that the atmospheric pressure DBD plasma treatment with ultrasonic irradiation can oxidise the cellulose surfaces efficiently.

## Conclusion

DBD plasma treatment of CNF coatings enhances the wettability by deionised water and glycerol. The plasma treatment oxidised the coating surface and etched it unevenly. However, ultrasonic irradiation enhanced the oxidation of the coating and the uniformity of the treatment. The said modifications are advantageous in enhancing the interaction of CNFs with a general organic solvent to improve their dispersion, and to ameliorate their adhesion with the polymer matrix during the manufacturing of CNF polymer composites. Thus, it is demonstrated that atmospheric pressure plasma treatment with ultrasonic irradiation is a promising technique to modify the surface of CNFs before composite processing.

## Acknowledgements

Alexander Bardenshtein (Danish Technological Institute, Denmark) and Niels Krebs (FORCE Technology, Denmark) are acknowledged for technical supports in acoustics.

## Disclosure statement

No potential conflict of interest was reported by the authors.

## Funding

This study has received funding from the European Union Seventh Framework Programme (FP7/2007–2013) under grant agreement no FoF NMP2013–10-608746 (INCOM).

## ORCID

*Yukihiro Kusano* http://orcid.org/0000-0003-3928-8729
*Linn Berglund* http://orcid.org/0000-0002-6247-5963
*Yvonne Aitomäki* http://orcid.org/0000-0002-2388-3358
*Kristiina Oksman* http://orcid.org/0000-0003-4762-2854

## References

[1] Peng BL, Dhar N, Liu HL, et al. Chemistry and applications of nanocrystalline cellulose and its derivatives: a nanotechnology perspective. *Can J Chem Eng*. 2011;89(5):1191–1206.
[2] Chirayil1 CJ, Mathew1 L, Thomas S. Review of recent research in nano cellulose preparation from different lignocellulosic fibers. *Rev Adv Mater*. 2014;37:20–28.
[3] Nakagaito AN, Yano H. Novel high-strength biocomposites based on microfibrillated cellulose having nano-order-unit web-like network structure. *Appl Phys A*. 2005;80(1):155–159.
[4] Herrera M, Mathew AP, Oksman K. Gas permeability and selectivity of cellulose nanocrystals films (layers) deposited by spin coating. *Carbohydr Polym*. 2014;112:494–501.
[5] Herrera M, Sirviö J, Mathew A, et al. Environmental friendly and sustainable gas barrier on porous

materials: nanocellulose coatings prepared using spin- and dip-coating. *Mater Design*. 2016;93:19–25.
[6] Industrial Production Processes for Nanoreinforced Composite Structures. (INCOM) financed under EU FP7-FoF.NMP.2013-10; 2015 [cited 2017 Jan 15], Avaiable from: http://www.incomproject.eu/index.htm.
[7] Siró I, Kusano Y, Norrman K, et al. Surface modification of nanofibrillated cellulose films by atmospheric pressure dielectric barrier discharge. *J Adhes Sci Technol*. 2013;27(3):294–308.
[8] Strobel M, Lyons CS, Mittal KL. Plasma surface modification of polymers: relevance to adhesion. Utrecht: VSP; 1994.
[9] Gorbanev Y, Soriano R, O'Connell D, et al. An atmospheric pressure plasma setup to investigate the reactive species formation. *J Visualized Exp*. 2016;117:e54735.
[10] Kogoma M, Kusano M, Kusano Y, editor. Generation and applications of atmospheric pressure plasmas. Hauppauge, NY: NOVA Science Publishers, Inc; 2011.
[11] Kusano Y. Atmospheric pressure plasma processing for polymer adhesion – a review. *J Adhes*. 2014;90 (9):755–777.
[12] Kusano Y, Andersen TL, Michelsen PK. Atmospheric pressure plasma surface modification of carbon fibres. *J Phys Conf Ser*. 2008;100:012002.
[13] Kusano Y, Salewski M, Leipold F, et al. Stability of alternating current gliding arcs. *Eur Phys J D*. 2014;68:319.
[14] Kusano Y, Sørensen BF, Andersen TL, et al. Adhesion improvement of glass-fibre-reinforced polyester composites by gliding arc discharge treatment. *J Adhes*. 2013;89(6):433–459.
[15] Sun ZW, Zhu JJ, Li ZS, et al. Optical diagnostics of a gliding arc. *Opt Express*. 2013;21(5):6028–6044.
[16] Kusano Y, Sørensen BF, Andersen TL, et al. Water-cooled non-thermal gliding arc for adhesion improvement of glass-fibre-reinforced polyester. *J Phys D Appl Phys*. 2013;46(13):135203.
[17] Zhu JJ, Gao JL, Ehn A, et al. Spatiotemporally resolved characteristics of a gliding arc discharge in a turbulent air flow at atmospheric pressure. *Phys Plasmas*. 2017;25:013514.
[18] Penkov OV, Khadem M, Won-Suk Lim W-S, et.al. A review of recent applications of atmospheric pressure plasma jets for materials processing. *J Coat Technol Res*. 2015;12(2):225–235.
[19] Kogelschatz U. Dielectric-barrier discharges: their history, discharge physics, and industrial applications. *Plasma Chem Plasma Process*. 2003;23(1):1–46.
[20] Siqueira G, Tadokoro SK, Mathew AP, et al. Re-dispersible carrot nanofibers with high mechanical properties and reinforcing capacity for use in composite materials. *Comp Sci Technol*. 2016;123:49–56.
[21] Moon RJ, Martini A, Nairn J, et al. Cellulose nanomaterials review: structure, properties and nanocomposites. *Chem Soc Rev*. 2011;40:3941–3994.
[22] Kusano Y, Norrman K, Singh SV, et al. Ultrasound enhanced 50 Hz plasma treatment of glass-fiber-reinforced polyester at atmospheric pressure. *J Adhes Sci Technol*. 2013;27(7):825–833.
[23] Kusano Y, Drews J, Leipold F, et al. Influence of ultrasonic irradiation on ozone production in a dielectric barrier discharge. *J Phys Conf Ser*. 2012;406:012006.
[24] Kusano Y, Singh SV, Norrman K, et al. Ultrasound enhanced plasma surface modification at atmospheric pressure. *Surf Eng*. 2012;28(6):453–457.
[25] Kusano Y, Singh SV, Norrman K, et al. Ultrasound enhanced plasma treatment of glass-fibre-reinforced polyester in atmospheric pressure air for adhesion improvement. *J Adhes*. 2011;87:720–731.
[26] Kusano Y, Singh SV, Bardenshtein A, et al. Plasma surface modification of glass fibre reinforced polyester enhanced by ultrasonic irradiation. *J Adhes Sci Technol*. 2010;24:1831–1839.
[27] Kusano Y. Plasma surface modification at atmospheric pressure. *Surf Eng*. 2009;25(6):415–416.
[28] Kusano Y, Zhu JJ, Ehn A, et al. Observation of gliding arc surface treatment. *Surf Eng*. 2015;31(4):282–288.
[29] Kusano Y, Mortensen H, Stenum B, et al. Atmospheric pressure plasma treatment of glass fibre composite for adhesion improvement. *Plasma Process Polym*. 2007;4: S455–S459.
[30] Herrera N, Matthew AJ, Oksman K. Plasticized polylactic acid/cellulose nanocomposites prepared using melt-extrusion and liquid feeding: mechanical, thermal and optical properties. *Comp Sci Technol*. 2015;106:149–155.
[31] Morkved TL, Lu M, Urbas AM, et al. Control of microdomain orientation in diblock copolymer thin films with electric fields. *Science*. 1996;283:931–933.
[32] Schwanninger M, Rodrigues JC, Pereira H, et al. Effects of short-time vibratory ball milling on the shape of FT-IR spectra of wood and cellulose. *Vib Spectrosc*. 2004;36:23–40.
[33] Belgacem MN, Czeremuszkin G, Sapieha S. Surface characterization of cellulose fibres by XPS and inverse gas chromatography. *Cellulose*. 1995;2:145–157.
[34] Kusano Y, Berglund L, Aitomäki Y, et al. Gliding arc surface modification of carrot nanofibre coating – perspective for composite processing. *IOP Conf Ser Mater Sci Eng*. 2016;139(1):012027.

# [Appendix A17]

Y. Kusano, K. Norrman, J. Drews, F. Leipold, S.V. Singh, P. Morgen, A. Bardenshtein, N. Krebs

## “Gliding arc surface treatment of glass fiber reinforced polyester enhanced by ultrasonic irradiation”

*Surface and Coatings Technology* 205 (2011) S490-S494.

Surface & Coatings Technology 205 (2011) S490–S494

Contents lists available at ScienceDirect

Surface & Coatings Technology

journal homepage: www.elsevier.com/locate/surfcoat

# Gliding arc surface treatment of glass-fiber-reinforced polyester enhanced by ultrasonic irradiation

Yukihiro Kusano [a,*], Kion Norrman [a], Joanna Drews [a], Frank Leipold [a], Shailendra Vikram Singh [a], Per Morgen [b], Alexander Bardenshtein [a,c], Niels Krebs [c]

[a] Risø National Laboratory for Sustainable Energy, Technical University of Denmark, P.O. Box 49, DK-4000 Roskilde, Denmark
[b] Department of Physics and Chemistry, University of Southern Denmark, Campusvej 55, DK-5230 Odense, Denmark
[c] FORCE Technology, Park Allé 345, DK-2605 Brøndby, Denmark

ARTICLE INFO

*Article history:*
Received 10 September 2010
Accepted in revised form 10 January 2011
Available online 3 February 2011

*Keywords:*
Gliding arc
Plasma treatment
Ultrasound
Glass-fiber-reinforced polyester

ABSTRACT

A gliding arc is a plasma generated between diverging electrodes and extended by a high speed gas flow. It can be operated in air at atmospheric pressure. It potentially enables selective chemical processing with high productivity, and is useful for adhesion improvement of material surfaces. The efficiency of such a plasma treatment at atmospheric pressure can be further improved by ultrasonic irradiation onto the surface during the treatment.

In the present work glass fiber reinforced polyester (GFRP) plates are treated using an atmospheric pressure gliding arc with and without ultrasonic irradiation to study adhesion improvement. The airflow at the arc ignition directed the GFRP surface at a grazing angle of approximately 30°. The ultrasonic waves of the frequency range between 20 and 40 kHz were introduced vertically to the GFRP surface through a cylindrical waveguide. It is found that ultrasonic irradiation reduced the OH rotational temperature of the gliding arc. The wettability of the GFRP surface was significantly improved by the plasma treatment without ultrasonic irradiation, and tended to improve furthermore at higher power to the plasma. Ultrasonic irradiation during the plasma treatment consistently improved the wettability. It is seen that polar functional groups were introduced at the surface by the gliding arc treatment, and that the treatment efficiency was enhanced by the ultrasonic irradiation, indicating that the adhesive property would be improved. TOF-SIMS ion images indicate that oxygen and nitrogen are uniformly attached at the treated surfaces with and without ultrasonic irradiation. The principal effect of the ultrasonic irradiation is attributed to enhanced oxidation during the plasma treatment.



## 1. Introduction

Development of atmospheric pressure plasma processing has attracted significant interests, and both basic and application-oriented researches are extensively progressing [1,2]. One of the challenges for atmospheric pressure plasma processing is to achieve high chemical selectivity and efficient productivity simultaneously [3]. High chemical selectivity can be expected with a high degree of non-equilibrium in a plasma, and efficient productivity can be demonstrated with high energy densities. However, typical thermal and non-thermal plasmas cannot provide high non-equilibrium and high energy density simultaneously. The use of a transient type of arc discharges can be a promising route to overcome this problem. Its present example is a gliding arc generated between diverging electrodes in a fast gas flow, potentially enabling selective chemical processing with high productivity [4]. Although a similar effect is expected for microwave plasmas, a gliding arc system is less expensive than microwave plasma devices. It is indicated that a gliding arc can be preferably applied for large scale exhaust gas cleaning, pollution control, fuel conversion, hydrogen production and surface modification [4]. In particular, the gliding arc combines a number of industrially attractive features of plasma-based surface treatments: it is environmentally much cleaner than mechanical or wet chemical processes, it operates well in air at atmospheric pressure with low costs; being a torch-like plasma source, it can treat surfaces of bulky objects, and it allows fast processing. Therefore it is useful in many industrial applications that involve coating, painting, printing, dying, and adhesion [5,6].

The efficiency of plasma processing can be further enhanced by external energy input. Among possible techniques, ultrasonic irradiation by a high-power gas jet ultrasound generator is attractive because of its simple setup, easy up-scaling, and high efficiency [7–9].

Glass-fiber-reinforced polyester (GFRP) materials are widely used for a variety of applications due to their high strength-to-weight ratios and corrosion resistance. They are often joined with

* Corresponding author. Tel.: +45 4677 4571; fax: +45 4677 4565.
*E-mail address:* yuki@risoe.dtu.dk (Y. Kusano).

0257-8972/$ – see front matter © 2011 Elsevier B.V. All rights reserved.
doi:10.1016/j.surfcoat.2011.01.061

components fabricated from similar or dissimilar types of materials using adhesives. However, they usually have smooth surfaces composed mainly of the polyester matrix materials with low surface energies, and thus careful surface preparation is normally necessary before adhesion. Some GFRP plate surfaces were treated by dielectric barrier discharge (DBD) at atmospheric pressure for adhesion improvement [10]. Here DBD is one of the commonly used non-thermal plasmas generated between electrodes covered with dielectrics. It is reported that the adhesion strength of the surface after 2-s DBD treatment was comparable to or higher than that achieved by the conventional abrasion method [10]. It is further reported that simultaneous ultrasonic irradiation during the DBD treatment enhances oxidation at the GFRP surfaces [8] and suppresses arcing [9]. A gliding arc was also used for the adhesion improvement of GFRP plates [6]. It is indicated that the treatment efficiency depends strongly on the temperatures of the electrodes and the gas of the discharge.

In the present work, GFRP plates are treated with the gliding arc with and without ultrasonic irradiation for the purpose of adhesion improvement. Optical emission spectroscopy (OES) was used for plasma diagnostics. The treated surfaces are characterized using contact angle measurement, X-ray photoelectron spectroscopy (XPS), time-of-flight secondary ion mass spectroscopy (TOF-SIMS) and atomic force microscopy (AFM).

## 2. Experimental methods

2-mm thick GFRP plates were used as specimens (G-Etronax PM. Elektro-Isola, Vejle, Denmark). They were cleaned and degreased with acetone and methanol. However, for XPS, TOF-SIMS and AFM analyses they were ultrasonically cleaned in deionized water for $2\times5$ min, acetone for $2\times5$ min and in methanol for 5 min before plasma treatment.

The gliding arc was generated between two 1-mm thick stainless steel blade-electrodes with a diverging configuration [6], driven by an alternating current (AC) power supply (Generator 6030. SOFTAL Electronic GmbH, Germany). The arc was ignited at the closest distance between the electrodes and extended by an airflow at a flow rate of 20 L/min. The airflow at the arc ignition was directed on the GFRP surface at a grazing angle of approximately 30°. The average power input was obtained by measuring voltage and current with a high-voltage probe and a 15.5 Ω current viewing resistor, respectively. The input power was adjusted by varying the frequency. A change of the frequency from 40 kHz to 33 kHz corresponds to an input power from approximately 300 W to 540 W without ultrasonic irradiation, and from approximately 260 W to 490 W with ultrasonic irradiation. In order to treat a GFRP plate surface, the plate was fixed on a holder which moved forward and back at a speed of 180 mm/s [6]. The specimen surfaces were exposed to the discharge twice in 5 s. The ultrasonic waves of the frequency range between 20 kHz and 40 kHz at a sound power level (SPL) of approximately 150 dB can be introduced vertically to the GFRP surface through a cylindrical waveguide using a high-power gas-jet ultrasonic generator (SonoSteam®, FORCE Technology, Denmark) which was placed near the top of the waveguide. The environments of the plasma treatment and the ultrasound generation were separated using a thin polyethylene film clamped in the waveguide in order to avoid the influence of the gas flow for the ultrasound generation on the plasma.

The OES measurements were performed without a GFRP plate using an optical fiber and a 0.75 m spectrometer equipped with a grating with 3600 grooves/mm and a charge-coupled device (CCD) camera (PI-MAX 1024, Princeton Instruments, USA) for the identification of excited species and estimation of the rotational temperature in the discharge. The data acquisition time was 3 s. The optical fiber faces the position at the discharge distancing approximately 50 mm from the arc ignition. The input powers to the gliding arc with and without ultrasonic irradiation were 490 W and 540 W, respectively. In order to estimate the temperature of the plasma, the spectra of the OH radicals in the gliding arc were measured and compared to the modelling of the Q1 branch of the OH (0–0) rotational band ($A^2\Sigma^+ \rightarrow X^2\Pi_{3/2}$). Measurements and simulations were normalized to the rotational transition $k''=8$ (309.239 nm) since this line is not superimposed by lines from other branches. The temperature can be obtained with an accuracy of 100 K. The spectral resolution (FWHM) is 18 pm. Data required for the simulation for the rotational system of the OH molecule were taken from Ref. [11].

Contact angles were measured with deionized water and glycerol in air at room temperature both before and after the plasma treatment for evaluation of the polar component of the surface energy using a contact angle measurement system (CAM100. Crelab Instruments AB, Sweden). Each result in the present work was the average of the at least ten individual measurements. The standard deviation of the resulting value is typically less than 1.5°. The polar component of the solid surface energy of the GFRP plates was determined by the two-liquid geometric method [12]. Its corresponding accuracy is approximately $\pm3$ mJ/m$^2$.

XPS data were collected using a double anode (Mg/Al) source, and for the present measurements the Mg $K_\alpha$ line with an energy of 1253.6 eV was used, with a lateral resolution of 2 mm to study the changes in elemental compositions and the functional groups on the GFRP surfaces. Atomic concentrations of all elements were calculated by determining the relevant integral peak intensities subtracting a Shirley-type background. A high-resolution analysis was performed on the carbon 1s (C1s) peak (pass energy 40 eV) acquired over 3 scans. The accuracy of the measurement is estimated to be better than 2%. The binding energies were referred to the hydrocarbon component (C–C and C–H) at 285 eV. The spectra were de-convoluted through curve fitting, taking purely Gaussian components with linear background subtraction. The instrumental full-width at half-maximum (FWHM) for all peaks of C1s was 1.6 eV which is the resolution of the spectrometer as well as the X-ray source. The fitted components had larger widths than this. Some of the widening of the peaks is due to various energy-loss phenomena at the polymer surface [13].

TOF-SIMS analyses were performed using a TOF-SIMS IV (ION-TOF GmbH, Münster, Germany). TOF-SIMS were acquired using 25 ns pulses of 25 keV $Bi^+$ that were bunched to form ion packets with a nominal temporal extent of <0.9 ns at a repetition rate of 10 kHz, yielding a target current of 1 pA. These primary ion conditions were used to acquire $500\times500$ μm$^2$ ion images of the sample surfaces with a lateral resolution of approximately 2 μm.

AFM imaging of the GFRP plates was performed on an N8 NEOS (Bruker Nano GmbH, Herzogenrath, Germany) operating in an intermittent contact mode and using SSS-NCLR cantilevers (NANOSENSORS™, Neuchatel, Switzerland). Images were recorded at a scan speed of 0.5 lines/min. The GFRP specimens for TOF-SÌMS and AFM were treated with the input powers to the gliding arc at 490 W and 540 W with and without ultrasonic irradiation, respectively.

## 3. Results and discussion

The OES was measured to identify excited species in the discharge and to evaluate the rotational temperature. A typical OES includes the emissions from $N_2$, $N_2^+$, NO, and OH [14]. The OH comes from ambient air humidity. The intensity of optical emission of gliding arc, including OH, NO, $N_2$ and $N_2^+$ bands, significantly decreased with ultrasonic irradiation. The rotational temperature in the discharge was determined by comparing the measured rotational band structure of OH A–X (0,0) with the simulated spectra at different temperatures. Fig. 1 (lower panel) shows the measured rotational spectrum of the OH radical between 308 and 312 nm without ultrasound (blue) and the simulated Q1 branch (red). The temperature of the simulation was varied for the best fit and here the best fit was obtained at 3500 K. Similarly the rotational

temperature of gliding arc with ultrasonic irradiation was estimated. Fig. 1 (upper panel) shows the comparison between OH emission of a gliding arc with ultrasonic irradiation (blue) and the simulated Q1 branch (red). In this case, the best fit for the spectra was obtained at a temperature of 3200 K. The large difference in some lines between measurement and simulation is due to the superposition of lines from different rotational branches in the measured spectra. The difference in the rotational temperatures of a plasma with and without ultrasound was discussed in Refs. [15–17]. It is reported that an increase in the acoustic wave intensity can lead to a growth in the plasma column diameter and the generation of a uniform non-contracted discharge at high gas pressures. More specifically, an audible resonant acoustic wave induces an acoustic flow that gives rise to a vortex motion in the plasma chamber and leads to the formation of a de-contracted, uniform stabilized positive column. Consequently, an acoustic wave can reduce the gas temperature of a plasma at high pressure. However, the acoustic waves delivered in a plasma are audible (<1 kHz) with SPL of less than 85 dB in Refs. [15–17], while those in the present work have the frequency diapason between 20 and 40 kHz at SPL of approximately 150 dB. Namely the acoustic energy in the present work is significantly higher than that in those references, and thus the mechanisms of interacting acoustic waves and the plasma might be different. In this connection further investigation is necessary for the understanding of detailed mechanisms involved.

The plasma treatment drastically changed the GFRP surface wettability. The water contact angle on the GFRP plate was approximately 72° before the treatment, dropped markedly to below 20° and tended to be lowered at high power to the plasma or with ultrasonic irradiation as shown in Fig. 2. The polar component of the surface energy of the GFRP plates treated at different input powers to the plasma is also shown in Fig. 2. The polar component of the surface energy significantly increased after the plasma treatment, and further increased with ultrasonic irradiation. However, it looks insensitive against increasing input power to the plasma. The result indicates that polar functional groups could be easily introduced at the surfaces and that the improvement of the wettability at higher input power to the plasma could be attributed to the increase of surface roughness. These effects potentially improve the adhesive property of the GFRP surfaces.

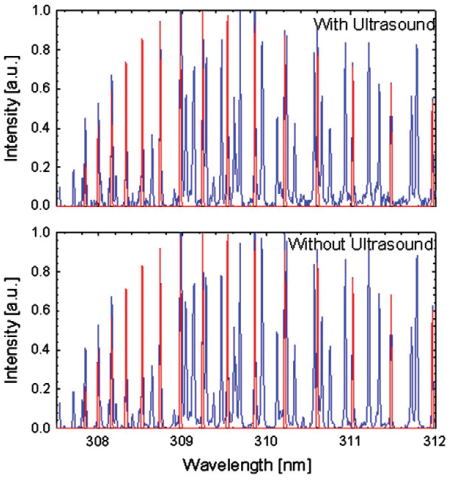


**Fig. 1.** Spectral measurement of the gliding arc with and without ultrasound (blue, upper and lower panels, respectively) and simulation of the Q1 branch of the rotational system of OH (red, upper and lower panels, respectively). The simulation results shown are performed at rotational temperatures of 3200 K (with ultrasound) and 3500 K (without ultrasound).

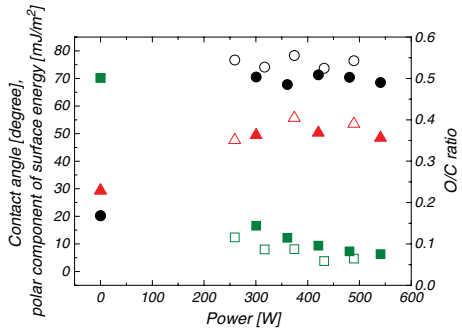


**Fig. 2.** Water contact angle (square), polar component of surface energy (circle), and O/C ratio (triangle) of GFRP plate surfaces before and after the plasma treatment with (solid) and without (open) ultrasonic irradiation.

XPS survey analysis was carried out to compare the elemental composition of the GFRP surfaces before and after the treatment. Carbon, oxygen and a small amount of nitrogen were detected at each surface. The nitrogen content was 0.4 at.% before treatment, and from 1 to 2 at.% after the treatment. Fig. 2 shows the O/C ratio at the GFRP surfaces before and after the treatment with and without ultrasonic irradiation. After the treatment without ultrasonic irradiation, the O/C ratio increased from 0.23 to approximately 0.36. When the input power was 370 W or higher with ultrasonic irradiation, the O/C ratio was as high as approximately 0.4. The results indicate that ultrasonic irradiation can enhance oxidation at the GFRP surfaces. On the other hand, the O/C ratio was only 0.35 at the surface treated at an input power of 260 W with ultrasonic irradiation. A possible explanation of this rather low O/C ratio is that the input power might not be high enough to sustain a stable discharge, since ultrasonic irradiation enhances observed fluctuations of the discharge.

The de-convolution of the C1s spectra of the GFRP surfaces before and after the treatment with and without ultrasonic irradiation is summarized in Fig. 3. Peaks at approximately 285 eV, 286.48 eV, 288.03 eV, 289.46 eV, and >290 eV can be assigned to C–H/C–C (A), C–O–C/C–OH (B), C=O (carbonyl) (C), C(O)O– (carboxyl) (D), and plasmon (π*–π shake-up) (E), respectively [6,10,13,14]. Due to the existence of an aromatic ring-structure in the polyester, the peak A at 285 eV should also contain a lower-energy peak (F) at approximately

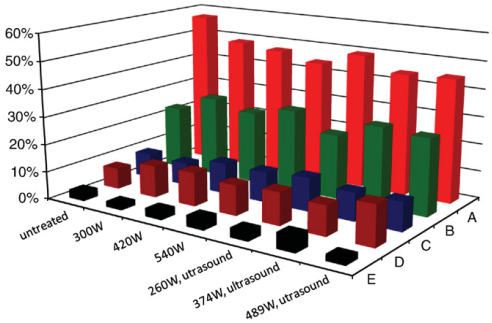


**Fig. 3.** C1s peak components of the GFRP surfaces before and after the treatments. Assignments correspond to A: C–H/C–C at 285 eV; B: C–O–C/C–OH at 286.48 eV; C: carbonyl at 288.03 eV; D: carboxyl at 289.46 eV; and E: plasmon at >290 eV.

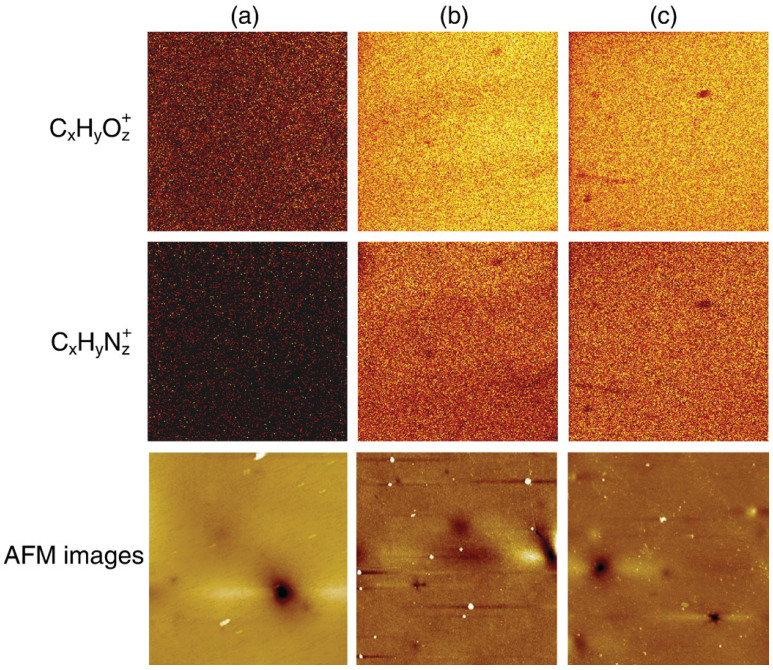


**Fig. 4.** TOF-SIMS ion images ($500\times500\ \mu m^2$) showing the lateral intensity distribution of $C_xH_yO_z^+$ (upper images) and $C_xH_yN_z^+$ (middle images) markers, and AFM images ($10\times10\ \mu m^2$) (lower images) of the GFRP surfaces: (a) untreated, (b) gliding arc treated without ultrasonic irradiation, and (c) gliding arc treated with ultrasonic irradiation. Black corresponds to no intensity, brown to some intensity, and white to 100% intensity in the TOF-SIMS ion images.

284.5 eV. However, the de-convolution of the peak F was not attempted, since the peaks A and F are too close to perform reliable de-convolution. The C1s component peaks of B, C and D increased after the plasma treatment with and without ultrasonic irradiation. The C1 component peak of D, corresponding to the carboxyl group seems to increase slightly with ultrasonic irradiation.

Fig. 4 (upper and middle images) shows TOF-SIMS ion images ($500\times500\ \mu m^2$) of the sample surfaces before and after the treatments. It is observed that both oxygen and nitrogen are homogeneously distributed after the plasma treatment with and without ultrasonic irradiation. These results contrast to that of Ref. [9] on DBD treatment in air, where significantly oxidized spots were randomly created without ultrasonic irradiation, while uniformly treated with ultrasonic irradiation. These results indicate that a gliding arc can preferably treat surfaces uniformly even without ultrasonic irradiation. The attachment of oxygen or nitrogen containing functional groups on the sample surfaces will most likely contribute to the increase in the polar component of surface energy and thus improve the adhesion properties of the surfaces.

Surface roughening is also useful for adhesion improvement because of the increased surface area and mechanical interaction with the adhesive. AFM was used to measure the surface roughness of the GFRP plates over $10\times10\ \mu m^2$ surface areas. Fig. 4 (lower images) shows the AFM images of the GFRP plates before the treatment, and after the treatment with/without ultrasonic irradiation. The average surface roughness ($S_a$) of the untreated surface was $1.2\pm0.2$ nm (Fig. 4a) (lower image)). The roughness increased to $1.9\pm0.2$ nm (Fig. 4b) (lower image)) and $2.3\pm0.6$ nm (Fig. 4c) (lower image)) after the plasma treatment without and with ultrasonic irradiation, respectively. It is therefore concluded that the treatment increases the surface roughness, but ultrasonic irradiation does not change the surface roughness to any detectable degree.

## 4. Conclusions

GFRP plates were treated by a gliding arc plasma with and without ultrasonic irradiation. Ultrasonic irradiation reduced the rotational temperature of the discharge. The polar component of the surface energy and the oxygen content at the GGFRP surface increased markedly after plasma treatment without ultrasonic irradiation. Ultrasonic irradiation during the treatment tended to increase them furthermore. Oxygen and nitrogen containing functional groups were uniformly attached at the surfaces by the treatment with and without ultrasonic irradiation. The surfaces were roughened by the treatments, but the simultaneous ultrasonic irradiation did not significantly improve surface roughening.

## Acknowledgements

This work is supported by a grant from the Proof of Concept Fund (07–017766). Søren Nimb is gratefully acknowledged for the design and construction of the gliding arc source.

## References

[1] A. Fridman, A. Chrirokov, A. Gutsol, J. Phys. A Appl. Phys. 38 (2005) R1.
[2] C. Tendero, C. Tixier, P. Tristant, J. Desmaison, P. Leprince, Spectrochimica B61 (2006) 2.
[3] Y. Kusano, Surf. Eng. 25 (6) (2009) 415.
[4] A. Fridman, S. Nester, L.A. Kennedy, A. Saveliev, O. Mutaf-Yardimci, Prog. Energy Combust. Sci. 25 (1999) 211.

[5] J. Janča, A. Czernichowski, Surf. Coat. Technol. 98 (1998) 1112.
[6] Y. Kusano, S. Teodoru, F. Leipold, T.L.L. Andersen, B.F. Sørensen, N. Rozlosnik, P.K. Michelsen, Surf. Coat. Technol. 202 (2008) 5579.
[7] N. Krebs, A. Bardenshtein, Y. Kusano, H. Bindslev, H.J. Mortensen, European patent No. 2153704 A1 (17th February 2010).
[8] Y. Kusano, S.V. Singh, A. Bardenshtein, N. Krebs, N. Rozlosnik, J. Adhes. Sci. Technol. 24 (2010) 1831.
[9] Y. Kusano, S.V. Singh, K. Norrman, F. Leipold, J. Drews, P. Morgen, A. Bardenshtein, N. Krebs, J. Adhesion. in press.
[10] Y. Kusano, H. Mortensen, B. Stenum, P. Kingshott, T.L. Andersen, P. Brøndsted, J.B. Bilde-Sørensen, B.F. Sørensen, H. Bindslev, Plasma Process. Polym. 4 (S1) (2007) S455.
[11] I. Ishii, A. Montaser, Spectrochim. Acta 8 (1991) 1197.
[12] D.H. Kaelble, J. Adhes. 2 (1970) 66.
[13] G. Beamson, D. Briggs, High Resolution XPS of Organic Polymers: The Scienta ESCA300 Database, Wiley, Chichester, 1992.
[14] Y. Kusano, S.V. Singh, K. Norrman, J. Drews, F. Leipold, N. Rozlosnik, A. Bardenshtein, N. Krebs, Surf. Eng. submitted for publication.
[15] G.A. Galechyan, Laser Phys. 4 (1) (1994) 23.
[16] G.A. Galechyan, Phys. Usp. 38 (12) (1995) 1309.
[17] G.A. Galechyan, Tech. Phys. Lett. 34 (1) (2008) 48.

# [Appendix A18]

Y. Kusano, J.J. Zhu, A. Ehn, Z.S. Li, M. Aldén, M. Salewski, F. Leipold, A. Bardenshtein, N. Krebs

## “Observation of gliding arc surface treatment”

*Surface Engineering* 31(4) (2015) 282-288.

# Observation of gliding arc surface treatment

**Y. Kusano*[1], J. J. Zhu[2], A. Ehn[2], Z. S. Li[2], M. Aldén[2], M. Salewski[3], F. Leipold[3], A. Bardenshtein[4] and N. Krebs[5]**

An alternating current (AC) gliding arc can be conveniently operated at atmospheric pressure and efficiently elongated into the ambient air by an air flow and thus is useful for surface modification. A high speed camera was used to capture dynamics of the AC gliding arc in the presence of polymer surfaces. A gap was observed between the polymer surface and the luminous region of the plasma column, indicating the existence of a gas boundary layer. The thickness of the gas boundary layer is smaller at higher gas flow-rates or with ultrasonic irradiation to the AC gliding arc and the polymer surface. Water contact angle measurements indicate that the treatment uniformity improves significantly when the AC gliding arc is tilted to the polymer surface. Thickness reduction of the gas boundary layer, explaining the improvement of surface treatment, by the ultrasonic irradiation was directly observed for the first time.

**Keywords:** Plasma treatment, Gliding arc, Gas boundary layer, Polyester, Ultrasound, Planar laser induced fluorescence

## Introduction

Non-thermal plasma processing at atmospheric pressure is widely used for surface modification.[1,2] Its applications include surface cleaning,[3] decontamination and sterilization,[4,5] deposition of functional coatings[6] and improvement of adhesion, wetting and paintability.[7–11]

One of the challenges in non-thermal plasma processing at atmospheric pressure is to achieve high reactivity and high productivity simultaneously.[12] Here, high reactivity is ensured by a high electron temperature in a non-equilibrium plasma so as to change chemical bonding of molecules in the plasma or the plasma treated surfaces. Meanwhile, high productivity can be demonstrated using high energy densities. However, most plasmas can hardly sustain a non-equilibrium state at high energy densities. Two possible approaches are proposed to overcome this issue: (1) development of a hybrid plasma with a high energy density in a non-equilibrium state and (2) plasma processing assisted by an external energy input.

A gliding arc is one of the hybrid plasmas,[13] generated between diverging electrodes as a low impedance thermal arc discharge, extended by a gas flow and quenched to non-thermal condition.[14] It can be operated in atmospheric pressure air and thus advantageously used for large-scale processing.[15–20] An alternating current (AC) gliding arc has a long lifetime extending over hundreds of AC periods without extinction. The plasma column can be elongated to approximately 20–30 cm.[16–20] The AC gliding arc is useful for adhesion improvement of glass fibre reinforced polyesters (GFRPs),[16,17] efficiently oxidising GFRP surfaces when the distance between the edge of the electrodes and the GFRP surface is up to 6 cm in open air. It is also demonstrated that optical techniques are promising for non-intrusive diagnostics of the AC gliding arc.[18,19] In particular, the dynamics of the gliding arc is observed by using a high speed camera. However, high speed observations of the AC gliding arc in the presence of a surface have not been intensively studied.

The efficiency of plasma processing can be improved by simultaneous high power ultrasonic irradiation to the plasma and material surfaces.[21–27] It is reported that high power ultrasonic irradiation during the gliding arc surface treatment enhances oxidation of GFRP surfaces. It has been proposed that a gas boundary layer sticking at a material surface reduces its thickness when the surface is irradiated with acoustic waves. Thus, the turbulent fluxes of the reactive species towards the surface increase and the surface modification is enhanced. However, this reduction of the boundary layer thickness in plasma processing was never visually demonstrated.

In the present work, the AC gliding arc is generated for surface treatment of GFRP plates. The performance of the AC gliding arc directing is captured by a high speed camera and OH planar laser induced fluorescence (OH-PLIF), while the surface modification effect is monitored by static water contact angle measurements and X-ray photoelectron spectroscopy (XPS). The effects of gas flow-rates, a tilted gliding arc and ultrasonic irradiation to the AC gliding arc are investigated.

## Experimental methods

The AC gliding arc was generated between two diverging tubular electrodes. The outer diameter of the

[1]Department of Wind Energy, Section for Composites and Materials Mechanics, Technical University of Denmark, Risø Campus, Frederiksborgvej 399, DK-4000 Roskilde, Denmark
[2]Division of Combustion Physics, Lund University, PO Box 118, S-221 00 Lund, Sweden
[3]Department of Physics, Section for Plasma Physics and Fusion Energy, Technical University of Denmark, DK-2800 Kgs. Lyngby, Denmark
[4]Danish Technological Institute, Gregersensvej 3, DK-2630 Taastrup, Denmark
[5]FORCE Technology, DK-2800 Brøndby, Denmark

*Corresponding author, email yuki@dtu.dk


Published by Maney on behalf of the Institute
Received 24 September 2014; accepted 23 November 2014
DOI 10.1179/1743294414Y.0000000429

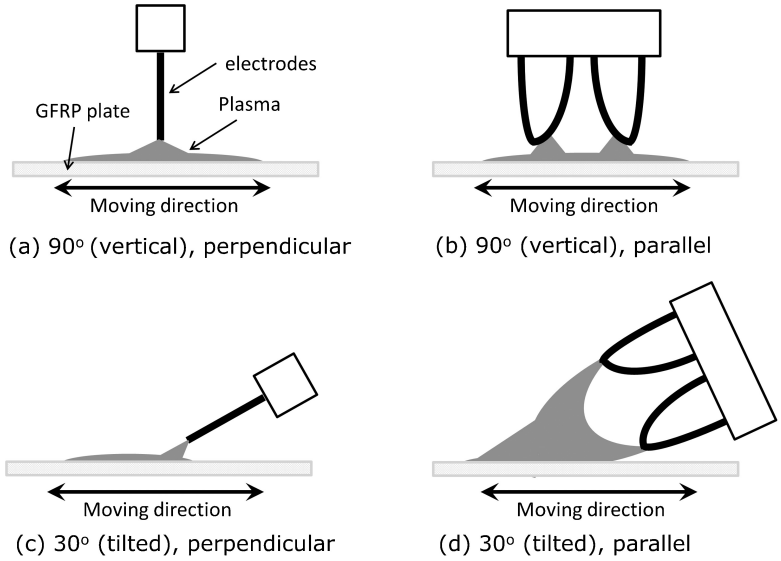


**1 Experimental arrangements of specimen and AC gliding arc: angle between the gas flow direction and specimen surface is either 90° (vertical: *a*, *b*) or 30° (tilted: *c*, *d*); arrangement between the moving direction of specimen and the line formed by the specimen surface and the plane containing electrodes is either perpendicular (*a*, *c*) or parallel (*b*, *d*)**

tubular electrodes is 3 mm. Cooling water was fed through the electrodes during operation.[16–20] An air flow was fed between the electrodes with flow-rates of 14·0, 17·5, 21·0, 31·5 or 42·0 standard liters per minutes (SLM). The AC gliding arc was driven by an AC power supply at a frequency of 31·25 kHz (Generator 6030; SOFTAL Electronic GmbH). Two millimeter thick GFRP plates were used as specimens (G-Etronax PM; Elektro-Isola). They were cleaned and degreased with acetone and methanol before the plasma treatment.

In order to treat a GFRP plate surface without excess thermal damage from the AC gliding arc, a poly(methylmethacrylate) holder was moved forward and backward at a speed of 180 mm $s^{-1}$ on which the GFRP plate was fixed. The angle between the gas flow direction and the specimen surface is approximately 30° (also referred to as "tilted") or 90° (also referred to as "vertical"). A line formed by the specimen surface and a plane containing the electrodes is perpendicular to the moving direction of the specimen, unless mentioned otherwise. Experimental arrangements of the specimen and the gliding arc are schematically illustrated in Fig. 1.

For the investigation of the effect of the ultrasonic irradiation, the angle between the gas flow direction and the specimen surface was fixed at approximately 30° and the acoustic waves were introduced vertically to the specimen surfaces through a cylindrical waveguide using a high power gas jet ultrasonic generator (SonoSteam; FORCE Technology). The acoustic frequency range is between 20 and 40 kHz, and a sound pressure level is approximately 150 dB.[21–27] A high-speed camera (Phantom v7·1) was used to capture the behaviour of the AC gliding arc during surface treatment. The high speed camera was operated at 20 kHz with exposure time of 30 μs and resolution of 256 × 256 pixels in the measurements.

PLIF is a powerful method for specific species detection and is widely used in the investigation of combustion[28] and plasma.[29] In order to visualize the spatial distributions of the reactive species generated by the AC gliding arc, OH-PLIF was performed in different directions. A Nd:YAG (Brilliant b) pumped dye laser (Continuum ND60) was tuned to 283·268 nm to achieve excitation of OH $X^2\Pi$–$A^2\Sigma^+$ (0,1). The resulting fluorescence at around 308 nm was collected by an ICCD camera (Princeton PI-MAX II) with an exposure time of 30 ns. Filters (UG5 + WG295) were added in front of the camera to reduce the laser scattering.

The static contact angles for deionized water on the GFRP surfaces were measured in air at room temperature using a contact angle measurement system (CAM100; Crelab Instruments AB).

XPS data were collected using a microfocused, monochromatic Al $K_\alpha$ X-ray source with a lateral resolution of 30 μm (K-alpha; ThermoFischer Scientific, UK) to study the changes of the elemental composition at the GFRP surfaces. Atomic concentrations of each element were calculated by determining the relevant integral peak intensities subtracting a linear background, and the O/C ratio was obtained.

## Results and discussion

### Effects of flow-rate and distance to surface

The angle between the gas flow direction and the GFRP surface is fixed at approximately 90° and the distance from the head of the electrodes to the specimen surface is 15 mm during the treatment. Averages of 10 000 images taken by the high speed camera and the temporal photoemission intensity from the projected squared area (0·5 mm high and 10 mm wide) near the specimen surface are shown in Fig. 2. The photos of the AC

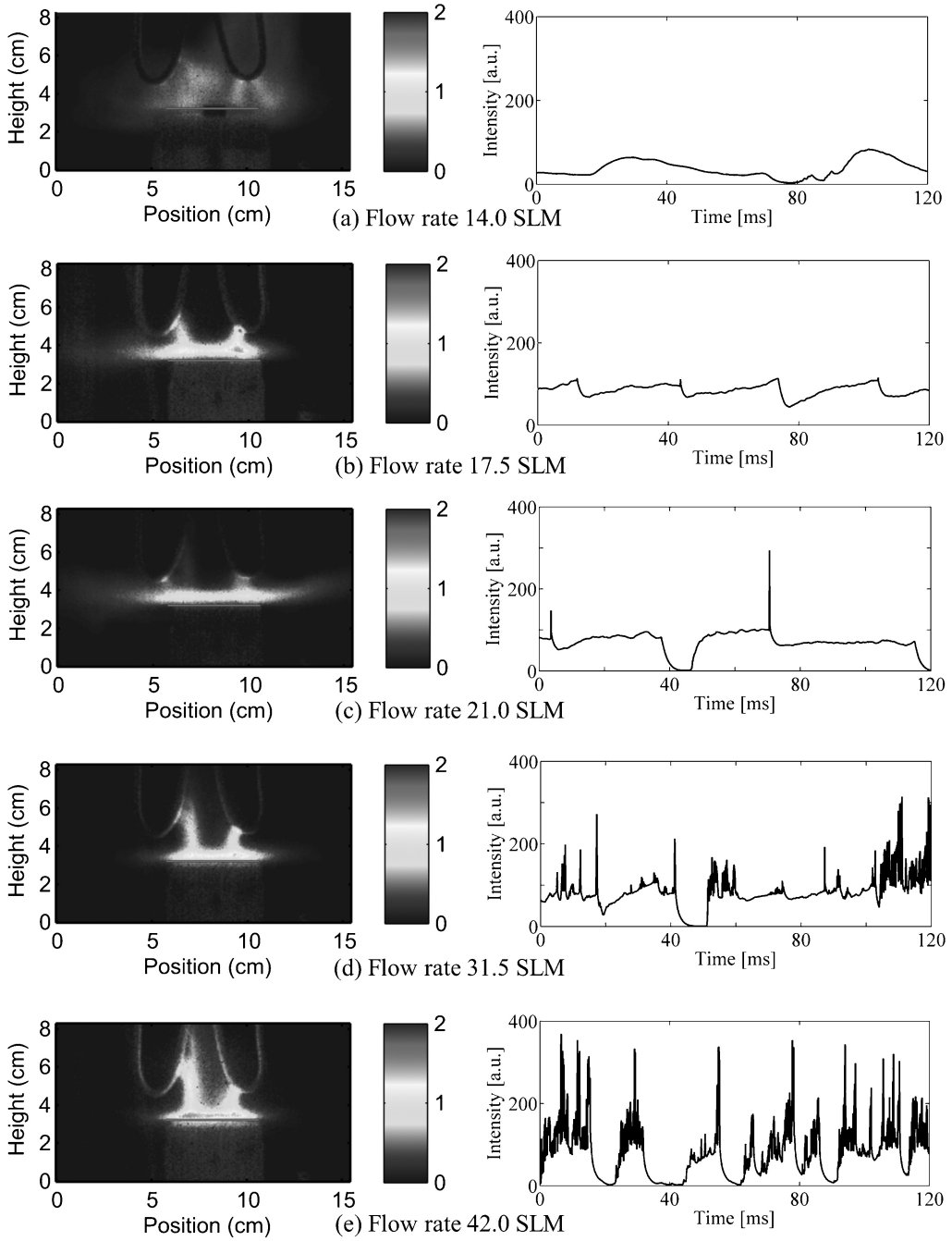


**2 Average of 10 000 images (left panels) and temporal photoemission intensity near the specimen surface (right panels) of the AC gliding arc at different flow-rates: *a* 14·0; *b* 17·5; *c* 21·0; *d* 31·5; *e* 42·0 SLM**

gliding arc in Fig. 2 indicate that a gap exists between the GFRP surface and a luminous region where the AC gliding arc is likely present. Here, the gap is different from a plasma sheath in that the AC gliding arc can be sustained regardless of the existence of the GFRP surface. Instead, the observed gap represents a gas boundary layer which is always formed close to the surface due to viscosity. The discharge tends to

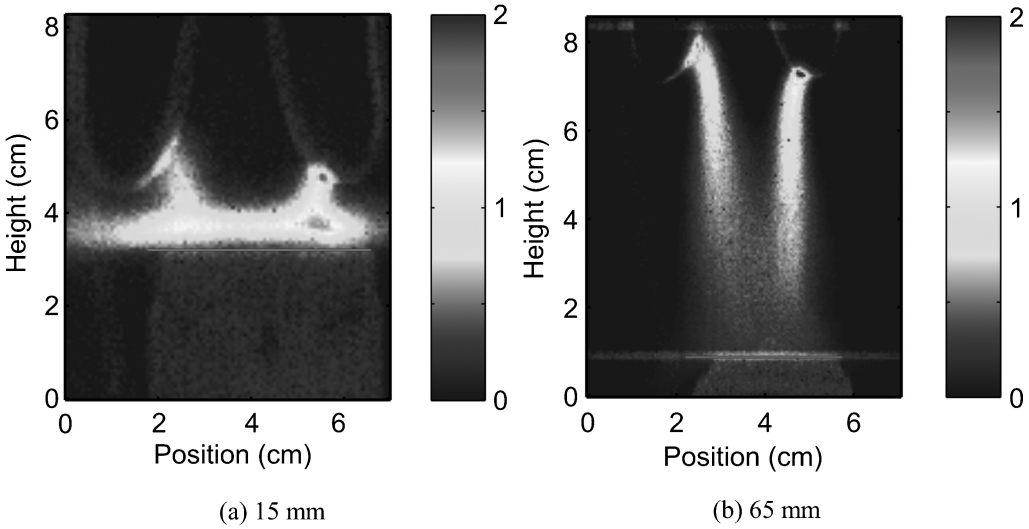


**3 Average of 10 000 images of AC gliding arc: distances of edge of the electrodes to the specimen surface are *a* 15 mm and *b* 65 mm**

approach the specimen surface at higher flow-rates. The time distribution of the photoemission in the region just above the surface in Fig. 2 shows that the overall photoemission intensity tends to increase as the gas flow-rate increases. The tendency of the photoemission of the AC gliding arc at different flow-rates is similar to the observation without a surface.[17]

The increasing overall photoemission at higher flow-rates results from more frequent conversions from glow type gliding discharge to spark type.[19] It is therefore indicated that the gas boundary layer can be detected by the high speed camera, and that the thickness of the gas boundary layer decreases at higher flow-rates. The result would suggest that at higher gas flow-rates, surface treatment effects would be improved due to a thinner gas boundary layer between the plasma and the surface. However, it is found in Fig. 2 that the photoemission intensity fluctuates more at higher flow-rates, affecting the treatment uniformity. Moreover, it is reported that as the gas flow-rate increases, the concentration of hydroxyl radical decreases, which is thought to be among the most important oxidative agents for plasma treatment,[19] and that the wettability of the treated GFRP surfaces decreases due to the excess quenching of the plasma.[16] In fact, when the flow-rate is higher than an optimal flow-rate, the photoemission intensity frequently goes down to zero, corresponding to a frequent extinction of the AC gliding arc by quenching. It is therefore expected that there is an optimum gas flow-rate for the gliding arc surface modification. Utilizing the same set-up and conditions, the optimum gas flow-rate of 17·5 SLM is reported in terms of the wettability as shown in Table 1, which agrees well with the previous work since the gas boundary layer at 17·5 SLM is modest and the intensity fluctuation is relatively small.

**Table 1 Water contact angles of GFRP plates after gliding arc treatment at different flow-rates: result is based on Ref. 17 (© IOP Publishing. Reproduced by permission of IOP Publishing. All rights reserved.)**

| Flow-rate/SLM | Water contact angle/° |
|---|---|
| 14·0 | 46·4 ± 10·2 |
| 17·5 | 25·7 ± 7·2 |
| 21·0 | 38·6 ± 11·1 |
| 31·5 | 43·9 ± 13·4 |
| 42·0 | 62·6 ± 12·6 |

Figure 3 shows averaged images of the AC gliding arc when the distances between the specimen surface and the edges of the electrodes are 15 and 65 mm. The photoemission intensity drops down when the distance increases. Similar results were reported in that at higher flow-rates, the wettability and the degree of oxidation[16,17] at the GFRP surface decrease and that the photoemission intensity decreases. The oxygen/carbon (O/C) ratio measured by XPS and the water contact angle of the GFRP plates after the gliding arc treatment are summarized in Table 2. The result indicates that the GFRP surface can be efficiently oxidized when the distance between the specimen surface and the edges of the electrodes is up to approximately 6 cm, and that the oxidation effect significantly decreases when it is larger than approximately 6 cm. More detailed surface characterization and dedicated adhesion tests after the treatment are reported by Kusano *et al.*[15–17]

## Tilted gliding arc

When a gliding arc is used for surface treatment, the gas flow direction is usually perpendicular to the surfaces due to a short extension of the general gliding arc reported in a literature.[30,31] That is, the gliding arc is usually directed perpendicular to the surface to be treated. However, even when the angle between the gas flow direction and the specimen surface is not perpendicular, the AC gliding arc in the present work can extend long enough (up to 20–30 cm at 17·5 SLM) to approach the surface. The static water contact angles were measured at four different conditions at the fixed distance of 15 mm between the edges of the electrodes

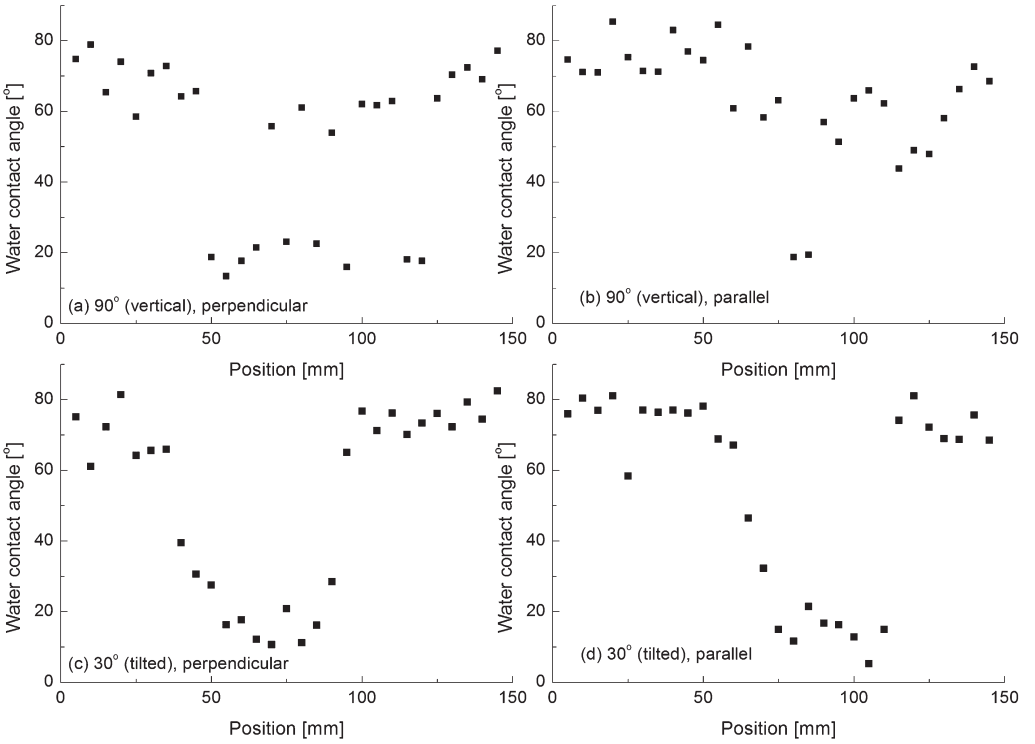


**4 Water contact angles of GFRP surfaces after AC gliding arc treatment: *see* Fig. 1 for conditions**

and the specimen surface. The gas flow-rate was 17·5 SLM. The power to the discharge was approximately 800 W. Each specimen surface was exposed to the discharge twice. The angle between the gas flow direction and the specimen surface was either 30° (tilted as shown in Fig. 1*c* and *d*) or 90° (vertical as shown in Fig. 1*a* and *b*). The arrangement between the moving direction of the specimen and the line formed by the specimen surface and the plane containing the two electrodes was either perpendicular or parallel. The results are shown in Fig. 4.

When the angle between the gas flow direction and the specimen surface is 90° (vertical), measured contact angles were scattered, indicating a poor treatment uniformity by the gliding arc. On the other hand, when the tilting angle was 30° (tilted), approximately 4 cm width was relatively uniformly and well treated, and thus, the tilting appears useful for improving the treatment uniformity. One possible explanation of the improvement is less fluctuation of the discharge column due to less streamline curvature and less shear in the tilted case. Furthermore, even when the arrangement between the moving direction of the specimen and the line formed by the specimen surface and the plane containing the two electrodes is parallel (Fig. 1*d*), the surface was uniformly treated within a certain region as shown in Fig. 4*d*. It is therefore indicated that the discharge column can dynamically fluctuate in a direction perpendicular to the plane containing the electrodes.

**Table 2 O/C ratios and water contact angles of GFRP plates after gliding arc treatment at different distances: result is based on Ref. 17 (© IOP Publishing. Reproduced by permission of IOP Publishing. All rights reserved.)**

| Distance/cm | O/C ratio | Water contact angle/° |
|---|---|---|
| 1·5 | 0·37±0·02 | 25·7±7·2 |
| 3·5 | 0·28±0·02 | 19·1±6·3 |
| 5·5 | 0·27±0·02 | 17·9±2·7 |
| 6·5 | 0·29±0·02 | 43·6±25·0 |
| 7·5 | 0·21±0·02 | 86·3±2·9 |

The OH-PLIF images of the AC gliding arc without the GFRP plates were collected to investigate the distribution of ground state OH radicals generated by the plasma. As shown in Fig. 5*a*, the asymmetric OH-PLIF image parallel to the plane containing the electrodes indicates that the plasma is partly out of plane of the laser sheet and is three-dimensionally distributed. It is confirmed in Fig. 5*b* that the plasma is also distributed perpendicular to the plane containing the electrodes. The observation in Fig. 5 shows good agreement with the result that the GFRP surface was uniformly treated even when the arrangement between the specimen moving direction and the line formed by the specimen surface and the plane containing the electrodes is parallel as shown in Fig. 4*d*. The relevant dynamics of the gliding arc discharge column is studied elsewhere.[19]

## Effect of ultrasonic irradiation

The advantage of tilting the AC gliding arc is not only the uniform treatment, but also easy introduction of

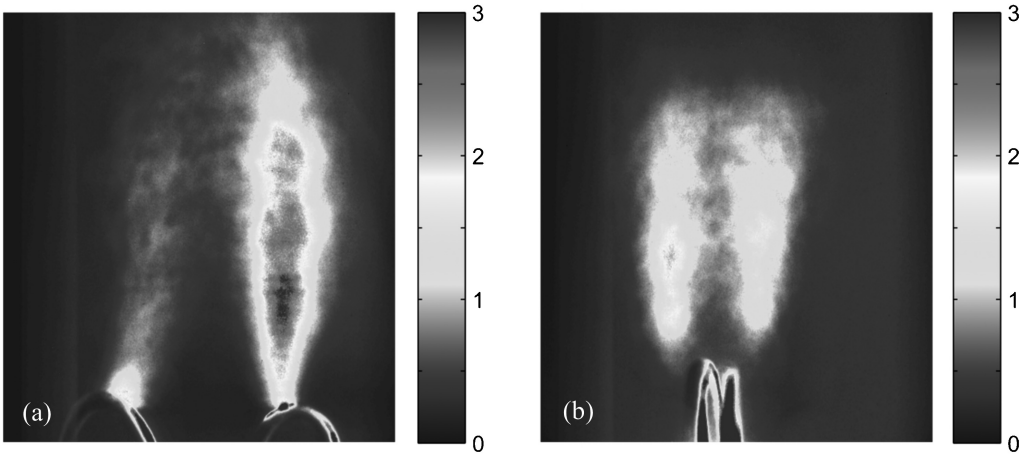


**5 Average of 500 OH-PLIF images of the AC gliding arc taken by the ICCD camera *a* facing and *b* perpendicular to plane containing electrodes: the laser sheet was located at plane parallel to OH image**

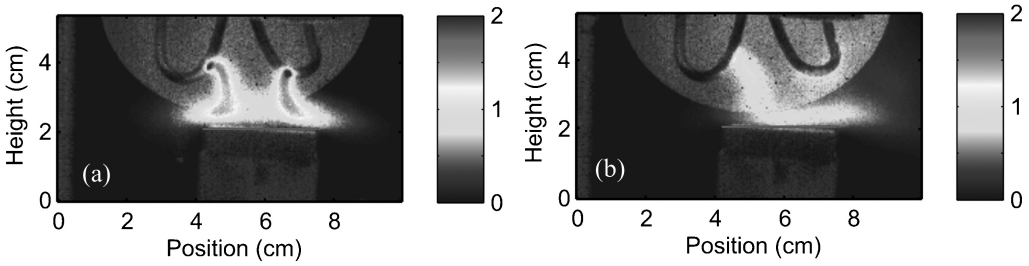


**6 Average of 10 000 images of the tilted gliding arc at gas flow-rate of 17·5 SLM *b* with and *a* without ultrasonic irradiation**

ultrasonic irradiation. It is reported that the treatment effects of the AC gliding arc are enhanced by the ultrasonic irradiation.[25] In the present work, high speed images were taken with and without ultrasonic irradiation. The gas flow-rate was 17·5 SLM, and the power to the gliding arc was approximately 800 W. A distance between the edges of the electrodes and the specimen surfaces was 15 mm. Without ultrasonic irradiation, a gap of a few millimeters was observed without strong photoemission between the surface and the photo emitting part as shown in Fig. 6*a*. However, with ultrasonic irradiation, the gap significantly reduced at the same flow-rate. This is the first direct observation of the thickness reduction of the gas layer attaching at the surface in plasma surface processing due to ultrasonic irradiation. The result corresponds to the improved plasma treatment effects by the ultrasonic irradiation[21–27] in which detailed surface characterizations are reported. More specifically, the surface density of the carboxyl group seems to increase with ultrasonic irradiation.[25] It is also noted that the ultrasonic irradiation induced observed spatial fluctuation and more frequent shortcutting events than the AC gliding arc without ultrasonic irradiation, and that the subsequent averaged image in Fig. 6*b* looks as if the discharge column would be discontinued.

## Conclusion

The performance of the AC gliding arc surface treatment was investigated using a high speed camera. The photographs revealed that the thickness of the gas boundary layer tended to decrease as the flow-rate increased so that the plasma column was observed closer to the surface on average. On the other hand, the photoemission intensity of the plasma fluctuated more and affected the treatment uniformity. The results indicate the existence of an optimum gas flow-rate for the surface treatment. The long extension of the discharge enables demonstration of plasma surface treatment with the tilted gliding arc. It is shown that the tilting improved uniformity of the treatment. For example, when the tilting angle was 30°, approximately 4 cm width of the specimen surface was relatively uniformly treated. Ultrasonic irradiation to the gliding arc also reduced the thickness of the gas boundary layer, indicating improvement of surface treatment effect. The effect of the thickness reduction by the ultrasonic irradiation, which has previously been predicted, was directly observed for the first time. It is concluded that direct observation of the AC gliding arc helps understanding of dynamics of plasma surface processing.

## Acknowledgements

The work had a partial financial support from the Swedish Energy Agency, Swedish Research Council (VR) and Knut & Alice Wallenberg Foundation. J.J. Zhu would like to thank China Scholarship Council for financial support.

## References

1. M. Kogoma, M. Kusano and Y. Kusano (eds.): 'Generation and applications of atmospheric pressure plasmas'; 2011, New York, NOVA Science Publishers, Inc.
2. U. Kogelschatz: 'Dielectric-barrier discharges: their history, discharge physics, and industrial applications', *Plasma Chem. Plasma Process.*, 2003, **23**, (1), 1–46.
3. C. H. Yi, Y. H. Lee and G. Y. Yeom: 'The study of atmospheric pressure plasma for surface cleaning', *Surf. Coat. Technol.*, 2003, **171**, 237–240.
4. F. Leipold, Y. Kusano, F. Hansen and T. Jacobsen: 'Decontamination of a rotating cutting tool during operation by means of atmospheric pressure plasmas,' *Food Control*, 2010, **21**, (8), 1194–1198.
5. F. Leipold, N. Schultz-Jensen, Y. Kusano, H. Bindslev and T. Jacobsen: 'Decontamination of objects in a sealed container by means of atmospheric pressure plasmas', *Food Control*, 2011, **22**, (8), 1296–1301.
6. C. E. Nwankire, G. Favaro, Q.-H. Duong and D. P. Dowling: 'Enhancing the mechanical properties of superhydrophobic atmospheric pressure plasma deposited siloxane coatings', *Plasma Process. Polym.*, 2011, **8**, 305–315.
7. M. Strobel, C. S. Lyons and K. L. Mittal (eds.): 'Plasma surface modification of polymers: relevance to adhesion'; 1994, Utrecht, VSP.
8. Y. Kusano, T. L. Andersen and P. K. Michelsen: 'Atmospheric pressure plasma surface modification of carbon fibres', *J. Phys. Conf. Ser.*, 2008, **100**, 012002.
9. Y. Kusano, S. Teodoru and C. M. Hansen: 'The physical and chemical properties of plasma treated ultra-high-molecular-weight polyethylene fibers', *Surf. Coat. Technol.*, 2011, **205**, 2793–2798.
10. S. V. Singh, Y. Kusano, P. Morgen and P. K. Michelsen: 'Surface charging, discharging and chemical modification at a sliding contact', *J. Appl. Phys.*, 2012, **111**, 083501.
11. Y. Kusano: 'Atmospheric pressure plasma processing for polymer adhesion: a review', *J. Adhes.*, 2014, **90**, (9), 755–777.
12. Y. Kusano: 'Plasma surface modification at atmospheric pressure', *Surf. Eng.* 2009, **25**, (6), 415–416.
13. A. Fridman, S. Nester, L. A. Kennedy, A. Saveliev and O. Mutaf-Yardimci: 'Gliding arc gas discharge', *Prog. Energy Combust. Sci.*, 1999, **25**, 211–231.
14. A. Czernichowski: 'Gliding arc. Applications to engineering and environment control', *Pure Appl. Chem.*, 1994, **66**, (6), 1301–1310.
15. Y. Kusano, S. Teodoru, F. Leipold, T. L. Andersen, B. F. Sørensen, N. Rozlosnik and P. K. Michelsen: 'Gliding arc discharge – application for adhesion improvement of fibre reinforced polyester composites', *Surf. Coat. Technol.*, 2008, **202**, 5579–5582.
16. Y. Kusano, B. F. Sørensen, T. L. Andersen and F. Leipold: 'Adhesion improvement of glass-fibre-reinforced polyester composites by gliding arc discharge treatment', *J. Adhes.*, 2013, **89**, (6), 433–459.
17. Y. Kusano, B. F. Sørensen, T. L. Andersen, H. L. Toftegaard, F. Leipold, M. Salewski, Z. W. Sun, J. J. Zhu, Z. S. Li and M. Aldén: 'Water-cooled non-thermal gliding arc for adhesion improvement of glass-fibre-reinforced polyester', *J. Phys. D: Appl. Phys.*, 2013, **46**, (13), 135203 DOI: 10.1088/0022-3727/46/13/13520328/2.
18. Z. W. Sun, J. J. Zhu, Z. S. Li, M. Aldén, F. Leipold, M. Salewski and Y. Kusano: 'Optical diagnostics of a gliding arc', *Opt. Express*, 2013, **21**, (5), 6028–6044 DOI: 10.1088/0022-3727/46/13/13520328/2.
19. J. J. Zhu, Z. W. Sun, Z. S. Li, A. Ehn, M, Aldén, M. Salewski, F. Leipold and Y. Kusano: 'Dynamics, OH distributions and UV emission of a gliding arc at various flow-rates investigated by optical measurements', *J. Phys. D: Appl. Phys.*, 2014, **47**, 295203.
20. Y. Kusano, M. Salewski, F. Leipold, J. J. Zhu, A. Ehn, Z. S. Li and M. Aldén: 'Stability of alternating current gliding arcs', *Eur. Phys. J. D*, 2014, **68**, 319.
21. Y. Kusano, T. L. Andersen, H. L. Toftegaard, F. Leipold, A. Bardenshtein and N. Krebs: 'Plasma treatment of carbon fibres and glass-fibre-reinforced polyesters at atmospheric pressure for adhesion improvement', *Int. J. Mater. Eng. Innov.*, 2014, **5**, (2), 122–137.
22. Y. Kusano, K. Norrman, S. V. Singh, F. Leipold, P. Morgen, A. Bardenshtein and N. Krebs: 'Ultrasound enhanced 50 Hz plasma treatment of glass-fiber-reinforced polyester at atmospheric pressure', *J. Adhes. Sci. Technol.*, 2013, **27**, (7), 825–833.
23. Y. Kusano, S. V. Singh, K. Norrman, J. Drews, F. Leipold, N. Rozlosnik, A. Bardenshtein and N. Krebs: 'Ultrasound enhanced plasma surface modification at atmospheric pressure', *Surf. Eng.* 2012, **28**, (6), 453–457.
24. J. Drews, Y. Kusano, F. Leipold, A. Bardenshtein and N. Krebs: 'Ozone production in a dielectric barrier discharge with ultrasonic irradiation', *Ozone: Sci. Eng.*, 2011, **33**, (6), 483–488.
25. Y. Kusano, S. V. Singh, K. Norrman, F. Leipold, J. Drews, P. Morgen, A. Bardenshtein and N. Krebs: 'Ultrasound enhanced plasma treatment of glass-fibre-reinforced polyester in atmospheric pressure air for adhesion improvement', *J. Adhes.*, 2011, **87**, 720–731.
26. Y. Kusano, K. Norrman, J. Drews, P. Morgen, F. Leipold, S. V. Singh, A. Bardenshtein and N. Krebs: 'Gliding arc surface treatment of glass-fiber-reinforced polyester enhanced by ultrasonic irradiation', *Surf. Coat. Technol.*, 2011, **205**, S490–S494.
27. Y. Kusano, S. V. Singh, A. Bardenshtein, N. Krebs and N. Rozlosnik: 'Plasma surface modification of glass-fibre-reinforced polyester enhanced by ultrasonic irradiation', *J. Adhes. Sci. Technol.*, 2010, **24**, 1831–1839.
28. M. Aldén, J. Bood, Z. Li and M. Richter: 'Visualization and understanding of combustion processes using spatially and temporally resolved laser diagnostic techniques', *Proc. Combust. Inst.*, 2011, **33**, 69–97.
29. R. Ono and T. Oda: 'OH radical measurement in a pulsed arc discharge plasma observed by a LIF method', *IEEE Trans. Ind. Appl.*, 2001, **37**, (3), 709–714.
30. J. Janča and A. Czernichowski: 'Wool treatment in the gas flow from gliding discharge plasma at atmospheric pressure', *Surf. Coat. Technol.*, 1998, **98**, 1112–1115.
31. J. Toshifuji, T. Katsumata, H. Takikawa, T. Sakakibara and I. Shimizu: 'Cold arc-plasma jet under atmospheric pressure for surface modification', *Surf. Coat. Technol.*, 2003, **171**, 302–306.